19th INTERNATIONAL CONFERENCE ON EXPERIMENTAL MECHANICS

ICEM·2022
17-21.07.2022 Kraków
POLAND

INTERNATIONAL CONFERENCE ON EXPERIMENTAL MECHANICS
19th INTERNATIONAL CONFERENCE ON EXPERIMENTAL MECHANICS

PROCEEDINGS

KRAKÓW, POLAND

17–21 July, 2022

X27 500μm   17 61 SEI

Edited by:
Zbigniew L. Kowalewski
Mateusz Kopec
Dariusz Rudnik
Jacek Widłaszewski

www.icem19.org

19th INTERNATIONAL CONFERENCE ON EXPERIMENTAL MECHANICS

PROCEEDINGS

Acknowledgement

19th INTERNATIONAL CONFERENCE ON EXPERIMENTAL MECHANICS

PROCEEDINGS

Edited by:

Zbigniew L. Kowalewski
Mateusz Kopec
Dariusz Rudnik
Jacek Widłaszewski

The selection and presentation of materiał and the opinion expressed
in this publication are the sole responsibility of the authors concerned.
No responsibility is assumed by the Publishers for any injury and/or
damage to persons or property as a matter of products liability,
negligence or otherwise, or from any use or operation of any method,
products, instructions or ideas contained in the materiał herein.

Typesetting and cover design: Dariusz Rudnik

PREFACE

There is a long tradition to organize International Conference on Experimental Mechanics (ICEM) in different locations in Europe to cover all areas of active experimental research in mechanics of materials and structures including interactive fields.

Conferences of the ICEM series have been initiated in 1959 in Delft, and further successfully continued in 1962 Paris, 1966 Berlin, 1970 Cambridge, 1974 Udine, 1978 Munich, 1982 Haifa, 1986 Amsterdam, 1990 Copenhagen, 1994 Lisbon, 1998 Oxford, 2004 Bari, 2007 Aleksandropoulis, 2010 Poiters, 2012 Porto, 2014 Cambridge, 2016 Rhodes and 2018 Brussels. The Conferences are organized under the auspices of the European Society for Experimental Mechanics (EuraSEM).

The ICEM events bring together internationally recognized experts and young researchers in an effort to exchange ideas on different topics having the common link „Experimental Mechanics". The conferences serve also a platform for establishing connections between different research teams and development of future scientific collaboration.

Based on the papers included in the Book of Abstracts one can conclude, that the engineering community is constantly moving towards a more globalized and digitalized world in which, thanks to the increased computational resources, problems of high complexity can be analyzed. Nevertheless, the relevance of Experimental Mechanics remains indisputable. Experimental Mechanics with the increased interest in reliable design, durability analysis, lifetime prediction, etc. unquestionably stays the ultimate source of information on the real behaviour of materials and structures. At the macro-, micro- and nano-scale, the broad discipline of Experimental Mechanics provides more and more advanced techniques to study the influence of defects such as inclusions, cracks, voids and/or inherent manufacturing defects on the nucleation and growth of failure mechanisms. Recent advances in scanning probe microscopy techniques, transmission electron microscopy or diffraction techniques greatly increased the fundamental understanding of the material response and failure processes which occur under different complex loading conditions. Additionally, they proved to be useful for the development of mathematical models that describe the material behaviour. At the meso-level the current trend shows increased use of full-field optical techniques for the monitoring of surface displacements and strains while embedded sensing systems like MEMS, optical fibers, piezoelectric sensors/actuators, etc. are extensively investigated for measurements inside the material. At the macro- or structural scale, the structural health monitoring techniques, including waves and vibrations, seem to be beneficial for proactive maintenance planning and for prolonging the safe service life.

Besides of the basic problems usually studied in the framework of Experimental Mechanics, the conference covers experimental, theoretical and numerical aspects of the mechanical behaviour of solids at high strain rates. The lack of knowledge on the behaviour and performance of structures/components against hazardous dynamic loads of human or nature origin, may result in catastrophic consequences for human life and structural systems. The experience and knowledge from extensive research, experimental testing and advanced computational techniques can provide feasible solutions to diminish these catastrophic effects. Therefore, the present 19th ICEM conference is focused not only on fundamental topics of Experimental Mechanics, but also aims to provide a forum for participants from around the world to show, review and discuss the latest developments in protection of materials and structures subject to hazardous loads.

This volume of the 19th ICEM Book of Abstracts contains 161 extended abstracts of papers out of 335 papers that were accepted for presentation. Due to the pandemic of COVID19 and the war in Ukraine as much as 174 presentations unfortunately were canceled. Despite all these extraordinary obstacles and difficulties, the conference has been prepared thank to the great effort of the Organizing

Committee members, as well as the support of public institutions and sponsoring companies. The program of the conference includes 8 Plenary Lectures, 14 Keynote Lectures and 139 contributed presentations.

International Conferences on Experimental Mechanics have maintained throughout the last 63 years a high scientific standards and served as a forum for the exchange of new ideas and research information. A considerable number of participants from different countries delivered here a fascinating lectures not a single time and certainly remember the period when they came for the first time as young, beginning researchers, while now they are presenting general or keynote lectures as eminent scientists. It is my great satisfaction to see again old friends with whom we shared our ideas and enthusiasm for Experimental Mechanics. It is also a great pleasure to meet here the young generation of researchers working in emerging fields and contributing new important results.

Besides the scientific program, the 19th ICEM participants will have an opportunity to explore and discover the city of Kraków, the former capital of Poland. Kraków is one of the most beautiful Polish cities with a tradition dating back over 1000 years. Everyone who was at least once in this city will not forget the impression left by the local atmosphere of the old castle walls, the Wawel Hill with the dragon's cave, stretching just above the lazily flowing Vistula River, a charming Sukiennice market with a beautiful St. Mary's Church and plenty of greenery. It is difficult to talk about the monuments of Kraków, because almost the whole city is one big monument, worth admiring during walks. Let me to acknowledge here, the great support of the Mayor of the City of Kraków Professor Jacek Majchrowski, in organizing the event.

I wish all participants a fruitful and enjoyable conference time in beautiful Kraków and look forward to the 19th ICEM, hoping that it will pave new ways for the development of Experimental Mechanics.

On behalf of the organizers, I would like to express our gratitude to the students and scientists who showed their interest and actively helped us in preparing the event.

Finally, it is a great pleasure to express my cordial thanks to all members of the Scientific Committee, to all members of the Local Organizing Committee, to all supporting institutions (all names enclosed separately), and to the Jordan Group – the official Conference Partner - for their help which cannot be overestimated.

Zbigniew L. Kowalewski

June, 2022

Chairman
of the 19th ICEM 2022

Kraków, Poland

CONFERENCE PLATINUM SPONSOR

CONFERENCE GOLD SPONSORS

CONFERENCE SILVER SPONSORS

PARTNERS

ORGANIZERS

EURASEM - European Society for Experimental Mechanics

Polish Society of Theoretical and Applied Mechanics

Institute of Fundamental Technological Research Polish Academy of Sciences (IPPT PAN)

ICEM 2022 ORGANIZING COMMITTEE

Zbigniew L. Kowalewski

Chairman of the 19th ICEM 2022

Elżbieta Pieczyska

Co-chairman of the 19th ICEM 2022

HONORARY PATRONAGE

Jacek MAJCHROWSKI

Mayor of the City of Kraków

CONFERENCE HONORARY COMMITTEE

Witold KOZŁOWSKI

Marshal of the Małopolska Region

Rector of the Cracow University of Technology

Rector of the University of Science and Technology

Rector of the Silesian University of Technology

Rector of the Warsaw University of Technology

President of the Polish Academy of Learning

Rector of the Poznan University of Technology

LOCAL ORGANIZING COMMITTEE

Professor Zbigniew Kowalewski
Chairman, IPPT PAN

Professor Elżbieta Pieczyska
Co-chairman, IPPT PAN

Professor Tadeusz Burczyński
Director of IPPT PAN

Professor Grzegorz Cieplok
AGH University of Science and Technology

Professor Jacek Janiszewski
Military University of Technology

Professor Jerzy Kaleta
Wroclaw University of Technology

Professor Małgorzata Kujawińska
Warsaw University of Technology

Professor Tomasz Krzyżyński
Koszalin University of Technology
President of the Polish Society of Theoretical and Applied Mechanics

Professor Włodzimierz Kurnik
Warsaw University of Technology
Vice-President of the Polish Society of Theoretical and Applied Mechanics

Professor Ryszard Pęcherski
IPPT PAN

Professor Paweł Pyrzanowski
Warsaw University of Technology

Professor Grzegorz Socha
Institute of Aviation

SECRETARIAT of the 19th ICEM

Mateusz Kopec	Tomasz Libura
Dariusz Rudnik	Tadeusz Szymczak
Aneta Ustrzycka	Jacek Widłaszewski

SCIENTIFIC ADVISORY BOARD

Ke, Changhong	*State University of New York, Binghamton, USA*
Kourkoulis, Stavros	*National Technical University of Athens, Greece*
Kowalewski, Zbigniew	*Polish Academy of Sciences, Poland*
Lacidogna, Giuseppe	*Politecnico di Torino, Italy*
Lacoviello, Francesco	*Università di Cassino e del Lazio Meridionale, Italy*
Lamberson, Leslie	*Drexel University, USA*
Langdon, Genevieve	*University of Cape Town, South Africa*
Lauro, Franck	*Université de Valenciennes, France*
Lavrov, Alexandre	*SINTEF Petroleum Research, Norway*
Lecompte, David	*Royal Military Academy, Belgium*
Li, Xide	*Tsinghua University, China*
Llorca, Javier	*Universidad Politécnica de Madrid, Spain*
Lu, Charles	*University of Kentucky, USA*
Mai, Yiu-Wing	*University of Sydney, Australia*
Mazeika, Liudas	*Kaunas University of Technology, Lithuania*
Mazza, Edoardo	*Eidgenössische Technische Hochschule Zürich, Switzerland*
Mileiko, Sergei T.	*Russian Academy of Sciences, Russia*
Mines, Robert	*University of Liverpool, United Kingdom*
Morimoto, Yoshiharu	*4D-sensors Inc., Japan*
Nie, Xu	*Southern Methodist University, USA*
Niezrecki, Christopher	*University of Massachusetts Lowell*
Okamoto, Satoru	*Shimane University, Japan*
Ostachowicz, Wieslaw	*Polish Academy of Sciences, Poland*
Osten, Wolfgang	*Universität Stuttgart, Germany*
Otani, Yukitoshi	*Utsunomiya University, Japan*
Özgüven, Nevzat	*Middle East Technical University, Turkey*
Pappalettere, Carmine	*Politicnico di Bari, Italy*
Pär, Jonsson	*Royal Institute of Technology, Sweden*
Parameswaran, Venkitanarayanan	*Indian Institute of Technology, India*
Passieux, Jean-Charles	*Institut Clement Ader, France*
Patterson, Eann	*University of Liverpool, United Kingdom*
Périé, Jean-Noël	*Institut Clément Ader/Université de Toulouse, France*
Pichler, Bernhard	*Vienna University of Technology, Austria*
Pieczyska, Elzbieta	*Polish Academy of Sciences, Poland*
Prakash, Vikas	*Case Western Reserve University, USA*
Qian, Kemao	*Nanyang Technlogical University, Singapore*
Qiu, Wei	*Tianjin University, China*
Ragulskis, Minvydas	*Kaunas University of Technology, Lithuania*
Rajapakse, Yapa	*Office of Naval Research, USA*
Ramesh, Kuruva	*Indian Institute of Technology Madras, India*
Ravi-Chandar, Krishnaswa	*University of Texas, USA*
Reu, Philip	*Sandia National Laboratory, USA*
Rittel, Daniel	*Israel Institute of Technology, Israel*
Rodriguez Perez, Jesus	*Universidad Rey Juan Carlos, Spain*
Rouillard, Vincent	*Victoria University, Australia*
Roux, Stéphane	*Université Paris Saclay, France*

Ruiz López, Gonzalo	*Universidad de Castilla-La Mancha, Spain*
Rusinek, Alexis	*Université de Lorraine, France*
Sakagami, Takahide	*Kobe University, Japan*
Shankar, Krishnakumar	*University of New South Wales, Australia*
Shilo, Doron	*Israel Institute of Technology, Israel*
Silva Gomes, Joaquim	*Universidade do Porto, Portugal*
Stockmann, Martin	*University of Technology Chemnitz, Germany*
Strantza, Maria	*Los Alamos National Laboratory, USA*
Su, Huaizhi	*Hohai University, China*
Takahashi, Hiroshi	*Tohoku University, Japan*
Tomlinson, Rachel	*The University of Sheffield, United Kingdom*
Toribio, Jesús	*Universidad de Salamanca, Spain*
Triantis, Dimos	*Technological Educational Institute of Athens, Greece*
Truman, Christopher	*University of Bristol, United Kingdom*
Tsouvalis, Nicholas	*National Technical University of Athens, Greece*
Van Hemelrijck, Danny	*Vrije Universiteit Brussel, Belgium*
Van Paepegem, Wim	*Universiteit Gent, Belgium*
Vassilopoulos, Anastasios	*Ecole Polytechnique Fédérale de Lausanne, Switzerland*
Vaz, Mario	*Universidade do Porto, Portugal*
Verleysen, Patricia	*Universiteit Gent, Belgium*
Voloshin, Arkady	*Lehigh University, USA*
Wang, Liliang	*Imperial College London, Kingdom*
Wang, Wei-Chung	*National Tsing Hua University, Taiwan*
Yoshida, Sanichiro	*Southeastern Louisiana University, USA*
Zhang, Qican	*Sichuan University, China*
Zhang, Xiaoxin	*Universidad de Castilla-La Mancha, Spain*
Zhao, Han	*University Pierre & Marie Curie, France*

PLENARY LECTURES

Abstract No.	Author	Title
PL1	*Professor* **George Z.Voyiadjis**	Gradient Enhanced Physically Based Plasticity: Size Effects and Shear
PL2	*Professor* **Jianguo Lin**	New Challenges on Developing Experimental Methods for Innovative Metal Forming Techniques
PL3	*Professor* **Paul Wood**	Selective Laser Melting of a High Precision Turbomachinery Application In IN718 Alloy
PL4	*Professor* **Małgorzata Kujawińska**	Full-Field Optical Methods In Experimental Mechanics: Past, Present And Future Challenges
PL5	*Professor* **Raj Das**	Virtual Forensic Laboratory - Developing Bio-Simulant Human Craniums for Extreme Injury Assessment
PL6	*Professor* **Błażej Skoczeń**	Plasticity, Damage and Fracture in the Proximity of Absolute Zero. From Experiment to Constitutive Models
PL7	*Professor* **Christian Hellmich**	Thermodynamics and Homogenisation Theory as Driving Forces in The Design of Novel Experiments and the (Re-)Evaluation of Data
PL8	*Professor* **Marek Stankiewicz**	Synchrotron SOLARIS - Applications for Experimental Mechanics

SYMPOSIUM

ID	Symposium	Organized by:
S1	Novel Applications of Experimental Mechanics	Wei-Chung WANG, *Taiwan*; Terry Yuan-Fang CHEN, *Taiwan*; Yu-Lung LO, *Taiwan*; Ming-Tzer LIN, *Taiwan*; Chi-Hung HWANG, *Taiwan*; Prof. Shyh-Tsong LIN, *Taiwan*

THEMATIC SESSIONS

ID	Thematic Sessions
TS1	Experimental Solid Mechanics
TS2	Experimental Fluid Mechanics
TS4	Computational Mechanics

SPECIAL SESSIONS

ID	Special Sessions	Organized by:
1	Additive Manufactured Materials: Production, Experiment and Applications	Dario CROCCOLO, *Italy*; Gorgio OLMI, *Italy*
2	Composites and Adhesives	Anastasios P. VASSILOPOULOS, *Switzerland*; Danny VAN HEMELRIJCK, *Belgium*
3	Dynamic Response of Materials and Structures	Bo SONG, *USA*; Vikas PRAKASH, *USA*
4	Innovative Testing Methods for Cementitious Materials and Structures	Bernhard PICHLER, *Austria*; Josef EBERHARDSTEINER, *Austria*; Mateusz WYRZYKOWSKI, *Switzerland*; Pietro LURA, *Switzerland*
5	Meso-Scale Mechanics: Between Micro- and Macro-	Sven BOSSUYT, *Finland*
6	Micro/Nano-Mechanical Testing of Materials	Xide LI, *China*
7	Non-Contact and Optical Dynamic Measurements	Christopher NIEZRECKI, *USA*
8	Recent Advances In Photoelastic Applications	Terry Yuan-Fang CHEN, *Taiwan*; Wei-Chung WANG, *Taiwan*; Ming-Jui HUANG, *Taiwan*; Po-Chi SUNG, *Taiwan*

ID	Special Sessions	Organized by:
9	Smart Materials and Structures	Hisaaki TOBUSHI, *Japan;* Qingping SUN, *China;* Ryosuke MATSUI, *Japan;* Kohei TAKEDA, *Japan;* Elżbieta A. PIECZYSKA, *Poland*
10	Structural Health Monitoring and Its Role in the Sustainability of the Built Environment	Dimitrios AGGELIS, *Belgium;* Tomoki SHIOTANI, *Japan;* Giuseppe LACIDOGNA, *Italy;* Danny VAN HEMELRIJCK, *Belgium*
11	Thermomechanical Behaviour of Metallic Alloys	Bonnie R. ANTOUN, *USA*

TABLE OF CONTENTS

THEMATIC SESSIONS 74

TS1. Experimental Solid Mechanics 74

4. Innovative Testing Methods for Cementitious Materials and Structures

5. Meso-Scale Mechanics: Between Micro- and Macro-

PLENARY LECTURES

GRADIENT ENHANCED PHYSICALLY BASED PLASTICITY: SIZE EFFECTS AND SHEAR

G.Z. Voyiadjis

Department of Civil and Environmental Engineering, Computational Solid Mechanics Laboratory, Louisiana State University, Baton Rouge, LA 70803, USA

Abstract

The objective of this work is to present a micromechanically based constitutive model for the modeling of heterogeneous media that assesses a strong coupling between (visco) plasticity and (visco) damage for high velocity impact related problems while considering the discontinuities on the macroscale level. The essential aspects of interest here can all be examined within the context of: (1) finite deformation kinematics; (2) rapid time variations in temperature, strain, strain rate, and other field variables; (3) equation of state; (4) thermal and damage softening; (5) strong viscoplasticity and viscodamage coupling; (6) long range microstructural interactions through the use of the nonlocal continua; and (7) numerical stability through the use of regularization approaches (i.e., using viscosity and gradient localization limiters).

1. Constitutive Model

The model is based on the nonlocal gradient plasticity and gradient damage theories. It includes the nonlocal von Mises yield criterion, the non-associated flow rules, isotropic and anisotropic strain hardening, strain rate hardening, softening due to adiabatic heating and anisotropic damage evolution, and finally a path dependent equation of state. The stress-strain rate relationship in the spatial and damaged configuration is given by

$$(1) \qquad \overset{\triangledown}{\tau} = \mathbb{Z} : \left(d - d^{vp} - d^{vd} \right) - A : \overset{\triangledown}{\phi} - \mathbb{Z} : \alpha_t \dot{T} \mathbf{1}$$

where $\mathbb{Z} = \widehat{M}^{-1} : \overline{\mathbb{Z}} : \widehat{M}^{-1}$ and $\widehat{M} = 2[(1 - \hat{\phi}) \otimes 1 + 1 \otimes (1 - \hat{\phi})]^{-1}$. The notation, $\triangledown$ indicates corotational objective derivative, τ is the Kirchhoff stress tensor, d is the total rate of deformation, $\boldsymbol{d^{vp}}$ is the viscoplastic rate of deformation, $\boldsymbol{d^{vd}}$ is the viscodamage rate of deformation, $\overline{\mathbb{Z}}$ and $\mathbb{Z}$ are the fourth-order undamaged and damaged elasticity tensors respectively, α_t is the thermal expansion coefficient, $\dot{T}$ is the rate of absolute temperature, and **I** is the second-order identity tensor.

The viscoplastic and viscodamage multipliers, $\dot{\lambda}^{vp}$ and $\dot{\lambda}^{vd}$, can be obtained in a nonlocal sense using the following generalized Kuhn-Tucker conditions for rate-dependent problems such that

$$(2) \qquad \dot{\lambda}^{vp} \geq 0, \quad f \leq 0 \Leftrightarrow \dot{\lambda}^{vp} f = 0 \quad and \quad \dot{\lambda}^{vd} \geq 0, \quad g \leq 0 \Leftrightarrow \dot{\lambda}^{vd} g = 0$$

The equation of state is a thermodynamic equation describing the state of matter under a given set of physical conditions. In this sense the thermodynamic pressure stress P for a shock compressed solid is given as follows:

$$(3) \qquad P = (1 - \gamma) c_v T^{ig} \varepsilon^e$$

where $T^{ig} = T_r \exp[(\eta - \eta_r)/c_v][1 + \varepsilon^e]^{(y-1)} exp[(\gamma - 1)(1/(1 + \varepsilon^e) - 1)]$

To establish the actual heat generation that occurs during the highly transient impact events of the thermo-mechanically coupled finite element, the development of a heat equation is imperative.

However, because the whole impact process lasts a few hundred of a μs, the effect of heat conduction is negligible over the domain of the specimen and therefore, an adiabatic condition is assumed such that the increase in temperature is calculated by the following heat equation:

$$(4) \qquad \rho_o c_p \dot{T} = \Upsilon \boldsymbol{\tau}' : \left(\boldsymbol{d}^{vp} + \boldsymbol{d}^{vd} \right) + J^e P(\boldsymbol{d}^e : \mathbf{1})$$

Voyiadjis and Abu Al-Rub (2005) showed that ℓ is not a fixed parameter and depends on the mean grain size d. This is in line with the dependence of the mean free path distance L_s on the plastic strain p, the hardening exponent m, and the grain size d. One, therefore, requires an evolution equation for the material length scale that is consistent with the experimental trends, such that the following expression for the length scale parameter ℓ can be adopted:

$$(5) \qquad \ell = \frac{\hbar D d}{D + d\, p^{1/m}}$$

2. Numerical Results

Fig. 1 shows the element distortion in the target plate just after impact. The final cross section of a target plate perforated by a blunt projectile at an impact velocity close to the ballistic limit is shown in Fig. 2. In Fig. 3 localization is presented for stainless steel using microstructure based viscoplastic model. Fig. 4 shows shear localizations in Hat-Shape specimens.
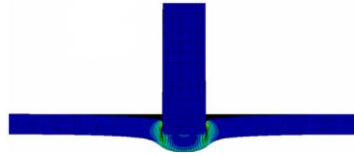
Fig. 1. Penetration of the target plate by a blunt projectile of initial impact velocity of $300\ m/s$ using ALE meshing, plotted as contours of accumulated viscoinelastic strain and showing details of element meshes just after adaptive remeshing (Voyiadjis and Abu Al-Rub, 2006)
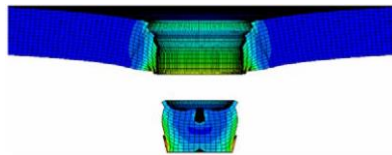
Fig. 2. Final cross section of the target plate perforated by a blunt projectile of initial impact velocity of $300\ m/s$ using ALE meshing and plotted as contours of accumulated viscoinelastic strain. The green indicates an accumulated damage between 0.25 and 0.30 (Voyiadjis and Abu Al-Rub, 2006)
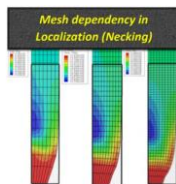
Fig. 3. Localization in Stainless Steel using Microstructural Based Viscoplastic Model. (Voyiadjis, G. Z., and Faghihi, D., 2013)
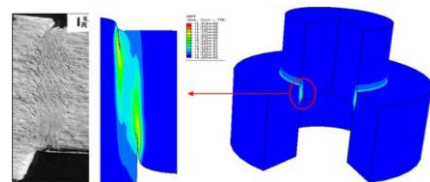
Fig. 4. Shear Localizations in Hat-Shape Specimens (Voyiadjis and Abed, 2008)

NEW CHALLENGES ON DEVELOPING EXPERIMENTAL METHODS FOR INNOVATIVE METAL FORMING TECHNIQUES

R. Zhang, Z. Shao and J. Lin

Department of Mechanical Engineering, Imperial College London, London, UK

1. Introduction to new metal forming processes and experimental challenges

In order to achieve energy savings and reduce CO_2 emissions in the transportation industries, significant efforts have been undertaken over the years to reduce the weight of vehicles by replacing the current heavy metallic structures with light alloys, such as aluminium alloys. However, the critical problem is that light alloys are brittle and difficult to be formed into complex-shaped structural components at room temperature. Thus new metal forming techniques have been developed to enable high strength alloys to be formed in one operation. These techniques include hot stamping for ultra-high strength steel [1] and HFQ® Technology for high strength aluminium alloys [2].

(a) Temperature profile in hot stamping   (b) Temperature distributions
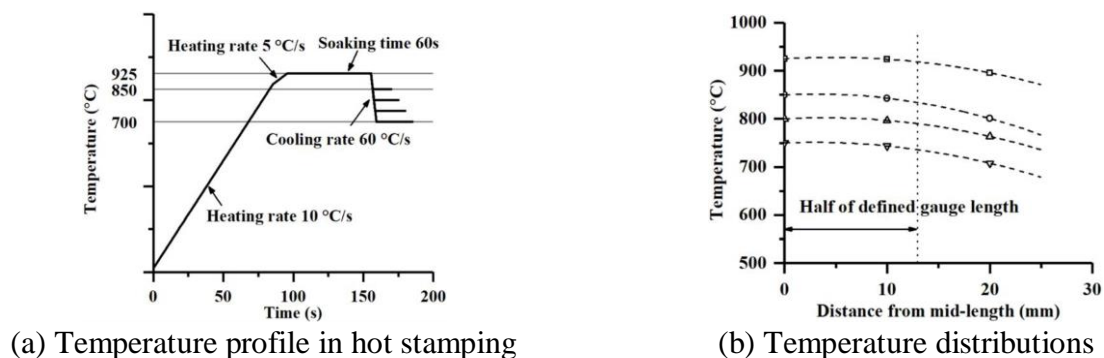
Fig. 1. A typical temperature profile for hot steel stamping (a)
and the challenges of non-uniform temperature distribution in uniaxial tensile tests (b)

Figure 1(a) shows a typical temperature profile in the hot stamping of boron steel. Characterisation of the thermo-mechanical behavior for boron steel needs to be carried out after the material is fully soaked and rapidly cooled to designated isothermal temperatures, so that the real manufacturing conditions can be simulated. There are similar testing requirements for HFQ® applications of aluminium alloys. The main challenges and difficulties include: (i) How to quench the hot material down to the designated testing temperatures at an accurately controlled cooling rate to meet the microstructure requirements, (ii) how to achieve the uniformity of temperature distribution along the gauge length of a dog-bone specimen throughout the entire testing processes, and (iii) how to measure accurate data through uniaxial tensile tests and also formability tests for calibrating material constitutive equations. The Gleeble materials simulator is often used for material thermo-mechanical tests, but the challenge is to obtain uniform temperature distribution within the gauge length of the specimen, as shown in Figure 1(b), which results in an issue of the accurate determination of stress-strain curves and forming limit diagram (FLD). Therefore, new experimental techniques need to be developed for the application to innovative stamping processes.

2. Material characterisation under thermo-mechanical testing conditions

For thermo-mechanical tensile tests in a Gleeble, the non-uniform temperature distribution leads to non-uniform deformation within the gauge length of a specimen. The obtained engineering stress vs. engineering strain curves vary significantly from the definition of gauge length in a range of 2 mm – 40 mm for a dog-bone specimen with a parallel length of 80 mm, as shown in Figure 2(a). Thus, the conventional uniaxial testing methods for determining the onset of necking at isothermal conditions cannot be used directly for the applications when complex thermal histories are introduced.

Formability test is needed to determine an FLD of material under hot stamping conditions. Forming limit curve varies from different temperatures and strain rates, as shown in Figure 2(b). It is impossible to accurately mimic the required thermal histories by using the conventional Nakajima test. The Gleeble was adopted for the multi-axial formability tests, so that the FLD data was generated for hot stamping applications [3]. The main challenges are (i) how to design the cruciform specimen used for this type of formability test, so that the strain field in the concerned area is uniform before necking occurs, and also the fracture initiates are close to the centre of the specimen for different materials at different straining states, and (ii) how to accurately measure the limit strains.

Research has been carried out to deal with the challenges and difficulties mentioned above and certain achievements have been made to date. A new spatio-temporal method has been proposed to determine limit strains for both uniaxial and FLD tests at different conditions for different materials. A novel biaxial testing system and the corresponding cruciform specimen geometries have been developed and used for generating the FLD data at hot stamping conditions. Further research needs to be carried out to standardise the testing methods for the hot stamping applications in industries.

| (a) Stress vs. strain curves for boron steel | (b) Determined FLD for AA6082 |
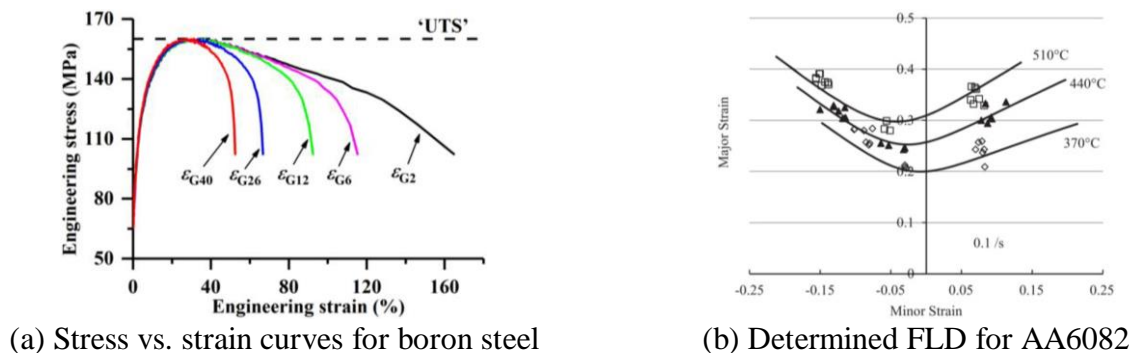
Fig. 2. Experimental results for (a) uniaxial testing at a strain rate of 0.2 /s and a temperature of 750 °C for boron steel, and (b) FLD at a strain rate of 0.1 /s for AA6082 [3]

3. Acknowledgements

4. References

[1] N. Li, J. Lin, D.S. Balint and T.A. Dean (2016). Experimental characterisation of the effects of thermal conditions on austenite formation for hot stamping of boron steel, *J. Mater. Process. Technol.*, **231**, 254-264.

[2] M.S. Mohamed, A.D. Foster, J. Lin, D.S. Balint and T.A. Dean (2012). Investigation of deformation and failure features in hot stamping of AA6082: experimentation and modelling, *Int. J. Mach. Tools Manuf.*, **53**, 27-38.

[3] Z. Shao, N. Li, J. Lin and T. Dean (2017). Formability evaluation for sheet metals under hot stamping conditions by a novel biaxial testing system and a new materials model, *Int. J. Mech. Sci.*, **120**, 149-158.

SELECTIVE LASER MELTING
OF A HIGH PRECISION TURBOMACHINERY APPLICATION IN IN718 ALLOY

P. Wood[1], U. Gunputh[1], G. Williams[1], W. Carter[1], F. Boud[1], S. Bahi[2], A. Rusinek[2,5],
Z.L. Kowalewski[3], Z. Nowak[3], T. Libura[3], G.Z. Voyiadjis[4], J. Díaz-Álvare[5] and M.H. Miguélez[5]

[1] *Institute of Innovation in Sustainable Engineering (IISE), University of Derby, UK*
[2] *Laboratory of Microstructure Studies and Mechanics of Materials, University of Lorraine, France*
[3] *Institute of Fundamental Technological Research, Warsaw, Poland*
[4] *Department of Civil & Environmental Engineering, Louisiana State University,*
Baton Rouge, USA
[5] *Department of Mechanical Engineering, University Carlos III of Madrid, Madrid, Spain*

1. Introduction

The paper describes the manufacture of an outlet guide vane (OGV) component, in IN718 alloy, used in jet engines by Selective Laser Melting (SLM). The OGV component is a static part in the last stage of the compressor and is characterised as a series of airfoils or vanes secured by two flanged rings. The part tolerances at the leading and trailing edge require a high dimensional precision of ±0.072 μm whilst the profile tolerances are slightly more generous. The current challenge to manufacture a prototype OGV in IN718 alloy from a wrought stock involves a lengthy machining process in a hard-to-machine alloy. The tooling access is greatly restricted between the curved vanes, and the process involves careful fixturing and process management to mitigate residual stress in the component arising from the removal of material.
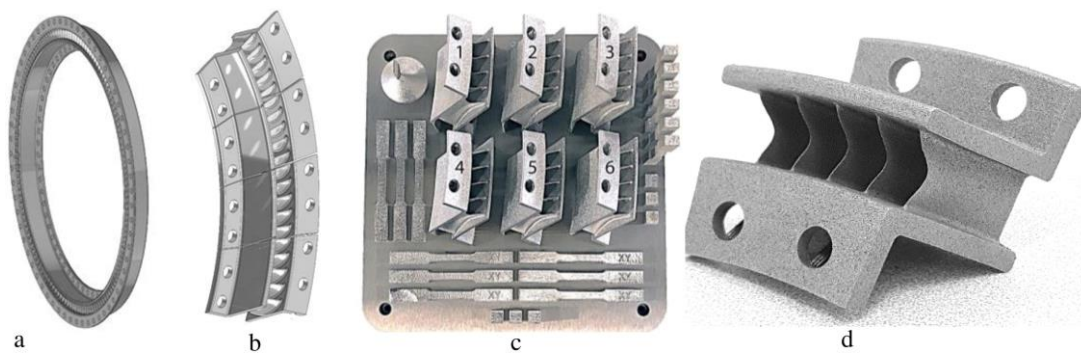
Fig. 1. (a) OGV; (b) Four segments; (c) Printed segments on build plate; (d) Printed segment

A case study OGV component with an outer diameter of 605mm was developed as displayed in figure 1a. There are 140 vanes equally spaced and the airfoil profile design was based on the NACA-6 series. The distance between the vanes with line of sight is roughly 6 mm. The OGV component was divided into an equal number of segments, each with five vanes and equal flow passages to enable the part to be printed by selective laser melting in a Renishaw AM250, see figure 1b. Parameter optimisation was performed with respect to the part orientation on the build plate, thickness change to the flanges, flange position and the influence of the support structure on print accuracy, to identify a build configuration which minimises dimensional error. The dimensions of interest were the inlet and exit angles at the leading edge, chord length, leading and trailing edge thickness, stagger angle and profile tolerance. In this paper, further refinements were performed, initially identifying the important laser process parameters in another build capable of achieving the precision required and

then verifying the process in a following build, see figure 1c and d. The post-process dimensional analysis was performed using the GOM ATOS triple scanning system, and in order to ensure consistency and accuracy of scanning, photogrammetry technology with two reference scale bars, having an average deviation of 0.85 μm, was utilized to calibrate the measurement system. The Airfoil Gauge software was used to establish the best fit of the measured scanned data to the nominal design and the deviations established. Other measurements included hardness, static tensile properties, density, porosity, CTScan, X-ray and surface roughness. This work established the capability of the SLM process to fabricate a high precision turbomachinery part in a high temperature superalloy.
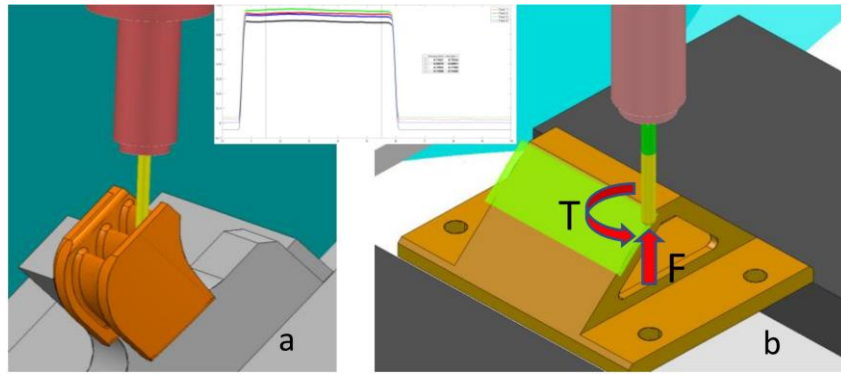
Fig. 2. (a) CAD model of printed segment; (b) Printed artefact to develop machining strategy

The paper further describes an approach to optimise the finishing by CNC machining to achieve the part tolerances and surface finish required of the SLM produced part. Within the study a suitable finish machining allowance was determined. An excessive allowance will consume more energy and tools and involves a multi-stage finishing process that could introduce residual stress in the part. If the allowance is too small, there is a risk of ploughing and smearing rather than cutting the alloy, which leads to rapid tool wear and a poor surface finish. A small diameter ball nose carbide cutting tool was used to machine the air foil profile surfaces between the vanes because tooling access was greatly restricted. The cutting tool stick out length is dictated by the distance to the midpoint of the air foil surface so that cutting forces must be minimized to limit tool deflection. The study uses an experimental approach to determine a suitable cutting strategy and process window for finish machining a high precision turbomachinery application in IN718 alloy produced by SLM. An artefact was printed in IN718 alloy that represents some of the challenges of machining the SLM OGV part. Experiments were performed using a precision machine tool instrumented with a rotating dynamometer to measure the torque, thrust and side cutting forces in machining the artefact. This paper reports the initial findings and identifies further work stages to develop an optimum machining protocol for SLM produced IN718 alloy.

2. Acknowledgements

FULL-FIELD OPTICAL METHODS IN EXPERIMENTAL MECHANICS: PAST, PRESENT AND FUTURE CHALLENGES

M. Kujawińska

Institute of Micromechanics and Photonics, Warsaw University of Technology, Warsaw, Poland

1. Introduction

The role of experimental mechanics involves the measurement of material parameters and physical-mechanical characteristics, stress analysis of large structures or models and the electromechanical analysis of micron-sized mechanical elements, the non-destructive flaw detection tests and development or advancement of computational models as well as design of structures. Full-field optical measurement methods, due to their generally non-contact and non-destructive character, relative ease to implement in a wide range of conditions, fast and high precision measurement process, represent the most important experimental mechanics and industrial control tools [1].

Up to the 60-ies of the last century the only optical tool practically useful for the purposes of experimental stress analysis was photoelasticity. This situation had tremendously changed with the invention of laser (1960), increasing computing power of computers and development of high resolution matrix detectors which brought the world into a digital era. Availability of coherent light (laser) influenced the development of such highly sensitive methods as holographic and electronic speckle interferometry, shearing interferometry, moiré interferometry and latter digital holography [2]. For lower sensitivity measurements incoherent light methods had been developed including wide range of grid (moiré fringe) based methods [2]. Both coherent and incoherent light methods delivered information about the changes in an object subjected to a load in the form of interferograms/fringe patterns. Starting from eighties of the last century multiple methods of automatic, phase based fringe pattern analysis have been proposed and implemented [2,3]. Parallelly with wide application of fringe based methods, simple vision based methods gained importance. Recently 2D and 3D digital image correlation methods have been applied to displacement/strain measurements of a variety macro and micro scale objects [4]. Both approaches resulted in fast and convenient delivery of quantitative displacement and strain data ready to be inserted into commercial CAD/FEM/CAE software and applied in hybrid opto-numerical methods for structural integrity analysis of complex mechanical structures.

2. Present and future challenges

Mechanical/material engineering and industrial demands for experimental techniques are continuously increasing due variety of technological, material and economic factors. It includes increasing shape and material composition complexity of functional surfaces (incl. the scale effect in microelements), the continuously decreasing feature sizes while simultaneous increase in field of view sizes, increased production output, high system performance, product reliability and lifetime. It also goes with increased requirements for working conditions (high temperature, humidity, pressure) and growing role of precision (alignment, placement, repositioning…) for the measurements distributed in time and space. There is also a continuous requirement for more ruggedness, higher resolution, faster measurement and evaluation to name only a few constraints. This situation not only calls for evolutionary improvement of the measurement methods, but also asks for new ideas or even revolutionary breakthroughs. Besides developing new experimental methods and paradigms, also rigorous modelling and simulations deserve due attention, especially in the emerging fields of hybrid and holistic metrology for experimental mechanics.

In the talk a historical overview of full-field optical experimental mechanics methods will be given followed by the overview of the present challenges and selected examples of new approaches to solve complex mechanical problems. The examples range from microscale interferometric measurements of MEMS/MOEMS [5] through monitoring of displacements and strains in complex composite structures [6] and in 3D cultural heritage objects [7]. Also the implementation of multimodal, hierarchical and synthetic aperture approaches to support development and validation of full FEM model of big engineering structures under complex load will be presented [8].

Finally the future trends in the development of full-field optical methods will be discussed in reference to the progress in optoelectronics, optomechatronics, computations, and machine learning (AI) as well as the new measurement and monitoring challenges in mechanics.

3. References

[1] A. S. Kobayashi (ed) (1998). *Handbook of Experimental Mechanics*, 2nd edition, Wiley-VCH Verlag GmbH

[2] M. Drzik, J. Chlpik (2014) Optical methods in experimental mechanics, Acta Physica Slovaca 64(2-3):101-216

[3] K. Patorski and M. Kujawinska (1993). *Handbook of moiré techniques*, Elsevier, Holland

[4] Servin M., Kujawińska M. (2001) Modern fringe pattern analysis in interferometry, in *Handbook of Optical Engineering*, D.Malacara (ed), Marcel Dekker Inc., 373-426

[5] M. A. Sutton, J. J. Orteu, H. Schreier (2009). Image Correlation for Shape, Motion and Deformation Measurements, Springer

[6] M. Kujawinska, M. Jozwik, A. Styk (2013) Parallel multifunctional system for MEMS/MOEMS and microoptics testing in Harding (ed) *Handbook of Optical Dimensional Metrology*, Taylor and Francis

[7] Gąsior P., Malesa M., Kaleta J., Kujawińska M., Malowany K., Rybczyński R. (2018) Application of complementary optical methods for strain investigation in composite high pressure vessel, Composite Structures, **203**, 718–724

[8] K. Malowany, L. Tyminska-Widmer, M. Malesa, M. Kujawinska, P. Targowski, and B. J. Rouba (2014)"Application of 3D digital image correlation to track displacements and strains of canvas paintings exposed to relative humidity changes", Applied Optics **53**(9), 1739–1749

[9] K. Malowany, A. Piekarczuk, M. Malesa, M. Kujawińska, P. Wiech (2019). Application of 3D digital image correlation for development and validation of FEM model of self-supporting arch structures, *Appl. Sci.*, **9**(7), 1305-1315

VIRTUAL FORENSIC LABORATORY - DEVELOPING BIO-SIMULANT HUMAN CRANIUMS FOR EXTREME INJURY ASSESSMENTS

E. Kwon[1], R. Das[2], J.W. Fernandez[3] and M. Taylor[4]

[1] Department of Mechanical Engineering, University of Auckland, Auckland, New Zealand
[2] School of Engineering, RMIT University, Melbourne, Victoria 3000, Australia
[3] Auckland Bioengineering Institute, University of Auckland, Auckland, New Zealand
[4] Institute of Environmental Science and Research (ESR), Christchurch, New Zealand

1. Introduction

In the context of the investigation of serious crimes and its resolution in court, some of the most difficult issues to resolve include distinguishing between accidental, intentional and suicidal causes of fatalities, the specific role of individuals in causing injury or fatality, especially their intent, determining the nature of the injuring cause (e.g. type of weapon used) and assessing the viable biomechanical scenarios for injury causing events. Essential to solving some of these problems is a thorough understanding of the mechanisms of wounding (including blood spatter) and the development of valid methods to be able to distinguish one mechanism from another. Relatively little information is known about the specific physics and fluid dynamics of blood spatter, but this has not deterred 'experts', with little or no appreciation of the science involved, giving sometimes controversial opinion evidence in courts around the world.

In cranial gunshot wounding it is thought that the initial contact between the projectile and the skin tissue produces spattered material with some sort of splashing mechanism [1]. This spattered material can transfer to the firearm or the shooter which is sometimes used as evidence of proximity. It would be valuable to be able to make predictions about the extent and range of this spatter. The objectives of this work are to develop an accurate physical model of the event of a projectile impact on a human cranium and to examine whether such models can be used to make realistic predictions about backspatter noticed during ballistic injury of human craniums. This work complements the associated computational model development reported previously [2].

2. Experimental methods

To develop a simulant human cranium, the essential components are scalp, skull and brain. In this paper, the simulant material development of one of the main components of the human cranium, i.e., the skull, is presented. A range of materials, including different types of Polyurethane resins, Urethane, Epoxy resins, Fibre-reinforced Concrete and Medium density fibreboard (MDF), were tested to evaluate suitable candidate simulants for human craniums. A number of additives were added to the selected skull simulant materials to further modulate their ballistic response. Two different types of animal bones (bovine scapulae and swine mandible) and two human skulls were also tested to provide reference data to validate the simulant performance. The skull simulant materials were fabricated into square test samples with thickness ranging from 4 to 8 mm. The animal bones and simulant materials were tested under ballistic conditions using 9 mm Luger calibre projectiles and filmed with a high speed camera. High speed digital imaging was used to acquire dynamic deformation data, and crack length and defect size were measured after the tests.

3. Results and discussion

The fragmentation characteristics of the animal bones and the human skull are shown in Figure 1 along with three of the simulant materials. In each case the fragments generally dispersed conically

in both the forward and backward directions with similar dispersion boundaries. As expected, significantly more fragments were produced in the forward direction. The human bone tended to produce fewer and smaller fragments than that by bovine scapulae and swine mandibles. These differences may reflect differences in the respective bone structures.
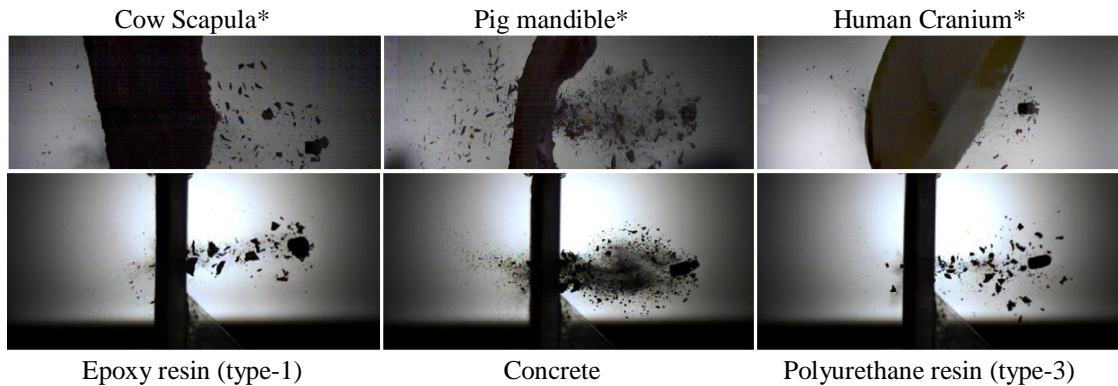
Fig. 1. Biological sample fragmentation behaviours (top row) compared to equivalent simulant material responses (bottom row) under the ballistic projectile impact

The skull simulants, Polyurethane resin and Urethane, provided the closest visual match to the human cranium fragmentation behaviour. Following penetration by the projectile, the human skull sample produced no cracks around the defect, with a bevelling extent of 6 mm, and maximum and minimum entry side defect diameters of 8.5 and 9.5 mm respectively. The skull simulants tested here were more brittle under ballistic impact, and all produced cracks around the entry defect. The number of complete cracks that traversed laterally through the sample was used as a primary indicator of sample brittleness, because complete cracks resulted in the total fracture of the samples. The use of an additive improved the performance of the skull simulants by changing the fragmentation behaviour. The lack of complete cracking in the Polyurethane samples mixed with 10% additive (Calcium metasilicate and silicon dioxide blend) implied that this material was the closest match to the human skull sample.

4. Summary

The key outcome of this work is the physical models with a skull simulant material emulating properties of biological structures for use in lieu of animal subjects to simulate ballistic-human interaction. Of the simulants for human skull considered in this study, the polyurethane resin (commercially Procast) mixed with an additive was deemed to be the most comparable simulant to the human skull. The overall outcome of this work would be a novel validated tool for the forensic scientists to inverse predict the possible causes of cranial injury incidents based on scene evidence, that will bring a new dimension to forensic science and crime scene investigation, whereby crime scene evidence could be analysed in-depth to provide new information and draw conclusions.

5. References

[1] G. E. Radford, M. C. Taylor, J. A. Kieser, J. N. Waddell, K. A. J. Walsh, J.C. Schofield, R. Das, E. Chakravorty (2015). Simulating backspatter of blood from human cranial gunshot wounds using animal models, *International Journal of Legal Medicine*, **130(4)**, 985-994.
[2] E. Kwon, M.R. Singh, R.D. Vallabh, R. Das, M.C. Taylor, J.W. Fernandez (2018). Modelling ballistic cranial injury and backspatter using smoothed particle hydrodynamics, *Computer Methods in Biomechanics and Biomedical Engineering: Imaging & Visualization*, 1-14.

PLASTICITY, DAMAGE AND FRACTURE IN THE PROXIMITY OF ABSOLUTE ZERO. FROM EXPERIMENT TO CONSTITUTIVE MODELS

B. Skoczeń
Cracow University of Technology, Cracow, Poland

1. Introduction

Design of modern scientific instruments (particle accelerators and detectors, superconducting magnets, NMR spectrometers, etc.), operating in the superconducting regime, involves rather complex constitutive modeling of materials suitable for use at extremely low temperatures. Many metals and alloys applied in the proximity of absolute zero, undergo at extremely low temperatures three coupled dissipative phenomena: discontinuous plastic flow (DPF), plastic strain induced phase transformation as well as evolution of micro-damage, including radiation induced damage. All three phenomena affect nucleation and propagation of a macro-crack, accompanied by substantial evolution of microstructure at the crack tip and along the fracture discontinuity.

2. Coupled dissipative phenomena in the proximity of absolute zero

DPF (serrated yielding) is characteristic of low (LSFE) and high stacking fault energy (HSFE) materials strained at extremely low temperatures. It represents oscillatory mode of plastic deformation and reflects discontinuous nature of plastic flow (discontinuous in terms of $d\sigma/d\varepsilon$). Low temperature serrated yielding (DPF) occurs below threshold temperature: T1 for LSFE materials and T0 for HSFE materials. From the phenomenological point of view, DPF consists in frequent abrupt drops of stress as a function of strain during kinematically controlled loading. There is enough experimental evidence to back the hypothesis that the mechanism of DPF is related to formation of dislocation pile-ups at the internal lattice barriers, such as the Lomer-Cottrell locks [2]. Accumulation of dislocations in the pile-up leads to increase of the resolved shear stress at the head of pile-up, until the stress reaches the level of cohesive strength and the lattice barrier breaks. General thermo-mechanical aspects of DPF are strictly linked to the so-called thermodynamic instability, which consists in strong oscillations of temperature due to heat accumulation in near adiabatic conditions, resulting from vanishing specific heat when the temperature approaches absolute zero. Another important phenomenon that occurs in the metastable materials at extremely low temperatures is the fcc-bcc phase transformation [1]. It manifests itself in the form of rapid change of crystallographic structure from face-centred-cubic parent phase to body-centred-cubic secondary phase. The plastic strain-induced martensitic transformation in the high-strength metastable stainless steels is related to TRIP (transformation-induced plasticity) effect, resulting in the uniform, unrecoverable, macroscopic strain. Finally, third important phenomenon is related to evolution of microdamage, including radiation induced damage. During irradiation, energetic particles penetrating lattice displace the atoms from their original positions. Exposure to a flux of particles leads to creation of clusters of defects in the material. As a result of cascade process, pairs of interstitial atoms and vacancies (the Frenkel pairs) are massively created. The vacancies often accumulate in clusters by means of diffusion. The nature of mechanically induced micro-damage, comprising micro-voids and micro-cracks, is different from the nature of radiation induced micro-damage. Nevertheless, all three phenomena discussed above are strongly coupled to each other and accompany nucleation and propagation of a macro-crack. The conditions of fracture in two-phase materials, and the evolution of microstructure at the crack tip and along the fracture discontinuity are investigated. In the course of macro-crack propagation, the plastic strain fields occurring in the vicinity of the crack tip induce

massive evolution of microstructure, consisting mainly in the fcc-bcc phase transformation. The analysis of morphology and orientation of grains, as well as the analysis of intensity of the phase transformation are carried out along the macro-crack path.

3. Experimental evidence

Experimental identification of the plastic strain induced phenomena at extremely low temperatures (in the near-0K regime) is quite complex. It involves a set-up consisting of double-wall cryostat, well instrumented insert containing the sample, cryogen transfer line linking liquid helium (or liquid nitrogen) dewar with the cryostat mounted in the standard traction machine. Moreover, the original set-up has been extended to include combined loads consisting in traction and torsion, which allows performing the non-proportional loading paths. The insert contains the piezoelectric load cell (for traction and torsion), pair of clip-on extensometers, set of special thermistors for extremely low temperatures (type cernox), set of tensometers, a ferritoscope and the acoustic emission sensors. The cryogen (liquid helium or liquid nitrogen) is supplied to the cryostat by means of the transfer line, until the specimen is immersed in the liquid helium or liquid nitrogen bath. The level of the cryogen is controlled by a thermistor mounted inside the cryostat. The kinematically controlled tests, with the crosshead velocity of the order of 1 mm/min, were carried out. High resolution and high quality data acquisition system has been applied. Both uniform and notched specimens were tested. The applied force (or torque) has been measured directly on the sample by means of the piezoelectric transducer. The thermistors, mounted in the gauge length of the specimen were used to measure the evolution of temperature. Specific and complex tests aimed at understanding the DPF as well as the plastic strain induced fcc-bcc phase transformation were carried out. Moreover, dedicated experiments related to the macro-crack initiation and propagation in the presence of DPF and fcc-bcc phase transformation were performed until fracture.

4. Physically based multiscale constitutive model

Multiscale constitutive model of DPF [2] involves microscopic approach based on the analysis of evolution of dislocations density and formation of dislocation pile-ups at the lattice barriers. The process of drop of stress during single serration is based on a criterion involving the number of lattice barriers accompanied by the dislocation pile-ups, and the average shear stress at the head of a pile-up. Formulation of the constitutive model of metastable material subjected to the plastic strain induced phase transformation is based on multiscale considerations [1]. The model involves the mechanism of strain hardening with two fundamental effects taken into account: interaction of dislocations with the inclusions of secondary phase, and evolution of tangent stiffness of two-phase continuum resulting from constantly evolving proportions between the hard martensite and the soft austenite. Radiation induced damage is combined with the evolution of mechanically induced damage within the common framework of Continuum Damage Mechanics (CDM). Coupling between all three phenomena has been implemented. Finally, based on the above models, the propagation of macro-crack in two-phase continuum has been numerically simulated, and the results were compared with the scanning electron microscope analysis and the synchrotron light microstructural observations.

5. References

[1] R. Ortwein, B. Skoczeń, J.Ph. Tock (2014). Micromechanics based constitutive modeling of martensitic transformation in metastable materials subjected to torsion at cryogenic temperatures, *International Journal of Plasticity*, **59**, 152-179.

[2] J. Tabin, B. Skoczeń, J. Bielski (2019). Discontinuous plastic flow coupled with strain induced fcc–bcc phase transformation at extremely low temperatures. *Mechanics of Materials*, **129**, 23-40.

THERMODYNAMICS AND HOMOGENISATION THEORY AS DRIVING FORCES IN THE DESIGN OF NOVEL EXPERIMENTS AND THE (RE-)EVALUATION OF DATA

Ch. Hellmich

Institute for Mechanics of Materials and Structures, Vienna University of Technology, Austria

1. General

There is broad consensus that theories may profit, or may essentially be built, on appropriate experiments. There is also broad consensus that experiments and theory, together, are the key fundaments of modern natural sciences. However, it is also important to remember that practically speaking, it is often not so much the theory which builds on experiments, but it is the "choice of (theoretical) problems" which actually drives the "experimental design" [1]: In this sense, it was BECAUSE Kepler wished to find a theoretically harmonious solution to astronomical problems, he TESTED, based on then known astronomical „experimental" observations, the significance of the ellipse as the path followed by the planets. In the context of experimental mechanics, we will discuss, in the lecture, two lines along which theoretical (and computational) methods can boost the significance of experimental methods:

(i)   massive re-evaluation of multi technique data from a multi-theoretical, truly unifying, approach;
(ii)   design of mechanical tests considering thermodynamics principles

Concerning (i) the lecture will cover a unified, mechanics-informed structural biology vision of mineralized tissues [2-5], integrating data from mechanical tests, ultrasonics, chemical analysis, light and electron microscopy, as well as small energy X-ray scattering; and concerning (ii) the lecture will cover the „true", i.e. rate-independent elasticity of cementitious materials, to be clearly distinguished from their creep characteristics with characteristic time ranging from minutes to decades [6-8].

2. References

[1]   Popper,K. Conjectures and Refutations: The Growth of Scientific Knowledge. New York: Basic Books, 1962. Print

[2]   Fritsch A1, Hellmich C. 'Universal' microstructural patterns in cortical and trabecular, extracellular and extravascular bone materials: micromechanics-based prediction of anisotropic elasticity. J Theor Biol. 2007 Feb 21;244(4):597-620. 2006 10.1016/j.jtbi.2006.09.013

[3]   Eberhardsteiner L1, Hellmich C, Scheiner S., Layered water in crystal interfaces as source for bone viscoelasticity: arguments from a multiscale approach, Comput Methods Biomech Biomed Engin. 2014;17(1):48-63. doi: 10.1080/10255842.2012.670227.

[4]   Morin,C., Hellmich, Ch., A multiscale poromicromechanical approach to wave propagation and attenuation in bone, Ultrasonics, Volume 54, Issue 5, 2014, 1251-1269, ISSN 0041-624X, doi.org/10.1016/j.ultras.2013.12.005.

[5]   Kurfürst, A., Henits, P., Morin, C., Abdalrahman, T., Hellmich, Ch., Bone Ultrastructure as Composite of Aligned Mineralized Collagen Fibrils Embedded Into a Porous Polycrystalline Matrix: Confirmation by Computational Electrodynamics, Frontiers in Physics, 6, 2018, 125, 10.3389/fphy.2018.00125

[6]   Königsberger, M., Pichler, B., Hellmich, Ch., Irfan-ul-Hassan, MInnovative creep testing combined with micromechanics modeling for deciphering creep of cementitious materials at

early ages. (2016). 33rd Danubia Adria Symposium on Advances in Experimental Mechanics, 10.13140/RG.2.2.10470.01607.

[7] M. Königsberger, M. Irfan-ul-Hassan, B. Pichler, and Ch. Hellmich: "Downscaling Based Identification of Nonaging Power-Law Creep of Cement Hydrates", J. Eng. Mech. (ASCE), 142, 04016106 (2016).

[8] Irfan-ul-Hassan, M.; Königsberger, M.; Reihsner, R.; Hellmich, C.; Pichler, B. How wateraggregate interactions affect concrete creep: Multiscale analysis. J. Nanomech. Micromech. 2017, 7, 04017019.

SYNCHROTRON SOLARIS - APPLICATIONS FOR EXPERIMENTAL MECHANICS

M. Stankiewicz

The Jagiellonian University, SOLARIS National Synchrotron Radiation Centre, Krakow

SYMPOSIUM

S1. Novel Applications of Experimental Mechanics

HIGH-TEMPERATURE INDENTATION CREEP TEST BY A FLAT-ENDED CYLINDER PUNCH

M. Arai[1], T. Doi[2] and K. Ito[1]

[1] Department of Mechanical Engineering, Tokyo University of Science, Tokyo, Japan
[2] Graduate School of Mechanical Engineering, Tokyo University of Science, Tokyo, Japan

1. Introduction

The design and remaining life prediction of a high-temperature component are required to determine the full set of material constants in a creep constitutive model. A uniaxial creep test has been conducted to identify the material constants involved in Norton's law:

$$(1) \qquad \frac{d\varepsilon}{dt} = k\sigma^n$$

where ε, σ, and t denote creep strain, stress, and time, respectively. Material constants k and n are called the creep coefficient and creep exponent, and are used to characterize creep deformability of engineering alloys. However, many specimens must be prepared in conventional uniaxial creep test procedures as each specimen can only be tested at a single temperature and stress condition. To overcome such difficulties, conventional creep tests that utilize a miniature-sized specimen [1] and a small punch test [2] were recently focused on. However, it was pointed out that the former includes a size-effect problem in the creep curve and rupture time; in the latter, the uniaxial and multi-axial creep states must be related based on the semi-empirical formula. Thus we proposed a ball indentation test to directly determine the material constants from changes in the impression size with creeping time [3], however, the indentation test had to be interrupted to measure the impression size, which complicated the test procedure.

In this study, an alternative technique based on creep indentation by a flat-ended punch is proposed. This technique can continuously obtain the required creep data. In addition, the exact solution formulated for the associated problem is applied to identify the creep coefficient and exponent.

2. Determination of creep constants based on flat-edged punch indentation

Mulharn et al. [4] formulated semi-infinite creeping media indented by a circular punch with a flat edge, demonstrating that it was possible to relate the indentation load P by the punch with radius a and indentation rate $\dot{h}$ as follows:

$$(2) \qquad \frac{P}{\pi a^2} = \left(\frac{\dot{h}}{a}\right)^{\frac{1}{n}} \left(\frac{1}{k}\right)^{\frac{1}{n}} \cdot F(n)$$

where $F(n)$ is a function of the creep exponent n. To consider the effect of a free edge in a circular indented sample with radius R, the correction factor η was included in Eq. (2), which was identified via finite element analysis conducted in advance.

$$(3) \qquad \frac{P}{\pi a^2} = \left(\eta \frac{\dot{h}}{a}\right)^{\frac{1}{n}} \left(\frac{1}{k}\right)^{\frac{1}{n}} \cdot F(n)$$

where function $F(n)$ and correction factor η of (a/R) are given.

(4) $\quad F(n) = -3.05n + 3.50$

(5) $\quad \eta = -5.127\left(\dfrac{a}{R}\right)^4 + 12.421\left(\dfrac{a}{R}\right)^3 - 8.791\left(\dfrac{a}{R}\right)^2 + 0.508\left(\dfrac{a}{R}\right) + 1$

An evaluation procedure based on Eq. (3) is described as follows: in performing the indentation test, a change in the indentation depth h with time t is monitored under a constant load P, whereas a logarithm of the indentation pressure $ln(P/\pi a^2)$ is plotted as a function of a logarithm of the indentation rate $ln(\eta \dot{h}/a)$. The gradient and the vertical axis intercept in this graph directly give the creep exponent n and creep coefficient k, respectively.

3. Identification of creep material constants

Creep material constants were identified following the procedure mentioned above. In this study, pure aluminum A1050-H24 with sample geometry of a 10×10×5 mm plate shape was prepared. The indentation tests were conducted using a circular indenter of alumina Al_2O_3 with a diameter of 2 mm. The tester was a hand-made lever-type device with an electric furnace. The indentation test results are shown in Fig. 1. Fig. 1 (a) indicates the relationship between the indentation pressure and indentation rate. Fig. 1 (b) and (c) are the results estimated by the proposed method compared to those obtained by a spherical indentation test [3] and typical uniaxial creep test. It was confirmed that the developed indentation test could precisely identify the material constants in Norton's law.

(a) Indentation results   (b) Creep exponent   (c) Creep coefficient
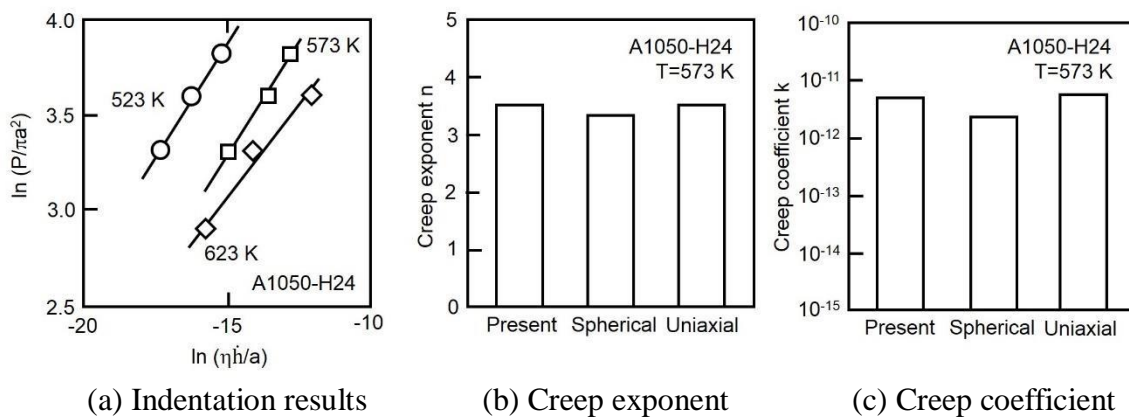
Fig. 1. The indentation test result obtained by a flat-ended punch

4. Conclusion

In this study, a creep indentation test by a flat-ended punch was proposed to identify the creep coefficient and exponent. The proposed method was shown to be able to obtain a full set of creep material constants.

5. References

[1] C. J. Hyde et al. (2013). Small ring testing of a creep resistant material, *Mater. Sci. Eng. A*, **586** (1), 358-366.

[2] T. H. Hyde et al. (2007). Requirement for and use of miniature test specimens to provide mechanical and creep properties of materials, *Int. Mater. Rev.*, **52** (4), 213-255.

[3] M. Arai (2017). High-temperature creep property of high-Cr ferritic heat-resisting steel identified by indentation test, *J. of Press. Vessel. Tech.*, **139**, 021403-1.

[4] A. F. Bower et al. (1993), Indentation of a power law creeping solid, *Proc. R. Soc. Lond. A*, **441**, 97-124.

CHARACTERIZING MECHANICAL PROPERTY OF NANOCOMPOSITES WITH ALIGNED GRAPHENE

L.-S. Su and J.-L. Tsai
Department of Mechanical Engineering, National Chiao Tung University, Hsinchu, 300, Taiwan

1. Introduction

The research aims to fabricate the nanocomposites with aligned functionalized graphene platelet and investigate the corresponding mechanical properties. The morphology of the nanocomposites was characterized by electrical microscopy. Moreover, the mechanical properties of the graphene nanocomposites were measured through tensile tests. Finally, the properties were characterized using micromechanical analysis.

2. Material Preparations and Characterization

The functionalized graphene modified with COOH and NH_2 groups were introduced into the epoxy matrix through mechanical mixing followed by sonication for homogeneous dispersion. Before curing, electrical field was applied on the epoxy-graphene compound to align the graphene platelets. Figure 1 demonstrates the evolution of the graphene during the aligning process (electrical field was applied in the horizontal direction). It can be seen that the graphene platelet is aligning gradually along the electrical field and the alignment is clearly observed after 20 minutes of electrical loading. In 40 minutes, the aligned network of graphene platelets is formed in the nanocomposites. The loading of graphene platelet in the current study is 0.3wt% and 0.6wt%. When the graphene platelets are aligned, the nanocomposites are regarded as orthotropic materials and the properties are evaluated from mechanical tests. For the sake of comparison, the nanocomposites without the alignment of graphene platelets were prepared and tested in the study.

3. Experiments

The nanocomposite samples were tested in the homemade tensile machine with stroke control. The strain rate for the tests was designated as 0.1mm/min. The slope of the tensile stress and strain curve is regarded as the Young's modulus of the nanocomposites. For each case, at least five samples were tested.
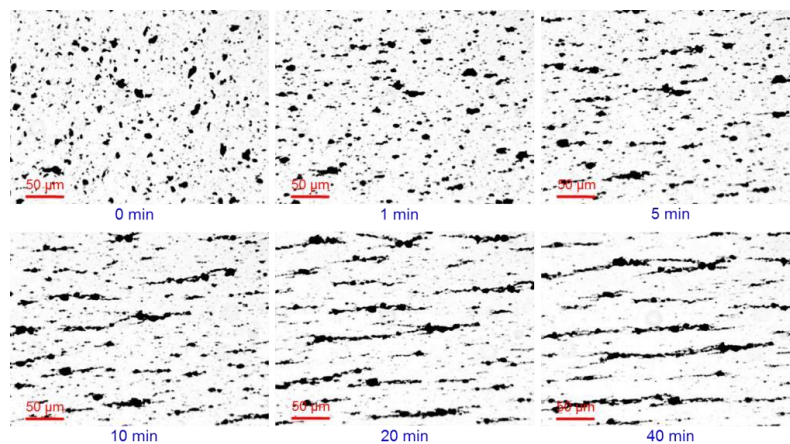
Fig. 1. The evolution process of graphene alignment under electrical field

4. Results and Discussion

In addition to the experimental measurement, the Young's moduli of the graphene nanocomposites were characterized using micromechanical analysis. Based on the Mori-Tanaka's average theory, the effective stiffness of the graphene nanocomposite can be expressed as [1]

$$(1) \qquad \overline{C} = C_m + f_p \left(C_p - C_m \right) A_p$$

where $\overline{C}$ is the effective stiffness matrix, C_m and C_p denote the stiffness matrix of the epoxy and graphene platelet, respectively. f_p is the volume fraction of graphene platelet, and A_p is the global strain concentration matrix of graphene platelet. The explicit form of the effective stiffness for the graphene nanocomposites can be found in literature [1]. It is noted in the model prediction, the continuum micromechanics concept was employed and the perfect bonding between the ingredients was assumed. In the modeling, the Young's modulus of epoxy resin is 2.94GPa, and the Poisson's ratio is 0.3. In addition, Young's modulus and Poisson's ratio of graphene platelet are 1060GPa and 0.48, respectively, which were obtained from molecular dynamic simulation [2]. The aspect ratio for the graphene platelet is assumed to be 700. Table 1 illustrates the moduli of the nanocomposites with aligned graphene and randomly orientated graphene. Apparently, the moduli of the nanocomposites with aligned graphene platelets are higher than that with randomly orientated graphene platelets. Furthermore, at the graphene loading of 0.3wt%, the micromechanical model prediction agrees well with the experimental data. However, when the graphene loading is 0.6wt%, the predictions are higher than the experimental data. This could be attributed to the aggregation of graphene platelets, which may dramatically diminish the moduli of the nanocomposites.

Graphene content (wt%)	Experiment (GPa)		Modeling (GPa)	
	Aligned	Random	Aligned	Random
0.3	3.82±0.04	3.44±0.02	3.82	3.43
0.6	4.25±0.02	3.65±0.02	4.69	3.92

Table 1. Comparision of Young's modulus obtained from experiments and model prediction for graphene nanocomposites

5. Conclusions

The graphene nanocomposites with aligned graphene can be fabricated by introducing electrical filed in the epoxy/graphene compound. The mechanical properties of the aligned nanocomposites can be characterized using micromechanical model and the model predictions are in good agreement with the experimental data.

6. References

[1] P. Lu, Y. W. Leong, P. K. Pallathadka, and C. B. He (2013). "Effective moduli of nanoparticle reinforced composites considering interphase effect by extended double-inclusion model-theory and explicit expressions" *Int. J. Eng. Sci.*, **73**, 33-55.
[2] T. Y. Wang, P. Y. Tseng, J. L. Tsai (2019). "Characterization of Young's modulus and thermal conductivity of graphene/epoxy nanocomposites" *J. Compos. Mater.*, **53(6)**, 835-847.

CREEP DEFORMATION AND DAMAGE ANALYSIS FOR HIGH-TEMPERATURE WELDED PIPING SUBJECTED TO LOAD COMBINED WITH BENDING MOMENT AND TORQUE

H. Kajita[1], T. Murai[2], M. Arai[3], K. Ito[3], K. Funakoshi[4] and A. Yoshimitsu[4]
[1] Graduate School of Engineering, Tokyo University of Science, Tokyo, Japan
[2] Subaru Corporation, Tokyo, Japan
[3] Department of Mechanical Engineering, Tokyo University of Science, Tokyo, Japan
[4] Mechanical & Materials Engineering Group, The Chugoku Electric Power Co., Inc., Hiroshima, Japan

1. Introduction

In aged thermal power plants, several cracks frequently form in welded pipes due to creep deformation. Creep deformation is induced by not only by axial force, but also torsional torque and bending moment. However, creep crack initiation life under such complex loading is predicted based upon the uniaxial creep test. In this study, a creep testing machine is developed, called the bending-torsional creep testing machine, that can apply both bending moment and torsional torque simultaneously at a high-temperature condition. In order to clarify the influence of complex loading on creep deformation and crack initiation, a 1Cr1Mo-0.25V steel pipe with weld part of 2.25Cr–1Mo steel was tested using the developed machine.

2. Development of bending-torsional creep testing machine

Figure 1 shows a schematic and photograph of the bending-torsional creep testing machine. A hollow cylindrical test piece is mounted on an electric furnace. One edge of the test piece is fixed and its center is simply supported. The free edge of the piece is subjected to both a vertical load and torsional torque by applying a weight on the tip of the two arms (Arm-1 and Arm-2 shown in figure). As the result, both bending moment and torsional torque are enforced at the center of the test piece.
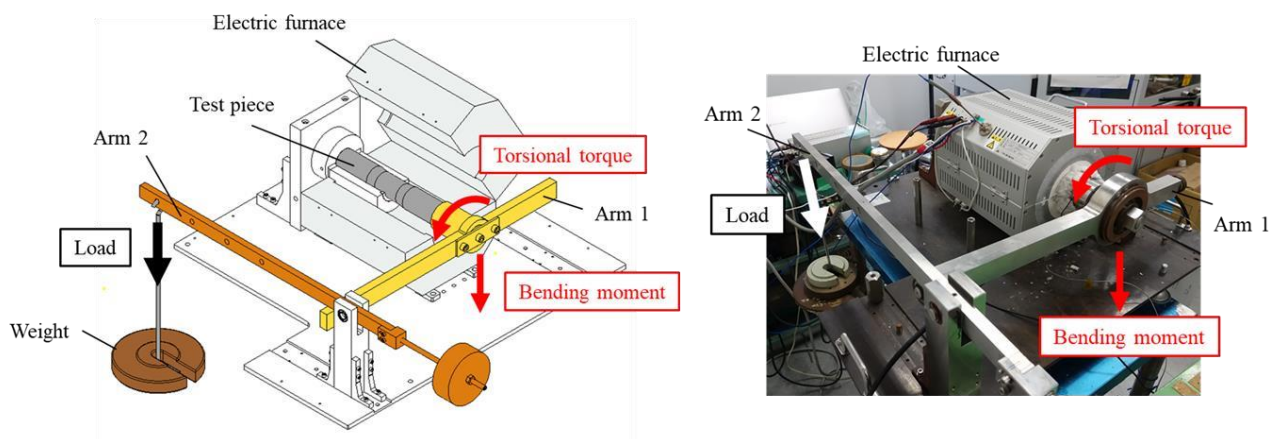
Fig. 1. The bending-torsional creep testing machine developed in this study

3. Test procedure and results

A 1Cr1Mo-0.25V steel pipe with the size of φ49 × φ41 × 320 mm was employed as the test piece. The pipe was butt welded with 2.25Cr–1Mo steel after cutting the center of the pipe. The creep test was conducted at 873 K. The weight and length of the two arms were determined so that bending moment and torsional torque were approximately 135 Nm and 270 Nm at the center of the test piece, respectively. Two displacement meters (DT-20D; Kyowa Electronic Instruments Co., Ltd., Japan) were set on Arm-1 to evaluate the deflection and twisting angle. The creep test was interrupted every 300 h to carry out metallographic replication around the welded region.

Figure 2 shows the variations of deflection and twisting angle with time. The deflection increased almost linearly up to 1000 h, and then increased rapidly. The twisting angle demonstrates similar behavior. From metallographic observations from replication, several creep cavities were observed at approximately 1000 h. Then, a macroscopic crack was observed near the welded region at 1600 h. As shown in Fig. 2, the macroscopic crack was inclined along the longitudinal direction of the test piece, which was attributed to the complex load.
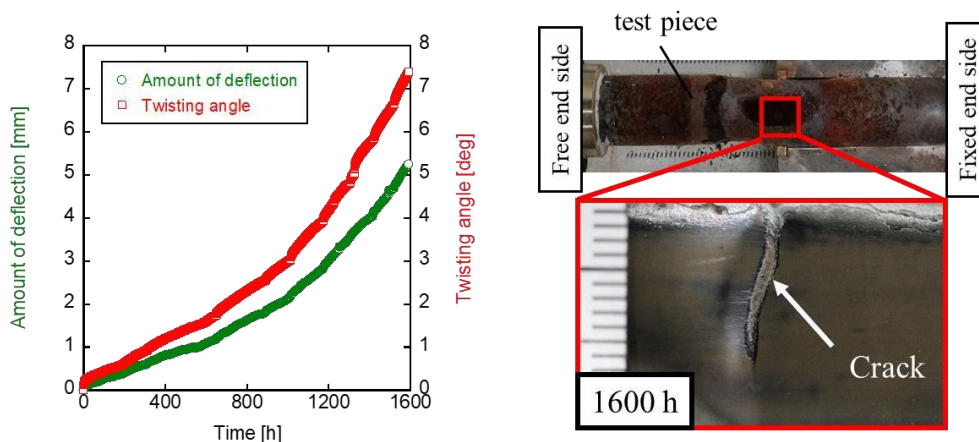
Fig. 2. Variation of deflection and twisting angle with time (left side)
and appearance of macroscopic crack initiated around the welded region (right side)

4. Creep deformation and damage evaluation by FEA

Finite element (FE) analysis was conducted using the commercial FE analysis code Marc (Ver.2010, MSC Software) to evaluate the stress distribution. The FE model with the same shape and material as the test piece was created. The material properties were obtained from the NIMS database [1]. Bending load and torsional torque were applied to the free edge of the FE model.

The FE analyses results confirmed that the direction of maximum principal stress was inclined approximately 23° along the longitudinal direction of the test piece, which corresponds to the angle of the macroscopic crack. Therefore, it was presumed that the creep crack under complex load is dominated by the maximum principal stress.

5. Conclusion

A bending-torsional creep testing machine, which can apply both bending moment and torsional torque to a hollow cylindrical welded pipe, was developed. It was revealed that an inclined macroscopic crack formed around the welded region at 1600 h. FE analysis showed that such a creep crack is dominated by the maximum principal stress.

6. References

[1] Creep data sheet, https://smds.nims.go.jp/MSDS/ja/sheet/Creep.html (accessed 2019-06-13)

EXPERIMENTS ON DAMAGE AND FAILURE BEHAVIOR OF BIAXIALLY LOADED SPECIMENS UNDER NON-PROPORTIONAL LOAD PATHS

M. Zistl, S. Gerke and M. Brünig
*Institut für Mechanik und Statik, Universität der Bundeswehr München,
85577 Neubiberg, Germany*

1. Introduction

This presentation deals with experiments and numerical simulations of non-proportionally loaded biaxial specimens. Due to technological progress and demand for economical use of resources, the requirements for materials and structures are increasing. However, this requires detailed knowledge of the deformation behavior of materials used under the expected, predominantly non-proportional loading conditions. It has already been shown that the loading history has a strong influence on the damage evolution and the failure processes as well as on the level of the final fracture load [1, 2]. Thus damage and failure mechanisms occurring under proportional load paths cannot be directly transferred to non-proportional ones. For this reason, the effects of the non-proportional load paths and the resulting changes of the stress states on the damage and failure mechanisms of metals will be investigated.

2. Phenomenological damage model

In this context, a thermodynamically consistent continuum damage model for ductile metals with stress-state-dependent criteria is presented. Its kinematics are based on the introduction of damaged and fictitious undamaged configurations [3]. A yield condition and a flow rule describe plastic behavior whereas a damage criterion and a damage rule characterize various damage processes in a phenomenological way. It takes into account different elastic potential functions to simulate the effect of damage on elastic material behavior. This leads to a damage affected elastic material law. It is well understood that plastic flow, damage and failure are dependent on stress intensity and stress triaxiality [4, 5, 6, 7]. Under tension dominated stress conditions damage in ductile metals is mainly caused by nucleation, growth and coalescence of voids whereas the formation of microshear-cracks is the predominant damage mechanism under shear and compression dominated stress states. Therefore, the damage model considers functions for both different damage modi. Numerical analyses on the micro-level examining deformation behavior of microdefect-containing unit cells have been performed to get information on stress-state-dependent damage and fracture mechanisms [8].

3. Biaxial experiments

To investigate non-proportional load paths and to validate the constitutive equations with its stressstate-dependent functions, a series of experiments with the biaxially loaded cruciform specimen [9, 10, 11] is performed. The specimens are taken from thin metal sheets and the results obtained from proportional loading paths will be compared with those based on non-proportional ones and among themselves. The loading is applied sequentially and thus the loading ratio and the stress-statedependent processes change during the biaxial experiments until failure. This gives chance to investigate superposition of different stress states with corresponding damage mechanisms. During the tests principal strain fields on the surfaces of critical regions of the specimen are monitored by digital image correlation technique (DIC) providing information on the formation of localized inelastic strain bands leading to damage and failure. Based on the examination of the fracture surface

under a scanning electron microscope (SEM) the different topologies are a clear indication that different micro-level mechanisms are present and distinct from proportional experiments.

4. Numerical Simulation

The corresponding numerical simulations with an user-defined material routine are presented and its results compared with the experimental data by force-displacement diagrams and with strain fields determined by DIC. The simulations are used to detect stress states as well as plastic and damage fields within the notched regions of the specimen. This different development of stress states is as well apparent in the numerical simulations and provides valuable information regarding the stress state and its influence on the ongoing material deterioration.

5. Conclusions

An experimental program with a biaxial specimen under proportional and non-proportional loading conditions has been presented. The exemplarily shown loading ratios displayed clear differences under proportional and non-proportional load in the localization development of principal strains in the critical notch area. A path-dependent damage behavior therefore is clearly indicated and thus additional information regarding the damage and failure processes can be extracted. Consequently, the presented specimen can be used to study the material behavior in an efficient way under different stress states and loading histories.

6. References

[1] J. Wang, CL. Chow (1989), Mixed mode ductile fracture studies with nonproportional loading based on continuum damage mechanics, *J. Eng. Mater. Tech.*, 111, 204-209.

[2] C. Chow, T. Lu (1992). An analytical and experimental study of mixed-mode ductile fracture under nonproportional loading, *Int. J. Damage Mech.*, 1, 191–236.

[3] M. Brünig (2003). An anisotropic ductile damage model based on irreversible thermodynamics, *Int. J. Plasticity* ,19, 1679-1713.

[4] Y. Bai, T. Wierzbicki (2008). A new model of metal plasticity and fracture with pressure and Lode dependence, *Int. J. Plasticity*, 24, 1071-1096.

[5] M. Brünig, O. Chyra, D. Albrecht, L. Driemeier, M. Alves (2008). A ductile damage criterion at various stress triaxialities, *Int. J. Plasticity*, 24, 1731-1755.

[6] X. Gao, G. Zhang, C. Roe (2010). A study on the effect of the stress state on ductile fracture, *Int. J. Damage Mech.*, 19, 75-94.

[7] L. Driemeier, M. Brünig, G. Micheli, M. Alves (2010). Experiments on stress-triaxiality dependence of material behavior of aluminum alloys, *Mechanics of Materials*, 42, 207–217.

[8] M. Brünig, S. Gerke, V. Hagenbrock (2013). Micro-mechanical studies on the effect of the stress triaxiality and the Lode parameter on ductile damage, *Int. J. Plasticity*, 50, 49–65.

[9] S. Gerke, P. Adulyasak, M. Brünig (2017). New biaxially loaded specimens for the analysis of damage and fracture in sheet metals, *Int. J. Solids Struct.*, 110-111, 209-218.

[10] S. Gerke, M. Zistl, A. Bhardwaj, M. Brünig (2019). Experiments with the X0-specimen on the effect of non-proportional loading paths on damage and fracture mechanisms in aluminum alloys, *Int. J. Solids Struct.*, 163, 157–169.

[11] M. Brünig, S. Gerke, and M. Zistl (2019). Experiments and numerical simulations with the Hspecimen on damage and fracture of ductile metals under non-proportional loading paths, *Eng. Fracture Mechanics*, 217, 106531.

INSPECTIONS USING DIFFERENTIAL INTERFERENCE CONTRAST MICROSCOPE BASED ON SHEARING INTERFEROMETRY

S.-T. Lin and H.-H. Lai

Department of Electro-Optical Engineering, National Taipei University of Technology, 1, Sec.3, Chung-Hsiao East Road, Taipei 10608, Taiwan

1. Abstract

In this research, a phase-shifting differential interference contrast microscope (DICM) using a Savart prism as the shear plate and rotatable analyzer as the phase-shifter is proposed; by which, the obtained phase-image is proportional to the derivative of optical path length of the beam through the sample, the defects of the sample can therefore be inspected with with higher image contrast. This paper introduces the apparatus, measurement theory, experimental setup, and experimental results of the proposed interferometer, the results agree the validity and feasibility of the DICM.

2. Introduction

The uses of transparent samples such as optical elements, glass- and silicon-wafers have increased over the past few years in fields of vision, bio-MEMs, CMOS and semiconductor industries. Since, there are several kinds of defects such as cracks, delamination, particles and voids that are affected to quality of their products; therefore four main instruments, scanning acoustic microscopes (SAMs) [1], scanning electron microscopes (SEMs) [2,3], optical instruments (OIs) [4], and optical interference microscopes (OIMs) [5], are proposed for detecting defects of transparent sample. However, SAMs have to soak samples in water (or other liquids), SEMs are time consuming, OIs are with low image contrast, and OIMs are sensitive to enviromental perturbations.

3. Apparatus and measurement theory
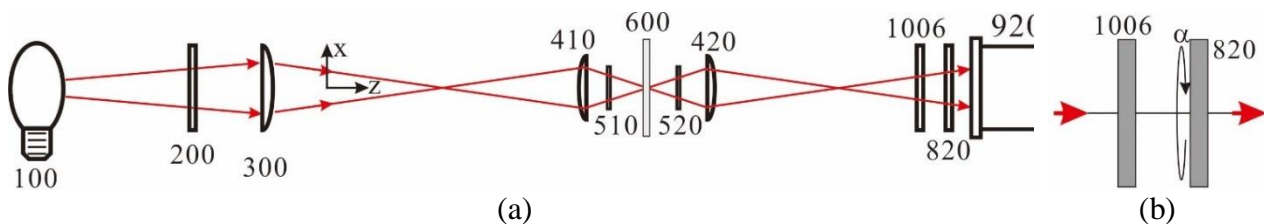
Fig. 1. (a) Apparatus of the proposed microscope, where 100, 200, 300, 410, 510, 600, 520, 420, 1006, 820, and 920 represent light source, polarizer, convergent lens, objective, Savart prism, sample, Savart prism, objective, quarter-wave plate, analyzer, and CCD sensor, respectively; (b) magnification of the phase-shifter

A phase-shifting differential interference contrast microscope (DICM) as that shown in Fig. 1 is proposed for surmounting the abovementioned problems, where the polarizer is with its transmission axis parallel to the x-axis, the left Savart prism is with its principal section having an angle of 45° with respect to the x-z plane, the right Savart prism which is an inverted one of the left one is utilized to shear the wavefront from the sample into two identical ones with perpendicular vibrations and a lateral shear distance of Δx, the quarter-wave plate is with its fast-axis parallel to the x-axis, and the analyzer is with its transmission axis having an angle α measured from the x-axis.

The sheared beams emerging from the right Savart prism then travel through the right objective, quarter-wave plate, and analyzer to generate a shearing interference pattern on the CCD sensor. A derivation and a numerical calculation regarding this pattern have been done, the results prove that the intensity of the interference pattern has a form of

$$(1) \qquad \mathbf{I} = \mathbf{I}_0[1 + \gamma \sin(\Delta\phi_x + 2\alpha)]$$

where

$$(2) \qquad \Delta\phi_x = \frac{4\pi}{\lambda_c}\Delta\Lambda(x,y) = \frac{4\pi}{\lambda_c}\frac{\partial\Lambda(x,y)}{\partial x}\Delta x$$

and λ_c and $\Lambda(x,y)$ in Eq.(2) symbolize central wavelength and optical path length, respectively, of the light source through the sample.

This convinces us that the proposed microscope is a DICM. Since, as conventional DICMs, it is able to acquire DIC images (i.e. images of Eq. (1)) by just recording the patterns on the CCD sensor and extract phase-DIC images (i.e. images of Eq. (2)) by phase- shifting algorithms [6]. Note the phase-shifting images for the phase-shifting algorithm are the DIC images with phase shifts of 2α.

4. Experimental setup and Experimental results

A setup of the proposed DICM was installed and then conducted to retrieve the DIC images and phase-DIC image of a transmission grating and contact lens with bubble defects, the results confirm the validity and feasibility of the proposed DICM.

To get the images with shear direction along the y-axis, the DICM can just rotate the Savart prism about the z-axis by 90° and then repeat the same process of x-direction measurements; this function has already been verified using experimental results.

5. Acknowledgement

6. References

[1] H. K. Wickramasinghe, "Scanning acoustic microscopy: a review," *J. of Microsc. 129*, 63-73, 1983.

[2] M. Kuwajima, J. M. Mendenhall, L. F. Lindsey, and K. M. Harris, "Automated Transmission-Mode Scanning Electron Microscopy (tSEM) for Large Volume Analysis at Nanoscale Resolution," *PLoS ONE 8*, e59573, 2013.

[3] R. Nakagaki, T. Honda and K. Nakamae, "Automatic recognition of defect areas on a semiconductor wafer using multiple scanning electron microscope images," *Meas. Sci. Technol. 20*, 075503, 2009.

[4] J. Höglund, Z. Kiss, G. Nadudvari, Z. Kovacs, S. Velkei, C. Moore, V. Vartanian and R. A. Allen, "Detection and characterization of three-dimensional interconnect bonding voids by infrared microscopy," *J. Micro/Nanolith. MEMS MOEMS 13*, 011208, 2014.

[5] V. H. F. Munoz, N. I. T. Arellano, D. I. S. Garcia, A. M. Garcia, G. R. Zurita, and L. G. Lechuga, "Measurement of mean thickness of transparent samples using simultaneous phase shifting interferometry with four interferograms," *Appl. Opt. 55*, 4047-4051, 2016.

[6] D. Malacara, Optical Shop Testing, 3rd. Ed, John Wiley & Sons (Hoboken, New Jersey), 547-666, 2007.

DEVELOPMENT OF NOVEL HOT STAMPING TECHNOLOGY PROCESS OF TITANIUM ALLOY

M. Kopec[1,2], K. Wang[3], Z.L. Kowalewski[1] and L. Wang[2]

[1] *Institute of Fundamental Technological Research, Polish Academy of Sciences, Pawinskiego 5B, 02-106 Warsaw, Poland*
[2] *Department of Mechanical Engineering, Imperial College London, London SW7 2AZ, UK*
[3] *State Key Laboratory of Advanced Welding and Joining, Harbin Institute of Technology, Harbin 150001, China*

1. Introduction

In order to meet fuel consumption targets for the aviation sector, increasing demands for low density and high strength materials were observed. In this specific sector, low strength structural components are commonly produced from aluminum alloys, and high strength structural components are made from titanium alloys [1]. The main problem during hot forming of complex-shaped components from titanium alloys is time, energy and cost intensive. The aircraft industry currently uses methods such as superplastic forming (SPF) [2], superplastic forming with diffusion bonding (SPF-DB) [3], hot stretch forming [4], creep forming [5], hot gas-pressure forming [6] or isothermal hot forming [7, 8] to produce complex-shaped structural components. However, these techniques usually require a very high temperature, slow strain rate and simultaneous heating of tools and sheet during the forming process. These characteristics gradually decrease productivity, and proportionally increase the cost of production. For example in conventional hot stamping using a furnace, the heating time of forming tools exceed the time of 2 h [9]. In order to increase the productivity of forming processes, new forming techniques such as the solution heat treatment, forming and in-die quenching [10], the Quick-plastic forming [11], and the hot stamping using rapid heating [9,12] have been developed. One promising solution to overcome low efficiency/high cost problem found in traditional techniques is using the hot stamping process to form complex-shaped components from sheet metal with cold dies, and rapidly quenching the workpiece in the dies simultaneously. The hot stamping process promises to reduce the tool wear commonly found in conventional hot forming processes and be an overall more efficient and economical process when compared to conventionally used isothermal hot forming techniques [9]. Traditional hot stamping processes have mainly focused on forming lightweight alloys, such as aluminium alloys and ultrahigh strength steels, for the automotive industry. However, few references can be found focusing on the hot stamping of titanium alloys. Recently, there has been an increased demand for titanium components in the aerospace industry due to their high strength to weight ratio, excellent temperature stability and corrosion resistance [13,14]. Therefore, there is a clear need to study the hot stamping of titanium alloys to achieve required mechanical performance whilst reducing manufacturing cost.

2. Results

A novel hot stamping process for titanium alloys using cold forming tools and a hot blank was studied in this work. Uniaxial tensile tests at temperatures ranging from 600 to 900 °C and strain rates ranging from 0.1 to 10 s^{-1} were conducted to investigate the formability of Ti6Al4V alloy. The microstructure and post-form properties of the material were monitored during tests to characterize the flow behaviour of investigated alloy. Hot stamping tests were performed in a wide temperature range to verify the feasibility of the novel process for the Ti6Al4V alloy. The formability of the material under isothermal conditions increased with the increasing temperature and decreasing strain

rate. A satisfactory elongation ranging from 30% to 60% could be achieved at temperatures ranging from 750 to 900°C respectively. During testing at various temperatures, a different microstructure evolution mechanisms were observed. In the range from 600 to 700°C, the main mechanism was recovery; whereas from 750 to 950°C, the main mechanism was transformation and recrystallization. The hardness of the material after deformation first decreased with the temperature due to recovery at 750°C, and subsequently increased due to the phase transformation and recrystallization at 900°C. During the hot stamping tests, qualified parts could be formed successfully at heating temperatures ranging from 750 to 850°C. By using the proposed novel hot stamping technology, a wing stiffener component made of Ti6Al4V titanium alloy was formed.

Keywords: Titanium alloys; Hot stamping, Formability; Post-form strength

3. References

[1] M. Peters, J. Kumpfert, C. H. Ward, and C. Leyens, "Titanium alloys for aerospace applications," *Adv. Eng. Mater.*, vol. 5, no. 6, pp. 419–427, 2003.

[2] D. Serra, "SUPERPLASTIC FORMING APPLICATIONS ON AERO ENGINES . A REVIEW OF ITP MANUFACTURING PROCESSES AERO ENGINES . A REVIEW OF ITP," 2009.

[3] H. Yang, X. G. Fan, Z. C. Sun, L. G. Guo, and M. Zhan, "Recent developments in plastic forming technology of titanium alloys," *Sci. China Technol. Sci.*, vol. 54, no. 2, pp. 490–501, 2011.

[4] A. Astarita, E. Armentani, E. Ceretti, L. Giorleo, P. Mastrilli, V. Paradiso, F. Scherillo, A. Squillace, and C. Velotti, "Hot Stretch Forming of a Titanium Alloy Component for Aeronautic: Mechanical and Modeling," *Key Eng. Mater.*, vol. 554–557, no. January, pp. 647–656, 2013.

[5] T. Deng, D. Li, X. Li, P. Ding, and K. Zhao, "Hot stretch bending and creep forming of titanium alloy profile," *Procedia Eng.*, vol. 81, no. October, pp. 1792–1798, 2014.

[6] K. Wang, G. Liu, K. Huang, D. J. Politis, and L. Wang, "Effect of recrystallization on hot deformation mechanism of TA15 titanium alloy under uniaxial tension and biaxial gas bulging conditions," *Mater. Sci. Eng. A*, vol. 708, pp. 149–158, 2017.

[7] T. Raghu, I. Balasundar, and M. Sudhakara Rao, "Isothermal and near isothermal processing of titanium alloys," *Def. Sci. J.*, vol. 61, no. 1, pp. 72–80, 2011.

[8] A. G. Ermachenko, R. Y. Lutfullin, and R. R. Mulyukov, "Advanced technologies of processing titanium alloys and their applications in industry," *Rev. Adv. Mater. Sci.*, vol. 29, no. 1, pp. 68–82, 2011.

[9] Z. Hamedon, K. Mori, and T. Maeno, "Hot Stamping of Titanium Alloy Sheet Using Resistance," pp. 12–15, 2013.

[10] J. Liu, H. Gao, O. El Fakir, L. Wang, and J. Lin, "HFQ forming of AA6082 tailor welded blanks," *4th Int. Conf. New Form. Technol.*, vol. 5006, p. 6082, 2015.

[11] P. F. Bariani, S. Bruschi, A. Ghiotti, and F. Michieletto, "Hot stamping of AA5083 aluminium alloy sheets," *CIRP Ann. - Manuf. Technol.*, vol. 62, no. 1, pp. 251–254, 2013.

[12] T. Maeno, K. ichiro Mori, and R. Yachi, "Hot stamping of high-strength aluminium alloy aircraft parts using quick heating," *CIRP Ann. - Manuf. Technol.*, vol. 66, no. 1, pp. 269–272, 2017.

WHICH PATTERN FOR MULTISCALE DIGITAL IMAGE CORRELATION?

R. Fouque[1,2], R. Bouclier[1,3], J.-C. Passieux[1] and J.-N. Périé[1]
[1] *Institut Clément Ader, CNRS UMR 5312, Université de Toulouse,*
INSA/ISAE/Mines Albi/UPS, Toulouse, France
[2] *DGA Aeronautical Systems, Balma, France*
[3] *Institut de Mathématiques de Toulouse, CNRS UMR 5219, Université de Toulouse,*
INSA/UT1/UT2/UPS, Toulouse, France

In Digital Image Correlation (DIC), patterns deposited on test objects are of great importance because measurement accuracy intensely relies on their characteristics. Numerous experimental methods are generally used in order to generate patterns on test samples such as airbrush and marker pen at large scales, or focused ion beam (FIB) technique and spin coating at small scales. For most of these techniques, corresponding measurement accuracy are strongly dependent on operators' experience. Concurrently, the need for test standardisation and robustness in the industrial context pushes towards the emergence of methods able to generate patterns with high reproducibility.

For these reasons, some work was done to assess the quality of a given pattern, so as to be able to generate patterns adequately in a second step. Some papers focused on the influence of speckle features, and an optimal speckle size of 2 to 5 pixels was defined. However, let us emphasize that this point of view is linked to some pattern generation techniques (particularly airbrush and marker pen), and assumes, for instance, that a typical speckle size can be defined.

At the same time, a need for full-field measurements at different scales arises [2,5] because it allows to reduce both computational cost and hardware requirements. In this context, defining pattern optimality in terms of pixel size seems problematic since different cameras with various optical resolutions will be used to observe it.

To circumvent this issue, another path is to build pattern quality criteria based on global parameters [1,3]. Strictly speaking, and until now, patterns generated for multiscale applications should be considered more as biscale patterns than as proper multiscale patterns, because they are optimised for two different camera magnifications [2,4]. However, in industrial contexts, the different scales of interest are not always known prior to the experiments, and an **actual multiscale pattern** would be of great help. In addition, pattern multiscale properties would facilitate the initialisation step in DIC when using a multigrid approach.

In this work, the main qualities expected from a pattern are reviewed and corresponding criteria based on its auto-correlation function are extracted. Then a method to numerically generate patterns from a desired auto-correlation function is proposed. As an illustration, Figure 1 shows the desired auto-correlation function for a suitable, multiscale pattern. We also plot in this Figure the autocorrelation function associated to the actual generated pattern using the proposed methodology. More precisely, a correlation-length-free pattern is obtained. It should be pointed out that, in this pattern, no speckle size is more prominent than another, which naturally makes it a suitable multiscale pattern, as demonstrated in Figure 2. In particular, this Figure also shows a 4x4-pixel subsampling of the pattern. In this subsampling, each pixel grey level value is equal to the mean over more than 260 000 pixels of the original 2048x2048-pixel picture. The subsampled picture dynamic range is still greater than 90 grey levels. Given the zoom level, this large dynamic range is an interesting result for multiscale applications where cameras with different levels of magnification are combined. Numerical experiments are performed for three different imposed displacement fields and results for the generated pattern are compared with a random one. Significant improvements in terms of robustness and accuracy are exhibited.
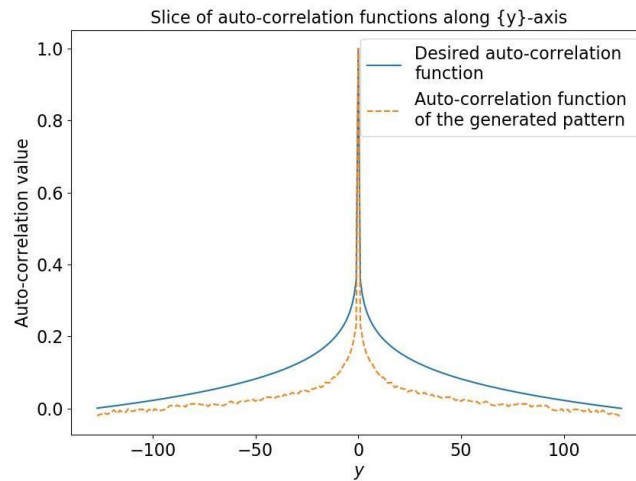
Fig. 1. Comparison between the desired auto-correlation function (solid blue curve) for the pattern and its actual auto-correlation (dashed orange curve)
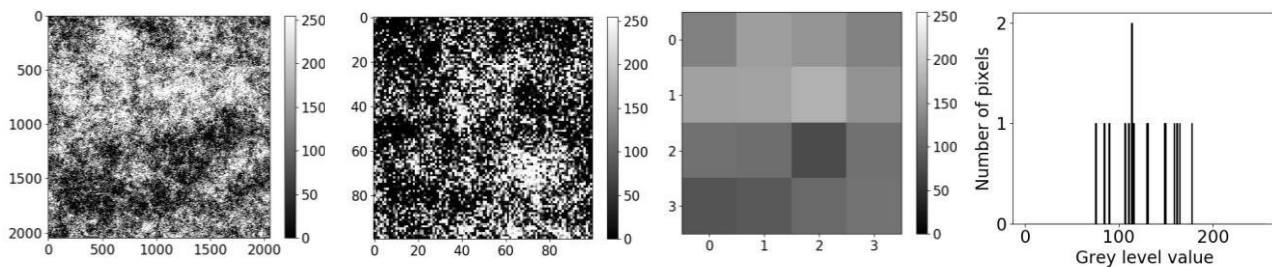
Fig. 2. The first picture is the generated pattern. The second picture is a zoom on a 100x100pixel square of the 2048x2048-pixel original one. The third picture is a subsampling of the considered pattern. The last one is the grey level distribution of the subsampling

References

[1] G. Bomarito, J. Hochhalter, T. Ruggles and A. Cannon. (2017). Increasing accuracy and precision of digital image correlation through pattern optimization, *Opt. Lasers Eng.*,**91**, 73 – 85.

[2] G. Bomarito, J. Hochhalter and T. Ruggles. (2018). Development of optimal multiscale patterns for digital image correlation via local grayscale variation, *Exp. Mech.*, **58**(7), 1169– 1180.

[3] S. Bossuyt (2013). Optimized patterns for digital image correlation. In: H. Jin, C. Sciammarella, C. Furlong, S. Yoshida (eds.) *Imaging Methods for Novel Materials and Challenging Applications*, Volume 3, 239–248. Springer New York, New York, NY.

[4] M. Mathew, A. Ellenberg, S. Esola, M. McCarthy, I. Bartoli and A. Kontsos. (2018). Multiscale deformation measurements using multi-spectral optical metrology. *Struct. Control Health Monit.*, **25**(6), e2166.

[5] J.-C. Passieux, F. Bugarin, C. David, J.-N. Périé, and L. Robert (2015). Multiscale displacement field measurement using digital image correlation: Application to the identification of elastic properties. *Exp. Mech.*, **55**(1), 121–137.

RESEARCH AND DEVELOPMENT OF A MULTI-FUNCTION CONFOCAL INTEFEROMETER USING DIFFRACTIVE OPTICAL ELEMENT

W.-C. Wang and C.-Y. Lin
Department of Power Mechanical Engineering, National Tsing Hua University
Hsinchu, Taiwan, Republic of China

1. Introduction

To improve the efficiency of the manufacturing process, a fast and accurate inspection device is essentially needed. By integrating a self-developed multi-wavelength confocal interferometer (MWCI) [1, 2] system with the confocal thickness measurement scheme [3], a multi-function chromatic confocal interferometric system (MFCCIS) [2] was constructed in this paper. By employing the axial dispersion feature of the diffractive optical element (DOE) [4], the MFCCIS can be used for real-time height and thickness measurements. In experiments, the measurement results of a standard step height specimen of step height 50μm was used to study the accuracy of the MFCCIS. Besides, thickness measurement results of the ultra-thin glass plate of thickness 103μm was obtained by the MFCCIS.

2. Experimental Setup

Based on MWCI, a self-constructed MFCCIS was developed, the broadband of spectrum of the light source was ~300nm and centered on 550nm. A combination of spatial filter and lenses was used to collimate the initial light field. A beam splitter was used to separate the collimated light field into objective light and reference light. In the objective light, a DOE was adopted to disperse the light field. Finally, after the objective light and the reference light were respectively reflected by specimens and the reference mirror and propagated back to the beam splitter, two light fields were merged into an interference light field. A single-point spectrometer was employed to capture the interference signal.

3. Results and Discussions

Figure 1 shows the result of profile reconstruction after two-dimensional scanning. It can be observed that the 3D profile of the standard step height specimen is well revealed.
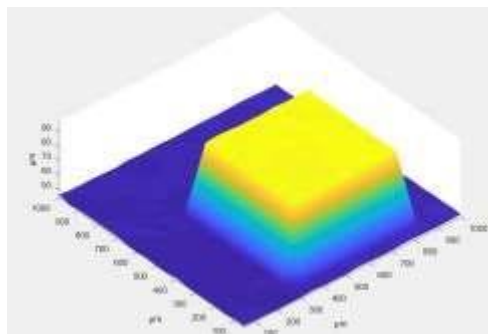
Fig. 1. Experimental result of standard step height specimen

The position chosen to analyze the accuracy of height measurement of MFCCIS was at the centerline of the specimen. The average height obtained from ten times measurement is 50.681µm with a standard deviation of 0.209µm. The accuracy can be obtained by the following equation

$$(1) \qquad Accuracy(\%) = \frac{Measurement\ Result - Actual\ Value}{Actual\ Value} \times 100\%$$

From Eq. (1), the average accuracy of MFCCIS in the measurement of a step height of 50µm is 1.332%.

For the experimental results of thickness measurement, the average thickness of the ultra-thin glass plate is 103.833µm with a standard deviation of 3.838µm from thirty times measurement. The sources of error could be inferred to the low signal to noise ratio caused by the non-equivalent light intensities between objective arm and reference lights and the spherical aberration caused by the optical elements used in the setup.

4. Conclusions

The MFCCIS was proposed in this paper. The interference signal can be used not only for height measurement but also for thickness measurement. At the current stage, the experimental height measurement results of a standard step height specimen and the thickness measurement results of an ultra-thin glass plate both show a quite high accuracy and prove the feasibility of MFCCIS.

5. Acknowledgements

6. References

[1] T. F. Wang, "Research and Development of Multi-wavelength Confocal Interferometer by Using Diffractive Optical Element", M. S. Thesis, Department of Power Mechanical Engineering, National Tsing Hua University, Hsinchu, Taiwan, Republic of China, November, 2018.

[2] C. Y. Lin, "Research and Development of A Multi-function Chromatic Confocal Interferometric System", M. S. Thesis, Department of Power Mechanical Engineering, National Tsing Hua University, Hsinchu, Taiwan, Republic of China, November, 2019.

[3] T. Boettcher, M. Gronle and W. Osten, "Multi-Layer Measurement Using a New Hybrid Single-Shot Technique: Chromatic Confocal Coherence Tomography (CCCT)," *Optics Express*, Vol. 25, pp. 10204-10213, 2017.

[4] D. Duque and J. Garzón, "Effects of both Diffractive Element and Fiber Optic Based Detector in a Chromatic Confocal System," *Optics and Laser Technology*, Vol. 50, pp. 182-189, 2013.

USE OF METALLIC STRAIN GAUGES FOR TORQUE MAGNETOMETRY: APPLICATION TO THE CONTACTLESS CHARACTERIZATION OF LARGE MAGNETIZED SUPERCONDUCTING SAMPLES

S. Brialmont[1,2], J.F. Fagnard[1] and P. Vanderbemden[1]
[1] University of Liege, Department of Electrical Engineering and Computer Science, Liege, Belgium
[2] Recipient of a FRIA FRS-FNRS fellowship

1. Introduction

The context of this research is the need of non-destructive characterization techniques for magnetized samples of relatively large size (> 10 mm). The magnetic materials of interest are either permanent magnets or bulk superconductors. Due to the ability of superconductors to carry large electric currents with no loss when cooled at cryogenic temperature (typically $T < 100$ K), they are able to trap large permanent current loops generating a strong magnetic field. A bulk magnetized superconducting material, therefore, behaves like a quasi-permanent magnet, also called 'trapped flux magnet'. Such trapped flux magnets may generate flux densities of several teslas [1], which is well beyond the flux density generated by conventional ferromagnets. Since the magnetic properties are due to macroscopic current loops, they depend on the size of the superconductor. A suitable characterization of the magnetic moment cannot be carried out on small samples cut out of the trapped field magnet. This requires the design of magnetometers that are able to accommodate samples of large size, typically above 10 mm in diameter. In this work we show how this can be achieved with torque measurement based on metallic strain gauges.

Magnetometry using torque measurements has been applied successfully in the last decades to measure accurately the magnetic moment of small samples (see e.g. [3]). The method usually relies on magnetizing the sample and then applying a magnetic field tilted at a given angle with respect to the magnetization direction. The resulting torque, measured experimentally, is used to determine the magnetization of the trapped field magnet. This technique, however, was demonstrated on samples of a few mm³, with torques typically smaller than 10^{-5} Nm. The purpose of the present work is to demonstrate that it can be applied to the measurement of torques up to 1 Nm.

2. Experiment

A bespoke torque magnetometer was constructed for operation either at room temperature or at liquid nitrogen temperature (77 K) [3]. The torque is measured with a metallic strain gauge bridge (HBM 1-VY43-3/350) mounted on an aluminum transmission shaft, as shown schematically in Fig. 1a. The shaft allows the sample to be located between two poles of a water-cooled electromagnet, the poles are 46 mm apart. The sample holder can accommodate samples up to 17 mm in diameter. The sample can be placed at two orthogonal directions with the applied field, namely with (i) the main axis parallel to the field during the magnetization procedure and (ii) the main axis perpendicular to the field for the generation of the torque to be measured. In so doing the sample is subjected to a field perpendicular to its main magnetization, which can lead to a demagnetization effect [4]. This effect is also worth to be investigated in view of engineering applications. When the magnetometer is operated at 77 K, the strain gauge bridge is maintained within its recommended operating temperature range (here ~ 242 K) using a Lake Shore temperature controller, a thermofoil heater and a Pt 100 temperature sensor thermally anchored to the shaft (Fig. 1b). The output signal of the bridge fed at 63 Hz is measured with an EG&G 7260 DSP Lock-in amplifier, allowing a relative bridge sensitivity down to ~ 2×10^{-8} to be achieved.

3. Results

Figure 1c shows the bridge output voltage as a function of the magnetic field, perpendicular to the axis of a calibration coil fed with a known DC current. The data are compared to the theoretical voltage expected from the bridge sensitivity, shear modulus and shaft diameter. Figure 1d shows the magnetic moment of a bulk sample made of a stack of $YBa_2Cu_3O_7$ superconducting tapes (12 x 12mm) at 77 K, measured experimentally with the torque magnetometer, and being slightly affected by the transverse applied field. Successful operation of the device was also demonstrated with a 15 mm diameter Nd-Fe-B magnet. The latter leads to measured magnetic moments > 1 Am², i.e. two orders of magnitude above what can be achieved with off-the shelf magnetometers.
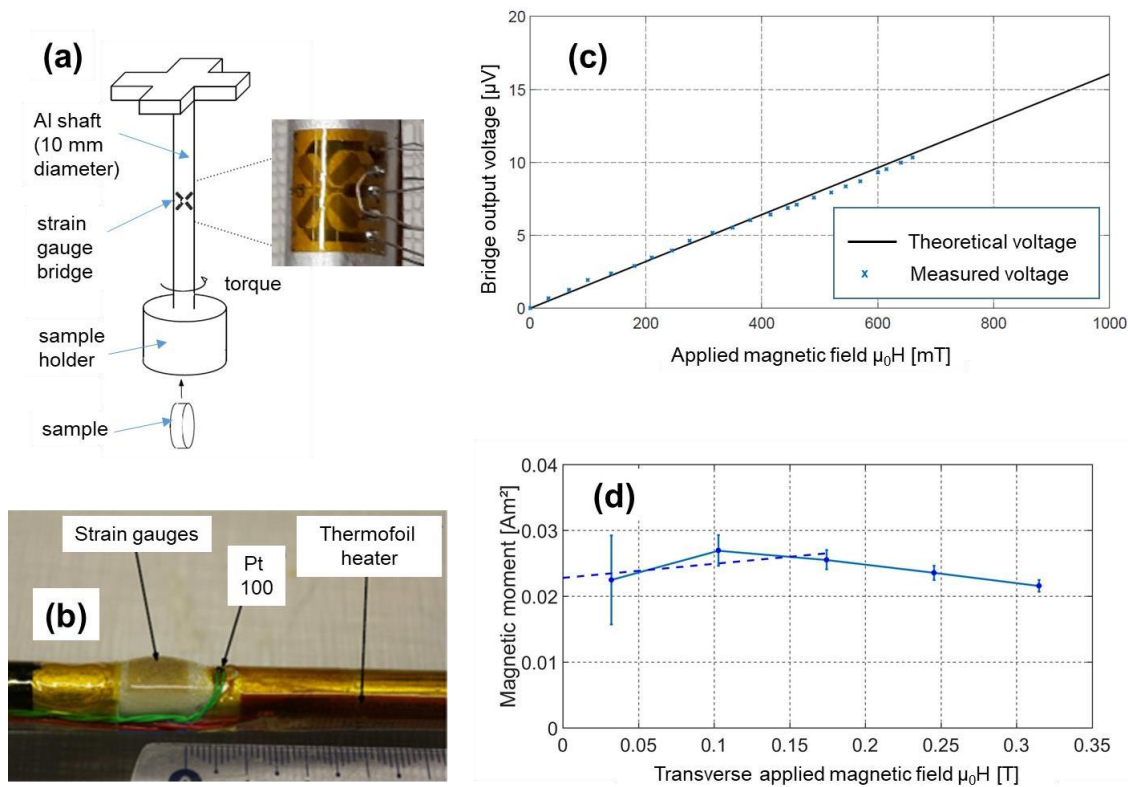
Fig. 1. (a) Schematic illustration of the torque transmission system (b) Photograph of the fully mounted bridge (c) Output signal measured at room temperature; the sample is a copper coil fed with DC current for absolute calibration (d) Magnetic moment at 77 K of a magnetized bulk stack of $YBa_2Cu_3O_7$ superconducting tapes as a function of the transverse applied magnetic field

4. References

[1] J. H. Durrell et al. (2018). Bulk superconductors: a roadmap to applications, *Supercond. Sci. Technol.* **31**, 103501.

[2] S. Kohout, J. Roos and H. Keller (2007). Novel sensor design for torque magnetometry, *Rev. Sci. Instrum.* **78**, 013903.

[3] S. Brialmont, J. F. Fagnard and P. Vanderbemden (2019). A simple torque magnetometer for magnetic moment measurement of large samples: Application to permanent magnets and bulk superconductors, *Rev. Sci. Instrum.* **90**, 085101.

[4] Z. Hong et al. (2008). The numerical modeling and measurement of demagnetization effect in bulk YBCO supercond. subjected to transverse field, *IEEE Trans. Appl. Supercond.* **18**, 1561.

MOISTURE CONTENT INFLUENCE ON THE ROLLING SHEAR BEHAVIOUR OF SPRUCE CLEAR WOOD

S.T. Akter[1], T.K. Bader[1] and L. Muszyński[2]
[1] Department of Building Technology, Linnaeus University, Sweden
[2] Oregon State University, Corvallis, OR, USA

1. Introduction

The use of wood as a construction, and thereby, structural material is increasing, due to the renewable characteristics of wood and its potential for reducing the carbon footprint of the construction sector. As a result, engineering wood-based products, such as cross-laminated timber (CLT), have gained much attention during the last decade. Particularly CLT has great potential to replace concrete in multi-storey buildings.

However, when loaded in bending, the transverse or cross-layers of CLT panels develop shear stresses in the radial-tangential plane of the orthotropic material, often referred to as rolling shear. Wood may be approximated as a cylindrical orthotropic material, in which stiffness and strength vary in three orthogonal directions. Since rolling shear modulus and strength of wood are comparably low, they play an important role in the overall mechanical response of CLT. Rolling shear however, is one of the least investigated properties of wood. Due to the cellular and hygroscopic structure of the wood tissue, stiffness and strength are strongly influenced by moisture content. This effect is considered in the European structural design standard, Eurocode 5 by service classes for certain temperature and moisture conditions. The coefficients, k_{mod} and k_{def}, account for moisture influence on the strength and stiffness of wood, respectively and they are equal for all strength and stiffness properties, respectively. However, alike stiffness and strength of wood, the effect of moisture varies with the loading direction and type of loading. This study aims at investigating the influence of moisture content on rolling shear modulus and strength by means of experimental investigations. Moreover, time-dependent effects in combination with moisture content are investigated and preliminary results are presented.

2. Previous research

Several researchers (see e.g. [1-2]) investigated the influence of moisture on mechanical properties of wood, except for effects on the rolling shear behavior. Gerhard [2] summarized effects of moisture content on mechanical properties of Norway spruce, but rolling shear was not included due to lack of data. Aicher and Dill-Langer [3] investigated the influence of annual ring patterns on rolling shear behavior and considered rolling shear as an intrinsic material property. To measure rolling shear behavior is a challenging task considering the difficulties of having uniform and pure shear stresses in a well-defined specimen volume. Several shear test fixtures have been developed for this purpose, e.g., Iosipesco, Arcan, Single cube apparatus and two or three-rail shear fixture [4]. Several modifications of these fixtures prove the complexity of developing pure shear in the region of interest in the specimen.

3. Materials and methods

A novel test set-up was developed for studying biaxial stress states in the transverse plane of wood [5]. Since this test setup allows to control the transverse force in shear loading, it was used herein to investigate the rolling shear behavior. Dog-bone shaped specimens with a size of 50×60×20 mm³

(width×height×thickness) and a load transfer set-up consisting of spiked steel plates were found suitable for shear testing. The present study was carried out on Norway spruce specimens at four different moisture contents from 3.5 (A), 13.0 (B), 18.6 (C) to 24.5% (D), spanning over all service classes according to Eurocode 5. Corresponding densities at the abovementioned moisture contents amounted to 437 (A), 457 (B), 470 (C), and 479 kg/m^3 (D). Specimens have been stored in a climate room at 20 °C and 65% relative humidity, or in closed plastic boxes with saturated salt solutions, at 20°C room temperature. Lithium bromide, potassium chloride and potassium sulphate were used for series A, C and D to maintain a relative humidity of about 8%, 80% and 92%, respectively. Tests have been performed in a biaxial test frame, which can be run in a load control or displacement control mode in two orthogonal directions. Shear tests were run in displacement control mode with a ramp rate of 0.5 mm/min.
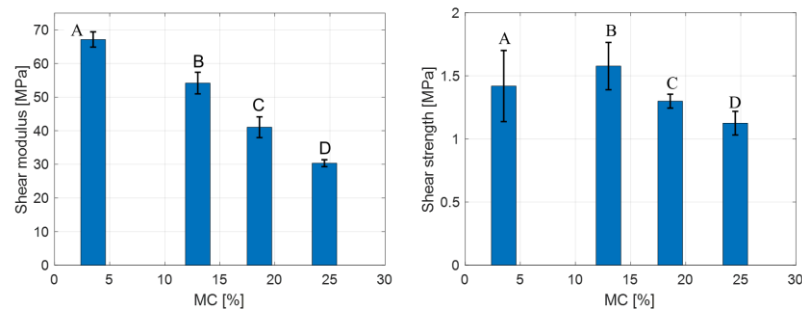
Fig. 1. Variation of shear modulus and strength with MC

4. Results

Results showed that the moisture content has a great influence on rolling shear modulus and strength. Shear modulus varied from 30 N/mm^2 at 24.5% MC to 67 N/mm^2 at 3.5% MC and strength varied from 1.12 N/mm^2 at 24.5% MC to 1.58 N/mm^2 at 3.5% MC. Rolling shear modulus increases with decreasing moisture content, which is in line with Gerhard's summarized results for longitudinal shear [2]. Strength increased with decreasing moisture content from 24.5% to 13%. A slightly decreasing trend was noticed with decreasing moisture content from 13% to 3.52%. The reason of decreasing rolling shear strength at low moisture contents could be related to the higher probability of cracks due to drying or local material imperfection. Time-dependent strains were strongly increasing with increased moisture content, which highlights the need for their assessment in the design of long-term displacements in CLT elements.

5. References

[1] Kollmann, F. (1941). The Mechanical Properties of Wood of Different Moisture Content Within -200 Degrees to +200 Degrees C Temperature Range. *VDI-Forschungsh*, 403(22), 118, (in German).

[2] Gerhards, C.C. (2007). Effect of moisture content and temperature on the mechanical properties of wood: an analysis of immediate effects. *Wood and Fiber-Science, 14*(1), 4-36.

[3] Aicher, S. and G. Dill-Langer. 2000. Basic considerations to rolling shear modulus in wooden boards. *Otto Graf Journal, 11*, 157.

[4] Dumail, J.F., Olofsson, K. & Salmen L. (2000). An analysis of rolling shear of spruce wood by the Iosipesco method. *Holzforschung, 54* (4), 420-426.

[5] Akter S.T., Bader, T.K. (2020). Experimental assessment of failure criteria for interaction of normal stress perpendicular to the grain with rolling shear stress in clear wood. *Submitted for publication.*

GALLING BEHAVIOUR IN ALUMINIUM STAMPING PROCESSES: MODELLING AND EXPERIMENTS

H. Liu, L. Wang, X. Yang and Y. Zheng
Imperial College London, London, UK

1. Introduction

Galling is a form of surface initiated damage arising from adhesive wear between sliding counterpart surfaces, and is expected to cause deteriorations of tribological performance and surface quality in aluminium stamping processes [1-3]. The galling mechanism can be classified into wear and material transfer processes. Figure 1 displays a schematic diagram of the feedback loop of source density (detachment of Al wear particles), ejection density (ejection of these particles) and third body internal density (entrapped particles at the contact) with outputs (I, III) and feedbacks (II, IV).

density of the source of third body

density of the entrapped third body at contact interface

density of the ejected third body
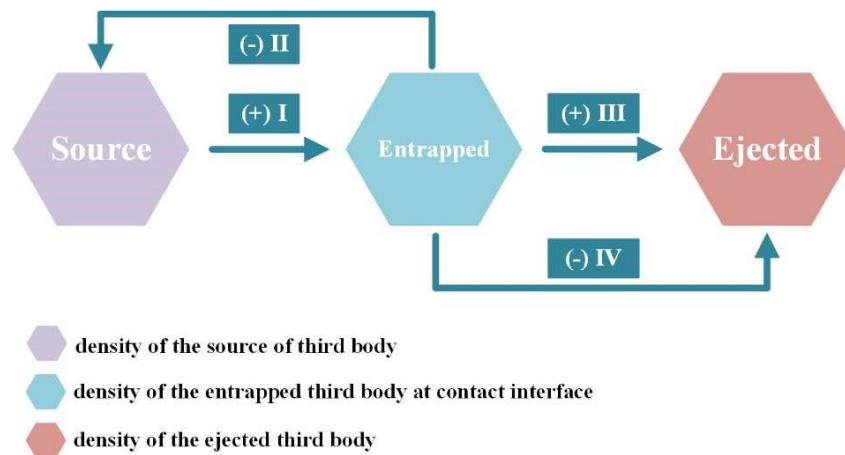
Fig. 1. Schematic illustration of material transfer loop during metal forming

Various adhesive wear or galling models have been developed by many researchers, most of them have been validated by the corresponding experiments. Hu et al. [3] proposed an interactive friction model of cold stamping process considering galling performance after the breakdown of lubrication. The density of material transfer area was applied to represent the severity of galling. Results show that higher contact loads will shorten the running-in stage and increase the saturated transfer amount as well as wear rate at the steady state. de Rooij et al. [4] discussed the galling phenomenon based on a soft workpiece contacting to a hard tool. The galling behaviour was represented as the increasing height and size of single or multi-lumps. Based upon this experimental verified lump growth model, the development of the summit height density of the tool surface caused by lump growth could be determined. Moreover, Liang et al. [5] evaluated the galling under press hardening conditions at high temperatures. The predicted galling height and growth rate were modelled and validated by corresponding tests.

However, the aforementioned galling models were established to reveal the characteristics of macro-scale performance. In addition, studies on the mechanisms of galling development and material transfer during metal forming process still needs further investigations. Hence, an experimental verified multi-scale galling model is necessary to be proposed to further reveal the galling mechanism during metal forming process.

2. Main objectives

With the view to revealing the underlying galling mechanism, experiments were conducted via an innovative autonomous testing system to characterise the galling process during aluminium stamping. The galling behaviour was multi-scale modelled incorporating the evolutions of the tribological performance and surface topography to represent the respective characteristics of various scales. Subsequently, the proposed galling multi-scale model was applied to predict the galling behaviour and was further verified by the experimental results. The multi-scale galling model is capable to reveal the multi-scale characteristics and improve the calculation efficiency simultaneously.

3. References

[1] MB. de Rooij (1998). Tribological aspects of unlubricated deepdrawing processes. Ph.D. Thesis, University of Twente, the Netherland.

[2] Gåård, Anders, Pavel Krakhmalev and Jens Bergström (2009). Influence of tool steel microstructure on origin of galling initiation and wear mechanisms under dry sliding against a carbon steel sheet. Wear, 267(1-4), 387-393.

[3] Y. Hu, Y. Zheng, D.J. Politis, M.A. Masen, J. Cui and L. Wang (2019). Development of an interactive friction model to predict aluminum transfer in a pin-on-disc sliding system. Tribol. Int., 130, 216-228.

[4] MB de Rooij, Matthias B., and Dirk J. Schipper (2001). Analysis of material transfer from a soft workpiece to a hard tool: part II—experimental verification of the proposed lump growth model. J. Tribol., 123(3), 474-478.

[5] D. Liang, L. Pelcastre, J. Hardell, B. Prakash and M. Oldenburg (2018). Experimental Evaluation of Galling Under Press Hardening Conditions. Tribol. Lett., 66(3), 93.

CURVATURE CHANGE IN LASER-ASSISTED BENDING OF INCONEL 718

J. Widłaszewski[1], M. Nowak[1], Z. Nowak[1] and P. Kurp[2]

[1] Institute of Fundamental Technological Research, Warsaw, Poland
[2] The Center for Laser Technology of Metals at the Kielce University of Technology, Kielce, Poland

1. Introduction

With a growing interest in application of high-strength and difficult-to-form materials, the processes of forming aided by local heating of the workpiece are under development in recent years. Laser-assistance has been successfully incorporated into numerous forming technologies, like bending, spinning, single point incremental forming (SPIF), roll profiling, stamping, deep drawing, stretch forming, hydroforming or wire drawing [1]. The aim of this study is an attempt to quantify the contribution of laser heating in the laser-assisted bending process.

2. Experiments

Thermo-mechanical bending experiments were conducted with specimens made of the annealed Inconel 718 nickel-based superalloy. Experimental setup is shown in Fig. 1. Each specimen (1) with the cross-section 20 x 1 mm was clamped in the cantilever arrangement. The initial pre-stress condition was realized with a holder of weights (3), which was attached at a distance 175 mm from the clamped end. In a series of five experiments the weights produced external mechanical load Q1 to Q5 of the values: 1.1, 1.57, 2.03, 2.98 and 3.91 N. Specimens loaded in the elastic range were next heated by a CO_2 laser beam (2) of CW power 500 W and laser spot 20 x 2 mm, which was moving with velocity $v = 3.33$ mm/s towards the clamped end. Each specimen was coated with a black paint in order to increase the absorption of the laser energy. The deflection (Fig. 2) of the specimen due to mechanical loading and laser heating was measured with the optical displacement sensor (5) and an auxiliary plate (4). Details of the experimental procedure are described in [2].
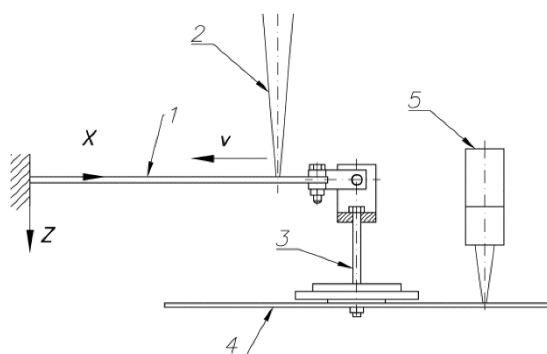
Fig. 1. Experimental setup (1 – specimen, 2 – laser beam, 3 – holder of weights, 4 – auxiliary plate, 5 – optical displacement sensor)
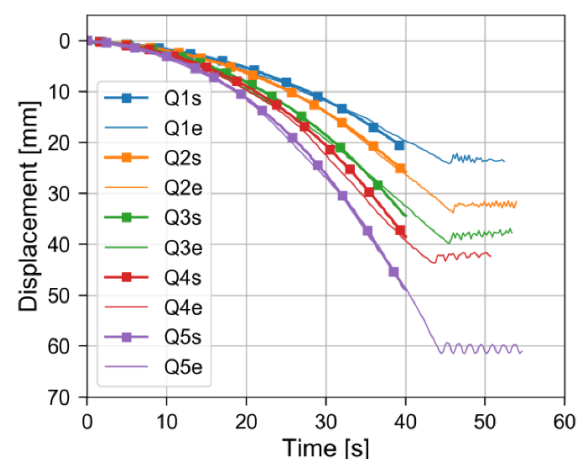
Fig. 2. A comparison of the deflection in: experiments (e) and numerical simulations (s)

3. Numerical analysis

A numerical FE model of the thermo-mechanical bending process was developed in order to: (1) validate the process modeling with the Johnson-Cook constitutive material model and (2) numerically determine the curvature (Fig. 3) of specimens in the XZ plane after mechanical loading (Q), laser heating (L) and final unloading (F). Detailed description of the material and processing modeling is presented in [2]. The curvature *C* was calculated using the parametric representation $x(s)$, $z(s)$ of the specimen configuration to account for the cases of large deflections:

(1)
$$C = \frac{|z''x' - x''z'|}{(x'^2 + z'^2)^{3/2}}$$

where ()' and ()'' denote the first and second derivative with respect to the parameter *s*, respectively.

4. Results and conclusions

The obtained dependence of specimen curvature on the bending moment is shown in Fig. 3. The red dot in Fig. 3 depicts curvature for the case of pure laser bending, i.e. without any external mechanical loading. The effect of "noise" seen in Fig. 3 can be attributed to the numerical differentiation procedure applied in calculating the curvature.
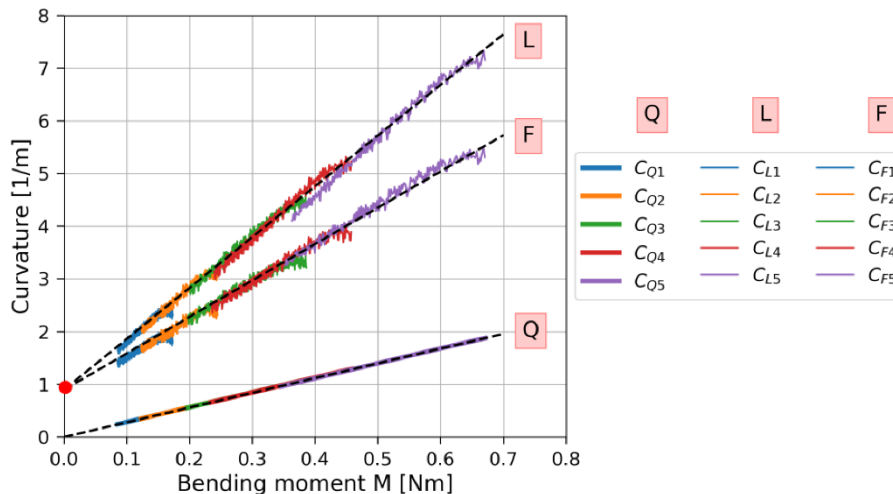
Fig. 3. Curvature dependence on the bending moment with loads Q1 to Q5, as calculated after: initial mechanical loading (Q), heating with a moving laser beam (L), final unloading (F)

The results presented in Fig. 3 suggest that the curvature after laser-induced thermo-mechanical bending process can be estimated as a linear function of the initial mechanically-induced curvature with the free term equal to the value of curvature resulting from the pure laser bending process.

5. Acknowledgements

6. References

[1] A. Kratky (2007). Laser Assisted Forming Techniques, *Proc. of SPIE,* **6346**, 634615.
[2] Z. Nowak, M. Nowak, R.B. Pęcherski, K. Wiśniewski, J. Widłaszewski and P. Kurp (2019), Computational modeling of thermoplastic behavior of Inconel 718 in application to laser-assisted bending of thin-walled tubes, *Int. J. for Multiscale Comp. Eng.*, **17** (3), 317-338.

NEW NANO INSERTS-BASED SOLUTION FOR MICRO DISPLAY OR SENSOR ASSEMBLY IN MICROELECTRONICS. EXPERIMENTS AND SIMULATIONS

C. Desbordes[1] [2], R. Pesci[2], B. Piotrowski[2], N. Raphoz[1] and O. Mailliart[1]
[1] *Univ. Grenoble Alpes, CEA, LETI, MINATEC Campus, F-38054 Grenoble, France*
[2] *ENSAM-Arts et Métiers Sciences et Technologies, LEM3 UMR CNRS 7239, 4 rue Augustin Fresnel, F-57078 Metz Cedex 3, France*

1. Introduction

The continuous evolution of microelectronic drives developments in photonic components packaging. Such components can be micro displays or sensors (in visible or IR ranges for example). Devices manufacturing requires making mechanical and electrical assemblies between a silicon reading circuit and a display or detection circuit, at the pixel scale. Improve the resolution of such devices without increasing too much components size (surfaces are already about one cm²) requires to reduce the pixel pitch (10 µm or less). A component at the SXGA resolution (HD) contains indeed more than one million micro assemblies, usually made by soldering. This hybridization technique involves to carry out thermal cycles at temperatures between 200°C and 260°C, which are not compatible with all types of components (ductile/brittle materials, thermomechanical stresses). The CEA LETI packaging laboratory develops hybridization solutions based on insertion at room temperature in order to solve this issue [1].

In this context, a new type of interconnection is developed, compatible with low pitch components (pixel pitch of 10 µm or less) [2]. The aim is to obtain efficient mechanical and electrical connections for each pixel through the interconnections. Those are composed of one or several "nano nails"-shaped inserts made of a hard material, manufactured on the reading circuit, inserted at room temperature in a ductile reception pad, manufactured on the active chip (figure 1).
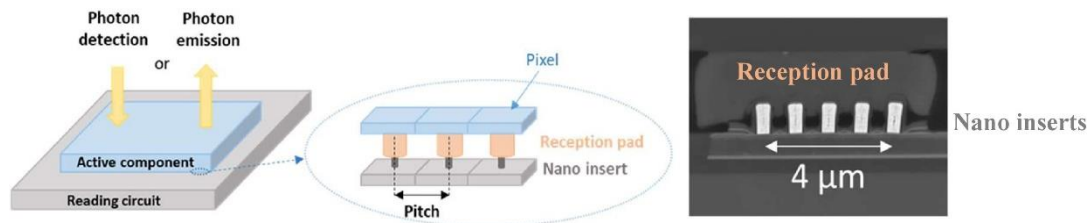
Fig. 1. Photonic component assembly solution using nano inserts-based interconnections SEM observation of an interconnection: several nano inserts pressed into an AlCu pad

2. Study and results

In order to optimize the performance of these components, it is necessary to focus on key parameters. The aim is to:
- minimize the force required for insertion while ensuring a sufficient mechanical contact,
- limit and homogenize residual stresses in the different chip layers by optimizing interconnection design,
- reduce deflection of components by improving interconnection design,
- get a good electrical conductivity in each interconnection.

Both experimental characterization and numerical simulations are investigated, through the assembly of test vehicles and finite element modelling using ABAQUS® software, respectively.

Concerning experimentations, test vehicles with different pixel pitch (equal and smaller than 10 μm) are manufactured. For each pitch, several variants of interconnection are defined with one or more nano inserts (Ø 0.5 μm) per pad and a particular arrangement of these nano inserts in the reception pad (square or round-shaped and made of aluminium alloy [3] or indium [4]). These test vehicles allow assembly process optimization on hybridization equipment and measurements of residual stresses (X-ray diffraction), electrical conductivity (probing) and deflection (interferometry).

A model of the layers stacking of the two chips with reception pad and insert(s) has been then designed at the scale of one pixel and then extrapolated to a matrix of 6*6. pixels. Numerical simulations are performed to reproduce the insertion process. A displacement is applied on the top chip to get a constant insertion of the inserts in the pads and compare all the interconnection configurations. Simulations highlight the influence of the main parameters and lead to determine an advantageous interconnection configuration since all the configurations cannot be easily experimentally tested (variation of nano inserts diameter for example).

The results show in particular for each interconnection that:
- the force required for insertion increases proportionally to the number of nano inserts pressed into the reception pad. Moreover, as the number of nano inserts increases, they are closer together and influence each other (figure 2); the force required for assembly is no longer proportional to the number of nano inserts but somewhat lower.
- for the same overall contact surface, decreasing the number of nano inserts while increasing their diameter allows an insertion at a lower force.

Finally, chip deflection and residual stress in reception pad show higher values for configurations with nano inserts larger in diameter.
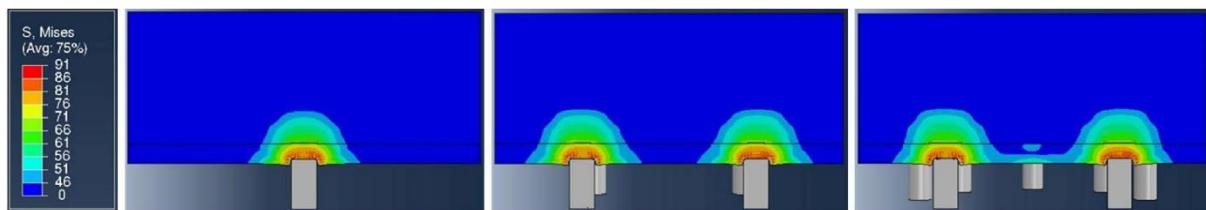
Fig. 2. Distribution of the Von Mises stress for 1, 4 and 8 nano inserts pressed into a reception pad (yield stress: 46 MPa)

3. Conclusions

Test vehicles first assemblies were successfully performed and in good agreement with the numerical model. XRD measurements allowed us to quantify the residual stresses induced by the assembly process for several interconnection designs. Deflection and electrical measurements lead us to determine the best configuration to optimize the assembly process and the reliability of photonic components.

4. References

[1] G. Lasfargues, B. Chambion, M. Volpert, F. Berger, D. Taneja, and D. Henry (2018). *Presentation of Different Fine Pitch Interconnection Technologies Developed for Optic Applications,* 7th Electronic System-Integration Technology Conference (ESTC), Dresden
[2] Interconnect, International Technology Roadmap for Semiconductors 2.0 (ITRS), (2015)
[3] D. T. Read, Y.-W Cheng, J. D. McColskey, R. R. Keller (2001). *Mechanical Behavior of Contact Aluminium Alloy,* Materials Research Society Online Proceedings Library, vol 695
[4] R. P. Reed, C. N. McCowan, R. P. Walsh, L. A. Delgado and J. D. McColskey (1988). *Tensile Strength and Ductility of Indium,* Materials Science and Engineering A

THICKNESS AND SOUND VELOCITY MEASUREMENTS IN THIN METAL FILM BY PICOSECOND ULTRASONICS

X. Tu, Y. Zeng, S. Wang and Z. Wang
Department of Mechanics, Tianjin University, Tianjin 300350, China

1. Introduction

Picosecond ultrasonics is an in-situ, non-contact and non-destructive experimental method based on the femtosecond laser pump-probe technique and it can be pioneered in the 1980s [1]. This method can characterize the solid materials includes metals and semiconductors by gigahertz–terahertz ultrasonic waves with nanometer spatial resolution [2]. In transparent materials, the picosecond ultrasonics was referred as time-domain Brillouin scattering and can measure the mechanical properties of nanoporous films, ion-implanted semiconductors, vegetable and animal cells in a contactless manner [3]. More recently, the capability of the technique to measure newly emerging field of homo- and heterostructures of van der Waals materials was demonstrated [4].

2. Experimental Methods
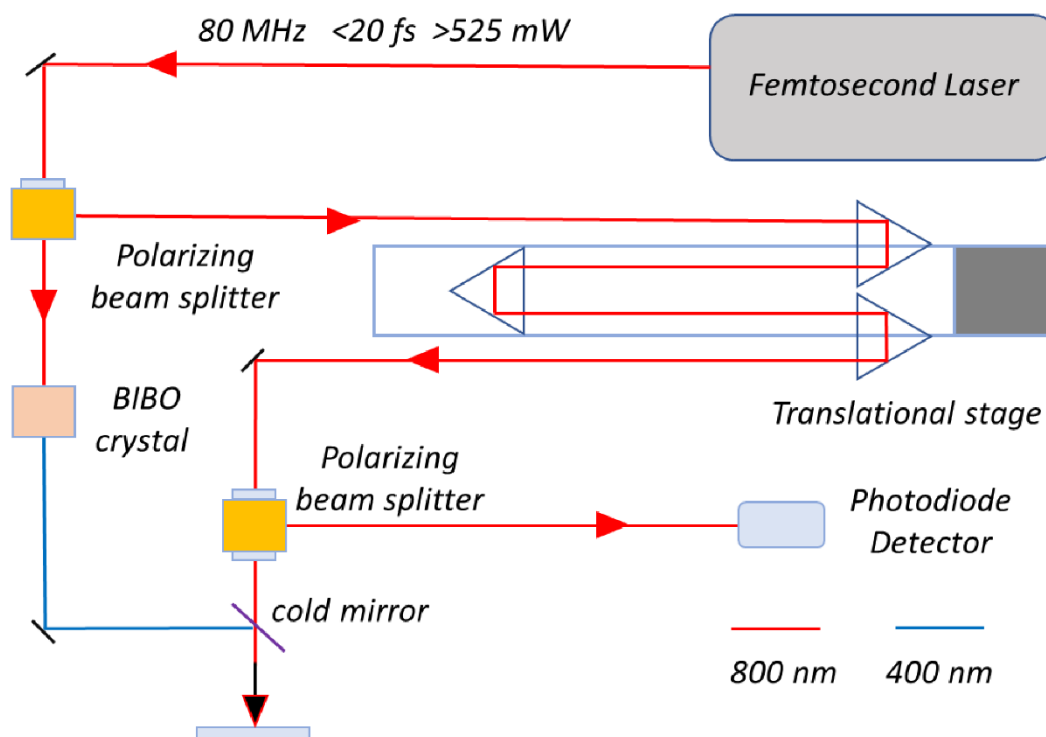
Fig. 1 Experimental setup

Thin metal film is both the transducer and sample in this study. The femtosecond laser beam (80MHz, 800nm, 20fs) was divided to pump and probe beam. We used a BIBO crystal and the second harmonic generation to obtain the pump beam (400nm). The different wavelength of pump and probe beam help us to improve the signal-noise ratio of experimental system. As shown in the Fig. 2 a), The pump beam heats the thin metal film and generate the acoustic strain waves through the thermoelastic mechanism. The thermal diffusion affects the temperature and acoustic strain waves cause the surface displacement. Both the temperature rise and surface displacement will change the reflectivity of metal

film. Then the time-delayed probe beam measured the reflectivity changes of thin metal film. The optical delay path is controlled by a stepping motor translation stage. Finally, we can get the reflectivity curve with 4000 ps time delay at 0.25 ps/point resolution.

3. Results
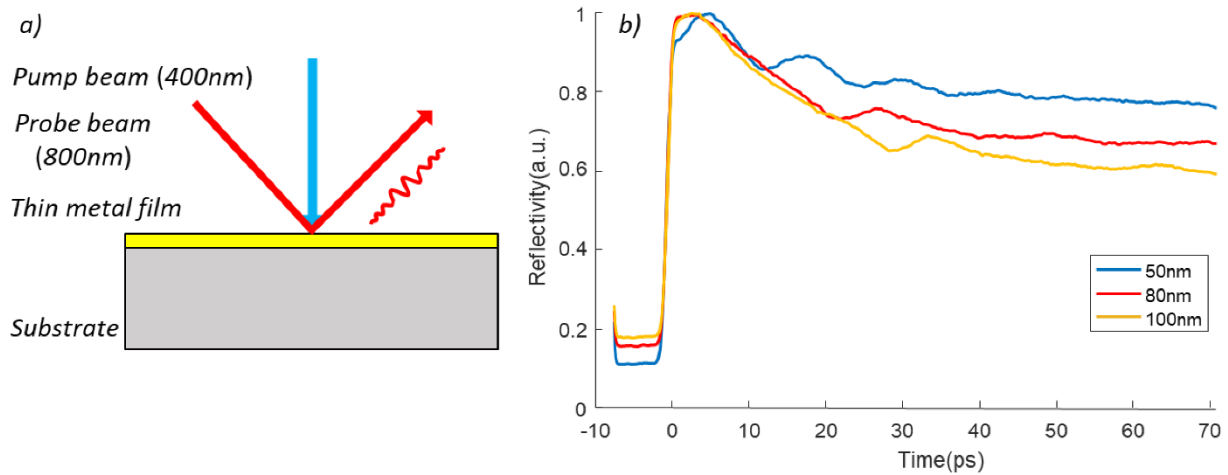
Fig. 2 a): the diagram of sample and b): the reflectivity response of Al film

We prepare and test three kinds of Al film with 50, 80 and 100 nm thickness on the same substrate. Fig. 2 b) shows several thickness-dependent acoustic echoes in their reflectivity response curves within 100ps. It corresponds to continuous bounce and back of the acoustic strain pulse as expected from the mechanical properties of Al film. The detected echoes are not the strain pulse itself but instead measure of its impact on the optical of Al film. If we assumed the sound velocity is equal to the bulk Al (6400m/s), we can calculate the accurate thickness of Al film. However, the sound velocity is significantly affected by scale effect at nanometer scale. And it is another option to investigate the influence of scale effect to sound velocity according to accurate thickness measurements by other method such as a SEM.

4. Discussion

The thickness and sound velocity of metal film measurement is the basic function of picosecond ultrasonics. By set the appropriate time resolution and delay, it can be used to investigate the pulse shape of acoustic strain and measure the mechanical and thermal properties of the metal film-transparent substrate assembly.

5. References

[1] Thomsen, C., et al (1986). Surface generation and detection of phonons by picosecond light pulses, *Physical Review B*, 1986. **34**(6): p. 4129-4138.
[2] Matsuda, O., et al (2015). Fundamentals of picosecond laser ultrasonics, *Ultrasonics*, **56.**
[3] Gusev, V.E. and P. Ruello (2018). Advances in applications of time-domain Brillouin scattering for nanoscale imaging, *Applied Physics Reviews*, **5**(3): p. 031101.
[4] Vialla, F. and N. Del Fatti (2020). Time-Domain Investigations of Coherent Phonons in van der Waals Thin Films, *Nanomaterials*, **10**(12).

THEMATIC SESSIONS

TS1. Experimental Solid Mechanics

BRICK MODEL FOR NONLINEAR DEFORMATION AND MICROCRACKING IN CERAMIC THERMAL BARRIER COATING

E. Yonemichi[1], H. Katori[2], M. Arai[3], K. Ito[3] and T. Suidzu[4]
[1] Graduate School of Engineering, Tokyo University of Science, Tokyo, Japan
[2] Softbank Corporation, Tokyo, Japan
[3] Department of Mechanical Engineering, Tokyo University of Science, Tokyo, Japan
[4] Tocalo Corporation, Hyogo, Japan

1. Introduction

Thermal barrier coatings (TBCs) are widely applied to gas turbine blades. A TBC is a multilayered system which contains a ceramic top coating (TC) with low thermal conductivity and a bond coating (BC) for improving adhesion strength between the TC and the metallic substrate. TC is usually deposited by an atmospheric plasma spraying (APS) technique which is based upon a continuous deposition process of small melted particles. This deposited particle is typically called splat. Due to the microstructure of TC based on the deposition of splats, the deformation behavior of TC becomes inelastic. In addition, cracks propagate intricately along splat boundaries and in intra-splats. However, it is difficult to accurately estimate the microscopic damage process and the crack propagation path via a finite element (FE) model based on continuum mechanics [1]. In this study, we propose a brick model where splats are replaced with rectangular bricks connected together by a cohesive model.

2. Nonlinear deformation and damage process of freestanding TC

A plate-shaped austenitic stainless steel AISI304 measuring 50×50×5 mm was prepared. CoNiCrAlY powder was deposited onto the surface of the plate by APS of up to 0.1 mm thickness as BC. YSZ powder was then deposited up to 0.5 mm of thickness as TC. In the deposition process of TC, three kinds of particle velocity condition were selected: 1. L (low speed), 2. Std. (standard speed), and 3. H (high speed). The TBC-coated plate was cut to a thinner specimen of 30×5 mm. A freestanding TC sample was then extracted from this specimen by chemical treatment with aqua regia. The hand-made bending test system was used to conduct a cantilever beam bending test for the freestanding TC sample. One end of the sample was fixed rigidly and the other free end was subjected to a bending load. Loading was measured with load cell (LUR-A-100NSA1, Kyowa Electronic Instruments Co., Ltd.) and load-point deflection was measured with a laser displacement sensor (LK500, Keyence). Data were recorded with a data logger (midi LOGGER GL220, GRAPHTEC). After the bending test, the cross-section of the fractured sample was observed using SEM (JCM-6000 neo score II, JEOL Ltd.).

The bending test revealed that the load was monotonously increased with displacement, irrespective of splay condition. It was found that the maximum load was increased with particle velocity, which implies that cohesive strength between splats was improved by higher particle velocity. In contrast, maximum deflection at fracture was increased with decreasing particle velocity. The cross sectional SEM image showed that cracks propagated, involving the splat boundaries and intra-splats. Furthermore, an increase of particle velocity led to an increase in the ratio of intra-splat cracking to fracture surface.

3. Numerical simulation

In this study, the microstructure of TC formed by deposition of splats was modeled based on brick structure where splats were replaced with bricks, and bricks were arranged periodically. Bricks were homogeneous isotropic elastic bodies, and the geometry of bricks was determined for the single splat deposition test. It was assumed that bricks fracture when normal stress exceed the allowable stress. The bricks were also connected together by a cohesive model expressed by:

$$(1) \qquad T = G_c \frac{\delta}{\delta_c^2} exp\left(-\frac{\delta}{\delta_c}\right)$$

where, T is traction binding between bricks, δ is relative displacement between bricks, G_c is material constant characterizing cohesive strength, and δ_c is critical relative displacement where bricks split off. In this study, bricks connected by the cohesive model are referred to as "Brick model".

Figure 1(a) shows the schematic image of the FE model. It consists of the brick model and the conventional model based on continuum mechanics. The brick model was used around the fixed point where bending stress becomes highest and the inelastic constitutive equation developed by Katori et al. (2018) was applied to the other area [1]. The FE analyses were performed using the commercial FE software Marc (Ver. 2010, MSC Software Corporation). The crack propagation path obtained from the FE analysis is shown in Figure 1(b). Red and green lines represent brick boundary cracks and intra-brick cracks, respectively. It was found that crack propagates involving the brick boundaries and intra-bricks. The ratio of intra-brick crack to fracture surface obtained from the FE analysis accurately corresponded to the experimental results. Figure 1(c) indicates the relationship between load and deflection. Both the results obtained from the FE analysis and the experiment are in concordance. From these results, it was demonstrated that the brick model can appropriately simulate the inelastic deformation and fracture behaviors based on the microstructure of TC.
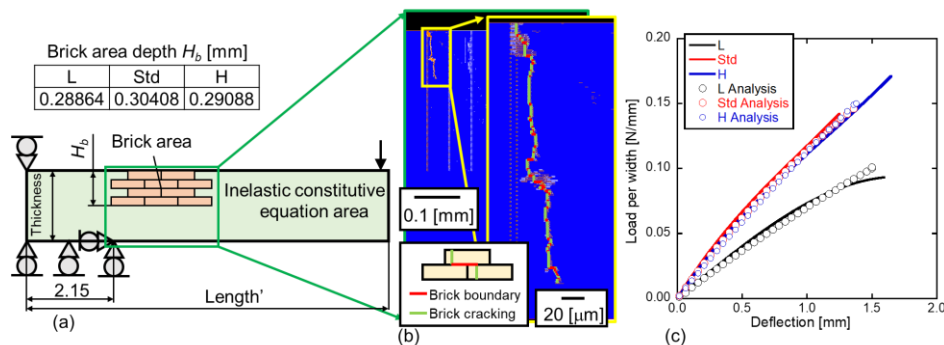
Fig. 1. FE analysis of deformation and fracture behaviors of a freestanding TC sample:
(a) schematic image of FE model with brick model, (b) crack propagation path and
(c) relationship between deflection and load per width

4. Conclusion

An FE model based on the brick model and the conventional inelastic constitutive equation was developed. As a result, it was confirmed that the FE model can simulate the relationship between load and load-point deflection and micro-crack propagation path obtained from the bending test.

5. References

[1] H. Katori, M. Arai, K. Ito (2018) "Comprehensive Numerical Simulation of Stress and Damage Fields under Thermo-Mechanical Loading for TBC-Coated Ni-Based Superalloy", Key Engineering Materials, Vol. 774.

EFFECT OF FIELD CAPROCK SHALE EXPOSURE TO CO_2 ON ITS MECHANICAL PROPERTIES – A COMPARISON OF EXPERIMENTAL TECHNIQUES

P. Cerasi[1], N. Agofack[2], S. Rørheim[2], L. Edvardsen[1] and H. Bhuiyan[1]
[1] SINTEF Industry, Trondheim, Norway
[2] Department of Geoscience and Petroleum, NTNU – Norwegian University of Science and Technology, Trondheim, Norway

1. Introduction

Carbon capture and storage (CCS) is now recognized as a necessary measure in order to satisfy the commitments in the Paris Agreement of 2015. Should global warming be kept under 1.5 °C, negative carbon emissions will be imperative; CO_2 storage is particularly suited for this goal, making use of tried technology from the oil and gas industry. More than 20 years of storage experience from pilot projects such as Sleipner and enhanced oil recovery (EOR) operations in North America prove that geologic storage is feasible and safe. Remaining gaps in research are mostly related to transition to large scale storage, capable of accommodating gigatons of CO_2 without compromising underground containment.

Pushing the storage envelope in terms of CO_2 volumes contained in a given high-permeability reservoir may lead to transient or permanent increases in reservoir pore pressure. This may lead to stress concentration effects and potentially, localized failure of the immediate barrier provided by the caprock formation. Once a fracture in the caprock develops, further evolution can either be fracture propagation leading to a potential leakage situation, or healing of the fracture and restored containment of the CO_2. These opposite scenarios will depend on the interaction of the caprock formation with the fluid entering the fracture, with chemical dissolution-precipitation effects depending on both formation and fracture fluid composition, as well as fluid flow rate and formation ductility change and straining capacity.

A North Sea caprock shale from the Draupne formation [1] was subjected to a panoply of experimental techniques involving various methods of exposure to CO_2, in order to assess its response in terms of changes, if any, in its mechanical properties. Depending on the exposure fluid composition and state, that is mixture with brine, liquid, gas or super-critical fluid, the chosen shale weakens or stiffens after exposure.

2. Experimental

Several techniques were used to assess mechanical properties and changes to these after varying exposure time. The experimental techniques vary from standard rock mechanical testing to newly developed or improved techniques at the SINTEF Formation Physics laboratory:

(a) Complex triaxial test using a dedicated, small sample cell developed at SINTEF (15 mm diameter and 30 mm high cylindrical plugs, Figure 1 left). The test was divided in two parts, where the first part had the shale exposed to seawater brine, while the second part had the shale exposed to super-critical CO_2 (scCO_2) dissolved into the same brine. Each part consisted of repeated unload-reload loops to probe the elastic properties of the plug. Note that plug to plug variability was eliminated in this technique since the same plug was exposed to the different fluids.

(b) Low frequency oscillation test [2], mimicking the passage of a seismic wave in terms of periodic straining of the plug (strain amplitude and cyclic frequency in the seismic ranges). Again, the same plug was used with exposure first to brine and then scCO_2 dissolved in brine. The test

probes elastic stiffness and its evolution with exposure time; the strains being very small, no fatigue effects can be expected, with the plug remaining in the elastic domain at all times (Figure 1, middle).

(c)   Shear strength of small shale disks (15 mm diameter and 5 mm thick disks) was probed using the punch test (Figure 1 right), whereby a specially designed piston inserted in a load frame cuts through the shale disk in a controlled manner. The applied force divided by the cut surface area provides an estimate of the compressive shear strength. The shale disks were exposed to brine, CO_2 gas dissolved in brine, $scCO_2$ dissolved in brine, dry $scCO_2$ and no exposure (air-dried shale).

3. Results and discussion

Depending on the fluid mixture and exposure time, weakening of the shale or slight stiffening was observed. These variations in results are thought to be a consequence of differing pH values for the different fluids, amount of diffusion into the shale bulk, associated changes in surface energy inside the shale's clay platelets and desiccation effects. Changes in stiffness need not be of the same sign as changes in compressive strength: loss of point cementation at grain contacts with no loss of large volumes of minerals or grains may lead to a weaker bulk but stiffer plug if finer material is trapped in the pore volume. In conclusion, an innovative caprock containment testing methodology is proposed, of interest for future large-scale storage site assessment.
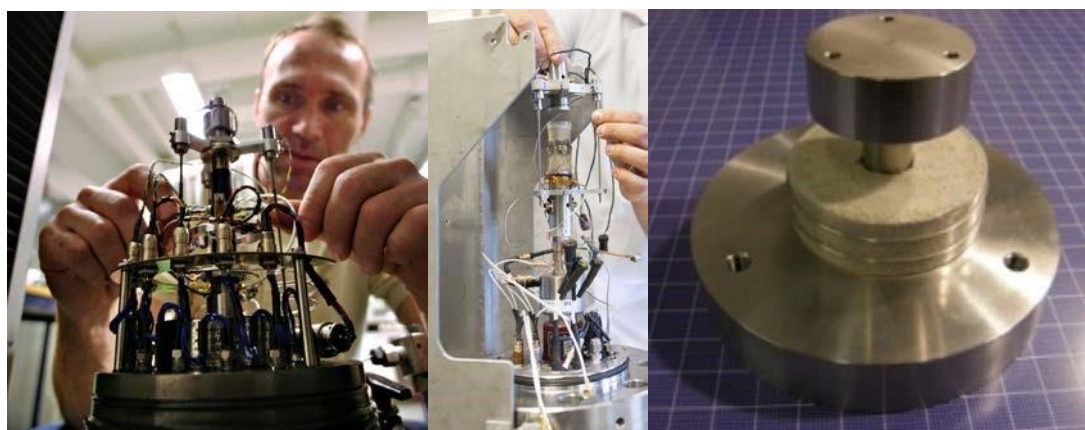
Fig. 1. Probing of Draupne shale mechanical properties using the small sample triaxial rig (left), the low frequency rig (middle) and the punch method (right), all developed at SINTEF

4. Acknowledgment

5. References

[1]   Skurtveit, E., Grande, L., Ogebule, O. Y., Gabrielsen, R. H., Faleide, J. I., Mondol, N. H., ... & Horsrud, P. (2015, November). Mechanical testing and sealing capacity of the Upper Jurassic Draupne Formation, North Sea. *In 49th US Rock Mechanics/Geomechanics Symposium*. American Rock Mechanics Association.

[2]   Agofack, N., Lozovyi, S., & Bauer, A. (2018). Effect of CO_2 on P-and S-wave velocities at seismic and ultrasonic frequencies. *International Journal of Greenhouse Gas Control*, **78**, 388-399.

EFFECT OF GRAIN SIZE AND FORCE RATIO ON FATIGUE CRACK PROPAGATION BEHAVIOR OF NANOCRYSTALLINE Ni THIN FILM

Y. Nakai[1], T. Hirai[1] and S. Kikuchi[2]
[1] Kobe University, Kobe, Japan
[2] Shizuoka University, Hamamatsu, Japan

1. Introduction

Nanocrystallization is one of the most promising techniques to improve the fatigue strength of metallic materials, and their thin films are now being widely used for micro-electro-mechanical systems. The electrodeposition method will be the easiest method to obtain a uniform nanocrystalline structure in thin films [1,2]. In comparison with hardness and tensile properties, fatigue properties of nanocrystalline metals are not well understood. It is well known for fracture mechanics studies of conventional metallic materials that the fatigue crack propagation behavior is affected by the force ratio and the grain size, and these effects have been explained by the difference in crack closure.

In the present paper, nickel nanocrystalline thin films were produced by electrodeposition using sulfamate solution, and the effects of the grain size and the force ratio on the fatigue crack propagation was investigated.

2. Material and Experimental Procedure

Nickel thin films were produced by electrodeposition using sulfamate solution. A polished stainless steel plate was used for a cathode and a pure nickel plate for an anode. The amount of brightener additive was either 0 or 0.8 g/L. Temperature of the bath was kept constant at 40 °C in a hot-water circulating bath. The pH value of the solution was maintained at 4.0 by adding sulfamate acid. The solution was stirred by a magnetic stirrer to avoid pit formation. The current density was kept constant at 0.25 mA/mm^2 by using a constant current supply. Deposition time was 30 min to obtain the thickness of 10 μm.

After deposition, the thin films were removed from the cathode and subjected to the characterization of the fatigue crack propagation as free-standing films. The microstructure of the thin films was examined by the electron backscatter diffraction (EBSD), where the step size was 15 nm. The grain size of the films in the cathode side was either 324 nm without brightener or 186 nm with brightener of 0.8 g/L. Single edge tension, SE(T), specimens with the length of 48 mm, the width of 10 mm, the initial notch length of 2.5 mm, and the thickness of 10 μm were employed for the fatigue crack propagation test. SE(T) specimens were glued to the grips of the test machine, where the distance between the edges of grips was 30 mm. To elucidate the effects of nanocrystallization and thickness, C(T) specimens made of commercially pure Ni with width of 18 mm and thickness of 1.5 mm were also employed for comparison, whose average grain size was 18 μm.

The crack propagation tests were conducted under stress-intensity-factor-range ($\triangle K$)-controlled conditions using a computer-controlled electro-dynamic testing machine with the loading capacity of 50 N for SE(T) specimen and 500 N for C(T) specimen. Sinusoidal loading wave with force ratio, *R*, from 0.1 to 0.5 and frequencies, *f*, of 10 Hz for SE(T) and 60 Hz for C(T) were employed for the crack propagation tests. The crack lengths were continuously monitored using compliance between the applied force and the load point displacement for SE(T) specimen, which was measured by a high resolution laser displacement meter. For C(T) specimen, backface strain was measured to determine crack length by the compliance method. Crack closure behavior was also determined by the compliance for both specimens.

3. Results and Discussion

Figure 1 shows the crack propagation behaviors, where (a) and (b) show the results for nanocrystalline thin firm (SE(T)), and C(T) specimens with conventional thickness and grain size, respectively. As shown in Fig. 1(a), almost unique relationship independent of the force ratio, R, was obtained for the same grain size material of nanocrystalline thin film, while the crack propagation rate, da/dN at the same stress intensity range, ΔK, is higher in the region near threshold, and the threshold stress intensity range, ΔK_{th}, is lower for smaller grain size material (0.8 g/L). Open marks in Fig. 1 (b) shows that the da/dN-ΔK relationship depends on force ratio, R, while da/dN-ΔK_{eff} relationship shown by solid marks is almost independent of the force ratio, R, indicating that the crack closure is responsible to the effect of force ratio. Since the force-displacement curve is almost linear for nanocrystalline thin film, crack closure must not have occurred and $\Delta K = \Delta K_{eff}$. The effect of grain size has been explained by the roughness induced crack closure because the roughness of fracture surface is depending on the grain size, and then the roughness of fracture surface of nanocrystalline material is very small to induce crack closure. The effect of grain size on the value of $\Delta K_{eff,th}$ was explained by the blocked slip band model proposed by Tanaka and Nakai [3]; however, the effect of thickness for thin film is not clarified.

4. Conclusions

Crack length and crack closure behaviors of nanocrystalline nickel thin film could be measured by the compliance method using high resolution laser displacement meter, and an automatic load shedding fatigue crack propagation testing system was successfully developed. As a result, and following results were obtained (1) For nanocrystalline thin film, crack closure was not observed. (2) Crack growth rate is higher and the value of ΔK_{th} Fig. 1. Crack propagation behavior. is smaller for smaller grain size material.
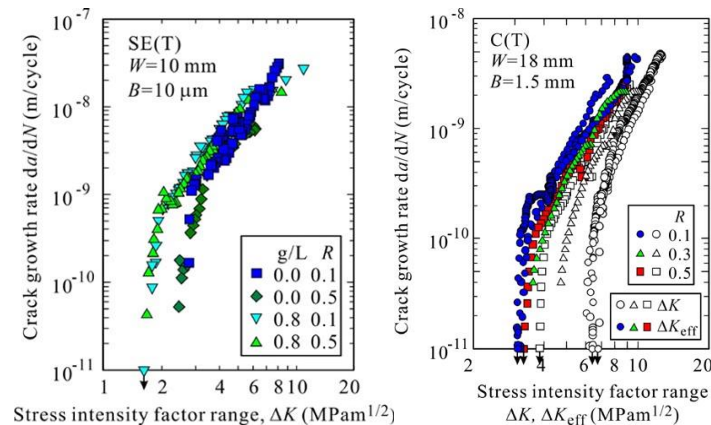
Fig. 1. Crack propagation behavior (a) Nanocrystaline thin film (b) Conventional material

5. References

[1] A.M. El-Sherik and U. Erb (1995). Synthesis of bulk nanocrystalline nickel by pulsed electrodeposition, .*J. Mat. Sci.*, **30**, 5743-5749.

[2] K. Tanaka, M. Sakakibara, and H. Kimachi (2011). Grain size effect on fatigue properties of nanocrystalline nickel thin films made by electrodeposition, *Procedia Eng.*, **10**, 542-547.

[3] K. Tanaka, Y. Nakai, and M. Yamashita (1981). Fatigue Growth Threshold of Small Cracks, *Int. J. Frac.*, **17**, 519-533.

RESIDUAL STRESS ESTIMATION
WITH VISUALIZATION OF THERMAL DEFORMATION
USING ELECTRONIC SPECKLE PATTERN INTERFEROMETRY

T. Sasaki[1], T. Ogawa[1] and S. Yoshida[2]
[1] Niigata University, Niigata, Japan
[2] Southeastern Louisiana University, Hammond, USA

1. Introduction

Nondestructive measurement of residual stress induced by the welding process is of a technical, as well as fundamental issue. Conventional residual stress evaluation methods which utilize X-ray, or ultrasound techniques allow accurate measurement in the microscopic level, while these have disadvantages of the small measurable area up to a few millimeters square and a time-consuming process. Optical techniques including electro speckle pattern interferometry (ESPI) can measure the surface deformation in full field, and are applied for the measurement of residual stress in combination with destructive methods. Our previous works [1] have demonstrated the feasibility of residual stress analysis with visualization of the least amount and reversible deformation of the measurement object. The present study focuses on a small thermal deformation to apply the least amount of deformation. Thermal deformation of the material under an external stress is visualized with the ESPI sensitive to two-dimensional in-plane displacement. Deformation process under local heating condition and the influence of the external stress initially applied on the deformation behavior are discussed.
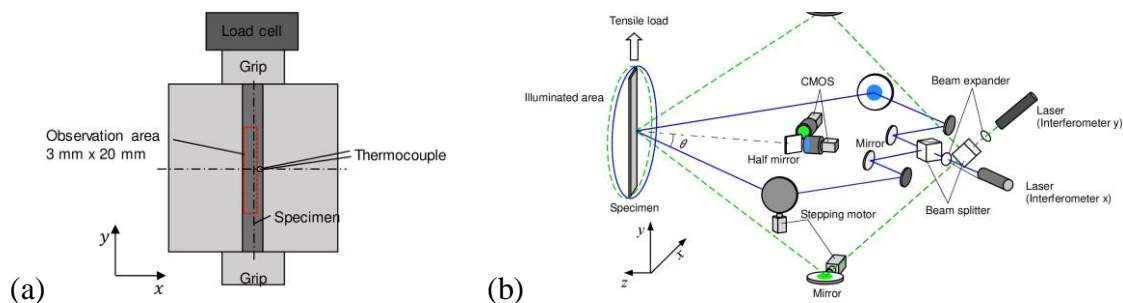
Fig. 1. (a) Schematic illustration of thermal expansion test and
(b) Optical setup of 2-D electronic speckle pattern interferrometer

2. Experiment

Metal sheets of aluminum alloy was used for the experiments. The sheets were annealed in the air at 300 °C for 24 hours (annealed specimen). Then, the surface of specimen was subjected to a bead-on-plate welding using TIG arc (welded specimen). First, external tensile load were applied to the annealed specimen using a crosshead of the tensile machine for a calibration test. This test aims to estimate residual stress based on the apparent thermal expansion coefficient under the known restraint conditions, assuming a situation that a tensile residual stress is introduced in the material due to a restraint of surrounding area. The specimen was locally heated from room temperature to about 28 °C at the heating rate of 0.1 °C /s by using a Peltier devise attached on the backside of specimen. Then, for the residual stress estimation, the welded specimen was spot heated using an infrared laser (spot size : 0.5mm). Deformation behavior during the above expansion tests were visualized using an ESPI.

Figure 1(b) shows an optical setup used in this study. Two optical configurations are arranged in a parallel direction and a perpendicular direction to a tensile machine. Displacement fields in each sensitive direction, x, and y on the measured surface can be individually obtained by two CMOS cameras via optical band path filters. The displacement fields on the measured surface can be individually obtained by computing the intensity difference for each camera as fringe contours.

3. Result and discussion

Figure 2(a) shows changes of the mean strain of specimen during the heating test. The applied stress condition "0MPa" indicates a condition that the test was conducted under the non-restraint condition. The strain values linearly increase as the heating temperature increase, showing the thermal expansion. Under the restrained conditions where both end of the specimen are gripped by the tensile machine, the strain is substantially smaller than the non-restraint condition. The slope of the line $d\varepsilon/dT$ indicates the apparent coefficient of thermal expansion (CTE). Figure 2(b) shows the apparent CTE plotted against the stress initially applied to the specimen. The CTEy in the tensile direction decreases depending on the external tensile stress. In contrast, the CTEx shows a trend to increase under the tensile stressed condition.

Figure 3(a) shows an example of fringe pattern in a spot heated specimen by the infrared laser. The spot laser was irradiated to the center of bead. Comparing the fringe pattern in the non-welded spcimen shown in Fig.3 (b), the fringe interval become slighlty smaller at the welded part. This may be due to that the residual stress induced by the welding influenced the thermal expansion behaviour. The result shows that the principal stress and its direction can be estimated by visualizing the thermal deformation.
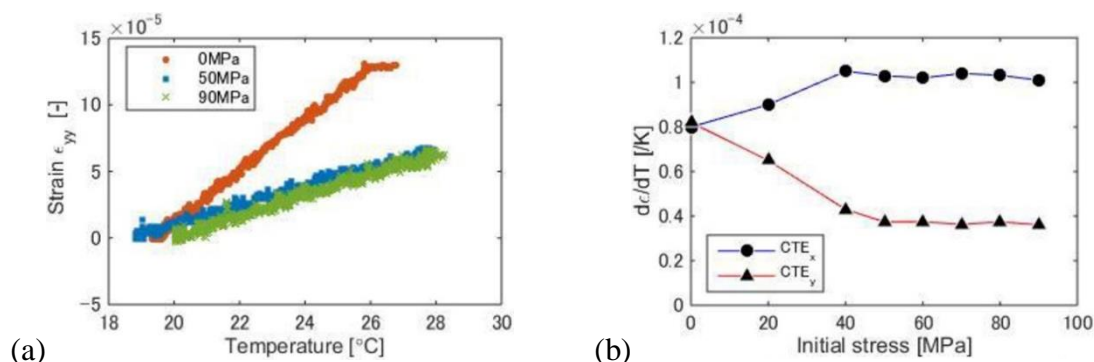
Fig. 2. (a) Changes of thermal strain and (b) apparent coefficient of thermal expansion
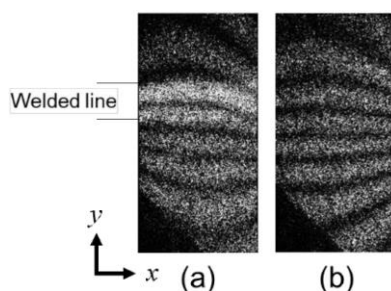
Fig. 3. Typical fringe pattern of spot heated specimen. (a) welded, (b) non-welded

4. References

[1] S.Yoshida, F.Miura, T.Sasaki, D. Didie, S. Rouhi (2017). Optical Analysis of Residual Stress with Minimum Invasion, Residual stress, *Thermomech Infrared Imag. Hybrid Tech. Inverse Probl.*, **8**, 65-72.

NEW BIAXIAL SPECIMENS AND EXPERIMENTS TO CHARACTERIZE SHEET METAL ANISOTROPY AND DAMAGE

S. Gerke, S. Koirala and M. Brünig
Institut für Mechanik und Statik, Universität der Bundeswehr München,
85577 Neubiberg, Germany

1. Introduction

Sheet metals are frequently characterized by plastic anisotropy and before final fracture ductile damage processes take place. In this context Brünig [1] presented a thermomechanically consistent continuum damage model which is enhanced to take into account plastic anisotropy. The anisotropic plastic material behavior is directly related to the material orientation while the damage behavior is strongly dependent on the stress state. Consequently, both processes have the need to be quantified under different loading conditions which can be realized by biaxial experiments.

2. Biaxial specimen

Classical cruciform geometries (see for instance [5]) have been designed to analyze the yield surface and the subsequent plastic behavior. Typically, these specimens are characterized by an extended central part where initially a homogeneous stress and strain state is obtained, but with ongoing deformation strains tend to localize and a well-controlled study of the material behavior is difficult to realize. In this context new biaxial specimens for sheet metals with moderate thickness have been presented [3]. Especially the X0- and the H-specimen (Fig. 1) indicated applicability in a wide range of loading conditions. The geometry of these cruciform specimens is characterized by central holes and the remaining connecting material is the region of interest. In addition, inelastic strains fields localize in notches in thickness direction from both sides and consequently the material behavior can be analyzed in detail [2,4].
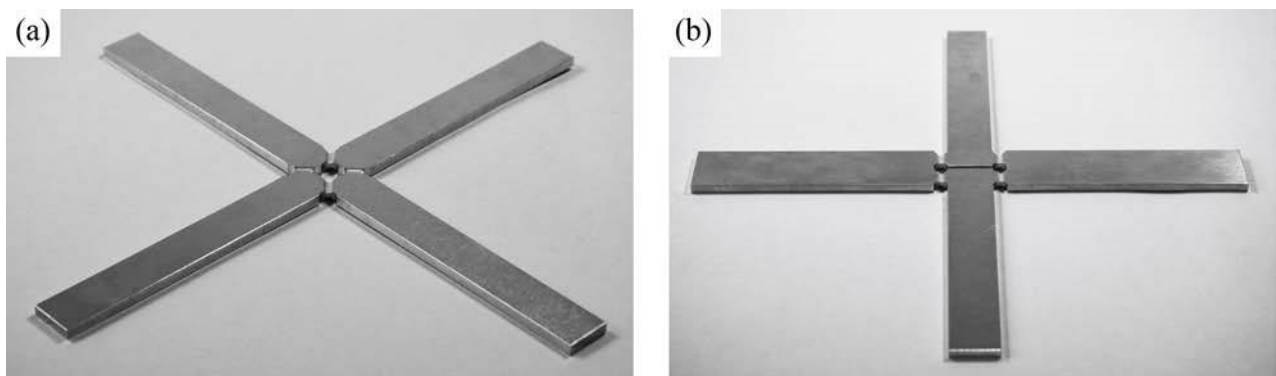
Fig. 1. Biaxial specimens: (a) X0- and (b) H-specimen

3. Experimental setup

All experiments have been performed with the biaxial test machine LFM-BIAX 20 kN produced by Walter+Bai, Switzerland. It contains four electromechanically, individually driven cylinders with load extrema of ±20 kN. To minimize non-symmetric behavior during the experiments a mainly displacement driven procedure has been used. During the experiments the displacement fields of the specimen surfaces have been monitored with a Q-400 digital image correlation (DIC) system

provided by Dantec/Limess. For the setup 6 Mpx cameras equipped with 75mm lenses have been used. The experimental setup is displayed in Fig. 2.

Fig. 2. Experimental Setup: Biaxial machine, digital image correlation system and lightning system

The experimental series includes experiments under different loading conditions leading to tension dominated stress states as well as shear stress states superimposed with tension or compression. In addition, all experiments have been realized under different material directions (0°, 45° and 90°). This approach facilitates a controlled study of the anisotropic and ductile damage behavior of the analyzed aluminum alloy AlCuMg1 (EnAw 2017). All experiments have been conducted till the occurrence of final fracture occurred and consequently the damage and fracture behavior could be investigated. In addition, the fracture surfaces have been analyzed by scanning electron microscopy (SEM).

4. Conclusions and perspective

The presented biaxial experiments with the X0- and the H-specimen facilitate the material characterization with respect to plastic anisotropy and ductile damage. Special focus has been given to the material orientation and different loading conditions. In the future this information has to be linked back to the material model to enable corresponding numerical simulations of components to be fabricated of these materials.

5. References

[1] M. Brünig. An anisotropic ductile damage model based on irreversible thermodynamics. International Journal of Plasticity, 19(10):1679–1713, 2003.

[2] M. Brünig, S. Gerke, and M. Zistl. Experiments and numerical simulations with the Hspecimen on damage and fracture of ductile metals under non-proportional loading paths. Engineering Fracture Mechanics, 217:106531, 2019.

[3] S. Gerke, P. Adulyasak, and M. Brünig. New biaxially loaded specimens for the analysis of damage and fracture in sheet metals. International Journal of Solids and Structures, 110111:209–218, 2017.

[4] S. Gerke, M. Zistl, A. Bhardwaj, and M. Brünig. Experiments with the X0-specimen on the effect of non-proportional loading paths on damage and fracture mechanisms in aluminum alloys. International Journal of Solids and Structures, 163:157–169, 2019.

[5] T. Kuwabara. Advances in experiments on metal sheets and tubes in support of constitutive modeling and forming simulations. International Journal of Plasticity, 23(3):385–419, 2007.

PRELIMINARY INVESTIGATIONS FOR RESIDUAL STRESS ANALYSIS INSIDE OF PLASTIC PARTS

E. Peretzki, T. Lehmann and J. Ihlemann
Chemnitz University of Technology, Chair of Solid Mechanics, Chemnitz, Germany

1. Motivation and introduction

In structural analyses and material characterisation, the determination of residual stresses is an important measuring task. In principle, every part contains residual stresses due to production. However, if a critical limit is exceeded, this can lead to distortion or even to premature failure. Usually residual stresses are measured using the hole drilling method with an electric strain gauge rosette. By drilling a small hole in the part, the residual stresses are rearranged, resulting in strains. Using mathematical evaluation methods, the residual stresses close to the surface can be determined.

This abstract describes a procedure that enables the analysis of residual stresses inside parts and specimens, the so-called staggered machining. Currently, this method is still a theoretical state. However, the suitability of the experimental setup required for this measuring task could already be tested in a simpler preliminary test, which will be described in this paper.

2. Principle of staggered machining

The principle of staggered machining was developed to measure residual stresses inside plastic parts. For this purpose, the well-known hole drilling method, which is only suitable for the determination of near-surface residual stresses, was modified. Instead of the previous usage of a strain gauge rosette, the displacements and strains are determined using Digital Image Correlation (DIC) as a field measurement method. Because the measuring fields are very small in this case, a very fine speckle pattern is required accordingly to obtain a high resolution. The pattern is produced on the basis of fine abrasive paper. The detailed description of this manufacturing process can be found in [1,2].

Figure 1 illustrates the procedure for staggered machining schematically. In the first step, a speckle pattern produced previously is applied to the test specimen using adhesive. An image of this pattern is captured by a CCD camera.
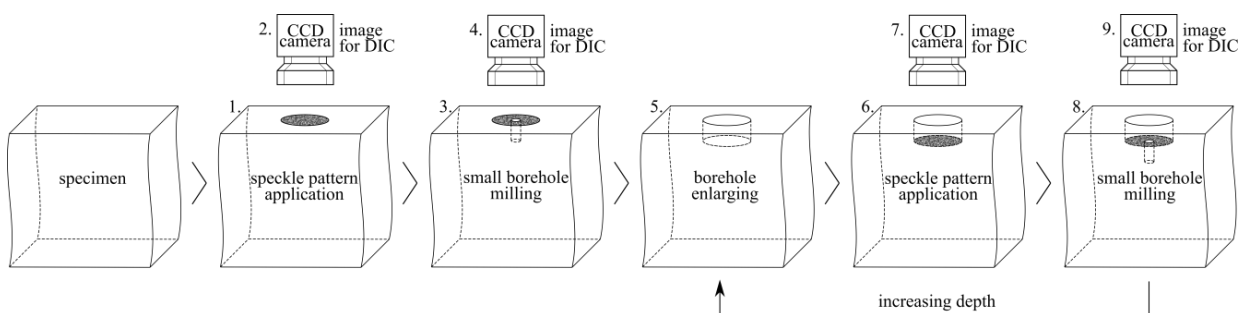
Fig. 1. Schematic sequence of the staggered machining

It serves as a reference image for the later evaluation. Now, as with the hole drilling method, a small hole is drilled in the centre of the pattern to rearrange the residual stresses. By a renewed capturing of the measuring field in step 4 the occurring displacement and strain fields can be determined using a DIC evaluation software. In step 6 the small borehole is enlarged to the size of

the speckle pattern. After this, a new speckle pattern is applied to this newly created plane. Then a reference image is taken again and a small borehole is milled. As in step 4, another image is taken to evaluate the displacement and strain fields of this plane. The steps 5 to 9 are repeated until the desired depth in the part is reached. The described machining steps are performed using a table portal milling machine.

3. Preliminary investigation, results and conclusion

In a preliminary test, the feasibility of capturing the speckle pattern by the CCD camera in a narrow deep borehole was investigated. The design of the used specimen is shown in Figure 2. The illumination of the borehole bottom is essential to achieve the image quality, which is required for the DIC. A beam splitter enables the illumination with simultaneous image acquisition. The setup is described in [2]. As the specimen itself does not contain any significant residual stresses, deformations in the borehole bottom are caused by an external load. The applied compressive force is monitored by means of a load cell. The evaluation is based on the reference image in the unloaded state (see Figure 2) and an image with applied compressive force on the test specimen. A detailed description of the evaluation strategy, using a special parameterisation, can be found in [1].

The displacement and strain fields in x- and y-direction of an annulus around the small borehole are the results of the evaluation. In Figure 2 the displacement and strain field of the x-direction at a load of 800 N are shown. It is a superposition of rigid body displacement and deformation. The displacement in x-direction increases with increasing distance to the bearing. The resulted strain field is almost symmetrical to the horizontal in the middle of the borehole.

The successful preliminary investigation allows the implementation of staggered machining in the experiment.
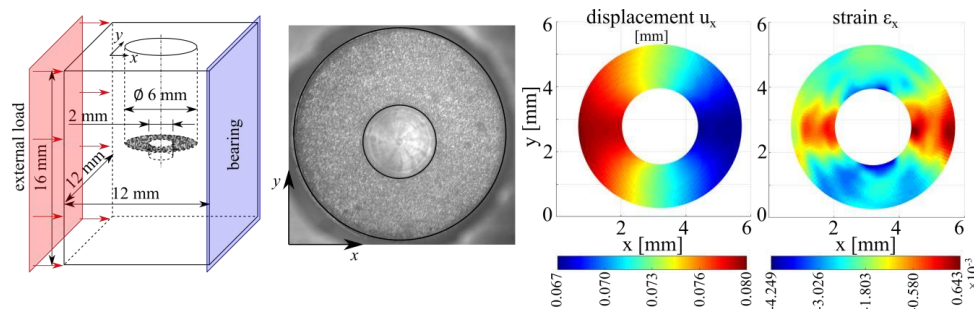
Fig. 2. Test specimen; captured speckle pattern; evaluation results

4. Acknowledgements

5. References

[1] Peretzki, E., Stockmann, M., Lehmann, T., Ihlemann, J. (2019) A new surface preparation method for microscopic digital image correlation applications, *Materials Today: Proceedings, Volume 12*, *Part 2,* Pages 377-382, ISSN 2214-7853, https://doi.org/10.1016/j.matpr.2019.03.138.

[2] Peretzki, E., Lehmann, T., Stockmann, M., Ihlemann, J. (2019) Strain analysis in narrow boreholes by means of microscopic Digital Image Correlation, *Proceedings of the 36th Danubia Adria Symposium*, Pilsen, ISBN 978-80-261-0876-4

INVESTIGATION OF THE ANISOTROPIC DAMAGE BEHAVIOR OF SMC COMPOSITES UNDER BIAXIAL STRESS STATES

J. Lang, C. Schmidt and T. Böhlke
Institute of Engineering Mechanics, Chair for Continuum Mechanics,
Karlsruhe Institute of Technology (KIT), Karlsruhe, Germany

1. Introduction

Sheet molding compound (SMC) composites are discontinuous fiber reinforced polymers. They combine high strength and low density with an economical production effort and represent, thus, an ideal lightweight material. The detailed understanding of the mechanical behavior, especially of the anisotropic damage behavior, presents still a challenge to composite material science. The characterization of damage also under multiaxial loading cases is indispensable to understand the various damage phenomena in fiber reinforced composites (cf. [1]) and to validate damage models. The focus of this study lies on biaxial tensile testing of an SMC composite using a special cruciform specimen design introduced by [2]. These experiments deliver results for anisotropic stiffness degradation as one phenomenon of damage.

2. Material and experimental methods

The investigated material is a SMC composite with an unsaturated polyester polyurethane hybrid (UPPH) as matrix and 23 vol% glass fibers of 25 mm length. The cruciform specimen introduced by [2] is reinforced by unidirectional carbon tapes on both sides and has a milled out center area exposing the pure SMC material. This design allows the observation of damage in the center area without preliminary failure of the specimen arms. Dependent on the manufacturing process of the material the specimens have different anisotropy ratios. Details of the manufacturing process can be seen in [3]. The experiments are performed with a biaxial testing device which consists of four electro mechanical actuators that are arranged perpendicular to each other. Each actuator is independently controllable. A digital image correlation system measures the strain field on the specimen.

The testing procedure is based on a quasi-static cyclic load with a stepwise load increase in each cycle. Different strain ratios between the two perpendicular directions are performed to cover different planar stress states. After each cycle the stiffness in each direction is evaluated. Since it is not possible to calculate the stress directly, the stiffness is defined by the force over strain difference in the corresponding direction:

$$(1) \qquad \tilde{E} = \frac{\Delta f}{\Delta \varepsilon}$$

3. Results and conclusion

Figure 1 shows exemplary results. The diagrams depict the stiffness over the maximum reached strain in the entire loading history. The values for the stiffness are normalized to their initial value for comparability. The left diagram shows results of a testing procedure with a uniaxial increasing load applied in the initially less stiff direction of the specimen. The dotted lines represent the stiffness in the non-loading direction and the continuous lines the stiffness in the loading direction. The stiffness decreases in both directions, but more in the loading direction. The right diagram shows the results of a testing procedure with equi-biaxial tension of specimens with initial anisotropy and with initial

planar isotropy which corresponds to an equal stiffness in the two tested directions. The stiffness degradation of the initial isotropic specimen is equal in both directions, the stiffness degradation of the initial anisotropic specimen is more pronounced in the initially less stiff direction.

The stiffness degradation in both perpendicular directions of the specimens depends on the initial anisotropy of the specimen and on the loading case. These results can be used for a better understanding of the various damage phenomena in SMC and to validate and deliver parameters for anisotropic damage models.
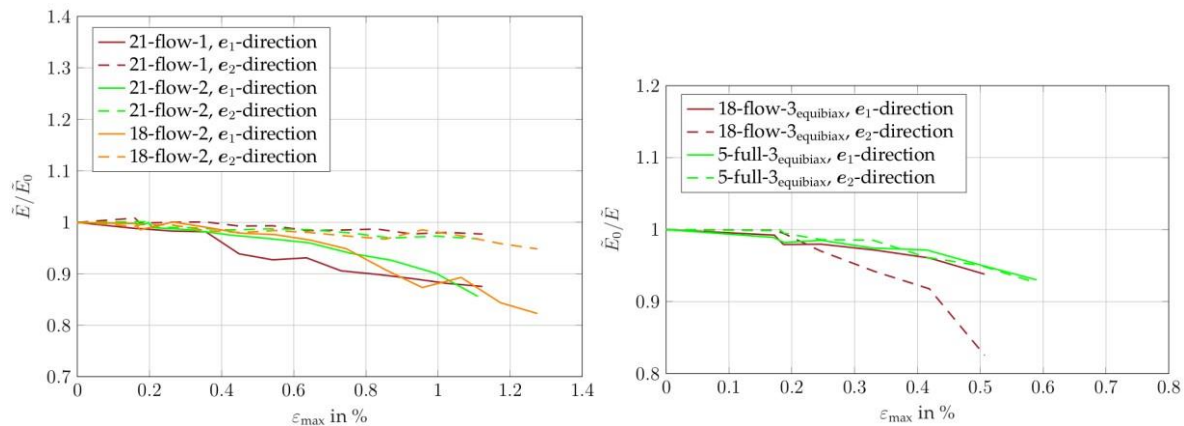
Fig. 1. Stiffness degradation of the biaxial specimens

4. References

[1] M. Schoßig. *Schädigungsmechanismen in Faserverstärkten Kunststoffen*. Springer Vieweg
[2] M. Schemmann, J. Lang, A. Helfrich, T. Seelig, and T. Böhlke (2018). Cruciform Specimen Design for Biaxial Tensile Testing of SMC. *J. Compos. Sci.*, 2(1), 12
[3] D. Bücheler (2017). *Locally Continuous-fiber reinforced Sheet Molding Compound*. Doctoral Thesis, Karlsruhe Institute of Technology (KIT)

EXPERIMENTAL STUDY OF REINFORCING MECHANICAL PROPERTIES OF NYLON-11 IN SELECTIVE LASER SINTERING

L. Andrusiv

United States Air Force Academy, Colorado 80840, USA

1. Abstract

The main objective of this project was to study the effect of kieselguhr (also known as diatomaceous earth – DE) on polymer reinforcement, in particular on nylon-11, when used as filler. A Selective Laser Sintering™ (SLS) machine was used to sinter nylon-11 with different percentages by volume of DE (10%, 15%, 20%, 25%, and 30%) to form composite mixtures and then rapidly prototype into the tensile bars to be tested in the Instron Tensile Testing machine.

The recorded results of experimental testing allow insight into the relationship between the specific mechanical properties of the reinforced nylon-11, predict its behavior as the percentage of filler varies, and demonstrate the trends in changes of yield strength, ultimate strengths, modulus of elasticity, and elongation of composite polymers.

The outcome of the investigation of the diatomaceous earth as a filler definitely indicated that this material is a feasible option for use as a reinforcement and it has more possibilities to strengthen physical properties of polyamides such as nylon when used in rapid prototyping.

2. Introduction

Polymer reinforcement through the use of fillers is a commonly accepted practice. Once bonded, the mechanical properties of the filler contribute to the overall physical and mechanical properties of the composite. A wide variety of fillers and their effects on new composites have been studied. The fabrication of functionally graded nylon-11 filled with different volume fractions of glass beads (0-30%) by SLS 3D was investigated in [1] and tested their composites in both tension and compression. [2] used silicon carbide (SiC) F240 blended with the Duraform Polyamide as an option for direct production in a SLS process. Selective Laser Sintering is one of the most rapidly developing prototyping techniques (RPT), which allows to create full-scale physical prototypes for testing or to rapidly produce 3-dimentional functional parts, but mainly due to its suitability to process almost any material: polymers, metals, ceramics, and many types of composites ([3]). Although the polyamides are the most suitable for SLS process, pure polyamide materials exhibit very large plastic deformation, thus their ultimate strengths are not that high. In order to increase the ultimate strength and improve the overall mechanical properties of the finished materials, some type of additive should be mixed with the polyamide.

3. Method and Materials

The key reasons for nylon-11 and DE to be selected for this work was that both materials can be bio-derived, they do not require as much energy to produce as compared to conventional materials, they are practically inexhaustible renewable resources, and SLS Nylon/DE would find many applications. Nylon-11 is a polymer from the polyamide family. Some of the important advantages of this material are that it has an ability to accept high loading of fillers, low water absorption, and good chemical resistance. Diatomaceous earth (DE) represents a highly porous material with a complex framework composed of the fossilized remains of diatoms, consisting almost entirely of silica, characterized by size in the range from under 5 to over 100 µm and porous structure with

openings as small as 0.1 μm in diameter. So, it was assumed that it might be possible to increase the nylon-11 stiffness by blending it with filler, like diatomaceous earth, which has a much lower density (0.152-0.208 g/cc) than the nylon-11 (1.0-1.05 g/cc), but a much higher melting point (1715 C°) than the nylon-11 (175-191 C°).

To obtain well-bonded blends within the composite specimens, rapid prototyping technique by the SLS machine was used. Five different blends by volume fraction (10%, 15%, 20%, 25%, and 30%) were created and five separate composite tensile bars from each blend were manufactured according to the ASTM D638 standard for plastics. Then each bar underwent a slowly increasing axial force in the Instron Tensile Testing machine until fracture occurred. The mechanical properties acquired for each specimen were then averaged to report them as the specific properties of each composite materials.

4. Main Results of the Research

The experimentally determined mechanical properties of pure nylon-11 were used as the basis for comparison with related properties of the tested specimens. The collected data showed that as the percentage of filler increases, the properties of the blend changed noticeably with respect to the native properties of the pure nylon-11.

The plots in Figure 1 clearly demonstrate the trends in changes of yield strength, ultimate strengths, modulus of elasticity, and elongation of composite polymers with increasing percentage of filler.
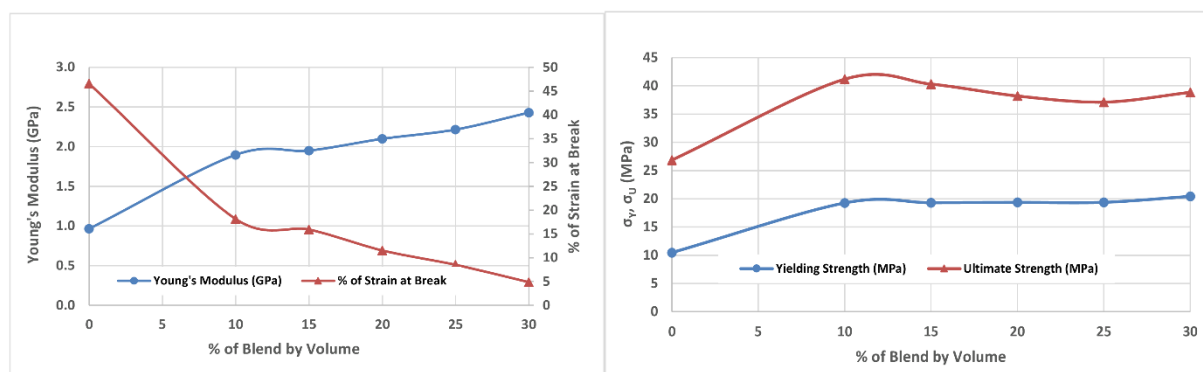
Fig.1. Mechanical properties of the composite polymer with respect to the percentage of the diatomaceous earth

It can be observed that the values of the yield strength and modulus of elasticity have the tendency to increase and the ultimate strength (almost up to 30%) and elongation tend to decrease as the fraction of DE in blend increases. If the material yields at a higher strength it will be stiffer and will be more resistant to elongation. The increase in ultimate strength can be seen as a result of the material becoming more brittle as it stiffens and the increase in modulus of elasticity can be due to the material becoming less elastic, which coincides with the other property trends.

5. References

[1] H. Chung and S. Das (2006). Processing and properties of glass bead functionally graded Nylon-11 composites produced by selective laser sintering, *J. of Mat. Sciences and Eng.*, **437**, 226-234.
[2] K.K.B. Hon and T. Gill (2003). Selective laser sintering of SiC/Polyamide composites, *CIRP Annals. Manufacturing Technology, Num. Meth. Eng.*, **52**, 173-176.
[3] J.P. Kruth, X. Wang, T. Laoui, L. Froyen (2003). Lasers and materials in selective laser sintering, *Assembly Automation*, **23** Issue: 4, 357-371.

STUDY ON CRACK EVOLUTION OF FILM-SUBSTRATE STRUCTURE UNDER PREFABRICATED CRACK

J. Li, L. Li, Q. Wang, S. Wang, C. Li and Z. Wang
Tianjin University, Tianjin, China

1. Introduction

Stiff thin film on soft-substrate structures have attracted with their broad application prospects of industrial fields such as electronics, manufacturing and biomedicine. However, in the actual service process, the film-substrate structure tends to be in a complex stress state, it is more likely to be damaged.Therefore, it is of great significance to study the fracture damage to the film-substrate structure and to explore the mechanism of crack initiation and evolution. As early as 2006, Khang, Jiang, Yu et al.[1] adopted transfer technology to transfer film elements to the surface of pre-stretched substrates by changing the strain of pre-stretching, the time of UV aging treatment, and Parameters.For example, PDMS elastic modulus are used to control the buckling wavelength. Since then, Nam et al.[2-4] achieved artificial control of the crack by changing the shape of the notch on the photoresist and controlling the direction of the crack to form the desired pattern. Amjadi M et al [5-6] began to use this technology to produce some high-sensitivity strain sensors, greatly improving the measurement accuracy of the sensor.However, the introduction of the incision needs too much manual intervention in the current study, which limits the application of crack modulation technology. The purpose of this study is to improve the convenience of the application by modulating the cracks in the film-substrate structure.

2. Theoretical model

A model is built in order to analyze the stress-strain relationship of the film under biaxial loading conditions, which is shown in Figure 1.
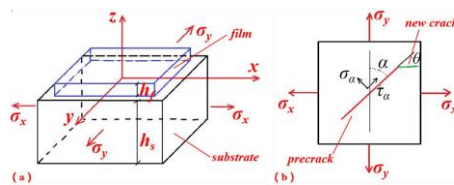
Fig. 1 Stress analysis model (a) Stress analysis of film-substrate structures;
(b) Stress analysis of crack tip

First, the normal and shear stresses of the crack surface are obtained according to the equilibrium conditions:(α is the pre-crack angle, β is the new crack angle)

(1) $\qquad \tau_\alpha = (\sigma_y - \sigma_x)\sin\alpha\cos\alpha$

(2) $\qquad \sigma_\alpha = \sigma_x \cos^2\alpha + \sigma_y \sin^2\alpha$

Considering the biaxial stretching, the crack propagation is formed by the coupling of type I and type II, and a new stress intensity factor under this coupling can be obtained.Substituting the new stress intensity factor into the following equation, we get the new theoretical model mentioned in this paper.

(3) $S = a_{11}K_I^2 + 2a_{12}K_IK_{II} + a_{22}K_{II}^2$

3. Experiment and Results

Combined with laser confocal microscopy to observe the crack morphology, the biaxial tensile damage experiment of film-substrate structure was carried out to study the effects of different loading ratios of crack initiation and the evolutionary behavior. In addition, the improved minimum strains energy density factor theoretical model was used in this study. The consequent expansion angle of the pre-crack (pre-cracked by focused ion beam technique) was predicted, and the experimental results agreed well with the theory. The experimental platform and test pieces are shown in Figure 2.
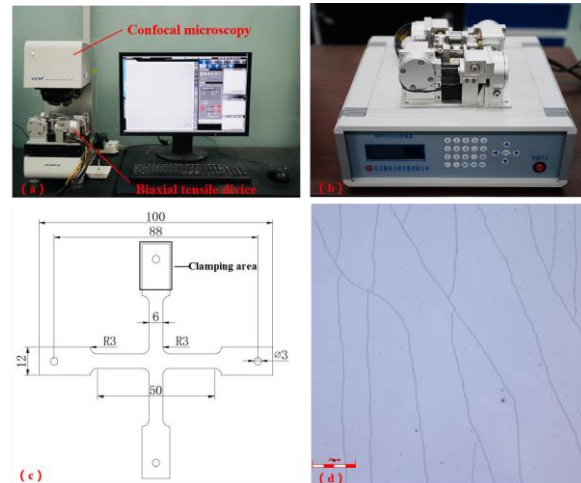
Fig. 2. The experiment platform (a) Confocal microscope (b) New biaxial tensile device
(c) Geometry size of the specimen (unit in millimeter) (d) Experimental results

4. Results and discussion

In this paper,a pre-cracked test piece was designed and the pre-cracked test piece is subjected to biaxial loading test.The relationship between the crack tip expansion angle and the loading ratio at different initial crack angles is obtained. The modulation effect of pre-crack and biaxial loading ratio on the film pre-crack expansion angle was achieved. On the angle of the new crack,the influence of loading ratio and pre-crack was analyzed by a theoretical model, so that the angle can be predicted. The experimental results agreed well with the theory.

5. References

[1] Khang, D. Y. A Stretchable Form of Single-Crystal Silicon for High-Performance Electronics on Rubber Substrates [J]. *Science*, 2006, 311(5758): 208-212.
[2] Nam K H, Park I H, Ko S H. Patterning by controlled cracking [J]. *Nature*, 2012, 485(7397): 221.
[3] Kim B C, Matsuoka T, Moraes C, et al. Guided fracture of films on soft substrates to create micro/nano-feature arrays with controlled periodicity [J]. *Scientific Reports*, 2013, 3(10): 3027.
[4] Kim M, Ha D, Kim T. Cracking-assisted photolithography for mixed-scale patterning and nanofluidic applications [J]. *Nature Communications*, 2015, 6: 6247.
[5] Amjadi M, Turan M, Clementson C P, et al. Parallel microcracks-based ultrasensitive and highly stretchable strain sensors [J]. *ACS applied materials & interfaces*, 2016, 8(8): 5618-5626.
[6] Choi Y W, Kang D, Pikhitsa P V, et al. Ultra-sensitive Pressure sensor based on guided straight mechanical cracks [J]. *Scientific Reports*, 2017, 7: 40116.

STRAIN MEASUREMENT BY MEANS OF CLIP-ON EXTENSOMETERS DURING DISCONTINUOUS PLASTIC FLOW AT 4 K

J. Tabin

Institute of Fundamental Technological Research of PAS, Warsaw, Poland
Cracow University of Technology, Cracow, Poland

1. Introduction

Until the 1980s, strain measurements in liquid helium (4 K) were complicated but tensometers for cryogenic temperatures were developed and reliable clip-on extensometers were fortunately introduced. Such transducers can work with high resolution, and reproducible signals for a variety of engineering measurement tasks such as tensile, fracture, compression, fatigue, flexural, and component tests at cryogenic environments. The correct measurement of strains is the key factor in the materials investigation and engineering design of complex structures. Properly designed and attached clip-on extensometers can transfer the strain information for further computation of mechanical parameters. Although different techniques are available at cryogenic temperatures, the strain gauge technology is still mostly used. Moreover, the clip-on extensometers based on strain gauges are recommended by the international standards (ASTM E 1450-16 or ISO 6892-4:2015) for tensile testing of metals at liquid helium. These transducers are often selected for strain measurement during cryogenic tensile tests of polycrystalline materials, composites or high-entropy alloys. Moreover, the International Electrotechnical Commission (IEC) supports the efforts to establish the international standards of the testing methods for superconducting technical wires at cryogenic temperatures, and the clip-on extensometers are considered as strain transducers to identify the tensile properties.
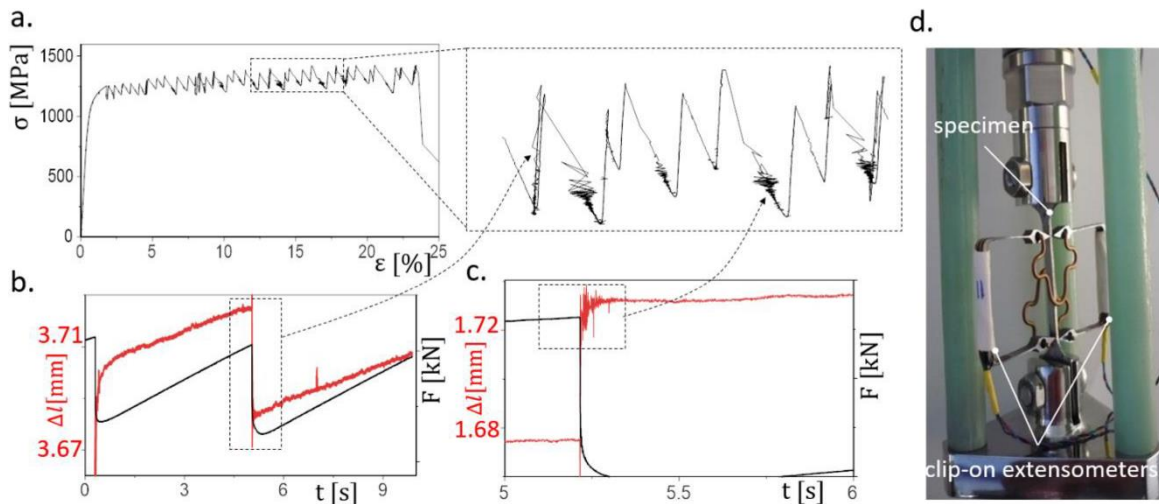
Fig 1. a) Artefacts on stress-strain curve of JK2LB during uniaxial tensile test at 4 K; b) time response of clip-on extensometers (red) and force transducer (black) when shear band occurs out of extensometers' gauge length; c) self-excited vibrations of extensometers induced by the plastic flow instability; d) strain measurement set-up

The most advanced material test laboratories, such as CryoMaK in Karlsruhe Institute of Technology in Germany, National Institute for Materials Science, or High Energy Accelerator

Research Organization (KEK) in Japan, CERN in Switzerland, or NASA in the USA, use clip-on extensometers to measure the elongation and to identify the mechanical parameters at cryogenic temperatures.

During tensile tests of the engineering materials at cryogenic temperatures, unusual behaviour is observed. When temperature tends to the absolute zero, below a transition temperature the discontinuous plastic flow (DPF) occurs. Until now, the DPF was successfully investigated by many prominent researchers. Nevertheless, they did not present the complex analysis of measurement artefacts during strain measurement at 4 K performed by the clip-on extensometers. In this study, the time responses of clip-on extensometers during the uniaxial tensile tests of the engineering materials at 4 K are analysed. It turns out, that the strong strain localization and the self-excited vibrations of extensometers, related to the plastic flow instability (DPF) disturb the strain measurement (Fig. 1). These measurement artefacts affect the identification of mechanical parameters, such as the proof stress or the total elongation [1]. 0 2. % R

2. Acknowledgments

3. References

[1] J. Tabin (2022). *Strain measurement by means of clip-on extensometers during discontinuous plastic flow at 4 K*. Cryogenics 123, 103451.

SIMPLE CALIBRATION OF MIXED, STRAIN-STRESS FAILURE CRITERION FOR 3D PRINTED METALLIC MATERIALS

G. Socha
Łukasiewicz Research Network - Institute of Aviation,
Al. Krakowska 110/114, 02-256 Warszawa, Polska

1. Introduction

Additive manufacturing is gaining increasing importance as the aerospace component manufacturing technology. Despite of significant progress in the production technology, 3D printed components still cannot challenge strength of precision castings, especially when it comes to high service loads and high temperatures. On the other hand, printed component can offer some advantages. One of them is the impact energy absorption ability. Due to incomplete fusion such components, when subject to compressive loads, can absorb significantly more energy in smooth manner (avoiding peak loads that can be dangerous from the point of view of passenger safety). Properly designed, 3D printed energy absorbing structures can offer some advantages but it's design and simulation process requires use of appropriate tools. Modelling and computer simulation of the impact requires use of appropriate yield condition, flow rule and failure criterion.

2. Failure criteria suitable for 3D printed materials

Effect of incomplete fusion on failure criterion can be easily deduced: failure strain shall be much higher under compression than that for tension. Many failure criteria taking into account this effect for metallic materials were proposed by researchers. A good review of criteria applied in the most popular FEM codes can be found in paper [1] together with an attempt of its calibration. One of them, proposed by Johnson [2] is very popular among researchers due to availability of calibration coefficients for some popular alloys. For other alloys however, calibration has to be performed if the criterion is going to be used for computer simulation. Experimental calibration of the above mentioned failure criterion, as it was reported in [1] is sophisticated, time consuming procedure. Much easier procedure can be applied for the criterion proposed by Xue and Wierzbicki. For the 3D printed alloy used in presented research, and for axisymmetric stress states, this failure criterion can be written in the following form [1]:

(1) $\qquad \varepsilon_f = C_1 exp(-C_2\eta)$

where ε_f is the equivalent failure strain, η is the triaxiality factor (ratio of first and second invariant of the stress tensor) and C_1, C_2 are coefficients to be determined.

3. Calibration procedure

The procedure of calibration for failure criterion (1) require performing at least two tests to failure at two different stress states. First of them is to be performed under pure shear. Procedure and accessory to be used in this case is described in patent description [3]. Simple fixture designed for determination of failure strain under pure shear stress at ambient and high temperatures is shown in figure 1 together with picture of specimen after test.
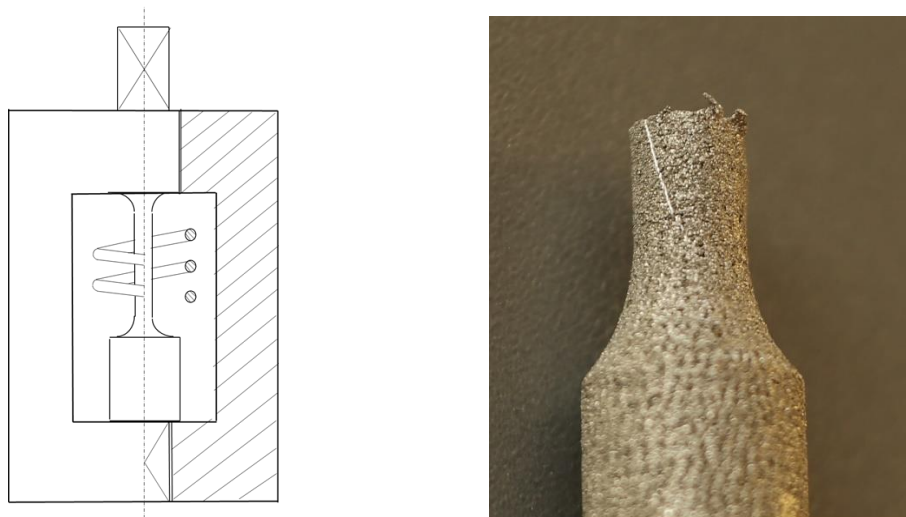
Fig. 1. Fixture and specimen for failure strain determination

As it can be seen in this figure, gage part of the specimen can be heated to required temperature using inductive heating. No testing machine is needed to load the specimen, hand tool can be used to twist gage part until failure of the material. On the right side of the figure, specimen after test is shown. Line visible on the gage part was marked parallel to the specimen axis before test. Gage part twist angle corresponding to material failure was measured to be 0.283 rad. This corresponds to equivalent strain 0.19 mm/mm.

Another test performed to calibrate failure criterion (1) is the static tension of the specimen shown in figure 1. Under this stress state material reached equivalent failure strain 0.0104 mm/mm. Two values of failure strain, obtained for different values of the triaxiality factor η were used to determine coefficients of the criterion (1). Finally failure criterion, calibrated for the material in question can be written in the following form:

(2) $\varepsilon_f = 0.19e^{-8.71\eta}$

As the conclusion it can be stated that Xue – Wierzbicki criterion seems to be suitable for 3D printed materials and, if properly calibrated, can be used for simulation of energy absorption process.

4. References

[1] Wierzbicki T. et al., Calibration and evaluation of seven fracture models, *International Journal of Mechanical Sciences*, Vol.47, pp. 719-743, 2005

[2] Johnson G. R., Materials Characterization for computations involving severe dynamic loading, *Proc. Army Symp. Of Solid Mechanics*, pp. 62-67, Cape Cod, Mass., 1980.

[3] Socha G., A method and accessory for determination of failure strain for ductile materials subject to arbitrary stress state in the wide range of temperatures, *Polish Patent Office*, patent pending 77P43754 PL00

STRAIN EVALUATION NEAR 3D CURVED BOUNDARIES BASED ON DIC DATA

T. Lehmann and J. Ihlemann
Chemnitz University of Technology, Chair of Solid Mechanics, Chemnitz, Germany

1. Introduction

Elastomer materials are used in many technical structural applications e. g. buffers, bearings, seals, tires, belts and air springs. The experimental investigation of these materials is of high importance and used for material characterization, parameter identification and the validation of numerical models. Furthermore, for field measurements high-performance measuring methods are required. This contribution deals with the experimental investigation of inhomogeneous strain fields on the surface of rubber specimens by Digital Image Correlation (DIC). In the presented case, the approximation of DIC data by B-Splines [1] with an additional parametrization around the hole geometry is performed as a basis for strain determination. The basic principle of this parametrization is given in [2]. An extension of this method for 3D geometries is demonstrated in the present paper using an example of a cylindrical specimen with a hole in radial direction.

2. Experimental setup

The tests were performed with filled EPDM specimens including a through-hole in radial direction in the middle of the specimen, see Fig. 1 (right). Compression loading was carried out using an electromechanical testing machine (Zwick/Roell 100 kN) with a device consisting of a punch and plates for load application and bearing, which is shown in Fig. 1 (left). The displacement-controlled load was applied monotonously (velocity 2 mm/min). For force measurement a 5 kN load cell was applied considering the low stiffness of the investigated material. Images were acquired in intervals of 0.25 mm as a database for the 3D DIC using a Gom Aramis 4M system, see Fig. 1 (left).
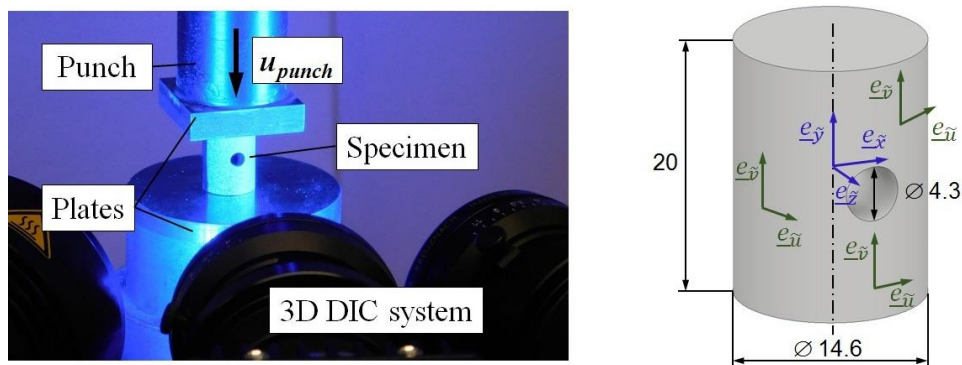
Fig. 1. left: experimental setup, right: nominal specimen geometry and evaluation directions

3. Strain evaluation method

The primary results of the DIC are the 3D coordinates of the surface in the reference (undeformed) and the deformed state. The data was approximated by B-spline surfaces using Matlab [2]. The performed procedure requires gridded data for the evaluation. To avoid interpolation of data in the section of the hole (without measuring data), which causes inaccuracies at the edges, a special developed parametrization (parameters s, $t \in [0,1]$) of an annulus surrounding the hole was applied in

the $\tilde{x}\,\tilde{y}$-plane. The relations between the parameters s, t and the coordinates in the reference state $\tilde{x}$, $\tilde{y}$ are based on geometrical conditions given in Fig. 2 (left) and calculated by:

$$(1) \qquad s(\tilde{x}, \tilde{y}) = \frac{\arctan(\tilde{y}/\tilde{x})}{2\pi}, \quad t(\tilde{x}, \tilde{y}) = \frac{\sqrt{\tilde{x}^2 + \tilde{y}^2} - r_{min}}{r_{max} - r_{min}}$$

The 2D deformation gradient regarding the global directions ($\tilde{x}$, $\tilde{y}$, x, y) is obtained using partial derivatives of the coordinates in the deformed state (x, y) with respect to the parameters (s, t) and partial derivatives of these parameters with respect to the coordinates in the reference state ($\tilde{x}$, $\tilde{y}$). Local tangential directions $\tilde{u}$, $\tilde{v}$ (see Fig, 1, (right)) and u, v are determined based on the 3D surfaces (given by $\tilde{x}$, $\tilde{y}$, $\tilde{z}$ and x, y, z) in the reference and the deformed state. On this basis, the 2D deformation gradient with regard to these directions is calculated. Finally, the Lagrangian Hencky strain tensor regarding the tangential directions is determined by:

$$(2) \qquad \underline{H} = 0.5\ln\left(\left(\underline{F}^T \cdot \underline{F}\right)\right), \text{ with } [H_{ab}] = \begin{bmatrix} H_{uu} & H_{uv} \\ H_{uv} & H_{vv} \end{bmatrix}$$

4. Results

In Fig. 2 (right) the distribution of the strain H_{uu} in a section surrounding the hole ($r_{min} = 2.4$ mm, $r_{max} = 4.3$ mm) is given for $u_{punch} = 1.5$ mm, $F_{punch} = 123$ N. An approximately symmetrical and inhomogeneous strain distribution with large gradients and changes of sign is observed.
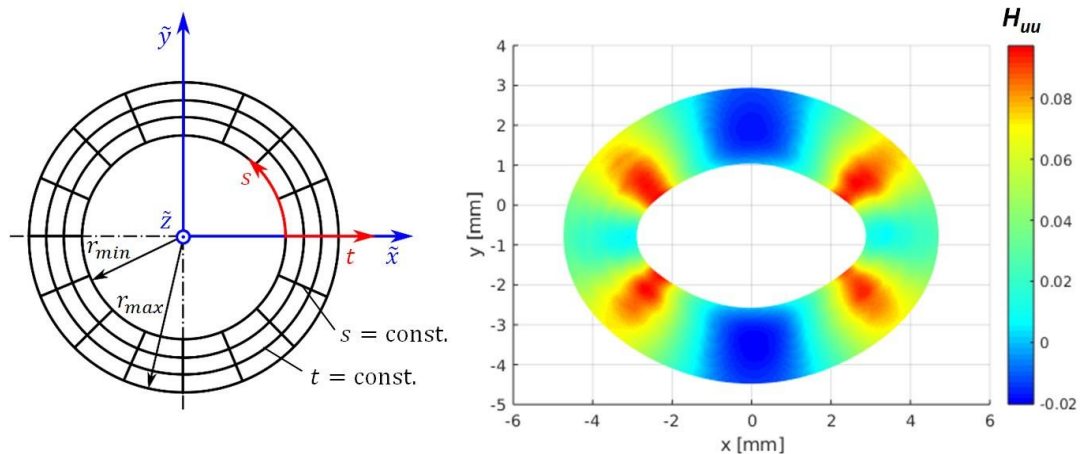
Fig. 2. left: principle of the parametrization, right: example of H_{uu} around the hole

5. Conclusions

The special evaluation procedure using B-spline approximation and parametrization enables precise strain determination near the edges of the hole. Furthermore, the presented evaluation method provides the determination of various tensorial strain measures.

6. References

[1] J. Hoschek and D. Lasser (1992). *Grundlagen der geometrischen Datenverarbeitung*, 2nd ed. Teubner, Stuttgart.

[2] T. Lehmann, M. Stockmann and J. Ihlemann (2019). A method for strain analyses of surfaces with curved boundaries based on measured displacement fields, *Mater. Today-Proc.*, **12**, 200-206.

STUDIES ON THE EFFECT OF DC HIGH VOLTAGE ON SAMPLES FROM GLASS-EPOXY CORE RODS FOR COMPOSITE INSULATORS

P. Ranachowski[1], K. Wieczorek[2], M. Jaroszewski[2] and Z. Ranachowski[1]
[1] Institute of Fundamental Technological Research Polish Academy of Sciences,
5b Pawińskiego Str., 02-106 Warsaw, Poland
[2] Wrocław University of Science and Technology, Faculty of Electrical Engineering,
Wybrzeże Wypiańskiego 27, 50-370 Wrocław, Poland

1. Introduction

In recent times growing interest in the transmission of electrical energy using High Voltage Direct Current (HVDC) lines have shown [1, 2]. However, in contrast to AC lines, the electrostatic phenomena can occur in DC lines. It can result in the degradation processes and electric strength can be affected [3, 4]. What is more, in comparison to AC systems, increase the accumulation of surface pollution can up to even four times [5]. The other problem is that in case of the DC polarization the ignition of concentrated surface discharges is not turned off as in the AC system - where the voltage curve passes through zero [5].

This work presents the results of an examination performed on a set of samples cut from glassepoxy core rods used in composite insulators with silicone rubber housings. There were tested a core rods of typical insulators operated in Alternating Current (AC) high voltage power transmission network. The idea is possibility of using such insulators in HVDC lines. In this connection the purpose of the tests was to check the aging resistance of the core material when exposed to DC high voltage. Long term exposure of a glass-epoxy core rod to DC high voltage may lead to the gradual degradation of its mechanical properties due to the flow of ion current. The ionic leakage current, the concentration of ions and their discharges at the electrodes may cause permanent changes to the structure of the glass-epoxy material. The process may lead to the creation of some more or less branched current paths, going from the negative electrode, as well as some micro or even macro fractures. Such effects would disqualify the analysed glass-epoxy material from being used in the presence of DC high voltage. Electrolysis of the core material (glass fiber) may cause such insulators to break and consequently result in a major failure.

2. Experimental

The samples were exposed to DC high voltage for 6000 hours. The assumed value of aging voltage was approximately twofold greater than the value of rated voltages in composite insulators. The average value of the electric field strength for insulators is about 1 kV/cm, while the value for the samples in the test was 2 kV/cm. The properties of the aged samples were compared with those measured in reference samples. It should be noted that the tested rods were made of ECR glass. Type E of glass is a special type of alkali-free glass designed for electrical application, CR means that the glass is corrosion resistant.

After being aged for 6000 hours under DC high voltage, the samples were subjected to microscopic analysis. Their chemical composition was also examined using Raman spectroscopy and their dielectric losses and conductance in the broad range of frequencies were tested using dielectric spectroscopy [6]. Another group of samples was subjected to mechanical tests. The research was also comparative. Therefore, the samples of the first series - marked as group A - were not subjected to any actions and reflected the initial structure of the material. The samples of the second series - group B - were for 6000 hours exposed to temperature increased to 50ºC. The samples of the third series -

group C - were exposed to temperature increased to 50ºC and first of all DC high voltage (2 kV/cm) for 6000 hours likewise. Samples of all three series – A, B and C - a total of 13 were tested using the three-point bend method. In addition to mechanical tests, the microhardness of the fresh and aged samples material was measured.

3. Results and conclusion

The comparative microscopic, Raman spectroscopy and mechanical examination of the reference samples and the aged samples from glass-epoxy core rods used in composite insulators showed no observable traces of degradation. Long term exposure to the influence of a DC voltage field in a direction parallel to the glass fibers and temperature increased to 50ºC caused neither any electrolysis in the material nor any deterioration of its electrical (electro insulation) or mechanical properties. Mechanical characteristics and microhardness of all three series of the tested samples showed no differences. What's more, very good repeatability of the characteristics and mechanical strength testing results of the samples of all three groups should be emphasized – table 1. Slight increasing polymerization of epoxy resin was the only phenomenon observed (using Raman spectroscopy) [6]. It does not cause any decrease in the operational properties of the glass-epoxy material. Dielectric spectroscopy confirmed the above results – as compared with the fresh samples, the aged samples showed no differences that could suggest any degradation processes. It has been proven that glass-epoxy core rods, made of ECR glass and operated in AC high voltage power transmission network, can be also used in HVDC lines.

Group of samples	A	B	C
Average strength [MPa]	572 ± 14.1	570 ± 17.1	5719.7

Table 1. Average strength of the three-point bend test of the samples of three groups, with standard deviation

4. References

[1] J.M. George, Z. Lodi (2009). *Design and selection criteria for HVDC overhead transmission lines insulators*, CIGRE Canada, Conference on Power Systems, Toronto, October 4-6.

[2] M. Kumosa, D. Armentrout, B. Burks, J. Hoffman, L. Kumosa, J. Middleton, P. Predecki (2011). *Polymer matrix composites in high voltage transmission line applications*, Proc. of the 18th International Conference on Composite Materials, Jeju Island, S. Korea August 2126.

[3] S. Gubański (2016). *Surface Charge & DC Flashover Performance of Composite Insulators*, INMR August 13.

[4] P. Morshuis, A. Cavallini, D. Fabiani, G.C. Montanari, C. Azcarraga (2015). Stress Conditions in HVDC Equipment and Routes to in Service Failure, *IEEE Trans. on Diel. and Elect. Insul.,* **22**, 1, February.

[5] CIGRE 518 (2012). *Outdoor Insulation in Polluted Conditions: Guidelines for Selection and Dimensioning*, Part 2: The DC case, Working Group C4. 303, December.

[6] K. Wieczorek, M. Jaroszewski, P. Ranachowski, Z. Ranachowski (2018). Examination of the properties of samples from glass-epoxy core rods for composite insulators subjected to dc high voltage, *Arch. Metal. Mater.*, **63**, 3, 1281-1286.

PHYSICAL AND MECHANICAL EFFECTS OF RADIATION DAMAGE

**A. Ustrzycka[1], F.J. Dominguez-Gutierrez[2,3], M. Nowak[1],
K. Mulewska[2], A. Azarov[4] and Ł. Kurpaska[2]**

[1] *Institute of Fundamental Technological Research, Warsaw, Poland*
[2] *NOMATEN Centre of Excellence, National Centre for Nuclear Research, Poland*
[3] *Institute for Advanced Computational Science, Stony Brook University, USA*
[4] *University of Oslo, Centre for Materials Science and Nanotechnology, Norway*

The present work focuses on the experimental analysis and the constitutive modeling of irradiation effect on mechanical properties of the materials subject in the nuclear installations design and the particle detectors.

Irradiation of materials leads essentially to severe degradation of material microstructure. In the materials, the displacements of atoms, caused by direct collisions of fast particles with the atoms, are the primary driving force of radiation defects creation. As a result of the collision cascade overlap, the creation of vacancy clusters (empty lattice sites) and/or interstitials clusters (atoms sharing lattice sites) occurs. Most of the point defects recombine within the time evolution of the displacement cascade. The remaining defects, voids, cavities, dislocation loops, and stacking-fault tetrahedral (SFTs) form stable defect configurations which are responsible for the radiation-induced microstructural changes, resulting in the evolution of the physical and the mechanical properties. All the physical processes in the irradiated materials occur during and soon after the interaction of energetic incident particles with lattice atoms. These processes are experimentally unobservable because a displacement phase of the collision cascade usually lasts even 10_{-12} seconds. The only approach that may address this issue is Molecular Dynamics (MD) simulations [1, 2]. At the atomic scale, the character and migration properties of self-interstitial clusters, dislocation loops kinetics, defect-dislocation interactions, void and gas bubble formation are studied by Molecular Dynamics simulations (Fig.1).

0.05 dpa   0.3 dpa   0.5 dpa
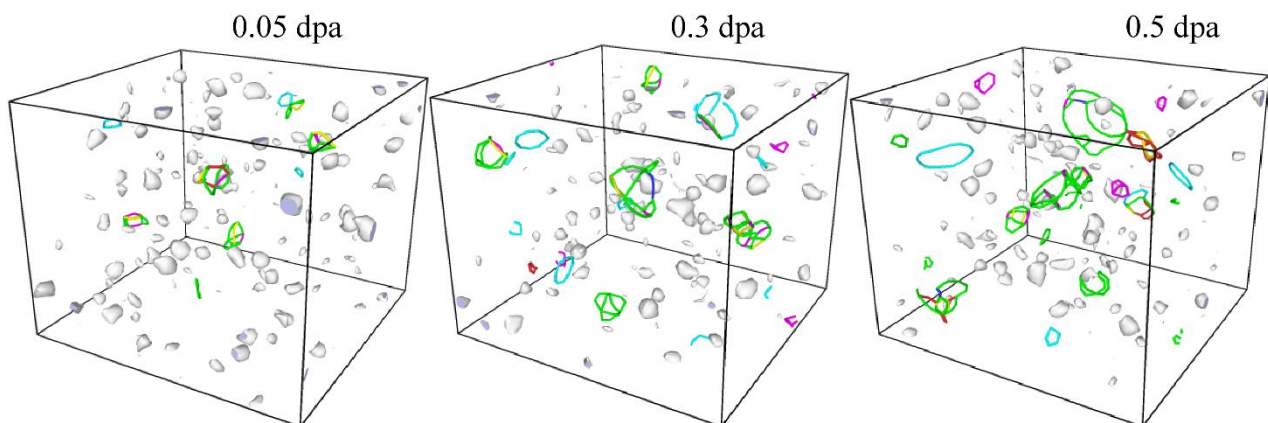
Fig. 1. Nucleation and evolution of radiation induced defects (voids, dislocation loops and stacking-fault tetrahedral formation) in austenitic stainless 310S

In order to validate molecular dynamics simulations, the ions irradiation campaign with MeV energies were carried out using a tandem accelerator in cooperation with the University of Oslo, Centre for Materials Science and Nanotechnology. Transmission electron microscopy (TEM)

investigations show the structural changes resulting from the ion beam irradiation. Direct observations of the defect structure, range, and the radiation-induced defect concentrations in the studied material was determined.

At the meso- and macroscopic levels, the irradiation of materials leads to drastic modifications of mechanical properties. The magnitude of the mechanical changes depends on multiple factors related to the irradiation conditions: radiation energy, particle fluence and flux, material composition and its history. In irradiated materials, the induced defects contribute to irradiation hardening, reduction in ductility, increased embrittlement, volumetric swelling, and helium accumulation. However, plastic deformation is based on similar mechanisms like in the virgin materials. In particular, the main mechanism of plastic flow is still slip. However, due to radiation induced defects the motion of dislocations within the easy slip planes is hindered by different obstacles, causing substantial increase of the flow stress.

In this work, the radiation-induced damage is defined in the framework of Continuum Damage Mechanics (CDM) [5, 6] and peridynamics theory (PD) [3] to solve the problem of further evolution of damage fields under mechanical loading. A novel material model based on nonlocal peridynamic theory is proposed to study irradiated materials [3]. The peridynamic theory is particularly powerful in modelling problems where spontaneous formation of discontinuities, like micro-damage, voids and cracks, occurs. The experimental characterization of the deformation process of the ion irradiated materials during the nano-indentation test is carried out. The numerically obtained curves were imposed on the experimental data [5].

Moreover, in the present work a physically-based constitutive model is proposed which allows to describe the effects of creep of irradiated materials at cryogenic temperatures and the physics of defect generation [4]. The quantum tunneling as the mechanism responsible for creep deformations at sufficiently low temperatures and relatively high-stress levels is adopted. Dislocations that are locally pinned can escape from their pinning points more rapidly via tunneling than by means of thermal activation. Peierls lattice resistance mechanism is used to explain creep produced by the elastic interaction of radiation-induced point defects with existing dislocations in materials. Furthermore, assuming the quantum tunneling mechanism, the kinetic law for the evolution of irradiation-induced dislocation loops is proposed. Predicted creep rate behavior as a function of stresses and *dpa* are presented.

References

[1] A. Ustrzycka, F. J. Dominguez-Gutierrez, U.von Toussaint and M. Alava (2022). Multiscale modeling of irradiation hardening in austenitic stainless steel, *(in preparation)*

[2] F. J. Dominguez-Gutierrez, K. Mulewska, A. Ustrzycka, R. Alvarez-Donado, A. Kosińska, W.Y. Huo, L. Kurpaska, I. Jozwik, S. Papanikolaou, M. Alava (2022). Mechanisms of strength and hardening in austenitic stainless 310S steel: Nanoindentation experiments and multiscale modeling, *(under review)*

[3] A. Ustrzycka, M. Nowak (2021). Microdamage and fracture initiation in the materials subjected to ion-irradiation, ICTAM2021, Italy, 1685-1686.

[4] A. Ustrzycka, (2021). Physical mechanisms based constitutive model of creep in irradiated and unirradiated metals at cryogenic temperatures, *Journal of Nuclear Materials*, **548**, 152851-1-15.

[5] A. Ustrzycka, B. Skoczeń, M. Nowak, Ł. Kurpaska, E. Wyszkowska, J. Jagielski (2020). Elastic-plastic-damage model of nanoindentation of the ion-irradiated 6061 aluminum alloy. *International Journal of Damage Mechanics,* **29**, 1271-1305.

[6] B. Skoczeń and A. Ustrzycka. (2016). Kinetics of evolution of radiation induced micro-damage in ductile materials subjected to time-dependent stresses. *International Journal of Plasticity*, **80**, 86-110.

ASSESSMENT OF HARDNESS EVOLUTION OF HEAT TREATED AMS6414 STEEL BY USING NON-DESTRUCTIVE METHODS

D. Kukla, M. Kopec and Z.L. Kowalewski

Institute of Fundamental Technological Research, Polish Academy of Sciences,
Pawinskiego 5B, 02-106 Warsaw, Poland

1. Abstract

This work concerns the development of procedures for assessing the hardness of AMS 6414 steel samples after the case-hardening and induction hardening process, by using non-destructive magnetic techniques. The eddy current and Barkhausen noise methods were used to assess the hardness of 7 samples subjected to tempering treatment in various temperatures ranging from 120 to 190°C. The eddy current method was used to measure the phase angle changes of the lift-off signal obtained from the measurements of samples with different hardness.

The phase angle of the eddy current signal strongly depends on the electrical conductivity and permeability changes of the investigated material. These specific physical properties of material are sensitive to stress and simultaneous hardness changes caused by heat treatment at different tempering temperatures. Therefore the hardness of material could be predicted by measurement of the phase angle changes.

Assessment of hardness by using non-destructive methods also based on the envelope analysis of Barkhausen effects signals. This method could be used to identify the hardness changes of tempered layers with an accuracy of 10HV. In order to verify the obtained results from both of nondestructive tests, the microstructure analysis were carried out and micro-hardness profiles were made on the cross sections of the samples.

In present work, non-destructive methods were also used to identify the changes of hardened layers thickness in materials characterized by microstructural gradient and thus different hardness distribution.

2. Keywords

Carburizing, induction-hardened layer, Barkhausen noise, eddy currents, micro-hardness profiles

3. References

[1] Kukla D., Grzywna P., Kopec M., Kowalewski Z.L., Assessment of hardened layer thickness for 40HNMA steel using eddy current method, INŻYNIERIA MATERIAŁOWA, ISSN: 0208-6247, DOI: 10.15199/28.2016.5.10, Vol.213, No.5, pp.263-266, **2016**

[2] Fryczowski K., Roskosz M., Kukla D., Szwed M., Wykorzystanie szumu Barkhausena w ocenie twardości warstw nawęglanych oraz hartowanych indukcyjnie na stali AMS 6414, PRZEGLĄD SPAWALNICTWA, ISSN: 0033-2364, Vol.89, No.11, pp.1-6, **2017**

[3] Kukla D., Grzywna P., Kopec M., Kowalewski Z.L., Eddy Current method for thickness assessment of carburized layers, AMT 2016, XXI Physical Metallurgy and Materials Science Conference - Advanced Materials and Technologies, 2016-06-05/06-08, Rawa Mazowiecka (PL), pp.BP7-1-3, **2016**.

CALCULATION AND FATIGUE TESTING OF STEEL P91 IN CONDITIONS OF VARIABLE LOAD AND CREEP

S. Mroziński[1], M. Piotrowski[1] and H. Egner[2]

[1] *University of Science and Technology, Faculty of Mechanical Engineering, Bydgoszcz, Poland*
[2] *Cracow University of Technology, Faculty of Mechanical Engineering, Kraków, Poland*

1. Introduction

The analysis of real load of machine structural elements indicates that it is most often subject to stress load. This includes facilities operated at elevated temperatures. This type of load can be accompanied by material creep, which causes a change of the load and the durability of the objects. Forecasting fatigue life in this case, considering only classic fatigue characteristics, can lead to differentiation of results obtained from calculations and tests.

Currently, there are several hypotheses for adding up fatigue damage in conditions of simultaneous occurrence of variable load and creep. They were presented in [1]. One of the models is a linear model, which refers directly to the proposal given in the work [2]. According to the proposed model, after the implementation of N_i load cycles, the fatigue damage D_t will be equal to:

$$(1) \qquad \sum \frac{N_i}{N_f} + \sum \frac{\tau_i}{T_c} = D_t$$

where: N_f – number of cycles till crake in the conditions of variable load (σ_a=const and τ=0), T_c – total time of creeping test (σ=const).

The research problem undertaken in the following work was determining the impact of creep on fatigue life under variable load and creep conditions.

2. Description of research

The samples for tests were made from steel P91 (*UTS*=716 MPa, *Yp*=564 MPa, *A₅*=35%). Shape of samples was based on proper standard [3]. Experimental studies included creep tests, fatigue tests and tests in which samples were simultaneously subjected to variable load and creep. The scheme of the load program and the parameters adopted are summarized in Figure 1. The tests were carried out at temperature of 20 and 600ºC.

τ_i, s	σ_{ai}, MPa		T, ºC	
0				
5	218,8	257,8	20	600
30				
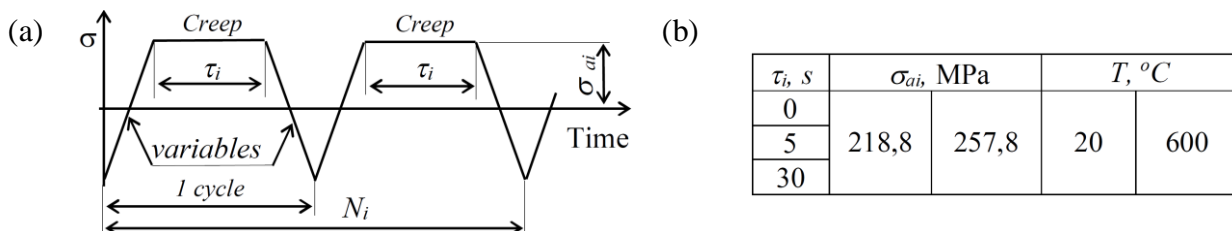
Fig. 1. Tests program: a) load program, b) load programs parameters

3. Results of the tests

The obtained test results were analyzed in the context of the influence of creep on changes in basic loop parameters as a function of the number of load cycles. To compare the results obtained under

the conditions of classic variable load and load containing creep, Figure 2 shows the changes in the maximum elongation ε_{max} of the sample registered during the tests at two stress levels.
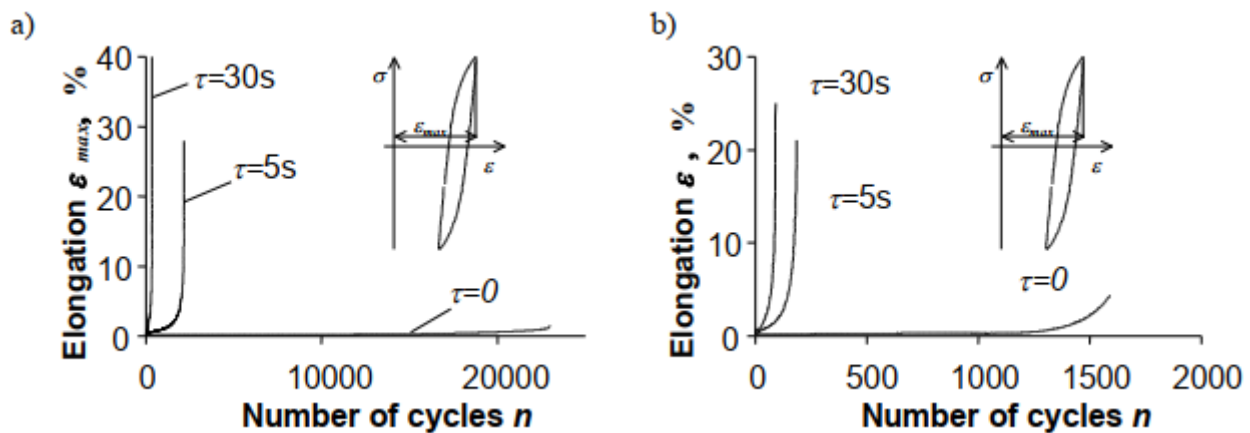
Fig. 2. Hysteresis loops in various test conditions: a) σ_a=218,8 MPa, b) σ_a=257,8 MPa

Based on the obtained results, it was found that the creep occurring during variable load causes a reduction of fatigue life and a clear increase in the elongation of the sample. Impact of the reduction fatigue life under variable load and occurrence of creep is the creep duration τ_i. Not taking this fact into account of fatigue life calculating leads to a significant differentiation in the results of calculations and tests.

4. Summary

If creep occur during variable load causes a reduction of fatigue life. As the creep time increases, the sample elongation increases and the fatigue life decreases. The temperature of the tests also has an impact on the reduction in fatigue life. At elevated temperatures, the effect of creep on reducing fatigue life is greater. The experimental verification of the classic fault of cumulative damage hypothesis showed that failure to consider creep durability in the calculations leads to a significant differentiation in the results of calculations and tests.

A clear improvement in the compliance of fatigue life results obtained from calculations and tests can be obtained by taking into account the creep during variable load summation.

5. Acknowledgment

6. References

[1] Zhuang W. Z., Swansson N. S.: T*hermo-Mechanical Fatigue Life Prediction: A Critical Review*, DSTO-TR-0609, DSTO Aeronautical and Maritime Research Laboratory, 1998.
[2] Miner, M., Cumulative Damage in Fatigue, J. Applied Mechanics. Trans. ASME, 1952.
[3] ASTM E606-92: Standard Practice for Strain -Controlled Fatigue Testing.

ANALYSIS OF FATIGUE CRACK INITIATION
IN CYCLIC MICROPLASTICITY REGIME

A. Ustrzycka, Z. Mróz, Z.L. Kowalewski and S. Kucharski
Institute of Fundamental Technological Research, Warsaw, Poland

The present work provides description of fatigue crack initiation in metals subjected to cyclic loading within the nominal elastic or initial elastic-plastic regimes. When a polycrystalline metal or alloy element is subjected to mechanical loading inducing uniform mean stress and strain states, the fluctuation fields develop due to material inhomogeneity related to grain anisotropy and inhomogeneity [1]. Due to imperfections (inclusions, cavities), grain boundaries, free boundary effects, dislocation microstructure, the local stress and strain concentrations develop (Fig. 1).
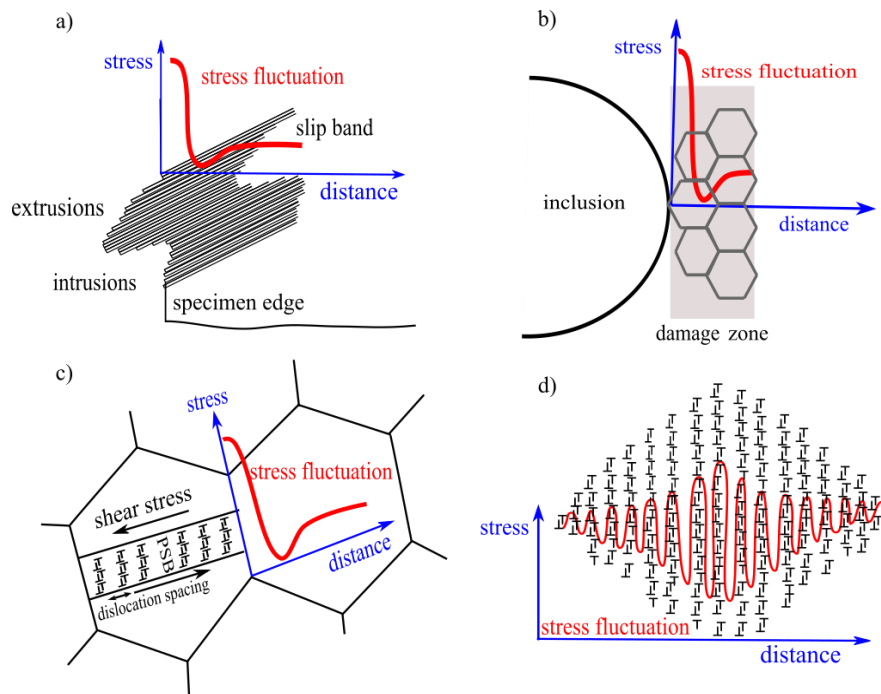
Fig. 1. Formation of stress and strain fluctuations a) boundary fluctuation,
b) stress fluctuation at the inclusion, c) grain boundary fluctuation
d) stress fluctuation due to dislocations microstructure

These stress fluctuations, developing at a fraction of the macroscopic elastic limit, are the source of initial structural defects and microscopic plastic mechanisms controlling the evolution of defect ensemble toward the state of advanced yielding.

The purpose of this work is to provide experimental and analytical description of stress and strain fluctuations and incorporate them into the fatigue criteria based on the local stress values. The analysis is also aimed at development of consistent description of the microplastic state of material [2]. The analysis of the stress and strain localization preceding crack initiation is performed by means of the optical method ESPI (Electronic Speckle Pattern Interferometry), apparatus using the coherent laser light. On the basis of strain fields specified at different load levels local hysteresis curves can be generated at selected points of specimen. The strain distribution maps, obtained for the first loading-unloading cycle, corresponding to the selected points of the curve are also presented in Fig. 2.

Additionally, the microindentation method has been applied to determine the damage variable from the data of the stiffness modulus.
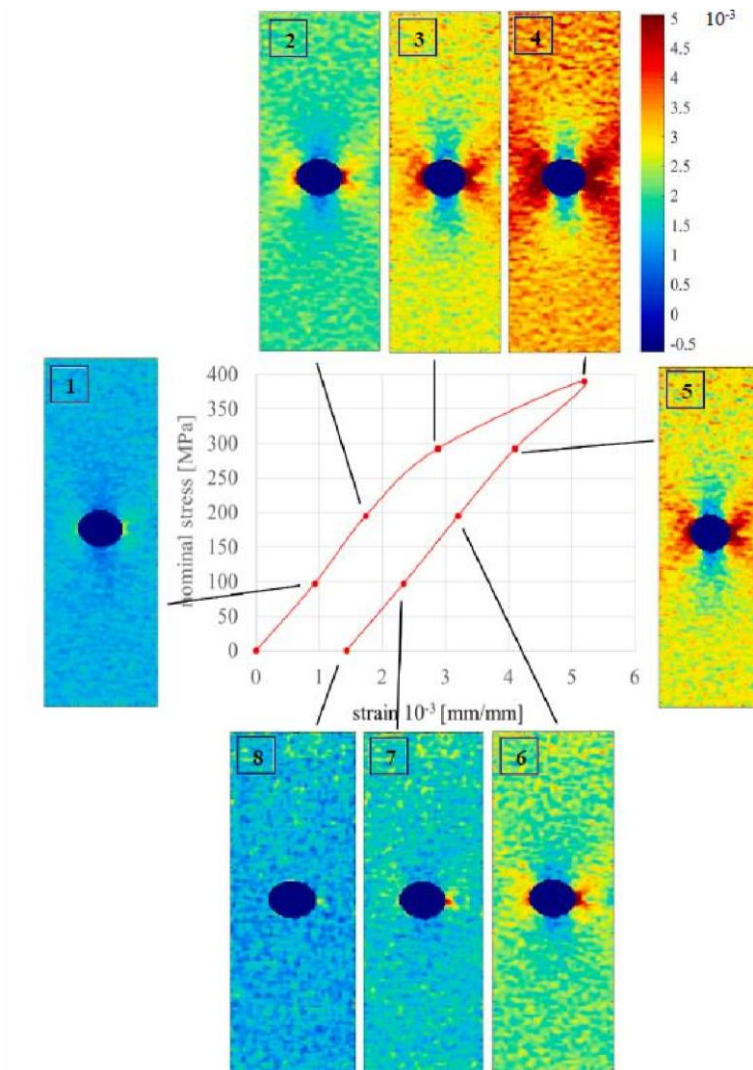
Fig. 2. Local hysteresis curve showing the first loading-unloading cycle
paused at selected stress levels for the strain distribution maps capturing

In this work, the new concept of constitutive modelling of fatigue crack initiation mechanisms is proposed. The new model is based on the continuum approach with account for local stress fluctuations, usually neglected in formulation of the damage models [3]. Depending on the accuracy of description of stress and strain fluctuations, such type of modelling may become close to microstructural models, usually requiring numerous material parameters.

References

[1] R. Maass and P.M. Derlet (2018). Micro-plasticity and recent insights from intermittent and small-scale plasticity, *Acta Materialia*, **143**, 338-363.
[2] A. Ustrzycka, Z. Mróz, Z.L. Kowalewski, (2017). Experimental analysis and modelling of fatigue crack initiation mechanisms, *JTAM*, **55**, 1443-1448.
[3] A. Ustrzycka, Z. Mróz, Z.L. Kowalewski, S. Kucharski, (2019). Analysis of fatigue crack initiation in cyclic microplasticity regime, *IJF*, https://doi.org/10.1016/j.ijfatigue.2019.105342.

POST-FORM STRENGTH PREDICTION
FOR HOT STAMPING OF AA6082 TAILOR WELDED BLANKS

J. Liu[1], S. Dhawan[2], A. Wang[2], Q. Zhang[2], N. Zuelli[1], D. Gonzalez[1] and L. Wang[2]
[1] Advanced Forming Research Centre, University of Strathclyde, Glasgow, UK
[2] Department of Mechanical Engineering, Imperial College London, London, UK

Abstract

As one of the lightweighting approaches, the use of aluminium has been increasing rapidly in recent decades so as to achieve desired weight saving without jeopardising the structural integrity of the products. The application of aluminium tailor welded blanks (TWBs) has exhibited its potential in weight reduction as this method can use the appropriate material/gauge in the target areas. In this work, aluminium AA6082 TWBs (with thickness combinations of 2.0-2.5 mm and 3.0-5.0 mm) made from friction stir welding have been used and successfully formed into automotive panel components (B-Pillar sectional parts) under hot stamping conditions. However, the final strength of the component may still depend on many factors from the forming process, e.g. solution heat treatment (SHT), transferring time, quenching efficiency (i.e. cooling rate), artificial ageing, etc. Prediction of the post-form strength is a challenge due to the effects of such factors. The precipitation reaction during cooling from SHT of Al-Mg-Si alloys has been reported over a wide range of cooling rates, and the effects of the cooling rate on the precipitation behaviour can be fundamentally described by continuous cooling precipitation (CCP) diagrams. Therefore, the post-form strength are determined by adopting the corresponding CCP diagram. A precipitation hardening model will be proposed to predict the precipitation hardening responses of AA6082 after hot stamping and the subsequent heat treatment. Material constitutive equations are used to model the viscoplastic flow of the TWB during forming, while age hardening theories are employed to simulate the evolution of microstructure and strength in the artificial ageing cycles. The effects of cooling rate/quenching efficiency on the formed TWB parts have been studied.

Keywords: Aluminium; Precipitation hardening; Hot stamping; Strength

INVESTIGATION ON FRICTION COEFFICIENT EVOLUTION AND LUBRICANT BREAKDOWN BEHAVIOUR AT ELEVATED TEMPERATURES IN A PIN-ON-DISC SLIDING SYSTEM

X. Yang, Q. Zhang, Y. Zheng, X. Liu, D. Politis, O. El Fakir and L. Wang
Department of Mechanical Engineering, Imperial College London, London, SW7 2AZ, UK

1. Abstract

The lubricant behaviour at elevated temperatures was investigated by conducting pin-on-disc tests between P20 tool steel and AA7075 aluminium alloy. The effects of temperature, initial lubricant volume, contact pressure and sliding speed on the lubricant behaviour, *i.e.* evolutions of coefficient of friction (COF) and breakdown phenomenon, were experimentally studied. The evolutions of COF at elevated temperatures showed three distinct stages: namely stage I (low friction stage), in which boundary lubrication was prevalent and the coefficient of friction was low; stage II (transient stage), in which the lubricant film thickness decreased to a critical value and the coefficient of friction increased rapidly; and stage III (breakdown stage), in which the lubricant was completely removed from the interface and the coefficient of friction was equal to its value under dry sliding conditions. The value of COF at the low friction stage was found to increase with increasing temperature. The increase of temperature, contact pressure and sliding speed as well as the decrease of initial lubricant volume caused earlier breakdown of the lubricant.

Keywords: elevated temperatures; friction evolution; lubricant breakdown behaviour;

Effect	Temperature °C	Speed mm/s	Load N	Lubricant volume g/m^2
Temperature	200	50	5	23.2
	250	50	5	23.2
	300	50	5	23.2
	350	50	5	23.2
	400	50	5	23.2
Speed	250	80	5	23.2
	250	100	5	23.2
Load	250	50	6	23.2
	250	50	8	23.2
Lubricant volume	250	50	5	9.3
	250	50	5	55.8

Table 1. Pin-on-disc test conditions
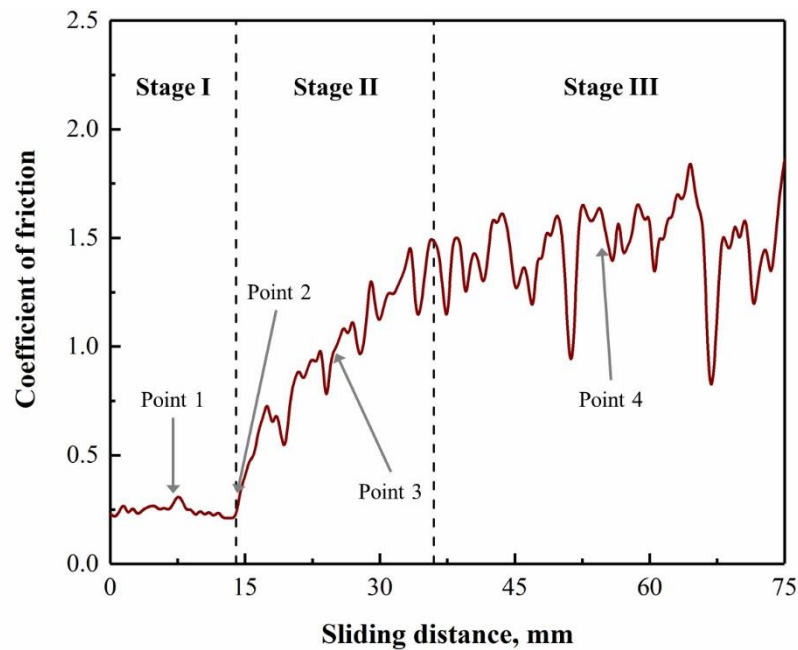
Fig. 1. Evolution of the coefficient of friction at elevated temperatures (300°C)

2. References

[1] Karbasian, H. and Tekkaya, A. E. (2010). A review on hot stamping. *Journal of Materials Processing Technology*, *210*(15), 2103-2118.

[2] Bhushan, B. (2013). *Introduction to tribology*. John Wiley & Sons.

[3] Chowdhury, M. A., Khalil, M. K., Nuruzzaman, D. M. and Rahaman, M. L. (2011). The effect of sliding speed and normal load on friction and wear property of aluminum. *International Journal of Mechanical & Mechatronics Engineering*, *11*(1), 45-49.

[4] Begelinger, A. and De Gee, A. W. J. (1976). On the mechanism of lubricant film failure in sliding concentrated steel contacts.

[5] Wang, W., Zhao, Y., Wang, Z., Hua, M. and Wei, X. (2016). A study on variable friction model in sheet metal forming with advanced high strength steels. *Tribology International*, *93*, 17-28.

[6] Hu, Y., Wang, L., Politis, D. J. and Masen, M. A. (2017). Development of an interactive friction model for the prediction of lubricant breakdown behaviour during sliding wear. *Tribology International*, *110*, 370-377.

[7] Amarnath, M., Sujatha, C. and Swarnamani, S. (2009). Experimental studies on the effects of reduction in gear tooth stiffness and lubricant film thickness in a spur geared system. *Tribology international*, *42*(2), 340-352.

FAILURE MECHANISMS OF STEEL LATTICE TOWERS ACCORDING TO FULL-SCALE TESTING

J. Szafran
Department of Structural Mechanics, Łódź University of Technology, Łódź, Poland

1. Introduction

Despite a long history of using space tower structures in industrial applications, they are still a subject of scientific research, optimization analyses, and implementation work. Global trends in this regard include mainly analyses of stochastic processes concerning loads, material properties, and geometrical imperfections, accompanied by modifications of analytical descriptions of structure behavior, complex computer simulations, and a wide range of experimental studies.

The experimental studies carried out by the author of this paper involved full-scale testing of six independent steel telecommunication towers. The assumptions of the tests, the equipment used, and details on how the tests were conducted and how measurements were taken are also provided in [1-5].

In this paper discussion of the failure mechanisms for two different type of lightweight, modern telecommunication towers will be presented.

2. Failure mechanisms of the tested structures

In the view of the author, understanding the failure mechanism of a tower structure is the key issue (particularly in the case of full-scale tests). The results in the form of displacements and deformations (stresses) are not sufficient to find out which member (joint) of the structure was the first to fail. Therefore, they do not provide a full insight into the behavior of the structure under breaking load conditions. For the two structures considered, identifying the failure mechanism seems to be yet more important; the towers are of similar selfweight but feature totally different bracing systems: with an asymmetrical (tower no. 1) and symmetrical (tower no. 2) support of the legs. Hence, a decision was made to make a full video recording of the tests using a number of cameras and views. In this way deformations of the structure with increasing external load as well as failure mechanisms of individual members could be observed in detail. The reader can find the videos showing the tower failure mechanisms by following the links:

- Tower no. 1 - https://www.youtube.com/watch?v=XfaMDHFowzQ
- Tower no. 2 - https://www.youtube.com/watch?v=7SbSVfdZ42M

As for tower no. 1, bracing members in segment S-3, located just below the point where load was applied, failed (Figure 1, left). It is where the cross-section of bracing members is smaller than that of bracing members in lower segments. Therefore, in this case the load-carrying capacity of the tower was determined by the buckling resistance of a diagonal brace. The buckling of the member occurred both in the plane and out of the plane of the tower wall. Referring to the assumptions of the test, it must be noted that the failure did not occur at the point where the largest axial forces were applied to members, since it was the compressed leg of the lower segment that was under the highest load. This mode of failure of the structure is undoubtedly a consequence of the single bracing system and asymmetrical support of tower legs, leading to a different redistribution of forces in members.

The resulting deformation was also affected by selected cross-sections of individual members; consequently, the effort of the diagonal brace was greater than that of the leg member. As soon as the diagonal braces lost their load-carrying capacity, specific deformations of the legs occurred: horizontal displacement of the upper part of the tower and its slight twist resulting from the asymmetrical arrangement of points of support of the legs.

Fig. 1. Mode of failure of tower no. 1 (left) and tower no. 2 (right)

Tower no. 2 had its legs stabilized by a symmetrical X-bracing system and the use of structural components (including diagonal braces) made only of circular sections of various diameters. The symmetrical X-bracing system provides two-sided support of the legs of tower structures and is commonly used in engineering solutions; nevertheless, a vast majority of diagonal braces in this system is made of hot-rolled L-sections or C-sections. Considering the solutions described above, one important observation of the recorded failure mechanism is that the first member that lost its load-carrying capacity was the compressed leg of the lower segment, and then, as a result of the buckling of the leg, bracing members deformed (Figure 1, right). This justifies the solutions used, since it was the member under the biggest load that failed. Significant plastic deformations of the member subject to failure, particularly in its lower part, should also be noted. Such large plastic deformations are due to the type of cross-section of the circular section, namely a circle of considerable diameter and a relatively small thickness of the wall. Gusset plates at the crossing of bracing members were also deformed to a large extent (due to lower rigidity than that of the members joined), and gussets at the joints of bracing members and the legs deformed as well.

3. References

[1] J. Szafran and M. Kamiński (2017). From full-scale testing of steel lattice towers to stochastic reliability analysis, *Archives of Mechanics,* **69(4-5)**, 371-388.

[2] J. Szafran and K. Rykaluk (2016). A full-scale experiment of a lattice telecommunication tower under breaking load, *Journal of Constructional Steel Research*, **120**, 160-175.

[3] J. Szafran (2015). An experimental investigation into failure mechanism of a full-scale 40 m high steel telecommunication tower, *Engineering Failure Analysis*, **54**, 131-145.

[4] J. Szafran, K. Juszczyk and M. Kamiński (2019). Experiment-based reliability analysis of structural joints in a steel lattice tower, *Journal of Constructional Steel Research*, **154**, 278292.

[5] J. Szafran and K. Rykaluk (2016). Diagonal bracing members of lattice towers - analytical versus experimental studies, Recent Progress in Steel and Composite Structures, Publisher: CRC Press/Balkema, pp. 94-95.

DATA MAPPING FOR HOT ALUMINIUM STAMPING TOWARDS TRIBOLOGICAL CHARACTERIZATION SCHEMES

H. Liu, X. Yang, Y. Zheng, Y. Hu, A. Wang, D. Politis, O. El Fakir, H. Shi and L. Wang
Department of Mechanical Engineering, Imperial College London, London, SW7 2AZ, UK

1. General

Research in metal forming processes has traditionally followed the convention of validating hypotheses with repeatable experimental trials. However, the reliable characterisation of boundary conditions remains challenging, which can be partly explained by the fact that the real boundary conditions in metal forming processes are not well understood. While the application of data science techniques in industries has been widespread, its utility in the metal forming research are limited. The wide usage of Finite Element software to aid in designing the forming strategy in metal forming industries, creates an opportunity for the vast amounts of data generated from the software to be processed in a variety of forms. In this work, data collected from experimentally verified Finite Element simulations demonstrated the capability of various data processing methods. With a focus on data filtering and weighting, a novel data visualisation scheme was developed to generate a tribo-map, where thermo-mechanical data such as the temperature difference between the workpiece and tool, relative sliding distance and contact pressure were characterised and adopted. It enables insight into the evolutionary boundary conditions at each different regions between the workpiece and tooling interface in a forming process. Three contact models were identified on forming tools, free-draw contact, restricted-draw contact and dynamic contact. Exploiting these data driven tribo-map procedures have opened up possibilities to spot new trends and analyse the significance of metal forming processes with a deeper understanding.

Keywords: Data-driven; Tribological test; Hot stamping; Aluminium alloy

REVIEW OF THE MODE I AND MODE II FRACTURE BEHAVIOUR OF HYBRID COMPOSITE MATERIALS FOR COMPOSITE REBARS

M. Barcikowski, W. Błażejewski, G. Lesiuk, J. Ławrecka, K. Rybkowska,
M. Smolnicki, S. Duda and P. Zielonka
Wroclaw University of Science and Technology, Department of Mechanics,
Materials and Biomedical Engineering, Wroclaw, Poland

1. Introduction

Nowadays, the general engineering idea is to design the structure lightweight - for this purpose; members are used to reducing weight without losing strength properties. An example of this solution is fibre-reinforced polymer rebars, which replace traditional steel reinforcing bars in civil engineering. Like any composite material, FRP rods are made of two different materials: matrix (which gives the shape of the composite) and reinforcement. Due to the many different types of reinforcements (fibrous, particulate, etc.) and the matrix, it is possible to design a composite material that has the appropriate properties. The mechanical properties of composite materials are dependent on the stiffness and strength of the fibres, matrix stiffness and adhesion between the matrix and the reinforcement. Composite materials which are reinforced with fiber are marked by the heterogeneity of structure, anisotropy of strength properties and sensitivity to surface condition between fiber and resin as well as sensitivity to technological and construction factors. The most severe defects of fiber-reinforced composite materials are structural porosity, delamination (only in layered composite materials), uneven or insufficient resin curing, fiber structure disturbances, fiber damage or breakage, local lack of reinforcement, wrinkled roving strip and matrix cracking. Interfacial fracture problems, the interfacial/bond strength plays an essential role in the strength of new hybrid composite material. Due to the different type of local loading composite and decohesion problem, the fracture mechanics approach is one of the most promising approaches. In work [1] is presented a complex study about the fracture mechanics models and testing including static, quasistatic strength and the most critical case based on cyclic loading. Typically based on fracture mechanics [2, 3, 4] for general behaviour of crack/interface delamination it is possible to describe the interfacial behaviour using three types of modes: I –tensile load, II – in-plane shear, III – out-ofplane shear. All modes are referred to as composite structures.

2. Materials and Methods

Due to the fact that the crucial damage mechanism depends on the mode I and mode II type of fracture – this was the object of Authors' interest. Static testing is applied to determinate onset and propagation of decohesion behaviour in the interface of the novel hybrid structure with regard to thermal and environmental loading conditions. The new structure is investigated according to norm ASTM D5528 [5], ASTM D7905 [6] and similar, so that, I mode, II mode and mixed-mode (I + II) are taken into account. Several test methods now offer spreadsheets for data analysis, including various correction factors and providing the opportunity to compare different approaches for analyses (e.g., beam theory based versus experimental compliance). Currently, the exact measurement of the delamination length has become a focus of attention, and recent models may provide an operator-independent determination of effective crack lengths. In the proposed experimental campaign, a hybrid experimental-numerical approach was involved. For the test, several combinations of the composite materials were selected. Typical measurement stand is shown in Fig. 1.

The materials used in this study are composites based upon a DGEBA epoxy resin. In order to improve epoxies fracture toughness, two reactive liquid polymer toughening agents additives were used, compared to unmodified epoxy resin. The resin was reinforced by glass-fiber roving and a particulate filler. Delamination in the composite material can be analyzed using the finite element method. Different approaches are used in this type of simulations and among them Cohesive Zone Model along with eXtended Finite Element Method is used successfully i.e. [7]. Cohesive Zone Model assumes that separation of surfaces is not sudden and cohesion between these surfaces is gradually reduced. Describe of this process is known as Traction Separation Law and is the input to eXtended Finite Element Method. This extension to standard FEM allows analysis with crack dividing elements.
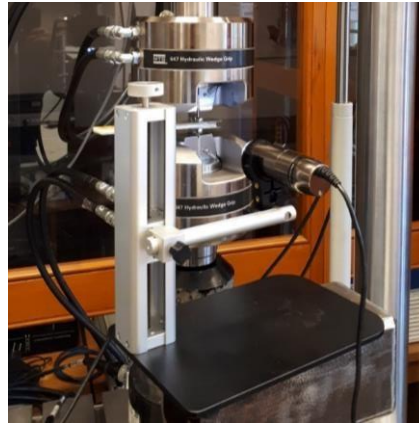
Fig. 1. Mode I - fracture toughness G_{IC} test - exemplary measurement stand

3. Acknowledgements

4. References

[1] A.J. Brunner, Fracture mechanics characterization of polymer composites for aerospace applications, Editor(s): P.E. Irving, C. Soutis, *Polymer Composites in the Aerospace Industry*, Woodhead Publishing, 2015, Pages 191-230, ISBN 9780857095237, https://doi.org/10.1016/B978-0-85709-523-7.00008-6

[2] Williams, J. G. (1989). The fracture mechanic delamination tests. *The Journal of strain analysis for engineering design*, 24(4), 207-214

[3] Broek, D. (2012). Elementary engineering fracture mechanics. *Springer Science & Business Media*

[4] Moore, D. R., Williams, J. G., & Pavan, A. (2001). Fracture mechanics testing methods for polymers, adhesives and composites (Vol. 28). *Elsevier*

[5] ASTM D5528 - Standard Test Method for Mode I Interlaminar Fracture Toughness of Unidirectional Fiber-Reinforced Polymer Matrix Composites

[6] ASTM D7905/7905M - Standard Test Method for Determination of the Mode II Interlaminar Fracture Toughness of Unidirectional Fiber-Reinforced Polymer Matrix Composites

[7] G. Giuliese, R. Palazzetti, F. Moroni, A. Zucchelli, A. Pirondi, Cohesive zone modelling of delamination response of a composite laminate with interleaved nylon 6,6 nanofibres, *Composites Part B: Engineering*, Volume 78, 2015, Pages 384-392

FRACTURE BEHAVIOUR OF THE NOTCHED PUR RIGID POLYURETHANE COMPONENTS – UNIAXIAL VS. MULTIAXIAL LOADING

K. Junik, M. Smolnicki, B. Babiarczuk, G. Lesiuk, S. Duda and P. Zielonka
Wroclaw University of Science and Technology, Department of Mechanics,
Materials and Biomedical Engineering, Wroclaw, Poland

1. Introduction

Polyurethane (PUR) material is a commonly used material, as a rubber replacement, in the suspension system of vehicles (Fig. 1). The knowledge about static and cyclic behaviour of these materials with consideration of the manufacturing discontinuities or fatigue cracks is limited.

Fig. 1. Typical polyurethane components in the vehicles suspension system

The standard fracture toughness tests are not suitable to the nonlinear and viscoelastic behaviour of such type materials like rubber or rubber-similar elastomers. However, the J-integral approach will be the most useful in many engineering tasks. On the other hand, its implementation could be not simple. In the last decade, the Essential Work of Fracture (EWF) [1, 2] is a promising substitution and alternative in polymer testing. It should be underlined that the physical explanation and relation with the J-integral approach are well documented in work [3].

2. Materials and Methods

In order to evaluate the essential critical work of fracture, the two types of specimens were prepared. According to the literature standardisation of the EWF test method, the 40-DENT (doubleedge-notched tension) specimens were fabricated from moulded plates (2 mm thick). The moulding process was performed with the accordance of the material manufacturer DOW Company using Hyperflex 101 material. Two types of specimens were obtained with different hardness respectively

80 and 90 ShA. During the experiments, the force, displacement and temperature were measured (with the additional channel from a thermo-vision camera). According to the numerical procedure prepared in HP VEE environment, all energy quantities responsible for the fracture process were obtained. The typical load-displacement curves were shown in Fig. 1. According to the EWF method, the W_e - specific, essential work of fracture was evaluated; for 80ShA – 26.8 $^{kJ}/_{m2}$ for 90ShA – 52.3 $^{kJ}/_{m2}$.
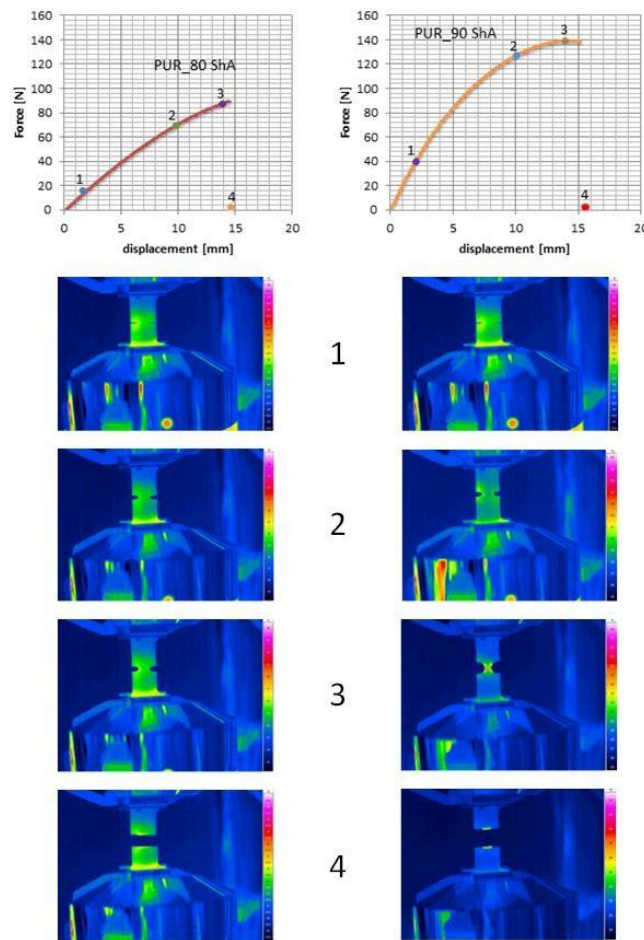
Fig. 2. Exemplary force-displacement diagrams for PUR materials 80ShA and 90ShA

It has been shown, based on results for the cracked DENT specimens, that the 80ShA and 90ShA materials demonstrate completely different behaviour under high-stress concentration condition . From the perspective of the usefulness of fracture mechanics, the energy approach seems to be crucial in the context of the real operating conditions of the bushing in the suspension system of vehicles. For this purpose, the fatigue crack growth rate test was performed. In full paper the problem of the multiaxial loading also has been discussed.

3. References

[1] N. Mehmood, T. Mao, G. Bhupati, „Fracture Mechanical Trouser Tear Testing In Thin Polymer Films", Department of Mechanical Engineering Blekinge Institute of Technology, Karlskrona, Sweden 2012, Str. 12-17.
[2] J. Gamez-Perez, M. Sanchez-Soto, J. Ignacio Velasco, M. LI. Maspoch, The Essential Work of Fracture (EWF) method – Analyzing the Post –Yielding Fracture Mechanics of polymers, *Engineering Failure Analysis*, December 2009.
[3] Arkhireyeva, A., and S. Hashemi. "Determination of fracture toughness of poly (ethylene terephthalate) film by essential work of fracture and J integral measurements." *Plastics, rubber and composites* 30.7 (2001): 337-350.

THE ANALYSIS OF THE IMPACT OF DIFFERENT CONFIGURATIONS OF FIXATION SYSTEM OF THE THORACOLUMBAR SPINE ON MECHANICAL PARAMETERS

K. Szkoda-Poliszuk, M. Żak and C. Pezowicz

Department of Mechanics, Materials and Biomedical Engineering, Wroclaw University of Science and Technology, Wroclaw, Poland

1. Introduction

Thoracolumbar spine is particularly exposed to injuries caused by the transmission of high load through its structures. According to statistics, account for almost 90% of all spinal fractures concerns fractures in thoracolumbar area [1-2]. This is mainly related to complicated structure of transition between the thoracic to the lumbar segment. The surgical treatment of vertebral fractures using implants has become a standard in clinical practice in recent years. However the literature shows that it is often a large clinical problem and leads to failures. Consequently, the use of an appropriate type of stabilization is crucial in the case of a vertebral fracture in the area of the thoracolumbar spine [3].

The main aim of study was the analysis of the impact of using different configurations of the fixation system on selected mechanical parameters of the thoracolumbar spine under conditions of its instability. The analysis was carried out for various transpedicular stabilization configurations (depending on the level of fixation), since it is most often used in the case of fractures related to the thoracolumbar spine. The assumed aim of the study was carried out through experimental research (on an animal model of the spine) and numerical simulations using the finite element method.

2. Materials and methods

The experimental study was conducted on preparations taken from 8 domestic pigs aged 6-10 months and weighing $90 \div 110$ kg. Preparations of the thoracolumbar spine (Th7-L5) were isolated, leaving intact intervertebral discs, ligaments, facet joints and parts of the ribs and muscles. Conducting experimental analysis required the development of own experimental research protocol. The implementation of the load was possible thanks to the MTS 858 MiniBionix Material Testing System. The preparations were assembled in a specially designed test system, which was equipped with two grips (upper and lower).

The numerical model of thoracolumbar spine (Th7-L3) was built on the basis of diagnostic computed tomography (CT). The geometric model was created in ANSYS Mechanical APDL 18.2 and divided into several structures with different tissues material properties. The vertebrae were modeled of a solid volume (cancellous bone) and a layer of vertebral cortical walls and were described by the isotropic, linear elastic material properties using tetrahedral 10-node elements. The models of the intervertebral disc were modeled of a solid volume and included the detailed structure. The difference between the nucleus pulposus and the annulus fibrosus was described by the nonlinear, hyper-elastic Mooney-Rivlin material. Additionally, three cylindrical layers of fibers

(outer, middle and inner) of the annulus fibrosus were modeled as a thick shell 4-node elements. The layers were described by the isotropic, nonlinear material properties with alternating fiber inclination (angle of 30º to the horizontal plane). The articulating facet surfaces were modelled using surface to surface contact elements (with a penalty algorithm and a friction coefficient of 0.1). The geometry of the stabilization system (screws and rods) was described by the isotropic, linear elastic material properties using tetrahedral 10-node solid elements.

In both cases, experimental study and numerical simulations, four configurations of the model were considered (Fig.1). In each of the considered cases, a pure unconstrained bending moment in

flexion (equal to 7 Nm) was applied to the superior endplate of the upper vertebral body (Th7). All configurations of the model were fixed by deducting all the degrees of freedom on the inferior endplate of the lower vertebral body (L3).
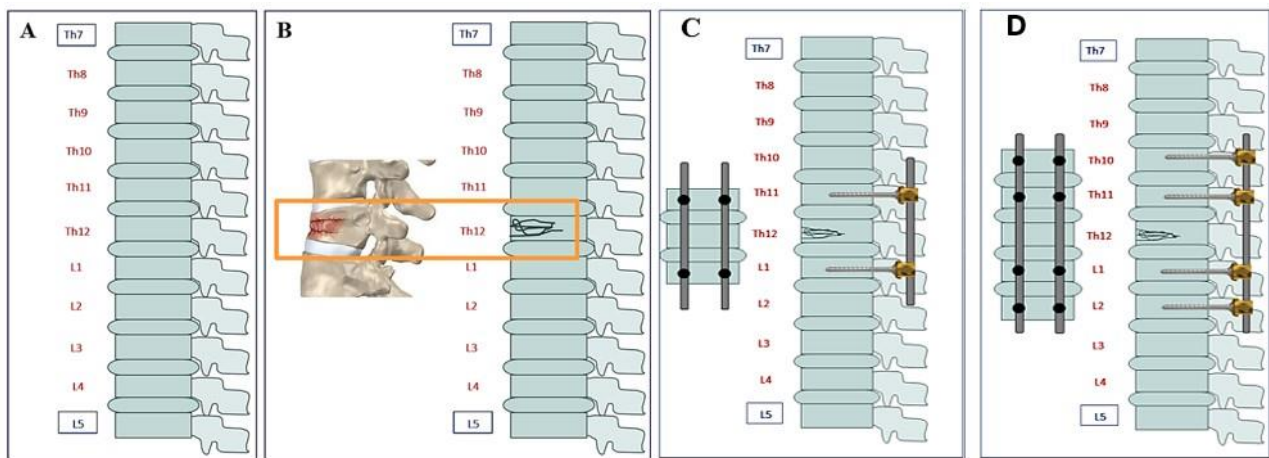
Fig. 1. Considered configurations of the fixation system: a) physiological, b) with compression fracture of Th12 vertebra, c) with short-segment stabilization, d) with long-segment stabilization

Additionally, in order to compare the prepared finite element method solution with the data obtained during experimental tests, the results were verified. The results obtained in the case of the physiological numerical model of the spine were compared with the results obtained for the same case during the experiment for a compressive load of 650 N.

3. Results and conclusions

The experimental and numerical study allowed to analyze the stiffness and the dissipation energy, as well as to assess the range of mobility of the spine during the use of various fixation system configurations. The intradiscal pressure in individual intervertebral discs and stresses on the surface of the joint processes were also analyzed. Performing numerical simulations also allowed to assess the distribution of strains and stresses in the construction of the implants subjected to load.
Research has shown that the use of a long construction of stabilization shows better results than short. It has been observed that the short construction does not provide sufficient stability, particularly when bending (extension). This stabilization affects the excessive mobility of the thoracolumbar spine, thus not providing adequate stiffness.

4.Acknowledgement

5. References

[1] B.B. Rosenthal et al. (2018). Thoracolumbar Burst Fractures. *Clin Spine Surg.*, 31(4): 143151.
[2] S.D. Daffner (2017). *Thoracolumbar Fractures. In Orthopedic Surgery Clerkship*. Springer, Cham, 475-480.
[3] C. Zoccali, B. Rossi et al. (2017). Short-Segment Versus Long-Segment Stabilization in Thoracolumbar Burst Fracture: A Review of the Literature. *J Orthop Spine Trauma*, 3(2).

EXPERIMENTAL IDENTIFICATION OF CRACK PROPAGATION IN AUSTENITIC STAINLESS STEEL AT CRYOGENIC TEMPERATURES

R. Schmidt[1], B. Skoczeń[1] and J. Tabin[2]
[1] Cracow University of Technology, Cracow, Poland
[2] Institute of Fundamental Technological Research of the Polish Academy of Sciences, Warsaw, Poland

1. Introduction

The scientific aim of the paper consists in analyzing the fracture mechanisms of austenitic stainless steel specimens subjected to fracture tests at extremely low temperatures (liquid helium, 4.2K). It is important to understand how the evolution of plastic strain induced phase transformation affects the propagation rate of a macrocrack in cryogenic conditions. On the other hand, fcc materials (austenitic stainless steels) exhibit the so-called discontinuous plastic flow (DPF, serrated yielding) when strained at extremely low temperatures [1], [2]. DPF manifests itself by the abrupt drops of stress against strain (or time), of the amplitude and the frequency depending on the material tested. Discontinuous plastic flow may have significant impact on the propagation rate of a macrocrack at very low temperatures. Therefore, experimental verification of these effects is crucial from the point of view of prediction of lifetime of materials in cryogenic conditions, down to absolute zero.

2. Experimental set-up and specimens

The kinematically controlled fracture tests at the liquid helium temperature were performed for austenitic stainless steel compact specimens [4]. Tensile tests were carried out on the unique experimental set-up [1]. The general scheme of the experimental set-up, as well as the cryostat interior, are presented in Fig. 1. The cryostat containing the specimen and the transducers were mounted between the grips of the tensile test machine. The cryogen (liquid helium) was fed to the cryostat by means of the transfer line, until the specimen with the transducers were immersed in the medium. The level of the cryogen was indicated by a thermistor mounted inside the cryostat. In order to measure the initiation of crack propagation and the rate of crack propagation, the crack detection gauge was mounted on the compact tension specimen. The initiation of macrocrack as well as its propagation were measured by means of the strain gauges. The phase transformation process at the vicinity of the crack tip was registered. The amount of the secondary phase, corresponding to the plastic strain induced fcc-bcc phase transformation, was measured be means of the ferritoscope as well as by direct electron microscope analysis. Also, a correlation of the way the macrocrack develops with the phenomenon of the discontinuous plastic flow was confirmed. In particular, a macroscopic increase of the crack length, correlated with each serration, has been observed. This, the macrocrack propagation at the extremely low temperatures is discontinuous by nature, and the reason has been associated with discontinuous (serrated) yielding represented by abrupt drops of stress against strain.

3. Conclusions

The present paper deals with the conditions of fracture in two-phase materials, and the evolution of microstructure along the fracture discontinuity. In the course of macro-crack propagation, the plastic strain fields occurring in the vicinity of the crack tip induce the evolution of microstructure, including the fcc-bcc phase transformation. Moreover, the macro crack propagation is determined by the stress-strain oscillations due to the DPF mode.

Fig 1. Experimental set-up for fracture tests at extremely low temperatures

4. Acknowledgments

5. References

[1] J. Tabin, B. Skoczeń, J. Bielski (2019). Discontinuous plastic flow coupled with strain induced fcc-bcc phase transformation at extremely low temperatures. Mechanics of Materials 129, 23-40.

[2] J. Tabin, B. Skoczeń, J. Bielski (2016). Strain localization during discontinuous plastic flow at extremely low temperatures. International Journal of Solids and Structures 97–98, 593-612.

[3] A. Das, S. Tarafder (2009). Experimental investigation on martensitic transformation and fracture morphologies of austenitic stainless steel. International Journal of Plasticity 25, 2222-2247.

[4] A. Nyilas, K. P. Weiss, S. Sgobba, M. Scheubel, P. Libeyre (2012). Fatigue crack growth rate and fracture toughness of ITER central solenoid jacket materials at 7 K. AIP Conference Proceedings 1435, 47-54

ASSESSMENT OF DAMAGE VIBRATION FEATURES IN A DEGRADED SUSPENSION FOOTBRIDGE

E. Caetano
Faculty of Engineering of the University of Porto, Portugal

1. General

The advance of the last decades in instrumentation and acquisition systems for assessment of civil engineering structures has led to a relevant progress in the understanding of their structural behavior and in the characterization of damage. The characterisation of damage from vibrationbased features implies intensive observation and the ability to detect associated variations of modal properties. (Un)fortunately, the limited number of structures exhibiting damage has prevented the validation of developed methodologies on the basis of full scale measurements and instead numerical simulations of data have been conducted, mostly by imposition of a degradation of mechanical properties at localized sections and at the structure supports.

The present paper departs from an old suspension footbridge (Figure 1) constructed by a rural population at the beginning of the 20th century. The footbridge is constructed from non-standardised local materials and exhibits an important level of degradation. The idea is to analyse features of measured ambient response of this structure and to compare to those of an equivalent non-degraded structure obtained numerically. The purpose of this study is to evidence other aspects of degradation rather than just frequency variations, as local modes and widening of the peaks of frequency response functions. In this context, an ambient vibration test has been conducted and, in parallel, a numerical model has been conducted in two conditions: assuming full integrity of the structure; assuming a degradation of similar type to the one observed. The latter model is calibrated with experimental data and the calculated dynamic response to an impact excitation is compared to that of the integral bridge model and also to experimental measured.

Fig. 1. View of the Ponte de Arame de St. Aleixo

2. Characteristics of the footbridge

The footbridge, designated as Ponte de Santo Aleixo, is located in the district of Vila Real, in the interior North of Portugal and used to provide a connection between the villages of Salvador and Santo Aleixo d' Além Tâmega in a time of mining exploration. The footbridge was constructed in 1913 and rehabilitated several times. Today, with the closing of mines and after construction of a road bridge, the footbridge has a very limited use and is considerably degraded. According to the

layout of Figure 2, the footbridge has a single span of 57.5 m and is formed from two pairs of cables suspended from two granite pillars and anchored directly on the ground and on the base of the pillars. In fact, a recent rehabilitation led to the addition of one of the pairs of cables which has a polygonal shape and appears to be inserted to suspend the central part of the footbridge. The footbridge deck is made from timber planks and has a width of 1.5 m.
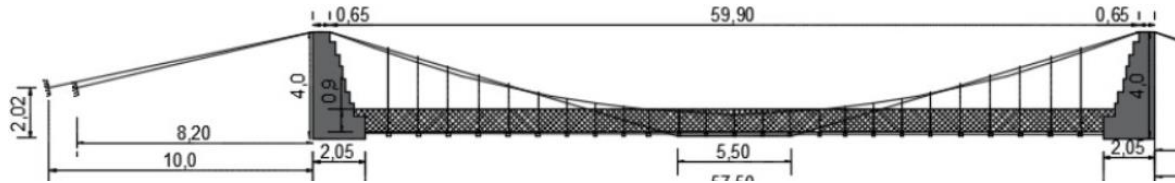
Fig. 2. Layout of the suspension footbridge: lateral (top) and bottom (bottom) views

3. Experimental testing vs numerical modelling

As part of the characterization of the footbridge, an ambient vibration test was conducted which allowed to identify the most relevant modal parameters of the footbridge. Figure 3 shows the singular values obtained from spectral estimates of the recorded ambient vibration accelerations. Calculated vibration modes are also represented which were obtained after calibration of the numerical model. This model was constructed on the basis of the asymmetric geometry of the structure assuming initially that all cables and connections were intact. In a second instance, some of the damage observed on site was simulated and the resulting modes and response compared. It was possible to identify features in the simulated and also the observed response that could be associated with damage. These included loss of symmetry and enlarging of frequency response peaks .
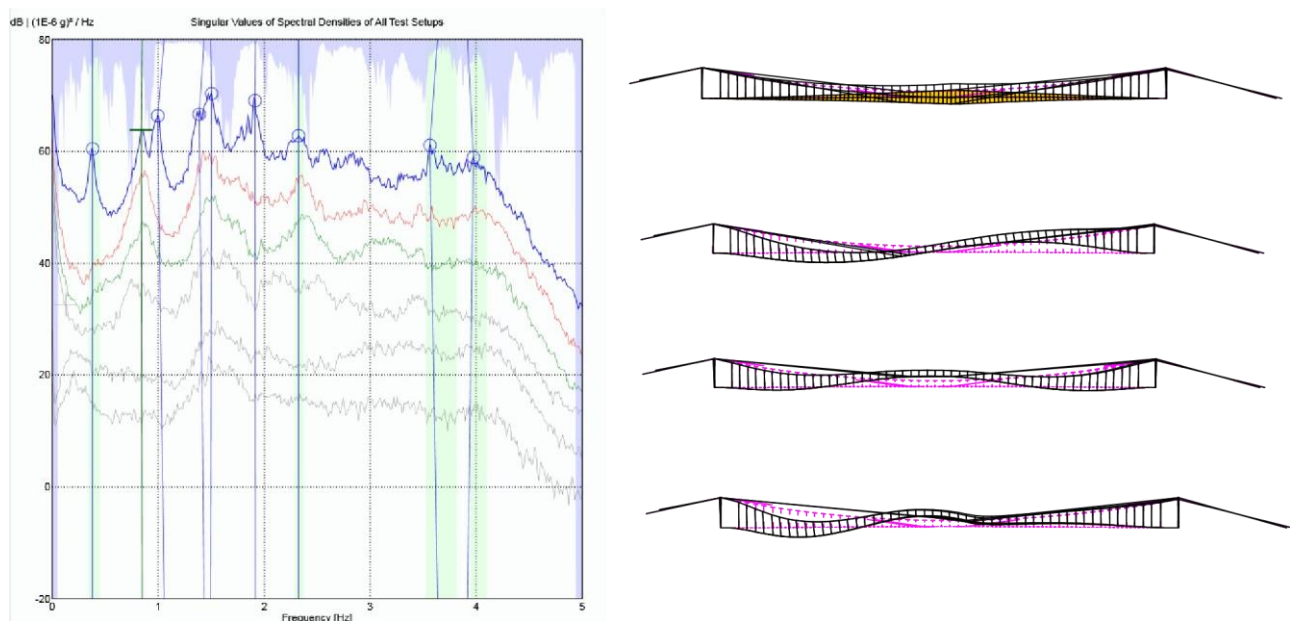
Fig. 3. Singular values of spectral densities of recorded accelerations (left).
Calculated modal configurations (right)

4. Acknowledgements

IN-PLANE LOAD-TO-GRAIN ANGLE DEPENDENCY OF THE COMPRESSIVE BEHAVIOR OF BIRCH PLYWOOD

T. Wang, Y. Wang, R. Crocetti and M. Wålinder
KTH Royal Institute of Technology, Stockholm, Sweden

1. Introduction

Steel plates with dowel-type fasteners are commonly used in modern timber structures for the connections of timber elements. As an alternative to the steel plates, plywood plates are considered to be more environmental-friendly, cost-efficient and less prefabrication/predrilling demanding. On the other hand, as an application in connection, plywood ought to be able to fulfill the structural design criteria. A connection is typically subjected to multiple types of stresses (e.g., compressive, tensile, bending and shear stresses, etc.) acting in different directions. In order to have a comprehensive insight on the load-displacement characteristics of the timber structures with plywood connections, it is of great significance to gain more knowledge on the in-plane mechanical properties of plywood at different loading angles to the face grain. Norris [1], Bier [2] and Popovska et al. [3] conducted experimental tests for yellow-poplar, pinus radiata and beech plywood with different cross-sectional patterns respectively. All of them observed the strong load-to-grain angle dependency of the strength properties of plywood.

In this study, plywood made of birch (*Betula pendula and Betula pubescens*) is investigated. Birch has wide natural distribution area in the Baltic and Nordic countries. However, it is rarely used in structural engineering applications and only the mechanical properties parallel and perpendicular to the face grain of birch is available in the literature [4]. This paper aims to (1) provide an experimental database of the compressive behaviors of birch plywood at varying angles to grain, (2) analyze the load-to-grain angle dependency of the elastic modulus and strength from the off-axis compressive specimens and (3) compare the tested strength data with the analytical predictions from different linear and quadratic failure criteria. This knowledge is considered to be vital for the structural design of connections that make use of birch plywood plates.

2. Materials and methods

The studied birch plywood is composed of 15 veneers with length, width and thickness of 100 mm, 50 mm and 21 mm, respectively. The plywood specimens are tested under five different loading angles to the face grain with the angle step of 22.5°, i.e. 0°, 22.5°, 45°, 67.5°, 90°, as shown in Figure 1, and with 12 repetitions for each test group. The relative humidity, indoor temperature and the motion rate of the loading head are controlled according to ASTM D3501 [5]. Moreover, one spherical bearing block is connected to the loading head and two 38mm-long strain gauges are attached on the side surfaces of the specimens. Test setup is illustrated in Figure 2. After the tests, experimental results including the elastic modulus, the characteristic and mean values of the strength with the standard deviation and coefficient of variance are obtained.

The compressive strength prediction is implemented based on the characteristic compressive strength parallel and perpendicular to the face grain (f_{c0k} and f_{c90k}) and the characteristic panel shear strength (f_{vk}) [4]. By transforming the uniaxial compressive stress to the normal stresses (σ_x and σ_y) and shear stress (τ_{xy}) in the local coordinate systems, two linear and three quadratic failure criteria are utilized to study the load-to-grain angle dependency of the compressive strength.
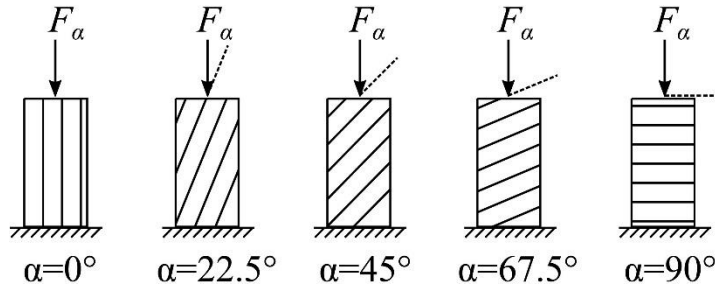
Fig. 1. Birch plywood specimens under five different loading angles

Fig. 2. Test setup

3. Results and discussions

The predicted effect of the load-to-grain angle on the compressive strength based on five failure criteria is revealed in Figure 3. The equation of each failure criterion is also shown in Figure 3.

$$(1)\ \frac{\sigma_x}{f_{c0k}}+\frac{\sigma_y}{f_{c90k}}=1$$

$$(2)\ \frac{\sigma_x}{f_{c0k}}+\frac{\sigma_y}{f_{c90k}}+\frac{\tau_{xy}}{f_{vk}}=1$$

$$(3)\ (\frac{\sigma_x}{f_{c0k}})^2+(\frac{\sigma_y}{f_{c90k}})^2+(\frac{\tau_{xy}}{f_{vk}})^2=1$$

$$(4)\ (\frac{\sigma_x}{f_{c0k}})^2-\frac{\sigma_x\sigma_y}{f_{c0k}f_{c90k}}+(\frac{\sigma_y}{f_{c90k}})^2+(\frac{\tau_{xy}}{f_{vk}})^2=1\ \text{or}\ \frac{\sigma_x}{f_{c0k}}=1\ \text{or}\ \frac{\sigma_y}{f_{c90k}}=1$$

$$(5)\ (\frac{\sigma_x}{f_{c0k}})^2-\frac{\sigma_x\sigma_y}{f_{c0k}^2}+(\frac{\sigma_y}{f_{c90k}})^2+(\frac{\tau_{xy}}{f_{vk}})^2=1$$
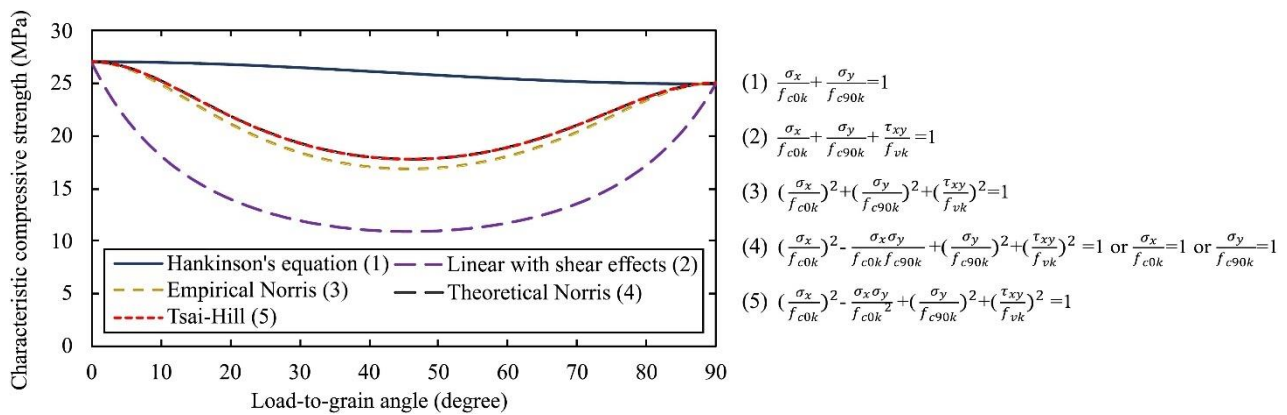
Fig. 3. The predicted characteristic compressive strength at varying load-to-grain angles

The results evaluated by the Hankinson's equation only vary between the strength at 0° and 90°. Three quadratic failure criteria exhibit similar results while the linear failure criterion considering shear effects predicts much lower values. All the criteria except the Hankinson's equation show the lowest compressive strength at approximately 45° to the face grain. More details regarding the experimental data and the comparative results will be presented and discussed in the full paper manuscript.

4. References

[1] C.B. Norris (1950). Strength of orthotropic materials subjected to combined stress. Forest Products Laboratory, Forest Service, U.S. Department of Agriculture. 30 p. [2] H. Bier (1984). Strength properties of pinus radiata plywood at angles to face grain, *N. Z. J. For.*, **14**, 349–367.

[2] V.J. Popovska; B. Iliev; G. Zlateski (2017). Impact of veneer layouts on plywood tensile strength, *Drv. Ind.*, **68**, 153-161. https://doi.org/10.5552/drind.2017.1634

[3] Finnish Forest Industries Federation (2002). Handbook of Finnish Plywood. https://www.koskisen.com/file/handbook-of-finnish-plywood/.

[4] American Society for Testing and Materials (2018). Standard Test Methods for Wood-Based Structural Panels in Compression. D3501-05a. Annual book of ASTM standards.

SPECIMEN SETUP FOR LIFETIME INVESTIGATIONS OF RUBBER MATERIALS IN THE COMPRESSION RANGE

L. Kanzenbach and J. Ihlemann

Chair of Solid Mechanics, Institute of Mechanics and Thermodynamics, Faculty of Mechanical Engineering, Chemnitz University of Technology, Reichenhainer Straße 70, Chemnitz

Abstract

This contribution deals with a new specimen setup with measuring device, which is tested for lifetime investigations of technical rubber materials in the compression range. The specimen setup enables high-precision compression tests up to 80 % (engineering compressive strain). Due to the design of the mounting geometry, a nearly homogeneous strain field can be achieved. In addition, first fatigue tests are carried out for such extreme compression levels.

1. Introduction

Lifetime predictions of elastomers are of high interest for many technical applications, like dampers, seals, tires, chassis bushings or medical equipment. In literature, a large number of durability specimens can be found (see exemplarily [1] and [2]). However, current durability specimens are not suitable for homogeneous compression tests with strains higher than 30 %. In the work of Kanzenbach [3] a new specimen setup (consisting of a new dumbbell specimen and a new mounting geometry) was developed, optimized and experimentally tested for quasi-static tests. The new specimen setup enables high-precision uniaxial tension-compression tests up to a compressive strain of approximately 80 %. Numerical studies have shown that the maximum stress occur in the nearly homogeneous measuring zone. Hence, the new specimen setup shall be applied for lifetime investigations of rubber materials in the compression range.

2. Experimental investigations

The experimental setup with measuring devices is illustrated in Fig. 1 (left).
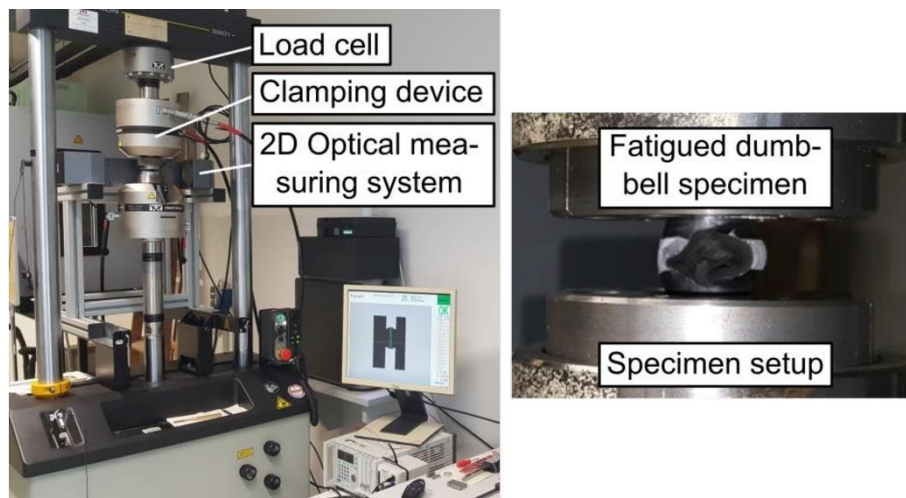
Fig. 1. Experimental setup for lifetime investigations of rubber materials in the compression range

The lifetime tests were performed with a servo-hydraulic testing machine from Instron. The force was measured with a load cell (nominal load 50 kN) and the deformation analysis was performed with a 2D optical measuring system from Keyence. Consider that especially for compressions > 50% the measuring zone of the dumbbell specimen is very limited. Thus, a new measuring strategy for strain measurement is applied. The main idea is to measure the tangential strain in the symmetry plane to obtain the axial strain via geometric considerations [3].

3. Experimental results

Lifetime investigations in the compression range were performed with specimens of a filled ethylene-propylene-diene monomer (filled EPDM). To this end, displacement controlled fatigue tests were carried out by a mean load of a displacement $u \, \epsilon \, [15, 15.5, 16]$ mm, an amplitude of 5 mm and a frequency of 1 Hz.
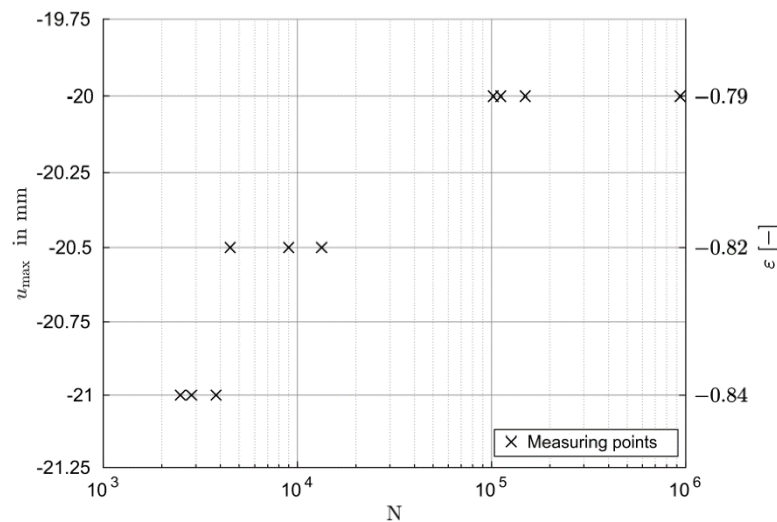
Fig. 2. Fatigue results for filled EPDM in the compression range

As a result, it can be determined that the dumbbell specimen fails in the nearly homogeneous measuring zone (cf. Fig. 1, right). A first fatigue curve is derived from the measuring points and illustrated in Fig. 2. These first results confirm the usability of the specimen setup for fatigue tests.

4. Conclusions

A new specimen setup for lifetime investigations of technical rubber materials in the compression range was successfully applied in this paper. As expected, the dumbbell specimen fails in the nearly homogeneous measuring zone. Finally, fatigue curves can be obtained from the measuring points in the compression range. In further investigations, Wöhler tests shall be conducted for tension/compression pulsating range and also for the alternating range.

5. References

[1] S.M. Cadwell, R.A. Merrill, C.M. Sloman and F.L. Yost (1940). Dynamic Fatigue Life of Rubber, Rubber Chem. Technol., **13** (2), 19-23.

[2] D. Juhre and M. Krause (2015). A study on the influence of mechanical preconditioning on the fatigue behavior of rubber materials, Constitutive Models for Rubber IX. Ed. from B. Marvalová & I. Petriková. Leiden: Balkema, 439-444.

[3] L. Kanzenbach (2019). Experimentell-numerische Vorgehensweise zur Entwicklung von Probekörper-Setups für die Charakterisierung technischer Elastomere, *PhD thesis, Chemnitz University of Technology*, https://nbn-resolving.org/urn:nbn:de:bsz:ch1-qucosa2-365142.

IMPROVEMENT METHOD FOR MEASURING KINEMATIC FIELD BY DIGITAL IMAGE CORRELATION FOR 2D TENSILE TEST AT HIGH TEMPERATURE

P. Luong, R. Bonnaire and L. Penazzi

Institut Clément Ader (ICA); Université de Toulouse; CNRS, IMT Mines Albi, INSA, ISAESUPAERO, UPS; Campus Jarlard, 81013 Albi, France

1. Introduction

In aerostructure industry, the shapes of some complex parts, e.g. pylons or engine air inlet made by Ti-6Al-4V (TA6V) titanium alloy sheet are manufactured by hot forming processes. To control the final geometry after forming operation at high temperature and/or to improve the accuracy of the Finite Element Method (FEM) model during the cooling phase, an access to continuous fullfield kinematic measurements would be appreciated. One solution is to use Digital Images Correlation (DIC) method. Although this method is relatively mastered at room temperature, it is more complex to implement at high temperatures (from 500°C to 800°C). This is due to two main factors, including the mirage effect (Mirage effect induces images deformed and blurred due to gradient of refractive index of air between a recorder (camera or human eyes) and a hot object [1]), the loss of image contrast decreasing DIC accuracy and precision. This communication develops a numerical spatial filter in DIC applied for planar tensile tests to eliminate errors due to temperature effects for the identification of Young's modulus.

2. Materials and methodology

Material studied is a TA6V alloy sheet of 1.6 mm thickness. The elastic behavior of TA6V at different temperatures (between 500°C and 700°C) is identified by uniaxial tensile tests (MTS with the measuring range of 0-15kN) and DIC system for full-field kinematic measurements. Tensile specimens (width 8 mm x height 25 mm) are heated by the electrical resistance oven AET. Images during tensile tests are captured by a fronto visible camera system (macro Tamron and sensor CCD 5M pixels AlliedVision) with a frame rate of 5fps. The Zone Of Interest (ZOI) dimensions are 8 mm x 15 mm equivalent to 757 x 242 pixels2.

Fig. 1. Transversal strain map at four different time measured by DIC at 600°C at static condition

Captured images are used to calculate strain maps by local DIC algorithm (VIC-2D, Correlated Solution®). Kinematic measurements are performed at three stages: i) room temperature served as reference images, ii) static stage (without load) and iii) during mechanical load at three temperatures: 500°C, 600°C and 700°C in nearly isothermal conditions (The thermal gradient is 1°C in ZOI of specimen). In static stage, since no load is applied on TA6V sample (Figure 1), the Background Oriented Schlieren (BOS) technique [2] is employed to characterize temperature dependence of DIC errors. To eliminate mirage effect, an algorithm based on a Gaussian low-pass filter [2] whose radius r and standard deviation σ depend on temperature is developed. This filter is optimized thanks to the

temperature – dependence of displacement/ strain errors measured in static stage. Gaussian filter allows to separate mechanical strain appeared at low frequency and error due to mirage effect mainly caused by convection flow in the oven appeared at high frequency.

3. Results and discussions

Firstly, by comparing mechanical strain in elastic domain obtained by the analytical solution and DIC measurements, we observed that mirage effect induces an error in DIC measurements at high temperature. The temporal and spatial DIC errors at a given time t are demonstrated in Figure 1.

Secondly, Figure 2a and 2b present longitudinal ε_{yy} strains at time t measured by DIC before and after eliminating temperature effects at 600°C. Before correction, the strain values (in absolute) are from 0 to 2.5×10^{-3}. After correction, the heterogeneous strain map is significantly reduced. Its range is from 0 to 1.0×10^{-3}. However, small part of DIC errors is still present probably due to the high dispersion of strain errors from the turbulent convection. Figure 3 presents stress – ε_{yy} strain curves of local subsets in Figure 2 before and after correction by Gaussian filter. Young's moduli are calculated from stress – strain curves in the elastic domain. After correction, Young's modulus of TA6V material at 600°C is 67 GPa, 12% lower than its value in literature at same conditions [3].
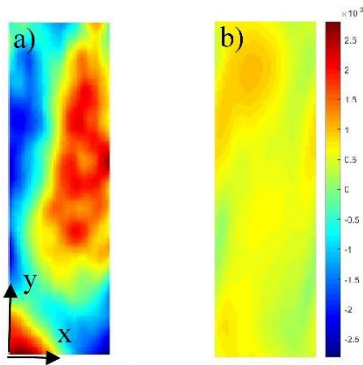
Fig. 2. a) Initial ε_{yy} strain map at time t, b) ε_{yy} strain map at time t after correction. Dashed rectangles represent local subsets
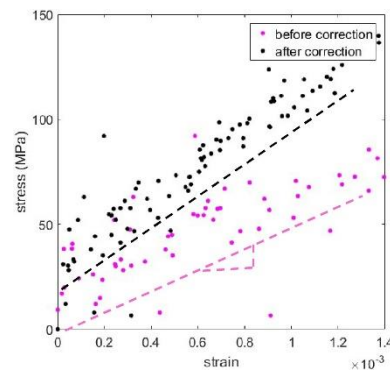
Fig. 3. Stress – ε_{yy} strain curves of tensile test measured on local subsets by DIC before correction (in rose) and after correction (in black) at 600°C

4. Conclusion and perspectives

The study aims to suggest a spatial filter adapted to temperatures to eliminate errors in kinematic measurement at high temperature. Preliminary result showed that at 600°C, Young's modulus after correction is 67 GPa, only 12% lower than the value in literature [3]. Future studies should be investigated to measure Young's moduli of others materials or others temperatures. Furthermore, studies would develop this method for any conditions. Finally, the spatial filter could be extended to temporal spatial filter to remove maximum errors due to temperature effects.

5. References

[1] A. Delmas. Y.L. Le Maoult. J.M. Buchlin. T. Sentenac and J.J. Orteu (2013). Shape distortions induced by convective effect on hot object in visible, near infrared and infrared bands, *Exp. Fluids,* 54(4), 1-26.
[2] E.M.C. Jones and P.L. Reu (2018). Distortion of Digital Image Correlation (DIC) displacement and strain from heat waves, *Exp. Mech,* 58(7), 1133-1156.
[3] M. Vanderhasten, Ti-6Al-4V: Deformation map and modelisation of tensile behavior, PhD thesis report, Katholike Universiteit Leuven, 2007.

EFFECT OF VIBRATION ON THE BEHAVIOR OF BLAHA EFFECT IN IRON SINGLE CRYSTAL USING MOLECULAR DYNAMICS

Y. Yuba and S. Arikawa
Meiji University, Kawasaki, Japan

1. Introduction

For plastic working of metals, stresses above the yield point must be applied for plastic deformation to occur. This is due to the generation of dislocations and slippage inside the metal crystal. If it becomes possible to process metals at a lower stress than their original yield stress, it will be easier to process difficult-to-process materials. One way to achieve plastic deformation at low stress is Blaha effect, in which the flow stress decreases when ultrasonic vibration is applied during plastic deformation. This phenomenon was discovered by F. Blaha, and B. Laungenecher, [1] in 1955. In their study, zinc was used and stress reduction was observed by adding ultrasonic vibration during tensile testing. The stress reduction was confirmed by adding ultrasonic vibration during tensile testing of zinc. However, there are many macroscopic research data by experiments and few microscopic researches such as analysis. It is very difficult to evaluate the internal conditions of metals and the movement of dislocations by experiments. In this study, molecular dynamics is used to evaluate the stress values of the metal including dislocations when they are subjected to vibration. There are many experiments of vibration loading in the direction of tensile test, and the case where other stress components of vibration are given has not been clarified. Therefore, molecular dynamics will be used to investigate whether Blaha effect can be reproduced and how the stress component is affected when other vibration components are applied.

2. Analysis

The molecular dynamics method, LAMMPS[2], is used for the analysis. The dimensions of the model are $4.1 \times 8.9 \times 13.3 \text{nm}^3$. The number of atoms in the model is 40482. There are two edge dislocation in the model. The interatomic potential is Finnis-Sinclair potential. Shear strain, γ_{xy}, is applied until the strain just before the yield point is reached, and then vibration of various stress components. The analysis conditions for the first step are a strain rate of $2.0 \times 10^5 \text{s}^{-1}$, temperature of 50K. For the second step, vibration of five cycles are applied at frequency of 258MHz and strain amplitude of 10^{-4}.
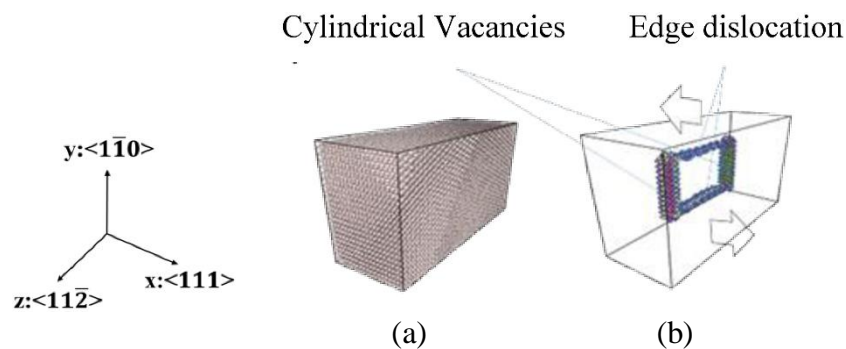
Fig. 1. Simulation Model

3. Result and Discussion

The analysis results were done as shown in the figure 2. The blue line shows the stress-time curve with strain above the yield point. On the other hand, the green line is the stress-time curve for a vibration of γ_{xz} and the red line is for a vibration of γ_{xy}. It can be seen that the stress decreases with the application of vibration. This shows that the material yielded at low stress. Therefore, Blaha effect can be reproduced. It was also found that the effect depended on the vibration applied, with the vibration of strain components, γ_{xz}, having the greatest effect. However, the detailed situation has not been clarified. So, clarification of the atomic behavior is important for understanding the phenomenon of Blaha effect.
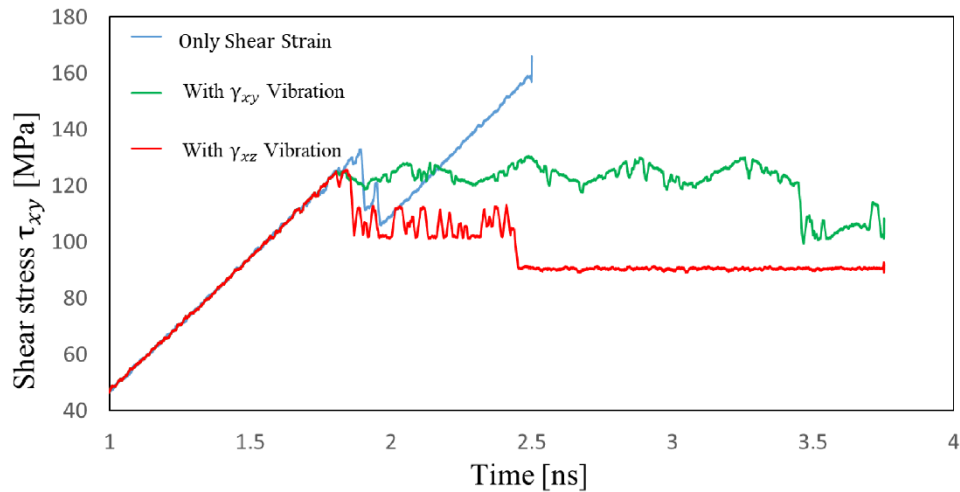
Fig. 2. Shear stress – time curve obtained by simulation

4. Conclusion

The following two points were found by the analysis. Blaha effect could be reproduced using the molecular dynamics method. It was found that the effect differs depending on the stress component to be vibrated. In the present analysis, the vibration of strain component γ_{xz} has the most influence. The detailed study is needed to clarify the factors for phenomenon.

5. References

[1] F. Blaha and B. Langenecker "Dehnung von Zink-Kristallen unterUltraschalleinwirkung" Naturwissenschaften Vol. 42, pp. 556 (1955)
[2] LAMMPS Molecular Dynamics Simulator : https://lammps.sandia.gov/.

FULL-FIELD EXPERIMENTAL STUDY AND NUMERICAL MODELING OF SOFT POLYURETHANE FOAMS SUBJECTED TO CYCLES LOADING

C. Casavola[1], L. Del Core[2], V. Moramarco[1], G. Pappalettera[1] and M. Patronelli[1]
[1] *Dipartimento di Meccanica, Matematica e Management, Politecnico di Bari, Bari, Italy*
[2] *Blackshape S.p.A., Monopoli, Italy*

Abstract

In this study the response of three soft, open cell polyurethane foams subjected to four incremental cyclic compression load steps of 20, 40, 60 and 80% of strain is analyzed by digital image correlation. The experimental results are compared with those obtained by a FEM analysis considering or not the influence of the Poisson's ratio.

1. Introduction

Polyurethane foam (PUf) is a versatile material commercialized both as rigid or soft. It is mainly used due to its good energy absorption capability combined with its lightweight. The exact structure and deformation mechanism of this material is a topic of great interest because at large deformations the material response becomes nonlinear. To analyze the mechanical behavior of soft polyurethane foam, full field, contactless and non distructive measurement techniques, like digital image correlation (DIC), should be used. In this work, the mechanical characteristics of three PUf: type A, B and C with densities respectively of 85, 63 and 46 kg/m3 are investigated by incremental DIC exploiting the natural speckle pattern of the specimens given by the presence of fireproof particles of expanded graphite [1]. Due to large deformation, the nonlinear response was analyzed, both experimentally and numerically (Abaqus 6.13), plotting engineering and true strain curves.

Stress-strain curves and energy absorbing capability were evaluated. An eventually auxetic behavior of the materials is investigated by a tangent Poisson's function formulation, more capable to capture the instantaneous behavior of the foam.

2. Results

Experimental stress-strain curves obtained for the compression step until 80% of strain are shown in Figure 1a on positive axis for easiness. The numerical output, obtained using the *hyperfoam* material model with a strain potential order $N = 2$, show that the experimental curves are well reproduced both considering $\nu = 0$ and $\nu \neq 0$. Transverse vs. axial strain curves in Figure 1b show that foams expand until 2% of transverse strain and then, at about 20% of axial compressive strain, there is an inversion of trend, well reproduced also by numerical simulations. This trend inversion points out the auxetic behavior of these foams, as confirmed by the tangent Poisson's functions (Figure 1c), which reach negative values. The specific strain energy absorbed by the foams increases with the amount of deformation and with the foams' density. Experimental displacement maps obtained by DIC along Y (Figure 2a, b) show horizontal bands due to the progressive cell's collapse; while those obtained along X (Figure 2c, d) confirm the tendency of the material to expand until 20% of strain and then shrinks at 80% of strain. Experiments are well reproduced by the *hyperfoam* model (Figure 2 e, f, g, h) but at high strain local effects are missed along the X direction.
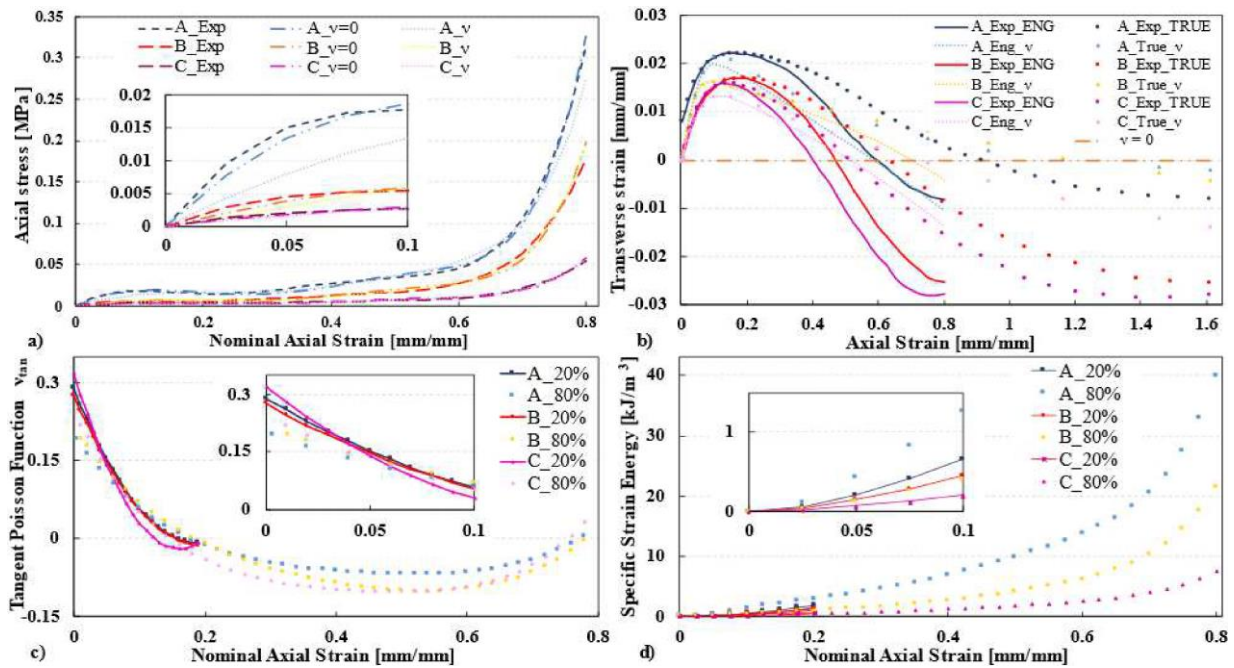
Fig. 1. Comparison of the experimental and numerical axial stress-strain (a) and transverse vs. axial strain (b) curves obtained at 80% of strain considering ν = 0 and ν ≠ 0. Tangent Poisson's function (c) and specific strain energy (d) for 20% and 80% of strain.
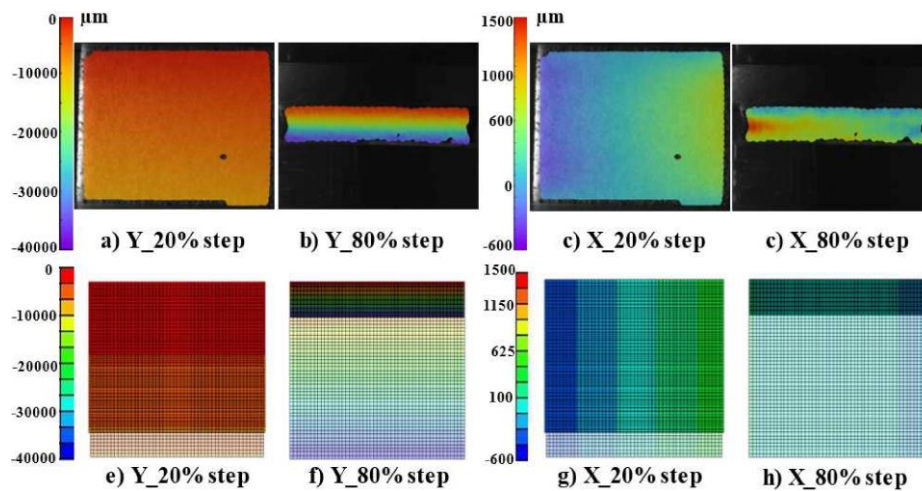
Fig. 2. Experimental displacement maps of type B foam along the load (Y) and transverse (X) direction (top row). Corresponding results obtained by numerical analysis (bottom row)

3. Conclusions

Large deformations are successfully captured by DIC on unpainted soft polyurethane foams and well reproduced by a *hyperfoam* material model. Th auxetic behavior of these conventional foams was studied by transverse vs. axial strain analysis and confirmed by a tangent Poisson's function.

4. References

[1] C. Casavola et al. (2021). Experimental and numerical analysis of the Poisson's ratio on soft polyurethane foams under tensile and cyclic compression load, *Mech. Adv. Mater. Struct.* DOI: 10.1080/15376494.2021.1994061.

CONTRIBUTION OF THERMOELASTIC COUPLING EVALUATION ON THE THERMOMECHANICAL CHARACTERIZATION OF 3D CARBON COMPOSITES

L. Navrátil[1], Y. Marco[1], V. Le Saux[1], S. Leclercq[2] and N. Carrere[1]
[1] ENSTA Bretagne, IRDL, UMR CNRS 6027 2, rue François Verny, 29806 Brest Cedex 9
[2] Safran Landing Systems, Vélizy-Villacoublay

1. Introduction

The broad implementation of composite materials in aircraft structures is the result of their excellent specific strength and specific stiffness properties. In industrial applications, woven or textile composites have been gaining popularity since they lack some drawbacks found in commonly used laminated composites: a low damage resistance or poor out-of-plane properties [1]. With this objective in mind, this study focusses on a three-dimensional woven composite with an organic matrix that was developed for research purposes by the Safran group. The present abstract shows how analyses of thermoelastic coupling maps can help in locating cracks appearing under cyclic loadings. The thermoelastic coupling maps are evaluated based on analyses of temperature variations occurring under cyclic loadings applied during a heat build-up protocol. The heat build-up phenomenon is often investigated in approaches that aim at accelerating the characterisation of the fatigue properties. The understanding of this dissipative mechanism is crucial for modelling fatigue properties based on the results of heat build-up experiments.

2. Thermoelastic coupling detection technique of thermal events

Thermal events are described as local irregularities appearing when the material undergoes cyclic loadings. A thermal event usually includes a steep increase in temperature that is limited to a few milliseconds. Furthermore, it was systematically observed that the occurrence of a thermal event is linked to a decrease in the thermoelastic coupling contribution [2]. Given that the thermoelastic coupling contribution is, under some assumptions, proportional to the local stress state [3], it is reasonable to assume that, as long as the material behaviour remains elastic, the thermoelastic coupling contribution remains proportional to the applied loading stress. This linearity can, therefore, be exploited in order to identify the thermal events that are characterised by the loss of thermoelastic contribution linearity described beforehand. In that respect, a detection procedure that permits to highlight the areas affected by the presence of thermal events was implemented. The concept of this detection technique is illustrated in Figure 1.
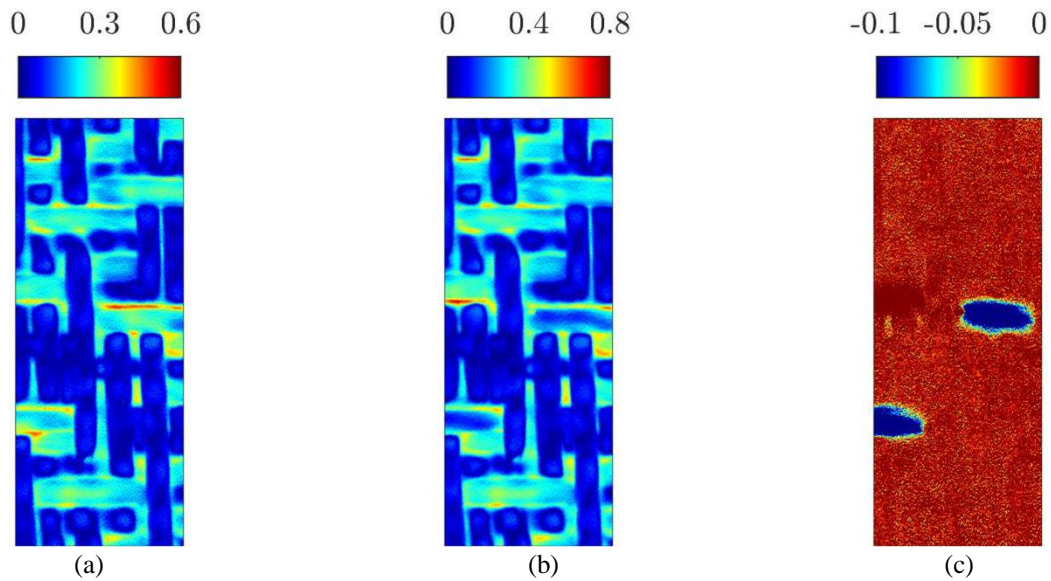
Fig. 1. Illustration of the thermal event detection process: (a) thermoelastic coupling map obtained for a normalised stress amplitude of 2.8 MPa/MPa, (b) thermoelastic coupling map obtained for a normalised stress amplitude of 3.8 MPa/MPa, (c) difference thermoelastic coupling map highlighting the thermal events occurring between the two loading steps

Furthermore, a posteriori microstructure observations revealed that the areas affected by thermal events are systematically marked by the presence of cracks. These observations confirmed the link between thermal events and the creation of local damage [2].

3. References

[1] P. E. Irving, C. Soutis (2015). *Polymer Composites in the Aerospace Industry.* PhD Thesis, ENSTA Bretagne.

[2] L. Navrátil (2021). *Apports de l'imagerie qualitative pour la caractérisation thermomécanique et le dimensionnement en fatigue de composites tissés 3D.* Woodhead Publishing.

[3] C. Doudard *et al.* (2010). Identification of heat source fields from infrared thermography: Determination of 'self-heating' in a dual-phase steel by using a dog bone sample. *Mechanics of Materials* 42.1, 55-62.

EVALUATION OF THE EFFECTIVE STRESS INTENSITY FACTOR USING THERMOELASTIC STRESS ANALYSIS AND 2D DIGITAL IMAGE CORRELATION

**A. Camacho-Reyes[1], F.A. Díaz[1], J.M. Vasco Olmo[1], E. López-Alba[1], L.A. Felipe-Sesé[2],
Á.J. Molina-Viedma[2], J.A. Almazán Lázaro[2]**

[1] *Departamento de Ingeniería Mecánica y Minera, Campus Las Lagunillas Universidad de Jaén,
23071 Jaén, Spain*
[2] *Departamento de Ingeniería Mecánica y Minera, Campus Científico Tecnológico de Linares,
Universidad de Jaén, 23700 Linares, Spain*

1. Introduction

Fatigue cracks have been one of the main sources of structural failures in real in-service structures. The application of fracture mechanics to engineering design has provided the possibility of understanding further into the study of failure and crack growth mechanisms. But there are still some aspects that remain not fully understood, such a case is the crack closure effect. This lack of understanding arises principally from the difficulties associated in quantifying the phenomenon and measuring its effect on the crack driving force [1]. Closure mechanisms reduce the effective crack driving force, and hence, the material shows an enhanced resistance to crack growth. Nevertheless, TSA [2] due to its physical nature appears to offer a direct means of measuring the effective crack driving force. This presumed ability arises from the fact that with TSA the near crack tip stress distribution is obtained from the temperature variations on the specimen's surface as a result of the thermoelastic effect, providing a direct assessment of cyclic strain around the crack tip. In the present paper, TSA and DIC [3] techniques are employed in combination with two mathematical models based on Muskhelishvili's complex potentials to evaluate the influence of shielding during fatigue experiments conducted with two commercial aluminium materials (Al2024-T3 and Al7050-T6) at different R-ratios.

2. Background of Thermoelastic Stress Analysis (TSA) and Digital Image Correlation (DIC)

Thermoelastic stress analysis can be defined as a non-contact, nondestructive and non-invasive experimental technique that provides fullfield stress maps by measuring temperature changes induced by the thermoelastic effect at the surface of a mechanical component as a result of a periodic change in the applied load. The deformation of a body is always associated with a change in its heat content and consequently, with a change in its temperature. The classical theory of thermoelasticity states that the application of a repetitive loading in a solid produces in it out-of-phase temperature changes that can be related to the variation in the sum of the principal stresses.

DIC is a full-field optical technique used for displacement measurements in structural components. The specimen surface must have a random grey intensity distribution (a random speckle pattern), which deforms together with the specimen. The basic principle of 2D DIC consists on tracking the displacement of points in two recorded images before and after deformation.

3. Experimental details

Fatigue tests were conducted using CT specimens 1mm thick. The two surfaces of each specimen were treated using different methods to enable simultaneous measurements of displacements by DIC and stresses by TSA. Figure 1 left shows the employed experimental setup.

4. Results

In figure 1 right it is plotted a comparison of ΔK at different R-ratios and different crack lengths. or R = 0.5 both techniques provide very similar values that agreed with ΔKnominal. On the other hand, for R = 0.1 experimental ΔK values obtained by DIC and TSA again provides very similar results but in both cases are lower than ΔKnominal. This demonstrates the ability of both techniques to account for the effective ΔK, that is related with a retardation effect on fatigue crack growth due to the shielding effect arising as a fatigue crack is growing.
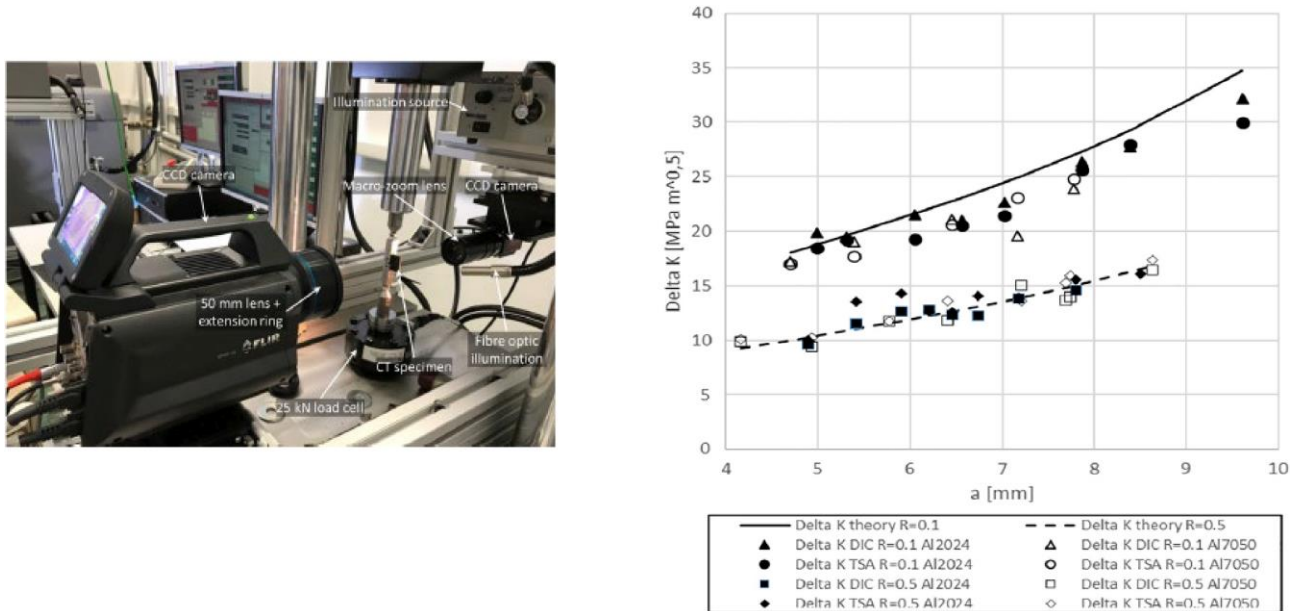
Fig. 1. Experimental set-up for fatigue testing and data acquisition (left). Comparison of ΔK nominal and ΔK effective obtained by DIC and TSA at different crack lengths (right)

5. Conclusions

Results obtained from both techniques show a great level of agreement, observing a variation in the range of stress intensity factor as the stress ratio changes from 0.1 to 0.5 and highlighting the potential ability of both techniques to account for the shielding effect during fatigue crack growth.

6. Acknowledgements

7. References

[1] James, MN. Some unresolved issues with fatigue crack closure – measurement, mechanism and interpretation problems. *Ninth International Conference on Fracture* 1997; 5: 2403–2414.
[2] Thomson W (Lord Kelvin). On the thermoelastic, thermomagnetic, and pyroelectric properties of matters. *Phil Mag* 1878; 5: 4–27.
[3] Sutton MA, Orteu JJ, Schreier HW. Image Correlation for Shape, Motion and Deformation Measurements: Basic Concepts, Theory and Applications. *Springer Science*, 2009.

YIELD SURFACE IDENTIFICATION OF Ti-Cu BIMETAL AND ITS EVOLUTION REFLECTING DEFORMATION HISTORY UNDER COMPLEX LOADINGS

V. Prakash Dubey[1], M. Kopec[1,2] and Z.L. Kowalewski[1]

[1] *Institute of Fundamental Technological Research Polish Academy of Sciences, Warsaw, Poland*
[2] *Department of Mechanical Engineering, Imperial College London, London, UK*

1. Introduction

Mechanical tests of materials generally performed under simple stress conditions do not simulate real-world stress conditions that can occur in most engineering applications. The characterization of materials using only uniaxial testing methods provides only limited data, that are not sufficient to identify all aspects of their behaviour like a texture or anisotropy coming from the manufacturing processes used to produce them [1]. Due to the combination of mechanical, thermal, and diverse functional properties, the bimetals formed from two dissimilar constituent materials have been used in many industrial applications [2][3]. Therefore, this article presents an experimental and theoretical investigations identifying the physical mechanisms responsible for the plastic deformation resulting from the complex mechanical loading and initiation and subsequent propagation of micro-cracks from inherent defects in the interface of titanium–copper bimetal.

2. Results

Complex loading tests were performed on tubular specimens under simultaneous application of axial force and torque to produce axial and shear stresses. Material characteristics of bi-metal (Ti-Cu) in the form of stress-strain are shown in Figure 1. The curve shows decrease in yield limit or increased inelastic response under simultaneous loading executed by the axial tension and proportional cyclic torsion. This effect is also shown in Figure 2, where an evolution of the initial yield surface of the bi-metal (Ti-Cu) is identified in the plane stress state.
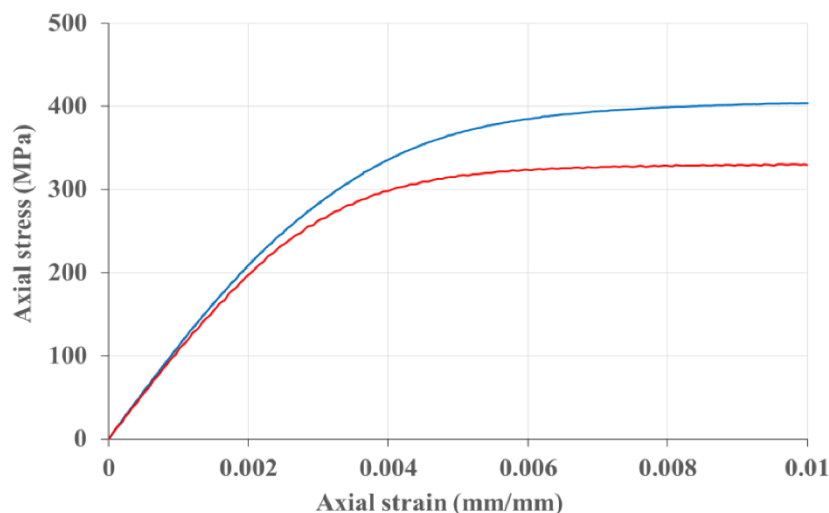
Fig. 1. Material characteristics of the bimetal (Ti-Cu) under monotonic axial tension (blue continuous line) and subjected to simultaneous monotonic axial tension and proportional cyclic torsion of strain amplitude ± 0.1% at 0.5 Hz frequency (red broken line)
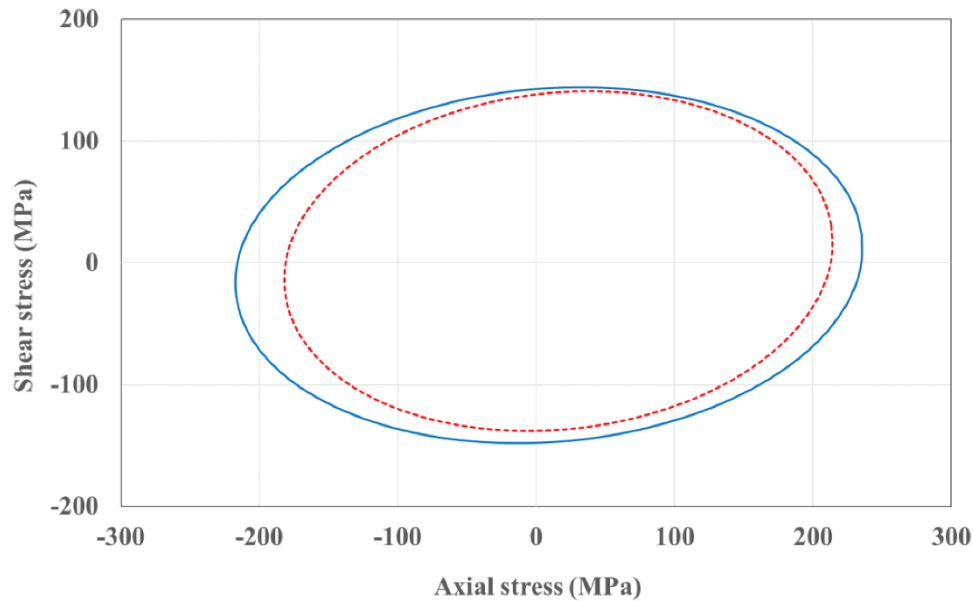
Fig. 2. Yield surfaces (1 * 10⁻⁴ offset strain) for the bimetal (Ti-Cu) in 'as received' state (blue continuous line) and in the pre-deformed state due to simultaneous monotonic axial tension up to permanent strain equal to 1% and proportional cyclic torsion of strain amplitude ± 0.1% at 0.5 Hz frequency (red broken line)

3. Conclusions

The effect of prior plastic deformation induced by cyclic torsion and monotonic tension on the shape and size of yield surface has been studied experimentally for the bimetal (Ti-Cu). Yield surfaces were determined by the technique of sequential probes of the single specimen along 17 different strain-controlled paths in the plane stress state.

(1) The material in its as-received state exhibits anisotropic behaviour for the defined plastic offset strain. Such an effect could have come from either the bimetal production, or specimen manufacturing process applied.

(2) The yield surface sizes of the material in the pre-deformed state are mostly reduced in the axial direction, especially for the compression. This means, that the complex loading of the bimetal (Ti-Cu) leads to the significant softening resulting from plastic anisotropy introduction, that may have created and then increased some of the defects . This issue will be studied in further steps of the experimental program.

4. Acknowledgement

5. References

[1] Socha, G. (2004). Prediction of the fatigue life on the basis of damage progress rate curves. *International Journal of Fatigue*, 26(4), 339-347.

[2] Li, L., Nagai, K., & Yin, F. (2008). Progress in cold roll bonding of metals. *Science and Technology of Advanced Materials*, 9(2), 023001.

[3] Ramadan, M., Fathy, N., Halim, K. A., & Alghamdi, A. S. (2019). New trends and advances in bi-metal casting technologies. *Int. J. Adv. Appl. Sci*, 6(2), 75-80.

REFLECTION INTERFERENCE CONTRAST MICROSCOPY: A VERSATILE TOOL FOR WETTING STUDIES

S.K. Mitra

Waterloo Institute for Nanotechnology, Department of Mechanical Engineering, University of Waterloo, Canada

1. Introduction

Wetting is fundamental to material characterization and discovery. Characterizing how a drop wets a given surface allows measuring the surface energy and associated material properties. Contact angle measurement has been the primary tool for this purpose. However, it often does not provide an opportunity to understand more intricate physical processes due to the interaction of the drop with the substrate (which can be solid or soft). In conjunction with traditional contact angle measurement, microscopy tools can provide a new way to investigate the wetting phenomena.

Reflection interference contrast microscopy (RICM) is a versatile tool to probe the wetting process (including static and dynamic characteristics). Typically, a dual-wavelength in a confocal mode is used in RICM. Sharp interferograms are obtained by controlling the confocal pinhole of the RICM imaging setup. A novel image processing framework [1] has been developed to interpret the experimental interferograms. Utilizing the reflected intensity pattern corresponding to two monochromatic laser sources, different characteristics of the wetting region can be captured.

2. RICM Setup

Figure 1 shows a typical RICM setup used in our studies. Using this setup, we have studied two classes of problems. First, we characterize the condensation process of microdroplets. The incident light rays get reflected from two interfaces, namely quartz/test liquid and test liquid/air interfaces, which interfere with one another. This interference results in bright and dark fringes depending on the difference in the light path. From experimentally obtained interferograms, the framework can reconstruct the three-dimensional topography of the microdroplets even when the contact line of the droplet is distorted due to strong local pinning. The interferograms provided interesting data regarding the flow physics associated with the process. We concluded that the ultrathin precursor film is formed only on the hydrophilic surface, which reduces a resistive force to migration. Also, the reduced size of droplets promotes the thermocapillary motion induced by a gradient in local temperature inside a small microdroplet arising due to the difference in the size of adjacent droplets [2].

Secondly, we investigate how soft solid (PDMS, silicone gels) deforms in the presence of a liquid drop at the three-phase contact line. Figure 2 shows the formation of the wetting ridge, whose height was further characterized using RICM [3]. This technique is further expanded to understand the dynamics of the wetting ridge for soft contact pairs, i.e., glass sphere in contact with gels and elastomers [4].
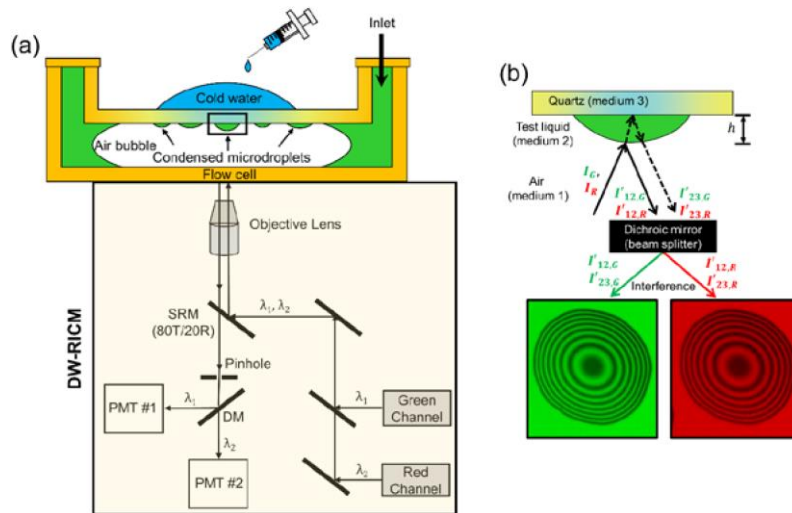
Fig. 1. (a) Schematic representation (not to scale) of the experimental setup for droplet condensation, (b) Simplified light path of the DW (Dual Wavelength) - RICM setup enabling interferometric imaging of the condensation dynamics from bottom view
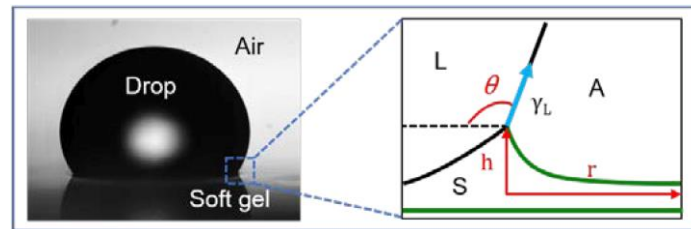
Fig. 2. A water drop on a soft gel coated glass surface. The region near the three-phase contact line is shown as an enlarged view to highlight the wetting ridge profile

3. Conclusions

We have demonstrated that RICM is a versatile tool for understanding the wetting characteristics, which conventional techniques are not feasible. RICM allows us to probe these characteristics as long as the access of the laser sources is made available to the probed interfaces from the bottom.

4. References

[1] S. Misra, H. Teshima, K. Takahashi, and S. K. Mitra (2021). Reflected Laser Interferometry: A Versatile Tool to Probe Condensation of Low-Surface-Tension Droplets, *Langmuir*, **27**, 8073-8082.

[2] H. Teshima, S. Misra, K. Takahashi, and S. K. Mitra (2020). Precursor film mediated thermocapillary motion of low surface tension microdroplets. *Langmuir*, **36**, 5096 – 5105.

[3] S. Mitra, S. Misra, T. Tran, and S. K. Mitra (2022). Probing liquid drop induced deformation on soft solids using Dual-Wavelength Reflection Interference Contrast Microscopy. *Submitted.*

[4] A.R. Kim, S. K. Mitra, and B. Zhao (2022). Capillary pressure mediated long-term dynamics of thin soft films, *Submitted.*

REVIEW OF RECENT ACHIEVEMENTS IN STRESS STATE EVALUATION IN TECHNICAL ELEMENT WITH BARKHAUSEN EFECT

B. Augustyniak[1], M. Chmielewski[1,2] and L. Piotrowski[2]
[1] *NNT Ltd, Gdansk, Poland*
[2] *Gdansk University of Technology, Gdansk, Poland*

1. Scope of the work

This is a short demonstration of achievements in stress state evaluation nondestructive technique development using innovative concept of the Barkhausen effect (BE) measuring devices. These portable devices convert in a few seconds the BE intensity into information about the stress state.

2. Introduction

The non-destructive testing and evaluation (NDT&E) of the stress state in steel construction elements exploited in industry is still a very important technical issue of great practical significance due to the obvious need to reduce the risk of failure of such elements. Our scientific experience with evaluation of magneto-mechanical properties with Barkhausen effect in various steels [1, 2] allows us to state that this phenomenon allows really quick and low cost detection of stress state in industrial environment. We present here the relevant examples of the application of such technique where two innovative devices elaborated by our spin-off company NNT Ltd are used. These devices analyze the BE voltage signal and provide within few second's time information about the stress level directly in MPa units. The first meter MagStress5C with unidirectional BE probe determines stress level in magnetization direction. The second meter – MagStress5D with the two core probe performs measurement of the angular distribution of BE intensity and provides automatically values of two main stress components *S1* and *S2* as well as the angle between *S1* and probe axis. It was constructed with financial support by the Polish research fund [3]. The calibration functions of BE vs. strain dependence, appropriate for the tested steel, are stored in the device memory.

3. Examples
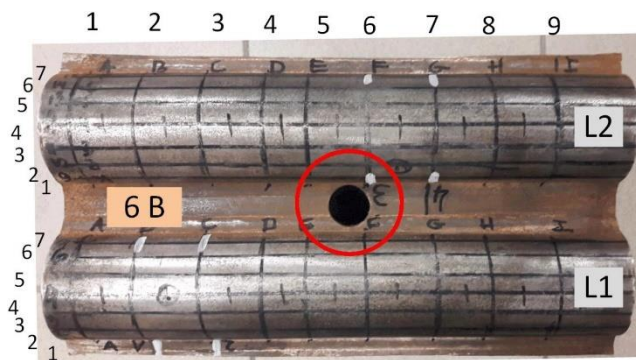
Fig. 1. The power plant boiler screen section with welded tubes L1 and L2
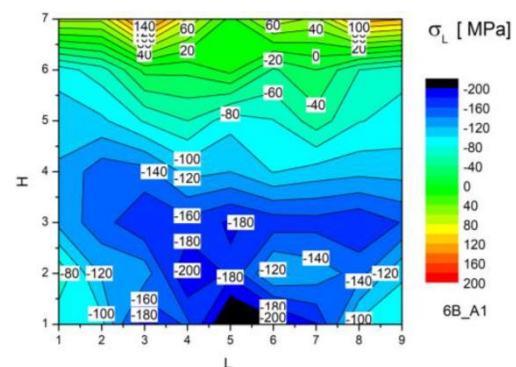
Fig. 2. Distribution of residual stress over the L1 tube (axial direction)

Figure 1 depicts a section of the power plant boiler curtain wall with two tubes welded in parallel and with a third tube welded in perpendicular direction to this section (seen as black hole). The intensity of the BE (*Int*) and corresponding strain *eps* was recorded with a MagStress5c meter at

selected points on the pipe surface in three main directions (circumferential direction (H), axial direction (A) and intermediate (T). Those *Int* values were transformed into corresponding three strain levels using the appropriate calibration function and from them the stress components in any direction can be calculated. The 2D map of stress in axial direction shown in Fig. 2 reveals the complex nature of stress distribution of such a section.

Fig. 3. Ship section tested with MagStress5D
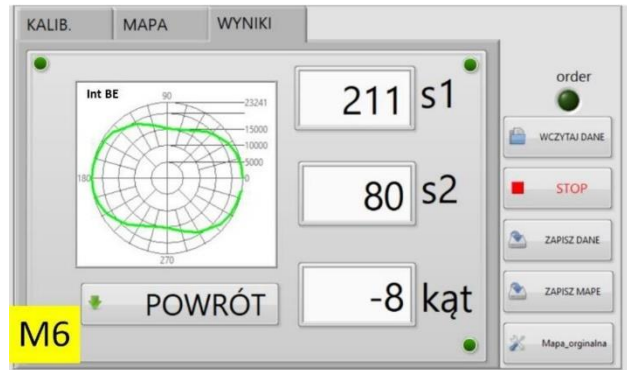
Fig. 4. MagStress5D readings - point M6 in Fig. 3

Exemplary result of biaxial stress state determination in a welded ship section (shown in Fig. 3) performed with the Magstress5D device is presented in Fig. 4. There is shown an angular distribution of BE intensity recorded at the point M6 in Fig. 3 with resulting values in MPa of stress components *S1* and *S2* and angle between *S1* and the axis of the probe (from which the orientation of main stress axes in the sample is obtained). It is worth noting that the new versions of the device can calculate the strains on the basis of full 2D BN intensity vs. strain dependence.

4. Conclusions

Our research on stress state determination included ferromagnetic steel components from the metallurgical, shipbuilding, automotive, and energy industries. The research was focused on the objects and technological processes where the high stress levels cause problems both at the construction and exploitation steps. The test results prove that the demonstrated innovative concept of BE devices application for stress state evaluation enables an effective and fast control of the many technological processes (e.g. welding, shot peening, as well as rolling or tensile leveling) as well as monitoring of safe operation of industrial components.

5. References

[1] B. Augustyniak; Magnetomechanical phenomena and its application in nondestructive testing of materials; *Monography* no 38, Gdansk University of Technology, Gdansk, 2003 (in Polish)
[2] B. Augustyniak, L. Piotrowski, M. Chmielewski, W. Kielczynski, K. Prokop; Progress in the post weld residual stress evaluation using Barkhausen effect meter with a novel rotating magnetic field probe,
[3] http://www.ndt.net/search/link.php?id=16857&file=events/ECNDT2014/app/content/Paper/ 647_Augustyniak.pdf
[4] Development and implementation of a measuring system to determine the state of stress in steel parts using the Barkhausen effect; National Centre for Research and Development; POIR.01.01-00-1094/18-00

THE EFFECT OF PRE-STRETCHING ON THE MECHANICAL PERFORMANCE OF Al-Cu-Li ALLOYS

C.M. Charalampidou[1], N.D. Alexopoulos[1], R.J. Mostert[2], M. Khodja[2] and S.K. Kourkoulis[3]

[1] *Department of Financial Engineering, School of Engineering, University of the Aegean, Kountourioti 41 str, 82132, Chios, Greece*
[2] *University of Pretoria, Department of Material Sciences and Metallurgical Engineering, 395, Pretoria, Republic of South Africa.*
[3] *Laboratory of Testing and Materials, Department of Mechanics, National Technical University of Athens, 9 Heroes Polytechniou Str,15773, Athens, Greece*

1. Abstract

The increasing demand for improvement in energy efficiency and mechanical performance along with decrease of maintenance costs lead the aviation industry to the development of new, lighter metallic structures. Third generation Al-Cu-Li alloys were developed to replace the conventional aluminum alloys, since they can offer approximately 5 % weight reduction of the structure as well as improved property balance and corrosion resistance. Their improved mechanical properties are often attributed to their precipitation hardening system including δ (Al3Li), θ (Al2Cu), T1 (Al2CuLi) and S (Al2CuMg) phases. The conventional manufacturing process of aerospace aluminium plate includes a stretching operation after solution heat treatment, for stress relief from the residual stresses developed on quenching, during which the material is typically plastically strained between 2 and 5% [1]. In 3rd generation Al-Cu-Li alloys this stretching operation enhances the optimum distribution of T1 precipitates, which is the main strengthening phase of these alloys and dislocation nucleated. It has been widely shown that a small pre-strain level prior to artificial ageing produces a uniform distribution of dislocations within the matrix, which act as heterogeneous nucleation sites for the T1 phase [2-3]. Additionally stretching was found to accelerate precipitation within the matrix, avoiding grain boundary precipitation which leads to a detrimental effect on toughness as well as to integranular corrosion attack [5-6]. The present work aims to examine the effect of increasing tensile pre-strains on a typical 3rd generation Al-Cu-Li alloy's ageing kinetics, microstructure evolution and yield stress.

The material used was a wrought aluminum alloy 2198-T8 which was received in sheet form of 3.2 mm nominal thickness. Tensile coupons were exposed to three different pre-stretching levels and a full characterization of microstructure evolution was perfromed through SEM and TEM analysis. The results showed that the grain size and the precipitates of the pre-stretched samples play a pivotal role on the corrosion susceptibility of the specimens and for the low stretching level.

2. Acknowledgements

3. References

[1] J.W. Martin, Precipitation Hardening (1998), 2nd ed., Butterworth-Heinemann, Oxford.

[2] B.M. Gable, A.W. Zhu, A.A. Csontos, E.A. Starke Jr. (2001). The role of plastic deformation on the competitive microstructural evolution and mechanical properties of a novel Al-Li-Cu-X alloy. J. Light Met. 1 1-14.

[3] W.A. Cassada, G.J. Shiflet, E.A. Starke (1991). The effect of plastic deformation on Al2CuLi (T1) precipitation. Metall. Trans. A 22 299-306.

[4] D. Tsivoulas, P. Prangnell (2014). Comparison of the effect of individual and combined Zr and Mn additions on the fracture behavior of Al-Cu-Li alloy AA2198 rolled sheet. Metall. Mater. Trans. A 45 1338-1351.

[5] Y. Ma, X. Zhou, Y. Liao, Y. Yi, H. Wu, Z. Wang, W. Huang (2015). Localised corrosion in AA2099-T83 aluminium-lithium alloy: the role of grain orientation. Corros. Sci. 107 41–48.

[6] Y. Ma, X. Zhou, W. Huang, Y. Liao, X. Chen, X. Zhang, G.E. Thompson (2015). Crystallographic defects induced localised corrosion in AA2099-T8 aluminium alloy. Corros. Eng. Sci. Technol. 50 420–424.

RESIDUAL STRESS CHARACTERIZATION AND PART DISTORTION IN EXTRUDED HEAT TREATED ALUMINUM ALLOY USED IN THE FABRICATION OF SECOND RIB STRUCTURE OF AN AIRCRAFT WING

M.S. Hossain[1], S. S.M. Al Hinai[1,2] and MD S. Miah[1]
[1] Department of Aeronautical Engineering, Military Technological College, Muscat, Oman
[2] Royal Flight Oman, Muscat, Oman

Abstract

This paper presents results of residual stress distribution measured by the neutron diffraction (ND) method in an extruded 7050 aluminum alloy used to fabricate a typical second rib structure of an aircraft wing. It is believed that the initial complex residual stress state introduced due to the heat treatment process still remains following stretching and extrusion, although the level of stress may be reduced during these stress relief steps. The distribution of the residual stress from this process is completely unknown and was predicted using the finite element analysis (FEA) technique using ABAQUS v12 commercial software. The presence of these complex residual stress fields may significantly influence the final distortion (in excess of several millimeters) during the fabrication of the wing rib 2 structure. The ND measured residual stresses were used to validate the FEA predicted stresses which can be further developed to model and explore different material removal strategies to minimize and alleviate undesired distortions.

The 7050 aluminum alloy extrusion sample was prismatic with an I cross-section and dimensions including 800 mm wide, 2650 mm long, 56 mm web thickness. The flange depths included 167 mm and 81 mm, with weight over 400 kg. The residual stress distribution was expected to be uniform along the longitudinal direction of the extruded alloy which was also confirmed by the FEA prediction. To optimize the allocated neutron beam time, the residual stress measurements spanned along the width of the extrusion sample, i.e. along the long-transverse *LT* direction, at three different thickness locations. These measurements were sufficient to provide a well-defined overall residual stress field in the sample and to validate the FEA predicted stress distributions. All three principal components of the strain field were considered in the ND measurement.

Keywords: Residual stress, neutron diffraction, time of flight technique, finite element analysis, part distortion

TS2. Experimental Fluid Mechanics

COALESCENCE OF DROPLETS CONTAINING PARTICLES IN CREEPING FLOW THROUGH A CYLINDRICAL TUBE

M. Muraoka and H. Sakurai

Department of Mechanical Engineering, Tokyo University of Science, Chiba, Japan

1. Introduction

Coalescence of droplets in creeping flow through a cylindrical tube is the basis for analyzing the flow of multiphase fluids through porous media such as for example in enhanced oil recovery (for instance, [1],[2]). We focus on a narrow passage in porous media, and if we assume the passage as a cylindrical tube, coalescence of droplets in creeping flow through the passage results in that through a cylindrical tube. Muraoka et al.[3] found out that coalescence time of droplets containing suspended particles was obviously shorter than that without particle in creeping flow through a cylindrical tube. The coalescence time is defined as the period between the instant when the relative velocity of the two droplets becomes zero after their apparent contact and when the coalescence takes place. Based on Aul and Olbricht's semi-theoretical formula [4], Muraoka et al.[3] proposed other semi-theoretical formulas of the coalescence time in terms of the resistance experienced by the liquid droplet in creeping flow through a cylindrical tube [5]. In the present study, coalescence time of droplets containing suspended particles in creeping flow through a cylindrical tube was experimentally measured and compared with the predictions of semi-theoretical formulas. Effect of different particle sizes and Reynolds number of the tube flow on coalescence of droplets were discussed.

2. Experiment

A cylindrical glass tube of inner diameter 2.0 mm, outer diameter 7.0 mm, and length 1500 mm was used as the test tube. Silicone oil with a kinematic viscosity of 3000cSt was employed as the test fluid of the droplet. Droplets include gold-coated acrylic particles. Two different particle sizes were employed, 15 μm in diameter, 1780kg/m^3 in density and 30 μm in diameter, 1490kg/m^3 in density, respectively. A mixture of glycerol and pure water was used as the surrounding fluid of the creeping flow through the tube. The density of the droplets was made equal to that of the surrounding fluid by the addition of carbon tetrachloride. The ratio of the viscosity of the droplet to that of the surrounding fluid was denoted by β; i.e., $β = μ_d/μ_s$, where the subscript d and s indicate droplet and surrounding fluid, respectively. In the present experiments, the densities of the droplet and the surrounding fluid were both $1.24×10^3$ kg/m^3, and $μ_s$ was 0.24 Pa·s, β≈1.0. A large volumetric syringe pump was employed to maintain steady flow through the tube at a designated average velocity. The two droplets were injected into the test tube using micro-syringes placed in front of the inlet of the tube. The behaviors of the droplets were monitored by a digital camera and two high-speed cameras placed on a sliding stage. The coalescence time of the two droplets was measured, as well as the diameter of the clearance area between them just before coalescence. The particle size and the Reynolds number of the tube flow were varied to investigate their effects on the film drainage and coalescence of the droplets containing particles. Experimentally measured coalescence time was compared with the predictions of semi-theoretical formulas.

3. Conclusions

Effects of conditions of contained particles and Reynolds number of the tube flow on the coalescence time were investigated. The coalescence time of droplets containing suspended particles

was obviously shorter than that without particle [6] in any of these cases. In the case of the leading droplets containing suspended particles 30 μm in diameter, coalescence time was dramatically shorter than that in any of these cases, though volumetric concentration of the particles was the same and number density of particle 30 μm in diameter was about 12% of that of particle 15 μm in diameter. It was found that particle size affected coalescence time of droplets containing suspended particles. In the case of Re=0.01, the experimentally measured coalescence time agreed roughly with the values by semi-theoretical formulas. The values by semi-theoretical formulas deviated from experimental values with increasing Re. In the case of Re=0.08, the experimentally measured coalescence time didn't agree with the values by semi-theoretical formulas due to increase of the effect of the rotation of the following droplet.

4. Acknowledgements

5. References

[1] J.J. Sheng (2013). *Enhanced Oil Recovery Field Case Studies*. ELSEVIER.
[2] J.J. Sheng (2011). *Modern Chemical Enhanced Oil Recovery*. ELSEVIER.
[3] M. Muraoka, et al.,(2013). Coalescence Phenomena of Droplets with Suspended Particles in a Tube Creeping Flow. *Proceedings of the 8th World Conference on Experimental Heat Transfer, Fluid Mechanics and Thermodynamics,* Paper No. 96.
[4] R.W. Aul and W.L.Olbricht (1991). Coalescence of Freely Suspended Liquid Droplets in Flow through a Small Pore. *Journal of Colloid and Interface Science.*, 145, No. 2, 478–492.
[5] J.J.L.Higdon, and G.P. Muldowney (1995). Resistance Function for Spherical Particles, Droplets and Bubbles in Cylindrical Tubes. *Journal of Fluid Mechanics*, 298, 193–210.
[6] M. Muraoka,et al.(2015).EFFECT OF REYNOLDS NUMBER ON COALESCENCE OF DROPLETS IN CREEPING FLOW THROUGH A TUBE, *Proceedings of the ASME-JSME-KSME Joint Fluids Engineering Conference 2015*, AJK2015-15106.

TS4. Computational Mechanics

IMPROVED DETECTION OF PROGRESSIVE TRANSVERSE CRACKING IN THE RAIL HEAD USING ULTRASONIC TECHNIQUE

T. Katz, S. Mackiewicz and Z. Ranachowski
Institute of Fundamental Technological Research, Warsaw, Poland

1. Introduction

Non-destructive detection of faults in track rails using ultrasonic technique (UT) have been performed for several decades throughout the European and world lines. In the European Union the standard EN 16729 is observed [1] in this respect. The standard specifies the requirements for testing principles and systems in order to produce comparable results with regard to location, type and size of typical faults occurring in rails. However the increasing speed and weight of exploited trains leads to new types of faults not entirely detected with the standard techniques. Especially difficult for detection are defects originating near the upper rail head corners and extending in the nearly transverse direction in respect to the rail axis [2]. These discontinuities are difficult to detect because of inefficient orientation of the beams emitted by the standard sets of ultrasonic transducers.

2. Comparison of effectivity of ultrasonic transducers with use of tools modelling the wave propagation

The authors applied a library of programs named BeamTool 9 of Eclipse Scientific Products Inc. to compare the effectivity of different transducer arrangements aimed at detection of transverse cracking in the rail head. The program allows for the tracing of ultrasonic beam path after specifying the properties of ultrasonic transducer, investigated material and geometry of the tested object. Modelling of the propagation of ultrasonic waves in the material is based on the concept of the ultrasonic beam produced by the vibrating transducer of the ultrasonic probe. This concept was introduced and described in detail in the basic monographs and textbooks on the ultrasonic testing [3].

The distribution of the ultrasonic field (more precisely distribution of its acoustic pressure) may be determined using the Huygens principle. It says that the acoustic pressure at a point defined by r is the sum of the pressures of spherical partial waves produced by all the points forming the active surface of the transducer. In the isotropic elastic body, this principle can be expressed in the form of the Rayleigh integral:

$$(1) \qquad p(\boldsymbol{r}) = \iint (p_0\, e^{-ikr}/\lambda r)\ dS$$

where: p is acoustic pressure at the point r, integration takes place over the entire active surface of the transducer; p_0 is the acoustic pressure at the transducer surface, k is the wave number, λ is wavelength, r is a distance between the point r, where the acoustic pressure is calculated and the current integration point on the transducer surface.

In Figure 1 an arrangement of ultrasonic transducer implemented in accordance to the standard practise is shown. The transverse wave transducer, operating at 2 MHz frequency emits a beam inclined at 70º in respect to the normal direction to the rail surface. Standard square 15 x 15 mm transducer was used for calculation of effective acoustic pressure. A standard circular fault of 8 mm diameter was placed in the nearly vertical direction (82 º) in the rail head. The incident beam produces reflection and scattering at the defect face but this configuration will not result in the good reception of the reflected signal by the transducer and thus the fault cannot be detected (see Fig. 1).
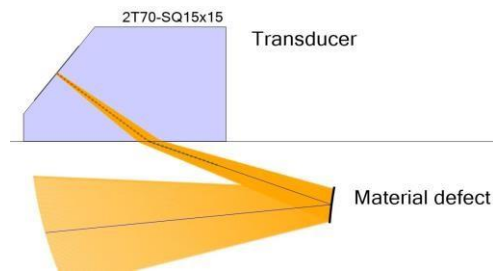
Fig. 1. The arrangement of UT transducer implemented in accordance to the standard practice

Figure 2 presents an another UT transducer configuration proposed by the authors for the same purpose. It is the 2 MHz probe emitting longitudinal wave at 80º angle in respect to the normal direction. To keep the ultrasonic beam near the rail surface, an elongated rectangular, 16 x 8 mm, transducer was used instead of a typical square transducer. The same circular model defect situated in the same manner as in Figure 1. was applied for the simulation. In this case however, the beam reflected from the defect face is much more diverged and some amount of energy reaches the testing transducer. The configuration presented in Figure 2 is currently being developed for the on-site tests realized by the authors.
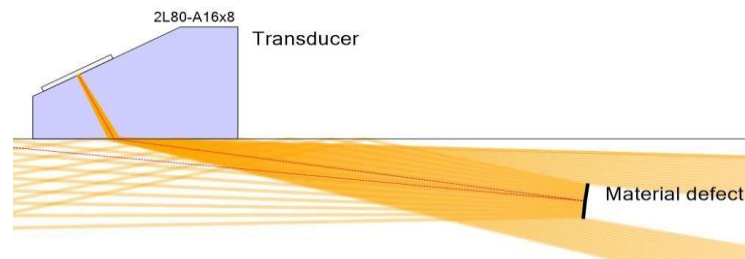
Fig. 2. The arrangement of an innovative UT transducer developed using the simulation

3. Acknowledgement

4. References

[1] European Standard EN 16729-1: 2016 Railway applications – Infrastructure–Non-destructive testing on rails in track – Part 1: Requirements for ultrasonic inspection and evaluation principles.
[2] G. Zumpano, M. Meo, A new damage detection technique based on wave propagation for rails, *Int. J. Sol. Struct.,* **43**, 1023-1046
[3] J. Krautkramer, H. Krautkramer (1990) *Ultrasonic Testing of Materials*., Springer-Verlag, Berlin, Heidelberg, New York, 20-160, ISBN 978-3-662-10680-8

GEOMETRIC REGULARIZATION OF MESH-BASED 3D SHAPE MEASUREMENTS USING MULTILEVEL SPLINES

M. Chapelier[1,2], R. Bouclier[1,2] and J.-C. Passieux[1]
[1]Institut Clément Ader (ICA), Université de Toulouse,
CNRS-INSA-UPS-ISAE-Mines Albi, Toulouse, France
[2]Institut de Mathématiques de Toulouse (IMT), Université de Toulouse,
CNRS-INSA-UT1-UT2-UPS, Toulouse, France

Digital Image Correlation (DIC) is a convenient way of performing full-field measurements on surfaces. It only requires one or several cameras to get a displacement field that can be used for model validation or parameter identification. Among the various methods to achieve DIC, Finite Elementbased (FE-based) methods are spreading, because of their ability to be coupled with numerical models. Indeed, measured and simulated kinematic fields can be defined at the nodes of the same mesh.

Stereo Digital Image Correlation enables to measure 3D surface fields, thanks to several cameras. Prior to any experimentation, a calibration phase must be carried out in order to determine the parameters of the cameras and the actual shape of the specimen. In Finite Element Stereo Digital Image Correlation (FE-SDIC), the shape is defined by the FE mesh. Although it facilitates the link with a FE simulation tool, it provides a fine description of both the geometry and the displacement field, which leads to an ill-posed problem when identifying the shape. When considering shape measurement problem or shape optimization, FE are known to generate unrealistic geometries. They often require the addition of a smoothing term, or a post-treatment phase, usually using smoothing filters. However, these filters may also affect the measurements.

Our approach consists in using another basis than FE Lagrange functions, so that shape measurement is directly performed on a more regular space [2,4]. We chose spline functions because of their high regularity. These functions are commonly used for describing geometries in ComputerAided Design (CAD). We then make a link between the spline geometry and the FE mesh in order to solve the shape measurement problem using a usual FE-SDIC software but with a smooth geometry in a non-invasive way, similarly to [3].

In FE-SDIC, camera calibration and specimen shape measurement are carried out simultaneously. We assume the intrinsic parameters of the cameras to be known, so only six extrinsic parameters have to be found for each camera, corresponding to their position and orientation. For two cameras, these parameters, denoted by $p^* \in \mathbb{R}^6 \times \mathbb{R}^6$, and the specimen shape, denoted by S^*, minimize the graylevel mismatch:

$$(1) \quad S^*, p^* = \underset{\substack{S \in L_2(\Omega_s) \\ p \in \mathbb{R}^{12}}}{\operatorname{argmin}} \frac{1}{2} \int_{\Omega_s} \left[\mathcal{I}_0\big(P_0(X + S(X), p_0)\big) - \mathcal{I}_1\big(P_1(X + S(X), p_1)\big) \right]^2 dX$$

with $\mathcal{I}_i(x)$ the ith image (x in pixels) and $P_i(X, p_i)$ the projection going from a point in the world space X and camera parameters p_i to a point in the pixel space.

A Gauss-Newton minimization is then performed [1]. Thus shape measurement is obtained by iteratively solving such equations:

$$(2) \quad H_{FE}^k \, dp^k = b_{FE}^k$$

We managed to link the FE operators to the CAD degrees of freedom so that the CAD geometry drives the shape measurement. We can then choose the number of control points that will describe the geometry, thus restricting the research space for admissible geometries to very smooth, realistic

shapes. This method does not need the addition of any regularization term, nor any smoothing filters. Furthermore, a multilevel approach was adopted. It is made possible by mathematical properties of splines, which can be refined while keeping the exact same geometry. The multilevel approach was found to be more effective than standard methods. As shown in Figure 1, a first measurement is made on a coarse CAD geometry with very few degrees of freedom. It is then used as an initialization for a finer CAD geometry, as many times as necessary to get the desired precision. Since the shape measurement problem regulation is based on CAD functions, which are usually used to describe geometries, we call our method Geometric Regularization.
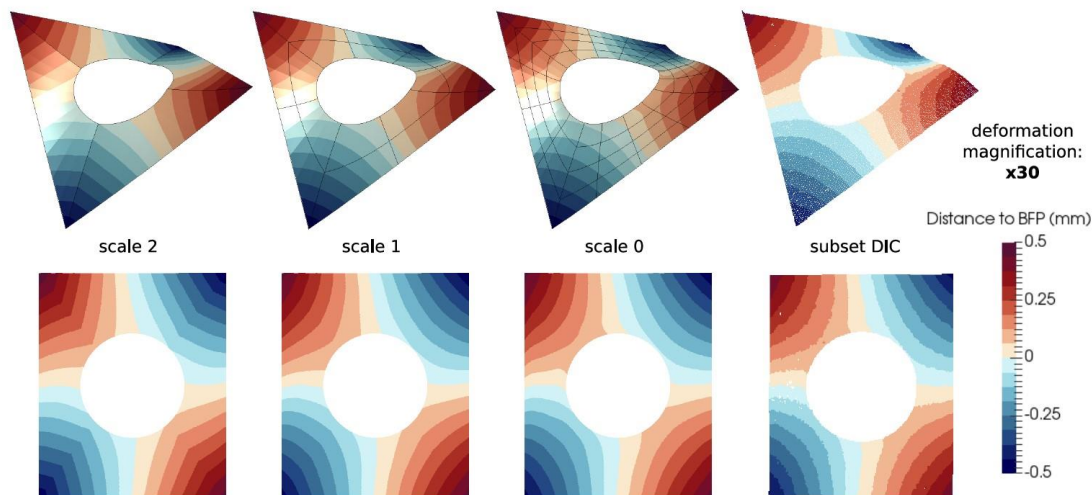
Fig. 1. Twisted specimen with the proposed geometric regularization.
The visible mesh is the CAD mesh, and analysis is performed on a finer FE mesh

The direct link between the CAD geometry and the FE model has multiple advantages. It allows using few degrees of freedom, making the problem both faster to solve and more regular. In addition, a FE meshing software has to be used only once even though the CAD geometry is changing. An important feature of our multilevel approach is that we benefit from spline ability to be refined without any change in the geometry. Finally, this approach enables using a standard FE-SDIC software in a non-invasive way, with an explicit link between the FE-mesh geometry and the CAD geometry.

References

[1] J.-C. Passieux, R. Bouclier, Classic and inverse compositional Gauss-Newton in Global DIC, International Journal for Numerical Methods in Engineering (2019).
[2] J.-E. Dufour, S. Leclercq, J. Schneider, S. Roux, F. Hild, 3D surface measurements with isogeometric stereocorrelation – application to complex shapes, Optics and Lasers in Engineering 87 (2016) 146 – 155.
[3] M. Tirvaudey, R. Bouclier, J.-C. Passieux, L. Chamoin, Non-invasive implementation of nonlinear Isogeometric Analysis in an industrial FE software, Engineering Computations, doi: 10.1108/EC-03-2019-0108.
[4] V. Braibant, C. Fleury, Shape optimal design using B-spline, Computer Methods in Applied Mechanics and Engineering 44 (1984) 247–267.

DEVELOPMENT OF A MULTI-OBJECTIVE FINITE ELEMENT SIMULATION FRAMEWORK FOR HOT STAMPING PROCESSES

X. Liu[1], S. Dhawan[1], Y.X. Lim[1], O. El Fakir[1], J. Liu[2], X. Yang[2] and L. Wang[1]
[1] Department of Mechanical Engineering, Imperial College London, London, UK
[2] Advanced Forming Research Centre (AFRC), University of Strathclyde Glasgow, Glasgow, UK

Abstract

Hot stamping is a novel non-isothermal forming technology to deform aluminum alloy blanks into complex-shaped components, in which a blank is first heated up to elevated temperature, rapidly transferred to a press machine and then formed by tools at room temperature, followed by a proper artificial ageing process [1]. In order to save experimental efforts, finite element (FE) simulation is performed to simulate the hot stamping process and predict the post-form properties of the formed components. Consequently, the geometries of the component and forming tools as well as the processing window could be optimized based on the simulated results to meet the desired requirement. Therefore, the FE simulation is required to enable multi-objective prediction, including thinning/wrinkling distribution, post-form strength distribution, springback analysis, formability/failure analysis, etc., in order to ensure reliable simulated results of the post-form properties of the formed components [2].

Three essential conditions are demanded to realize the multi-objective FE simulation of a hot stamping process, namely experimental characterization of the material properties and boundary conditions, predictive modelling of the material properties and boundary conditions, and integration of the modelling with FE simulation software. Specifically, the material properties and boundary conditions, e.g. flow stress [3], coefficient of friction [4], interfacial heat transfer coefficient (IHTC) [5] and forming limit curves (FLC) [6], determine the material behaviors under the non-isothermal forming conditions, while their predictive modellings can be integrated with the FE simulation, saving the development of multi-disciplinary subroutines tailored to the software being used [7].

The present research demonstrated a multi-objective FE simulation of hot stamping of a panel component made from 7075 aluminum alloy. The flow stress, coefficient of friction, IHTC and FLC under various experimental conditions were characterized and then modelled, as shown in Fig. 1. Through the integration of the material models with the FE simulation, the multi-objective predictions of the temperature, thinning, failure and post-form strength of the formed component were achieved, and they were subsequently compared to the experimental results obtained from hot stamping of the AA7075 panel components. The good agreement between the experimental and simulated results verified that the demonstrated framework of the multi-objective FE simulation is reliable and feasible to be applied in the hot stamping of the aluminum alloys.
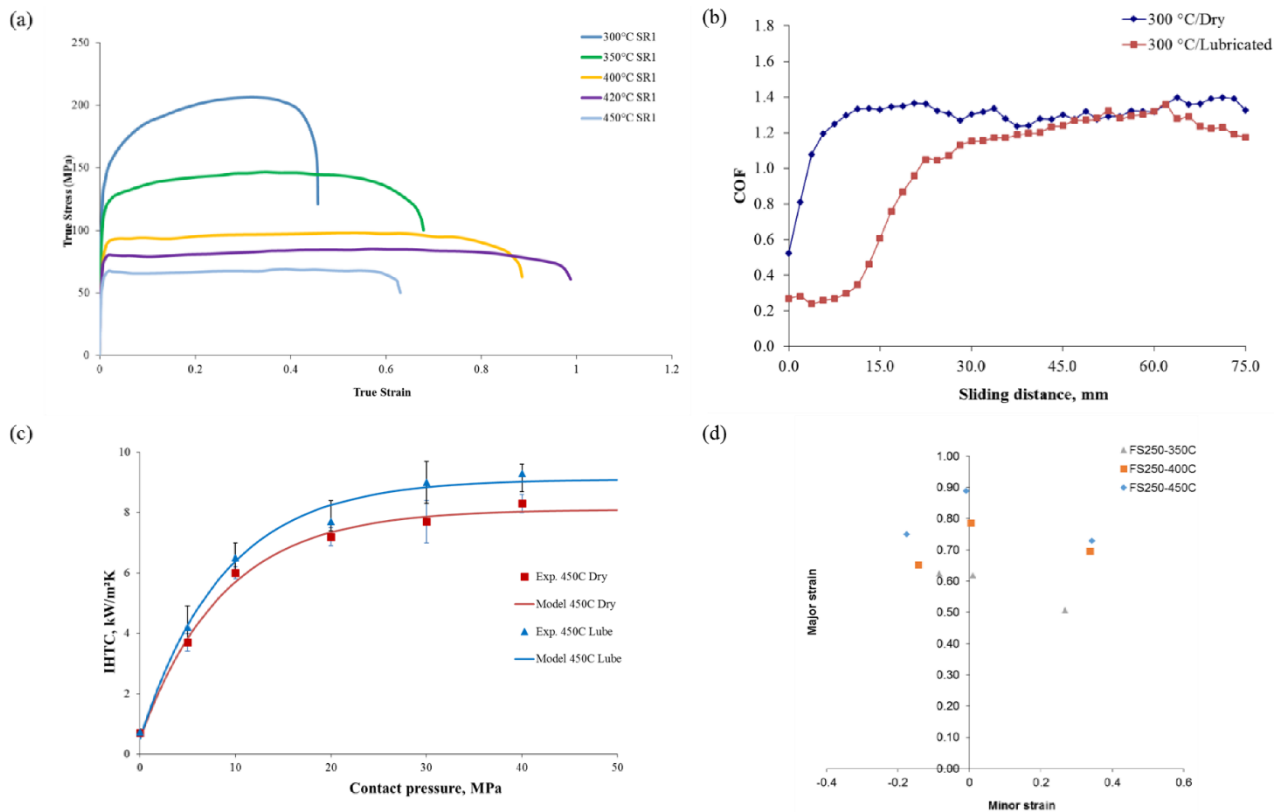
Fig. 1. (a) The flow stress; (b) the coefficient of friction; (c) the interfacial heat transfer coefficient; and (d) the forming limit curves of the AA7075

References

[1] J. Liu et al. (2018), Transition of failure mode in hot stamping of AA6082 tailor welded blanks, *J. Mater. Process. Technol.*, **257**, 33–44.

[2] A. Wang, O. El Fakir, J. Liu, Q. Zhang, Y. Zheng, and L. Wang (2018), Multi-objective finite element simulations of a sheet metal-forming process via a cloud-based platform, *Int. J. Adv. Manuf. Technol.*, **100**, 2753–2765.

[3] O. El Fakir, L. Wang, D. Balint, J. P. Dear, J. Lin, and T. A. Dean (2014), Experimental and numerical studies of the solution heat treatment, forming, and in-die quenching (HFQ) process on AA5754, *Int. J. Mach. Tools Manuf.*, **87**, 39–48.

[4] Y. Hu, L. Wang, D. J. Politis, and M. A. Masen (2017), Development of an interactive friction model for the prediction of lubricant breakdown behaviour during sliding wear, *Tribol. Int.*, **110**, 370–377.

[5] X. Liu, K. Ji, O. El Fakir, H. Fang, M. M. Gharbi, and L. Wang (2017), Determination of interfacial heat transfer coefficient for a hot aluminium stamping process, *J. Mater. Process. Technol.*, **247**, 158–170.

[6] H. Gao, O. El Fakir, L. Wang, D. J. Politis, and Z. Li (2017), Forming limit prediction for hot stamping processes featuring non-isothermal and complex loading conditions, *Int. J. Mech. Sci.*, **131**, 792–810.

[7] D. Zhou *et al.* (2016), Knowledge based cloud FE simulation of sheet metal forming processes, *J. Vis. Exp.*, **118**, 1-9.

OPTIMIZATION OF TRANSIENT STATES OF SURGICAL ROBOT TO SOFT TISSUE SURGERY USING MOGA GENETIC ALGORITHM

G. Ilewicz and A. Harlecki

Department of Combustion Engines and Vehicles, Faculty of Mechanical Engineering and Computer Sciences, University of Bielsko-Biala

1. Introduction

Surgical robots have been used to carry out soft tissue treatments around the world for many years due to the positives of minimally invasive surgery. Doctors since the use of artificial organs in the human body formulate a belief in the effectiveness of medical robots for their repair and maintenance in hospitals due to the high accuracy of robot positioning and thus a quick and effective service of the mechatronic structure of the artificial organ using them.
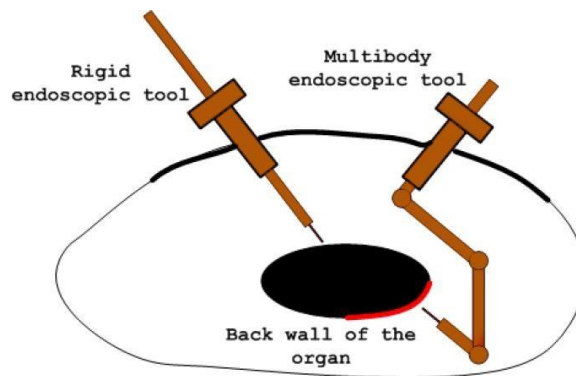
Fig. 1. Rigid and multibody effector that can reach to the back wall of the operating organ

From the point of view of economic rights, doctors in Poland take the position that medical robots are only profitable to apply in urology because of the costs of their use.

2. Matherials and methods

The medical robot considered in the work is characterized by an open structure RRRS in the kinematic chain due to the possibility of reaching such a structure, to the back wall behind the organ or artificial organ.
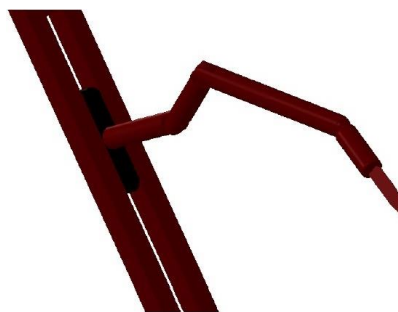
Fig. 2. The model of the RRRS structure of the medical robot

The robot is ended with a scalpel due to the possibility of cutting soft tissue during surgery inside the body to reach through the body shells to the pathological organ. It is an elementary surgical operation performed by a doctor during surgery.

The authors used (finie element method) FEM when formulating a physical model of medical robot to determine mechanical quantities such as stresses and deformations in the robot structure, especially in places that they considered to have an impact on the construction safety criterion and that could contribute to improving dynamic properties during medical robot work.
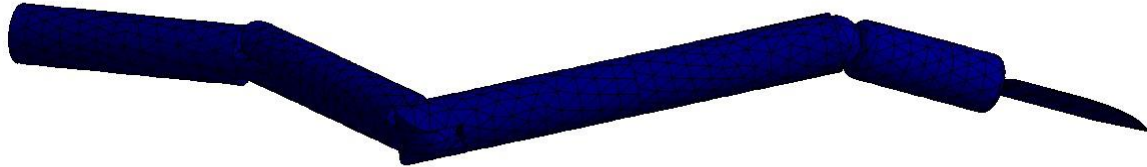
Fig. 3. The FEM model of the RRRS structure of the medical robot

These values were determined during transient states to determine near-real strength reactions occurring inside the material structure due to motion.

Particular attention was focused on the phenomenon of friction in joints occurring during movement due to the fact that authors wanted to know its impact on the structure of the medical robot.

An optimization model was formulated to obtain the correct mass and stress values for given constraints and boundary conditions of the FEM discrete model. The multi-criteria objective function was solved using a genetic algorithm MOGA.

The stiffness of the medical robot for optimal solution was also examined.

3. Results

The authors illustrated the results of stress and strain distribution arising on the basis of the FEM model. The values of decision variables of objective function needed to obtain the geometrically optimal structure of the medical robot was also determined.

The charts show the impact of friction on the structure of the medical robot to determine its quantitative effect on the dynamics of the medical robot.

Charts of natural frequencies during bending and torsional vibrations of the optimal structure of the medical robot were also determined.

4. Conclusions

The optimization model allows obtaining the correct mechanical structure of the medical robot for the adopted criteria (mass, stress) and limitations (safety factor). It is stated that friction has a significant effect on the structure of the medical robot.

The formulation of frequency charts allows to infer about the work of a medical robot in the areas of the resonance curve.

5. References

[1] G. Ilewicz (2017). Natural frequencies and multi - objective optimization of the model of medical robot with serial kinematical chain, *Advances in Intelligent Systems and Computing*, **519**, 371-379.

[2] G. Ilewicz, A. Harlecki (2018). Full Dynamics and Optimization of a Controllable Minimally Invasive Robot for a Soft Tissue Surgery and Servicing Artificial Organs, *Lecture Notes in Networks and Systems*, **53**., 204-2011.

DIRECT AND INVERSE CHARACTERIZATION
OF THE ASYMMETRIC HARDENING BEHAVIOR OF BULK TI64 ALLOY

V. Tuninetti[1], G. Gilles[2], P. Flores[3], G. Pincheira[4], L. Duchêne[5] and A.M. Habraken[5,6]
[1] Department of Mechanical Engineering, Universidad de La Frontera, Temuco, Chile
[2] Samtech S.A., a Siemens Company, Digital Factory Division, Product Lifecycle Management,
Simulation and Test Solutions, Angleur, Belgium
[3] Department of Mechanical Engineering, Universidad de Concepción, Concepción, Chile
[4] Department of Industrial Technologies, Universidad de Talca, Curicó, Chile
[5] ArGEnCo Department, MSM team, University of Liège, Liège, Belgium 6 Fonds de la Recherche
Scientifique – F.N.R.S.–F.R.S., Belgium

1. Introduction to the two identified CPB06 models

The finite element (FE) material model selected to simulate the evolving quasi-static, anisotropic and tension-compression asymmetric mechanical response until the onset of fracture of bulk Ti64 alloy is based on five distorted CPB06 plasticity surfaces [1]. The model considers that the different yield surfaces follow the Voce hardening law in the reference direction of the alloy, while the other directions are modelled by distortional hardening. The anisotropic plasticity parameters applied to the CPB06 model have been previously identified with mechanical experiments performed in the three dimensions of the alloy [2]. Two sets of constitutive hardening parameters were identified with direct and inverse strategies. The parameters considered are the tension-compression asymmetry k-value of the CPB06 criterion and the constants of the Voce law representing the reference tensile hardening. The first identification strategy is mainly based on the experimental actual stress-strain data until the necking point computed with the Considère criterion (CPB06 direct), and the second is performed by reducing the FE prediction errors of load-displacement curves of both tensile test of a cylindrical bar and compression test of an elliptic cylinder sample [3]. The latter strategy allows to obtained a model called here CPB06 (inverse), which gives more accurate predictions specially for simulation of necking instability.

Digital image correlation has been applied to all the experiments to evaluate the two identification strategies and the model capabilities about the shape prediction. Large prediction errors of area reduction and load in a simple uniaxial tensile cylindrical bar confirm that the second strategy is essential to plastic instability. The validity of this claim has been proved here in this work only for bulk material and should be further verified for sheet metals and forming limit diagram prediction.

2. Evaluation of numerical predictions of shape and load of Ti64 samples

The FE code LAGAMINE developed at the University of Liège since 1985 is used to simulate the experiments. The results obtained for the tensile of cylindrical bar and compression of elliptic cylinder, both axially loaded in the reference direction are shown in Figure 1. The predictions capabilities of the two models are also been tested in cylindrical bar with 5 different U-notches radii and V-notch as well but are not shown in this abstract. The predictions of load and shape are accurate for the inversely identified CPB06 model, from initial plasticity till the onset of necking, with an increasing prediction error until just before fracture. This comparison allows us to confirm that for accuracy increase of load and transverse area prediction during plastic deformation of the Ti64 until fracture, asymmetrical hardening should be identified for values of plastic work higher than the values reached at the onset of necking, or stress-strain curves until 0.1 (CPB06 direct). The prediction

accuracy of the load and shape just before fracture in cylindrical tensile test were increased by identifying a new set of hardening parameters and *k* values with inverse modeling.

Higher accuracy decreases the load predictions in the samples with higher stress triaxilities and at the same time reduces the prediction errors of shape in notched bars. To accurately predict the mechanical deformation of Ti64 in specimens with several combined stress state and high stress triaxilities, further research required an asymmetric anisotropic pressure sensitive plasticity-damage model.
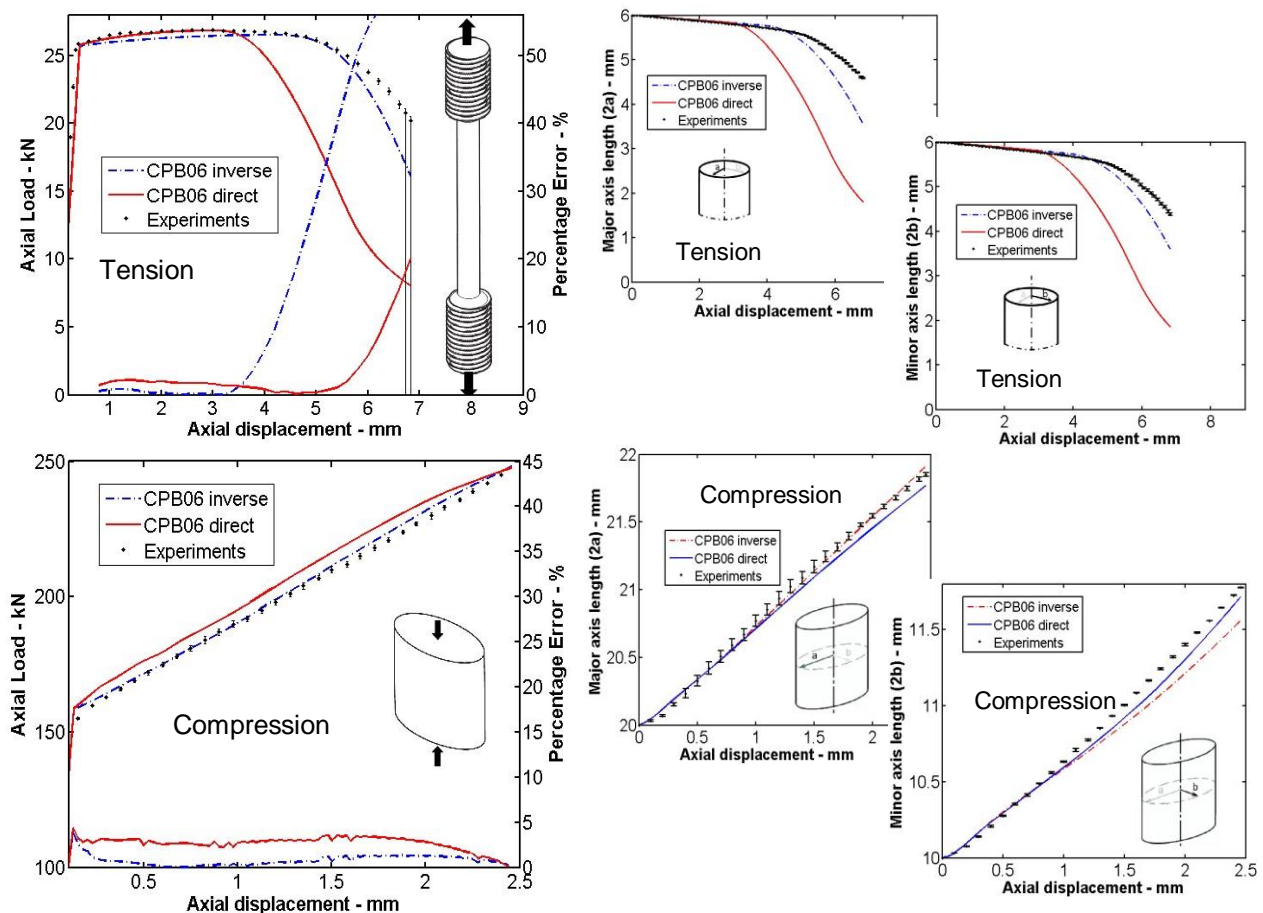
Fig. 1. Experimental load and transverse area measured by DIC vs. predictions of the two identified CPB06 models in Tensile with necking and compression in elliptical cylinder

3. Acknowledgments

4. References

[1] O. Cazacu, B. Revil-Baudard, N. Chandola (2018). *Plasticity-Damage Couplings: From Single Crystal to Polycrystalline Materials,* Springer, Switzerland.
[2] V. Tuninetti, G. Gilles, O. Milis, T. Pardoen, A.M. Habraken (2015). Anisotropy and tension–compression asymmetry modeling of the room temperature plastic response of Ti–6Al–4V, *Int. J. Plasticity,* **67**:53–68.
[3] V. Tuninetti, P. Flores, G. Pincheira, G. Gilles, L. Duchêne, A.M. Habraken (2019). Impact of distortional hardening and the strength differential effect on the prediction of large deformation behavior of the Ti6Al4V alloy, *Meccanica*, **54**(11), 1823–1840.

SPECIAL SESSIONS

1. Additive Manufactured Materials: Production, Experiment and Applications

FATIGUE STRENGTH OF AS FABRICATED DMLS PRODUCED 15-5 PH STAINLESS STEEL AND EFFECTS OF POST-MANUFACTURE TREATMENTS

**D. Croccolo[1], M. De Agostinis[1], S. Fini[1], G. Olmi[1], L. Paiardini[1],
F. Robusto[1], S. Ciric Kostic[2] and N. Bogojevic[2]**

[1] *Department of Industrial Engineering (DIN), University of Bologna, Bologna, Italy*
[2] *Faculty of Mechanical and Civil Engineering in Kraljevo, University of Kragujevac, Serbia*

1. Introduction

Additive Manufacturing (AM) techniques are capable of producing complexly shaped parts in a short time and with high flexibility and customization. Further advantages arise from a faster time-to market and a high efficiency in material utilization [1]. A possible drawback of AM techniques consists in the residual stresses that may be generated during part building. Moreover, AM produced parts may have their fatigue strength, detrimentally affected by defects, due to unmolten particles, entrapped gas bubbles, lack of penetration of the molten pool between adjacent layers [1]. A further drawback arises from poor surface finishing in the "as fabricated" state.

15-5 PH stainless steel is commonly used in applications involving aircraft components, or parts, such as valves, fasteners or gears, under high pressure or in corrosive environments [2]. This material has been developed, in order to improve toughness with respect to 17–4 PH. This enhanced feature arises from the reduced content of delta ferrite and an accurate monitoring of inclusion size and shape [3]. A controlled precipitation mechanism is the metallurgical process being used to fulfil this goal. The present study is focused on this material: at a previous stage [4] the combined effects of build orientation and of machining and its allowance were studied. A beneficial impact of greater allowance and of slanted orientation upon building were observed. A literature survey indicates that extensive studies dealing with the fatigue response of as built parts and with the effects of heattreatment, machining or surface treatments like shot-peening are currently missing. However, the possible use of AM fabricated components in their "as built" state furtherly enhances the great potentials of this production technique. This paper tackles the topic of the fatigue response for finite and infinite life with regard to DMLS built parts (by DMLS EOS M280 machine) of PH Stainless Steel. The response of as built parts and the effects of heat, machining and peening treatments are investigated by statistical methods, thus providing useful recommendations for design purposes. Issues of novelty arise from providing data to improve the post manufacture treatments and from the use of advanced methodologies to isolate the effects of the investigated factors.

2. Materials and Methods

The experimental two-factor design involving 15-5 PH Stainless Steel is resumed in Table 1. Heat treatment (H900 heat treatment: parts kept at the temperature of 482°C for 2 hours after a ramp increase from the room temperature in 1 hour time.) was regarded as a two-level (on-off) factor. The effect of machining or surface treatment was investigated over three levels: only shotpeening after heat treatment, shot-peening and machining, machining and subsequent peening treatment. The rationale of performing shot-peening after machining derives from the need of leaving the yielded beneficial compressive residual stress state unchanged by further processing. Previous studies on a different material [5] indicated that proceeding this way, unlike the recommendations by powder suppliers, may be highly beneficial, despite higher surface roughness. The results were processed by Standard ISO 12107 for determining the S-N curves and by an ANOVA-based methodology for their comparison.

		Machining		
		No	Yes	Yes, with subsequent shot-peening
Aging Heat	No	Set 23	Set 24	Set 27
Treatment	Yes	Set 25	Set 26	Set 28

Table 1. Experimental design (involving 15-5 PH stainless steel samples)

3. Results and conclusions

The retrieved fatigue curves are plotted together in Fig. 1. The statistical assessment indicates that machining is able to yield a beneficial effect on the fatigue strength for finite life and that subsequent shot-peening is able to induce a further enhancement, consistently with [5]. Conversely, the heat treatment does not have a significant impact.
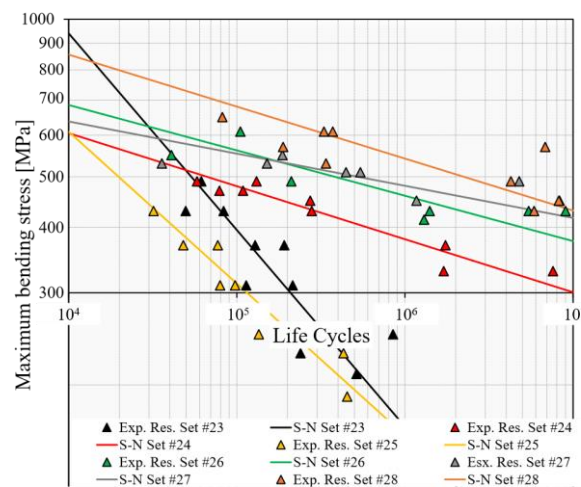
Fig. 1. S-N curves in the finite life domain for the six sample sets included in the experiment

4. Acknowledgements

5. References

[1] S.M.J. Razavi, P. Ferro, F. Berto and J. Torgersen (2018). Fatigue strength of blunt V-notched specimens produced by selective laser melting of Ti-6Al-4V. *Theor. Appl. Fract. Mec.*, **97**, 376–384.

[2] H.K. Rafi, T.L. Starr and B.E. Stucker (2013). A comparison of the tensile, fatigue, and fracture behaviour of Ti–6Al–4V and 15-5 PH stainless steel parts made by selective laser melting. *Int. J. Adv. Manuf. Technol.*, **69**, 1299–1309.

[3] V. Muthupandi, P. Bala Srinivasan, V. Shankar, S.K. Seshadri, S. Sundaresan (2005). Effect of nickel and nitrogen addition on the microstructure and mechanical properties of power beam processed duplex stainless steel (UNS 31803) weld metals. *Mater. Lett.*, **59**, 2305–2309.

[4] D. Croccolo, M. De Agostinis, S. Fini, G. Olmi, N. Bogojevic, S. Ciric-Kostic (2018). Effects of build orientation and thickness of allowance on the fatigue behaviour of 15–5 PH stainless steel manufactured by DMLS, *Fatigue Fract. Eng. Mater. Struct.*, **41**, 900–916.

[5] D. Croccolo, M. De Agostinis, S. Fini, G. Olmi, F. Robusto, S. Ćirić-Kostić, A. Vranic and N. Bogojevic (2018). Fatigue Response of As-Built DMLS Maraging Steel and Effects of Aging, Machining and Peening Treatments, Metals, 8, 1–21.

EFFECT OF THE POSITION IN THE BUILD CHAMBER ON THE FATIGUE RESPONSE OF DMLS PRODUCED MARAGING STEEL

D. Croccolo[1], M. De Agostinis[1], S. Fini[1], G. Olmi[1], L. Paiardini[1],
F. Robusto[1], S. Ciric Kostic[2] and N. Bogojevic[2]
[1] Department of Industrial Engineering (DIN), University of Bologna, Bologna, Italy
[2] Faculty of Mechanical and Civil Engineering in Kraljevo, University of Kragujevac, Serbia

1. Introduction

There is nowadays an increasing interest towards Additive Manufacturing (AM) techniques, from the point of view of process optimization and of the achievable mechanical properties. AM makes it possible to produce even highly complicated parts in a short time and as a monolithic component. Maraging steel MS1 is one of the most promising materials for use in AM [1]: high density, 95% or higher, can be generally achieved; moreover, a 50 HRC hardness can be fulfilled, following a suitable heat treatment, thus making this feature comparable to that of wrought material. Moreover, it has good static and fatigue properties [2-4] and good corrosion resistance and machinability [5-6]. Previous research [2] was aimed at investigating the effect of build orientation on the fatigue strength of DMLS produced samples by EOS M280 machine. The retrieved results indicate that build orientation does not have a significant effect, when considering, micro-shotpeened, heat-treated and machined parts. This study was then extended in [3], focusing on the effect of build orientation for incremented allowance to be removed by machining, as well as on the combined effect of these two factors. The outcomes of this study confirmed the fatigue strength keeps unaffected by the mentioned factors. The study in [4] investigated the response of the same material in the "as fabricated" state and the effects of heat treatment, machining and shot-peening to be run after machining, highlighting the beneficial outcomes of the latter procedure.

This study can be regarded as a follow-up of that put forward in [4] and deals with the effect of part position in the build chamber on the fatigue response. Previous investigations on a different material indicated that powder residuals may affect the achievable mechanical response. The amount of these residuals may be, in turn, due to the position of the built part in the chamber with respect to the path of the inert gas flowing from the rear side to the front sides. Regarding this point, it may be argued that parts being built at the backside are closer to the gas outlets and are therefore more protected against powder residuals that are spread away by the gas flow. Conversely, the parts being built closer to the frontal door are more exposed to powder residuals. Issues of novelty arise from the lack of studies in the literature dealing with this topic.

2. Materials and methods

The present study dealt with DMLS produced Maraging steel MS1 (AISI 18Ni300). The experimental plan investigated in [4] was extended to the vertically built heat-treated (age-hardening at 490°C for 6 hours) and 0.5 mm allowance machined samples with shot-peening (400 μm shots, 5 bar pressure) being performed after machining. This treatment combination was split into three different cases (Table 1), accounting for different positions in the build chamber: upstream midstream and downstream positions were considered with respect to the gas flow. 12 samples were considered for each case and fatigue tests were run for determining the three S-N curves in the finite life domain based on ISO 12107 Standard. These curves were then compared by an ANOVA-based statistical method for the comparison of S-N curves [2-4]. A fatigue limit was finally estimated based on the same standard, taking a runout of 10 million cycles into account.

Position in the chamber		
Upstream	Midstream	Downstream
Set HMP-U	Set HMP-M	Set HMP-D

Table 1. Experimental design (involving MS1 heat-treated machined peened samples)

3. Results and conclusions

The retrieved curves are plotted together in Fig. 1, along with dots indicating the experimental data. The statistical test indicates the differences among the curves are not significant, i.e. they are confounded by the experimental uncertainty. Therefore, the results were then sorted out, to determine a unique fatigue limit.
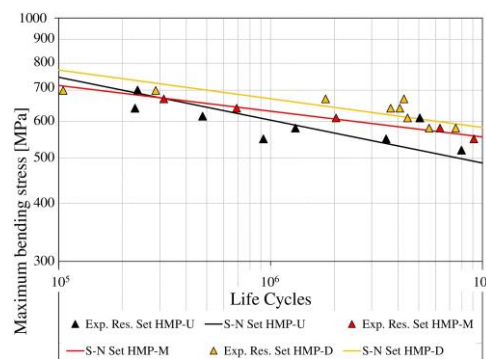
Fig. 1. Fatigue curves in the finite life domain for the three sample sets

4. Acknowledgements

5. References

[1] K.J. Brookes (2016). Maraging steel for additive manufacturing-Philipp Stoll's paper at DDMC., *Met. Powder Rep.*, **71**, 149–152.

[2] D. Croccolo, M. De Agostinis, S. Fini, G. Olmi, A. Vranic and S. Ciric-Kostic (2016). Influence of the build orientation on the fatigue strength of EOS maraging steel produced by additive metal machine. *Fatigue Fract. Eng. Mater. Struct.*, **39**, 637–647.

[3] D. Croccolo, M. De Agostinis, S. Fini, G. Olmi, F. Robusto, S. Ćirić-Kostić, S. Morača and N. Bogojević (2019). Sensitivity of direct metal laser sintering Maraging steel fatigue strength to build orientation and allowance for machining, *Fatigue Fract. Eng. Mater. Struct.*, **42**, 374– 386.

[4] D. Croccolo, M. De Agostinis, S. Fini, G. Olmi, F. Robusto, S. Ćirić-Kostić, A. Vranic and N. Bogojevic (2018). Fatigue Response of As-Built DMLS Maraging Steel and Effects of Aging, Machining and Peening Treatments, *Metals*, **8**, 1–21.

[5] K. Kempen, E. Yasa, L. Thijs, J.P. Kruth and J. Van Humbeeck (2011). Microstructure and mechanical properties of Selective Laser Melted 18Ni-300 steel. *Phys. Proc.*, **12**, 255–263.

[6] G. Casalino, S.L. Campanelli, N. Contuzzi and A.D. Ludovico (2015). Experimental investigation and statistical optimisation of the selective laser melting process of a maraging steel. Opt. Laser Technol., 65, 151–158.

MECHANICAL STUDIES ON 3D REGULAR CELLULAR STRUCTURES UNDER QUASI-STATIC AND IMPACT LOADING

P. Dziewit, P. Płatek, J. Sienkiewicz, J. Kluczyński and J. Janiszewski
Military University of Technology, Warsaw, Poland

1. Introduction

Regular cellular materials are a new class of materials that have attracted great interest among scientists over the last decade. The increase in this interest is generally due to the fact that cellular structures possess a high mechanical strength with (at the same time) significantly reduced mass in comparison to their bulk equivalents [1]. Additionally, nowadays development in the field of additive manufacturing (AM) techniques cause that these types of materials have been started to be used in selected branches of industry (e.g. aviation, automotive), as well as in bio-engineering, art or civil engineering. Based on the results of literature study, regular cellular materials are classified in two main groups: 2D and 3D. The 2D structures are well-known and one of the most popular representative of this group is a honeycomb structure. The other group is represented by 3D lattice materials which indicate lower mass in comparison to 2D structures, however they demand more sophisticated AM techniques with powder bed feeding system to perform a manufacturing process. Based on the data presented in many scientific papers, lattice structures are listed as multifunctional, ultralight materials dedicated to application in cutting-edge products. For this reason, many of undertaken studies are focused on the mechanical response of the lattice structures depending on adopted elementary unit cell topology and origin material used during manufacturing process [2,3].

The main aim of this paper is to present the results of authors investigations related to mechanical response of additively manufactured 3D lattice structures subjected to compression tests under quasi-static and dynamic loading conditions. Authors focused their attention on imperfections of produced specimens and their influence on the deformation processes also taking into account strain rate effects. Based on obtained results an energy absorption efficiency of proposed topologies was evaluated.

2. Experimental procedure

Initial experimental tests were conducted with the use of additively manufactured 3D cellular structures (Fig. 1.) designed on the basis of 2D topologies tested both numerically and experimentally [3,4]. The structure design process was associated with replacement of walls in 2D models by cylindrical struts in 3D models (Fig. 2.). Developed models were manufactured with use of SLS technique. A Sinterit Lisa 3D PA12 Polyamide was used to conduct this process. Adopted AM technique, as well as PA12 material enabled obtaining a high geometrical quality of fabricated lattice specimens.
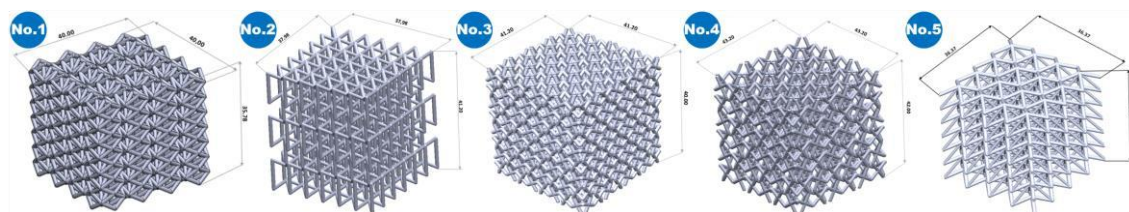
Fig. 1. View of developed 3D lattice structure models

Fig. 2. The general view of lattice design process (a) 2D structure, (b) an exemplary unit cell
(c) 3D lattice structure (d) fabricated via SLS technique specimen

3. Results and conclusion

Based on result of carried out uniaxial compression tests, the deformation energy curves presented in Fig. 3 were defined. Referring to the presented history plots of deformation energy, a bending dominant deformation mechanism during loading can be observed.
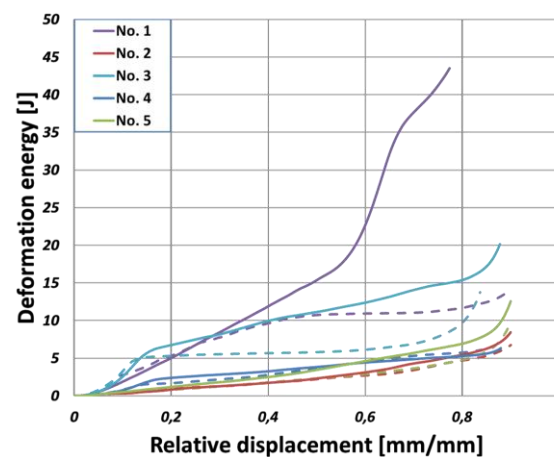
Fig. 3. Energy absorption curve determined for different topologies at different strain rates:
continuous line $\dot{\varepsilon}=0,001$; dotted line $\dot{\varepsilon}=0,1$

Based on obtained results of conducted studies it was noticed that geometrical features of structure topology have a great influence on lattice structure deformation process. Furthermore, it can be assumed, that crashworthiness properties of structures depend not only on adopted topology, but also on strain rate effects.

4. References

[1] L.J. Gibson, M.F. Ashby (1997). *Cellular Solids*; Cambridge University Press: Cambridge, ISBN 9781139878326
[2] Yongle Suna, Q.M. Li Dynamic compressive behaviour of cellular materials: A review of phenomenon, mechanism and modelling. International Journal of Impact Engineering, 2018, 112, p. 74-115.
[3] Q. Gao, C. Ge, W. Zhuang, L. Wang, and Z. Ma, "Crashworthiness analysis of double-arrowed auxetic structure under axial impact loading," Mater. Des., vol. 161, pp. 22–34, 2019.
[4] L. Yang, O. Harrysson, H. West, and D. Cormier, "Mechanical properties of 3D re-entrant honeycomb auxetic structures realized via additive manufacturing," Int. J. Solids Struct., vol. 69–70, pp. 475–490, 2015.

INFLUENCE OF THE CRYSTALLIZATION KINETIC IN THE THERMOPLASTIC POLYMERS ON VOLUMETRIC SHRINKAGE IN ADDITIVE MANUFACTURING PROCESSES

P. Bajerski[1] and R.B. Pęcherski[2]

[1] *ABB Sp. z o.o. Corporate Technology Center, Kraków, Poland*
[2] *Institute of Fundamental Technological Research, Polish Academy of Sciences, Warsaw, Poland*

1. General

Additive Manufacturing (AM) process is a very popular field of fast prototyping of machine components. The main materials for producing are metals and polymers. Usage of polymers in AM techniques give many advantages like very low mass of part, low cost of detailing and acceptable mechanical strength. Polymers are usually used in Injection Molding (IM) or Casting processes, where the material description and also behavior are well known. Therefore, the prediction of warpage and residual stresses of the producing object in IM provides satisfactory conformity with experimental data. AM processes are more complex, so the available commercial tools to predict volumetric shrinkage and residual stresses of simulated parts are still developing and require description of complex phenomena. The main challenge that is usually neglected by engineers in calculations is description of polymer crystallization process. This phenomenon has a strong influence on final volumetric shrinkage of produced component. The presented investigations describe the influence of crystallization process on the volumetric shrinkage and show how to perform whole process of AM in Abaqus software. Expanding Abaqus solver capabilities and writing in Fortran user-subroutines will help to predict crystallinity, temperature distribution, warpage and residual stress of produced part. Furthermore, Differential Scanning Calorimetry (DSC) results will help to describe material model for implementing in FE analyses [1-4].

2. Experimental background

The crystallization kinetics theory describes the evolution of the degree of crystallization $\alpha(t)$ in semi-crystalline polymers. The process of crystallinity is a function of time t and time-dependent temperature $T(t)$. The fundamental model describing degree of crystallinity is general Avrami equation for isothermal crystallization. Nakamura expanded Avrami model (equation 1) for nonisothermal crystallization [2].

$$(1) \qquad \frac{d\alpha}{dt} = nK[T(t)](1-\alpha)\left[ln\left(\frac{1}{1-\alpha}\right)\right]^{\frac{n-1}{n}}$$

where $K(T)$ is a crystallization rate function. The Nakamura and Avrami theories can be directly related to the crystallization half time $t_{1/2}$ expressed by the Hoffman-Lauritzen theory [2].
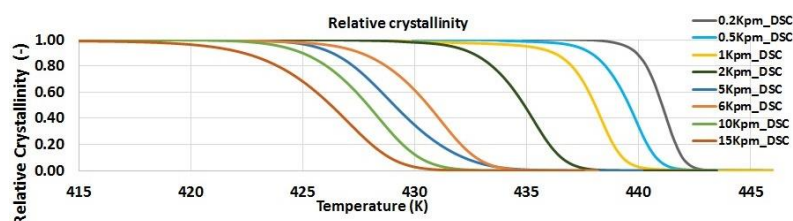
Fig. 1. DSC curves of the relative crystallinity of PA 2200 at several cooling rates

The material parameters needed to implement in FE analysis are directly taken from DSC tests. The example of curves of the obtained relative crystallinity for Polyamide 2200 at several cooling rates are presented in Figure 1. Calculating the strength of the material and implementing in FE model is also supported by Dynamic Mechanical Analysis (DMA) tests. Based on the DMA test, the stress relaxation of the material can be extracted, and the calculated parameters in type of Prony series can give more accurate numerical results of volumetric shrinkage.

3. Process simulation in FEM

Based on the theoretical and empirical model description of crystallization kinetics, melting process, DSC results and heat transfer description in real process, one can analyze volumetric shrinkage in FE analyses. The total volumetric shrinkage S_{total} is described by equation 2, where the most important components are S_c – shrinkage caused by crystallinity process, S_T – shrinkage caused by temperature effects and S_{tech} – shrinkage caused by density of input material [5].

(2) $\qquad S_{total} = S_C + S_T + S_{tech}$

The overall process of simulation is based on the manufacturing and information of the CNC machine steps directly taken from G-code files. Furthermore, crystallization and melting parameters are calculating from DSC measurements. The prediction of crystallinity of produced objects in AM process and assessment of crystallinity influence on volumetric shrinkage and mechanical strength is validated with experimental measurements [1], [2].

4. Further investigations

Behaviour of thermoplastic polymers in AM processes indicates that the crystallization process cannot be neglected in the investigating of the volumetric shrinkage. Furthermore, the nonisothermal conditions accompanying presented AM techniques causes that component manufacturing is very complex and difficult to optimize. The implementation of prediction of the volumetric shrinkage in the FE computations including influence of the crystallinity of the material is the main step in assessment of residual stress and strength of manufactured components. This approach will allow to perform mechanical analyses of the component without the costly and timeconsuming producing of real prototypes and functional tests.

5. References

[1] P. Bajerski, R. Pęcherski, D. Chudy (2019), *Virtual Additive Manufacturing Based on Semicrystalline Polymer Polyetheretherketone (PEEK)*, Engineering Transactions, **67(2)**, 157165.
[2] P. Bajerski, R. B. Pęcherski, D. Chudy, and L. Jarecki (2019), *Crystallization kinetics of polyamide 2200 in the modelling of additive manufacturing processes by FE analyses*, Eng. Trans., **67(3)**, pp. 301–309.
[3] B. Brenken, E. Barocio, A. J. Favaloro and R. Byron Pipes (2017), *Simulation of SemiCrystalline Composites in the Extrusion Deposition Additive Manufacturing Process*, Science in the Age of Experience, pp. 90-102, Chicago.
[4] A. J. Favaloro, B. Brenken, E. Barocio, and R. Byron Pipes (2017), *Simulation of Polymeric Composites Additive Manufacturing using Abaqus*, Science in the Age of Experience, pp. 103114, Chicago.
[5] L. Benedetti, B. Brulé, N. Decreamer, K. E. Evans, and O. Ghita (2019), *Shrinkage behaviour of semi-crystalline polymers in laser sintering: PEKK and PA12*, Mater. Des., **181**.

ADDITIVE MANUFACTURING OF LATTICE STRUCTURED HOT STAMPING DIES WITH IMPROVED THERMAL PERFORMANCE

D. Chantzis, X. Liu, D. Politis and L. Wang
Department of Mechanical Engineering, Imperial College London, London SW7 2AZ, UK

1. Introduction

Currently, the most established and cost-effective method of manufacturing internal cooling channels for hot stamping dies is conventional drilling. The profound disadvantage of this approach is that can only produce straight line cooling channels which are unable to maintain an equidistance from a complex 3D geometry of the tool working surface [1]. Consequently, "hot spots" are obtained which are essentially areas on a final component that have been cooled at different rates compared to the rest of the component and inherently exhibit varied mechanical properties [2]. On the other hand, AM technologies allow for greater design freedom and complexity, allowing manufacturing of conformal cooling channels [3]. Moreover, lattice structures can be integrated into the die's body. This enables enhanced heat control, where the area far from the cooling channel can be selectively insulated, while the region in proximity to the cooling channel remains solid and comparatively conductive [4]. Moreover, there is a significant reduction of the overall thermal mass, which needs to be cycled during the heating and cooling of the die. In the current study, a design method for Additevely Manufactured Hot Stamping dies is proposed and relevant results are presented.

2. Proposed design of Additively Manufactured Hot Stamping Dies

The basic element of the proposed design method is the definition of solid – lattice structure interface within the die body. The proposed solid-lattice structure interface is a straight line and defined by two points which are the result of the intersection between the effective cooling angle (θcool) [5] and the circumference of the circular cooling channel. The effective cooling angle is selected at 100o and defined as the vertex angle of an isosceles triangle, drawn from the centre of the cooling channel and the working surface of the die .
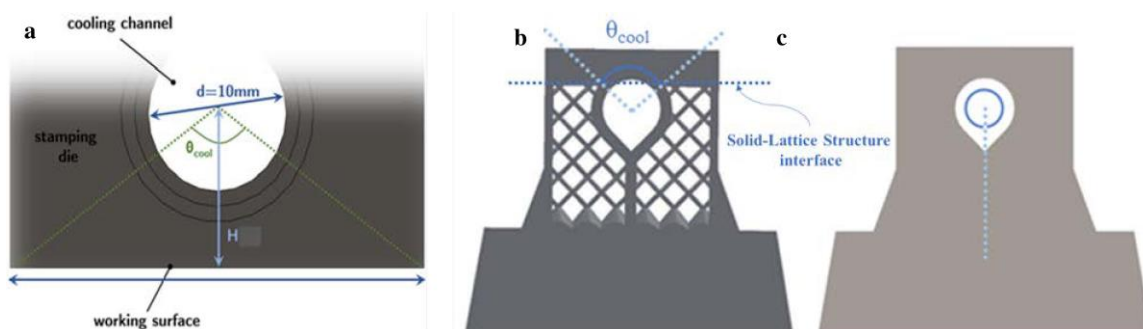
Figure 1: (a) Representation of the effective cooling angle (b) Proposed hot stamping die (c) Solid hot stamping die

3. Experimental Setup

The thermal performance of the two dies shown in Figure 1b and Figure 1c, were evaluated using a Gleeble 3800 thermo-mechanical simulator, which allows the realisation of hot stamping process at a small scale. The testing apparatus and procedure are shown in Figure 2a and Figure 2b respectively.
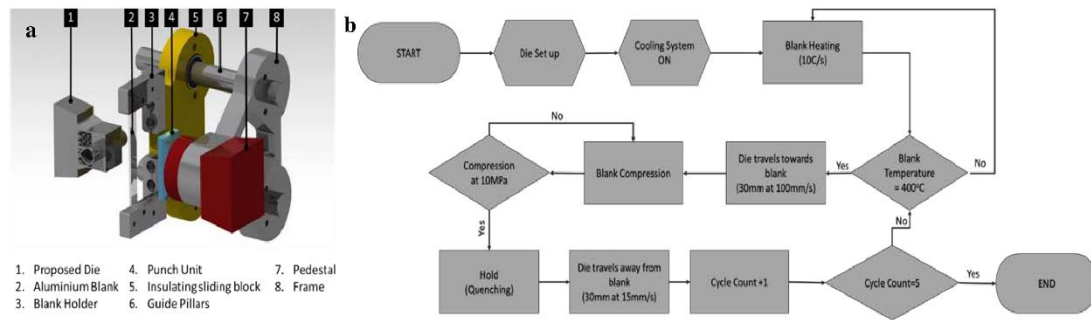
Figure 2: (a) Testing apparatus (b) Testing Procedure

4. Results

In this study, the effect of lattice structures in the body of a hot stamping die is investigated. A method for the identification of the solid-lattice interface is described as well. The proposed die was evaluated in a 5 cycles hot stamping scenario and its thermal performance is compared with a fully solid die, which represents, geometry wise, the current state of the art. In Figure 3a, the blank temperature evolution for each die is presented. Although in the first cycle both dies are quenching the blank with almost the same rate, during the rest of the cycles the proposed die quenches the blank at a higher cooling rate and at a lower temperature. Moreover, the proposed die operates at a lower temperature than the solid one (Figure 3b) which can lead to other benefits, such as improved thermal fatigue resistance, except better quenching performance.
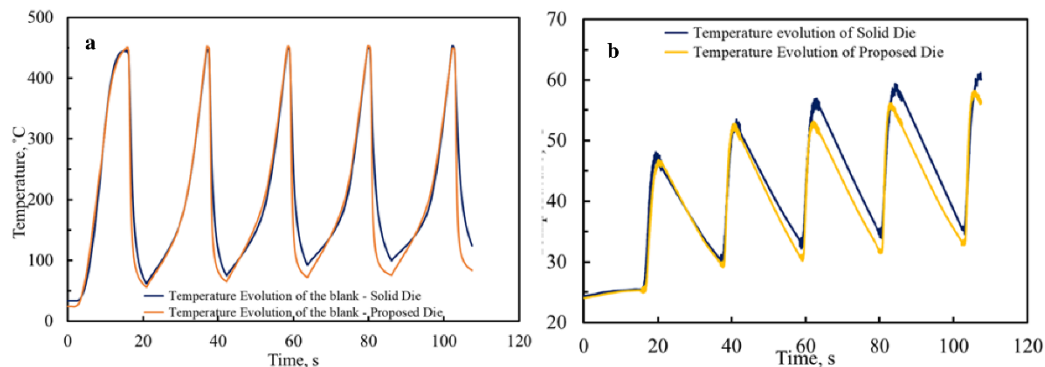
Figure 3: (a) Blank temperature evolution (b) Die Temperature evolution

5. References

[1] H. Hoffmann, H. So, and H. Steinbeiss, "Design of hot stamping tools with cooling system," *CIRP Ann. - Manuf. Technol.*, vol. 56, no. 1, pp. 269–272, 2007.

[2] H. Karbasian and A. E. Tekkaya, "A review on hot stamping," *J. Mater. Process. Technol.*, vol. 210, no. 15, pp. 2103–2118, 2010.

[3] M. Cortina, J. Arrizubieta, A. Calleja, E. Ukar, and A. Alberdi, "Case Study to Illustrate the Potential of Conformal Cooling Channels for Hot Stamping Dies Manufactured Using Hybrid Process of Laser Metal Deposition (LMD) and Milling," *Metals (Basel).*, vol. 8, no. 2, p. 102, Feb. 2018.

[4] M. Mazur, M. Leary, M. McMillan, J. Elambasseril, and M. Brandt, "SLM additive manufacture of H13 tool steel with conformal cooling and structural lattices," *Rapid Prototyp. J.*, vol. 22, no. 3, pp. 504–518, 2016.

[5] W. S. Lim, H. S. Choi, S. Y. Ahn, and B. M. Kim, "Cooling channel design of hot stamping tools for uniform high-strength components in hot stamping process," *Int. J. Adv. Manuf. Technol.*, vol. 70, no. 5–8, pp. 1189–1203, 2014.

EFFECT OF ELEMENT WALL THICKNESS ON THE HOMOGENEITY AND ISOTROPY OF HARDNESS IN SLM IN718 USING NANOINDENTATION

G.Z. Voyiadjis[1], R.A. Znemah[1] and P. Wood[2]
[1] *Computational Solid Mechanics Laboratory, Louisiana State University, USA*
[2] *Institute of Innovation in Sustainable Engineering (IISE) University of Derby, UK*

1. Introduction

Utilizing Additive Manufacturing (AM) in metals and super alloy production have witnessed progressive development since the 1980s. The process is based on melting successive layers of metal powder typically with a laser beam. Selective Laser Melting (SLM) technique introduced in 1999 enabled a full melting of the current powder layer and hence achieving a higher density compared to the previous techniques; almost 99.9 % density without sintering, post infiltration or hot isostatic pressing (HIP) can be achieved [1]. IN718 is used in the mechanical applications operating at elevated temperatures where many of them require complex hollow shaped elements to obtain specific physical or mechanical properties, weight reduction, fluid flow or heat transfer. However, even in its fully annealed condition IN718 is difficult to machine using subtractive methods needing expensive tools, with high rates of tool wear and low metal removal rates. This work examines the uniformity and isotropy of the mechanical properties in AM produced thin-walled structures by SLM as an alternative to formative manufacturing methods.

2. Methodology

AM produced honeycomb samples of different ligament thicknesses by SLM were received from the IISE, University of Derby, UK. Samples are termed S1, S2, and S3 for the thicknesses 0.8, 0.6 and 0.4 mm respectively. Their composition was analyzed using Energy Dispersive spectroscopy (EDS), and the results were found to conform to the standard composition of IN718 specified by the ASTM [2]. For each sample successive rows of indents were performed to scan the variation of the hardness across the ligament area on the top plane (XY plane). Also, three groups of nine indents were performed on the joint area on the top plane and other groups on the lateral plane (XZ plane) to examine the isotropy. The method used is the continuous stiffness method (CSM) in which the hardness is obtained as a continuous function of the penetration depth.

3. Results

Indentation Size effects (ISE), which is characterized by the decrease in hardness values as the indentation depth increases and finally reaching a constant value after certain depth, was observed for all indents. For the ligament area the plateu value of the hardness for each indent is plotted for Sample S1 (Fig. 2 (a)). It is observed that the hardness values in the vicinity of the boundaries are 4-6 % lower than in the intermediate areas for all of the three samples (not shown in this work). This phenomenon can be related to the inherent porosity that was observed by Sangid et al. to be higher at the boundaries [3]. Also, the hardness values in the intermediate area drops as the ligament thickness decreases; that is ~ 4.20 GPa for S1, ~ 4.13 GPa for S2 and ~ 3.54 GPa for S3. However, the rate of change is higher between the 0.6 mm and 0.4 mm thickness than between the 0.8 mm and 0.6 mm thickness. This suggest that there is a threshold minimum value for the element thickness below which the manufacturing process will drastically affect the hardness values.

For the same sample the average hardness for each one of the three groups of indents on the top and lateral planes against depth is ploted in Fig. 2 (b). Hardness values are found to be anisotropic in all samples; the hardness values on the top plane are higher than on the lateral plane. However, no fixed ratio among the three samples is defined. For the sample S3 indentations showed a local hardening in the hardness- indentation depth curve over the depth range of 50-100 nm. This local hardening can be related to the interaction between the volume of the geometric necessary disolcations (GNDs) created by the indenter and the grain boundary first approached by this volume [4]. Fig. 2 (c) shows this behaviour for selected indents.
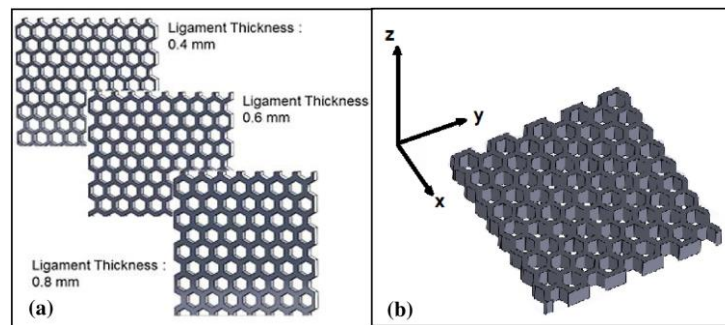
Fig. 1. Samples geometry: (a) top view, (b) samples orientation
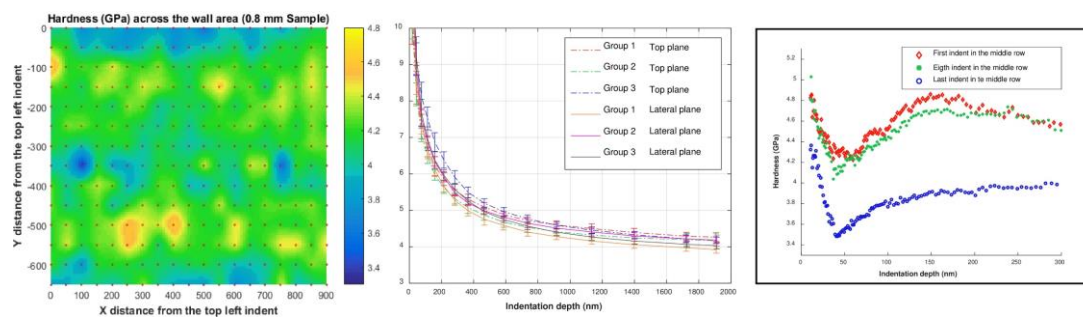
Fig. 2. Selected results: (a) Hardness values across the ligament area of S1
(b) Average hardness-indentation depth curves for the top and lateral planes of S1
(c) Local hardnenig in selected indents of sample S3

4. Acknowledgements

5. References

[1] Gu, D D, et al. (2012). Laser Additive Manufacturing of Metallic Components: Materials, Processes and Mechanisms, *International Materials Reviews*, 57, 133–164.
[2] ASTM B670 – 07 (2018) Standard Specification for Precipitation-Hardening Nickel Alloy (UNS N07718) Plate, Sheet, and Strip for High-Temperature Service.
[3] Sangid, Michael D., et al. (2018). Role of Heat Treatment and Build Orientation in the Microstructure Sensitive Deformation Characteristics of IN718 Produced via SLM Additive Manufacturing. *Additive Manufacturing*, 22, 479–496.
[4] Voyiadjis, George Z., and Cheng Zhang (2015). The Mechanical Behavior during Nanoindentation near the Grain Boundary in a Bicrystal FCC Metal. *Materials Science & Engineering A*, 621, 218–228.

EFFECT OF PRINTING DIRECTION IN TECHNICAL ELASTIC PROPERTIES OF NYLON 3D-PRINTED MATERIALS

P. Efstratios and P. Lincy
Department of Mechanics of Materials and Constructions, Vrije Universiteit Brussel (VUB), BE-1050, Brussels, Belgium

1. Introduction

Additive manufacturing or 3D printing is regarded a highly applicable manufacturing process in areas like the automotive and aerospace industry. One of the main techniques is the Fused Filament Fabrication (FFF), a simple layer by layer deposition of the filament which is fairly simple and inexpensive. Main thermoplastic materials that are utilized in FFF are Nylon, ABS and PEI. Qualities that make the 3D printed materials attractive are the very low waste percentage in cases that thermoplastic polymers are used and the fast and accurate prototyping that aids the reduction of manufacturing process[1].

However, the use of those promising materials is inhibited by problems of the final product that are mainly due to the manufacturing process. During the deposition of successive beads, the filament is heated up to become malleable and to increase the interface bonding sequence[2]. This behavior has been studied before for materials like ABS where the meso structure of tested specimens is clearly defined. The individual beads and the form of voids created during the manufacturing is obvious and the meso-structure follows a specific pattern. This behavior is attributed to the lack of excessive deformation of the material. The meso-structure is where the anisotropy due to manufacturing process has its main effect. Void models have been developed for the meso-structure to define properly the decrease of the material properties due to this effect[3]. For nylon specimens, however, the meso-structure is not clearly defined and is more or less random. This phenomenon is a possible indication that conventional techniques, used for ABS many not be useful in the case of nylon. Therefore, the understanding of the nylon's structure is of major importance in order to define precisely its impact on the macroscopic properties, the elastic behavior and strength.

2. Manufacturing of specimens and experimental procedure

For the study of the meso-structure, three different categories of 3D printed nylon specimens where studied. Each of those categories contained rectangular specimens that were printed with the beads aligned in the 0°, 45° and 90° direction respectively. For each case a plate was printed and then 3 specimens were cut with the use of a diamond saw to eliminate the effect of heat. In 3D printed structures with nylon (using the same printer), Iragi *et al.*[4] record the temperature magnitude against the distance from the nozzle. At a distance greater than 15-20mm the temperature has dropped to that of the base plate. Therefore, it is crucial that the plate is long enough, either wise the material will be in a higher temperature for a longer time, which might affect the intra-bead bonding and affect the experimental results. Furthermore, the excessive warping of nylon at the edges was not taken into account since those regions were removed from the specimens. After the manufacturing the specimens were carefully prepared and tested in tension using an Instron 5885 H (Instron, Norwood, USA) tensile testing machine. The strain field was monitored with 3D DIC and not extensometers, in order to have a better understanding of the phenomena that take place during testing. All specimens were constructed by the use of the Markforged Mark Two printer.

3. Results

The results of the meso-structure show similar characteristics to those observe in other materials. Unfortunately, the unclear positioning of the voids renders the already existent models inaccurate but in a great degree usable with proper assumptions. The stress-strain curves depict a consistency among the specimens of each category. The results coincide with those tested from other printers like the Mark One for nylon specimens[5]. Finally, this study is a clear indication that the bead interface properties play a major role in the materials' macroscopic properties.
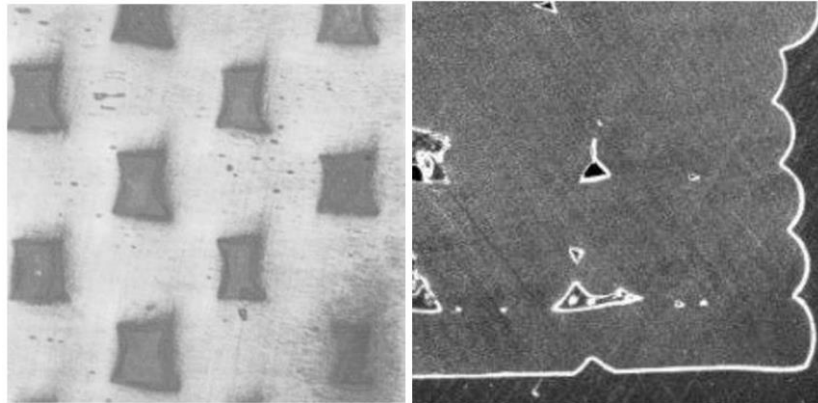
Fig. 1. Comparison of the meso-structure and the voids of ABS (left[3]) and nylon SEM micrographs of a neatly polished cross section image from MeMC laboratory(right)

* Scanning Electron Microscope

4. References

[1] B.Brenken, E. Barocio, A. Favaloro, V. Kunc, and R. B. Pipes (2018). Fused filament fabrication of fiber-reinforced polymers: A review.*Additive Manufacturing*, **21**(January):1–16.

[2] N.Van De Werken, H. Tekinalp, P. Khanbolouki, S. Oz-can, A. Williams, and M. Tehrani (2019). Additively Manufactured Carbon Fiber-Reinforced Composites: State of the Art and Perspective Ad-ditively Manufactured Carbon Fiber-Reinforced Composites: State of the Art and Perspective. *Additive Manufacturing*, **301**:100962.

[3] J. F.Rodriguez, J. P. Thomas, and J. E. Renaud (2003). Mechanical behavior of acrylonitrile butadiene styrene fused deposition materials modeling.*Rapid Prototyping Journal*, **9**(4):219–230.

[4] M. Iragi, C. Pascual-Gonzalez, A. Esnaola, C. S. Lopes, and L. Aretxa-baleta (2019). Ply and interlaminar behaviours of 3D printed continuous carbonfibre-reinforced thermoplastic laminates; effects of processing conditions andmicrostructure. *Additive Manufacturing*, **30**(July):100884.

[5] F. Van der Klift, Y. Koga, A. Todoroki, M. Ueda,Y. Hirano, and R. Matsuzaki (2016). 3D Printing of ContinuousCarbon Fibre Reinforced Thermo-Plastic (CFRTP) Tensile Test Specimens. *Open Journal of Composite Materials*, **06**(01):18–27.

MICROSTRUCTURAL AND MECHANICAL CHARACTERIZATION OF CuSn10 ALLOY FABRICATED ADDITIVELY BY THE SLM

P. Płatek, J. Janiszewski, J. Kluczyński, K. Grzelak,
M. Sarzyński, K. Makowska, M. Polański
Military University of Technology, Warsaw, Poland

1. Introduction

On the basis of the state-of-the-art survey, it can be observed that the number of publications related to Cu-based metal powders dedicated to the additive manufacturing laser powder bed fusion technique is currently limited. However, the mentioned group of materials has started to attract the attention of many researchers because of the specific physical and mechanical properties. One of the most important issues highlighted in many papers refers to the high thermal conductivity of Cu-based metal powders and results from this problem of significant heat loss that exists during the melting process. The main research problem related to the additively manufactured CuSn10 alloy refers to optimizing the technological process and determining the influence of the technological parameters of 3D printing on the microstructure and mechanical behavior of the material [1]. Nevertheless, many of the published articles generally focus on mechanical studies carried out under quasi-static loading conditions [2]. The main aim of this paper is related to this problem, nevertheless, the authors extend the range of performed studies taking into account determination of the mechanical properties of CuSn10 material under dynamic loading conditions, as well as determination of material model parameters that can be used in numerical investigations. Due to the fact that CuSn10 alloy is characterized by high thermal conductivity, two variants of semi-finished material samples, i.e, thin-walled and bulk were considered.

2. Optimization of the 3D printing parameters of the SLM technological process

The first stage of the carried out investigations was related to the selection of the technological parameters of the SLM process two variants of semi-finished CuSn10 alloy samples (Fig. 1). They were fabricated as 12 x 12 x 12 mm cuboids and thin-walled structure with dimensions 12 x 12 x 3 mm using CuSn10 powder (Carpenter Additive, Windness, UK) and an SLM 125 HL machine (SLM Solutions, Lubeck, Germany). On the basis of the obtained results of microstructural and porosity tests it was possible identification the most effective sets of 3D printing parameters that were further used in fabrication process of tensile tests samples. The porosity of the material samples in both cases was less than 0.1 % (calculated based on planimetric method).
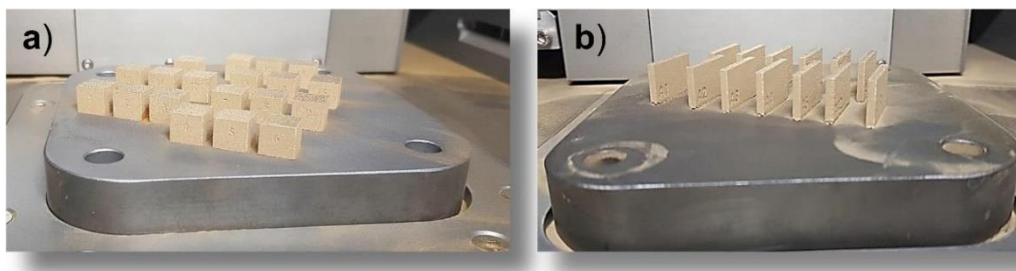
Fig. 1. The main view of two variants of semi-finished specimens fabricated via the SLM technology to optimize the material porosity: a) cuboids samples; b) thin-walled samples.

3. Mechanical characterization of the CuSn10 material under dynamic loading conditions

High strain rate tensile tests were carried out with the use of geometry of non-standardized material samples presented in Fig. 2. The proposed shape and dimensions of the material samples resulted from the necessity of ensuring a relatively high elongation of the material and a high value of the strain rate during tension. Dynamic tensile tests were carried out with the use of two variants of material samples which were prepared from the thin-walled and bulk material elements.
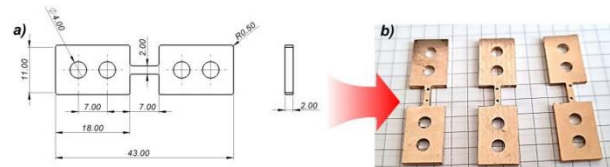
Fig. 2. Material specimens used in dynamic tensile tests:
a) dimensional drawing; b) view of specimens after manufacturing

Dynamic tensile tests were performed with the use of a split Hopkinson pressure bar laboratory stand illustrated in Fig. 3. Its design solution is based on the idea proposed in [3]. Due to applying a "inversion grip" mounted at the end of input bar, the compression loading pulse is converted into tensile loading on the specimen. The bar system consists of a striker bar, input bar, and output bar, the diameter of which is 12 mm and they are made of high-strength steel. A high speed camera system (Phantom v1612) was used to measure the displacement history at the specimen during high strain rate tension. The movies were analyzed in Tema Motion software, with the use of which the fracture strain was also estimated.
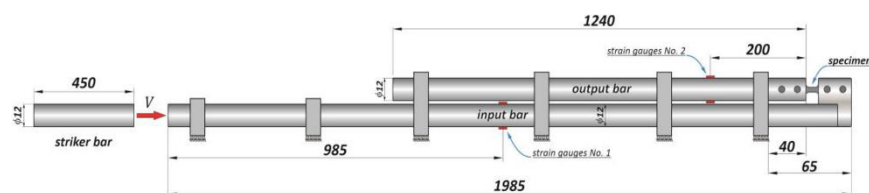
Fig.3. The scheme of laboratory stand used for dynamic tensile tests

Based on the results obtained, it was revealed that the CuSn10 alloy manufactured with the use of the SLM technique demonstrates higher mechanical properties compared to material samples made from plate obtained in the standard metallurgical approach. The estimated elongation value for the CuSn10 thin-walled variant is changed in the range from 20% to 30%, while the estimated elongation for the CuSn10 bulk variants ranges from 20% to 40%. Furthermore, the bulk variant of CuSn10 demonstrates higher values of plastic flow stress in comparison to thin-walled variants. The values are equal to 580, 620, 630 MPa for cases where the strain rates were 1200, 2100 and 2500 s-1, respectively. In turn, the values of plastic stress estimated for CuSn10 thin-walled variants are lower in comparison to bulk variants and their values are 570, 580 and 590 MPa for the case of strain rates of 1200, 2000 and 2600 s-1, respectively.

4. References

[1] C. Deng, J. Kang, T. Feng, Y. Feng, X. Wang, P. Wu (2018). *Study on the selective laser melting of CuSn10 powder*, Materials, **11.**
[2] S. Scudino, C. Unterdörfer, K.G. Prashanth, H. Attar, N. Ellendt, V. Uhlenwinkel (2015). *Additive manufacturing of Cu – 10Sn bronze*, Materials Letters. **156,** 202–204.
[3] C.C. Roth, G. Gary, D. Mohr (2015). *Compact SHPB System for Intermediate and High Strain Rate Plasticity and Fracture Testing of Sheet Metal,* Exp. Mechanics, **55**(9), 1803–1811.

SUITABILITY OF LASER ENGINEERED NET SHAPING TECHNOLOGY FOR INCONEL 625 BASED PARTS REPAIR PROCESS

I. Barwinska[1], M. Kopec[1,2], M. Łazińska[3], A. Brodecki[1], T. Durejko[3] and Z.L. Kowalewski[1]
[1] Institute of Fundamental Technological Research, Polish Academy of Sciences, Poland
[2] Department of Mechanical Engineering, Imperial College London, London
[3] Faculty of Advanced Technologies and Chemistry, Military University of Technology, Poland

1. Introduction

Nickel alloys, despite their excellent resistance to high temperature, tend to form brit- tle intermetallic phases, which decrease the mechanical properties of the material. Moreover, the high production cost of parts made of the Inconel alloys demands new techniques, that enable the fabrication of complex geometries or repair the broken part without the necessity of their replacement. Therefore, the main aim of this work was to assess the suitability of the Laser Engineering Net Shape Technology to repair parts made of the Inconel 625 nickel-based superalloy deposited using the optimized process parameters. Moreover, since the LENS technology reduces an area of heat-affected-zone and does not change the physical characteristics of the deposited material and the substrate, such aspects of this technique were also studied with regard to damaged parts re- pair.

2. Results and discussion

In this paper, the Inconel 625 laser clads characterized by microstructural homogeneity due to the application of the Laser Engineered Net Shaping (LENS, Optomec, Albuquerque, NM, USA) technology were studied in detail. The optimized LENS process parameters (laser power of 550 W, powder flow rate of 19.9 g/min, and heating of the substrate to 300 °C) enabled to deposit defect-free laser cladding. Additionally, the laser clad was applied in at least three layers on the repairing place. The deposited laser clads were characterized by slightly higher mechanical properties in comparison to the Inconel 625 substrate material. Microscopic observations and X-ray Tomography (XRT, Nikon Corporation, Tokyo, Japan) confirmed, that the substrate and cladding interface zone exhibited a defect-free structure. Moreover, the relatively thick heat-affected zone of about 35 μm was generated. It should also be highlighted, that the higher temperature of the material substrate (300°C) and relatively low power of laser reduced the significant phase transformations commonly found in the conventional repair process. Mechanical properties and flexural strength of the laser cladding were examined using microhardness and three-point bending tests. It was concluded, that the LENS technology could be successfully applied for the repair since a similar strain distribution was found after Digital Image Correlation measurements during three-point bending tests (Figure 1). Moreover, an observation of the test specimens did not reveal the surface cracks (Figure 2) [1, 2].
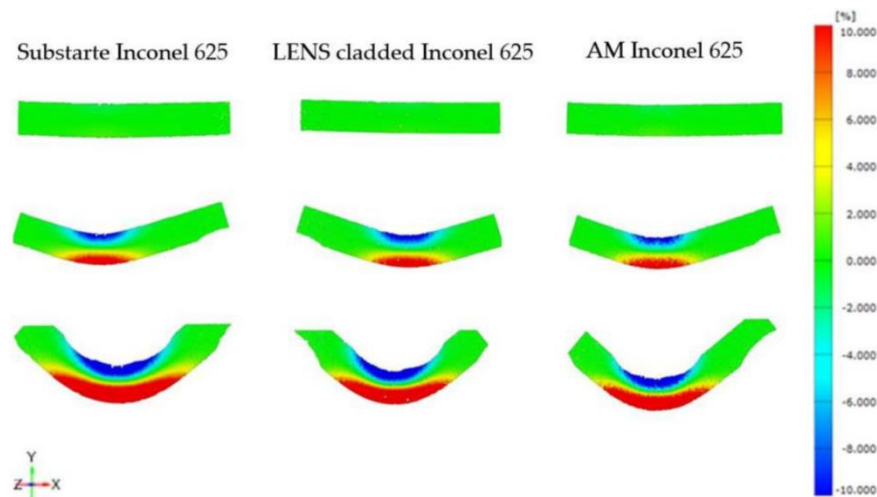
Fig. 1. DIC strain distribution maps of the Inconel 625 in the as-received state, with additional clad and additively manufactured [1]
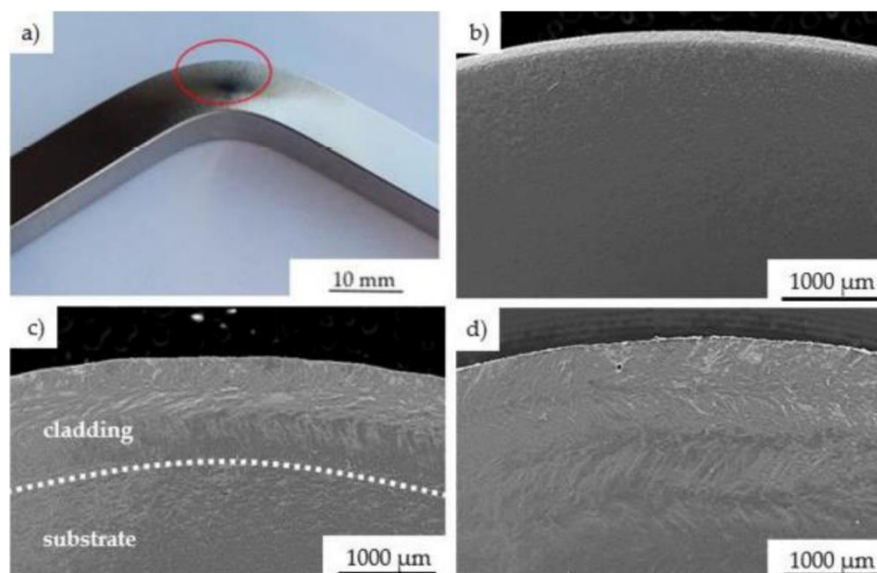
Fig. 2. Surface of the specimen after bending test: area of microscopic observations (a); substrate Inconel 625 (b), LENS cladded Inconel 625 (c), AM Inconel 625 (d) [1]

3. Conclusions

Optimization of the LENS parameters for the Inconel 625 nickel-based superalloy with respect to the repair process enabled obtaining a non-defected laser clad with the specified thickness of about 1 mm. The laser clad was characterized by a very good ad- herence to the substrate material and even improved mechanical properties.

4. References

[1] I. Barwinska, M. Kopec, M. Łazińska, A. Brodecki, T. Durejko, Z.L. Kowalewski (2021) Suitability of Laser Engineered Net Shaping Technology for Inconel 625 Based Parts Repair Process. *Materials 2021*, 14, 7302. https://doi.org/10.3390/ma14237302
[2] T. Durejko, M. Łazińska, C. Senderowski, W. Napadłek, (2017) The FeAl coatings deposited by Laser Engineered Net Shaping, *Inżynieria Materiałowa*, 125-130, https://doi.org/10.15199/28.2017.3.3

2. Composites and Adhesives

INFLUENCE OF TRANSVERSAL CONNECTION TYPE ON FLEXURAL BEHAVIOUR OF 3D TEXTILE REINFORCED CEMENT COMPOSITES (TRC)

M. El Kadi, T. Tysmans and D. Van Hemelrijck

Department Mechanics of Materials and Constructions, Vrije Universiteit Brussel (VUB)

1. Abstract

Textile Reinforced Cement Composites (TRCs) are composite materials characterized by the combination of a cementitious matrix with textile reinforcement. The matrix material guarantees the structural integrity of the composite, while the textile reinforcement warrants a ductile and hence controlled tensile response. TRCs have proven to be a promising alternative to traditional construction elements both for repair and strengthening realizations as well as structural elements such as sandwich panels [1], pedestrian bridges [2] and shell structures [3-4].

Traditionally, two-dimensional, planar textile reinforcement layers have been used as reinforcement for TRCs (see Figure 1 a) and b)). A new iteration in textile reinforcements are 3D textiles. These textiles are characterized by two or more textile layers, distanced by means of transversal connections. These connections can be knitted, woven or manually inserted at discrete positions (see Figure 1 c), d) and e) respectively).
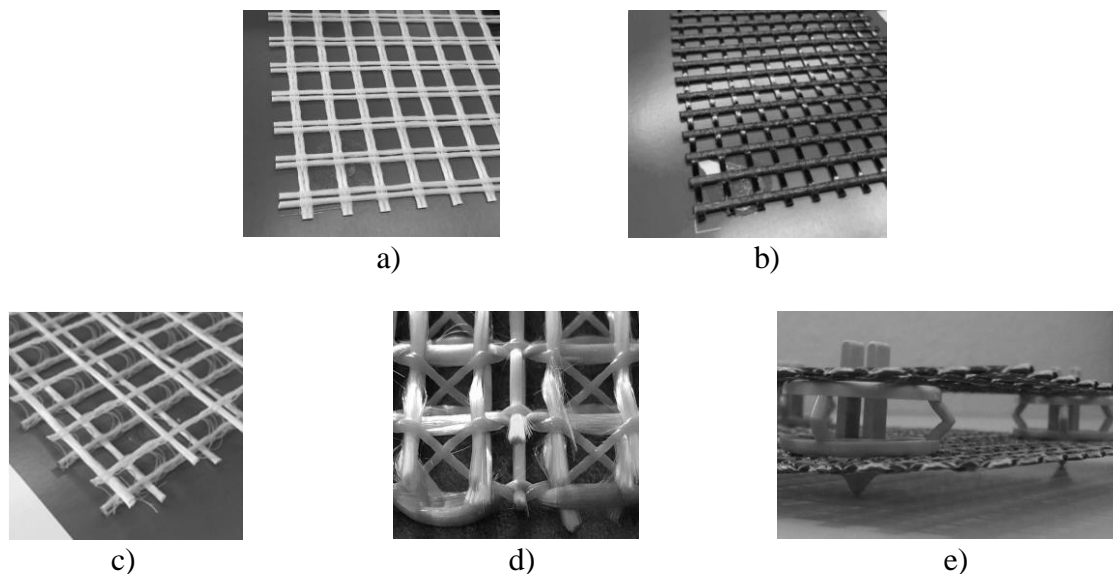
Fig. 1. a) planar 2D glass textile, b) planar 2D carbon textile, c) 3D knitted textile, d) 3D woven textile and e) 3D discretely connected textile

The original goal of employing 3D textiles is their manufacturing ease: due to their spaced configuration they allow for a manufacturing process by pouring. Several experimental campaigns have however shown that apart from their manufacturing proficiency, 3D textiles also provide an improved mechanical behaviour in flexural applications compared to 2D equivalent layups (without transversal connections) [5-7]. Preliminary comparisons of the anchorage effect provided by the knitted and woven transversal connections have been performed in literature [7] for layups combining 3D and 2D textiles. A full-fledged comparison of the three connection types on layups containing only 3D textiles is still lacking in literature and is the research objective of this article.

For the experimental comparison six different TRC layups have been considered in TRC samples of 450 mm x 60 mm x 15 mm. For each layup, six samples have been tested in four point bending during the experimental campaign, the layups were: the original (i) 3D knitted and (ii) 3D woven layups depicted in Figure 1 c) and d) respectively, (iii) the 3D knitted textile where the transversal connections were removed, resulting in a 2D equivalent layup with the same amount of in-plane textiles, (iv) the 3D knitted textile where the knitted connections were replaced by the discrete connections shown in Figure 1 e), (v) a 2D equivalent layup using the 2D textiles depicted in Figure 1 a), without transversal connections and lastly (vi) a 3D textile containing the planar textiles of Figure 1 a), connected by the discrete connections shown in Figure 1 e). In all cases, the transversal connections were made of non-structural materials (e.g. polyester) and the interlayer distance was 8.5 mm.

The four point bending experiments provided greater insight on the anchorage mechanism provided by the different types of transversal connections. All layups containing transversal connections exhibited a clearly improved post-cracking stiffness compared to the 2D equivalent layups, without connections. The increase of up to three times the 2D equivalent stiffness confirmed the potential of these connections towards the optimal material solicitation within the TRC.

Between the different types of transversal connections, the woven connections provided a superior post-cracking regime. These connections were fully intertwined over the length of the textiles (rather than providing discrete bridges between the textile layers) and therefore provided an improved anchorage mechanism due to an optimal stress redistribution over the composite's length during loading.

2. References

[1] J. Vervloet, T. Tysmans, M. El Kadi, M. De Munck, P. Panagiotis, P. Van Itterbeek, J. Wastiels and D. Van Hemelrijck (2019). Validation of a Numerical Bending Model for Sandwich Beams with Textile-Reinforced Cement Faces by Means of Digital Image Correlation, *Applied Sciences*, **9**, 1253–1269.

[2] T. Helbig, S. Rempel, K. Unterer, C. Kulas and J. Hegger (2016). Fuß- und Radwegbrücke aus Carbonbeton in Albstadt-Ebingen. Die weltweit erste ausschließlich carbonfaserbewehrte Betonbrücke, *Beton- und Stahlbetonbau*, **111**, 676-685.

[3] A. Scholzen, R. Chudoba and J. Hegger (2015). Thin-walled shell structures made of textilereinforced concrete Part I: Structural design and construction, 106–114.

[4] E. Verwimp, T. Tysmans, M. Mollaert and S. Berg (2015). Experimental and numerical buckling analysis of a thin TRC dome. *Thin-Walled Structures,* **94**, 89–97.

[5] E. Amzaleg, A. Peled, S. Janetzko and T. Gries (2013). Flexural Behaviour of Cement Based Element Reinforced with 3D Fabric, *VIII International Conference on Fracture Mechanics of Concrete And Concrete Structures*, 10 pages.

[6] A. Peled, R. Haik and E. A. Sasi (2017). Influence of three-dimensional (3D) fabric orientation on flexural properties of cement-based composites, *Cement and Concrete Composites*, **80**, 1-9.

[7] M. El Kadi, T. Tysmans, S. Verbruggen, J. Vervloet, M. De Munck, J. Wastiels and D. Van Hemelrijck (2019). Experimental study and benchmarking of 3D textile reinforced cement composites, *Cement and Concrete Composites*, **104**. 10 pages.

COMBINATION OF DIGITAL IMAGE CORRELATION AND ACOUSTIC EMISSION FOR DAMAGE ASSESSMENT OF V-SHAPE CARBON/EPOXY SUB-COMPONENTS

K.-A. Kalteremidou[1], B.R. Murray[1,2], D. Carrella-Payan[3], D. Van Hemelrijck[1] and L. Pyl[1]
[1] *Mechanics of Materials and Constructions, Vrije Universiteit Brussel, Brussels, Belgium*
[2] *SIM M3 program, Zwijnaarde, Belgium*
[3] *Siemens Digital Industries Software, Leuven, Belgium*

1. Introduction

The usage of composite materials in engineering applications has seen a rapid increase recently. Especially in the automotive sector lightweight carbon/epoxy composites have shown their benefits compared to traditional metallic materials, and they are used in several parts of vehicles, from frames and chassis to bumpers and spoilers [1]. In such structural sub-components, different crosssection geometries are utilized and the material can be subjected to various loading combinations. Considering the complex damage sequence in composites due to their anisotropy as well as the nonuniformity of such geometries, it is expected that the mechanisms through which intralaminar and interlaminar damage develops, under fatigue loading especially, becomes very complicated [2]. Determining the precise damage development in such geometries is therefore of great importance in order to obtain improved designs, avoiding overdesigned parts as well as unexpected early failure.

To that end, V-shape carbon/epoxy specimens have been experimentally characterized in this work both under quasi-static and fatigue, tensile and compressive loads. The main target is to mimic the corner of a square beam component with a potential usage in a vehicle frame for a suspension mount and to evaluate the conditions leading to failure. The potential of Non-Destructive Testing (NDT) for damage characterization of composite sub-components is explored at the same time by using Digital Image Correlation (DIC) and Acoustic Emission (AE). The outcome of both methods is compared to traditional Strain Gauge (SG) measurements to indicate the early damage detection they can offer and their benefits in real applications for the establishment of reliable safety margins.

2. Experimental details

Quasi-static tensile and compressive tests were initially conducted for the V-shape specimens. Fatigue tests were then performed at five load levels and a frequency of 2 Hz with two R-ratios equal to 0.1 and 10. The tests were run up to 500000 cycles. A DIC system from Correlated Solutions with two cameras was used to obtain 3D strain information through the thickness of the samples and to assess the occurring intralaminar and interlaminar damage modes. A Mistras Group AE system with two Pico sensors was used to obtain the acoustic activity of the material during loading and the exact location of damage through linear localization of AE events. Multiple SGs were applied during all tests, indicating the way the specimens were strained in different directions.

3. Main findings

DIC and AE techniques have shown significant benefits over traditional SG measurements, providing precise damage information at early loads, related both to the mode and to the location of damage. DIC has demonstrated its potential for damage identification using the sigma parameter, representing the confidence in correlation, apart from extracting the widely used strain information (Figure 1). By evaluating the AE activity of the material during loading, the AE method has shown its advantages for early damage detection (Figure 2a). At the same time, selection of the most

appropriate features of the AE signals, like the Rise Time (RT), has demonstrated that the transition from moderate to severe damage or to certain damage modes can be strongly indicated (Figure 2b). Moreover, the exact damage locus along the length of the specimen can be detected using linear localization algorithms. Fatigue life curves based on the prediction of the first damage event from the different techniques are constructed, showing that DIC and AE provide much more conservative estimates (in terms of fatigue cycles N) compared to traditional SG outputs.
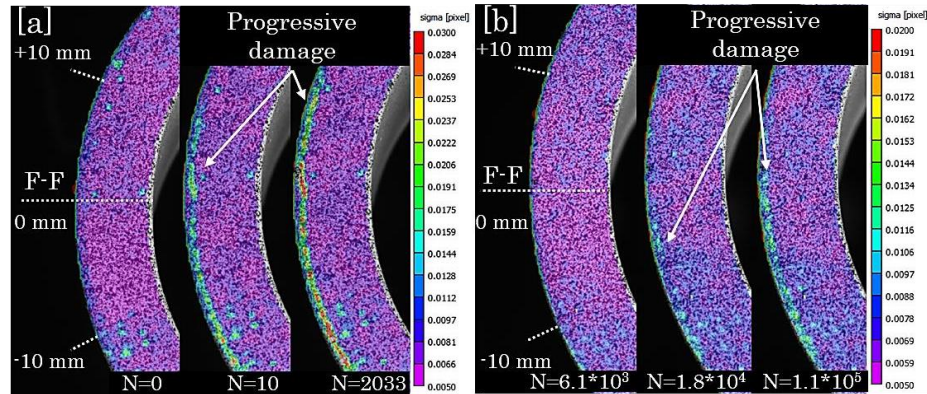
Fig. 1. DIC images showing progressive damage in fatigue compression samples
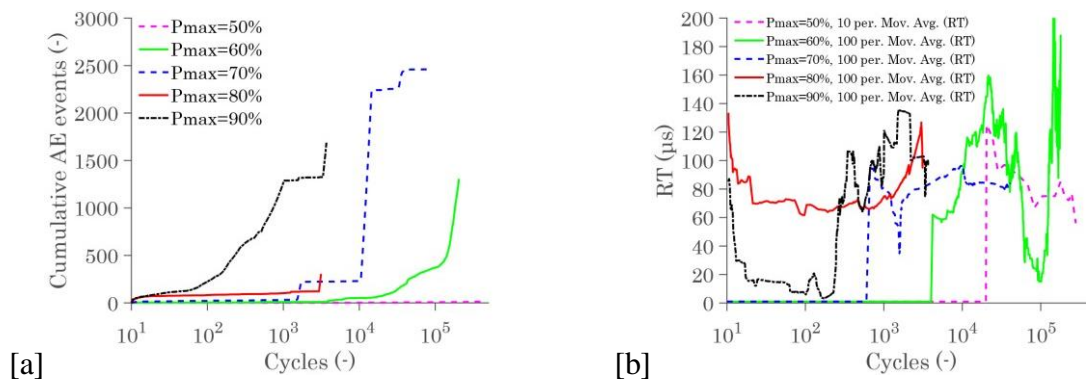
Fig. 2. [a] AE activity and [b] average RT of AE signals in the fatigue compression tests

4. Acknowledgements

5. References

[1] D.W. Lim, T.H. Kim, J.H. Choi, J.H. Kweon and H.S. Park (2008). A study of the strength of carbon-carbon brake disks for automotive applications, *Compos. Struct.*, **86**, 101–106.

[2] G. Savage and M. Oxley (2010). Repair of composite structures on Formula 1 race cars, *Eng. Fail. Anal.*, **17**, 70–82.

INFLUENCE OF FATIGUE AGING AND FIBER ORIENTATION ON THE HIGH VELOCITY IMPACT RESISTANCE OF GLASS WOVEN REINFORCED ELIUM ACRYLIC LAMINATES

T. Libura[1], A. Rusinek[2], R. Matadi Boumbimba[2], Z.L. Kowalewski[1] and P. Gerard[3]
[1] Institute of Fundamental Technological Research, Pawińskiego 5B, 02-106 Warsaw, Poland
[2] Laboratory of Microstructure Studies and Mechanics of Materials,
7 rue Félix Savart, 57073 Metz, France
[3] ARKEMA, Groupement de Recherche de Lacq, F-64170 Lacq, France

1. Abstract

Ballistic impact loading is one of the most critical conditions to which structures can be subjected. Therefore, the examination of a new material such as fully recyclable thermoplastic ELIUM Acrylic resin reinforced by glass fabric woven has a fundamental importance. Its high strength and lightweight as well as low production cost contribute to its wide application in the automotive industry as a replacement of the thermoset-based laminates [1]. The study presents an experimental and numerical work concerning an effect of damage due to fatigue aging on the process of perforation of thin (four layer) laminated composite plates using a hemispherical projectile.

2. Experimental work

Fatigue tests were carried out on two groups of specimens with 100 mm x 100 mm x 2 mm dimensions prepared by an infusion process at room temperature. The first group was cut out along the fiber, while the second one with a 45 degree angle, GFRE $[0°/90°]_4$ and $[45°/45°]_4$, respectively. Cyclic loading was executed under force control with a frequency of 2 Hz. The sinusoidal loading signal was characterized by $R = Ϭmin/Ϭmax = 0,1$. Two stress levels were taken into account. The first one was planned to be below the yield point. In the second, a similar program was arranged, however, the maximum force was chosen, so that the stress level exceeded the yield point. The fatigue aging program did not led to a destruction of the laminated composites during cyclic loading, but to stiffness reduction of the tested specimens, only. Therefore, using an extensometer with the strain range of ±0.2, the Young's modulus variations were monitored as well as an evolution of the hysteresis loop width [2]. The fatigue aging program was stopped before the specimen failure. Subsequently, the aged specimens were dismounted from the testing machine and subjected to perforation tests using a gas gun testing stand. The projectile for impact tests had a hemispherical shape with a diameter of 12 mm, and total mass of 29,1 g, approximately. It was made of maraging steel and subsequently heat treated to reach a yield stress over 2 GPa. Therefore, the projectile had no visible permanent deformation during the penetration. All perforation tests were carried out at room temperature for an impact velocities up to 180 m/s. During experiments an initial and residual values of projectile velocity were measured. The following formula proposed by Recht and Ipson [3] for ballistic impact was used:

$$(1) \qquad V_R = (V_0^K - V_B^K)^{1/K}$$

where V_0 is the initial velocity, V_B is ballistic limit velocity and K is a shape coefficient. The parameters of Eq.(1) were calculated using the least squares method based on experimental results.

The energy absorbed by a target *Ed* were estimated using the following equation:

$$(2) \qquad E_D = \frac{m_p}{2}(V_0^2 - V_R^2)$$

where m_p is the projectile mass.

Having these results a ballistic curve of the tested plates as well as absorbed energy vs initial impact velocity were established. In order to obtain comparison of numerical and experimental results, simulations were carried out using 3D solid element meshes within Abaqus software.

3. Conclusions

The experimental results show that all groups of specimens after fatigue loading exhibited a clear strain-softening effect and a lower impact resistance in comparison with the non-aged specimens. It is clearly visible for the specimens cut out at 45 degree angle, $[45°/45°]^4$. Examination of images captured using the scanning electron microscope and microtomography showed that the fatigue aging deteriorates the interface between matrix and glass fibres due to an appearance of cracks in the transverse yarns. This leads to the inter-yarn decohesion between longitudinal and transverse yarns (meta-delamination), and as a consequence, induces the softening of the reinforcing phase responsible for the stiffness of the composite and its impact resistance.

4. Acknowledgements

5. References

[1] R. Matadi Boumbimba, M. Coulibaly, A. Khabouchi, G. Kinvi-Dossou, N. Bonfoh, P. Gerard (2017). Glass fibres reinforced acrylic thermoplastic resin-based tri-block copolymers composites: Low velocity impact response at various temperatures, *Composite Structures*, **160**, 939–951.

[2] A. Niesłony, Chalid el Dsoki, H. Kaufmann, P. Krug (2008). New method for evaluation of the Manson–Coffin–Basquin and Ramberg–Osgood equations with respect to compatibility, *International Journal of Fatigue*, **30**, 1967–1977.

[3] R.F. Recht, T.W. Ipson (1963). Balistic perforation dynamics, *Journal of Applied Mechanics*, **30**, 384-390.

USING EMBEDDED OPTICAL FIBRES TO MEASURE RESIDUAL STRAIN IN RAPIDLY CURING EPOXY COMPOSITES

B. Seers, R.A. Tomlinson and P. Fairclough
Department of Mechanical Engineering University of Sheffield

1. Introduction

Carbon fibre reinforced plastics are becoming more and more popular in the aerospace and automotive industries due to their high specific strength and stiffness. However, one major drawback of more traditional composite manufacturing techniques is that they have very long processing times. This is primarily due to the need to slowly increase and decrease the processing temperature to avoid residual stress formation and warpage after cure. In recent years, "snap-curing" or very fast curing resins, have been developed to reduce the processing time required to cure parts. However, the effect of shorter processing times on residual stress formation is still not well understood and if these manufacturing techniques are to be adopted for structural applications this gap in knowledge must be addressed. Therefore, this research programmme aims to investigate ways in which to evaluate residual stress in fast curing composites and to determine the effect that residual stress has on the mechanical performance of the finial composite part. While there are many ways in which to monitor residual strain in composites [1], this work will focus on the applicability of the use of embedded optical fibres with Fibre Bragg Gratings (FBGs) in fast-curing composite systems to measure residual strain. The use of FBGs in standard curing resin systems has been growing ever more common in recent years with ever more accurate results [2] [3] [4]. However, the basis of this technique relies on the assumption that there is a sufficient bond strength and transfer of strain between the embedded optical fibre and the epoxy matrix. It is the aim of this work to prove the validity of this assumption for the case of fast-curing resin systems.

2. Method

The use of FBGs in fast-curing resins is still a relatively unexplored area and it is the aim of this research to investigate the interfacial shear strength of epoxy-carbon bonding and epoxy-optical fibre bond. Work by Gao et al [5] found that the interfacial shear strength of a carbon-epoxy bond is influenced by the degree of conversion and diffusion temperature which are two factors that are affected by increasing the curing rate of an epoxy matrix. Recent work by Qi et al [6] has found that increasing the curing rate of epoxy matrices decreases the thickness of the interfacial region between carbon and epoxy within a laminate. These factors have led to the need for an investigation into the effect of an increased cure rate on the interfacial shear strength of carbon-epoxy bonds as it is clear that multiple factors affect this region.

In the current research, single fibre fragmentation testing (SFFT) is conducted on carbon-epoxy and carbon-optical fibre specimens with both conventional and fast curing resins. In this case, SFFT is conducted by preparing a sample consisting of a single carbon or optical fibre running along the centre of an epoxy dog-bone sample. This sample is then strained which causes the single fibre to fracture. The applied load is then transferred to the remaining fibre fragments via the shear lag effect of the epoxy matrix. The applied strain is then further increased and more fibre fractures occur. This continues until the fibre lengths are insufficient to cause enough load introduction into the fibre fragment and any further fibre breaks to occur [7]. At this point it is possible to calculate the interfacial shear strength of the fibre/matrix interface by measuring the length of the fibre fragments. To aid this process, polarised light is shone through the specimen as it is loaded at the saturation point which

clearly shows the fibre breaks. These data are then analysed and comparisons between all cases can be made. The bonding is then qualitatively evaluated with the use of scanning electron microscope images to ensure no debonding in the interfacial region has occurred. Initial experiments have shown promising results; detailed analysis will be presented at the conference. This research is key to the advancement of the use of optical fibre sensors in fast curing resin systems as without the validation of the key assumptions as previously outlined it is not possible to make any meaningful correlation between experimental results and the system under investigation.

3. Future work

Using embedded FBGs, it is possible to both monitor thermal/chemical expansion/contraction, laminate temperature and resin modulus (degree of conversion) *in situ* during the cure of a laminate [8]. Additionally, the same embedded sensors can be used for structural monitoring of the part during its life. Therefore, this technique allows for an unmatched insight into the real time state of a composite laminate during and after cure. Work is underway to use embedded FBGs to investigate the effect of varying the cure rate on the residual strain and strain distribution within a rapidly cured laminate. This will give an insight into the mechanisms behind the formation of residual stress in rapidly curing laminates and thus provide a tool to optimise future fast curing resins systems and their cure cycles for structural applications.

4. References

[1] B. Seers, R. Tomlinson, and P. Fairclough, "Residual stress in fiber reinforced thermosetting composites: A review of measurement techniques," *Polym. Compos.*, pp. 1–17, 2020.

[2] P.P. Parlevliet, "Residual Strains in Thick Thermoplastic Composites," Technische Universiteit Delft, Delft, 2010.

[3] M. Mulle, R. Zitoune, F. Collombet, P. Olivier, and Y.-H. Grunevald, "Thermal expansion of carbon-epoxy laminates measured with embedded FBGS-Comparison with other experimental techniques and numerical simulation," *Compos. - Part A Appl. Sci. Manuf.*, no. 38, pp. 1414–1424, 2007.

[4] S.S. Kim, H. Murayama, K. Kageyama, K. Uzawa, and M. Kanai, "Study on the curing process for carbon/epoxy composites to reduce thermal residual stress," *Compos. - Part A Appl. Sci. Manuf.*, no. 43, pp. 1197–1202, 2012.

[5] A. Gao, Y. Gu, Q. Wu, C. Yuan, M. Li, and Z. Zhang, "Influence of processing temperature on interfacial behavior of HKT800 carbon fiber with BMI and epoxy matrices," *Chinese J. Aeronaut.*, vol. 28, no. 4, pp. 1255–1262, 2015.

[6] Y. Qi, D. Jiang, S. Ju, J. Zhang, and X. Cui, "Determining the interphase thickness and properties in carbon fiber reinforced fast and conventional curing epoxy matrix composites using peak force atomic force microscopy," *Compos. Sci. Technol.*, vol. 184, pp. 266–3538, 2019.

[7] L.A. Carlsson, D.F. Adams, and R.B. Pipes, *Experimental Characterization of Advanced Composite Materials*, 4th ed. Boca Raton: Taylor & Francis Group, 2014.

[8] S. Minakuchi, S. Niwa, K. Takagaki, and N. Takeda, "Composite cure simulation scheme fully integrating internal strain measurement," *Compos. Part A*, vol. 84, pp. 53–63, 2016.

EVALUATION OF DEBONDING TOUGHNESS OF BONDED LAYERS USING WITH THE SHAFT LOADED BLISTER TEST

S. Devi and V. Parameswaran

Department of Mechanical Engineering, Indian Institute of Technology Kanpur, 208016, India

Abstract

Shaft loaded blister test (SLBT) was employed to evaluate the debonding toughness of a polymer layer adhesively bonded to a steel substrate. As the blister grows the mode-mixity does not remain constant in SLBT. Finite element analyses (FEA) were performed to obtain the variation of mode-mixity with change in blister size. Experiments were performed in which the load, load-point displacement and de-bond (blister) size were recorded synchronously. The variation of toughness with mode-mixity was obtained.

Keywords: Blister test, debonding, energy release rate, mode-mixity, bimaterial

1. Introduction

In recent years, the use of adhesive bonding has increased in several sectors, such as automotive, aerospace, defence, electronics and naval industries. SLBT is considered more effective than other conventional adhesive tests (Pull-off test, peel test and indentation test) as delamination can be obtained even at low displacements. Malyshev and Salganik [1] used SLBT on the polymer coating to obtain the energy release rate of adhesives. This work aims to evaluate the debonding toughness of PMMA layer bonded to steel plate.

2. Details of experiment and analysis

Circular PMMA sheet of thickness 1.4 mm and diameter 90 mm was bonded to a steel plate of thickness 3 mm using an epoxy adhesive. Using the experimental setup as shown in Fig. 1, the load, load-point displacement and de-bond (blister) size were recorded synchronously. The variation of the force and blister radius as a function of displacement is shown in Fig. 2(a).
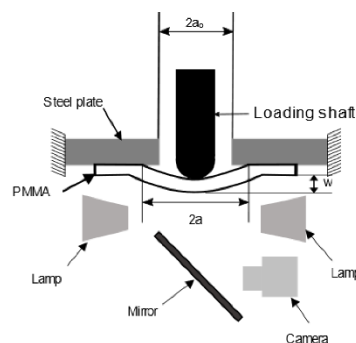
Fig. 1. (a) Schematic diagram for SLBT

In the experiment, the behaviour of the de-bonding layer transitions from flexure dominated response to membrane dominated response. The energy release rate (ERR) can be calculated using equation (1) for small deflection of PMMA layer [1]. When the deflection exceeds the PMMA layer thickness, membrane effects become dominant and equation (2) can be used to calculate the ERR [2].

$$G_T = \frac{3(1-v^2)P^2}{8\pi^2 E h^3}$$

(1)

$$G = \left(\frac{P^4}{\pi a^4 E h}\right)^{1/3}\left[\frac{1}{8\gamma} + \frac{\gamma^2(1-v^2)}{2}\right]$$

(2)

where, P is the load, E and h are respectively the elastic modulus and thickness of PMMA layer, w the displacement of PMMA layer, a the blister radius, v the Poisson's ratio of PMMA. The parameter γ is defined in [2]. Following [3], the variation of toughness with mode-mixity was assumed as

$$G_c = G_{Ic}(1 + (1-\lambda)tan^2(\psi))$$

(3)

where $tan\ (\psi)$ is the mode-mixity, *GIC* is the mode-I toughness, and λ is free parameter. FEA was performed to determine the mode-mixity as a function of blister radius and deflection. The data shown in Fig. 2(a) was used with the FEA results to determine the variation of mode-mixity as a function of blister radius in the experiments.

3. Results

The variation of mode-mixity as a function of blister radius is shown in Fig. 2(b). Equation (1) and (2) and the mode-mixity variation obtained from FEA were used to obtain the parameters of equation (3) were determined from the experimental data. The variation of toughness (Gc) as a function of the blister radius is shown in Fig. 2(b). It is observed that the toughness increases by 10% for the range of mode-mixity and blister growth observed in the experiments.
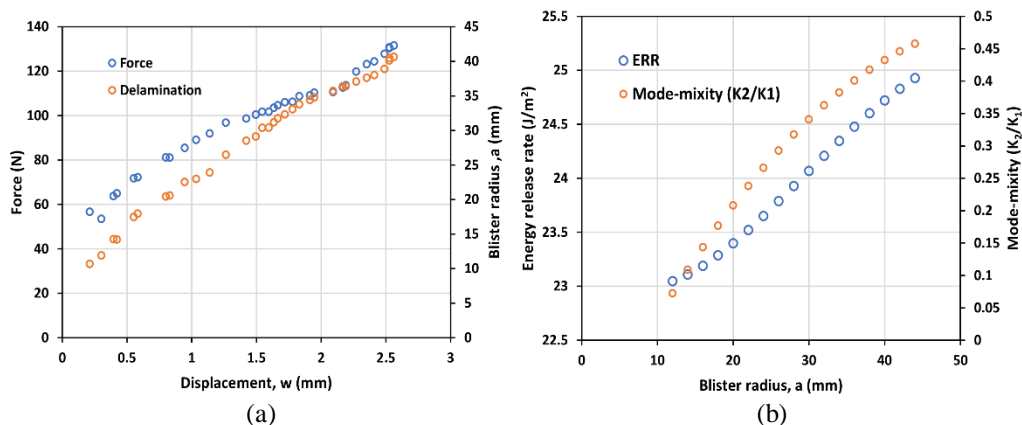
Fig. 2. (a) Variation of force and blister radius with displacement
(b) Variation of ERR and Mode-mixity with blister radius

4. References

[1] Malyshev BM, Salganik. The strength of adhesive joints using the theory of cracks. *Int. J. Fract. Mech* 5; 1:114–29,1961.
[2] Jensen HM. The blister test for interface toughness measurement. *Eng. Fract. Mech.*;40(3):475–86,1991.
[3] Jin ZH, Sun CT. Cohesive zone modeling of interface fracture in elastic bi-materials. *Eng. Fract. Mech.* 2005; 72:1805–17

3. Dynamic Response of Materials and Structures

ANOMALOUS DYNAMIC BEHAVIOR OF POLYCRYSTALLINE PURE ALUMINUM AT ULTRA-HIGH SHEARING RATES AND ELEVATED TEMPERATURES

B. Zuanetti, T. Wang and V. Prakash
Case Western Reserve University, Cleveland, OH 44106-7222, USA

1. Introduction and motivation

Plastic flow of metals at large strains and high strain rates, studied extensively for nearly fifty years, has recently attracted renewed interest because of the discovery of strong effects at very high strain rates and elevated temperatures, and because of the growing acceptance of the importance of these effects in dynamic failure mechanisms. At low loading rates, it is well accepted that mobility of dislocations is controlled by the stress-temperature assisted glide past short-range obstacles; however, as the strain rates are increased, the dominant mechanism controlling the mobility of dislocations can shift from thermal activation to a viscous-drag mediated regime, where temperature may play a positive role in the determination of flow stress.

The present study is facilitated by the recent developments in experimental techniques in our laboratory that enable thin metal foil specimens placed on the flyer-plate to be heated to temperatures in excess of 1000°C prior to impact, thereby extending the capability of conventional high-strain-rate combined pressure-and-shear plate-impact experiments to elevated temperatures. These developments include the introduction of a breech-end machined steel tube that extends the length of the gun-barrel and carries a vertical heater-well that accommodates a z-axis manipulated resistance coil heater. Moreover, an all-fiber optics-based heterodyne interferometer has been implemented that enables simultaneous measurements of both normal and transverse components of the particle velocity at the rear-surface of the target plate. Using these new capabilities, we have conducted elevated temperature combined pressure-and-shear plate-impact experiments on polycrystalline commercially-pure Al samples to investigate the effect of temperature on their dynamic shearing resistance at strain-rates $>10^5$ s^{-1}, temperatures of up to 600°C, and shear strains approaching 100%. The characterization of the plastic deformation of Al (T_m= 660°C) at elevated temperatures and very high strains rates is particularly valuable because of its usefulness in understanding the shearing resistance of fcc metals at high plastic strains as they approach their melt point, and for the immediate contribution to improved high temperature constitutive models.

2. Experimental methods and results

The elevated temperature combined pressure-and-shear plate-impact experiments were conducted using the 82mm bore gas-gun facility at CWRU. A schematic of the experimental configuration is shown in Figure 1(a). The gun barrel has a broached keyway along its entire length, which makes the rig well suited for conducting both normal and oblique plate impact experiments. The front of the sabot is skewed with respect to the gun barrel axis. The flyer plate assembly comprises a thin metal foil specimen diffusion bonded to a high hardness and high impedance pure (99.9%) tungsten carbide flyer plate. In the experiments reported herein, the flyer and the target plates are pre-aligned to a 22° angle of inclination with respect to the direction of approach. At impact, both normal and transverse components of the sabot velocity are imposed on the sample and flyer assembly and the target plate, resulting in the thin metal foil specimen to be essentially sandwiched between the WC back-flyer and the target plates. Consequently, the metal samples are subjected to an in-plane shearing deformation at high shearing rates under a superimposed hydrostatic pressure. The impact velocity and the skew angle of the projectile are controlled such that the target and the flyer plates remain elastic during

impact. On the rear-surface of the target plate a 500 lines/mm holographic grating is fabricated using lithography together with standard liftoff procedures. The grating allows simultaneous measurements of normal and the transverse particle displacement history of the free surface of the target plate by using the all-fiber-opticsbased heterodyne combined NDI/TDI.

Figure 1(b) summarizes the results obtained from the elevated temperature combined pressureand-shear plate impact (PSPI) experiments on Al foil samples at test temperatures of 23°C, 224°C, 320°C, 501°C, 549°C, and 593°C. In all the experiments, 99.9% pure WC is used for the flyer and target plates. The impact velocity is kept within the narrow range of 99 to 105 m/s with the skew angle of impact maintained at 22°. The corresponding hydrostatic pressure in the sandwiched samples was ~ 4.6 GPa. The thickness of the samples was varied from 70 to 45 microns. The corresponding plastic shearing rates in the samples are in the range ~ 3.9×10^5 s^{-1} to 7×10^5 s^{-1}. The initial steeply rising portions of the stress-strain curves correspond to intervals in which the stress state in the specimen is not uniform because of insufficient time for wave traversals through the thickness of the specimens. At room temperature, the flow stress is observed to saturate at a strain level of ~ 0.12. This behavior has also been reported by other investigators in constant high strain rate tests in pure Al, suggesting that a nominally steady dislocation structure evolves in the samples in these experiments at modest strains. It is noteworthy to highlight the increased rate sensitivity at high strain rates (~ $4-7 \times 10^5$ s^{-1}) of pure Al at room temperature, where the flow stress is observed to increase by nearly 140% when compared to that measured at a strain rate of 1.5×10^3 s^{-1} at a shear strain of 0.1. This rate sensitivity is observed to further increase at elevated temperatures - the flow stress at 320°C is more than 160% higher than that measured at 350°C at 1.5×10^3 s^{-1}, and is almost 260% higher at 549°C at a similar strain rate. What is more striking is the flow stress at 593°C, where an anomalous increase is observed when compared to that at 549°C at all levels of plastic strain. Moreover, the flow stress in the 549°C experiment shows thermal softening at plastic strains larger than 0.22, whereas the 593°C experiment shows hardening at plastic strains of ~ 0.3 and higher.

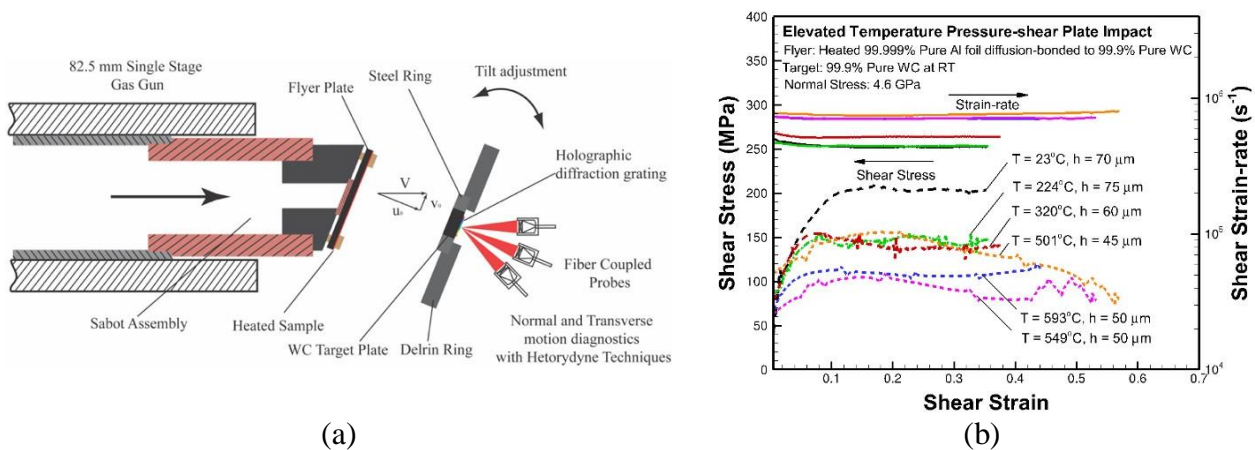(a)   (b)

Fig. 1. (a) Schematic of the elevated temperature combined pressure-and-shear experimental configuration used in the present study; and (b) Stress vs. strain profiles for the polycrystalline commercial-purity aluminium samples obtained as a function of temperature

3. Acknowledgment

THE EFFECT OF SABOT MASS AND THE INTERFACIAL FRICTION BETWEEN THE SABOT AND STRIKER ON THE INCIDENT SIGNALS OF A SPLIT-HOPKINSON BAR

D. Kumar and S.N. Khaderi

Department of Mechanical and Aerospace Engineering, Indian Institute of Technology Hyderabad, Kandi, Sangareddy, Telangana 502285, India

1. Introduction

In a typical split Hopkinson bar setup, the striker impacts on the input bar to give rise to an input pulse, which is nearly rectangular in shape. Usually, the inner diameter of the gun barrel, which accelerates the striker, is slightly larger than the striker. In such situations, nylon, Teflon, or brass sabots are fitted on the striker so that the striker can travel concentric in the barrel. The effect of the mass and material of the sabot may considerably influence the incident signals. Forrestal et al. [1] showed that the nylon sabots increase the effective density of the striker, which is defined as equivalent density, $\rho_{st} = (m_{st} + m_{sa})/AL$, where m_{st} and m_{sa} are the mass and density of sabot, respectively, and *A* and *L* are the area and length of the striker. As a consequence, the magnitude of the incident signal is slightly higher when sabots are used. Song et al. [2] also investigated the effect of sabot mass on the incident signal. They also assumed that the striker has a higher equivalent density when compared to the input bar. Using one-dimensional analysis, it was shown that this slight mismatch of densities, in addition to causing a higher incident pulse, has the effect of increasing the pulse width of the incident pulse. Specifically, the unloading portion of the incident pulse is very long (typically in the order of the width of the incident pulse) whose magnitude progressively decreases with time. However, Chen et al. [2] did not include any experimental data that validates this feature.

From the above studies, we see that the sabot mass increases the magnitude and time duration of the input pulse only through the equivalent density. Therefore, it is hypothesized that the fabrication or the installation methods for the striker should have no influence on the incident signals. To test this hypothesis, we performed experiments in which a striker-sabot assembly is fabricated from a rod, whose initial diameter is the same as the gun barrel, using the turning process on a lathe. This sabot is further referred to as an integral sabot, to represent that the sabot is an integral part of the striker.
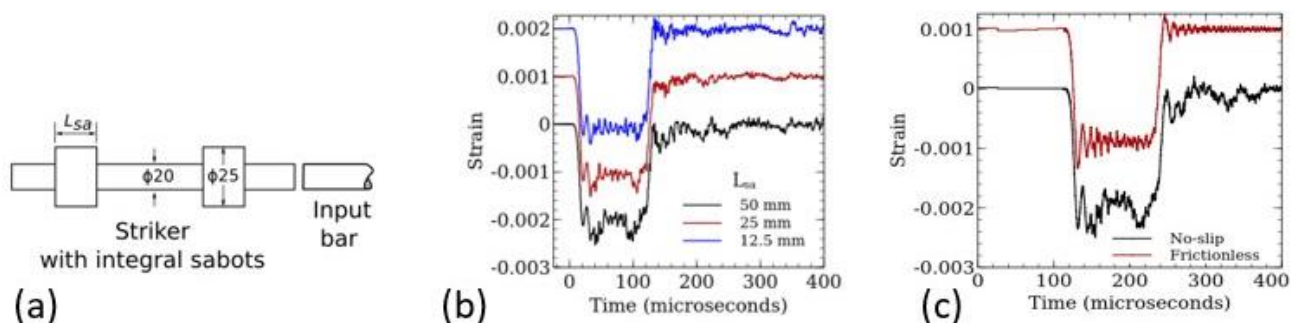
Fig. 1. (a) Striker with an integral sabot. (b) Incident signals for various values of length of sabot (L_{sa}). (c) Incident signals obtained from finite element simulations by varying the interface conditions between the sabot and striker

In this talk we present the results of the experiments performed using the integral sabots. We demonstrate that the use of integral sabot, in contrary to the hypothesis, give additional features to

the incident signals which are not usually observed in the literature when non-integral sabots (such as polymeric/brass) are used. The causes of these additional features and their dependence on the integral sabot dimensions are reported using a combined experimental and finite element analysis.

2. Experiments

Experiments have been conducted to test the hypothesis that an integral sabot would result in incident signals which are similar to the references [1] and [2]. Integral sabot strikers are fabricated using D2 steel alloy (see Fig. 1(a)). The outer diameter of the integral sabot is the same as the gun barrel (25 mm). The lengths of the integral sabot (L_{sa}) are chosen as 50 mm, 25 mm or 12.5 mm. The striker and the input bar have a diameter of 20 mm. The incident signals are recorded through strain gauges connected in a half-bridge configuration on the 1200 mm-long incident bar, at a distance of

500 mm from the impacting end. The striker-sabot assembly is accelerated to a velocity of 21 m/s. The incident signal for the three lengths of the integral sabots are shown in Fig. 1(b). We observe that the magnitude of strain at the beginning and the end of the incident pulse is larger than that of the plateau. This enhancement is larger when the length of the integral sabot is larger. These features of the incident signals have not been reported in the literature. The main reason seems to be that in our work, the sabot is integral to the striker and in the literature the sabots are either shrunk or pressfitted. From these results, we infer that in addition to the mass of the sabots, the way they are fabricated/fitted on to the striker also determines the nature of the incident signal.

3. Discussion

The main difference between our integral sabot and the conventional brass/polymeric sabots is that there is a possibility of relative motion between the sabot and striker in the latter, whereas a noslip condition exists in the former. We therefore anticipate that the interface friction between the sabot and the striker plays a vital role in determining the nature of the incident signal. This assertion is substantiated by performing detailed finite element simulations in which the interfacial friction between the sabot and striker is accounted for (see Fig. 1(c)). The finite element simulation results reveal that the distortion of the incident signals happens when the interface between the striker and sabot is of no-slip type. When the interface is frictionless, the incident signals have no additional features as shown in Fig. 1(b). We also provide guidelines for the typical dimensions of sabot so that the incident signal is not corrupt due to the mass of sabot.

4. References

[1] M. J. Forrestal, D. J. Frew and W. Chen, (2002) The Effect of Sabot Mass on the Striker Bar for Split Hopkinson Pressure Bar Experiments, *Experimental Mechanics*, **42**, 129-131.

[2] B. Song, K. Connelly, J. Korellis, W. Lu and B. R. Antoun, (2009). Improved Kolsky-bar design for mechanical characterization of materials at high strain rates, *Measurement Science and Technology*, **20**, 115701.

MODAL VERIFICATION OF ROTOR BLADES OF TOP-PRESSURE RECOVERY TURBINES

H.T. Chiang, M.H. Lin, C.H. Hsu and C.S. Lin

Department of Vehicle Engineering, National Pingtung University of Science and Technology, Pingtung, Taiwan

1. Abstract

The topic of this paper aims to investigate the dynamic characteristic of the turbine blades under the operation of turbine. At first we did the validity of the finite element model by experimental modal analysis for actual a turbine blade, also verify the agreement with value of modal criterion between the mode shapes obtained from the theoretical modal analysis and the experimental modal analysis. Furthermore, we did the theoretical modal analysis for turbine to understand the turbine dynamic characteristic. Moreover, we evaluate the turbine blades high cycle fatigue Relevance with dynamic characteristic by Campbell diagram and SAFE (Singh's Advanced Frequency Evaluation) diagram.

2. Introduction

Top-Pressure Recovery Turbines (TRT) is an energy recovery equipment operated by the gas generated in a blast furnace. TRT has following tow functions. One is control the top pressure of a blast furnace. The other one is generated electric power by driving turbine. The TRT turbine blades is subjected to centrifugal and fluctuating force. The centrifugal force is caused by turbine rotating, and fluctuating force yielded by nozzle passing frequency excitation and the running speed harmonic excitation. M.P. Singh et al [1] presented the SAFE diagram to evaluate interference. The SAFE diagram compares not only the frequencies of exciting harmonies with natural frequencies of blades, but also the shape of these harmonies with the normal mode shapes of a completely turbine with packed blade. M. Zhang et al. [2] concluded that the fatigue failure of turbine blades is cause by the resonance generated by the aerodynamic load.

3. Metrology

The aim of this paper is investigate the dynamic characteristic of the turbine blades. It has been shown in a previous study [2] that the fatigue failure of blades was cause by the aerodynamic load and centrifugal force. Based on the finite element analysis, through the commercial CAE software to simulate the turbine blades. The modal parameter of blade could be determined by the modal analysis and harmonic analysis. Moreover, through the commercial software, the exact modal parameter of blade can be carried out in experimental modal analysis. In addition, via modal assurance criterion to check the similarity of the mode shapes of simulation result and experiment result. In order to determine the mode shapes of blade disk that we did the modal analysis of the well packed turbine blades. Furthermore, we evaluate the dynamic characteristic of the turbine blades through Campbell diagram and SAFE diagram.

4. Result

From the result of blade modal analysis that table. 1 shown, we could observe the mostly mode shapes are bending mode on blade instead of dovetail. So we chose our excitation point on the blade but dovetail. We arranged the measurement point to did the modal testing following as fig.1 shown. After we finished verification between the theoretical modal analysis and experimental modal

analysis by modal assurance criterion. Consider the blades are assembly on the disk that constraint on axis. We did the theoretical modal analysis of the well packed turbine blades. The result of the theoretical modal analysis that blade disk The result table 2 shown the theoretical modal analysis that blade disk has a lot of close modes as a result of the blade disk is an axial symmetry model. In addition, in order to understand the dynamic characteristic of blade disk in operation. Through the change rotation velocity of the blade disk. Plot the various of modal frequencies on different rotation velocity in campbell diagram following as Fig. 2.
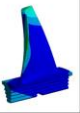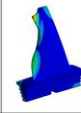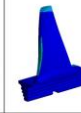
Table 1. The results of modal analysis for a blade
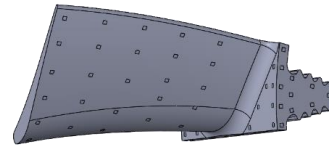
Fig. 1. The experiment modal analysis grid planning
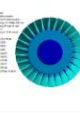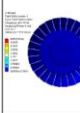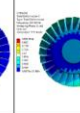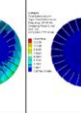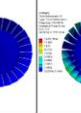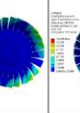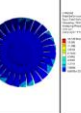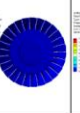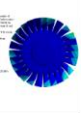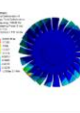
Table 2. The theoretical modal analysis result of blade disk
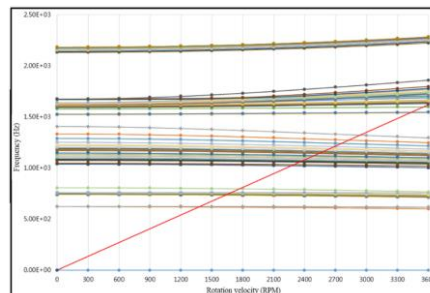
Fig. 2. The Campbell diagram of blade disk

5. Conclusion

From the result of the theoretical modal analysis, some conclusions drawn form the result as follows:

1. In the case didn't consider aerodynamic of blade and rotation velocity. We could observe the mostly mode shapes locate on the blade instead of dovetail.
2. The Campbell diagram of blade disk shown that the mode shape might cause high-cycle fatigue are happening frequencies range of 1500~1700Hz.

6. References

[1] M. P. Singh, J. J. Vargo, D. M. Schiffer and J. D. Dello (1988). *SAFE Diagram – A Design and Reliability Tool for Turbine Blading,* Texas A&M University. Turbomachinery Laboratories.
[2] M. Zhang, Y. Lin, W. Wang, P. Wang and J. Li (2016). The Fatigue of Impellers and Blades, *Engineering Failure Analysis.*, **62**, 208–231.

PREDICTING THE BEHAVIOUR OF PREDAMAGED CONCRETE UNDER BALLISTIC LOADING

G.R. Tear[1], A.H. Cohen[2] and W.G. Proud[1]
[1] Physics Department, Imperial College London, London, UK
[2] Dynamic Physics Group, NRCN, Be'er Sheva, Israel

1. Introduction

Concrete is a complex material which undergoes several modes of failure when loaded ballistically. Often different parts of the sample will undergo different modes of failure as ballistic impact creates an extreme stress and strain rate loading on the sample. Hydrostatic pressures in excess of 20 GPa may be experienced by some parts of the sample at the impact site, whilst some distance from impact large shear strains may be induced. The key failure modes for ballistic impact of concrete are ductile flow, brittle fracture and granular flow. These different failures lead to different post failure behavior, which is necessary to accurately predict if we wish to understand multiple impact scenarios.

This research aims to combine numerical and experimental techniques to accurately predict the thresholds at which different failure modes occur. In this presentation, Kolsky bar techniques [1] have been used to characterize the concrete.

2. Experimental Methodology

Experiments were conducted at the European Synchrotron Radiation Facility (ESRF) in Grenoble, France using the NRCN's Kolsky bar setup. The Kolsky bar was used to load the samples whilst a Shimadzu camera captured radiographic images of the sample's failure. Kolsky bar impact velocities varied between 8 m/s and 17 m/s using steel Inconel bars. Whilst strain gauge measurements were taken, the sample did not reach equilibrium as brittle and granular flow behavior initiated.

Samples were prepared using techniques developed in [2] and were 10mm square, 4mm thick. The method is designed to produce samples which represent Ultra High Performance Concrete (UHPC), and the mix is close to core tuff. The main difference is the aggregate size distribution which we have limited in order to ensure repeatability at the small scale. The weights of each component are given in table 1.

Cement / g	Water / g	Basalt Microspheres / g	Plasticiser / g
147.8	59.1	285.1	0.9

Table 1. Mix details for the samples in this set of experiments

3. Results

The preliminary results from ESRF show samples with both granular flow and fracture. We have evidence of both occurring in the same sample. Additionally sub-surface behavior is evidenced which is different from surface fracture, as can be seen in figure 1 left.

Methods developed previously [2] to threshold Kolsky bar images and estimate regions of failure have been applied, as in figure 1 right. The results of this thresholding algorithm identify failed material and allow a numerical metric to be calculated which can then be compared to numerical simulations.
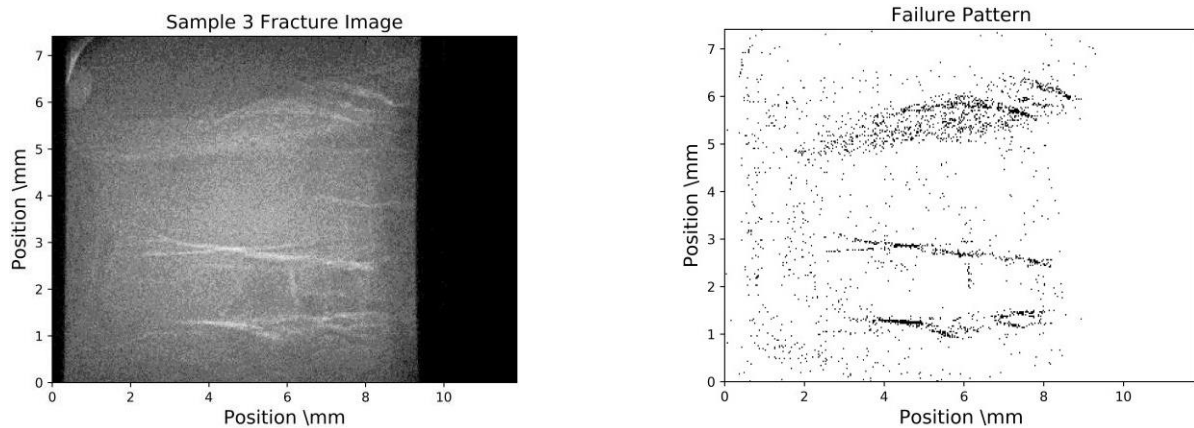
Fig. 1. (*left*) Sample 3 fracture frame, and (*right*) failure thresholding algorithm which identifies regions of material failure

4. Numerical Methods

Numerical simulations were conducted in the finite element code Abaqus. The Kolsky bar was simulated with both the input and output bars, the model geometry is shown in figure 2. Gauge outputs were simulated using the average longitudinal strain over a surface area of nodes corresponding to the gauge size. We have taken inverse methods developed for ductile materials on a Kolsky bar [3] and extended them to brittle materials in order to find the numerical parameters for this specific concrete sample.
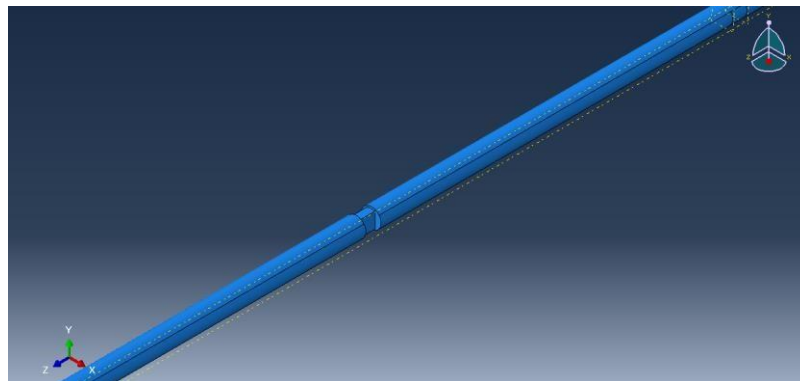
Fig. 2. Geometry of numerical model in Abaqus, designed to represent the Kolsky bar

5. References

[1] W. W. Chen and B. Song (2011). *Split Hopkinson (Kolsky) Bar Design, Testing and Applications.* Springer, New York.

[2] Tear, G. R., Cohen, A. H., Magnus, D., Sory, D. R., & Proud, W. G. (2018). Damage Characterisation for Cement and Concrete Using Microwave Induced Damage. *MDPI Proceedings*, *2*(8), 525.

[3] Oliveira, I., Teixeira, P., Ferreira, F., & Reis, A. (2015). Inverse Characterization of Material Constitutive Parameters for Dynamic Applications. *Procedia Engineering*, *114*, 784–791.

USING FULL-FIELD STRAIN AND TEMPERATURE MEASUREMENTS TO DETERMINE THE TAYLOR-QUINNEY COEFFICIENT IN DYNAMIC TENSILE TESTS

J. Smith, J. Seidt and A. Gilat

Ohio State University, Department of Mechanical and Aerospace Engineering,
Columbus, Ohio, USA

1. Introduction

Plastic deformation generates heat and the Taylor-Quinney coefficient is the ratio between the energy dissipated as heat and the overall work invested in producing the deformation. Knowing the value of the Taylor-Quinney coefficient is of great importance. It can provide insight into the microstructural evolution that occurs during the deformation, and it can play an important role in numerical simulations of applications that involve plastic deformation and failure. Accurate simulation of the temperature rise during the deformation is essential since a rise in temperature may offset the increase in stress due to strain hardening. This effect can be substantial when high strain rates and dynamic loading are involved where there is little or no time for the generated heat to dissipate and the temperature rise can be significant.

Measurements of the Taylor-Quinney coefficient during high strain rate deformation have been mostly done in compression experiments conducted with the split Hopkinson bar (Kolsky) apparatus (SHB) [1, 2]. In these tests the nominal stress and strain in the specimen during the tests were determined from the measured waves in the incident and transmitter bars assuming that the strain in the specimen is uniform. The temperature of the specimen was only measured at one, or a few, points using infrared (IR) detectors. In one investigation [3] the Taylor-Quinney coefficient was determined in tensile SHB experiments. In this case the temperature was measured at only one point and the average strain was determined from the recorded waves in the incident and transmitter bars. Consequently, valid values of the Taylor-Quinney coefficient were obtained only for small strains since the average strain that is determined from the waves is valid only during uniform deformation before localization (necking) starts.

In the present paper the Taylor-Quinney coefficient is determined from tensile tests over a wide range of strain rates including high strain rates which are conducted in a tensile SHB apparatus. In these tests simultaneous full-field strain and full-field temperature measurements are made on the surface of the specimens. The strains are measured using the Digital Image Correlation (DIC) method with high-speed cameras, and the temperature is measured with a high-speed IR camera. Both, strain and temperature are measured throughout the test including in the necking region during the localization. By combining these measurements with force measurements, the TaylorQuinney coefficient can be determined when the strain is uniform and in the necking region at large strains. Results from testing AISI 316L austenitic stainless steel show that the strain in the necking region can exceed 0.8 and the temperature rises by more than 200C. The Taylor-Quinney coefficient increases with strain and reaches a plateau value of about 0.8 at large strains.

2. Experimental setup

Quasi-static tests (stain rates 10^{-2} to 1 s^{-1}) are done using a servo-hydraulic load frame. Dynamic tests at strain rate of 200 s^{-1} are done using a special intermediate strain rate apparatus [4], and high strain rate tests (3,000 s^{-1}) are done using a tensile split Hopkinson (Kolsky) bar (SHB) apparatus. The experimental setup is shown in Figure 1. The optical setup consists of one or two visual cameras

on one side of the specimen and a high speed IR camera on the other side. The specimens are flat and thin with a gage length of 8 mm, width of 3.8 mm and thickness of 1.85 mm.
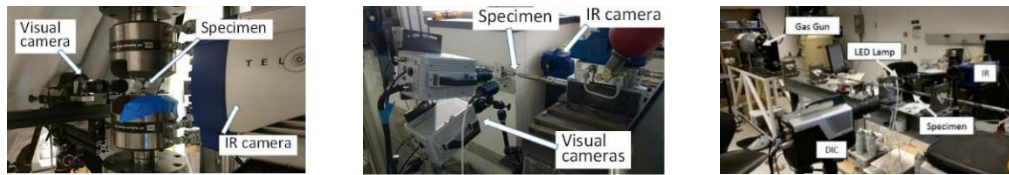
Fig. 1. Experimental setup, static (left), intermediate rates (middle), high rates (right)

3. Results

Example of results are presented from testing of 316L stainless steel. Figure 2 shows images of the deformation (DIC axial strain) and temperature during a test at nominal strain rates of 200 s^{-1}. Figure 3 shows the history of strain (engineering and true) and temperature at the necking point in the gage section. The figure shows a moderate temperature increase during the uniform deformation (up to a strain of about 0.3 at 1.7 ms) and a significant temperature increase up to 300°C when the specimen fractures. The calculated values of the Taylor-Quinney coefficient as a function of strain from tests at different strain rates are shown in Figure 4. The figure shows values that range between 0.75 and 0.82 at strains larger than 0.15. There is no significant difference between the tests at the different strain rates. It should be pointed out that at small strains (less than 0.15) the calculated values are less accurate due to a larger tolerance in the temperature measurement.
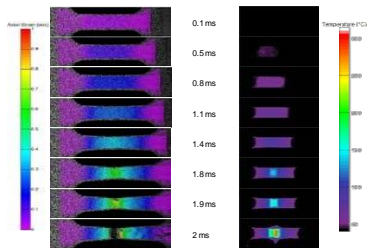
Fig. 2. Images of strain (left) and temperature (right)	Fig. 3. Strain and temperature history	Fig. 4. Taylor-Quinney coefficient
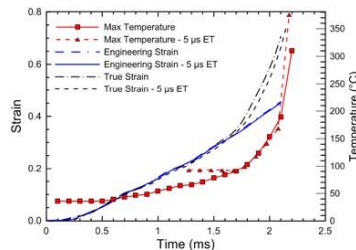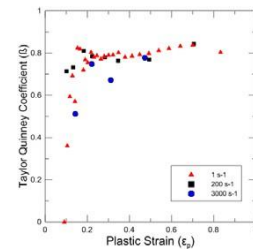
4. Conclusions

The Taylor-Quinney coefficient can be determined in tensile tests from simultaneous measurements of strain and temperature in the necking region. Results from testing AISI 316L austenitic stainless steel at strain rates of 1.0, 200 and 3,000 s^{-1} show an average value of 0.8. The research was supported by the U.S.A. Federal Aviation Administration, Grant No. 11-G-004.

5. References

[1] J.J. Mason, A.J. Rosakis, and G. Ravichandran (1994). On the Strain and Strain Rate Dependence of the Fraction of Plastic Work Converted to Heat: An Experimental Study Using High Speed Infrared Detectors and the Kolsky Bar *Mech. Mater.*, **17**, 135–145.

[2] J. Hodowany, G. Ravichandran, a Rosakis, and P. Rosakis (2000). Partition of Plastic Work into Heat and StoredEnergy in Metals, *Exp. Mech.*, **40**, 113–123.

[3] D. Rittel, L.H. Zhang, S. Osovski (2017). The dependence of the Taylor–Quinney coefficient on the dynamic loading mode , *J the Mech and Physics of Solids* **107**, 96–114.

[4] A. Gilat, J.D. Seidt, T.A. Matrka, K.A. Gardner (2019). A New Device for Tensile and Compressive Testing at Intermediate Strain Rat, *Exp. Mech.*, **59**, 725–731.

SEQUENT INVESTIGATION ON FIBER REINFORCED SELF-COMPACTING CONCRETE UNDER DYNAMIC LOADINGS

M. Pająk[1], J. Janiszewski[2] and L. Kruszka[2]
[1] *Silesian University of Technology, Department of Structural Engineering, Gliwice, Poland*
[2] *Military University of Technology, Warsaw, Poland*

1. Introduction

The concrete reinforced with the randomly distributed fibres is believed to be the best material that can effectively face the high strain rates coming from explosions or blasts. To properly design the concrete structure to withstand that kind of loadings the knowledge about the influence of the high strain rates on the mechanical parameters of concrete reinforced with fibres is crucial.

The paper display the sequent investigation of self-compacting concrete (SCC) reinforced with different types of fibres. The aim of the present research was to examine the strain rate sensitivity of the mixes with a use of the Split Hopkinson Pressure Bar (SHPB). One of the objectives was to reaffirm the correctness of the SHPB technique procedures adopted in the previous work to achieve the repeatable results.

2. Materials and experimental technique

The SCC specimens containing fibres coming from the end-of-life tires (R) and the combination of these fibres with the polypropylene ones (RPP) were experimentally tested. The applied volume ratio of recycled fibres was equal to 1.5% and 0.25% for polypropylene fibres. The compressive strength of the SCC matrix was equal to 57.7 MPa.

The SHPB used in the laboratory investigation was equipped with the bars with a diameter equal to 40 mm. The high and the diameter of the samples with cylindrical shape were equal to 40 mm. The specimens were tested under the range of strain rates from 138 s^{-1} to 194 s^{-1}. The appropriate pulse shaper was experimentally selected for each test to achieve the equilibrium stress state in the specimen. The pulse shaper diameter was equal to 8 mm and the high was equal to 1.5 mm or 2.5 mm depending on the applied pressure. The extensive description of the material of the specimen, their preparation and the testing procedure can be found in [1,2].

3. Results and discussion

The stress-strain curves obtained in the SHPB tests on the R-SCC and RPP-SCC mixes are presented in the Fig. 1. Three specimens were investigated under each strain rate. The average results were summarized in the Table 1. The results from SHPB tests presented in details in the previous work [1] are depicted with a dashed line in the Fig. 1. The average strain rate noted in these research were equal to 108 s^{-1} and 100 s^{-1} for R-SCC and RPP-SCC, respectively. The mechanical response of the material to quasi-static strain rate ($5.6 \cdot 10^{-5}$ s^{-1}) is marked with dotted lines. In the paper they were used for comparison purpose.

The mix containing one type of fibers (R-SCC) was investigated under two ranges of strain rates with the average: 173 s^{-1} and 193 s^{-1} (Fig. 1a). In the case the mix exhibit pronounced enhancement of compressive strength with the increase of strain rate. For the highest strain rate the DIF exceed 2.5. These results match very good to the results from the previous research [1]. The response of the RPP-SCC specimens the high strain rates is presented in the Fig. 1b. In the case of the increase of the compressive strength for the average strain rate equal to 144 s^{-1} was slightly higher than in the case

of strain rate equal to 100 s^{-1} acc. to [1]. In the research a very good repeatability of the results in every range of strain rate was obtained, what can be noted in the Fig. 1.

The value of compressive strength of the R-SCC and RPP-SCC specimens was comparable for average strain rates: 173 s^{-1} and 144 s^{-1}, respectively. Analyzing the Fig. 1a it can be concluded that the compressive strength of R-SCC would be probably lower for strain rate around 140 s^{-1}. Thus, the SCC containing both types of fibres was less strain rate sensitive than the mix where only one type was applied. It can be concluded that the increase of the amount of fibres, in the case of the PP fibres, caused the reduction of the strain rate sensitivity of the SCC.
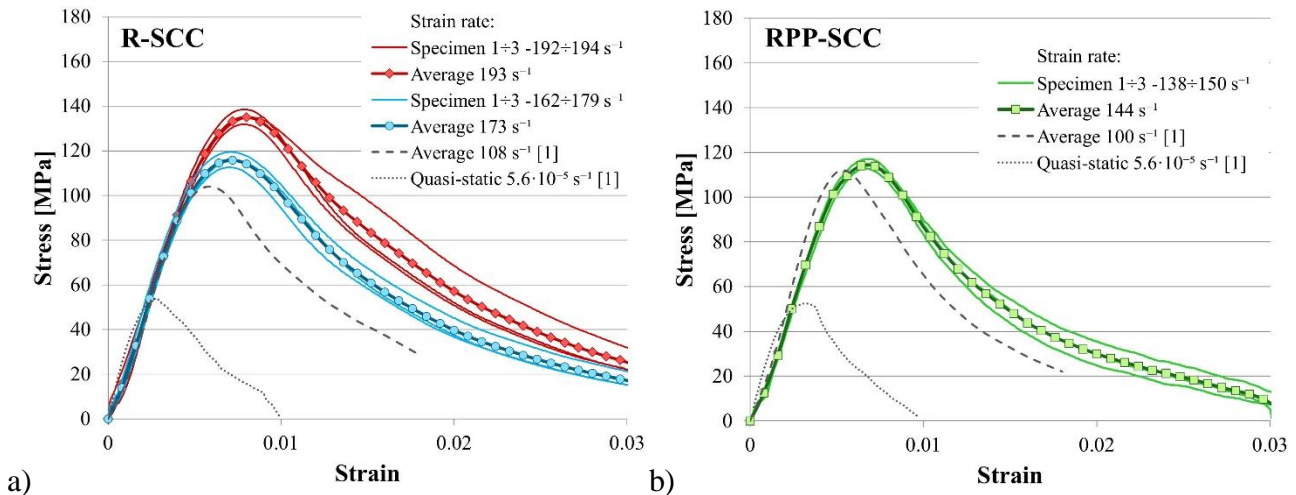
Fig. 1. Stress-strain curves obtained in the compression tests for R-SCC (a) and RPP-SCC (b) mixes

Mix	Strain rate [s^{-1}]	Dynamic compressive strength [MPa]	Strain at peak stress x10^{-3}	Quasi-static compressive strength [MPa]	DIF
R-SCC	173 (6)	115.8 (3)	0.0071 (3)	53.5 (2)	2.16
	193 (1)	135.1 (2)	0.0080 (3)		2.52
RPP-SCC	144 (4)	114.7 (2)	0.0068 (2)	52.7 (1)	2.17

Table 1. The average results from the SHPB compression tests

4. Results and discussion

The SHPB research on the SCC reinforced with different kinds of fibres revealed that:
- Fibre reinforced SCC was strain rate sensitive material;
- The strain rate sensitivity of the SCC reinforced with recycled fibres decreased with the addition of polypropylene fibres;
- The procedure of the performing of the SHPB tests (choosing the pulse shaper) is appropriate because it leads to achieving the repeatable test results.

The results are in a good agreement with the results from the previous research [1,2].

5. References

[1] M. Pająk, J. Janiszewski, L. Kruszka (2019). Hybrid fiber reinforced self-compacting concrete under static and dynamic loadings. *Concrete - Innovations in Materials, Design and Structures*, ed. W. Derkowski et al., Lausanne, 766-772.

[2] M. Pająk, J. Janiszewski, L. Kruszka (2019). Laboratory investigation on the influence of high compressive strain rates on the hybrid fibre reinforced self-compacting concrete. *Constr. Build. Mater.*, 227, 116687.

EXPERIMENTAL METHODOLOGY FOR THE CHARACTERIZATION OF THE STRAIN RATE EFFECT ON THE NONLINEAR DAMAGEABLE BEHAVIOR OF A CFRP

J. Berton[1,2], F. Coussa[1], J. Berthe[1,2], M. Brieu[3] and É. Deletombe[1,2]
[1] ONERA-The French Aerospace Lab, F-59014, Lille, France
[2] Univ Lille, CNRS, Centrale lille UMR CNRS 9013 - LaMCube
[3] ECST College, California State University, USA

CFRPs are now widely used in the aeronautic industry. Due to their optimale mass-stiffness ratio, they allow to lighten the structures while respecting design criteria. During crash or impact loading, aeronautical structures are subjected to strain rate gradients from quasi-static to dynamic. The CFRPs exhibit a nonlinear shear behavior. This nonlinear shear behavior is therefore dependent on the strain rate [1]. It is well known that the stress and strain at failure are both rate dependent [2]. However, to the author knowledge no study has been able to study the strain-rate effect on the nonlinear behavior up to failure**.** To improve the predictivity of numerical simulations it is required to characterize the strain rate effects on the nonlinear mechanical behavior. Especially the strain-rate effect on the damageable behavior and the nonlinear viscoelastic phenomena.

One of the solutions to characterize the nonlinear behavior of a material lies to the realization of incremental cyclic tests. These tests allow to assess the evolution of the elastic properties according to the degradation and the damage up to failure. The experimental protocol used for the dynamic characterization do not allow to directly perform incremental tests. The servo system in open loop of servo-hydraulic jacks does not allow to control test interruptions while loading. To interrupt dynamic tests, there are currently two main experimental approaches in the literature: the interruption in stress and the interruption in displacement.

The first interrupted tests on servo-hydraulic jacks have been proposed for glass fiber reinforced polymers with the stress interruption method [4]. A study has extended this application to a carbon fiber reinforced polymer composite [2]. Finally, the evolution of the different kinds of damage in a CFRP has been studied using a holding system [3]. Concerning the displacement interruption, a specific device has allowed the analysis of the effect of the strain rate on the nonlinear behavior of a glass fiber reinforced thermoplastic matrix [5]. This work allowed to assess the level of degradation of the same specimen, in particular thanks to its holding in displacement and to its possibility to reattach the device with the jack after the load.

It should be noticed that the shear tests are usually performed on [±45°] specimens. However, dynamic tests with [±45°] specimens are not standardized. To answer this lack of standardization, the specimen geometry used in this work respects the criteria of [6]. These criteria allow to guarantee the nonlinear behavior representativeness until failure of a standard [±45°] specimens. They are defined by the characterization of the geometrical parameters influence on the nonlinear behavior in shear and more particularly as a function of the irreversible strains.

The objective of the present work is to develop a methodology of interrupted displacement tests suited to CFRP and servo-hydraulic jacks. This methodology is based on the design of a test device allowing the interruption and the holding of the loading. As the load cell will never be dissociated from the device, the tests can be performed on the same test specimen. The developed protocol will allow to control and measure the decrease of the load of the specimen after the holding for the all incremental cyclic tests. To ensure the consistency of the protocol, it has been validated experimentally by verifying that the device did not perturb the measurement of the physical quantities in comparison with quasi-static conventional machine. In addition, it has been verified that the

specimen did not undergo compression following the elastic return introduced by the experimental methods of loading interruption on servo-hydraulic jacks.

Within this presentation, the possibilities that the device offers for the characterization of the nonlinear behavior of a CFRP will be highlighted. The analysis can be conventionally studied by the strain rate effect evaluation on the scalar damageable variable. Moreover, the device also allows to measure the decrease of the load phases and enable to evaluate the fibers reorientation during the hysteretic behavior by using a digital image correlation system.

Another advantage lies in the possibility to perform and analyze recovery tests after dynamic loading (*Figure 1*). These analyses have been performed by the measurement of the nonlinear strains recovery after a decrease of the load phase (nonlinear viscoelastic phenomena). The *Figure 1* depicts the comparison of nonlinear strains recovery for tests at 1m/s and at 6mm/min, for a same displacement increment fixed at $\delta = 1$ mm (*Figure 1a*), $\delta = 1.5$ mm (*Figure 1b*) and $\delta = 2$ mm (*Figure 1c*). These preliminary tests tend to illustrate that the strain rate seems to influence the strain retrieval ability of CFRPs after a nonlinear mechanical loading.

(The results presented in Figure 1 are preliminary work. It will be completed for the conference.)
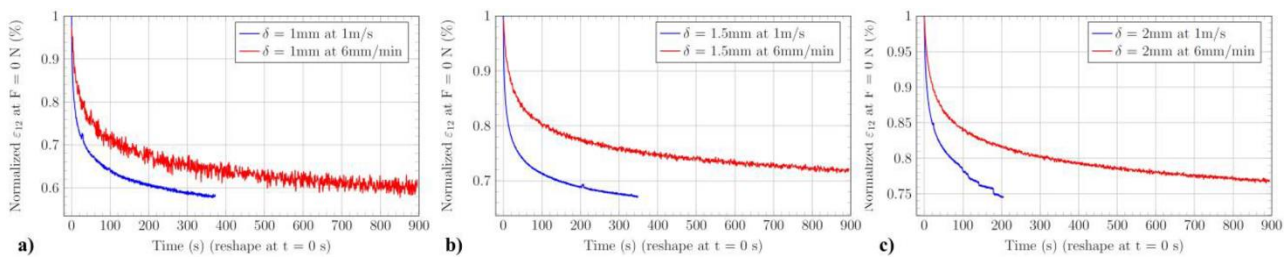
Fig. 1. Comparison of the nonlinear shear strains recovery of the T700/M21 CFRP
at 6mm/min and 1m/s loading for a) $\delta = 1$mm, b) $\delta = 1.5$mm and c) $\delta = 2$mm

References

[1] J. Berthe, et al., *Consistent identification of CFRP Viscoelastic models from creep to dynamics loading*, Strain Vol. 49, pp. 257-266, 2013.

[2] J. Fitoussi, et al., *Experimental methodology for high strain-rates tensile behaviour analysis of polymer matrix composites*, Composites Science and Technology, Vol. 65, Issue 14, pp. 2174-2188, 2005.

[3] G. P. Battams and J. M. Dulieu-Barton, *Data-rich characterisation of damage propagation in composite materials*, Composites: Part A, Vol. 91, pp. 420–435, 2016.

[4] J. L. Lataillade, et al., *Effects of the intralaminar shear loading rate on the damage of multi-ply composites*, Int. J. Impact Eng Vol. 18, No. 6, pp. 679 699, 1996.

[5] F. Coussa, et al., *A consistent experimental protocol for the strain-rate characterization of thermoplastic fabrics*, Strain, 53(3), p. e12220, 2017.

[6] J. Berton, et al., *Definition of ±[45°]ns specimen geometry to characterize CFRP nonlinear shear behavior in dynamic loading*, Composites Communications, Vol. XX, pp. XX, 2021. (Submitted)

CHARACTERISING THE MECHANICAL PROPERTIES OF SHORT POLYETHYLENE FIBRE AND BIOGLASS REINFORCED SILICONE COMPOSITE SKIN SIMULANTS

A. Chattrairat[1], R. Das[1], P. Tran[1] and S. Aimmanee[2]
[1] *RMIT University, Melbourne, Australia*
[2] *King Mongkut's University of Technology Thonburi, Bangkok, Thailand*

1. Abstract

To develop equivalent mechanical properties and biological structure similar to the human scalps, the present study proposes a novel silicone-based composite skin simulant development. This utilises randomly distributed short polyethylene (PE) fibres and bioglass (BG) particles as reinforcements. The composites with a range of (1 to 5%) filler weight concentrations were characterised with four quasistatic tests - tensile, compressive, hardness, and stress relaxation. Experimental results highlight that the polyethylene fibres have the advantage of enhancing the elastic modulus up to 44% when using 5% filler weight fraction, and bioglass can help maintain hardness and viscoelastic properties. The study has established that the proposed composite skin simulants are suitable as a human scalp simulant than pure silicone.

2. Introduction

In the forensics field, silicone elastomers are widely adopted by scientists as artificial skins to avoid ethical concerns arising from human cranial impact experiments [1]. Although silicone elastomer and human skin constitutive responses are comparable [2], it is still challenging to fabricate an ideal silicone skin simulant. The integration of additives into the silicone elastomer can enhance its mechanical behaviour and other desired functional properties. Nonetheless, the primary interest of most silicone-based composite studies is to maximise the functional properties rather than directly mimick the biological structure and mechanical behaviours of the human skin.

Short polyethylene (PE) fibres possess comparable length, diameter, and elastic modulus to the collagen fibres in human skin [3] and can also strengthen the mechanical properties of the matrix. Bioactive glass (BG), a composition of 45% by weight of silica, is a particle that is believed to increase the stiffness and maintain the hardness of the silicone [4]. The characterisation of both composites is yet to be comprehensively determined, particularly their hardness and viscoelastic properties. The present study investigates the influences of short PE fibres and bioglass particles, with different filler concentrations (1-5%), in the platinum silicone on the tensile, compressive, hardness, and viscoelastic properties via experiments to develop suitable skin simulant candidates.

3. Methodology

Short high-density PE fibres with a diameter of 15 μm and a length of 0.7 mm were treated with $KMnO_4$ solution. PE fibres and Bioactive glass particles (45% SiO_2, 24.5% CaO, 24.5% Na_2O, and 6% P_2O_5) with two different diameters of 10 and 53 μm were mixed randomly with the platinum silicone in a centrifugal mixer at 2000 rpm for 5 minutes. Afterwards, the skin simulants were processed with compression moulding and cured for 12 hours at room temperature. The composites contain the filler weight fractions of 1%, 3% and 5% of the total weight. The hybrid composite specimens were also fabricated by including both fillers. Tensile, compressive, hardness, and stress relaxation tests were performed with five samples in each category according to ASTM standards of D412 at 0.012 s-1, D575 at 0.016 s-1 and 0.48 s-1, D2240, and D6147, accordingly.

4. Results

Figure 1a reveals that the presence of both additives increases the elastic moduli up to 44% and 22% for the treated PE fibre and bioglass (both 5%) reinforcement compositions, respectively. Smaller particle size leads to greater tensile strength and modulus. Due to improved interfacial interlocking, treated PE fibres produce a greater elastic modulus than that by the untreated fibres. While the short PE fibres significantly influence the hardness growth with 7% per 1% filler concentration, bioglass can maintain the hardness of its composite within 5% from the baseline silicone. In the compressive tests, the stiffness of the hybrid composite has a very low sensitivity to the filler type, but it is highly sensitive to the filler weight fraction. Composites with both types of inclusions cause the reductions of force decay. In Figure 1b, tensile properties of the silicone can be improved by PE fibres to make it closer to the middle range of human scalps, which would be the primary interest in cranial injury study using artificial scalp simulants.
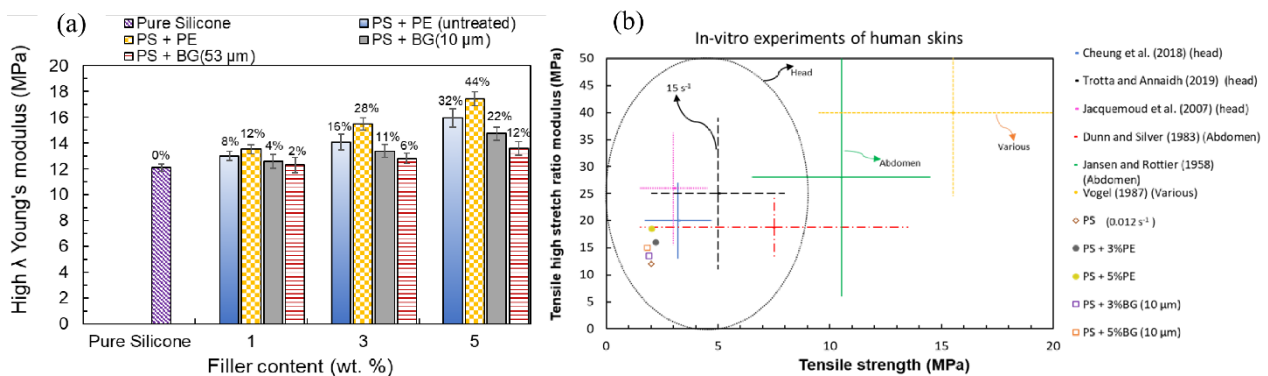
Fig. 1. (a) High stretch ratio ($\lambda > 1.6$) Young's modulus of the three types of composites skin simulants at different filler weight concentrations, and (b) comparisons of tensile strength and high stretch ratio modulus of the proposed composites with studies from the literature

5. Conclusions

The proposed PE fibres and bioglass integrated silicone composites generate more potent and suitable overall mechanical responses as compared to the human skin and scalp than the pure platinum silicone. The characterised outcomes can be adopted for physical and numerical cranial models in the forensic field.

6. References

[1] S. C. Taylor and E. F. Kranioti (2018). Cranial trauma in handgun executions: Experimental data using polyurethane proxies, *Forensic Sci Int*, **282**, 157-167.

[2] L. Meunier, G. Chagnon, D. Favier, L. Orgéas, and P. Vacher (2008). Mechanical experimental characterisation and numerical modelling of an unfilled silicone rubber, *Polymer Testing*, **27**, 765-777.

[3] M. P. Wenger, L. Bozec, M. A. Horton, and P. Mesquida (2007). Mechanical properties of collagen fibrils, *Biophysical journal*, **93**, 1255-1263.

[4] N. H. Cohrs, K. Schulz-Schönhagen, F. Jenny, D. Mohn, and W. J. Stark (2017). Bioactive glass containing silicone composites for left ventricular assist device drivelines: role of Bioglass 45S5® particle size on mechanical properties and cytocompatibility, *Journal of Materials Science*, **52**, 9023-9038.

THE EFFECT OF CARBON BLACK CONTENT ON VISCOELASTIC PROPERTIES OF VULCANIZED NATURAL RUBBER

S. Bandyopadhyaya, R. Kitey and C.S. Upadhyay
Aerospace Engineering Department, IIT Kanpur, Kanpur, India

Abstract

The effect of filler content on viscoelastic properties of carbon black filled vulcanized natural rubber is studied. The filled rubber specimens are subjected to dynamic mechanical loading with the temperature varying from -80°C to 100°C. While the storage modulus of unfilled and filled rubber materials remains nearly the same in glassy state, the glass transition temperature significantly increased in the case of the latter. The data also indicates that the rubbery modulus of filled rubber increases with increasing CB content. The loss factor data suggest that the damping characteristics of filled rubber decrease with increasing CB content.

1. Introduction

Natural rubber (NR) reinforced with different grades of carbon black (CB) are extensively used in modern industries owing to their deformability and damping characteristics. Among them, high abrasion furnace (HAF) CB of grade N330 is used for tyres, O rings and conveyor belts due to their good tear-resistance and energy absorption properties [1]. The mechanical properties of filled rubber have been of great interest for a long time due to its hyperelastic [2] and viscoelastic [3] nature. The viscoelastic behaviour is studied either by conducting creep and relaxation experiments or by obtaining a steady-state response by subjecting the material to oscillatory loading. Often for the latter mode of study, Dynamic Mechanical Analyzer (DMA) is used to assess the viscoelastic response of the rubbery materials. DMA helps in the measurement of storage modulus and loss modulus. While storage modulus corresponds to the elastic behaviour of the material, loss modulus indicates the dissipation associated with the same. Temperature sweep and isothermal frequency sweep can be carried out in the DMA to analyze the variation of the properties of the vulcanizates. The rubbery storage modulus and the loss tangent (tan δ) have been used to investigate the molecular weight across cross-links and damping characteristics of polymers, respectively [4]. The thermorheological behaviour of vulcanized NR, across a temperature and frequency range, has been documented with the help of these experiments [5]. However, the effect of the presence and proportion of CB on the viscoelastic properties of vulcanized NR compared to the properties of an unfilled NR remains of interest. In this study, NR filled with CB at four different proportions was subjected to temperature sweep experiments in DMA at a single frequency, in tensile loading. The materials' response was recorded, and the effect of CB content on the variation of viscoelastic parameters such as storage and loss moduli and glass-transition temperature was analyzed.

2. Material and experiment description

Vulcanized NR sheets filled with N330 grade CB were obtained from Supreme Rubber Industries, Coimbatore. The CB was reinforced into the NR with 0, 20, 40, and 60 PHR. The associated sheets are referred to as VR00, VR20, VR40 and VR60, respectively. The test specimens are prepared by cutting 2-mm-thick sheets into 30 mm x 10 mm rectangular strips with a gauge length of 30 mm for the experiments. A dynamic mechanical analyzer Metravib DMA+ with 100 N loadcell is employed to conduct temperature sweep experiments. The specimens were loaded in tension at 1 Hz with 80 μm

static displacement (0.27% strain) in combination with an excitation displacement of amplitude 20 μm (0.07% strain). The temperature was swept from -80°C to 100°C at 2°C/min rate, and storage modulus (E'), loss modulus (E'') and loss factor (tan δ) are recorded as a function of temperature.

3. Results and discussion

The storage modulus as a function of temperature is plotted in Fig. 1(a). While all test specimens exhibit nearly the same storage modulus in the glassy state, their glass transition behaviour significantly differs in the presence of the CB fillers. In the case of unfilled NR, the glass transition process begins at -65°C, whereas this transition in the filled rubber specimens commences at -45°C.

The plots show that the storage modulus in the rubbery plateau increases with increasing CB content. The increase in rubbery modulus is significantly high when the CB content is increased from 20 PHR to 40 PHR. The plots show that the CB reinforcement significantly increased the glass transition temperature (T_g) of NR, but its proportion appears to have negligible influence on T_g.
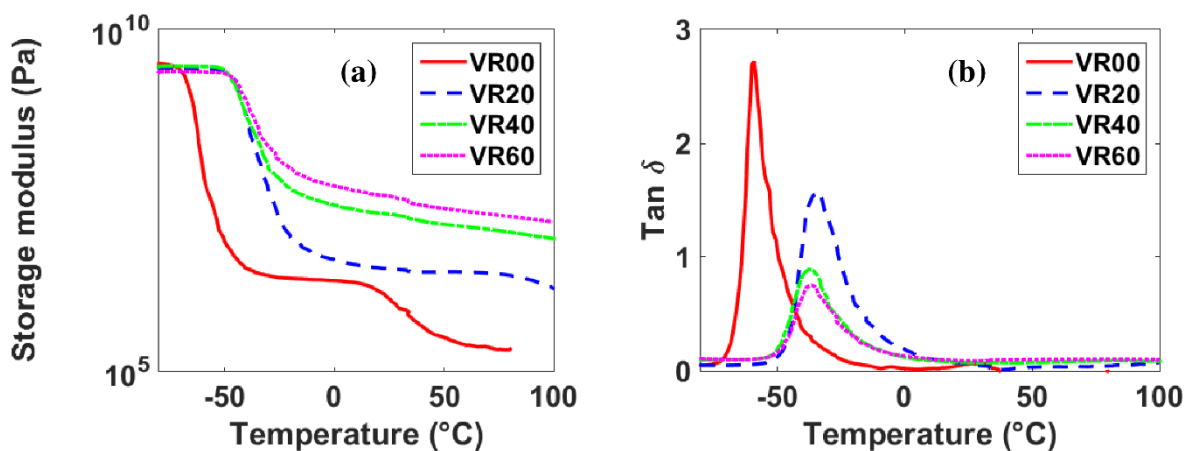
Fig. 1. (a) Variation of storage modulus and (b) tan δ with temperature for NR

The variation of tan δ with temperature is plotted next in Fig. 1(b). While the unfilled NR shows tan δ peak at -67°C, the peaks associated with VR20, VR40 and VR60 specimens are observed to be at -47°C. The decreasing peak value of tan δ with an increase in the filler content indicates decreasing damping characteristics of the filled rubber.

4. References

[1] M. Bhattacharya and A. K Bhowmick (2010). Synergy in carbon black-filled natural rubber nanocomposites. Part I: Mechanical, dynamic mechanical properties, and morphology, *J.Mater. Sci.*, **45**, 6126-6138.

[2] M. Mooney (1940). A Theory of Large Elastic Deformation, *J. Appl. Phys.*, **11**, 582-592.

[3] J. Lubliner (1985). A Model of Rubber Viscoelasticity, *Mech. Res. Commun.*, **12(2)**, 93-99.

[4] R. Rahul and R. Kitey (2016). Effect of cross-linking on dynamic mechanical and fracture behaviour of epoxy variants, *Compos. B*, **85**, 336-342.

[5] X. Hu, W. Luo, X. Liu, M. Li, Y. Huang and J. Bu (2013). Temperature and frequency dependent rheological behaviour of carbon black filled natural rubber, *Plast. Rubber Compos.*, **42**, 416-420.

EFFECT OF MATRIX MODIFICATION ON POST IMPACT FLEXURAL CHARACTERISTICS OF GLASS FIBER LAMINATED COMPOSITE

M.K. Singh and R. Kitey

Indian Institute of Technology Kanpur, Kanpur, Uttar Pradesh, India

Abstract

For enhancing impact characteristics of glass fiber laminated composites, chopped fiber reinforced epoxy system is used as the matrix material. The laminates are machined into beam specimens and impacted at two different energy levels. The data suggest that the impact resistance as well as the elastic response of the laminates increase with increasing short fiber content. Flexural tests are performed on the impacted specimens to study their post-impact residual characteristics. The flexural-after-impact tests exhibit higher post-impact flexural modulus and strength in the case of chopped fiber reinforced laminates, especially at higher impact loading case. Microscopic analysis of the impacted sample shows lesser damage in the reinforced laminates as compared to the unreinforced ones.

1. Introduction

Glass fiber laminates have become key components of aerospace and high-performance automotive structures due to their high specific strength and stiffness. Besides being cost effective they are also corrosion resistant and show good dielectric properties but their lower out-of-plane properties have always been a cause of concern. While, the laminates in general are susceptible to impact damage, the low-velocity impact needs special attention because often failure remains obscured in between the laminae which significantly deteriorates load carrying capacity of the laminates. Among various techniques adopted in past to enhance the impact characteristics of the laminates [1-2], employing chopped fiber reinforced matrix to prepare the laminates is somewhat difficult because of the processing complexities. Compression after impact (CAI) test is commonly used method to get post-impact residual properties of the laminates [1]. The method requires a large robust setup with precise data acquisition system. Recently, a few researchers have adopted a simpler flexural after impact (FAI) technique as an alternative to CAI [2]. In this study, the effect of chopped fiber reinforcement on the impact response and post-impact residual properties of laminated composites is analysed by employing FAI protocol.

2. Fabrication and experimental techniques

Sixteen ply bi-directional plain-weave glass fabric laminates are fabricated where 1/4" long chopped glass fiber reinforced epoxy matrix is used as the matrix material. A requisite amount of chopped fibers are added into the Diglycidyl Ether of Bisphenol-A (DGEBA) resin. The fillers are uniformly dispersed into the resin by mechanical stirring and sonication. Methyl Tetra Hydrophthalic Anhydride (MTHPA) hardener is then mixed in 1:1 resin/hardener ratio with a small quantity of 2,4,5-tris[(dimethylamino)methyl]-Phenol accelerator. Thus developed matrix system is used for preparing laminates by hand lay-up technique, followed by curing them in vacuum-assisted hot press. In this study three different matrix systems are used, unfilled epoxy and the epoxy embedded with chopped fibers at 2% and 4% volume fractions, which are referred as 'UR', '2% R' and '4% R', respectively.

Beam specimens of dimension 110 mm × 16 mm × 4.5 mm are machined form the cured laminates and tested under low velocity impact in INSTRON CEAST 9340 by following ASTM D7136

standards [4]. The specimens were constrained in a 75 mm diameter circular clamp and impacted at 7.5 J and 12.5 J energy levels. Force histories are acquired from instrumented tup at 100 kHz. Next, quasi static flexural tests on pristine and impacted samples are conducted in symmetric four-point bend configuration [ASTM D6272] with subjecting the impacted face under flexural tension. The force vs. displacement data obtained from the tests are analysed to characterize post-impact residual strength and the residual elastic modulus of the laminate.

3. Results and discussion

Upon subjecting the test specimens to 12.5 J impact, the energy absorption in the specimens is plotted with time in Fig. 1 (a). After attaining the maximum value, the curves monotonically decrease until a plateau value is attained, which signifies the energy dissipated in the failure process. The elastic energy stored in the laminate system is determined by the difference between the maximum energy and the dissipated energy. From the plots it is evident that with increasing chopped fiber content, the elastic energy in the laminate increases whereas the energy available for failure decreases. The flexural stress vs. strain curves associated to the specimens impacted with 12.5 J energy are plotted in Fig. 1(b). For comparison the stress-strain curve associated to the pristine specimen is also included in the figure. The plots show that the residual flexural modulus and strength of the laminates increase with increasing filler content. Interestingly, the laminate prepared with 4% filler reinforcement exhibits nearly the same flexural strength and stiffness as noted in the case of pristine specimen. Microscopic failure analyses performed on the test specimens (not included here for brevity) correlates well with the experimental measurements.
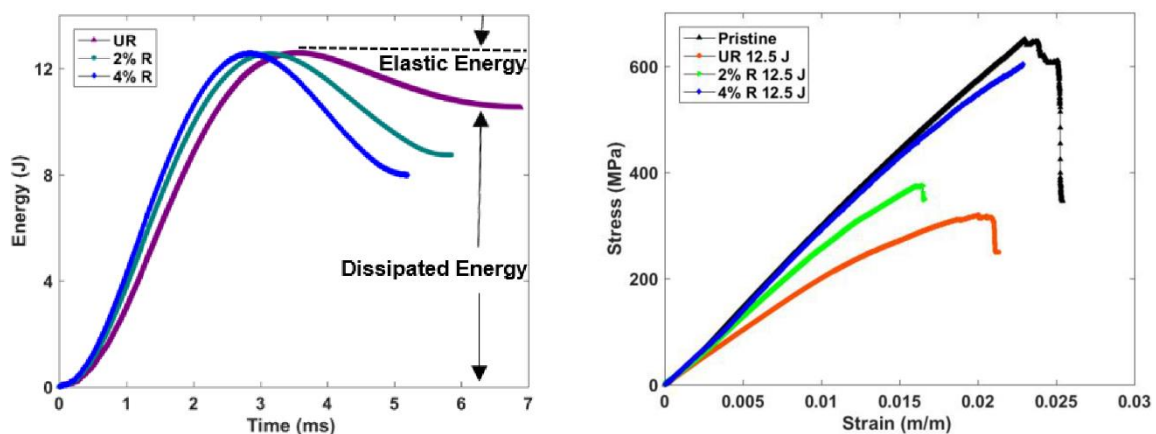
Fig. 1. (a) Energy-time plot of beam impact at 12.5 J (b) flexural stress-strain curves

4. References

[1] W. J. Cantwell, and J. Morton (1991). The impact resistance of composite materials - a review, *Compos.*, *22*(5), 347-362.

[2] B. Yuan, M. Ye, Y. Hu, F. Cheng, and X. Hu (2020). Flexure and flexure-after-impact properties of carbon fibre composites interleaved with ultra-thin non-woven aramid fibre veils, *Compos. - A: Appl. Sci. Manuf.*, *131*, 105813.

[3] ASTM D7136/D7136M-12 (2012). Standard test method for measuring the damage resistance of a fiber-reinforced polymer matrix composite to a drop-weight impact event.

[4] ASTM D6272-10 (2010). Standard Test Method for Flexural Properties of unreinforced and reinforced Plastics and Electrical Insulating Materials by Four-Point Bending.

SHEAR BANDING - A KEY MECHANISM CONTROLLING VISCOPLASTIC FLOW. I. DEVELOPMENT OF CONSTITUTIVE RELATIONS

R.B. Pęcherski and Z. Nowak
Institute of Fundamental Technological Research, Warsaw, Poland

It was recently shown that two types of shear banding mechanisms control viscoplastic flow in any solids.

- The instantaneous multiscale shear banding system formed by micro-shear bands of the thickness of the order of 0.1 μm, the clusters of micro-shear bands producing the discontinuity of the microscopic velocity field vm and the macroscopic zone of shear strain localization spreading through the representative volume element (RVE) of a polycrystalline metallic solid. In Pęcherski [1], [2], [4], a new concept of the RVE with strong singularity was introduced, and the instantaneous shear banding contribution function was defined.

- The cumulative organization of micro-shear bands is based on the accumulation of the particular contribution of micro-shear bands forming clusters in specific volumes contained in RVE. The micro-shear bands gradually contribute to such a case in the development and growth of micro-shear bands clusters. Finally, the clusters accumulate in the macroscopic localization zone spreading across the macroscopic volume of considered material. Such deformation mechanism is observed in the inelastic deformation of gum metals, where the giant faults play the role of elementary micro-shear bands. Also, micro-shear bands play the local shear transformation zones (STZ) in amorphous solids such as glassy metals or polymers. Finally, the phenomenological viscoplasticity model introduces the cumulative shear banding contribution function, Nowak et al. [3] and Pęcherski [4].

Both types of the abovementioned shear banding mechanism often appear with variable contributions during the deformation processes. Such a situation can occur in polycrystalline metallic solids, subjected to the deformation with a distinct change of deformation or loading paths. Also, materials that reveal the hybrid structure characterizing with amorphous, ufg and nanostructural phases are prone to the mixed shear banding responsible for inelastic deformation. Finally, some recent results are discussed and confronted with earlier approaches related to the instantaneous shear banding contribution function.

References

[1] R.B. Pęcherski (1997). Macroscopic measure of the rate of deformation produced by microshear banding, Arch. Mech., 49, 385–401.

[2] R.B. Pęcherski (1998). Macroscopic effects of micro-shear banding in plasticity of metals, Acta Mechanica, 131, 203–224.

[3] Z. Nowak, P. Perzyna and R.B. Pęcherski (2007). Description of viscoplastic flow accounting for shear banding, Archives of Metallurgy and Materials, 52, 217–222.

[4] R.B. Pęcherski (2022). Viscoplastic Flow in Solids Produced by Shear Banding, John Wiley & Sons Ltd.

SHEAR BANDING - A KEY MECHANISM CONTROLLING VISCOPLASTIC FLOW. II. NUMERICAL SIMULATIONS OF SOME EXPERIMENTALLY PERFORMED PROCESSES

Z. Nowak and R.B. Pęcherski
Institute of Fundamental Technological Research, Warsaw, Poland

1. Introduction

The metallic materials undergo various manufacturing operations such as forming, forging, extrusion, machining, and cold working. Experimental investigations of the behaviour of high strength metallic materials under quasistatic and dynamic loading conditions related to microscopic observations show that in many cases, the dominant mechanism of plastic strain is multiscale development of shear deformation modes–called shear banding [1]. The Viscoplasticity model with the overstress function proposed earlier by Perzyna [2] was extended to describe the new mechanism of inelastic deformation [1, 3, 4].

The paper aims to study the application of the new description of viscoplastic deformation, which accounts for the observed shear banding phenomena. The numerical simulations of the deformation processes of metallic specimens in the channel-die test are performed.

2. The channel-die test

The compressive loading in the channel-die test was carried on the OFHC copper at strain rates of 10^{-3} s^{-1} in the loading direction and described by Bronkhorst et al. [5], Kalidindi et al. [6]. In the experiment, all contacting surfaces of the specimen and the die were ground smooth and well lubricated. Two types of sample shapes were tested. One type of specimen was machined in a rectangular block of dimensions 9.52 mm in height (loading direction), 26.4 mm and 23.5 mm in the other two directions [5]. The another, specimen was machined in the form of a prism that had the following initial dimensions: height (compression direction), 13.97 mm; length (flow direction), 23.5 mm; width (constrained direction), 26.4 mm. Plane strain can be applied almost perfectly, but friction, which extends to the lateral faces of the sample, is likely to play a more critical role. Thin Teflon films or "classical" lubricants such as graphite or boron nitride powders can lubricate the sample surfaces, leading to a quasi-zero friction coefficient.

The paper aims to interpret the channel-die compression tests at room temperature, where friction effects can be neglected. Isotropic viscoplastic incompressible materials submitted to large strains are considered. The constitutive viscoplastic model accounting for micro-shear bands of OFHC copper is applied. The compression test is carried out at a constant equivalent strain rate of 10^{-3} s^{-1}. A power law describes the flow stress of the material in the overstress function Perzyna type viscoplastic equation. The material parameters obtained for the annealed OFHC copper used in Kalidindi et al. [6] experiments are applied in the simulation.

3. Numerical simulations and identification of the model parameters

The ABAQUS software performed the numerical simulations of the channel-die quasistatic and dynamic compression tests. Due to the symmetry of the experimental setup, only half of the geometry was modelled. The vertical plane (walls of the channel) and one horizontal plane (bottom of the channel) represent the channel-die device. These two planes are embedded by their reference nodes, whose degree of freedom is set to zero. The tool is represented by an additional horizontal

plane whose reference node controls the sample's nominal strain and nominal strain rate. The planes representing the walls of the channel and the tool are rigid since the elastic deformation of the mechanical device can be neglected. The specimen is meshed using C3D8R elements (8 integration points). The power hardening law described the material's stress-strain curve [1]. A global surface contact was defined with the option available in the ABAQUS. The action of the tools is simulated by the definition of the contact pairs between the specimen surface and the vertical and horizontal surfaces. The friction coefficient was chosen equal to zero for all the friction surfaces, although a specific coefficient can be applied to the various boundaries of the specimen.

The model was tested and validated for the homogeneous case (no friction on all the surfaces) and the conditions that lead to symmetric law (no friction on the lateral surfaces and friction on the horizontal surfaces). This result indicates and justifies the possible assumption of local plane strain. The basic idea of the identification procedure was to determine all material constants of the shear banding influence function using the inverse solution of the boundary value problem simulating the compression test process numerically. The least-squares method requires the residual sum in nominal stress between the experimental observations, σ_{Exp}, and model results, σ_{Model}, to be minimised. Finally, it implies that the proposed model of rate-dependent plasticity can be entirely calibrated by minimising the residual function $F(\sigma_{eqv}^{pl})$, which refers to the residual of the constitutive model and the experimental data as a function of equivalent plastic strain σ_{eqv}^{pl}.

4. Conclusions

This paper presents the description of the rate-dependent plastic behaviour of polycrystalline copper OFHC and the new feature of our proposition to account for shear banding. The multiscale shear band formation mechanisms are responsible for accommodating the inelastic deformation. Therefore, the proposed description can also be applied to other ufg, nc-metals, and harddeformable materials. Finally, the identification of constitutive relations of viscoplastic flow was made for *fcc* metal. Finally, the derived constitutive equations will be applied to solve an inverse problem and the verification behaviour of such materials using other independent experimental tests.

5. References

[1]   Z. Nowak, R.B. Pęcherski (2002). Plastic Strain in Metals by Shear Banding. I: Numerical Identification and Verification of Plastic Flow, Arch. Mech., **54**, 621–634.
[2]   P. Perzyna (1966). Fundamental Problems in Viscoplasticity, Adv. Mech., **9**, 243–377.
[3]   R.B. Pęcherski (1992). Modelling of Large Plastic Deformation Produced by Micro-Shear Banding, *Arch. Mech.*, **44**, 563–584.
[4]   Z. Nowak, P. Perzyna and R.B. Pęcherski (2007), description of viscoplastic flow accounting for shear banding, *Arch. Metall. Mat*, **52**, 217–222.
[5]   A. Bronkhorst, S.R. Kalidindi and L. Anand (1992), Polycrystalline Plasticity and the Evolution of Crystallographic Texture in FCC Metals, Phil. Trans. R. Soc. Lond. A, **341**, 443–477.
[6]   S.R. Kalidindi, C.A. Bronkhorst and L. Anand (1992). Crystallographic texture evolution in bulk deformation processing of fcc metals, *J. Mech. Phys. Solids*, **40** (3), 537–569.

4. Innovative Testing Methods

for Cementitious Materials and Structures

THREE-MINUTES CREEP TESTS AND ULTRASONIC EXPERIMENTS OF CEMENTITIOUS MATERIALS AT EARLY AND MATURE AGES

B.L.A. Pichler, J. Eberhardsteiner and Ch. Hellmich
Institute for Mechanics of Materials and Structures
TU Wien - Vienna University of Technology, Austria

1. Three-minutes creep tests and evaluation protocol

Three-minutes creep tests provide quantitative insight into the elastic stiffness and the nonaging creep properties of specific microstructures of cementitious materials [1]. Performing such ultrashort tests once every hour is a well-suited approach for characterizing cementitious materials at early ages, because the duration of the experiments is so short that the ongoing chemical reaction between cement and water cannot make a significant progress, while one hour is enough such that the microstructure changes measurably [1].

Significant creep deformation develops already during the initial loading ramp which is used to reach the desired load level for the creep test. The reason for this is that the creep function starts, in good approximation, with an infinite slope. Thus, a very short period of time is sufficient for the development of significant creep deformation [1].

2. A validated multiscale creep model for hydrating cementitious materials

Several hundreds of three-minutes creep tests were performed on hydrating cement pastes during the first week after production [1]. The tested materials differed in the initial water-to-cement mass ratio. The collected experimental data were used to identify the isochoric creep constants of microscopic hydrate gel needles [2]. The developed model is capable of predicting the creep activity of a thirty-years-old cement paste, in a thirty-days-long creep test [2].

Extending the model to concrete, a water migration process was found [3]. During mixing of fresh concrete, oven-dried aggregates take up a part of the mixing water, such that the effective water-to-cement mass ratio of the cement paste is smaller than expected based on the mix proportions. The uptaken water is later sucked back to the cement paste matrix, driven by selfdesiccation [3]. Notably, the model for cement paste was also extended to polymer-modified cement pastes [4,5].

3. Model-Code-inspired formulas for the early-age creep evolution of modern concretes

Hourly-repeated three-minutes creep experiments were also carried out in order to characterize several concretes which are used in Austria in the field of bridge engineering. In addition, standard tests regarding the evolution of the compressive strength and Young's modulus were performed during the first 28 days after production.

The test database allowed for assessing and improving formulae of the *fib* Model Code 2010, see [6]. This includes formulae for (i) the evolution of the uniaxial compressive strength during the first four weeks after production, such that the 28-days-value is reached in the end, (ii) the correlation between the 28-days-values of the uniaxial compressive strength and Young's modulus, as well as (iii) the evolution of Young's modulus during the first four weeks after production, such that the 28days-value is reached in the end. In addition, formulae were developed for (i) the correlation between the 28-days-values of the uniaxial compressive strength and the creep modulus, and (ii) the evolution of the creep modulus during the first four weeks after production, such that the 28-days-value is reached in the end. It was found that the creep modulus increases significantly slower

compared to Young's modulus and the compressive strength. This implies that concretes, which appear to be already quite mature in terms of their strength, are still highly creep active [6]. This finding is relevant for construction methods in which concrete is loaded at early material ages.

4. Identification of the modulus of elasticity from quasi-static and ultrasonic experiments

The "static" loading modulus is smaller than the modulus of elasticity. The latter is smaller than the "dynamic" modulus obtained from ultrasonic testing. Provided that tests are evaluated carefully, the same modulus of elasticity can be determined from both three-minutes creep tests and ultrasonic pulse velocity experiments [7]. As for the three-minutes creep tests, it is essential to consider that significant creep strains develop already during the loading, see above. As for the ultrasonic experiments, it is essential that the separation-of-scales requirement is satisfied and that the correct effective mass density of the material is determined [7].

5. Conclusion

Hourly-repeated three-minutes creep tests have led to valuable progress in fundamental and applied science of cementitious materials, both at early and mature material ages.

6. References

[1] M. Irfan-ul-Hassan, B. Pichler, R. Reihsner, and Ch. Hellmich (2016). Elastic and creep properties of young cement paste, as determined from hourly repeated minute-long quasistatic tests, *Cem. Con. Res.*, **82**, 36-49; http://doi.org/f8hgjp

[2] M. Königsberger, M. Irfan-ul-Hassan, B. Pichler, and Ch. Hellmich (2016). Downscaling based identification of nonaging power-law creep of cement hydrates. *J. Eng. Mech.*, **142**, 04016106; http://doi.org/f9cxv4

[3] M. Irfan-ul-Hassan, M. Königsberger, R. Reihsner, Ch. Hellmich, and B. Pichler (2017). How Water-Aggregate Interactions Affect Concrete Creep: Multiscale Analysis. J. Nanomech. Micromech., 7, 04017019; http://doi.org/cqq9

[4] L. Göbel, M. Königsberger, A. Osburg, and B. Pichler (2018). Viscoelastic behavior of polymer-modified cement pastes: Insight from downscaling short-term macroscopic creep tests by means of multiscale modeling. *Appl. Sci.*, **8**, 487; http://doi.org/crnk

[5] L. Göbel, A. Osburg and B. Pichler (2018). The mechanical performance of polymermodified cement pastes at early ages: Ultra-short non-aging compression tests and multiscale homogenization. *Constr. Build. Mat.*, **173**, 495-507; http://doi.org/crnj

[6] M. Ausweger, E. Binder, O. Lahayne, R. Reihsner, G. Maier, M. Peyerl, and B. Pichler (2019). Early-Age Evolution of Strength, Stiffness, and Non-Aging Creep of Concretes: Experimental Characterization and Correlation Analysis, *Mat.*, **12**, 207; http://doi.org/czmn

[7] E. Binder, M. Königsberger, H. Mang, C. Hellmich, and B. Pichler (2019) Temperaturedependent non-dissipative (elastic) and dissipative (viscous) deformation of cement paste, Manuscript in preparation for submission to *Cem. Con. Res.*

A COMPREHENSIVE EXPERIMENTAL PROGRAM FOR DETERMINING THE TIME-DEPENDENT MATERIAL BEHAVIOR OF SHOTCRETE AT EARLY AGE

S. Smaniotto[1], M. Neuner[1], T. Cordes[2] and G. Hofstetter[1]
[1] Unit of Strength of Materials and Structural Analysis, University of Innsbruck, Austria
[2] Brenner Base Tunnel BBT-SE, Innsbruck, Austria

1. Introduction

The Brenner Base Tunnel (BBT) is a priority European infrastructure project under construction. From 2028 the tunnel will be an essential part of the European high-speed railway corridor from Helsinki (Finland) to La Valletta (Malta) [1]. The tunnel system of the BBT comprises the total length of 230 km with an overburden of up to 1800 m. It consists of two main tubes complemented by exploration, emergency, ventilation and access tunnels. About half of the total tunnel length is driven by the drill and blast method using shotcrete linings as a securing measure.

Shotcrete linings of deep tunnels may be heavily loaded at early age, resulting in high stresses in the lining, potentially accompanied by the development of cracks. Hence, the temporal evolution of the shotcrete properties, like the Young's modulus, the compressive and tensile strength as well as the shrinkage and creep behavior, are required for determining the limit state of such linings from early ages up to the intended lifetime of 200 years. This holds especially in the case of permanent single shell linings, which are used for tunnels with lower requirements (e.g. exploration and emergency tunnels).

2. Experimental program

Motivated by the progress in shotcrete technology, which resulted in modified shotcrete compositions with enhanced material behavior, a new experimental program was designed for determining the time-dependent material behavior of a modern shotcrete employed at the BBT. It is designated as SpC25/30/(56)/J2/GK8 according to the Austrian guideline for shotcrete [2]. SpC25/30/(56) characterizes the shotcrete strength class, J2 the early age strength class according to [3], and GK8 the maximum aggregate size of 8 mm. The composition is typical for commonly employed modern shotcrete compositions used in the framework of the New Austrian Tunneling Method.

The first part of the experimental program [4] comprised tests at early age (starting 8 h after spraying the specimens) for determining the evolution of (i) the Young's modulus and uniaxial compressive strength and (ii) the total time-dependent strain in shrinkage and creep tests on sealed specimens.

Hence, the latter tests were restricted to autogenous shrinkage and basic creep. In the creep tests the specimens were loaded at the two different shotcrete ages of 8 h and 24 h for considering the influence of the material age at loading on the creep behavior. The sustained compressive stresses were sufficiently low ensuring linear creep behavior.

In the second part of the experimental program, currently under way, in addition, tests are conducted for determining the early age evolution of (iii) the splitting tensile strength and the specific mode I fracture energy, (iv) the combined autogenous and drying shrinkage strain and (v) the combined basic and drying creep strain at low, moderate and high levels of the sustained compressive stress.

All specimens are sampled directly at the tunnel face with the on-site equipment.

The material parameters (Young's modulus, uniaxial compressive strength, tensile splitting strength, specific mode I fracture energy) are determined at shotcrete ages of 8, 16 and 24 hours and 2, 7, 28 and 365 days. The evolution of the basic creep strain and of the combined basic and drying creep strain is measured on specimens loaded at shotcrete ages of 8, 16 and 24 hours and 2 and 7 days to compressive stresses of 40%, 60% and 80% of the uniaxial compressive strength at the age of loading. Hence, the experimental program surpasses previous test programs on shotcrete, available in the literature, by a considerably wider range of tests.

Fig. 1. Test setup for the creep and shrinkage tests: Creep test bench with one sealed and one unsealed specimen (left) and detail view of a sealed specimen (right), showing displacement transducers and piezoelectric transducers for acoustic emission measurements

Fig. 1 depicts the test setup for the creep and shrinkage tests. In Fig. 1 (left) a test bench for creep tests is shown. In each creep test bench one sealed and one unsealed shotcrete specimen are mounted one above the other for determining the basic creep strain and the combined basic and drying creep strain, respectively. The evolving axial strain in the shrinkage and creep tests is determined from the length changes, measured by three displacement transducers, fixed at equal distances along the perimeter of a specimen. The latter are shown in Fig. 1 (right), together with the additional equipment for acoustic emission measurements for capturing the spatial and temporal evolution of micro cracks in the specimens [5]. For this purpose six piezoelectric transducers are placed on a specimen for registering acoustic events and localizing such events in the threedimensional space of the specimen.

Results of the comprehensive experimental program for determining the time-dependent material behavior of shotcrete will be presented at the conference.

3. References

[1] K. Bergmeister (2011). *Brenner Basistunnel - Brenner Base Tunnel - Galleria di Base del Brennero*, Tappeiner Verlag, 2011.

[2] Österreichische Vereinigung für Beton und Bautechnik (2009). Richtlinie Spritzbeton; *Österreichische Vereinigung für Beton und Bautechnik (ÖVBB)*, Vienna, Austria.

[3] European Committee for Standardization (2006). Sprayed Concrete—Part 1: Definitions, Specifications and Conformity; EN 14487-1; *European Committee for Standardization*, Brussels, Belgium.

[4] M. Neuner, T. Cordes, M. Drexel, G. Hofstetter (2017). Time-Dependent Material Properties of Shotcrete: Experimental and Numerical Study, *Materials*, **10**, 1067.

[5] P. Rossi, J.-L. Tailhan, F. Maou, L. Gaillet, E. Martin (2012). Basic creep behavior of concretes investigation of the physical mechanisms by using acoustic emission. *Cement and Concrete Research*, **42**, 61-73.

MICROSTRUCTURAL AND MICROMECHANICAL CHARACTERIZATION OF ALKALI-ACTIVATED SLAG-FLY ASH SYSTEMS

L. Zelaya-Lainez[1], M. Königsberger[2], O. Lahayne[1], B.L.A. Pichler[1] and Ch. Hellmich[1]
[1] *Institute for Mechanics of Materials and Structures, Vienna University of Technology, Austria*
[2] *Civil Engineering Laboratory, Université libre de Bruxelles, Belgium*

1. Introduction

Clinker-free alkali-activated materials (AAMs), exhibit a lower CO_2 footprint than ordinary Portland cement (OPC) [1] and therefore contribute to the urgent need of increasing the sustainability of modern concretes. Recent alkali activated slag-fly ash systems can in a near future replace traditionally used OPC. The macroscopic mechanical properties such as stiffness and strength of AAMs are significantly different than the counterparts in OPC materials. Herein, we are exploring the reason for the observed by means of studying AAMs at the microscopic scale. Nanoindentation campaigns, along with their statistical interpretation, have been widely proven indispensable used to obtain quantitative micromechanical outline information for OPC [2] and AAMs [3] [4]. We complemented nanoindentation techniques with light microscopy were applied to slag-fly ash material systems.

2. Materials and Methods

Ground granulated blast furnace slag and fly ash were used as binder materials. Their chemical composition was determined by x-ray fluorescence spectroscopy (XRF) and is shown in Table 1. Alkaline solutions (mass s) contained either pure sodium hydroxide (molarity: 8) or a mix of sodium hydroxide and sodium silicate. Solution and binder material (b) were mixed at different s/b ratios ranging from 0.5 to 0.8 and then cast in cubes with dimensions of 5x5x5 cm^3 and stored for at least three months at 20 centigrade and 70% relative humidity.

component	SiO_2	Al_2O_3	Fe_2O_3	CaO	MgO	SO_3	K_2O	Na_2O_3
slag	36.2	12.4	0.6	39.8	7.3	-	0.5	-
fly ash	54.5	26.5	6.6	3.5	2.0	1.3	2.9	1.0

Table 1. Mass percentage of the chemical components of slag and fly ash

Smaller cubes with dimensions 1x1x1 cm^3 were extracted from center of the large cubes by means of a diamond band saw (EXAKT Technologies, USA). The smaller cubes were embedded with an epoxy resin (Struers GmbH, Germany) and latterly cut in half by means of a low speed saw (Buehler, USA). The cut surfaces were milled to micro-leveled height difference by means of an ultramiller with an attached rotating diamond tip (Leica, Germany) and further polished by means of a PM5 rotating polishing system (Logitech, UK) and diamond suspensions with 3µm and 1µm polycrystalline diamond grains. The finishing was inspected by means of light microscopy as seen in Fig. 1(a) and the roughness was measured by means of scanning probe microscopy. A nanoindentation campaign was carried out on the specimen's polished surface by means of a Triboindenter (Hysitron Inc., USA), equipped with a three-sided pyramid-shaped tip (Berkovich type). A total of 3000 indents were performed for each sample in three different areas, following the

protocol of [2]. The indentation chamber was saturated with nitrogen gas to prevent carbonation and conditioned to 20 centigrade while maintaining a relative humidity of more than 70%.
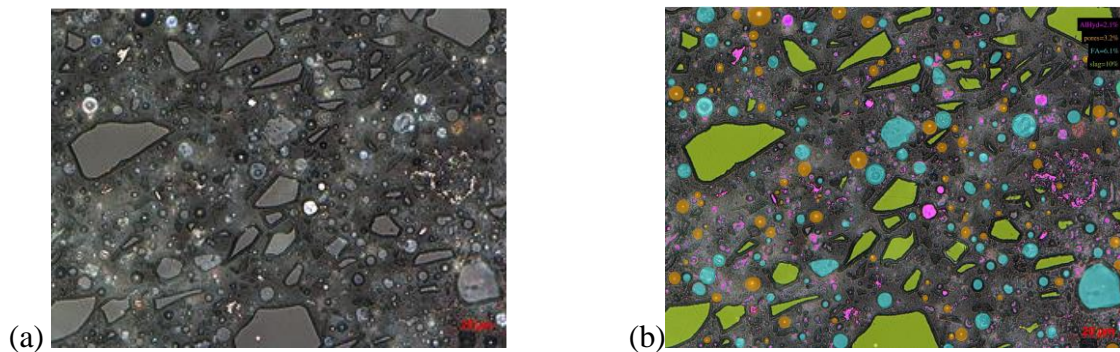

(a)   (b)

Fig. 1. Light microscopy images of alkali-activated slag-fly ash material
(a) 500-fold magnification; (b) color assigned to phases

3. Results

Discussion of results is herein limited to the slag-fly ash mix with both activators and s/b=0.55. Analyses of the light microscopy images revealed the presence of around 10% (area fraction) of anhydrate slag with polygonal shape, less than 6% fly ash particles with spherical shape, 3% of hydration-induced air voids (separated based on the spherical shape and on the grey value), and traces of very bright crystalline alumino-hydrates, as seen in Fig. 1(b). The remaining porous matrix is considerably inhomogeneous. The dark rims around the anhydrate slag grains indicate a weak interface potentially altered by shrinkage-induced microcracks.
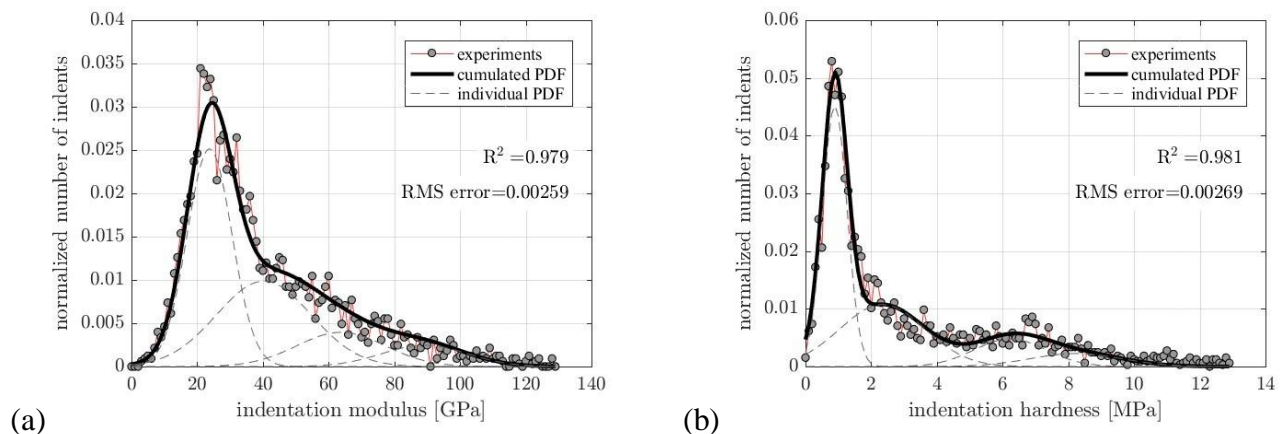

(a)   (b)

Fig. 2. Probability density functions (PDF) and histogram related to:
(a) indentation modulus; (b) indentation hardness

4. References

[1] P. Duxson, J. Provis, G. Lukey and J. (2007). The Role of Inorganic polymer Technology in the Development of Green Concrete, *Cement Concrete Research*, 37, 1590-1597.

[2] G. Constantinides, F. -J. Ulm and K. Van Vliet (2003). On the use of nanoindentation for cementitious materials, *Materials and Structures*, 36, 191-196.

[3] J. Němeček, V. Šmilauer and L. Kopecký (2011). Nanoindentation characteristics of alkaliactivated aluminosilicate materials, *Cement & Concrete Composites*, 33, 162-170.

[4] R. Thomas and S. Peethamparan (2015). Alkali-activated concrete: Engineering properties and stress –strain behavior, *Construction and Building Materials*, 93, 49-56.

SIZE EFFECT ON THE COMPRESSIVE FATIGUE OF STEEL-FIBER REINFORCED CONCRETE CYLINDERS

D.C. González[1], M.A. Vicente[1], G. Ruiz[2], R.C. Yu[2], Á. Mena[1], J. Mínguez[1] and E. Poveda[2]
[1] E. Politécnica Superior - Universidad de Burgos, Burgos, Spain
[2] ETSI Caminos, C. y P. - Universidad de Castilla-La Mancha, Ciudad Real, Spain

1. Introduction

The compressive strength of concrete depends on the size and shape of the specimens used to perform the tests [1]. Besides, compressive properties are also affected by fibers when they are used to reinforce the concrete matrix. Their distribution in the specimen is highly conditioned by the shape of the mold and the casting protocol. Fibers tend to align in parallel to the mold walls, and, in cylinders, this leads to a type of tubular reinforcing region whose thickness depends on the fiber length and the radius of the cylinder. This wall effect interacts with those of the size and shape in fiber-reinforced concrete specimens. We are particularly interested in how these effects influence the fatigue behavior of steel-fiber concrete and in determining which type of specimen yields reliable constitutive equations for structural elements. Therefore, we did tests on cubes of various sizes [2] and on cylinders of three sizes, namely 75 mm × 150 mm, 100 mm × 200 mm, and 150 mm × 300 mm (diameter × height), which results are presented here and described detailly in [3].

2. Experimental procedure

The experiments consisted firstly in determining the compressive strength of each size, followed by immediate testing of 15 cylinders of each size in compressive fatigue, with cycles of 0.25 Hz going from 20% to 85% of the respective compressive strength. The material was the same as the cubes in [2], and the fatigue setup was analogous to that of cubes.

Figure 1 shows computed tomography (CT) scans of the fiber distributions in the small and intermediate cylinders. Porosity distribution in the cylinders' volume was determined as well by CT.
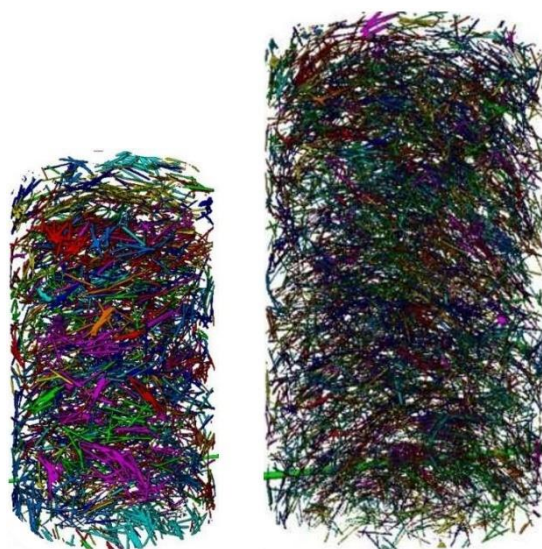

Fig. 1. CT scans showing the fibers within the small and intermediate cylinders

3. Results and discussion

Figure 2 plots the cumulative probability of the number of cycles resisted by each cylinder size and the corresponding Weibull fit to each case. We also represent —washed-out symbols and curves— the results obtained for cubes [2]. Large and medium cylinders stand fewer cycles than the small ones, roughly two orders of magnitude less for the 50% probability case, whereas small cylinders roughly match the results obtained for the 80 mm and 150 mm cubes. We attribute these size and shape effects to several causes: (1) the constrain exerted by the platens is weaker in the cylinders, which results in shorter fatigue life for them; (2) CT scans showed that maximum pore size is higher in larger cylinders, which leads to shorter number of resisted cycles; (3) contrariwise, porosity gets reduced with size when close to the walls, which originates an inverse size effect in the static compressive strength, i.e., larger cylinders yield higher strengths, which may be influencing the fatigue results since absolute stress limits result to be higher for larger specimens; and (4) cyclic induced maturation may also be working in the small cylinders, as described in [2], although not to the extent of getting runouts like in cubes.
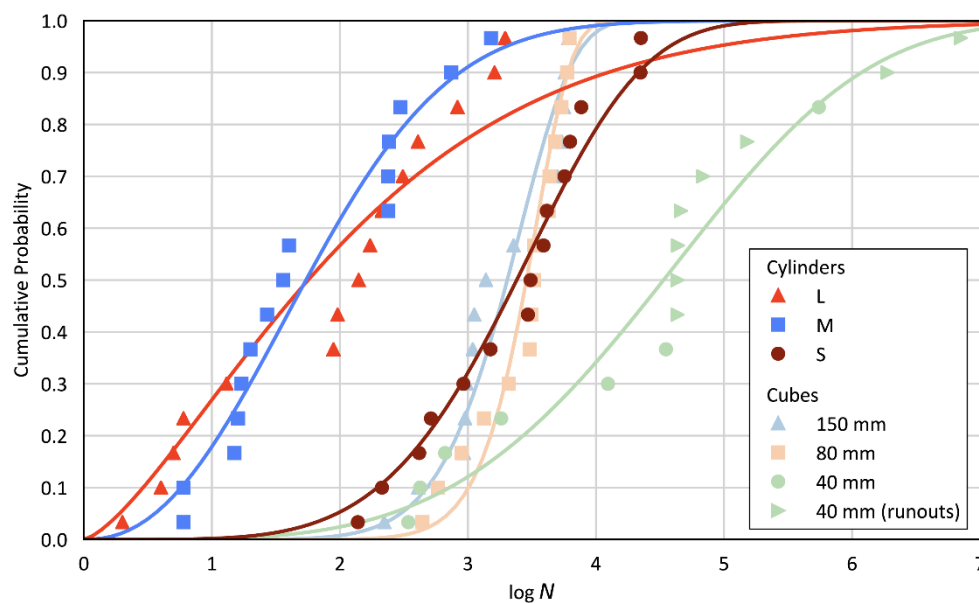

Fig. 2. Cumulative probability life distributions and fitted Weibull functions for all the specimens

4. Conclusion

Fatigue life is very sensitive to the shape and size of the specimens used in the fatigue tests. These effects mix with those of the porosity and fiber distribution. A careful selection of the correct testing specimen is crucial when determining the constitutive laws for the fatigue of steel-fiber concrete.

5. References

[1] J.R. del Viso, J.R. Carmona, G. Ruiz (2008). Shape and size effects on the compressive strength of high-strength concrete, *Cem. Concr. Res.*, **38**, 386–395.

[2] J.J. Ortega, G. Ruiz, E. Poveda, D.C. González, M. Tarifa, X.X. Zhang, R.C. Yu, M.Á. Vicente, Á. De La Rosa and L. Garijo (2022). Size effect on the compressive fatigue of fibre-reinforced concrete. *Constr. Build. Mater.*, **322**, 126238.

[3] D.C. González, Á. Mena, G. Ruiz, J.J. Ortega, E. Poveda, J. Mínguez, R.C. Yu, Á. De La Rosa, and M.A. Vicente (2022). Size effect of steel fiber–reinforced concrete cylinders under compressive fatigue loading: Influence of the mesostructure. *Under review*.

SIZE EFFECT ON THE COMPRESSIVE FATIGUE OF STEEL-FIBER REINFORCED CONCRETE CUBES

G. Ruiz[1], R.C. Yu[1], J.J. Ortega[2], E. Poveda[1], D.C. González[3] and M.A. Vicente[3]
[1] ETSI Caminos, C. y P. - Universidad de Castilla-La Mancha, Ciudad Real, Spain
[2] ETSI Minas y Energía - Universidad Politécnica de Madrid, Madrid, Spain
[3] E. Politécnica Superior - Universidad de Burgos, Burgos, Spain

1. Introduction

The size of concrete specimens influences the value of the strength obtained from the tests due to the development of fracture processes before the maximum load [1, 2]. Small specimens yield higher strengths than larger ones, and so the size effect becomes an issue since material properties in large structural elements may be smaller than those measured in the Lab. Regarding the fatigue life of concrete and fiber concrete in compression, there are very few studies on the effect of the specimen size in the resisted number of cycles, which justifies a work on this topic. This study presents the results obtained with a series of fatigue tests on cubes of three edge lengths, 40 mm, 80 mm, and 150 mm, but made of the same material, a self-compacting steel-fiber reinforced concrete. You can find a detailed description of the tests and results in [3].

2. Experimental procedure

We performed 10 quasi-static tests for each size to obtain the quasi-static compressive strengths, which we did right before testing 15 cubes of each size in fatigue, with cycles ranging from 20% to 85% of the corresponding strength at 0.25 Hz. Figure 1 shows cubes of the three sizes and the set-up used in the tests, which included scaled ball-and-socket joints to minimize load eccentricity.

Fig. 1. (a) Cubes and (b) ball-and-socket joints of the three sizes; (c) large cube being tested

3. Results and discussion

Figure 2 shows the cumulative probability of the fatigue life for the cubes of the three sizes and the Weibull fit to each case. Symbols with an arrow pointing to the right represent runouts. Large and intermediate cubes have similar behavior, but 40 mm cubes resist significantly more cycles than the others, 1.5 orders of magnitude above their larger counterparts for the 50% probability. Interestingly, all the cubes follow the Sparks and Menzies' law regardless of their size, that is, the secondary strain rates of all broken specimens fall aligned with the corresponding number of cycles in a log-log plot [3], which attests to the ability of strain-based methodologies to predict the failure life [4].

The reason behind this size effect can be partially attributed to the constraining effect of the platens, which affects the contact side differently, causing different crack patterns for the various sizes. In addition, the research shows that the effect of the size couples with the effect of fatigue induced maturation, which is fully activated in the case of small cubes, as proven by mercuryintrusion porosimetry [3]. In addition, the residual compressive strength of runouts was 43% higher than the corresponding quasi-static strength [3].
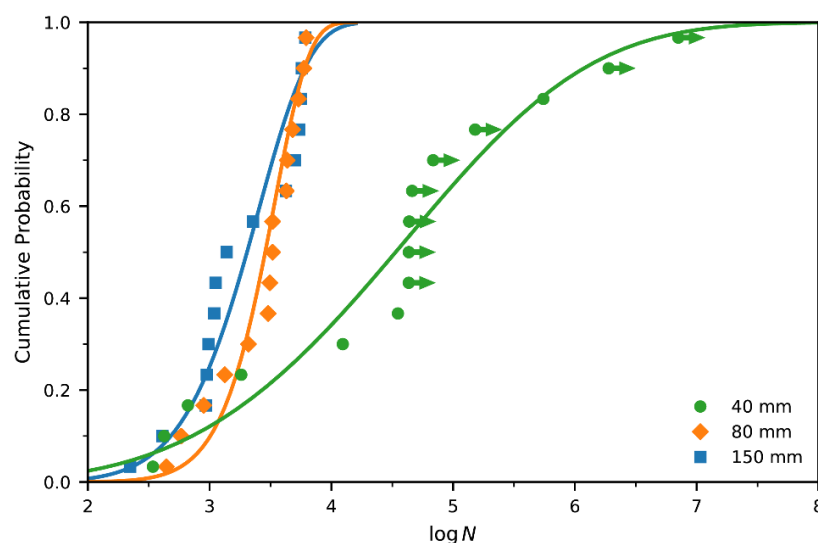

Fig. 2. Cumulative probability life distributions and fitted Weibull functions for all the cubes

4. Conclusion

The self-compacting fiber-reinforced concrete tested in this work exhibits a strong size effect coupled with maturation induced by cyclic loading. *S-N* or *ε-N* curves obtained with small cubes may overestimate the fatigue life.

5. References

[1] Z.P. Bažant, J. Planas (1998). *Fracture and Size Effect in Concrete and Other Quasibrittle Materials*, CRC Press, Boca Raton, Florida, USA.

[2] J.R. del Viso, J.R. Carmona, G. Ruiz (2008). Shape and size effects on the compressive strength of high-strength concrete, *Cem. Concr. Res.*, **38**, 386–395.

[3] J.J. Ortega, G. Ruiz, E. Poveda, D.C. González, M. Tarifa, X.X. Zhang, R.C. Yu, M.Á. Vicente, Á. De La Rosa and L. Garijo (2022). Size effect on the compressive fatigue of fibre-reinforced concrete. *Constr. Build. Mater.*, **322**, 126238.

[4] S. Blasón, A. Fernández Canteli, E. Poveda, G. Ruiz, R.C. Yu, E. Castillo (2022). Damage evolution and probabilistic strain-lifetime assessment of plain and fiber-reinforced concrete under compressive fatigue loading: Dual and integral phenomenological model, *Int. J. of Fatigue*, **158**, 106739.

5. *Meso-Scale Mechanics: Between Micro- and Macro-*

MONITORING OF TWINNING-DETWINNING IN A TWIP STEEL UNDER REVERSED CYCLIC LOADING BY IN SITU TESTS UNDER AN AFM OR IN A SEM WITH HR-DIC

C. D'Hondt[1,2], V. Doquet[1] and J.P. Couziniè[2]
[1] *CNRS, Laboratoire de Mécanique des Solides, Ecole Polytechnique - Palaiseau (France)*
[2] *CNRS, Institut de Chimie & Matériaux - Thiais (France)*

1. Motivation of the study

While the tensile behavior of TWIP steels has been thoroughly investigated, the literature on their cyclic behavior is more limited. In particular, the role played by mechanical twinning under cyclic loading is not clear. This, to a large extent, is due to the small thickness of the twins (a few tens of nanometers) that makes the measurement of the twin volume fraction a challenge. Detwinning upon load reversal, has recently been reported in TWIP steels [1-2], but the condition for de-twinning and its kinetics are yet unclear. This work investigates the contributions of twinning and detwinning to the cyclic plastic deformation of a Fe-22Mn-0.6C-0.2V TWIP steel.

2. Experimental study

A push-pull testing machine with $\pm$ 4 KN load capacity was designed to work either under the scanner of an AFM or inside a FEG-SEM, in order to monitor twinning/de-twinning events in ionpolished specimens with a 1.2 mm long, 10 mm wide and 0.6 mm thick gage length. Before the tests, an EBSD mapping of crystals orientations in the gage length was performed. To track the deformation during a cyclic test run in a SEM, a dense and uniform distribution of gold nano-particles with a diameter of about 20 nm, formed by vapour-assisted remodelling of a gold film, was deposited on the surface of the sample. The specimen was then cycled at a fixed stress range of $\pm$ 475 MPa and unloaded at selected stress levels for measurements of the plastic strain field, with a gage length between 150 and 250 nm, in a few selected grains by correlation of SEM images with a resolution of 5 nm/pixel. This allowed a detection of twins that are too thin to be detected by EBSD, thanks to the large shear strain $\gamma f \sqrt{2}$ that they carry [3], where f denotes the twin fraction on system t in the subset. Furthermore, after an identification of active slip and twinning systems, a post-treatment of plastic strain maps allowed the determination of f since:

$$(1) \qquad \varepsilon_{ij} = \sum_t \frac{f^t}{\sqrt{2}} R_{ij}^t + (1 - f^t) \sum_s \gamma^s R_{ij}^s$$

where γ^s is the strain produced by a slip system s, and $R_{ij}=(1/2)(n_i m_j + n_j m_i)$ the orientation tensor of a slip or twinning system characterized by a plane normal $\vec{n}$ and a shearing direction $\vec{m}$.

Figure 1 shows plastic strain maps in a grain with a (1 0 1) orientation at various stress levels, as well as a twin fraction map at 475 MPa and a curve correlating the evolution of the mean twin over the area marked by a red rectangle with the evolution of the applied stress. A twinning/detwinning process is clearly observed, where the stresses required for twinning and detwinning are nearly equal. Moreover, during reloading in tension up to 475 MPa, retwinning is only partially achieved (the twin fraction reaches 25% instead of 37%).
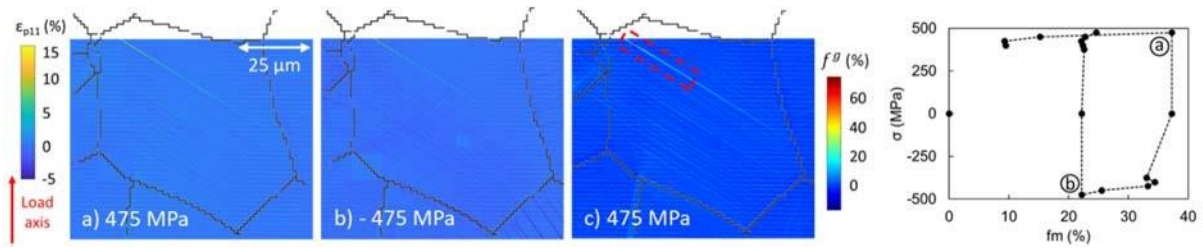
Fig. 1. a-b) Plastic strain field in a grain at various stress levels, c) map of the twin fraction corresponding to (a) and d) stress versus twin fraction in the area marked by a red rectangle

Push-pull tests were run under an AFM, which can unambiguously distinguish a nanotwin from a slip line due to the uniformity of the shear strain inside the twins, that induces a saw-tooth surface topography with a specific tilt angle. Figure 2a shows fine twins, of height 20-55 nm formed under a 556 MPa tensile stress, appearing as bright lines in a 30 x 30 μm² Peak-Force error image with an inplane resolution of 58 nm inside a grain close to (2 1 3) orientation. The saw-tooth height profiles captured normal to these twins, along the long side of the rectangular box (Fig 2b), for different stresses from tension upon subsequent compression down to – 515 MPa, show that beyond - 400 MPa the twins height starts decreasing, some of them even nearly disappearing. The variation in the twin fraction during each cycle, Δf^t, was measured in a few grains during push-pull tests run either under a fixed stress range or a fixed plastic strain range. In the first case, Δf^t and the plastic strain range accomodated by twinning/detwinning, $\Delta \varepsilon_{pij}^t = \Sigma_t R_{ij}^t \cdot \Delta f^t \cdot \varepsilon^t$, decreased with the number of cycles, while in the latter, it increased, due to cyclic hardening resulting in the nucleation of new twins rather than the growth of existing ones.
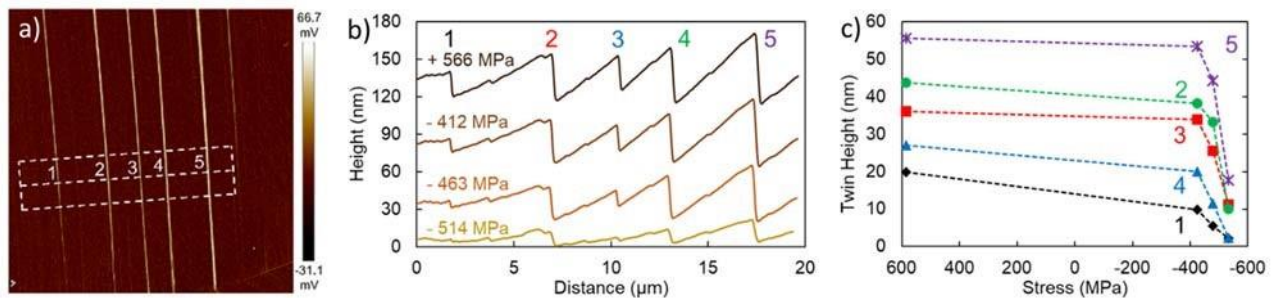

Fig. 2. a) AFM Peak-Force error image of a twinned grain at 566 MPa,
b) Evolution of surface topography and c) Evolution of twins height upon load reversal

3. References

[1] Xie Q., Liang J., Stoica A.D., Li R., Yang P., Zhao Z., Wang J., Lan H., Li R., An K. (2017) In-situ neutron diffraction study on the tension-compression fatigue behavior of a twinning induced plasticity steel, *Scripta Mater.,* **137**, 83–87

[2] McCormack S.J. , Wen W., Pereloma E.V., Tome C.N., Gazder A.A., Saleh A.A. (2018): On the first direct observation of de-twinning in a twinning-induced plasticity steel, *Acta Mater.,* **156,** 172-182

[3] H.K. Yang, V. Doquet, Z.F. Zhang (2016) Micro-scale measurements of plastic strain field, and local contributions of slip and twinning in TWIP steels during *in situ* tensile tests. Mater. Sci. Engng **A 672** 7-14

MULTISCALE MODELING OF THE ELASTICITY OF THIN FILMS DEPOSITED AT OBLIQUE INCIDENCE

E. Zgheib[1,3], A. Alhussein[1], M.F. Slim[2], K. Khalil[3] and M. François[1]
[1] Laboratory of Mechanical Systems and Concurrent Engineering (LASMIS),
University of Technology of Troyes, Nogent, France
[2] Institut Jean Lamour (IJL), University of Lorraine, Nancy, France
[3] Mechanical and Civil Engineering Unit (MGC), Lebanese University, Tripoli, Lebanon

1. Introduction

Thin films are developed in order to protect structures from environmental hazards and mechanical damage and to enhance the surface properties to meet the requirements and application. Thin films can be made by different techniques, among which we will focus on thin films deposited by magnetron sputtering with GLAD (GLancing Angle Deposition).

Nano-sculptured thin films are new types of films deposited on substrates with controlled tilt angle. They are attracting more and more interest, thanks to their nanostructure that can be produced with nano-elements of various shapes (inclined, zigzag, helicoidally, etc.), with their controlled texture and their anisotropic properties. They are used in different applications, such as electromechanical systems, sensors, photovoltaics, energy storage technology and optical anisotropy engineering allowed by GLAD. In addition, they can be used as an interface between two different materials to compensate the difference between their thermal expansion coefficients or to reduce the coupling between the normal and shear deformations.

2. Objective

The mechanical properties of thin films, especially the elastic ones, have an important role in preventing cracks and structural failure. The elasticity of thin films depends on their microstructure controlled by the process parameters. This study deals with the characterization and the modeling of the elastic behavior of sputtered films at oblique incidence.

3. Methods

The elastic anisotropy was taken into account using a new analytical model developed based on the laminated theory for the characterization of thin films. A finite element model was developed to validate the analytical model.

A multiscale model was developed using Kröner-Eshelby model, which is a self-consistent model to study the influence of the microstructure on the macroscopic and microscopic elastic behavior of the film [1]. The effect of the glancing angle on the microstructure has been studied and its features have been correlated with the mechanical properties of the film. The microstructure of the film (texture, morphology, porosity) has been taken into account in the micro-mechanical modeling.

4. Experiments

Titanium films were deposited with different glancing angles on glass, stainless steel and silicon substrates. The macroscopic elastic behavior of the deposited films was characterized using the Impulse Excitation Technique [2]. The microstructure of the deposited films was characterized by X-ray diffraction and Scanning Electron Microscopy. The microscopic elastic behavior of the deposited Ti films was investigated by X-ray diffraction under imposed loading. The deformation measurement

of the hexagonal crystal lattice under imposed loading was carried out on three different families of planes (114), (203) and (211) of α-Ti phase. The evolution of the residual stresses within films as a function of the columns tilt angles and the texture was studied. The evolution of hardness and reduced modulus of the films as a function of glancing angles was investigated.

5. Results

The microstructure analysis shows that the Ti film exhibits a single α-Ti hcp phase independent of the glancing angle. From the morphology, a columnar growth of the film was observed and these columns were influenced by the glancing angle. We found that the microcolumns tilt angle increases with the glancing angle. The experimental pole figures of α-Ti show that the film exhibits a fiber texture with (002) out-of-plane orientation that will be shifted with some texture tilt angle when the glancing angle increases.

It has been shown that a large glancing angle led to high anisotropy in the film. This elastic anisotropy is due to the film microstructure. The film's hardness and reduced stiffness decrease when the micro-column angle increases. It can be explained by the increase of the porosity rate within the film by increasing the glancing angle.

6. References

[1] M.F. Slim, A. Alhussein, E. Zgheib and M. François (2019). Determination of single-crystal elasticity constants of the beta phase in a multiphase tungsten thin film using impulse excitation technique, X-ray diffraction and micro-mechanical modeling, *Acta Materialia*, **175**, 348-360.

[2] E. Zgheib, A. Alhussein, M.F. Slim, K. Khalil and M. François (2019). Multilayered models for determining the Young's modulus of thin films by means of Impulse Excitation Technique, *Mechanics of Materials*, **137**, 103143.

UNDERSTANDING THE EFFECT OF PRIOR PLASTICITY ON PRIMARY CREEP ACCUMULATION

C. Allen, H. Coules and C. Truman
Solid Mechanics Research Group, University of Bristol, United Kingdom

1. Introduction

In the United Kingdom, the current fleet of civil power Advanced Gas Cooled (nuclear) Reactors (AGRs) are operated by EDF Energy and have now existed for several decades, hence are entering the end-of-life phase. These reactors contain a graphite core and are primarily cooled by carbon dioxide gas. Of key interest are the steel components in the boilers, which experience temperatures ranging from 480°C to 650°C. Due to this temperature regime, the aforementioned steel components can undergo creep deformation which could reduce the lifetime and cause a loss of structural integrity. By improving understanding of creep and its interaction with plasticity, more effective models can be developed. These models can aid in structural integrity analysis thus assist the AGR life extension program currently under operation.

Literature has shown that there is a clear interaction between creep and plasticity under certain conditions. Experiments performed at both 550°C and 650°C have shown increased plastic pre-straining results in a reduction in creep ductility in both tensile and compression loading scenarios [1-2]. Whilst it is generally clear the effect prior plasticity has on creep accumulation, it is less apparent the effect pre-load strain rate has on creep accumulation. Hence, these experiments performed at the University of Bristol were designed to explore both the effects of prior plasticity and pre-load strain rate on creep accumulation. The results of these experiments are then to be utilised with crystal plasticity simulations using ABAQUS.

2. Experimental Design & Methodology

The material utilised for these experiments was a cast of austenitic 316H stainless steel provided by EDF Energy. This specific cast was chosen due to its chemical and microstructural similarity to 316H stainless steel in use in current AGRs. Specimens were heated to 550°C and plastically loaded to 8% and 10% strain. The strain rates to obtain the aforementioned strains for different specimens was $2.5E\text{-}4 \ s^{-1}$, $2.8E\text{-}5 \ s^{-1}$ and $5.5E\text{-}6 \ s^{-1}$. Upon reaching the desired plastic strain, specimens were unloaded and cooled to room temperature. The extensometer was then exchanged for one that is more suitable for high temperature, long-term, testing. The samples were then finally reheated to 550°C, loaded to 280 MPa and (approximately) 200 hour creep tests were performed. A diagrammatic summary of this procedure can be shown in figure one. Specimen pre-straining conditions can be found summarised in table one.

Specimen Number	Strain Rate (s-1)	Plastic Strain (%)
1	2.5E-4	8
2	2.5E-4	10
3	2.8E-5	8
4	2.8E-5	10
5	5.5E-6	8
6	5.5E-6	10

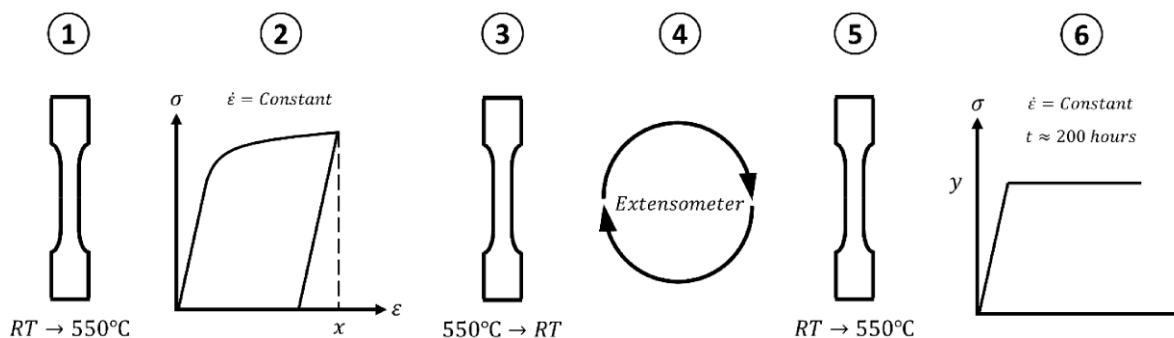Table 1. Summary of loading conditions to the 316H specimens

Fig. 1. Diagrammatic summary of experimental methodology. 1 – Sample heated to 550°C.
2 – Sample plastically strained, x = 8 or 10%. 3 – Sample cooled to room temperature.
4 – Extensometer changed. 5 – Sample reheated to 550°C.
6 – Sample loaded and held for approximately 200 hours, y = 280 MPa

3. Crystal Plasticity Simulations

A Crystal Plasticity Finite Element Model (CPFEM) has been developed in the Solid Mechanics Research Group (SMRG) at the University of Bristol, dubbed BRISTOL. This takes the form of crystal plasticity constitutive laws integrated into an ABAQUS UMAT. This model is applied to a Representative Volume Element (RVE) which consists of grains made up of C3D8 elements. The model aims to capture the deformation and granular activity of 316H stainless steel at the microstructural level in order to better represent the overall material.

The experimental results are being utilised to calibrate this newly developed model and simulations performed to observe whether the model can capture the physical behaviour, especially the effect of the different loading strain rates. The results of these simulations can go on to further inform model development. The models are being calibrated using the 8% strain results and these can be used to simulate up to 10% to see if this calibration is suitable to extend to higher plastic strains.

4. Future Work

Future work will involve more experimentation to analyse the creep-plasticity interaction further and utilise a sub-modelling approach to generate improved deformation calculations which can thus be useful for better estimates of damage.

5. References

[1] A. Mehmanparast, C. M. Davies, D. W. Dean and K. Nikbin (2016). Effects of plastic pre-straining level on the creep deformation, crack initiation and growth behaviour of 316H stainless steel, *Int. J. Pres. Ves. Pip.*, **141**, 1-10.

[2] Y. Ohashi, M. Kawai and T. Momose (1986). Effects of prior plasticity on subsequent creep of type-316 stainless-steel at elevated-temperature, *J. Eng. Mater-T. ASME*, **108**, 68-74.

NEUTRON DIFFRACTION STUDY OF STRESSES LOCALISED AT GROUPS OF GRAINS IN TEXTURED MAGNESIUM ALLOY UNDER MECHANICAL LOADING

P. Kot[1], A. Baczmański[1], S. Wroński[1], M. Wroński[1], M. Wróbel[2], J. Pilch[3] and K. Wierzbanowski[1]

[1] *AGH University of Science and Technology, Faculty of Physics and Applied Computer Science, al. Mickiewicza 30, 30-059 Kraków, Poland*
[2] *AGH University of Science and Technology, Faculty of Metals Engineering and Industrial Computer Science, al. Mickiewicza 30, 30-059 Kraków, Poland*
[3] *Nuclear Physical Institute, ASCR, Hlavní 130, 25068 Řež, Czech Republic*

1. Introduction

A new methodology based on neutron diffraction experiment was developed in order to measure stresses localised in polycrystalline materials during plastic deformation. The method was applied to textured Mg alloy and the components of stress tensor were determined directly from measured lattice strains corresponding to chosen orientations of crystallite lattice. Using the experimental data the evolution of stress was calculated for selected groups of grains, showing a large difference in the hardness of crystallites having different lattice orientations. Moreover, the critical resolved shear stress (CRSS) for basal slip system and for group of non-basal systems was determined directly from the experiment. It was found that the activation of basal glide, having small CRSS, does not lead to significant plastic deformation, and the activation of other non-basal systems (with higher CRSS) requires the development of plasticity at macroscopic scale. The experimental results were compared with the modified version of elastic-plastic self-consistent model.

2. Stress evolution at groups of grains in Mg-alloy

The diffraction measurements were done during tensile test performed at the HK9 strain diffractometer (NPI, Rez, Czech Republic) using 2θ-dispersion method (neutron diffraction). The lattice strains in Mg-alloy were measured in-situ at directions corresponding to selected grain orientations for which stress tensor was determined. The so obtained results allowed us to develop an experimental methodology based on the so-called crystallite group method [1,2] in order to determine the evolution of the stresses localised in polycrystalline grains having different crystallographic orientations. This methodology was applied to textured Mg AZ-31 alloy subjected to tension and the components of stress tensor were determined for chosen groups of crystallites [3].

The results obtained in this work show that, during plastic deformation different stresses are localised in the grains having different lattice orientations, due to anisotropy of crystal plasticity related to the crystallographic glides. Analysing evolution of von Mises stress, it was found that the grains for which the load is parallel to basal plane (crystal orientations A and B, cf. Fig. 1) are much harder than the grains tilted from this orientation (crystal orientation C) Fig. 2.

The values of critical resolved stresses (CRSS) for different slip systems were determined in the studied Mg alloy, activation of basal system occurs for non-preferred crystal orientations, therefore the basal system does not lead to significant macroscopic plastic deformation. Important macroscopic plastic deformation occurs when the non-basal systems are activated, for significantly higher applied stress comparing to the one required to activate basal system (CRSS is much higher for non-basal slips as compared with basal glide).

Modified elasto-plastic self-consistent EPSC model was also used to determine the CRSS values from the lattice strains measured "in-situ" during tensile test. The value of CRSS for basal slip system and probable set of CRSS values for non-basal slip systems determined with the help of the modified

EPSC model agree with these obtained from a direct method. The predictions of the model agree with experiment if significant plastic accommodation is introduced for the plastically deformed grains.
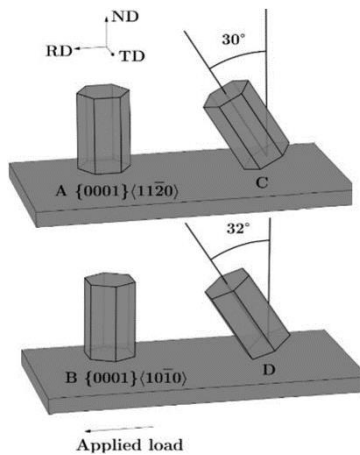

Fig. 1. Visualization of the tested orientations in relation to the sample coordinates: RD, TD and ND
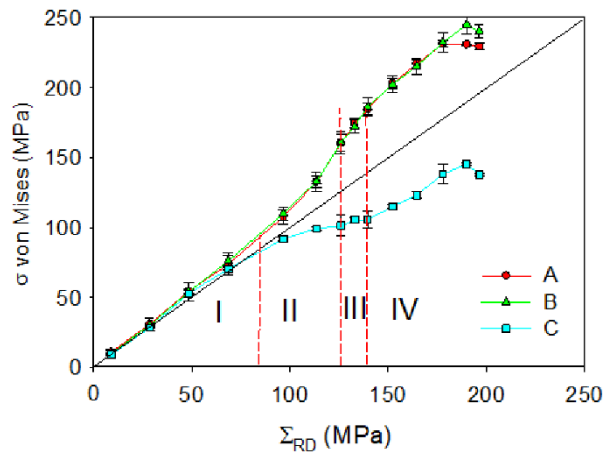

Fig. 2. Von Mises stresses for orientations A, B and C in function of the applied stress ΣRD. The trend changes caused by slip systems activations are marked

3. Conclusions

A new methodology of stress measurement using neutron diffraction allowed us to study stress state in textured magnesium alloy subjected to elastoplastic deformation. The main achievement of this work are as follows:

- Stresses localized at groups of grains having different orientations with respect to the applied load were determined showing significant differences between grains from groups A and B (preferred orientations) and C and D (inclined orientations).
- It was shown that, the determined CRSS value for basal slip system is much smaller compared to those found for the non-basal systems.
- The measured CRSS values were used in calculations performed with EPSC model, confirming stress distribution between grains having different orientations.

4. Acknowledgements

5. References

[1] B. Ortner, On the selection of measurement directions in second-rank tensor (e . g . elastic strain) determination of single crystals , J. Appl. Crystallogr. 22 (1989) 216–221.

[2] R. Dakhlaoui, V. Klosek, M.H. Mathon, B. Marini, Orientation stress field analysis in polycrystalline bcc steel using neutron diffraction, Acta Mater. 58 (2010) 499–509.

[3] A. Baczmański, P. Kot, S. Wroński, M. Wróbel, M. Wrofński, J. Pilch, M. Muzyka,K. Wierzbanowski, Y. Zhao, L. Le Joncour, M. François, B. Panicaud, Direct diffraction measurement of critical resolved shear stresses and stress localisation in magnesium alloy, Materials Science & Engineering A 801 (2021) 140400.

6. Micro/Nano-Mechanical Testing of Materials

ACOUNTING FOR SHEAR STRESS EFFECT: RAMAN-STRESS RELATIONSHIP FOR ARBITRARY CRYSTAL ORIENTATION

W. Qiu[1], L. Ma[1,2], Y. Chang[1], H. Xing[1], M. Wang[1] and X. Fan[2]
*[1] Tianjin Key Lab Modern Engineering Mechanics, Department of Mechanics,
Tianjin University, Tianjin 300350, China*
[2] Department of Mechanical Engineering, Lamar University, Beaumont, TX 77710 USA

1. Introduction

Micro-Raman Spectroscopy (μRS) is increasingly used as an effective technique to measure local strain and/or residual stress at microscale level due to its nondestructive and noncontact feature with high spatial resolution ($\sim 1\mu m$) [1,2]. In order to calculate the strain/stress from the measured Raman wavenumber shift, the uniaxial or biaxial stress are often assumed by neglecting shear stress component.

During the manufacturing process, nevertheless, intrinsic and/or processing complicated states of stress always be introduced into the semiconductor structures and devices, especially those applying the "Strain Engineering". However, most of the existing research are based on the Raman relationship of typical crystal orientation with simple stress assumptions by neglecting shear stress component, which can't obtain the real stress state and the actual magnitude of stress components in most cases.

In this paper, we will establish a general model for Raman-mechanical measurement on arbitrary crystal orientation and present an analytical solution based on (110) silicon considering the general stress state. In addition, the calibration experiments are also carried out to verify the theoretical derivation.

2. General model for Raman-mechanical measurement

To establish the Raman-stress relationship for an arbitrary crystal orientation, it is necessary to first define the crystal coordinate system with the axes $X_1 = [100]$, $X_2 = [010]$, $X_3 = [001]$ and the sample coordinate system of the measured surface, $X_1'X_2'X_3'$, as shown in Fig.1.
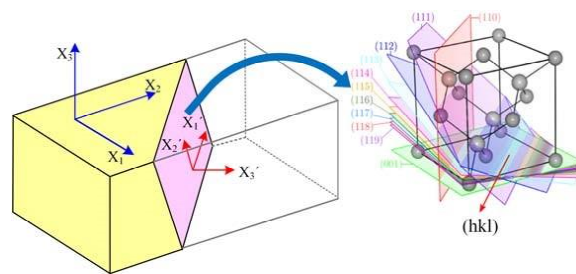

Fig. 1. Illustration of different crystal planes about silicon

Because, owing to crystal symmetry, the mechanical, physical and optical parameters of different crystal planes show obvious anisotropy, leading to the Raman-mechanical relationship dissimilar on the different crystal planes. The spectral parameters and mechanical parameters are usually given in crystal coordinate system. Through coordinate transformation, the parameters in the sample coordinate system are obtained. The equations of both the stress– strain relationship and the lattice dynamics in the sample coordinate system were obtained firstly. Then, the relationship between the stress and the observed Raman shift was determined by using the Raman selection rules.

3. Raman strain rosette

For the given polarized angle of the incident light (θ) and the Raman scattered light (φ), the Raman shift of material surface that contains three stress components (σ_x, σ_y, τ_{xy}), $\Delta\omega_{obs}$, is generally a function of θ and φ, as follows

(1) $\qquad \Delta\omega_{obs}=f(\sigma_x, \sigma_y, \tau_{xy}, \theta, \varphi)$

If at least three independent Raman shifts $\Delta\omega_{obs}$ can be obtained by controlling θ and φ at the same point during the experiment, the three stress components σ_x, σ_y, τ_{xy} can then be derived accordingly. Based on the general model for Raman-mechanical measurement of arbitrary crystal orientation, the expression of the stress components of (110) silicon can be written as Eq. (2)

(2)
$$\begin{cases} \sigma_x = 549\Delta\omega_{obs}\big|_{\theta(0°)} - 1122\Delta\omega_{obs}\big|_{\theta(45°)} \\ \sigma_y = -1122\Delta\omega_{obs}\big|_{\theta(0°)} + 1404\Delta\omega_{obs}\big|_{\theta(45°)} \\ \tau_{xy} = 248\Delta\omega_{obs}\big|_{\theta(0°)} - 434\Delta\omega_{obs}\big|_{\theta(30°)} + 186\Delta\omega_{obs}\big|_{\theta(45°)} \end{cases}$$

where $\Delta\omega_{obs}|_{\theta(0°)}$, $\Delta\omega_{obs}|_{\theta(30°)}$ and $\Delta\omega_{obs}|_{\theta(45°)}$ are the Raman shift with the three different sets of the polarization angles (0°, 90°), (30°, 120°), and (45°, 135°), respectively.

4. Experiment

To verify the above theoretical results, a series of experiments were performed. Table 1 gives the measured stress components with the comparison to the actual given stress state. All three measured stress components are within 10% error from the actual given stress state. If we assume that the stress state is uniaxial, the stress σ_x can also be calculated in a traditional manner. The results are also shown in Table 1. It clearly shows that uniaxial stress condition assumption gives erroneous result.

Actual given stress: $\sigma_x = \sigma_y = \tau_{xy} = -95$	Present prediction			Simple stress assumption
	σ_x	σ_y	τ_{xy}	$\sigma_x|_{uniaxial}$
	-102.9	-86.0	-86.3	-174.8
Error	8.3%	9.5%	9.2%	84.0%

Table 1. Stress prediction based on the measured $\Delta\omega_{obs}$ (stress unit: MPa)

5. Conclusions

This paper presents an approach that can effectively and accurately calculate both normal and shear stress components through polarized Raman spectroscopy. The polarized Raman spectroscopy acts as "strain rosette" to determine all in-plane stress components. For (110) silicon, this paper gives an analytical and linear solution for Raman-stress relationship based on the general model for Raman-mechanical measurement of arbitrary crystal orientation. The approach is transferable to other material systems, even though an analytical solution is not available. Provided that the Raman shift data under different polarized angles are obtained, the numerical solutions can be applied to determine each stress component in actual applications.

6. References

[1] W. Qiu, L. L. Ma, Q. Li, H. D. Xing, C. L. Cheng, and G. Y. Huang (2018). A general metrology of stress on crystalline silicon with random crystal plane by using micro-Raman spectroscopy, *Acta Mech. Sin.*, **34**, 1095-1107.

[2] Y. Kang, Y. Qiu, Z. Lei, and M. Hu (2005). An application of Raman spectroscopy on the measurement of residual stress in porous silicon, *Opt. Laser Eng.*, **43**, 847-855.

INVESTIGATION OF THE LOCAL MECHANICAL PROPERTIES OF LASER BEAM WELDED AA2198 (Al-Cu-Li ALLOY) JOINTS USING MICRO-MECHANICAL CHARACTERISTICS

T.N. Examilioti[1,2], N. Kashaev[3], B. Klusemann[2] and N.D. Alexopoulos[1]

[1] *School of Engineering, Department of Financial Engineering, University of the Aegean, Chios, Greece*

[2] *Institute of Product and Process Innovation, Leuphana University of Lüneburg, Lüneburg, Germany*

[3] *Institute of Materials Research, Materials Mechanics, Helmholtz-Zentrum Geesthacht, Geesthacht, Germany*

1. Objective

The last decade's trend of aluminum alloy producers is to manufacture new aluminum alloys that are even lighter, have increased mechanical properties as well as to have the ability to be welded in order to compete the composite materials in aeronautical applications [**1**]. Third generation Al-CuLi alloys are highly promising materials, which provide improved mechanical properties and damage tolerance when compared to the already commercially available Al alloys [**2, 3**]. The improved mechanical properties are quite often associated with the lithium (Li) concentration that enables the formation of additional strengthening precipitates besides the *S* type particles, e.g. δ' (Al$_3$Li), δ (AlLi), T_1 (Al$_2$CuLi), θ' (Al$_2$Cu) and *S'* (Al$_2$CuMg) particles [**4**]. It is mentioned in the literature [**5**] that the addition of 1 wt. % Li to Al reduces the density by 3 % and the modulus of elasticity increases by almost 6 %. These alloys have already been established as structural materials for aerospace applications mainly because of the reduced density and increased specific strength. It was estimated that the use of high strength Al-Cu-Li alloys instead of conventional AlCu-Mg alloys, could approximately reduce the structural weight by 10 – 15 % and increase the stiffness by 20 % [**6**]. Additionally, further reduction of manufacturing costs and structural weight can be achieved with the introduction of alternate joining processes such as advanced welding methods in order to replace the conventional rivets where necessary.

2. Material and method(s)

Aluminum-copper-lithium (Al-Cu-Li) alloy 2198 in T3 heat treatment condition with nominal thickness of 5.0 mm was laser beam welded (LBWed) using aluminum-silicon (Al-Si) 4047 filler material with diameter of 1.2 mm. The effect of post weld heat treatment (PWHT) on tensile mechanical behaviors of butt joints was also investigated under different ageing conditions. Artificial ageing heat treatment conditions were performed at 170 ºC and for different ageing times, selected from Alexopoulos et al. [**7**], that corresponds to all possible ageing tempers, namely, underageing (UA), peak-ageing (PA) and over-ageing (OA) conditions.

From the rectangular plates, micro-flat tensile specimens were machined in Longitudinal (L) direction, according to ASTM E8 specification with electron discharge machine (EDM). The specimens were machined horizontal and vertical to the weld seam, from the highly important regions namely, base material (BM) and fusion zone (FZ). The gauge length of the micro-flat tensile specimens was approximately 10 mm and the respectively thickness was 0.5 mm. The received microstructure of the joints was investigated by optical microscope (OM), scanningelectron microscopy (SEM), electron backscatter diffraction (EBSD) and micro-hardness measurements.

3. Result(s) and conclusion(s)

Preliminary results for horizontal and vertical micro-flat tensile specimens presented similar conventional yield stress results for the base material. However, vertical micro-flat tensile specimens exhibited slightly higher ductility when compared to horizontal specimens. With applying heat treatment, conventional yield stress increases up to peak-ageing (PA) and 48 hours and then decreases to over-ageing (OA) condition, for both directions.

Horizontal micro-flat specimens from the fusion zone (FZ) present approximately 47 % low yield stress in T3 condition compared to base material (BM) specimens. With increasing artificial ageing yield stress increases up to 98 hours and over-ageing (OA) condition for horizontal specimens from the FZ. Total elongation at fracture, for both BM and FZ specimens, decreases approximately 7 % at T3 condition. Increasing artificial ageing, total elongation at fracture decreases for both locations up to 98 hours. Silicon intensity in the FZ affects the local tensile mechanical properties of AA2198 as a result the decrease of strength and with an increase in elongation.

4. References

[1] J. Montgomery, Aircraft primary structure and materials, National Institute of Aerospace Workshop, *Revolutionary Aircraft for Quite Communities*, Hampton, VA, (2007).

[2] E.J. Lavernia, T.S. Srivatsan, F.A. Mohamed (1990). Strength, deformation, fracture behaviour and ductility of aluminium-lithium alloys. *Journal of Materials Science*, 25, 1137– 1158.

[3] T. Dursun and C. Soutis (2014). Recent developments in advanced aircraft aluminum alloys, *Materials and Design*, 56, 862-871.

[4] R. Yoshimura, T.J. Konno, E. Abe, K. Hiragaa (2003). Transmission electron microscopy study of the evolution of precipitates in aged Al–Li–Cu alloys: the θ′ and T1 phases, *Acta Materialia*, 51, 4251-4266.

[5] S. Zhang, W. Zeng, W. Yang, C. Shi (2014). Ageing response of a Al-Cu-li 2198 alloy, *Materials and Design*, 63, 368-374.

[6] S.G. Pantelakis and N.D. Alexopoulos (2008). Assessment of the ability of conventional and advanced wrought aluminum alloys for mechanical performance in light-weight applications, *Materials and Design*, 29, 80-91.

[7] N.D. Alexopoulos, A. Proiou, T.N. Examilioti, N. Kashaev, S. Riekehr, S.K. Kourkoulis (2016). Effect of artificial aging on the mechanical performance of (Al-Cu) 2024 and (Al-CuLi) 2198 aluminum alloys, *Procedia Structural Integrity*, 2, 3782-3783.

A MULTI-PURPOSE, HYGRO-THERMO-MECHANICAL, IN-SITU X-RAY CT TESTER

J.P.M. Hoefnagels, N.H. Vonk, E.C.A. Dekkers and M.P.F.H.L. Van Maris
Dept. of Mechanical Engineering, Eindhoven University of Technology, the Netherlands

1. Extended abstract

X-ray Computed Tomography (CT) is a powerful non-destructive technique used to obtain highresolution 3D description of samples. In the past decade, a growing interest has arisen in combining CT scanning with mechanical testing. Hence, several in-situ testing devices have been developed, each with their own merits and limitations, see brief literature review in [1]. However, none of them can perform advanced hygro-thermo-mechanical tests on specimens subjected to multiple loading modes, while accurately controlling and measuring the force, displacement, temperature and relative humidity in real time. Therefore, a compact, light-weight, climate-controlled, high force and displacement resolution, stationary ROI, multiple loading in-situ CT device has been realised which allows such complex experiments. The device is designed to fit the compact design space of lab-scale CT scanners. The conceptual design is based on a comprehensive literature study in which various possible options were discussed [1]. A stationary ROI is realized with a smart planetary gear to convert rotational motion into both up-and downwards translation, see Fig. 1.

Accurate force and displacement measurements are attained by, respectively, allowing exchangeable loadcells and three accurate extensiometers (LVDT's) inside. A maximum stroke of 20 mm was realized along with a maximum applied load of 2 kN, allowing testing of a wide variety of materials. A modular clamping method was realized that allows fixation of rectangular and circular samples which require minimal sample geometry adjustments, while additionally, allowing fixation of specific loading modules such as three- and four-point bending clamps. To enable a controlled climate (temperature and relative humidity) around the sample, an external climate box is connected to the sample tube.

Various validation experiments were conducted.[1] CT reconstruction quality was found to be sufficiently high to characterize delamination in cardboard down to the level of individual fibres, which is known to be challenging. Accurate force and displacement measurements are validated by successfully determining the Young's modulus of three brass shafts. Proper climate control inside the sample tube is realized, well within the specified requirements.

The setup's potential is demonstrated by performing the creasing and folding and subsequently relaxation process of cardboard within a climate-controlled environment, see Fig. 2. Three- and four-point bending clamps are used to, respectively, crease and fold cardboard. Each process is performed in multiple increments and intermittent CT scans on the sample are performed. This allowed full 3D characterization of the material, which can directly be linked to the properly captured mechanical response, allowing identification and analysis of micro-mechanical failure modes, in this case plie delamination during the folding process.[1]

2. References

[1] N. H. Vonk, E. C. A. Dekkers, M. P. F. H. L. van Maris & J. P. M. Hoefnagels (2019). A multi-loading, climate-controlled, stationary ROI device for in-situ X-ray CT hygro-thermomechanical testing. *Exp. Mech.*, **59**(3), 295-308.
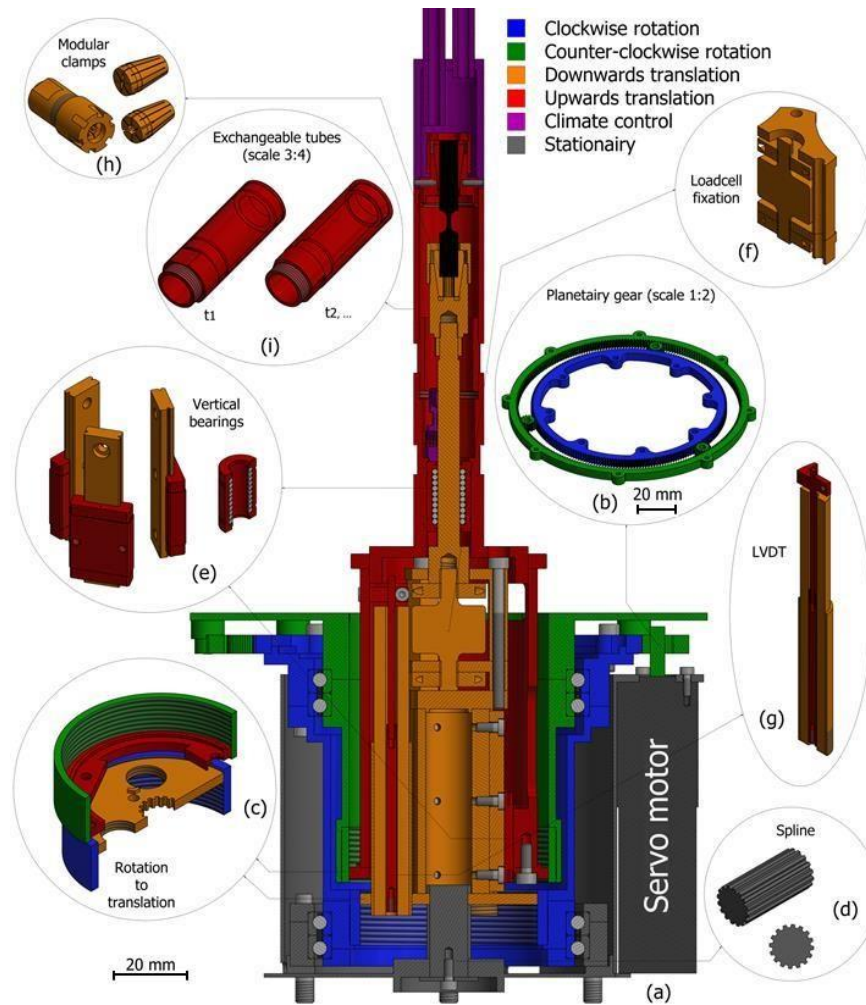
Fig. 1. CAD model of the detailed design of the in-situ CT tester. (a) Section view of the realized setup, (b) planetary gear which is driven by three servo motors, (c) two large threaded cylinders (green and blue) in combination with a spline (d) and vertical bearings (e) to convert the rotational motion into vertical translational motion of the upper (red) and lower (orange) plate which are connected to the sample clamps, (f) exchangeable loadcell which is fixed under the clamp for accurate force measurement, (g) three LVDT's which accurately monitor the relative displacements of the cylinders, (h) exchangeable tubes and (i) universal clamps which are easily exchangeable. Legend: each color indicates a different type of motion
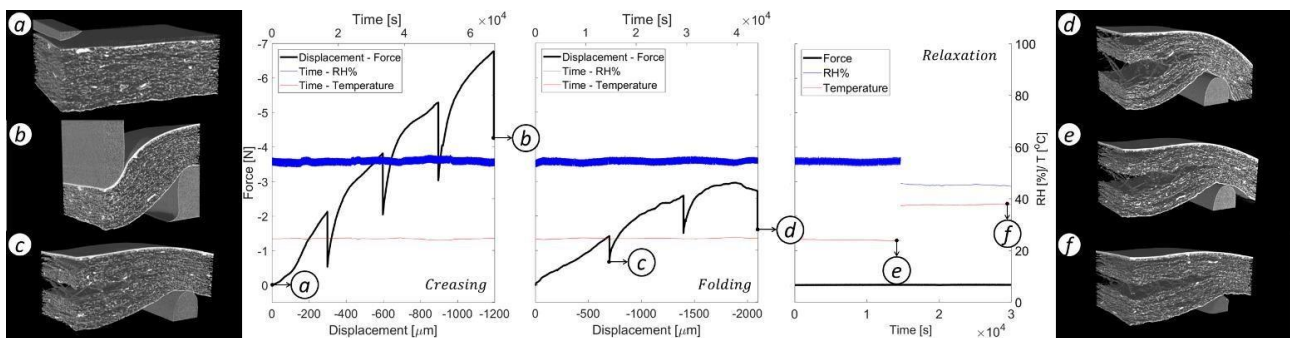
Fig. 2. High resolution 3D CT characterization
of hygro-thermo-mechanical response of cardboard under creasing and folding

7. Non-Contact and Optical Dynamic Measurements

AN IMPROVED PHOTOELASTIC SKIN TISSUE SURROGATE FOR INVESTIGATION OF NEEDLE FORCES

S. Falconer[1], Z. Taylor[2] and R.A. Tomlinson[1]
[1] The University of Sheffield, Sheffield, UK
[2] University of Leeds, Leeds, UK

1. Introduction

This research aimed to investigate the forces that both needle and tissue experienced during a needle insertion, and how they altered the needles trajectory. An investigation into the current literature showed that existing skin tissue surrogates did not perform similarly to real skin tissue *in vivo* during needle insertions. A new surrogate is required to aid with validation for computational models of needle insertions, while avoiding the ethical issues raised from testing real tissue. This study developed an improved skin tissue surrogate for use in photoelastic testing which focused on replicating the fracture mechanism observed during a needle insertion through human skin tissue.

2. Surrogate

It was found that konjac gel fractures in the same way as human skin tissue. The photographs in figures 1 and 2 illustrate the similarities in the fracture profiles between konjac and human skin tissue. Experimental assessments determined that at a concentration of 1.5% gel powder to water konjac jelly had a stiffness which closely matched the stiffness of human skin tissue *in vivo*.

Fig. 1. BD blood fill needle inserted into skin *in vivo*

Fig. 2. BD blood fill needle inserted into konjac jelly

3. Photoelastic analysis

Photoelastic analysis was used to assess the principal strain distribution in the surrogate material caused by a needle insertion. Within photoelastic analysis a complete and continuous strain field is acquired, rather than discrete points. A GFP2500 poleidoscope was used for the analysis; it is a digital polariscope which allowed for the capture of instantaneous, dynamic, full field magnitude and directional data using one piece of apparatus [1]. Existing research within needle insertion investigation only the magnitude of the force response is reported, with use of the GFP2500 poleidoscope directional data was also obtained. It is hoped that this directional data will shed light on the circumstances which cause needle deflection through soft tissue.

4. Experimental results

A variety of needle insertion experiments were conducted which assessed how varying the insertion speed, needle length, and needle gauge affected the overall response. The results proved that konjac jelly accurately replicated needle insertion response through soft tissue better than existing surrogates. Figure 3 shows an example of the data acquired from the GFP2500 poleidoscope of a biopsy needle insertion into the konjac surrogate. The poleidoscope data revealed never-before-seen data regarding the strain distribution during a needle insertion. Locations of maximum principal strains were identified against the side of the bevel tip, and at the entry point; which has not been reported before. These locations of maximum principal strain difference were consistent across the range of needle experiments. The new directional information, illustrated by the yellow lines in figure 3, visualised the bending pattern as the needle was inserted. The utilisation of the GFP2500 poleidoscope with the newly developed skin tissue surrogate revealed how the needle affected the surrogate as a whole.
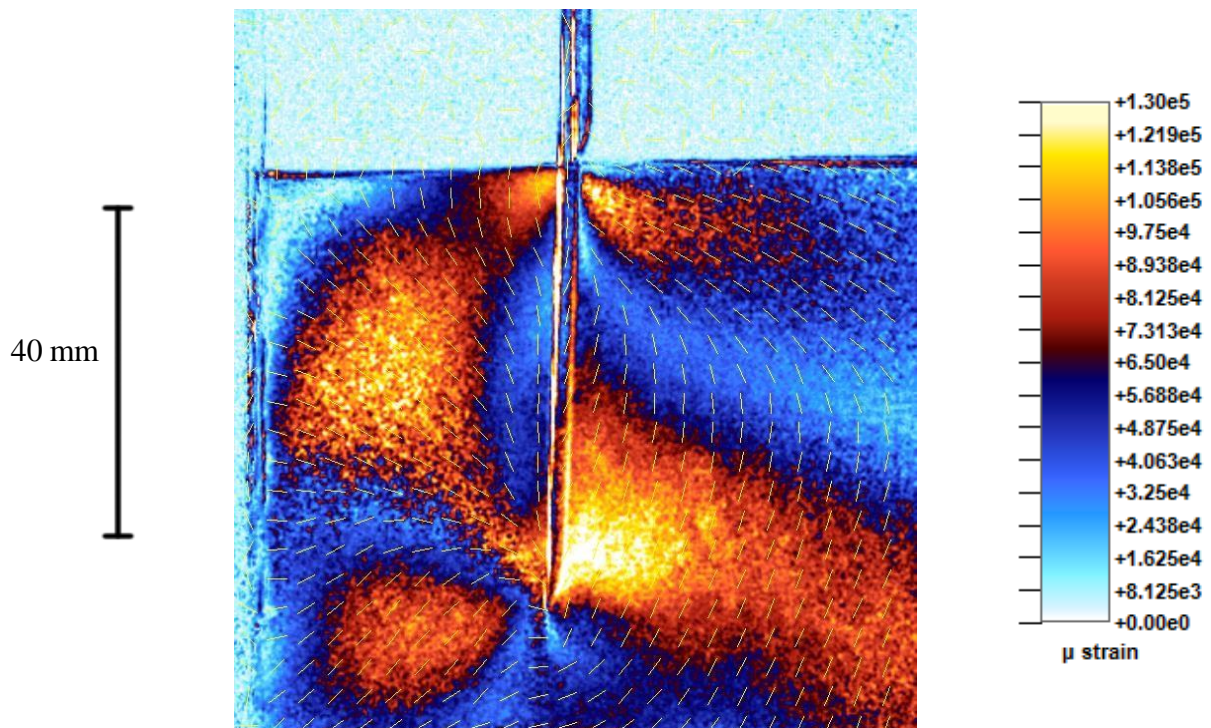
Fig. 3. Principal strain difference diagram of needle insertion

5. References

[1]　J. Lesniak, S. J. Zhang, and E. A. Patterson, "Design and Evaluation of the Poleidoscope A Novel Digital Polariscope," *Experimental Mechanics,* vol. 44, no. 2, pp. 128-135, 2004.

**MEASUREMENT OF CONTINUOUS DEFORMATION
BY SPECKLE INTERFEROMETRY USING ONE STEP PHASE ANALYSIS
WITH INTENSITY NORMALIZATION**

S. Arikawa and K. Takahashi
Meiji University, Kawasaki, Japan

1. Introduction

Speckle interferometry [1], [2] is an effective technique for measuring very small deformations in high spatial resolution. The sensitivity reaches nano-meter order. For the phase analysis, several phase stepping techniques can be applied. General phase stepping methods are not suitable for measuring dynamic phenomena. Accordingly, some phase analysis techniques for measuring dynamic phenomena have been developed, such as Fourier transform method [3] and Hilbert transform method [4]. However, these methods have some limitations for the measurements. On the other hand, a phase stepping method for dynamic phenomena called one-step phase analysis [5] was developed by L. Bruno et. al. in 2008. This method uses the randomness of the phase of the speckle pattern effectively. In this method, the average intensity and the modulation amplitude values are assumed as constant during the measurement. However, the average intensity and the modulation amplitude gradually vary when the object is deformed. In such case, one-step phase analysis method cannot be applied for all the deformation process. Accordingly, we have proposed a new one-step phase analysis method [6] which can adapt the variations of the average intensity and the modulation amplitude. In this study, a continuous deformation is measured by the new one-step phase analysis method for verifying the effectiveness of the proposed method.

2. Phase analysis method

Outline of the new one-step phase analysis is described as follows. In this method, interfered speckle images and average intensity images must be captured simultaneously. As written in Eq. (1), normalized intensity I' is calculated by the subtraction of the average intensity A from the intensity I.

$$(1) \qquad I'_{ij} = I_{ij} - A_{ij} = B_{ij}cos(\varphi_j + \Delta\varphi_{ij})$$

Where B, φ and $\Delta\varphi$ are the modulation amplitude, the initial phase and the phase change respectively. i and j denote the i-th deformation state and the pixel number in each image. When a_{ij} and b_{ij} are defined as following Eq. (2), Eq. (1) can be rewritten as Eq. (3).

$$(2) \qquad \begin{Bmatrix} a_{ij} \\ b_{ij} \end{Bmatrix} = \begin{Bmatrix} B_{ij}cos\Delta\varphi_{ij} \\ -B_{ij}sin\Delta\varphi_{ij} \end{Bmatrix}$$

$$(3) \qquad I'_{ij} = a_{ij}cos\varphi_j + b_{ij}sin\varphi_j$$

A kernel as a local calculation region is set on the speckle image. If the initial phase is known, a_{ij} and b_{ij} are calculated using least squares method by assuming the phase changes in the kernel are the same value. The phase change $\Delta\varphi$ is then obtained by Eq. (4).

$$(4) \qquad \Delta\varphi_{ij} = tan^{-1}\left(-b_{ij} \Big/ a_{ij} \right)$$

3. Experimental result and discussion

An in-plane rotation is measured using a speckle interferometer which can capture the interfered intensity and the average intensity images simultaneously by two cameras. One of the phase analysis results is shown in Fig. 1. The phase value is slightly fluctuated, but a reasonable tendency of the phase distribution can be obtained. It is expected that the reason for the phase fluctuation is the effect of miss alignment of the interferometer. The interferometer used in this experiment is relatively complicated, because polarizations of laser beams are controlled and superposed for capturing the interfered intensity and the average intensity images simultaneously. Therefore, improvement of the interferometer is required.
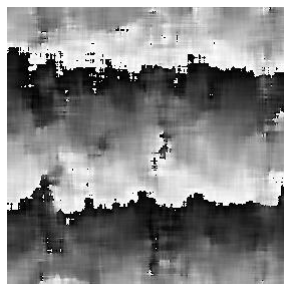
Fig. 1. Phase map obtained by new one-step phase analysis method

4. Conclusion

A new one-step phase analysis method with an intensity normalization is applied for measuring an in-plane rotation measurement. The phase analysis can be available to measure a continuous deformation. It is expected that various continuous deformations can be measured by the proposed method by improving the interferometer.

5. References

[1] Chiang, F. P. (1989). *Speckle Metrology*, ASM handbook Vol.17, Nondestructive Evaluation and Quality Control, 432.
[2] Sirohi, R. S. (2002). Speckle Interferometry, *Contemporary Physics*, 43(3), 161–180.
[3] Kaufmann, G. H. and Galizzi, G. E. (2002). Phase measurement in temporal speckle pattern interferometry: comparison between the phase-shifting and the Fourier transform methods, *Applied Optics*, 41(34), 7254–7263.
[4] Madjalova, V. D. , Kadono, H. and Toyooka,S. (2003). Dynamic electrinic speckle pattern interferometry (DESPI) phase analyses with temporal Hilbert transform, *Optics Express*, 11(6), 617-623.
[5] Bruno, L. and Poggialini, A. (2008). Phase shifting speckle interferometry for dynamic phenomena, *Optics Express*, 16(7), 4665-4670.
[6] Takahash, K. and Arikawa, S. (2019). A new phase analysis method using mean intensity on speckle interferometry for measuring dynamic phenomena, *Proc. SPIE 11205, Seventh International Conference on Optical and Photonic Engineering*, DOI:10.1117/12.2542764.

OPTICAL MOTION MAGNIFICATION ENHANCEMENT AND QUANTIFCIATION FOR STRUCTURAL DYNAMIC MEASUREMENT

N.A. Valente, M. Southwick, Z. Mao and C. Niezrecki
Department of Mechanical Engineering, University of Massachusetts Lowell,
Lowell, MA, United States

Abstract

Traditional distributed dynamic measurement on a structure with complex geometry can be an arduous task especially if the structure is large. Optical sensing for structural dynamic measurement has recently gained significant interest as a diagnostic tool for metrology as well as structural health monitoring because of its non-contact nature. In particular, motion magnification has gained popularity within the scientific community for its non-invasive approach by using a single camera to observe motion. Phase-based motion magnification (PME) permits an amplification of small motions that are not visible to the naked eye. Although PME offers a potential alternative to traditional manual instrumentation, the extracted motion may contain artifacts due to the amplification factor or may be difficult to quantify. Depending upon the value of magnification, noisy displacement measurements can be present which tend to produce inconclusive results concerning frequency content. This paper presents the application of total variation (TV) to improve the signal to noise ratio (SNR) of extracted phase displacements and explores ways to quantify the amplified motion. In the presence of large artifacts that come as a result of the magnification factor, the improvement of SNR produces a more conclusive frequency response of the experimental structure. Prior work has attempted to zoom into a small range of pixels to increase SNR; however, this limits the field of view and does not capture a large dynamic range of motion. Total variation has the capability of improving SNR without having to spatially zoom in on a group of pixels. In this work, the modified method of motion magnification and total variation (MMTV) is applied to a simple geometric structure for structural dynamic identification. Other approaches are also presented to help quantify the physical motion that is derived from the motion magnified videos.

ELASTIC REGULARIZATION OF DIGITAL IMAGE CORRELATION: AN APPLICATION TO CELLULAR MATERIALS

A. Rouwane[1,2], R. Bouclier[1,2], J.-C. Passieux[1] and J.-N. Périé[1]

[1] *ICA, Université de Toulouse, UPS, INSA, ISAE-SUPAERO, MINES-ALBI, CNRS,
3 rue Caroline Aigle, F31055 31400 Toulouse, France*
[2] *IMT, Université de Toulouse, UPS, UT1, UT2, INSA, CNRS, 135 avenue de Rangueil,
F-31077 Toulouse Cedex 04, France*

1. Introduction

Characterizing the mechanical behavior of materials with complex microstructures has become necessary in order to design low-priced and efficient structures. In the aerospace industry, for example, complex materials such as foams or honeycombs are widely used in sandwich panels due to their low density and high stiffness. However, the need is not limited to industry. In biology, for instance, an accurate characterization of the mechanical behavior of bones could contribute to a better design of bone grafting components. In this context, Computed Micro-Tomography (μ-CT) has clearly become one of the most efficient non-invasive imaging tools for representing and inspecting the physical reality of such materials.

The present work aims at developing a procedure to identify mechanical properties of cellular materials (see Fig.1) using a rigorous dialogue between full field measurements and numerical simulations based on CT images. This kind of dialogue is practically inscribed in the Finite Element Method Updating (FEMU) class of algorithms [1]. On the one hand, it is necessary to simulate the mechanical response of the material (direct problem). Given the CT images, we can try to build a faithful Digital Image Based (DIB) model [2]. On the other hand, such an experimentation/simulation coupling requires minimally invasive measurements. Those measurements can nowadays be easily obtained using Digital Image Correlation (DIC, also named Image Registration in other fields of study) [3] or its three-dimensional variant called Digital Volume Correlation (DVC) [4, 5]. Unlike local matching techniques [6], the global DVC method facilitates this dialogue through finding a smooth unknown displacement field in a space of approximation suited for analysis. As a first step towards this long-term goal, our present contribution focuses only on the strain field assessment.

DVC in complex microstructures presents multiple changes and challenges when compared to 2D DIC. For instance, in most two-dimensional cases, a speckle pattern can be deposited onto the sample in order to introduce sufficient gray-level gradient values in the images. However, for DVC, the only information available is the intrinsic gray-level values of the material. That is why it seems that conventional DVC algorithms can only be applied when materials exhibit a natural speckle pattern (for instance graphite nodules [7]). In addition, the interpolation of the displacement field can be tricky. For example, when deforming cellular materials (see Fig.2 as illustration), localized deformations could occur. These deformations cannot be captured by low order shape functions used in traditional subset-based or finite element algorithms.

Our contribution concerns the development of a Free-form DIC algorithm that is capable of characterizing local deformations in cellular materials. For that we construct an automated DIB mechanical model and use it as a regularization for the DIC problem as proposed by Réthoré et al. [8]. When using voxel-based methods, which consist of converting the voxel data into a low order finite element mesh, a large number of degrees of freedom is obtained. Furthermore, when images are poorly resolved, non-smooth strain fields may be obtained due to the irregularities of the finite element mesh. In order to overcome the geometric problem, we use a B-spline level-set method in

order to give a smooth description of the geometry represented by the voxel data [9]. Using this level-set function, the mechanical solution is computed using non-conforming meshing techniques as proposed in [10].
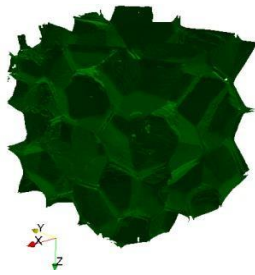
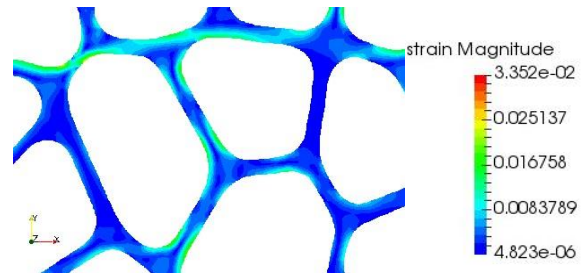Fig. 1. Three-dimensional reconstruction of a Polymethacrylimid closed foam

Fig. 2. Strain field in a simplified dimensional cellular material. Local flexions are observed on the microscopic scale

2. References

[1] Avril, S., Bonnet, M., Bretelle, A. S., Grédiac, M., Hild, F., Ienny, P., ... & Pierron, F. (2008). Overview of identification methods of mechanical parameters based on full-field measurements. *Experimental Mechanics*, 48(4), 381.

[2] Hollister, S. J., & Kikuchi, N. (1994). Homogenization theory and digital imaging: a basis for studying the mechanics and design principles of bone tissue. *Biotechnology and bioengineering*, 43(7), 586-596.

[3] Horn, B. K., & Schunck, B. G. (1981). Determining optical flow. *Artificial intelligence*, 17(13), 185-203.

[4] Bay, B. K., Smith, T. S., Fyhrie, D. P., & Saad, M. (1999). Digital volume correlation: threedimensional strain mapping using X-ray tomography. *Experimental mechanics*, 39(3), 217226.

[5] Gomes Perini, L. A., Passieux, J. C., & Périé, J. N. (2014). A multigrid PGD- based algorithm for volumetric displacement fields measurements. *Strain*, 50(4), 355-367.

[6] Hild, F., & Roux, S. (2012). Comparison of local and global approaches to digital image correlation. *Experimental Mechanics*, 52(9), 1503-1519.

[7] Leclerc, H., Périé, J. N., Roux, S., & Hild, F. (2011). Voxel-scale digital volume correlation. *Experimental Mechanics*, 51(4), 479-490.

[8] Réthoré, J., Roux, S., & Hild, F. (2009). An extended and integrated digital image correlation technique applied to the analysis of fractured samples: The equilibrium gap method as a mechanical filter. *European Journal of Computational Mechanics/Revue Européenne de Mécanique Numérique*, 18(3-4), 285-306.

[9] Verhoosel, C. V., Van Zwieten, G. J., Van Rietbergen, B., & de Borst, R. (2015). Imagebased goal-oriented adaptive isogeometric analysis with application to the micro-mechanical modeling of trabecular bone. *Computer Methods in Applied Mechanics and Engineering*, 284, 138-164.

[10] Schillinger, D., & Ruess, M. (2015). The Finite Cell Method: A review in the context of higher-order structural analysis of CAD and image-based geometric models. *Archives of Computational Methods in Engineering*, 22(3), 391-455.

LASER ULTRASOUND FLEXIBLE SYSTEM
USING MID-WAVE INFRARED GENERATION LASER
FOR NON-CONTACT INSPECTION OF COMPOSITE STRUCTURES
MADE OF CARBON FIBER REINFORCED POLYMER

J.-F. Vandenrijt, F. Languy and M. Georges
Center Spatial de Liège, University of Liège, Liège, Belgium

1. Introduction

Ultrasonic testing (UT) [1,2] is commonly used in the industry for the investigation of carbon fiber reinforced polymer (CFRP). It is wide-spread and very efficient but, major problems arise when the shape of the element to be investigated is complex (peak, valley, small radius of curvature…). To overcome these problems laser ultrasonic testing (LUT) can be used and the recent developments show promising results.

Compared to classical UT, LUT offers the advantage that no contact nor couplant are needed and points difficult to access can be illuminated by laser beams at distance. LUT usually combines two principles: the first one is the generation of an ultrasonic wave by a laser [2]. For generation, CO_2 lasers emitting at 10 μm wavelength are usually used. However, the optical fibers for 10 μm wavelength are not capable to cope with laser ultrasonic system needs. Therefore, infrared systems use a jointed articulated beam delivery system which limits the flexibility of the arm. To circumvent this limitation, an all-fibered laser ultrasonic system can be used. For this purpose, visible wavelengths are becoming more common. However, visible generation is more likely to damage the sample under investigation.

Halfway between these two technologies, OPO lasers are commercially available in the range of 3 to 3.5 μm wavelength. They already have been considered in earlier experiments with CFRP which show that it is an advantageous wavelength compared to visible/near infrared or far infrared generation. Mid-infrared (MIR) generation is expected to combine both advantages of visible and far-infrared. Solutions now exist for transporting MIR light of OPO lasers into fiber, thus avoiding articulated beam delivery system. Also MIR can be used at higher power than visible light without damaging the surface of the sample under investigation. For these reasons, we have started developing a fully-fiber coupled laser ultrasonics head with MIR OPO generation to put on a robot arm for the non-destructive inspection of CFRP components. In this conference, we will present the first step of this development, and results obtained on a reference plate with the OPO and are compared to those obtained with the green (532 nm) and far infrared (10.6 μm) generations.
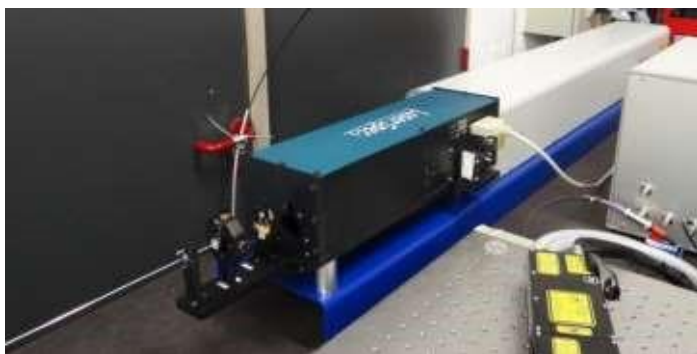
Fig. 1. General view of the OPO laser
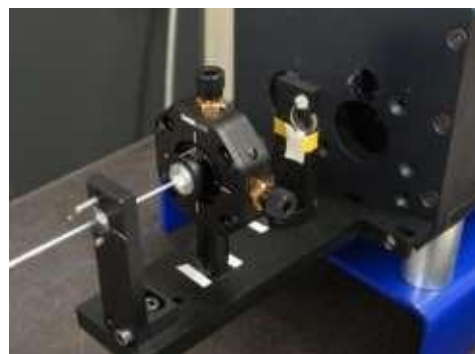
Fig. 2. Fiber injection assembly

2. Effect of Generation Laser Wavelength

We started investigation of a high power midwave infrared (MWIR) optical parametric oscillators (OPO) pulsed laser tunable between 2.9 and 3.5 μm. In the past, such lasers were difficult to find with fiber coupling, which is no longer the case. Such wavelength is believed to give better performances than other wavelengths [3]. We took this opportunity to test MWIR laser with our system and compare the results. The current system is not yet implemented on the robotic arm.

In this conference, we present the first step of the development of the mid-infrared generation system, still under work and the expectations we have for the future instrument. First, we present the investigations of the performances of a 4-meters long fiber. Then we show C-scan of a CFRP sample and compare it with the same plate measured realized in visible and in MWIR, and with another one which uses the same detector (Tecnar TWM) but a TEA CO2 laser from Light Machinery for the generation. We analyze and show the main differences on the A-scans and Cscan generated by each system. From these elements, we show the expectation we have for the final instrument, and the planning of the rest of the development activities.
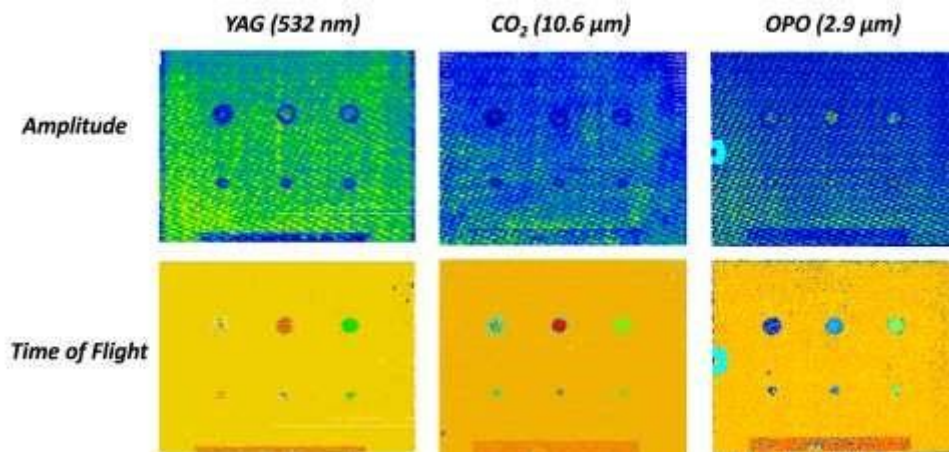
Fig. 3. C-scans scans in amplitude and time-of-light with three different generation wavelengths

3. References

[1] Scruby, C.B.; Drain, L.E. (1990). *Laser Ultrasonics. Techniques and Applications*; Adam Hilger: Bristol, UK; New York, NY, USA; Philadelphia, PA, USA.

[2] Monchalin, J.-P. (2004). Laser-ultrasonics: From the laboratory to industry. *AIP Conf. Proc. 2004*, **700**, 3–31.

[3] Lorraine, P.; Dubois, M.; Bauco, A.S.; Filkins, R. (2000). A new laser source for ultrasound generation in composites. *AIP Conf. Proc. 2000*, **509**, 295–301.

FULL-FIELD IDENTIFICATION OF MIXED-MODE ADHESION PROPERTIES IN MICROELECTRONICS FROM MICROGRAPHS ONLY

J.P.M. Hoefnagels[1], A.P. Ruybalid[1], O. Van der Sluis[1,2] and M.G.D. Geers[1]
[1] Dept. of Mechanical Engineering, Eindhoven University of Technology, the Netherlands
[2] Philips Research Laboratories, Eindhoven, the Netherlands

1. Extended abstract

Identifying the adhesion properties of interfaces in multi-layer, microelectronic devices, e.g., light-emitting diodes, is challenging due to (1) the small-scale deformations requiring appropriate microscopic techniques, (2) the small, multi-directional forces within the different material layers and their interfaces, and (3) the complex loading conditions to which these systems are subjected during fabrication and operation. Because of the large variability in thermo-mechanical properties and fabrication-dependent loading conditions, identifying the relevant adhesion properties is most accurately done on actual microelectronic devices, rather than on dedicated specimens. This necessitates high resolution testing setups in combination with robust and accurate parameter identification tools, both of which are de- veloped and realized in this dissertation. The strategy of investigation adopted here is to first generate virtual experimental data (by numerical methods) in order to develop and optimize the proposed methods, after which they are applied in real experiments.

The identification of mechanical model parameters can be achieved by utilizing full-field kinematic data in the form of micrographs, in combination with finite element simulations, as done in, e.g., Finite Element Model Updating (FEMU) and Integrated Digital Image Correlation (IDIC) [1,2]. The performances of these seemingly similar methods has been compared in order to select the most appropriate of the two for mechanical characterization of microelectronic systems. Based on virtual experimentation, in which a variety of realistic error sources are investigated, it is concluded that IDIC is more reliable than FEMU, especially for cases involving the abovementioned challenges that are typical for microelectronic devices.

Subsequently, the method of IDIC has been advanced for identifying the mechanical parameters of a cohesive zone model.[3,4,6] The complications arising in microelectronic specimens are investigated by artificially imposing important error sources in a well-known test-case, involving a small-scale, virtual double cantilever beam specimen.[3] Erroneous boundary conditions in the employed finite element model were identified as the most critical error source, mainly because the far-field boundary conditions applied in the experiment lie outside the microscopic field of view, and for which assumptions would be required. Instead of assuming the experimentally applied, farfield boundary conditions, a method is developed that enables adequate measurement and application of local boundary conditions in a finite element model that corresponds to the restricted, microscopic field of view. A mode-I interface delamination experiment on a real double cantilever beam specimen subsequently demonstrates that, when the elasticity parameters of the deforming cantilever beams are known, no force data is required for accurately identifying cohesive zone parameters with the developed method.[3]

The next step was the extension of the method for identifying mixed-mode cohesive zone parameters from a single experiment on a small-scale, double cantilever beam specimen, i.e., without the need for performing multiple tests under different levels of mode-mixedness.[4] Virtual experimentation provides a comprehensive understanding of the intricate role of the method's kinematic sensitivity towards the parameters of interest. By assessing kinematic sensitivity fields, the most appropriate experimental data and boundary conditions can be utilized in order to ensure high

accuracy and robustness of the identification method. Indeed, realistic virtual experiments showed that for optimized load cases, robust identification of the elusive interface parameters with errors below 1% is possible [4]. The method has been validated by conducting real mixed-mode bending experiments on double cantilever specimens and identify the mixed-mode cohesive zone parameters.[4]

To mechanically deform multi-layer material/interface systems, a micro-mechanical testing apparatus, composed of commercially available piezoelectric actuators, is devised and described in [5]. The testing rig can impose a variety of loading paths in different directions (resulting in tension, compression, bending, shear, out-of-plane deformation, etc.) to approach the realistic loading conditions that microelectronic systems experience during fabrication and operation. A force measuring algorithm is developed and implemented in the actuators' controlling software, which solves the corrupting drift effects associated with piezoelectric actuators. High-resolution force measurements in all directions are thereby made possible, without the need for external force sensors. Furthermore, the compact design and the vacuum compatibility of the setup allow for insitu testing of small-scale specimens in combination with a variety of microscopic techniques.[5]

Finally, the realized micro-mechanical testing apparatus has been used to deform a multi-layer barrier stack of a flexible, organic light-emitting diode (OLED), with the eventual goal of identifying the relevant adhesion properties by IDIC.[6] Before parameter identification is realized, virtual experiments have been conducted to simulate the loading conditions imposed by the mechanical test setup, in order to understand the required experimental conditions, as needed for reliable identification results.[6] Subsequently, real experiments have been used together with IDIC, extended with the developed methods for boundary condition application and kinematic sensitivity optimization, in order to identify the mechanical parameters of the considered material/interface system. It was found that for optimized experimental load cases, the IDIC optimization scheme robustly converged to a unique solution for the mixed-mode CZ parameters [6].

2. References

[1] J. Réthoré, S. Roux, F. Hild (2009). An extended and integrated digital image correlation technique applied to the analysis of fractured samples, *Eur. J. Comp. Mech.* **18**, 285.

[2] A.P. Ruybalid, J.P.M. Hoefnagels, O. van der Sluis, M.G.D. Geers (2016). Comparison of the identification performance of conventional FEM-Updating and Integrated DIC, *Int. J. Num. Meth. Eng.* **106**, 241.

[3] A.P. Ruybalid, J.P.M. Hoefnagels, O. van der Sluis, M.G.D. Geers (2018). Image-based interface characterization with a restricted microscopic field of view, *Int. J. Solids. Struct.* **132**, 218.

[4] A.P. Ruybalid, J.P.M. Hoefnagels, O. van der Sluis, M.G.D. Geers (2019). Mixed-mode cohesive zone parameters from integrated digital image correlation on micrographs only, *Int. J. Solids. Struct.* 156, 179.

[5] A.P. Ruybalid, O. van der Sluis, M.G.D. Geers, J.P.M. Hoefnagels (2019). *An in-situ, micromechanical setup with accurate, tri-axial, piezoelectric force sensing and positioning*, accepted for publication in Experimental Mechanics

[6] A.P. Ruybalid, O. van der Sluis, M.G.D. Geers, J.P.M. Hoefnagels (2020). Full-field identification of mixed-mode adhesion properties in a flexible, multi-layer microelectronic material system, *Eng. Fract. Mech.* **106879**.

MODAL SHAPE VISUALIZATION EMPLOYING FP+2D-DIC AND PHASED-BASED MOTION MAGNIFICATION

M. Pastor-Cintas[1], L.A. Felipe-Sesé[1], Á.J. Molina-Viedma[1], E. López-Alba[2] and F.A. Díaz[2]
[1] *Departamento de Ingeniería Mecánica y Minera, Campus Científico Tecnológico de Linares, Universidad de Jaén, 23700 Linares, Spain*
[2] *Departamento de Ingeniería Mecánica y Minera, Campus Las Lagunillas Universidad de Jaén, 23071 Jaén, Spain*

1. Introduction

In the last years the combination of Fringe Projection (FP) and Digital Image Correlation with one camera (2D-DIC) techniques have been applied to different mechanical analysis such as vibration with low frequency excitation [1,2]. As DIC and FP is a displacement measuring technique, low level of displacements related to high frequency excitation represents a challenging task. In this work, a new tool has been explored for FP+DIC in the interpretation of subtle periodic motion. It consists in phase-based motion magnification using image decomposition through complex steerable pyramid filters which has been previously employed with 3D-DIC [3].

2. Background

Technique FP + 2D DIC

Digital Image Correlation (DIC) has been presented in the last decades as an alternative to classical transducers in vibration analysis [1]. 2D–DIC allows the measurement of displacements on a plane perpendicular to the optical axis (in-plane displacements) with one camera. When two cameras are employed, the 3D–DIC technique enables the measurement of displacements experienced in the three spatial directions [4]. Fringe Projection (FP) is an alternative full-field optical technique that can be used to determine displacements in the direction of the camera optical axis for a deformed object by obliquely project a fringe pattern [5].

The combination of both 2D–DIC and FP techniques was demonstrated by authors to provide a low-cost alternative to 3D–DIC for measuring in- and out of-plane displacements maps with only one CCD camera and a fringe projector [1].

Phase-based motion magnification + 2D DIC

High speed video cameras provide valuable information in dynamic events facilitating mechanical characterization. In modal analysis, videos contribute to the evaluation of mode shapes, but motion could be too subtle to be interpreted. Recently, image treatment algorithms have been developed to generate a magnified version of the motion that could be interpreted by naked eye. In this work, magnification of the captured images sequence in each test was performed according to the phase-based magnification method proposed by Wadhwa et al. [6]. By this methodology, the sequence is decomposed using complex steerable pyramids. Temporal variation of the local phase is found as an indicator of the motion. By analysing the phase signal in the frequency domain, a magnification factor can be applied to a desire band and reconstruction video.

3. Methodology

In this work, images after magnification process have been analysed with FP+2D DIC methodology to evidence displacements hidden to human eye. To illustrate this capability, the displacement behaviour of a cantilever beam was studied at different natural frequencies. In fact, test

has been performed on a polycarbonate beam of 160 x 40 x 2 mm exited at one and end with a shake. Images along the test were captured using strobe method with a 3CCD camera and processed with FP and 2D-DIC algorithms to quantify the periodic movement. Specifically, phase based motion magnification was used when the mode shape was not clear.

4. Results

It will be presented the results of the measurements of the mode shapes obtained during vibration at the first (20 Hz), second (160 Hz) and third (450 Hz) resonance frequencies (Fig. 1 and 2). For, third mode shape required the performing of the motion magnification as observed in Fig 2.
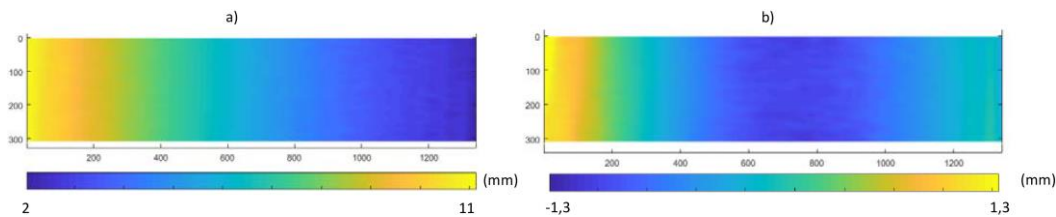
Fig. 1. Displacement fields obtained with FP+2D DIC for a) first mode shape
and b) second mode shape
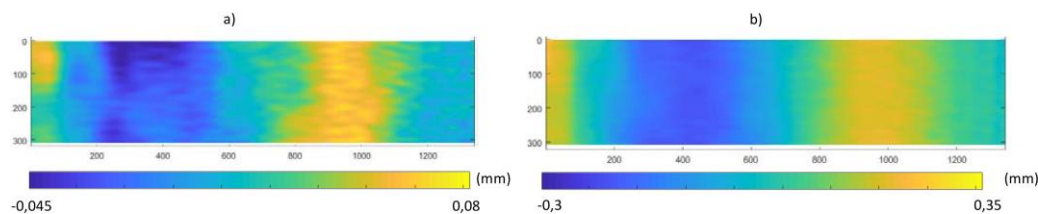
Fig. 2. Displacement fields obtained with FP+2D DIC for a) third mode shape and displacement
field result after performing magnification x5

5. Conclusions

Phase motion Magnification has been demonstrated to be a valuable tool to evidence subtle displacement, which could also be quantified in displacement fields employing FP+2D DIC.

6. References

[1] L. Felipe-Sesé, P. Siegmann, F.A. Díaz, E.A. Patterson, Simultaneous in-and-out-of-plane displacement measurements using fringe projection and digital image correlation, Opt. Lasers Eng. 52 (2014) 66–74.

[2] L. Felipe-Sesé, F.A. Díaz, Damage methodology approach on a composite panel based on a combination of Fringe Projection and 2D Digital Image Correlation, Mech. Syst. Signal Process. 101 (2018). doi:10.1016/j.ymssp.2017.09.002.

[3] A.J. Molina-Viedma, L. Felipe-Sesé, E. López-Alba, F.A. Díaz, 3D mode shapes characterisation using phase-based motion magnification in large structures using stereoscopic DIC, Mech. Syst. Signal Process. 108 (2018). doi:10.1016/j.ymssp.2018.02.006.

[4] M.A. Sutton, J.J. Orteu, H.W. Schreier, Image Correlation for Shape, Motion and Deformation Measurements- Basic Concepts, Theory and Applications, Image Rochester NY. (2009) 341. doi:10.1007/978-0-387-78747-3.

[5] M. Takeda, K. Mutoh, Fourier transform profilometry for the automatic measurement of 3-D object shapes, Appl. Opt. 22 (1983) 3977. doi:10.1364/AO.22.003977.

[6] N. Wadhwa, M. Rubinstein, F. Durand, W.T. Freeman, Phase-based video motion processing, ACM Trans. Graph. 32 (2013) 1. doi:10.1145/2461912.2461966.

DIC VERIFICATION OF FEA DATA MODELED ON REAL CT SCANS

M. Kneć[1], M. Wątrobiński[2], P. Golewski[3] and J. Andrzejewski[4]
[1] Lenso Sp. z o.o., Poznań and Lublin University of Technology, Poland
[2] Syntplant Sp. z o.o., Poznań, Poland
[3] Lublin University of Technology, Poland
[4] Poznań University of Technology, Poland

1. General

FEA modeling is almost always based on FEA meshes built on CAD objects. CAD objects are created in the software so they always have ideal tolerance dimensions and so on.

One of the methods of verification of FEA models is to measure the actual object and analyze it using the DIC ARAMIS system, and then compare the corresponding inspections, e.g. major strain and present the results as a 3D differences map between FEM analysis and real measurement with maintaining similar boundary conditions.

ARAMIS measures the actual object, therefore the results that will be calculated will automatically contain all components affecting the FEM analysis – e.g. CAD discrepancy to the real object, other than the material data used in modeling, or not taking into account all phenomena that occur in the places of support.

Having the results of analyzes from the ARAMIS system, in the next steps it is possible to improve the FEM mesh by replacing it with a mesh built on the scan with a 3D scanner (e.g. ATOS), change the material data or the entire FEM material model to measured and not use tabular data, take into account friction or other phenomena in modeling. After several iterations and imports of the FEM model into the ARAMIS system, the values of the analyses should approach those obtained from the measurements and finally it will be possible to consider the FEA model as validated (with the percentage difference of results assumed at the beginning).

However, in cases where it is not possible to create a FEM model correctly or scan it with a 3D scanner, you need to use other methods to model FEM. An example of such situation is an attempt to model an organic object printed with a 3D printer.

During surgical operations related to the removal of a fragment of the skull, there is a need to renew the skull-shaped defect after surgery. One of the methods is to print a special overlay - a scaffolding around which over time the bone will grow back and the shape of the skull will be recreated.

The material from which such elements are printed must be bio-safe and bio-resorbable. The development and validation of the FEA model will allow it to be used later to create organically appropriate shapes depending on the individual patient. The CT scanner (GOM Metrotom 1) allowed to obtain an STL mesh taking into account all invisible places as well as places of voids inside the overlay structure.

In the next step, ARAMIS tests were performed on these scanned samples and FEM analysis was performed using the STL mesh from the GOM Metrotom 1 scanner.

Fig. 1 a) represents STL mesh view, b) inside mesh view including voids.

To create the FEM model, after many attempts, HyperMesh software from the HyperWorks package was finally used, provided for testing by the company (Endego Sp. z o.o. Poland). The FEM model taking into account the lack of material in the places of voids, containing a properly created filling using C3D10 elements is visible in Fig. 1b. Silver zones are places of lack of material. In the further analysis of FEM, a model visible as brown taking into account voids, was used.
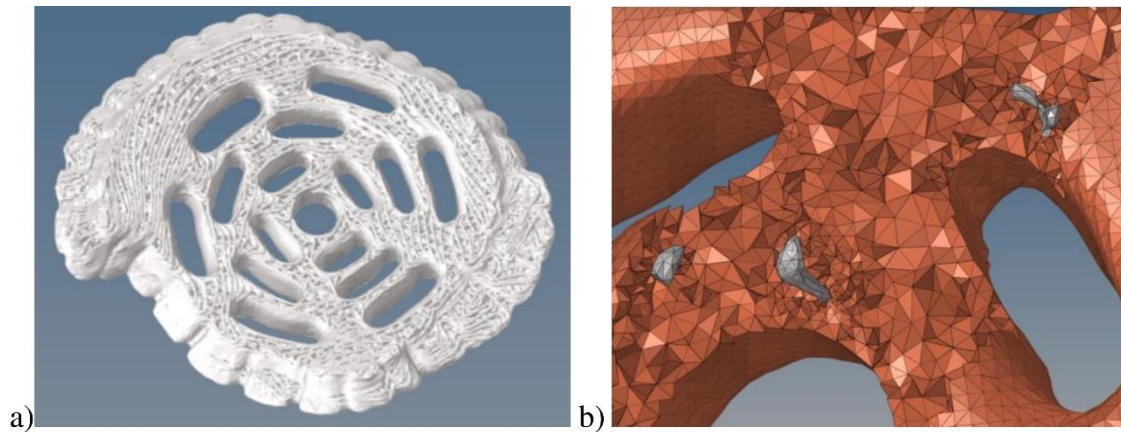
Fig. 1. a) STL model b) FEA model with empty spaces

The way the implant works may vary depending on the patient, conditions and many other factors. In order to determine which solution is most suitable (type, print, direction, method, shape), it was decided to perform comparative tests in a simple compression test with the same test conditions. After the ARAMIS test, comparisons of FEM analysis to measurement were made, Fig.2.
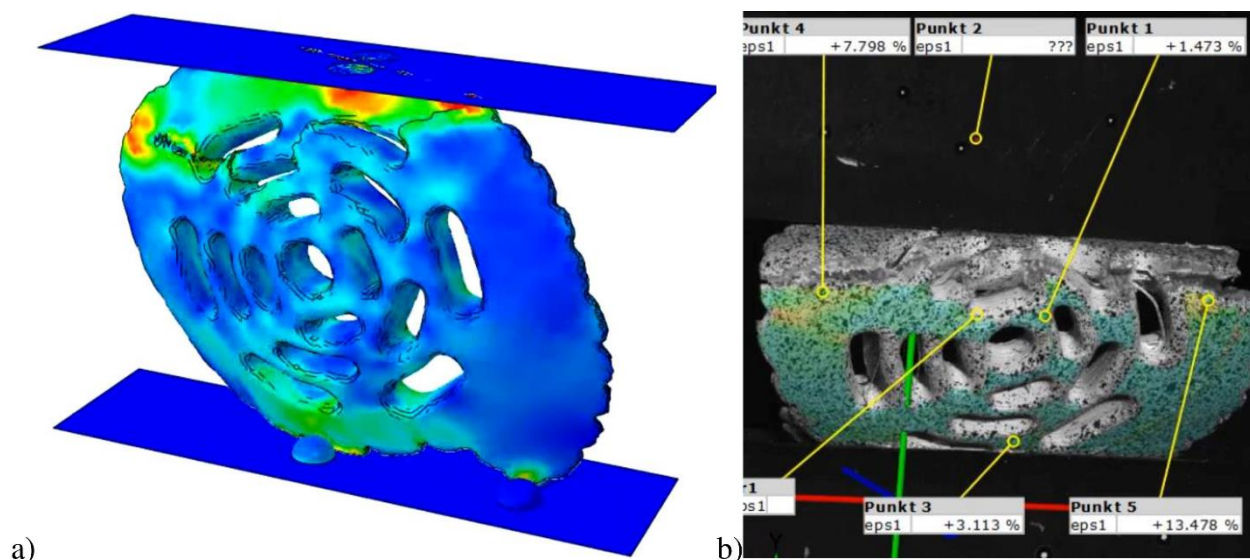
Fig. 2 Major strain analysis a) FEA b) ARAMIS

2. References

[1] L. Marsavina, T. Sadowski and M. Kneć (2013). Crack propagation paths in four point bend Aluminium–PMMA specimens, *Engineering Fracture Mechanics,* **108**, 139–151.

[2] T. Łusiak and M. Kneć (2018) Use of Aramis for fatigue process control in the accelerated test for composites, International Conference on Air Transport – INAIR 2018, *Transportation Research Procedia*, **35**, 250–258.

8. Recent Advances in Photoelastic Applications

A PHOTOELASTIC METHOD BY ENHANCED EXPOSURE FOR LOW-LEVEL STRESS MEASUREMENT IN THIN GLASS PLATE

P.-C. Sung, W.-C. Wang and Y.-L. Yeh
Department of Power Mechanical Engineering, National Tsing Hua University
Hsinchu, Taiwan, Republic of China

1. Introduction

Glass plate has been one of the most important elements in high-tech products and industries. Due to the low temporary birefringent property and the thinner and thinner thickness of the glass plate, the measurement of the low-level stress in the thin glass plate has been quite difficult for the conventional photoelastic techniques [1]. Besides, most of the instruments which are able to measure the low birefringence have to additionally use expensive devices such as the photoelastic modulator and/or the lock-in amplifier. Moreover, these instruments can only perform the single point measurement.

In this paper, based on the phase-shifting technique, a new measurement method named enhanced exposure theory of photoelasticity (EEToP) [2] was proposed to determine the low-level stress in the thin glass plate. The EEToP is implemented by a basic plane polariscope. In addition, owing to the use of CCD camera, the full-field stress distribution can be obtained simultaneously. Furthermore, the principle of EEToP can be used in not only the phase-shifting technique but also the white light photoelasticity and the transmissivity extremities theory of photoelasticity (TEToP) recently proposed by Sung and Wang et al. [3]. A Soleil-Babinet compensator (SBC) was employed to verify the feasibility and the measurement accuracy of the EEToP. The results show that the retardation smaller than 10nm still can be accurately measured.

2. Concept of EEToP

When the thin glass plate is with low-level stress, the light intensity of the isochromatic fringe pattern is too weak so that it is difficult to be detected by the conventional photoelasticity. The concept of the EEToP is to measure the relationship between the exposure time of the camera and the light intensity value evaluated by the camera. Then, the intensified light intensity of the isochromatic fringe pattern is captured by enhanced exposure. Finally, by using the relationship between the exposure time and light intensity value, the low-level stress can be calculated from the intensified light intensity of the isochromatic fringe pattern. The advantage of EEToP is as follows:
1. the low-level stress in ultra-thin glass plate can be determined,
2. the measurement resolution of EEToP can be increased without the need of improving the equipment, and
3. only two polarizers, a light source, and a camera are used in the measurement setup.

3. Experimental setup, specimen, and results

To implement the EEToP, a plane polariscope was employed. A sodium lamp with wavelength of 589.2nm was used as the light source. A 16bit CCD camera (STF-8300, SBIG) was used to capture the phase-shifting images of EEToP.

Before measurement, the SBC (SBC-VIS, THORLABS) needs to be calibrated in the plane polariscope to make the retardation of the SBC can be generated correctly. After the calibration of the SBC was done, three standard retardations, i.e. 3.326nm, 6.652nm, and 9.979nm were generated

by the SBC and were measured by the EEToP. The measurement results of EEToP to these three standard retardations were 3.261nm, 6.591nm, and 9.936nm, respectively. The corresponding absolute differences between these three standard retardations and measurement results were 0.065nm, 0.061nm, and 0.043nm, respectively. It is demonstrated that the EEToP can measure the low retardation with high accuracy.

4. Conclusions

In this paper, the low-level stress measurement method EEToP was proposed so that the stress in the ultra-thin glass plate can be actually measured. The feasibility and the measurement accuracy of EEToP was verified by the SBC. Therefore, the EEToP has been able to be applied in industry to help the manufacturer inspect the stress and defect of product and improve the manufacturing process.

5. Acknowledgements

6. References

[1] K. Ramesh (2000). *Digital Photoelasticity: Advanced Techniques and Applications*, Springer, Berlin, Germany.

[2] W.C. Wang, P.C. Sung, Z.Y. Lu, Y.L. Yeh, and P.Y. Chen, (2018) Stress Measurement Method and System for Optical Materials, *United States Patent*, Patent Application Number: 15/618,145, Publication Number: US20180164169A1, Patent Number: 10067012, Application Date: 2017/6/09, Publication Date: 2018/6/14. Issued Date: 2018/09/04.

[3] P.C. Sung, W.C. Wang, C.H. Hwang, and G.T. Lai (2018) A low-level stress measurement method by integrating white light photoelasticity and spectrometry, *Optics and Laser Technology*., **98**, 33-48.

RATIONAL DESIGN OF A NEW REFLECTION PHOTOELASTIC COATING

W.H. Fraser[1], R.A. Tomlinson[1] and A.J. Parnell[2]
[1] Department of Mechanical Engineering, The University of Sheffield, Sheffield, UK
[2] Department of Physics and Astronomy, The University of Sheffield, Sheffield, UK

1. Introduction

Reflection Photoelastic Stress Analysis (RPSA) is an experimental technique used in industries to assist in a variety of design and manufacture processes. Users can benefit from immediate qualitative and quantitative information, for example, about maximum shear strains in complex geometries. Recent developments, and commercial availability, in automated collection and analysis of photoelastic data has given potential for RPSA to be a truly effective method. However, current RPSA methods are hindered by complicated coating application processes, a need for skilled engineers and large timescales for data collection. These issues all stem from one vital component – the photoelastic coating material. This research has demonstrated the possibility of improving upon these drawbacks by designing a new coating material that is thinner (~50 μm), easy-to-apply, and curable in a matter of minutes. Furthermore, this new coating has been shown to be comparable to commercially available photoelastic materials in its response.

2. Photoelastic coating

Common reflection photoelastic materials utilise thermoset resins as either an adhesive for a polycarbonate sheet or as a mouldable coating for use on complex geometries. Application processes are difficult to perfect and often produce undesirable qualities that affect a coating's photoelastic response. Such effects include non-uniform adhesive layers creating residual stresses or air bubbles in transparent coating, distorting captured photoelastic images. Another inconvenient attribute of thermoset resins is their long cure times, often upwards of twenty-four hours.

This research investigated the potential of UV curable resins to produce rapid, energy efficient and low-cost chemical reactions when compared to thermosets. A variety of resins were chosen and combined in different quantities to form thirty formulations. After initial photoelastic testing, the resin compositions of formulations that presented ideal properties (low residual birefringence, high sensitivity to strain, curing performance etc.) were analysed further using a Design of Experiments (DOE) statistical package, utilising a mixture design, to optimise the resin blend.

3. Photoelastic analysis and experimental setup

To investigate a formulation's photoelastic performance, coatings were cured onto aluminium beams at a thickness of approximately 50 μm. The beams were subjected to various cantilever deflections with a consistent location chosen for photoelastic analysis. Photoelastic analysis was used to measure the induced retardation between two mutually perpendicular components of light that interacted with the coating. The formulation's normalised retardation data were compared directly to beams coated with a commercially available polycarbonate sheet, Micro-Measurements' PS-1E sheet adhered with PC-10 two-part adhesive (www.micro-measurements.com).

A GFP1600 grey-field polariscope (www.stressphotonics.com) was used, in conjunction with the DeltaVision image and acquisition software, to provide automated full-field magnitude and directional data with a sub-fringe resolution of better than 0.1 nm, figure 1. Once the formulation

composition was finalised, its strain-optic coefficient can be calculated and inputted into the software to translate retardation data into micro-strain with a 20 micro-strain resolution.
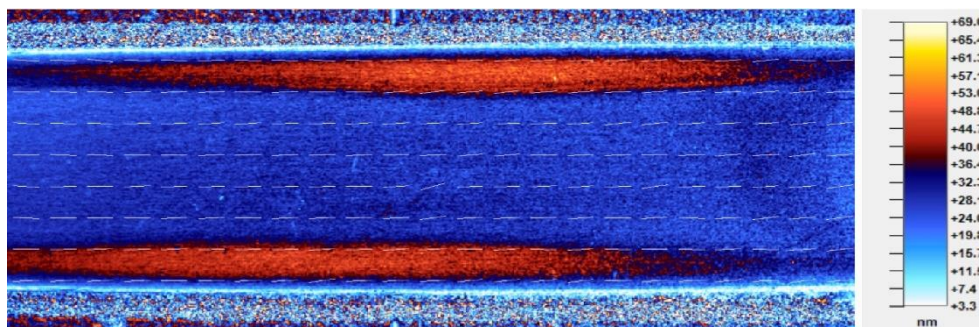
Fig. 1. Photoelastic analysis of an aluminium beam at a maximum cantilever deflection of 20.32mm. Directional vectors represent the orientation of the first principal strain. Orange regions represent the edges of the beam where a meniscus has formed increasing coating thickness.

4. Experimental results

Through rational design, a potential UV curable coating was established. It's response to cantilever deflections was linear and it possessed only a small initial residual birefringence, comparable to the PS-1E sheet. Strain gauges were then used to measure the principal strains at the point of measurement. As a result, the formulation's strain-optic coefficient (K) was calculated to be 0.042 which demonstrates a suitable sensitivity for use in photoelastic analysis. Figure 2 compares the principal strain difference determined using strain gauges and the two coatings and demonstrates that the UV curable coating is linear throughout the deflection whilst the PS-1E sheet's strain limit is breached beyond a 0.8 mm deflection. This it is concluded that this new coating shows great potential in comparison to existing technologies.
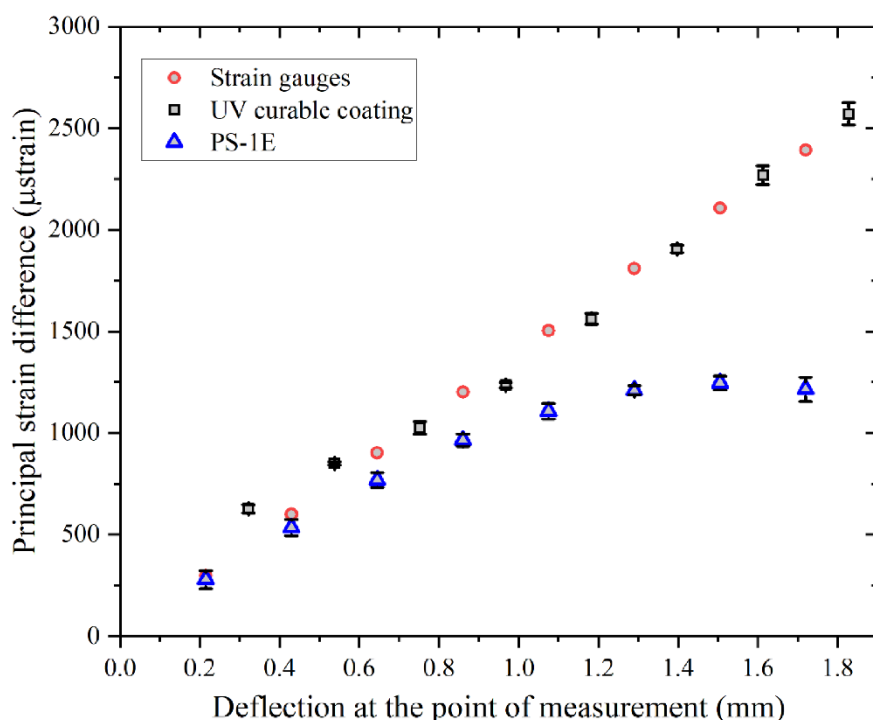
Fig. 2. Comparison of principal strain difference of the cantilever beam

9. Smart Materials and Structures

OBSERVATION OF PLASTIC DEFORMATION IN GUM METAL BY IN-SITU COMPRESSION IN TEM

S. Kuramoto[1], K. Onose[2], E. Nakagawa[3] and T. Ohmura[3,4]
[1] *Ibaraki University, Hitachi, Japan*
[2] *Graduate School, Ibaraki University, Hitachi, Japan*
[3] *National Institute of Materials Science, Tsukuba, Japan*
[4] *Kyushu University, Fukuoka, Japan*

The beta titanium alloy, called " Gum Metal " [1,2], with a typical composition of Ti-23Nb-0.7Ta-2.0Zr-1.2O (at.%) has been of great interest since bulk samples of this alloy remains elastic until loaded to near ideal strength. The niobium, tantalum and oxygen in Gum Metal are important alloying elements in terms of obtaining the critical phase stability which is considered to be responsible for outstanding mechanical properties and the unique deformation behavior. The alloy also has unusual physical properties, including Invar-like thermal expansion and Elinvar-like thermal dependence of the elastic modulus [1]. The Invar-like property of Gum Metal is reversible from 173 to 473 K without any phase transformations [1]. However, the mechanism for these properties is not fully understood.

In the present study, deformation behavior has been studied in Gum Metal using in-situ nanopillar-compression tests in transmission electron microscope (TEM). The sample was solution treated at 900 ºC for 30 min and quenched in water at room temperature. Pillar specimens with 100 nm in thickness and 400 nm in width were made using focused ion beam (FIB) device to have <001> direction along compression direction. In-situ observations for dislocation activity and phase transformation during compression test of these pillars have been performed in bright-field and diffraction modes in TEM (JEM 2010F) and Hysitron PI 95 TEM PicoIndenter [3].

Figure 1 shows an example of an image obtained from a video in bright-field mode test of a Gum Metal pillar just after unloading of the compression test. The pillars were loaded with a flat punch which appears in the lower right of the figure and the compression direction is shown in the figure.
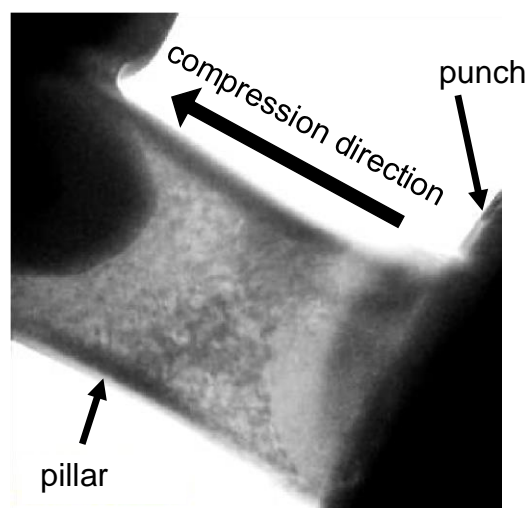
Fig. 1. Bright field image of a pillar just after unloading of compression test

During the compression test, the pillar of the Gum Metal specimen was plastically deformed in compression, but distinct contrast of dislocations has not been observed during the tests in bright field

mode. However subtle contrast change, which might be related to dislocation motion, has been observed in localized areas. After the compression test, the pillar was observed using a 2-axis-tilting TEM holder to enable a detailed observation with various diffraction conditions. Again, distinct contrast of dislocations was not observed in the Gum Metal pillar after compression.

Figure 2 shows a load-displacement curve during the compression test of the pillar shown in Fig. 1. The pillar showed elastic deformation in the early stage of compression and started to deform plastically after about 50 nm in displacement. The load-displacement curve appears very smooth and continuous. Previous researches have shown that nano-pillar specimens which has very low dislocation density before compression often show sudden large load drops during compression tests. This implies that local strain burst occurred in the pillars in relation to multiplication of dislocations or dislocation avalanche [4, 5]. In the present observation in Gum Metal pillars, such activity related to dislocation motion has not been observed.
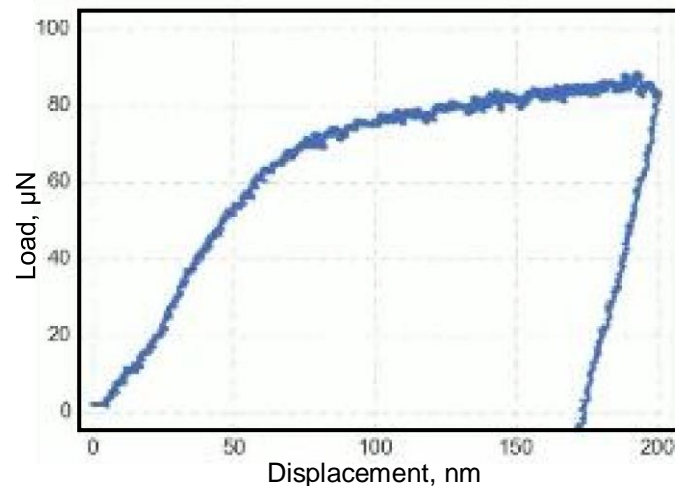
Fig. 2. Load-displacement curve of a pillar shown in Fig. 1

In the diffraction mode, pre-existing diffraction from omega phase decreased, and diffraction from α" Gum Metal with large length-to-thickness ratio showed a large amount of pseudoelastic deformation after unloading. These results will be discussed in relation to the effect of bcc phase stability on plastic deformation mechanism in beta titanium alloys.

References

[1] T. Saito, et al., Science 300 (2003) 464.
[2] T. Furuta, et al., Mater. Trans. 12 (2005) 3001.
[3] K. Onose, et al., J. Japan Inst. Light Metals 69 (2019) 273.
[4] L. Zhang, et al., Mater. Sci. Eng. A, 611 (2014), 188. [5]
[5] Y.-C. Hsieh, et al., Scr. Mater., 125 (2016), 44.

THERMO-ELECTRO-MECHANICAL CHARACTERIZATION OF A SHAPE MEMORY COMPOSITE DURING ELECTRIC ACTIVATION

C. Pereira Sánchez[1], M. Houbben[2], J.F. Fagnard[1], P. Harmeling[1], C. Jérôme[2], L. Noels[3] and P. Vanderbemden[1]

[1] *University of Liège, Sensors and electrical measurement systems, Liège, Belgium*
[2] *University of Liège, Centre for education and research on macromolecules, Liège, Belgium*
[3] *University of Liège, Computational and multiscale mechanics of materials, Liège, Belgium*

1. Introduction

Shape memory polymers (SMP) and their composites (SMC) are smart materials having morphing capabilities that can be applied in aerospace, biomedical or textile engineering. Conventionally, the shape change is triggered with direct heating close to a heat source. This reduces drastically the range of applications of SMC since having a heater next to the material is sometimes impossible, problematic or even hazardous. In the recent years, effort has been put into generating the shape memory effect of SMC remotely by using an electric current, a magnetic field, light, or pH [1].

The present experimental research consists on the detailed thermo-electro-mechanical characterization of a nanocomposite with shape memory properties activated by an electric current. The SMC is functionalized polycaprolactone (PCL) doped with 5%wt of multiwall carbon nanotubes (MWCNT). The PCL has a melting temperature of 60 °C [2] at which the crystalline phase melts and the material becomes rubbery thanks to its covalent crosslinks. The SMC can be formed into its temporary shape, which will be kept when cooling down below its crystallization temperature. The permanent shape can be recovered by heating up the SMC again above 60 °C. There are, however, very few reports on the strain dependence of the electrical resistance R of the SMC, except in [3]. In addition, the monitoring of the electrical properties of the SMC during the shape memory cycle has, to our knowledge, not yet been covered in spite of its vital importance for accurately and efficiently controlling the heating of the SMC with minimum electric power. Under an electric current, the precise temperature T depends on the resistance R of the SMC, the latter being in turn dependent on T and applied strain. Simultaneous monitoring of strain, stress, T and R is carried out in the present work to better understand the interplay between mechanical, electrical, and thermal properties of such SMC.

2. Methodology and preliminary results

A bespoke tensile test bench has been built for the characterization of SMC. The test bench includes additional features enabling, for example, to inject a current in the composite and measure its electrical properties while heating up and deforming. The deformation is measured by 2D Digital Image Correlation (DIC). The change of temperature on its surface is measured in a contactless fashion using an infrared camera previously calibrated in the lab. The preliminary results (Figure 1) are explained hereinafter:

i) Heating: from the permanent shape, heating at zero stress is achieved with the injection of an electric current I. Energy is dissipated in the form of Joule losses, which depend on the resistivity ρ and geometry of the material. For this SMC when T increases, R decreases.

ii) Loading: during loading, the sample is elongated to the temporary shape. The MWCNT are placed further apart from each other. This results in an increased R that would cause the sample to cool down. To compensate and maintain a constant temperature on the samples, R and T need to be monitored and I controlled accordingly.

iii)   Cooling: the current source is switched off to let the SMC cool down by natural convection under constant deformation. *R* increases due to the drop of *T*.

iv)   Loading release: at room temperature the stress is released by removing one of the grips.

v)   Heating: when re-heating, the SMC goes back to its original shape. *R* decreases because MWCNT are place closer together.
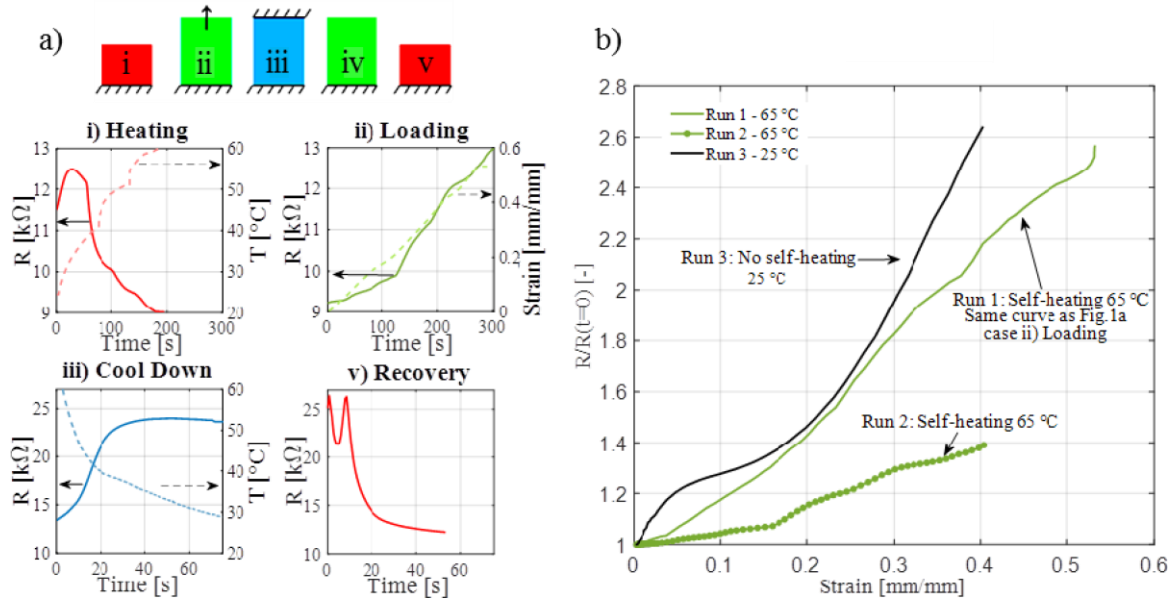
Fig. 1. a) Schematic illustration and measurement of the *R* of PCL 5%wt MWCNT to the shape memory cycle: i – Heating, ii – Loading, iii – cooling, iv – Loading release and v – Heating.
b) Variation of *R* normalised to its first value with respect the to *ε* for two runs of the shape memory cycle performed at 65 °C, and a conventional tensile test performed at 25 °C where *R* is measured

Figure 1b shows that the strain dependence of *R* is significant as well as run dependent. After the first shape memory cycle is performed, the change of *R* decreases considerably to that of Run 1. After the second shape recovery, a conventional tensile test is performed at room temperature. The variation of *R* is found to be much bigger than that for Run 2. Such results demonstrate that *R* should be monitored and characterised for a full understanding of the electric triggering of SMC.

3. Acknowledgements

4. References

[1]   X. Xin et al. (2019). Mechanical models, structures, and applications of shape-memory polymers and their composites, *Acta Mech. Solida. Sin.*, **32**, 535-565.

[2]   T. Delfize et al. (2012). Multifunctional poly(ε-caprolactone)-forming networks by Diels-Alder cycloaddition: effect of the adduct on the shape-memory properties, *Macromol. Chem. Phys.*, **213**, 187-197.

[3]   K. Yu et al. (2011). Conductive shape memory polymer composite incorporated with hybrid fillers: electrical, mechanical and shape memory properties, *J. Intel. Mat. Syst. Str.,* **22**, 369-379

DYNAMIC MECHANICAL ANALYSIS
IN INVESTIGATIONS OF SMART MATERIALS: A POLYMER CHEMIST THINKING

M. Cristea[1], D. Ionita[1] and E.A. Pieczyska[2]
[1] "Petru Poni" Institute of Macromolecular Chemistry, Iasi, Romania
[2] Institute of Fundamental Technological Research, Warsaw, Poland

1. Introduction

Smart materials are simply defined as stimuli-responsive materials that experience reversible changes of their properties under the action of external stimuli like temperature, pH, electric/magnetic field. The most known smart materials are shape-memory materials (polymers, metal alloys or ceramics) that have the ability to fix a temporary shape, and recover later to original shape upon the application of an external stimulus, mostly temperature [1]. Even if dynamic mechanical analysis (DMA) is the method of choice for determining the glass transition temperature of polymers, it provides much more. A meaningful dependence of their viscoelastic parameters (elastic modulus E', viscous modulus E'' and loss factor tan δ) with temperature/time is required in order to establish the adequate conditions for featuring the shape memory process.

The presentation aims to put forward the utility of the method as a research instrument in the field of smart materials, with connections to examples encountered in the polymer domain.

2. Methods

The DMA experiments were performed on a Perkin Elmer Diamond DMA instrument, in tension, bending and shear mode. The isochronal experiments were run on various types of elastomers by increasing the temperature in ramp mode until the E' value was too small to allow the experiment to be continued. Multifrequency experiments were conducted in order to establish the nature of some transitions and to construct master curves by using the time-temperature superposition principle [2].

3. Discussions

Specialists in polymers have a good understanding of the structure-property relation. They can choose reactants, modify the synthesis conditions or the processing parameters in order to get polymeric materials with appropriate characteristics. A DMA isochronous experiment will emphasize the main four characteristic regions: glassy, glass transition, rubbery plateau and flowing. Any atypical trend of E', E'' or tan δ in any of these regions can be a clue for a specific phenomenon (solvent removal, crystallization, melting) that can take place with increasing temperature and or under the action of the small oscillatory deformation [3]. Their identification is of foremost importance because that transition temperature can represent the external stimulus for the shape memory process or may interfere with an ongoing process.

The glass transition temperature represents a key index for the glass transition-type shape memory polymers. Nevertheless, the argumentation of the structure-property relation by considering only one value of temperature is a simplistic approach that frequently turns into wrong conclusions. The glass transition process is not indicated by a single temperature value, but by an interval, as large as the structure of the polymer is less homogeneous. The E' drop of three orders of magnitude during the glass transition of a polymer indicates its amorphous nature. Still, a DMA multifrequency experiment can help in assessing whether other phenomena occur during glass transition that can interfere with the classic behavior of an amorphous polymer.

These materials will be thoroughly perceived only by taking into account the dynamic relation between mechanics and phase structure, that depends invariably on chemical structure. On one side, the phase-structure of the material depends invariably on mechanical loads: external load can prevent or enhance phase separation. Here the changes in temperatures that may accompany mechanical deformation with perceptive effects on phase structure can be mentioned [4]. On the other side, the structural changes result in strong mechanical response.

4. References

[1] M.R. Aguilar and J. San Roman (2014*). Smart polymers and their applications*, Woodhead Publishing, Cambridge, 1-11.

[2] D. Ionita, M. Cristea, C. Gaina (2020). Prediction of polyurethane behavior via timetemperature superposition: meanings and limitations, *Polym. Test.*, **83**, 106340.

[3] R.P. Chartoff, J.D. Menczel, S.H. Steven (2009). *Thermal analysis of polymers. Fundamentals and applications*, John Wiley & Sons Inc., Hoboken, 387-495.

[4] E. Pieczyska, M.Maj, K. Kowalczuk-Gajewska, M. Staszczak, A. Gradys, M. Majewski, M. Cristea, H. Tobushi and S. Hayashi (2015) Thermomechanical properties of polyurethane shape memory polymer-experiment and modelling, *Smart Mater*

SEMI-ACTIVE MITIGATION OF STRUCTURAL VIBRATIONS IN 2D FRAMES BY ON/OFF NODAL RECONFIGURATION

G. Mikułowski, B. Poplawski and Ł. Jankowski

Institute of Fundamental Technological Research, Polish Academy of Sciences, Warsaw, Poland

1. Introduction

An important part of the research in structural control is devoted to mitigation of structural vibrations. The basic strategy is to properly design the structure, but such a passive approach might be insufficient in many applications. An example is constituted by space structures: due to their low weight and high slenderness, they are inadequately damped by the natural mechanisms of material damping and susceptible to prolonged free vibrations and excessive forced vibrations.

When passive structural optimization is not sufficient, an active or semi-active system might be applied. Active systems are based on the paradigm of active counteraction: actuators are employed to generate control forces that counteract structural motion. Such systems are well-researched and extremely efficient [1]. However, these advantages often come at the cost of a 1) large power consumption required by the external actuators, and 2) danger of instabilities, especially in case of a control system failure, which is related to the relatively large forces generated by the actuators.

In contrast to the active counteraction employed in the active control systems, there is a class of systems that employ the Nature-inspired paradigm of self-adaptation to variable external conditions. Such systems are called semi-active [2,3], and they exert control through online modification of selected structural parameters rather than large counteracting forces. Such an approach is clearly advantageous in terms of the power consumption (power is required to change the structural or material characteristics only rather than to generate large forces) and significantly decreased danger of instabilities. The cost is a slightly reduced effectiveness and an often larger design complexity.

2. Structural reconfiguration

One of the approaches in the area of semi-active control can be identified as controllable structural constraints or dynamic structural reconfiguration. It can be traced back to the switchablestiffness truss elements proposed in 1990s [3], and includes controllable delamination [4], jammed granular material [5] and nodes with a controllable ability to transfer moments [6,7]. In all these reports, the structural control has been enforced by means of a controllable structural constraints.

An example is the temporary decoupling of rotational degrees of freedom in a frame node, which has been first studied numerically in [7] and then experimentally in [8], in an application to damping of free vibrations. Such a decoupling turns an originally frame node (with full transmission of moments between the adjacent beams) into a hinge, which no longer transmits the bending moments. In practice, such nodes can be friction-based and controlled by an actuator that exerts a normal force of a controllable level.

3. Experimental results

This contribution discusses a semi-active vibration damping system for slender 2D frame structures and proves its effectiveness in various loading conditions. Significant mitigation of vibration amplitudes have been achieved in free vibrations, as well as in harmonic and random forced vibrations. The actuators have the form of frame nodes with a controllable ability to transfer moments.

In all tested cases the laboratory experimental results have been confirmed with numerical simulations. Exemplary results in damping of harmonic vibrations are shown in Fig. 1.
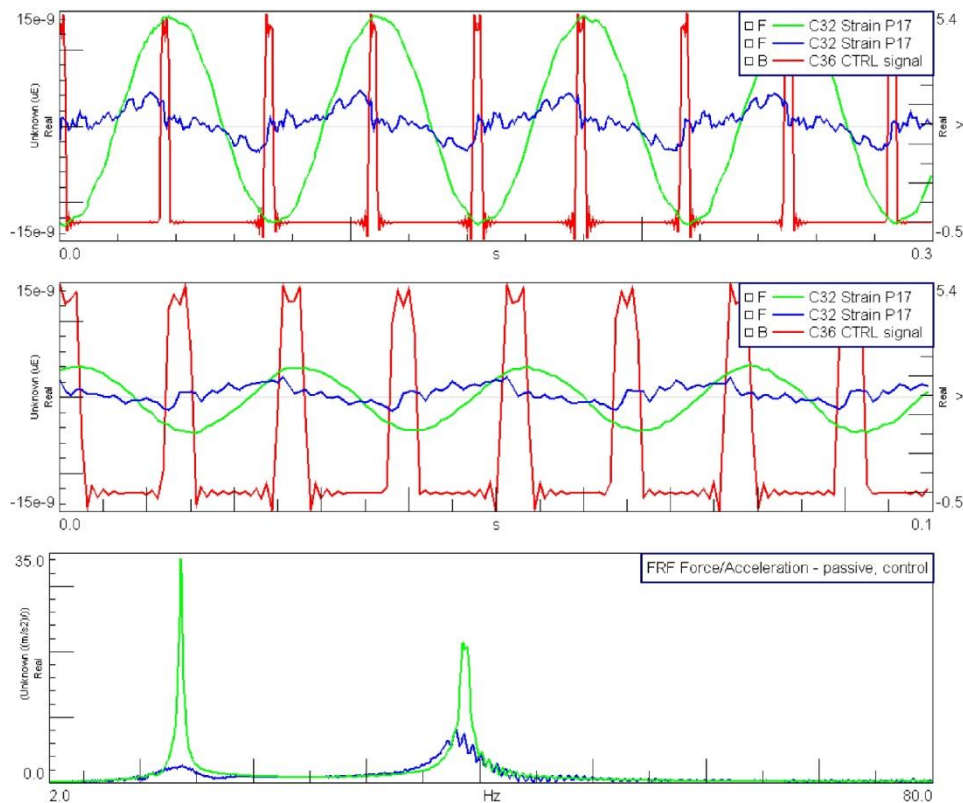
Fig. 1. Strains at a selected sensor location in a passive and semi-actively controlled structure and the control signal (top, middle); the corresponding accelerances of the frame tip (bottom)

4. Acknowledgments

5. References

[1] A. Preumont (2018). *Vibration control of active structures: an introduction*. Springer.

[2] S. Hurlebaus, L. Gaul (2006). Smart structure dynamics, *Mech Syst Signal Pr*, **20**, 255–281.

[3] J. Onoda, T. Endo, H. Tamaoki and N. Watanabe (1990). Vibration suppression by variable stiffness members, *AIAA Journal*, **29**(6), 977–983.

[4] A. Mroz, A. Orlowska and J. Holnicki-Szulc (2010), Semi-active damping of vibrations. Prestress Accumulation-Release strategy development, *Shock and Vibration*, **17**(2), 123–136.

[5] J.M. Bajkowski, C.I. Bajer, B. Dyniewicz, D. Pisarski (2016). Vibration control of adjacent beams with pneumatic granular coupler: an experimental study, *Mech Res Comm*, **78**, 51–56.

[6] A. Mróz, J. Holnicki-Szulc and J. Biczyk (2015). Prestress accumulation-release technique for damping of impact-born vibrations: Application to self-deployable structures, *Math Probl Eng*, **2015**, 720236.

[7] B. Poplawski,G. Mikułowski, A. Mróz and Ł. Jankowski (2018). Decentralized semi-active damping of free structural vibrations by means of structural nodes with an on/off ability to transmit moments, *Mech Syst Signal Proc*, **100**, 926–939.

GUM METAL SUBJECTED TO COMPRESSION LOADING
IN A WIDE SPECTRUM OF THE STRAIN RATES

E.A. Pieczyska[1], K.M. Golasiński[1], M. Staszczak[1], J. Janiszewski[2],
J. Sienkiewicz[2], S. Kuramoto[3] and N. Takesue[4]
[1] *Institute of Fundamental Technological Research, Warsaw, Poland*
[2] *Warsaw Academy of Military, Warsaw, Poland*
[3] *Department of Mechanical Engineering, Ibaraki University; Hitachi, Japan*
[4] *Fukuoka University, Japan*

1. Introduction

Gum Metal stands for a group of multifunctional β-Ti alloys, which was developed by the Toyota Central Research and Development Laboratories at the beginning of the 21st century. Typical composition of Gum Metal Ti–36Nb–2Ta–3Zr–0.3O (in mass %), the fabrication process including cold working and the role of oxygen in the composition are critical for the unique mechanical performance of the alloy, i.e. low Young's modulus, large nonlinear recoverable deformation, and high strength [1]. The understanding of mechanical characteristics of the alloy subjected to loading at various strain rates is critical for its application in a variety of engineering solutions [2-4]. This work presents the behavior of Gum Metal in compression under quasi-static and dynamic loadings.

2. Methods

Mechanical behavior of the Gum Metal was investigated by conducting compression tests in a wide spectrum of strain rates, including impact loading: $10^{-3}s^{-1}$ - $10^3 s^{-1}$. An MTS testing machinewas used to measure the quasi-static behavior of the alloy (strain rates $10^{-3}s^{-1}$ and $100 s^{-1}$) under uniaxial compression. High strain rate uni-axial testing was performed using a Split Hopkinson Pressure Bar (SHPB) system (strain rates 940 s^{-1}, 1460 s^{-1}, and 2200 s^{-1}). Microscopic evaluation was realized by using KEYENCE VHX-6000 digital microscope. Cross-sections of Gum Metal samples were metallographically ground and polished. To reveal the microstructure, the samples were etched with the use of Kroll's Reagent (20 ml H_2O + 4 ml NHO_3 + 1 ml HF).

3. Results and discussion

The obtained results of quasi-static and dynamic mechanical behavior of Gum Metal under compression at strain rates of 10^{-3} s^{-1}, 100 s^{-1}, 940 s^{-1}, 1460 s^{-1}, and 2200 s^{-1} are shown in Figure 1a. It can be noticed that Gum Metal is very sensitive to the strain rate applied during the compression loading. The rule the faster the stronger was confirmed.
Elastic-plastic transition during quasi-static compression appears at the stress level between 900 MPa and 1000 MPa. Almost no strain hardening is observed for the strain rate 10^{-3} s^{-1}. Slight strain softening is visible for the strain rate of 100 s^{-1}.At the significantly higher strain rates, the phenomenon of strain softening is present for each of the dynamic strain rates. During dynamic compression loading the peak flow stresses are on the order between 1200 MPa – 1400 MPa.

Optical microstructure of Gum Metal after Hopkinson test at the strain rate 2200 s^{-1} is presented in Figure 1b. In the micrograph the loading direction is vertical. It was noticed that equiaxed grains observed at the initial state are deformed after dynamic testing and are elongated in a direction perpendicular to the deformation direction. Fully developed adiabatic shear band (ASB) with the crack inside arose roughly at ~45˚ with respect to the loading direction indicating the maximum shear

stress plane. Width of the shear band is near ~50 µm. Within the ASB structure composed of ultrafine equiaxed grains is observed. Such remarkable grain refinement had place since great temperature rise occurred during dynamic loading [5]. It can be also noticed that there is a temperature gradient athwart the adiabatic shear banding, leading to much refined grain size in the middle of ASB against ASB/matrix boundaries.
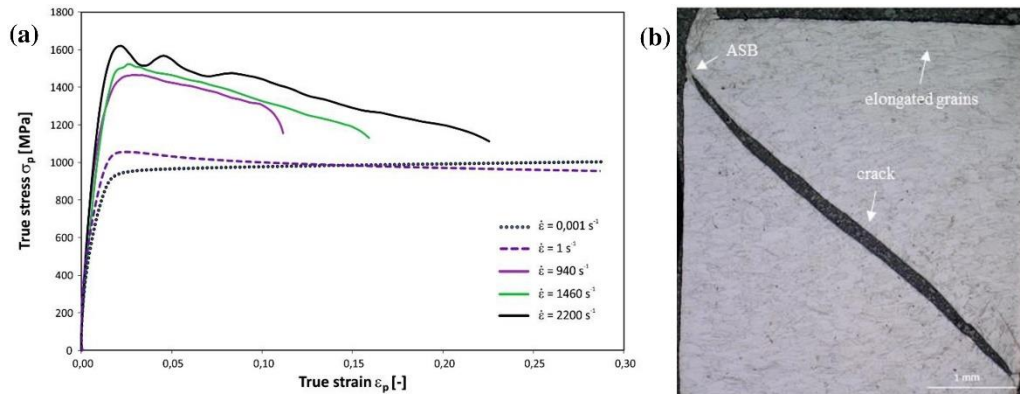
Fig. 1. a) Stress vs. strain curves of Gum Metal under compression at various strain rates; b) Optical micrograph of Gum Metal after dynamic loading at the strain rate 2200 s^{-1}

4. Acknowledgments

5. References

[1] T. Furuta, S. Kuramoto, J. Hwang, K. Nishino, T. Saito (2005). Elastic deformation behavior of multi-functional Ti-Nb-Ta-Zr-O alloys, *Mater. Trans.* **46** 3001–3007.

[2] E.A. Pieczyska, M. Maj, K. Golasiński, M. Staszczak, T. Furuta, S. Kuramoto (2018). Thermomechanical Studies of Yielding and Strain Localization Phenomena of Gum Metal under Tension, *Materials*, **11**, 1-13.

[3] K. Golasiński, E.A. Pieczyska, M. Maj, S. Mackiewicz, M. Staszczak, Z. Kowalewski, L. Urbański, M. Zubko, N. Takesue (2019). Anisotropy of Gum Metal analysed by ultrasonic measurement and digital image correlation, *Materials Science and Technology*, 1-7.

[4] K. Kowalczyk-Gajewska, E.A. Pieczyska, K. Golasiński, M. Maj, S. Kuramoto, T. Furuta (2019). A finite strain elastic-viscoplastic model of Gum Metal, *International Journal of Plasticity*, **119**, 85-101.

[5] Q. Wei, Z.L. Pan, Y.H. Zhao, T. Topping, R.Z. Valiev, X.Z. Liao, E.J. Lavernia, Y.T. Zhu, (2017). Effect of strain rate on the mechanical properties of a gum metal with various microstructures, *Acta Mater.* **132** 193–208.

PIEZORESISTIVE PROPERTIES OF CARBON – BASED CEMENTITIOUS NANOCOMPOSITES

N.D. Alexopoulos[1], A. Dimou[1], Z.S. Metaxa[2] and S.K. Kourkoulis[3]
*[1] University of the Aegean, School of Engineering, Department of Financial Engineering,
821 32 Chios, Greece*
*[2] International Hellenic University, School of Science and Technology, Department of Chemistry,
Hephaestus Laboratory, St. Luke 654 04, Kavala, Greece*
*[3] National Technical University of Athens, Department of Mechanics,
Laboratory of Testing and Materials, 9 Heroes Polytechniou Str., 15780 Athens, Greece*

Abstract

Carbon-Based Nanomaterials (CBNs) have gained a lot of interest for use in cement-based materials because they can improve their electrical properties and can provide them with the self-sensing ability. The aim of the present study is twofold; to develop a compatible matrix that can be used for the restoration of Cultural Heritage Monuments made from cementitious materials and to successfully reinforce the matrix at the nanoscale so as the material itself can act as a self-sensor. The composite under study is based on a cementitious matrix, in which metakaolin and lime are also added. Two different types of CBNs were selected to reinforce the matrix, namely modified Multi-Wall Carbon Nanotubes (MWCNTs) and Graphene Oxide (GO), at percentages of 0.05 %, 0.1 % and 0.2 % on the total amount of binder so as to investigate which CBN type and concentration gives the best results in terms of piezo resistivity. The samples were subjected to different mechanical loadings and simultaneously measuring their electrical resistance; the results indicate that the nanocomposites can be applied for the restoration of concrete Monuments, while acting as sensor for non-destructive evaluation of structural damages.

Keywords: Composites, Multi-Wall Carbon Nanotubes, Piezoresistivity

1. Introduction

In order to develop multifunctional construction materials, different nanomaterials have been applied in the past decade [1]. The extensive focus on nanomaterials results from their extraordinary physical and chemical characteristics, which leads to the properties enhancement of the materials that they are added to [2]. In this study, the incorporation of two different CBNs, e.g. MWCNTs and GO as reinforcement is studied. MWCNT and GO composites possess excellent electrical properties and have been gaining scientific interest. These electrical properties are attributed to the conductive networks that are formed after dispersing the nanostructures [3-4]. Moreover, studies have shown that the electrical response of composites is affected by the application of mechanical loads [5]. In the present work, this concept, i.e. the stress-dependent electrical response of MWCNT cementitious composites, is examined for the first time in a cementitious matrix containing metakaolin and lime. The aim of this study is to develop a smart restoration nanocomposite to be used for interventions on Monuments of Cultural Heritage.

2. Materials and Methods

2.1. Nanocomposites Preparation

The CBNs were prepared in the Department of Materials Science, University of Ioannina under the framework of the research project 'AKEISTHAI'. Initially, dispersions of the two different

nanomaterials (MWCNTs and GO) were prepared by mixing different wt.% concentrations of MWCNTs, namely 0.05 %, 0.1 % and 0.2 % on the total amount of binder, with water and applying ultrasonic energy of 60 kJ per 100 mL of suspension using a tip ultrasonicator. Following, the nanocomposites were prepared by mixing the cementitious matrix (CEM I, Lime, Metakaolin) with the MWCNT suspensions according to the ASTM C305. The water to binder ratio was kept constant at w / c = 0.55. After mixing, the nanocomposites were placed into prismatic molds and were demolded after one day and were cured for 28 days in a water bath saturated with lime until testing.

2.2. Nanocomposites Testing

The piezoresistive behavior of the nanocomposites was investigated under monotonic compression as well as under different loading – unloading loops. The experiments were performed under displacement control. During testing, time, mechanical force and crosshead displacement were recorded from the loading frame. At the same time, electrical resistance measurements were conducted with the use of a digital multimeter.

3. Results and Discussions

The compressive stress and the relative change of resistance ($\Delta R/R_0$) were studied for both types CBNs nanocomposites. The ratio $\Delta R/R_0$ was observed to be inversely analogous to the compressive stress, since an increase in load leads to a decrease in resistance. This behavior can be attributed to the decrease of the distance between the nanoparticles in the nanocomposite, thus leading to a more conductive network. Although the compressive strength shows similar values for all concentrations of nanoparticles, the 0.05 wt.% samples show the smallest sensitivity regarding their electrical properties. On the contrary, higher concentrations of nanoparticles lead to greater sensitivity and clear piezoresistive properties.

4. Conclusions

The findings of the present study suggest that the composite material under investigation exhibits piezoresistive characteristics when nanomaterials at concentrations higher than 0.05 wt.% are used. The results indicate that the produced nanocomposites can be used for restoration interventions on Monuments of Cultural Heritage that require such compatible matrices.

5. Acknowledgements

6. References

[1] S. Chandra Paul, A. S. van Rooyen, G. P. van Zijl and L. F. Petrik (2018). *"Properties of cement-based composites using nanoparticles: A comprehensive review,"* 1019-1034.

[2] H. S. Siad, M. Lachemi, M. Sahmaran, H. A. Mesbah and K. A. Hossain (2018). *"Advanced engineered cementitious composites with combined self-sensing and self-healing functionalities,"* *Constr. Build. Mater*, **176**,313-322

[3] T. Shi, Z. Li, J. Guo, H. Gong and C. G. Gu (2019), *"Research progress on CNTs/CNFs-modified cement-based composites – A review,"* *Constr. Build. Mater.* **202**,290-307.

[4] Z. Li, L. Wang, Y. Li, Y. Feng and W. Feng (2019), *"Carbon-based functional nanomaterials: Preparation, properties and applications,"* *Compos Sci Technol*, **179**, 10-40.

[5] Z.S. Metaxa (2016), "Exfoliated graphene nanoplatelet cement-based nanocomposites as piezoresistive sensors: influence of nanoreinforcement lateral size on monitoring capability," *CTMAT*, **28**, 73-79.

DEVELOPMENT OF ACTUATOR MATERIALS USING PHOTOTHERMAL CONVERSION BY LOCALIZED SURFACE PLASMON RESORNANCE

K. Fukazawa and S. Arikawa
Meiji University, Kawasaki, Japan

1. Background

Actuators are devices that convert an energy source such as electricity or hydraulic pressure into mechanical power. Conventional actuators use conductors to transmit energy, which limits their shape and arrangement. There are methods to transfer energy for non-contact. For example, CNT/graphene composite that deforms when it is exposed to infrared radiation [1] has been studied. The material proposed in this study converts light energy into heat energy and then thermally contracts. Specifically, rubber/metal nanoparticles composite that is deformed by exposing it with light of a specific wavelength is investigated. Localized surface plasmon resonance (LSPR) of the metal nanoparticles is used for high photothermal conversion. LSPR causes the composite to instantly rise in temperature. The composite is then deformed by thermal contraction. The change in wavelength of LSPR in water and natural rubber, and the conditions under which natural rubber undergoes thermal contraction are investigated. It is expected that a flexible actuator that can be operated by laser light from a remote location can be realized by developing this rubber/metal nanoparticles composite film.

2. Experimental method

The rubber/metal nanoparticles composite films were made by mixing natural rubber (NR) latex with metal nanoparticle solution. The used metal nanoparticles were spherical Au nanoparticles (diameters of 15 nm and 100 nm) and Ag nanoplates. In addition, a NR-only film was also prepared. Fig.1 shows three rubber/metal nanoparticles composite films. Captions in the Figure, Au15n, Au100n and Agnp indicate rubber films containing Au nanoparticles (diameters of 15 nm and 100 nm) and Ag nanoplates, respectively.
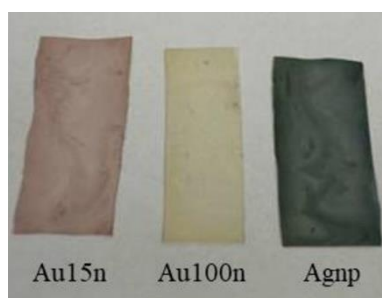
Fig. 1. Image of the rubber/metal nanoparticles composite films

Firstly, the wavelength of light at which metal nanoparticles undergo LSPR in NR has been investigated by measuring absorbance.

Secondly, the four films were exposed to LED light with wavelength of 365nm and output power of 50mW for 5 minutes, and the temperature was measured every minute.

And finally, the conditions for thermal contraction of NR-only films were investigated. Thermal deformation was measured by digital image correlation method. The surface of films is colored black,

and white random pattern are placed on the surface to be photographed by a camera. The temperature and deformation were measured when the suspended film was exposed to white light. Thermal deformations of NR-only film with 50% initial strain and without any strain are measured.

3. Experimental results
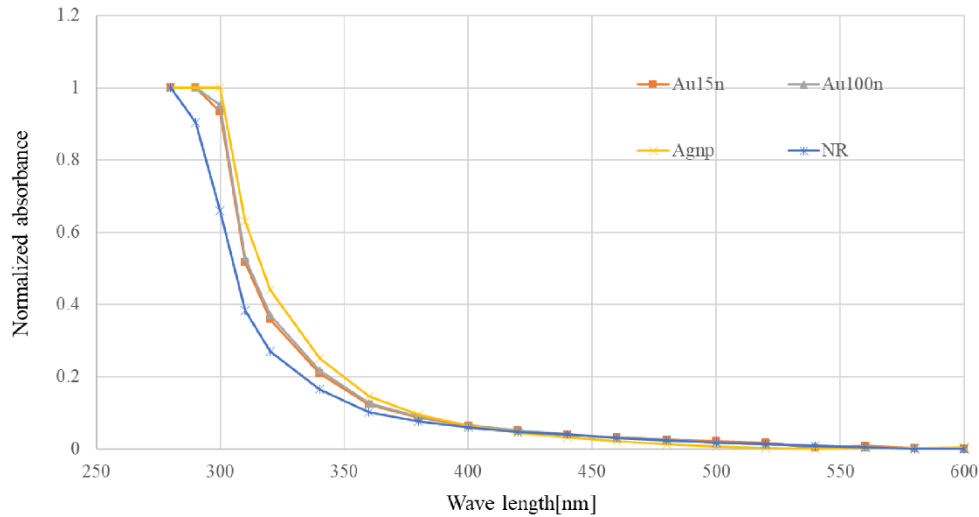
Fig. 2. Absorbance measurement results

Figure 2 shows the results of normalized absorbance measurements for the four films. The absorbance of the composite films is higher than that of the NR-only film at wavelength between 300nm and 380nm. It is thought that the metal nanoparticles in the rubber underwent such a change due to LSPR.

When four films were exposed to LED light of 365nm wavelength, the temperature increase for Au15n, Au100n, and Agnp was 9.3°C, 7.5°C, and 13.9°C, compared to 3.9°C for NR-only film. The rubber films containing metal nanoparticles underwent efficient photothermal conversion by LSPR.

When measuring the thermal deformation, the temperature of NR-only film was increased from 26.0°C (room temperature) to 61.0°C by white light. NR-only film with 50% initial strain was thermal contracted with an average strain of 1.78%, while the film without any initial strain had thermal expansion of 0.86%.

4. Conclusion

Rubber/metal nanoparticles composites were investigated. The composites were efficiently converted to photo-thermal energy by exposing it with near-UV light. It was also confirmed that NR-only film with initial strain was thermal contracted. It is necessary to investigate the optimal type and dispersion method of metal nanoparticles so that the composite film can cause LSPR in visible light. Furthermore, improvement of the thermal contraction of rubber films should be investigated.

5. References

[1] B. Panchapakesan, F. Khosravi, J. Loomis, and Eugene M. Terentjev (2017). Photomechanical Effects in Polymer Nanocomposites, *Photomechanical Materials, Composites, and Systems: Wireless Transduction of Light into Work*, John Wiley & Sons, Hoboken, 179–231.

INVESTIGATION OF PERIODIC CELLULAR STRUCTURE EXPANDED BY ACOUSTIC WAVES

H. Koyama and S. Arikawa
Meiji University, Kawasaki, Japan

1. Introduction

An actuator is a device that converts energy sources such as electricity into mechanical energy. Actuators have long been developed to be lightweight and compact. However, since a power supply is installed, it is limited by the weight of the power supply and the shape of the wiring to connect to the power supply. In order to overcome these limitations, some research have been conducted on actuators that can be operated by non-contact energy supply. Examples of research is giant magnetostriction materials using magnetic fields [1] and a polyelectrolyte gel using electric fields [2]. In most of such research, the actuators were fabricated from materials with deformable properties. On the other hand, Igaki conducted research on non-contact deformation of materials without such properties [3]. Acoustic energy was used to deform the periodic cellular structure. Its unit structure consists of a hexagonal frame structure and a membrane bonded to it on a pair of edge line. Using Finite Element Method, it was proved that by applying sound waves of the resonant frequency to the membrane, the frame structure contracts, and a static displacement can be obtained. However, the amount of contraction in contrast with the oscillation amplitude was small. It should be large for the performance of the actuator. Therefore, the purpose of this research is to establish a deformation principle in which the amount of deformation in contrast with the oscillation amplitude is large.

2. Principle

In this research, the frame structure is expanded rather than contracted. As shown in Fig. 1, asymmetrically shaped membrane in a curved state is bonded to the frame structure. The principle is that when sound waves of a resonant frequency are applied to the membrane, the tips of the membrane oscillate back and forth, and the central part of the membrane is stretched in the height direction, causing the frame structure to expand. By connecting these unit structures, it is thought that the amount of expansion of the frame structure would increase, and a material that could be used as an actuator could be realized.
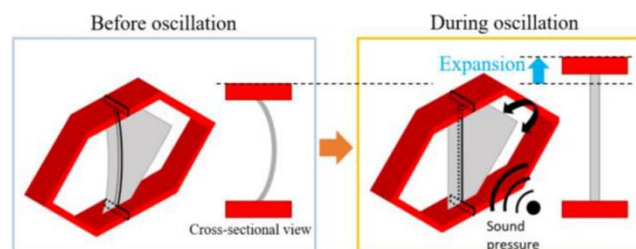
Fig. 1. Deformation principle of the unit structure

3. Experimental method

The frame structure was fabricated using a 3D printer. This 3D printer uses Fused Deposition Modeling method. The material is polylactic acid. A stainless-steel foil with a thickness of 20 μm was used for the membrane. Fig. 2 shows the test specimen made. Fig. 3 shows schematic diagram

of experimental setup. The underside of the specimen was fixed. Sound waves of the designated frequency were output from the speaker. The displacement in a perpendicular direction of the upper surface of the frame structure was measured by a laser displacement meter.
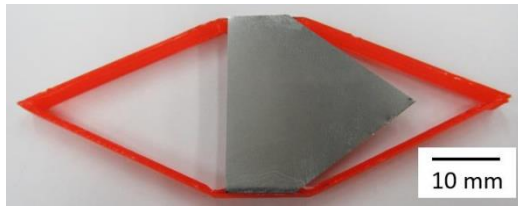
Fig. 2. The test specimen used in this experiment
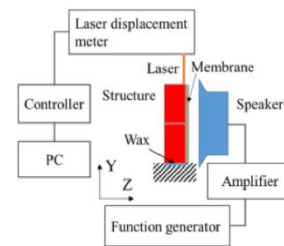
Fig. 3. Schematic diagram of experimental setup

4. Experimental result and discussion

The results are shown in Fig. 4 at 120 Hz. It can be seen that the frame structure was expanded. The oscillation is always about 2.5 μm apart from zero during the application of the sound waves. The average displacement at the time from 6 to 7 seconds is about 4.0 μm, and the amplitude is about 3.0 μm, the amount of deformation in contrast with the oscillation amplitude is larger than the preceding research. The details of the oscillation state need to be clarified in the future. Moreover, increasing the amount of expansion in the unit structure, stabilizing the frequency, and investigating the effects of connecting the unit structure should be considered.
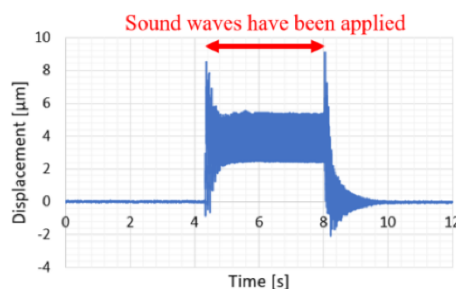
Fig. 4. Displacement-time profile obtained by the experiment

5. Conclusion

The principle of expanding the frame structure having an asymmetrically shaped membrane by applying sound waves was proposed. The experimental results showed that the amount of expansion in contrast with the oscillation amplitude is large. If the amount of expansion can be increased and the unit structure can be connected, a non-contact actuator using sound waves, in which any material can be used can be realized.

6. References

[1] H. Eda, M. Sahashi and T. Kobayashi (1990). Study on giant magnetostriction actuator (1st report), *Journal of the Japan Society for Precision Engineering*, **56**-2, 388-392.
[2] T. Shiga, Y. Hirose, A. Okada and T. Kurauchi (1989). Bending of high strength polymer gel in an electric field, Japanese Journal of Polymer Science and Technology, 46-11, 709-713.
[3] Y. Igaki and S. Arikawa (2019). Study on regular structure deformed by acoustic waves, *Proceedings of The 14th International Symposium on Advanced Science and Technology in Experimental Mechanics*.

THE EFFECT OF SHAPE MEMORY BEHAVIOR
ON THE MICROSTRUCTURE OF THE PU-SMP ($T_g = 45°C$)

M. Nabavian Kalat, M. Staszczak, Y. Ziai, A. Gradys, L. Urbański and E.A. Pieczyska
Institute of Fundamental Technological Research, Polish Academy of Sciences,
Pawińskiego 5b, 02-106, Warsaw, Poland

1. Abstract

In this study, the mechanical deformation and shape recovery of the polyurethane shape memory polymer (PU-SMP) with T_g of 45°C are investigated from the microscopic point of view. For this purpose, the influence of the shape memory effect on the microstructure of the PU-SMP was studied by Scanning Electron Microscope (SEM) and Differential Scanning Calorimetry (DSC). The results proved that the macroscopic deformation and recovery of the PU-SMP are resulted from the microstructure changes induced during the loading, and further thermal shape recovery processes.

2. Introduction

Shape memory polymers (SMPs) are stimuli-responsive materials that have attracted great attention as smart materials due to their high shape recovery characteristics. The SMP is capable of recovering the original shape, which is changed by mechanical loadings by exposing the SMP to an external stimulus, such as heat. Polyurethane shape memory polymers are especially distinguished owing to their good shape memory and high mechanical properties [1]. The mechanical deformation of the PU-SMP specimen and shape recovery of the original shape are resulted from the microstructural changes and mechanical reinforcement during the tension and stress relaxation during the heating [2]. In this study, the effect of one and five cycles of tensile loading-unloading and thermal shape recovery on the microstructure of the PU-SMP with Tg of 45˚C are studied, by using SEM and DSC analysis.

3. Materials and characterization methods

The investigation was conducted on the PU-SMP with T_g of 45˚C, produced by the *SMP Technologies Inc.,* Tokyo, Japan. The tensile mechanical loading program of PU-SMP was conducted by INSTRON 5969 testing machine at room temperature. The cycles of the loading were performed with strain rate of 10^{-2} s^{-1} within the strain range of 0.33. The DSC measurement was carried out by power-compensation calorimeter Pyris1 DSC (Perkin-Elmer., USA) the samples were heated from -20°C to 200°C, at the rate of 10 K/min. SEM investigation of the PU-SMP surface was conducted using a scanning electron microscope JEOL JSM-6390LV. Before the measurement the samples were sprayed with 8 nm layer of gold in order to obtain a better conductivity.

4. Results and discussion

The SEM images of the specimen surface under tension in 5 states are presented in Fig. 1. Fig. 1a represents the surface roughness of the PU-SMP specimen before the loading. Fig. 1b shows the formation of the micro-cracks in the direction of the loading on the surface of the same specimen after one cycle of tensile mechanical loading-unloading at room temperature. As seen in Fig. 1c, the surface of the specimen looks smooth without the presence of micro-cracks after the thermal shape recovery at the temperature above T_g (T_g+15°C). Therefore, besides macroscopic shape recovery of the deformed specimen by heating, the defects are also healed in the microscopic point of view.

Fig. 1d displays the surface of the specimen after 5 cycles of loading-unloading. Despite the absence of micro-cracks on the surface of the specimen, the effect of strain hardening and orientation in the tension direction is quite visible. Fig. 1e shows the surface of the specimen represented in Fig. 1d after the heating and thermal shape recovery at $T_g + 15°C$. No big difference is noticed between the surface of the specimen before and after the thermal shape recovery in the specimen subjected to five loading-unloading cycles.
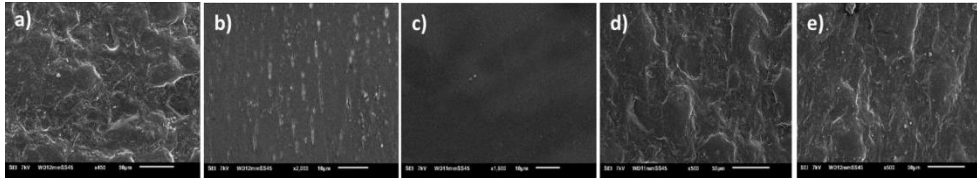
Fig. 1. SEM images of the PU-SMP specimen surface in 5 states: a) before loading at the scale of 50 μm. b) after one cycle of loading-unloading at the scale of 10 μm c) after thermal shape recovery at the scale of 10 μm d) after five cycles of loading-unloading at the scale of 50 μm e) after thermal shape recovery at the scale of 50 μm

The effect of deformation and shape recovery on the microstructure of the PU-SMP were also investigated by DSC. In order to not change or erase the microstructure of the specimens after the loading, the results obtained during the 1st heat flow were considered. Therefore, the quantity of T_g differs from the given quantity by the producer (45°C). As demonstrated in Fig. 2, all the specimens except of the undrawn one, show the stress relaxation peak right after the T_g step. The second endothermic peak which happens in about 80°C in all 5 specimens, attributes to melting crystallization (MC) peak. The peak area is increased in PU-SMP1 in comparison with the peak in PU-SMP0 due to strain-induced crystallization. The MC peak is decreased in PU-SMP2 compared to PU-SMP1, because of the shape recovery of PU-SMP1 after the heating. However, there is no huge difference in the MC peaks in PU-SMP3 and PU-SMP4, before and after shape recovery when the specimen is deformed in a cyclic deformation.
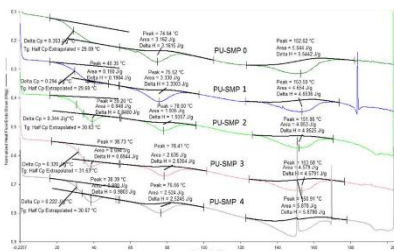
Fig. 2. DSC measurement of the PU-SMP specimen in 5 states: a) before loading (**PU-SMP0**) b) after one cycle of loading-unloading (**PU-SMP1**) c) after shape recovery (**PU-SMP2**) d) after five cycles of loading-unloading (**PU-SMP3**) e) after shape recovery (**PU-SMP4**)

5. Conclusion

In this study it was demonstrated that, the macroscopical shape memory behavior of the PU-SMP subjected to loading, is resulted from the microstructure changes that occur during the deformation and shape recovery, namely the strain-induced crystallization, melting crystallization and healing effects.

6. References

[1] Pieczyska, E.A.; Maj, M.; Staszczak, M.; Gradys, A.; Majewski, M.; Cristea, M.; Tobushi, H.; Hayashi, S. Thermomechanical properties of polyurethane shape memory polymer – experiment and modelling. *Smart Mater. Struct.*, **2015**, *24*, 45043.

[2] Candau, N.; Stoclet, G.; Tahon, J.F.; Demongeot, A.; Yilgor, E.; Yilgor, I.; Menceloglu, Y.Z.; Oguz, O. Mechanical reinforcement and memory effect of strain-induced soft segment crystals in thermoplastic polyurethane-urea elastomers. *Polymer.* **2021**, *223*, 123708.

INFLUENCE OF STRAIN RATE AND COOLING RATE ON THE MECHANICAL BEHAVIOUR SHAPE MEMORY POLYURETHANE WITH *Tg* = 65 °C

M. Staszczak[1], M. Nabavian Kalat[1], L. Urbański[1], M. Cristea[2] and E.A. Pieczyska[1]
[1] Institute of Fundamental Technological Research, PAS, Warsaw, Poland
[2] Petru Poni Institute of Macromolecular Chemistry, Iasi, Romania

1. Introduction

Shape memory polymers (SMP) are stimuli-responsive smart materials that are able to fix its temporary shape and recover the original shape when exposed to an appropriate external stimulus, e.g. heat, light, water. Due to the properties, the SMP have attracted tremendous attention and are applied in various areas, such as biomedical, smart textiles, food protection, toys, as well as aircraft and space industry [1]. Polyurethane shape memory polymer (PU-SMP) is specially distinguished and characterized by a good processability, wide-range of shape recovery temperature and high recoverable strain, resulting in the high mechanical and the related functional properties [2, 3]. The purpose of this paper is to discuss selected results of investigation of the PU-SMP in order to demonstrate how significantly its mechanical properties change at various strain rates during the loading and deformation. This investigation helps to predict the PU-SMP behavior in application. Moreover, PU-SMP is extremely sensitive to the surrounding conditions [2]. Therefore, the effect of cooling rate during the initial thermal treatment is also taken into consideration. The obtained results will be useful in further investigation of the PU-SMP shape memory properties, since the strain rate and thermal treatment before the loading are influential factors which determine their shape memory performance.

2. Materials and experimental procedure

The investigation was conducted on shape memory polyurethane with glass transition temperature T_g = 65°C, manufactured by *SMP Technologies Inc.*, Japan. For the initial characterization of the PU-SMP and establishing the nature of transition, such as relaxation, melting or crystallization, the multifrequency dynamic mechanical analysis (DMA) in the temperature range from -150°C to 160°C was performed.

The tension loading was conducted on Instron 5969 testing machine at room temperature till rupture with various strain rates: 10^{-3} s^{-1}, 10^{-2} s^{-1}, 10^{-1} s^{-1} and 100 s^{-1}. Before the loading, the PU-SMP specimens were heated up to 80°C (T_g +15°C) during 30 minutes in order to uniform their microstructure and erase the mechanical history. After that, some of the specimens were cooled down quickly to the room temperature by taking them out from the thermal chamber, whereas others were cooled down slowly inside the thermal chamber.

3. Results and discussions

The obtained DMA results, namely the temperature dependencies of storage modulus E' and loss factor tan δ, are presented in Fig. 1a. The glass transition is followed by a phenomenon which is frequency independent. Considering decrease of E' by increase of the temperature in the temperature region of 100°C - 150°C, it is very probable to have a succession of overlapping melting and crystallization phenomena. The glass transition temperature, determined as the tan δ peak, is equal to 65.2°C. The value is in agreement with T_g value given by the PU-SMP producer.
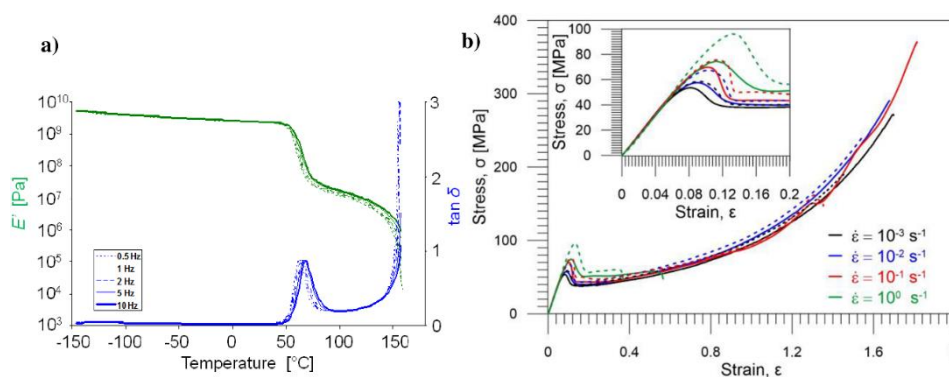
Fig. 1. a) Multifreqency DMA diagram: storage modulus E' and loss factor tan δ tan vs. temperature; b) stress vs. strain obtained during the PU-SMP tension till rupture conducted at various strain rates - 10^{-3} s^{-1} (black), 10^{-2} s^{-1} (blue), 10^{-1} s^{-1} (red) and 100 s^{-1} (green): the solid and dashed lines correspond to specimens cooled down quickly and slowly, respectively; insert shows the part of this graph obtained till strain value 0.2

The experimental results of the PU-SMP tensile loadings performed till rupture at various strain rates are presented in Fig. 1b. As it is noticed, the obtained stress becomes higher with the increase in the strain rate, since the deformation process of the polymer is more dynamic. This tendency is observed both for the specimens cooled down quickly and slowly. The stress values of the specimens which were cooled down slowly, are higher than those of the specimens cooled down quickly at all the strain rates applied, which is related to the special microstructure of the polymer. Before the loading, during the heating process of the specimen to the temperature above T_g, the soft segments of the polyurethane chains, located between the hard segments, become highly flexible and the rotations of the segments around the bonds are significantly increased. By cooling down the polymer to the temperatures below T_g the flexibility and mobility of the polymer chains become limited and PU-SMP reaches its glassy state. Slow cooling allows the polymer reach this state more completely. Thus, a slower cooling rate gives the material more time to evolve to an equilibrium configuration during the cooling process. This phenomenon improves their mechanical properties.

4. Conclusions

It was experimentally demonstrated how significantly the polyurethane shape memory polymer PU-SMP (T_g=65°C) is affected by the strain rate and the cooling rate, which is closely connected with the polymer microstructure evolution.

5. Acknowledgments

5. References

[1] A. Lendlein and S. Kelch (2002). Shape-memory polymers, *Angew. Chem. Int. Ed.*, **41**, 2034–2057.

[2] H. Tobushi, R. Matsui, K. Takeda and E.A. Pieczyska (2013). *Mechanical Properties of Shape Memory Materials*, Nova Science Publishers, New York.

[3] E.A. Pieczyska, M. Staszczak, K. Kowalczyk-Gajewska, M. Maj, K. Golasiński, S. Golba, H. Tobushi, S. Hayashi (2017). Experimental and numerical investigation of yielding phenomena in a shape memory polymer subjected to cyclic tension at various strain rates, *Polym. Test.*, **60**, 333–342.

STUDY OF BOND LENGTH AND ITS EFFECT ON GUIDED WAVES USING FIBER OPTIC SENSORS

K. Balasubramaniam, R. Soman, P. Fiborek, P. Kudela and P.H. Malinowski
Institute of Fluid Flow Machinery, Polish Academy of Sciences, Gdansk, Poland

Abstract

Fiber optic grating (FBG) based structural health monitoring applications are being used in different types of damage prediction, detection analysis in various fields of engineering. FBG can serve as an effective sensor for data monitoring applications as they are more robust in harsh environmental conditions and can be embedded directly into the structure. The paper aims to study the effect of GWs relative magnitude based on the bond and bond length of the FBG sensor. The paper compares the signal amplitudes between the directly bonded and remotely bonded FBG in the structure. Apart from this, a parametric study was also conducted based on signal attenuation to show the change in the bond length affecting the GW and wavelength shift. The study is conducted on subsystem level aluminium and composite specimens. The bond length wave attenuation based studies were done by applying glue at various distances (H1 to H4 as shown in Figure 1) from the FBG sensor and glue of various spread lengths (G1 to G4) to facilitate the concept of remote and direct bonding effects. The paper tends to predict different lamb wave modes based on the time of arrival and also to check which type of bonding is effective in producing effective signal amplitude. The experimental process is also replicated via a spectral element based numerical simulation.
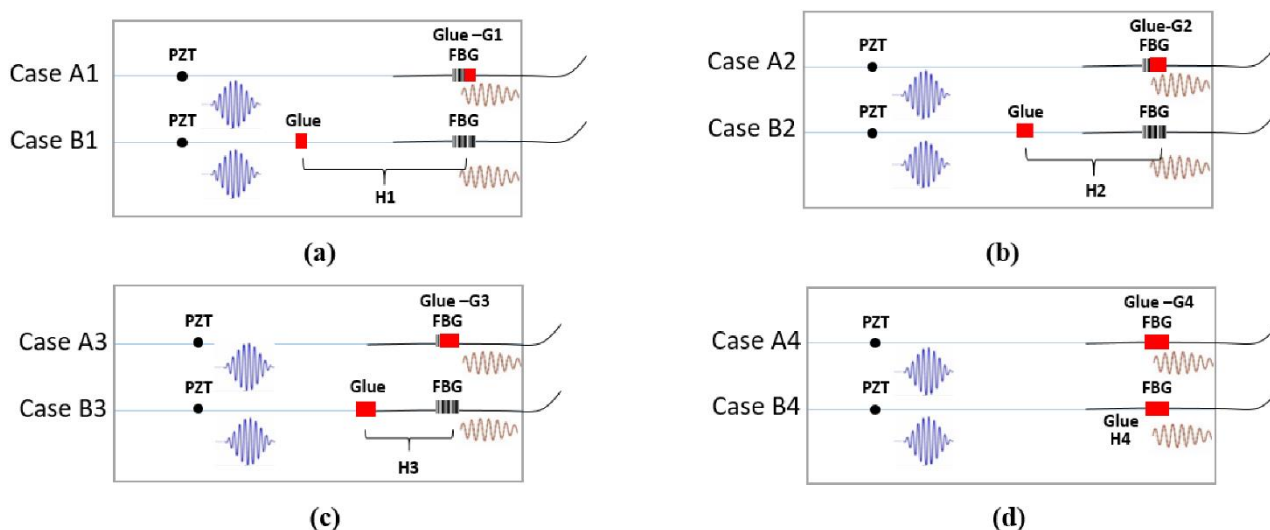
Fig. 1. GW analysis using FBG at different (a) H1 ,G1, (b) H2 ,G2, (c) H3,G3 , (d) H4,G4

Keywords: Fiber optics, guided waves, bond length, parametric study, numerical studies.

References
[1] Wee, J., Wells, B., Hackney, D., Bradford, P. and Peters, K., 2016. Increasing signal amplitude in fiber Bragg grating detection of Lamb waves using remote bonding. *Applied optics*, *55*(21), pp.5564-5569.

[2] Soman, R., Balasubramaniam, K., Golestani, A., Karpiński, M., Malinowski, P. and Ostachowicz, W., 2021. Actuator placement optimization for guided waves based structural health monitoring using fibre Bragg grating sensors. *Smart Materials and Structures*, *30*(12), p.125011.

[3] Goossens, S., Berghmans, F., Muñoz, K., Jiménez, M., Karachalios, E., Saenz-Castillo, D. and Geernaert, T., 2021. A global assessment of barely visible impact damage for CFRP sub-components with FBG-based sensors. *Composite Structures*, *272*, p.114025.

EFFECT OF OXYGEN ON MECHANICAL BEHAVIOR
OF Ti-25Nb BASED SHAPE MEMORY ALLOYS

K.M. Golasiński[1], W. Tasaki[1], M. Maj[2], E.A. Pieczyska[2] and H.Y. Kim[1]
[1] Division of Materials Science, University of Tsukuba, Tsukuba, Japan
[2] Institute of Fundamental Technological Research, Warsaw, Poland

1. Introduction

Ti-Nb based alloys are very attractive candidates for biomedical shape memory alloys (SMAs) [1]. Their Ni-free composition is a solution to the issue of hypersensitivity and toxicity of Ni (e.g. in Ti-Ni SMAs) [2]. Shape memory and superelastic properties of Ti-Nb alloys are associated with martensitic transformation from β to α''. However, oxygen-added Ti-Nb SMAs significantly change their mechanical behavior due to formation and activity of nanodomains [3, 4]. In this work, the effect of oxygen on superelastic properties of Ti–25Nb–xO (at. %, x = 0, 0.3, 0.5, 0.7, 1.0) SMAs under tension is discussed.

2. Methods

The Ti–25Nb–xO (at. %, x = 0, 0.3, 0.5, 0.7, 1.0) alloys were prepared using the Ar arc melting method. The ingots were sealed in a vacuumed quartz tube and homogenized at 1273 K for 7.2 ks, and then cold-rolled with a reduction in thickness of 95%. Specimens for X-ray diffraction (XRD) measurements and mechanical tests were cut using an electro-discharge machine. The damaged surface was removed by mechanical polishing and chemical etching. The specimens were solution-treated at 1173 K for 1.8 ks in an Ar atmosphere, followed by water quenching. The oxidized surface was removed by chemical etching. XRD measurements were conducted at room temperature with Cu Kα radiation. Displacement-controlled load-unload tensile tests were carried out using an MTS 858 testing machine at room temperature. The gauge area of each specimen (4 mm x 6 mm) was covered with speckle pattern. The deformation process was monitored by a visible range camera Manta G-125B. A function of virtual extensometer was used to measure elongation. The displacement rate was 0.06 mm·s−1 which corresponded to strain rate of 10^{-2} s−1.

3. Results and discussion

A comparison of stress-strain curves of Ti–25Nb–xO (at. %, x = 0, 0.3, 0.5, 0.7, 1.0) SMAs under load–unload tension is shown in Fig. 1(a). The yield stress tends to increase with an increase in oxygen content. The Ti–25Nb alloy shows a shape memory behavior associated with the martensitic transformation from β to α''. In oxygen-added alloys, the β–α'' martensitic transformation is suppressed by generation of nanodomains. Oxygen atoms expand the surrounding Ti and Nb atoms, then generate and promote the shuffling and shearing processes of the β–α'' martensitic transformation [3,4]. A comparison of XRD profiles of Ti–25Nb and Ti–25Nb–0.3O alloys is presented in Fig. 1(b). Only the α'' martensite phase was observed in the Ti–25Nb alloy, whereas only the β parent phase was observed in the Ti–25Nb–0.3O alloy. The addition of oxygen stabilizes the β phase in Ti-25Nb alloys. It results in the reduction of the hysteresis loop causing the nonlinear superelastic-like deformation and the increase of flow stress. Similar phenomena are observed in the mechanical behavior of Gum Metal (Ti–23Nb–0.7Ta–2.0Zr–1.2O, at. %) [5, 6].
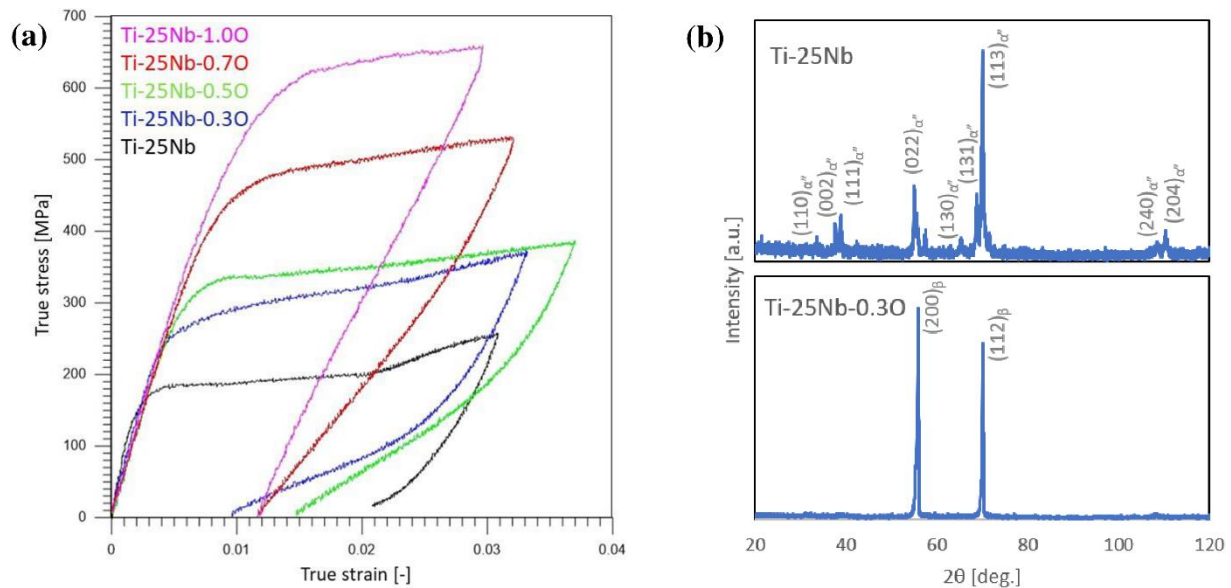
Fig. 1. Comparison of (a) stress-strain curves of Ti–25Nb–*x*O (*x*=0, 0.3, 0.5, 0.7, 1.0) SMAs under load-unload tension; (b) XRD profiles of Ti–25Nb and Ti–25Nb–0.3O SMAs

4. Acknowledgments

5. References

[1] H.Y. Kim, Y. Ikehara, J.I. Kim, H. Hosoda, S. Miyazaki (2006). Martensitic transformation, shape memory effect and superelasticity of Ti–Nb binary alloys, *Acta Mater.*, **54**, 2419-2429.

[2] H.Y. Kim, S. Miyazaki (2016). Several Issues in the Development of Ti–Nb-Based Shape Memory Alloys, *Shap. Mem. Superelasticity.*, **2**, 380–390.

[3] M. Tahara, H.Y. Kim, T. Inamura, H. Hosoda, S. Miyazaki (2011). Lattice modulation and superelasticity in oxygen-added β-Ti alloys, *Acta Mater.*, **59**, 6208-6218.

[4] M. Tahara, T. Inamura, H.Y. Kim, S. Miyazaki, H. Hosoda (2016). Role of oxygen atoms in α″ martensite of Ti-20at.% Nb alloy, *Scripta Mater.*, **112**, 15-18.

[5] K. Golasiński, E.A. Pieczyska, M. Maj, P. Świec, T. Furuta, S. Kuramoto (2020). Investigation of strain rate sensitivity of Gum Metal under tension using digital image correlation, *Archiv. Civ. Mech. Eng.*, **20**, 53.

[6] E.A. Pieczyska, M. Maj, K. Golasiński, M. Staszczak T. Furuta, S. Kuramoto (2018). Thermomechanical studies of yielding and strain localization phenomena of Gum Metal under Tension. *Materials.*, **11**, 567.

10. Structural Health Monitoring

and Its Role in the Sustainability of the Built Environment

COMBINATION OF MILIMETER WAVE SPECTROSCOPY, ULTRASONIC TESTING AND INFRARED THERMOGRAPHY TECHNIQUES TO MONITOR CURING EVOLUTION OF TRC PLATES

N. Ospitia[1], A. Pourkazemi[2], E. Tsangouri[1], H. Azzam[1], J.H. Stiens[2] and D.G. Aggelis[1]

[1] Department of Mechanics of Materials and Constructions, Faculty of Engineering, Vrije Universiteit Brussel, Brussels, Belgium
[2] Department of Electronics and Informatics ETRO-IR, Faculty of Engineering, Vrije Universiteit Brussel, Brussels, Belgium

1. Extended abstract

Non-destructive testing (NDT) techniques are used to study mechanical properties of the materials without destroying, nor compromising such properties [1]. This paper focuses on three types of NDT methods in order to follow the curing process of textile reinforced cementitious (TRC) composites and study the impact of the temperature, humidity and curing time: Millimeter wave (MMW) spectroscopy, ultrasonic testing (UT) and infrared thermography (IR). Hence, the evolution of the curing process will be followed by an experimental setup in which two NDT established techniques (UT and IR) will serve as benchmark for the MMW spectroscopy which has not been applied in TRC.

At regular intervals, ultrasonic pulses are applied to the samples from an emitter transducer and received by a receiver transducer, measuring the velocity and the attenuation of elastic waves [2]. For the purpose of this research, resonant AE sensors are used as ultrasonic receivers, registering the changes on the material stiffness as it increases with time due to curing.

On the other hand, thermography, an IR non-contact technique, usually used to record electromagnetic rays in the infrared spectrum, allowing a full-field thermal imaging of the surface. Therefore, it was used to passively monitor the heat evolution and the uniformity of TRC during curing [3]–[5]. It is expected to obtain a uniform thermal distribution, with slightly higher temperatures in the center of the plates.

Finally, MMW spectroscopy due to the nature of the technique (electromagnetic waves), provides contactless measurements, allowing correlations between the three NDT techniques. This novel NDT technique that - by means of electromagnetic transmission and reflection, measures through a frequency sweep in the mm wave band - monitors the physical and chemical parameters and specifically the changes during curing stage, showing sensitivity to the chemical processes in particular at the level of intermolecular forces. In addition, it is influenced by the consumption or evaporation of water due to either the exothermal stages during cement hydration (initial exothermal reaction, acceleratory period, or due to cement bleeding), or external environmental conditions [6], [7].

The transmission coefficient progress during curing is illustrated in Figure 1 from a preliminary experiment. In Fig. 1a) as it is evident, during the first 9 hours after casting there is a high influence of the exothermic reactions and in which the transmission drops from -20 to -35 dB divided in two stages: the first 5 hours in which the transmission coefficient is barely decreased and it is attributed to the cement dormant period. Later, from 5th hour to the 9th hour, the transmission drops due to

exothermic reactions which leads to increasing losses. Finally, after the 9th hour, a high increase of the transmission coefficient can be seen attributed to the stiffness development [6], [8].

On the other hand, the reflection coefficient increases the first 13 hours after casting due to the increase of the bonds in fresh mortar. However, later it drops as a result of water evaporation [6].

a)   b)
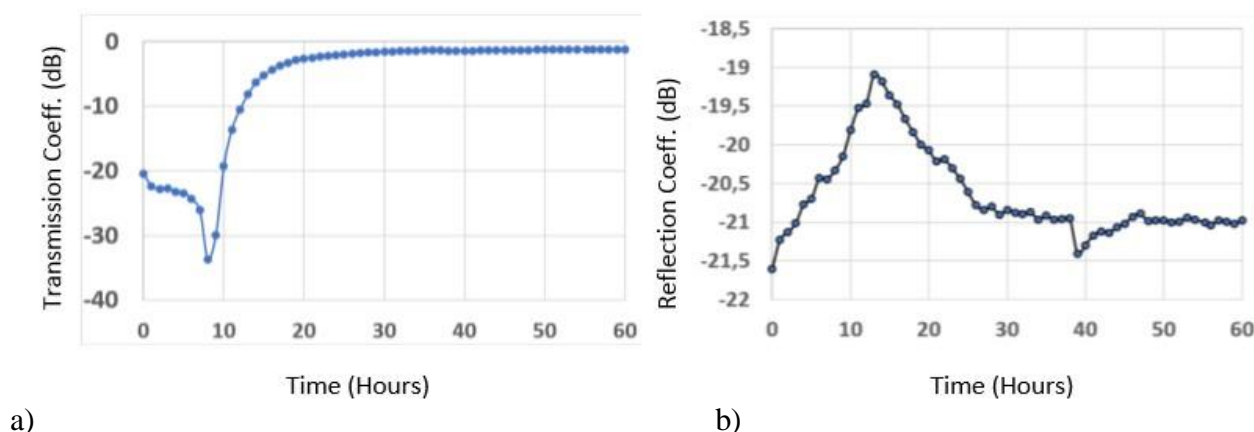
Fig. 1. a) Transmission coefficient [6];
b) Reflection coefficient with respect to curing time for fresh mortar [6]

This study shows the good agreement between the findings of the different techniques, while apart from the experimental observations, it attempts to explain the behavior based on the chemical reactions and the stiffness gain in the matrix. The possibility for industrial application is also discussed.

2. References

[1] P. J. Schull (2013). *Nondestructive Evaluation*, vol. 53, no. 9, Marcel Dekker, INC, New York.

[2] *Denys Breysse* (Ed.) *Non-Destructive Assessment of Concrete Structures: Reliability and Limits of Single and Combined Techniques, State-of-the-Art Report of the RILEM Technical Committee 207-INR*, (2012) Springer Netherlands.

[3] O. Gunes (2013) *Failure modes in structural applications of fiber-reinforced polymer (FRP) composites and their prevention*. In Developments in Fiber-Reinforced Polymer (FRP) Composites for Civil Engineering 115-147. Elsevier Inc.

[4] L. Nilsson (Ed.) *Methods of Measuring Moisture in Building Materials and Structures*, State-of-the-Art Report of the RILEM Technical Committee 248-MMB (2018) Springer.

[5] C. Sirieix, J. F. Lataste, D. Breysse, S. Naar, and X. Dérobert (2007) "Comparison of nondestructive testing: Infrared thermography, electrical resisitivity and capacity methods for assessing a reinforced concrete structure," *J. Build. Apprais.*, vol. 3, no. 1, pp. 77–88.

[6] A. Pourkazemi *et al. (2017)* "Combination of Acoustic Emission and Millimeter Wave Spectroscopy Techniques to Investigate Damage on Cementitious Materials," Proceedings of the *2nd Int. RILEM/COST Conference on Early Age Cracking and Serviceability of Cementitious Materials and Structures.*,Brussels, 12-14 September 2017, 155–160.

[7] J. Hu, Z. Ge, and K. Wang (2014) "Influence of cement fineness and water-to-cement ratio on mortar early-age heat of hydration and set times," *Constr. Build. Mater.*, vol. 50, pp. 657– 663.

[8] P. Bismpas (2016), *Damage monitoring of composite plates by combined Millimeter-wave and Acoustic emission techniques,* Master thesis Vrije Universiteit Brussel, Brussels.

MONITORING OF LARGE CIVIL STRUCTURES – HOUSE CHARLIE

M. Dorn[1], O. Abdeljaber[1] and J. Klaeson[1]
[1] *Department of Building Technology, Linnaeus University, Växjö, Sweden*

1. Introduction

Wooden structures are increasingly built whereby the advantages of engineered wood products are exploited. Glulam has been used for centuries but e.g. Cross-Laminated Timber (CLT) is relatively new. With this, new types of structures and ways of production are possible, such as a high grade of prefabrication and a quick construction phase.

Nevertheless, wood and wood-based materials are subjected to changes of the environment, particularly time-dependent and humidity effects are visible. Additionally, wood is non-homogenous and of natural origin and, hence, can be predicted only to a certain degree. The condition of the structure is therefore of high interest for the designers, the constructors and not at the least for the owner and user.

In an on-going project, a four-story office structure was equipped with a network of sensors [1]. The building, House Charlie in Växjö, Sweden, comprises 3,700 m^2 of office space and 2,000 m^2 of conference and shared space. The load-bearing structure consists beams and columns in glulam with the flooring made from CLT. The elevator shafts in concrete together with diagonal bracings in the façade provide horizontal stabilization.

2. Sensors and measurement network

House Charlie was equipped with a multitude of sensors: potentiometers for displacement measurement; conductivity for moisture content; combined temperature and humidity sensors; geophones and triaxial accelerometers for vibrations; a weather station for outdoor conditions (rain, wind direction, wind speed, temperature, humidity, pressure). The sensors were placed in groups at certain positions in the building on all floors (see Figure 1).

Floor 1   Floor 2

Floor 3   Floor 4

Fig. 1. Layout of the sensors and sensor groups (floor 1 to floor 4)

SAAB and LNU developed a sensor card as part of this project. Two of such cards were deployed, collecting data at floors 1 and 2 as well as floors 3 and 4, respectively. The sensor cards are synced

so that data is logged at the same time point. The sensor card handles analog and digital signals, additionally, a CAN bus is available.

The sensor card allows for multiple signal reading in one channel if the data comes from a microcontroller. In four positions, groups of six temperature/humidity sensors were placed in the outer facades in six different depths. Temperature/humidity sensors and conductance measurements were put into a CLT-floor at different layers of the CLT. Displacement measurements on columnbeam connections were done at three positions. The sampling interval is set to 10 min.

ADC cards were used to operate the geophones and the accelerometers. Sampling is done at 120 Hz for a duration of 90 min twice a day. Additionally, measurement is triggered by the weather station if a certain wind speed is reached.

A RaspberryPi is deployed to collect data from the sensor cards for storage. It also serves as a gateway via a SSH- and web-interface. Thereby, data can be downloaded but also the sensor network is managed via the interface.

3. Selected results

The vibration data allowed to determine eigenfrequencies and damping of House Charlie [2]. It allows hereby also verifying structural models of House Charlie.

Figure 2 shows the moisture content in the CLT-flooring at three different depths from, both, the temperature/humidity sensors and the conductance measurements. Moisture level was obviously high in July 2018 when the construction was finished. There was a clear dry-out phase during winter 2018/19, followed again by an increase of moisture during the warm season of 2019. Nevertheless, the maximum levels from the beginning where not reached again. The overall pattern is the same for the three depths; nevertheless, the increase during spring/summer was much lower in positions 1 and 2 as compared to position 3.
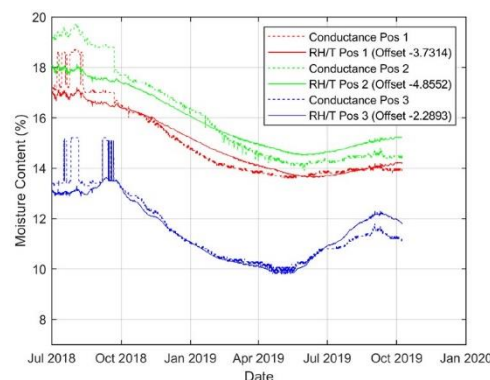
Fig. 2. Comparison of moisture data in a CLT flooring at different depths

4. Conclusions and outlook

The measurement network in House Charlie feeds two goals simultaneously: for the first, it allows monitoring the structure and the conditions. Secondly, the project is used as a prototype to learn how to lay out such a network. It is already planned to deploy similar networks in the future to monitor timber structures.

5. References

[1] O. Abdeljaber, J. Klaeson, and M. Dorn, "Structural Health Monitoring of House Charlie." Department of Building Technology, Linnaeus University, 2019.
[2] T. V. Rasmussen, "Vibration in Timber Constructions", University of Southern Denmark, 2019.

LOGISTIC REGRESSION AIDED PHASE UNWRAPPING ALGORITH

M.J. Huang, S.C. Cheng and Y.C. Yang
National Chung Hsing University, Taichung, Taiwan

1. Introduction

Phase unwrapping is a key technique in many phase retrieving applications, e.g. photoelasticity, shearography, ESPI, and other fringe pattern analysis. The wrapped map that produced by these applications should be successfully unwrapped first to form a continuous phase distribution so that their corresponding physical characteristics can then be built. Therefore, a robust and efficient unwrapping algorithm is definitely needed for finishing the jobs well.

In this article, a machine learning skill – logistic regression is utilized for isolating zones with and without 2π phase discontinuities. After that, regional phase recovery can be continued to eliminate the 2pi phase ambiguities of the phase maps.

2. The unwrapping algorithm

The unwrapping algorithm used herein is based on a previously published paper "A quasi-one-frame phase-unwrapping algorithm through zone-switch and zone-shifting hybrid implementation" [1]. It is classified as a regional retrieving branch [2] and therefore bears the inherent advantages of a regional approach – fast, clear and robust.

But instead, we will use an artificial intelligence tool – the logistic regression to locate its necessary transition and global zones so as to improve its efficiency and correctness of the zone partition.

3. Logistic regression

Logistic regression is a statistic model for modeling a probability of an even such as pass/fall, win/lose, alive/dead or healthy/sick. Using it, the binary variable of our problems where the zones with and without 2π phase discontinuities locate can be decided with ease.

For best correctness of the result, lots of training data (, including at least the similar scenario study of the solved problem) should be fed into the model to build a useful weighting coefficient set for the logistic regression of the real problem. A centered mask is placed on each pixel of the training phase map to calculate all the differences of the surrounding with respective to the centered pixel and then classified the differences into partitioned ranking levels. In this approach, factor of fringes' orientation will automatically die out. This makes the training work easier and more structured. With this inherency, trained coefficients set from regular vertical fringes can be applied for horizontal, inclined or even non-regular experimental analysis of real case.

4. Photoelastic and ESPI verification

Two real cases, photoelastic and ESPI, are verified by the proposed algorithm. The first case is the well-known study of disk under diametric compression. As the figures shown in Fig. 1, the wrapped maps are very clear (i.e., noise-free) and could be processed with ease. But as stressed on the literature [3] the wrapped isochromatic of Fig. 1(b) is coupled by isoclinic. The coupled map should be decoupled first, before the proposed algorithm applying on it, to get a correct result. The second case was the ESPI study shown as Fig.2, which was a highly noisy case and it was very difficult to be processed by most proposed unwrapping algorithms. In present study, the proposed algorithm was successfully verified on both cases.

5. Conclusion

Logistic regression is successfully applied for the unwrapping on both the simulated and experimental photoelastic phase maps. With its designed rule, trained weighting coefficients built from vertical, straight and regular fringes can be applied on the retrieval of non-regular fringes acquired from real photoelastic experimental work. In addition, the present study not only can be applied on clear data coming from the photoelasticity experiment but also can be applied on highly noisy experimental works such as the ESPI (electronic speckle pattern interferometry) or ESPSI (electronic speckle pattern shearing interferometry) experiment.
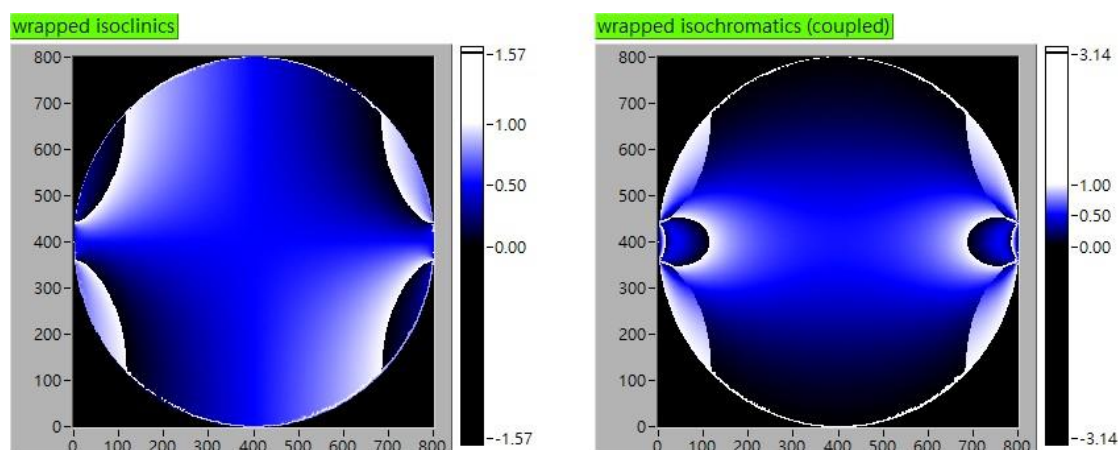
Fig. 1. A simulated photoelastic study of disk under diametric compression,
(a) wrapped isoclinic and (b) wrapped isochoromatic but with isoclinic factor coupling on
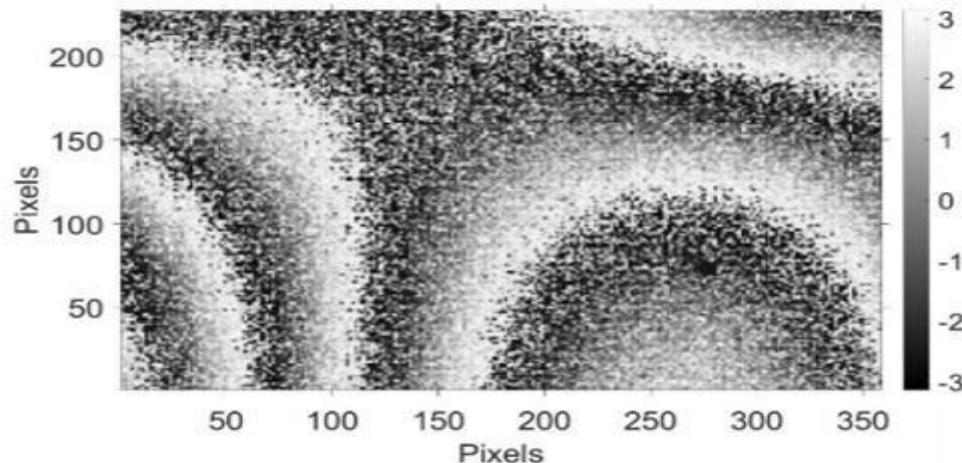
Fig. 2. An ESPI experimental case

6. References

[1] M.J. Huang (2002). A quasi-one-frame phase-unwrapping algorithm through zone-switching and zone-shifting hybrid implementation, *Opt. Comm.*, **210**, 187-200.

[2] R.M. Goldstein., H.A. Zebker, and C.L. Werner (1988). Satellite radar interferometry: Two-dimensional phase unwrapping, *Radio Science*, **23**, 713-720.

[3] Y.T. Zhang, M.J. Huang, H.R. Liang, and F.Y Lao (2012). Branch cutting algorithm for unwrapping photoelastic phase map with isotropic point, *Optics and Lasers in Engineering*, **50**, 619-631.

A STUDY ON STABILITY
OF THE MEDIEVAL "TWIN TOWERS" OF BOLOGNA IN ITALY

G. Lacidogna[1], G. Niccolini[1], O. Borla[1] and A. Carpinteri[1]
*[1] Politecnico di Torino, Department of Structural, Geotechnical and Building Engineering,
Torino, Italy*

1. Abstract

Extending the lifespan of monumental structures is of fundamental importance for the sustainability and safety of the built environment. It is society's duty to preserve these unique monuments and keep the memory of the historical and cultural roots for future generations. In this context, has been demonstrated as monitoring systems and especially the Acoustic Emission (AE) Technique, combined with laboratory and nondestructive testing methods, allow to reliably evaluate the state of conservation of historic towers and its evolution in time. In this contribution, after a brief summary on the results already obtained from the the "Asinelli" Tower monitoring, carried out by the authors a few years ago, the preliminary outcomes from the "Garisenda" Tower structural stability analysis are discussed. As a matter of fact, the two Towers, recognized as the "*Twin Towers*" of Bologna, represent a remarkable symbol of the City in the Italian Architectural Heritage, and they must be preserved.

2. The "Twin Towers" of Bologna: Asinelli and Garisenda

The Authors of the City of Bologna history all agree in dating the Asinelli and Garisenda Towers (Figure 1) to the early twelfth century. The Asinelli Tower was built in 1109–1119. It rises to a height of 97.30 metres above the ground, and shows a deviation from verticality of 2.38 metres. It has a square cross-section, tapering along its height, the sides measure ca. 8.00 metres at the base and 6.50 metres at the top. From the structural standpoint, the Tower can be subdivided into four segments, depending on type of masonry.

The Garisenda Tower, built around the same time, is much smaller (48 metres), but with a steeper leaning (3.22 metres) due to an early and more marked subsidence of soil and foundation. In the middle of the 14th century the Tower, which was 60 metres high, was cut by 12 metres reaching the current 48 metres. In addition, the ashlar covering in "selenite" stone of the base dates back to the late 19th century.

Fig. 1. The Asinelli Tower (right) and the Garisenda Tower (left) in the city centre of Bologna

3. Results of the structural stability of the Asinelli Tower

AE monitoring on the Asinelli Tower lasted 122 days from September 23, 2010 to January 28, 2011. The data collected during the monitoring period were analyzed to evaluate crack growth and its possible correlation with: (i) seismic activity; (ii) vehicle traffic and wind effects on the Tower. The AE transducers were applied to the north-east corner over the arcade of the Tower. Historic series of the AE differential count showed a strong correlation with seismicity, and a statistically unrelated behaviour between AE counts and urban traffic or wind phenomena [1, 2].

4. Preliminary results of the structural stability of the Garisenda Tower

AE monitoring on the Garisenda Tower started on May 31st, 2019 and it is still in progress. The adopted AE equipment consists of a device connected to 8 piezoelectric sensors, fine-tuned by the authors. This system allows to perform a real-time analysis of the signals. The piezoelectric sensors have been fixed to the inner wall of the Tower basement, composed of blocks of "selenite". A seismometer was also fixed at a height of about 150 cm from the floor basement. Thanks to this arrangement, the AE signals distribution can be related with the data measured by the seismometer in order to obtain correlations between the actions generated by the environment, as seismic vibration, vehicle traffic, wind, and the Tower damage. In Figure 2, the early results in terms of AE cumulative function, hourly monitoring rate, frequencies and amplitudes, and micro-crack sources localization are reported for the first monitoring period (until to September 30, 2019).
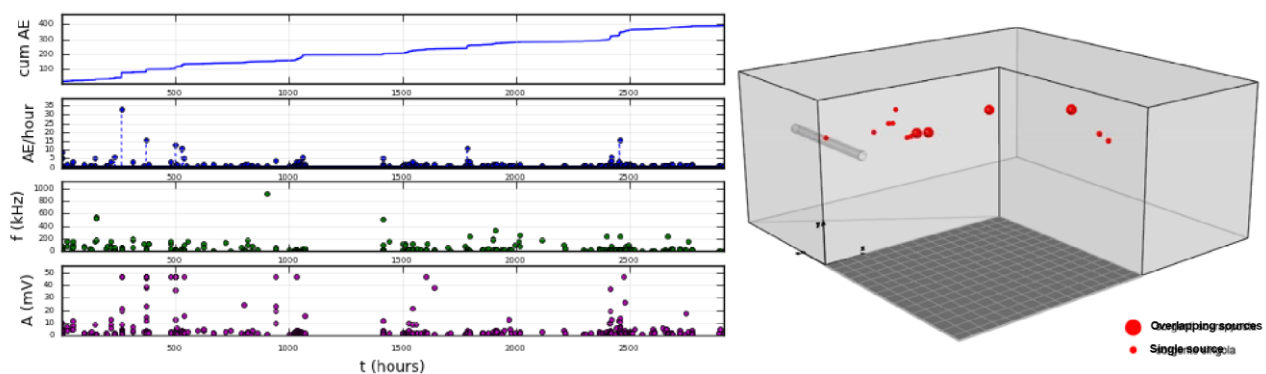
Fig. 2. (left) AE data; (right) Axonometry representation of the AE sources localization

In this preliminary analysis some of the AE sources have been localized in the masonry of the "selenite" basement, and in particular some of them have been detected along the so-called "*unloading arch*", formed in the masonry due to the dissolving action of humidity. Other laboratory tests were carried out on specimens of different shape and size extracted from the Tower and tested in compression, with the simultaneous detection of the AE activity. In this contribution a statistical correlation between the *in situ* monitoring data and the external environmental actions will be provided, therefore the most damaged areas of the Tower will be identified. Moreover, a comparison between the structure data and those obtained from the specimens tested in the laboratory will be presented, in an attempt to experimentally identify the masonry state of damage and stress.

5. References

[1] A. Carpinteri, et al. (2016). A study on the structural stability of the Asinelli Tower in Bologna, *Structural Control and Health Monitoring*, **23**, 659-667.
[2] A. Carpinteri, et al. (2018). Time series analysis of acoustic emissions in the Asinelli Tower during local seismic activity, *Applied Sciences*, **8**, Paper N. 1012.

DIGITAL IMAGE CORRELATION ANALYSIS APPLIED TO MORTAR SHRINKAGE TESTS FOR THE DURABILITY OF RESTORATION WORKS

A. Grazzini[1], G. Lacidogna[1], M. Zerbinatti[1] and S. Fasana[1]

[1] *Politecnico di Torino – Department of Structural Geotechnical Building Engineering, Turin, Italy*

1. Abstract

The use of repair mortars for restoration and strengthening works applied on existing buildings must be carefully studied regarding the compatibility of the mechanical characteristics. In fact, the use of mortars with very different physical-chemical-mechanical characteristics respect to the original ones and the support on which they are applied can compromise the durability and sustainability of the repair intervention [1-3]. Often the use of new mortars is aimed for restoring old plaster or for strengthening work of historic masonry wall. The mechanical incompatibility between repair mortars and masonry structures can cause the detachment of the strengthening material, thus making ineffective the repair work [4, 5]. It's important to set up an atlas of reference, compared to many mixtures of mortars and conglomerates, useful to support the operational choices in the project of restoration, recovery, and maintenance of historical buildings [6].

In the case of repair plaster or strengthening mortars it is very important to evaluate the consequences of the shrinkage after the application of the repair mortar. It is known that during the setting and hardening phenomena of concrete or mortar, there is a change in volume known as "shrinkage". It is a function of time, independent of the loads acting and originates from the movement of water inside the binding paste. If the shrinkage-induced stress exceeds the tensile strength of the mortar, the shrinkage would inevitably cause the mortar to crack. However, shrinkage can be reduced by using particular precautions during the design of the blends (paying attention to the mix design of aggregates and to the adequate ratio binder/aggregates, e.g.), the execution of the castings and the seasoning. High shrinkage values can cause aesthetic inconsistencies on the repaired plaster or even favor internal coercion forces that determine the detachment of the repair mortar. It is very important to be able to analyze and measure the phenomenon of shrinkage of specific repair mortars in the laboratory, in order to test their durability when applied *in situ*.

In this experimental work, the trend of shrinkage on repair mortars was assessed by specific shrinkage laboratory tests using the new measure technique by Digital Imaging Correlation (DIC). In the field of non-destructive diagnostics, the DIC represents a very advanced technique for monitoring the diplacements and deformations of materials in the laboratory tests [7].

The shrinkage tests were performed by packaging specimens of mortars of different mixtures inside specific moulds for shrinkage tests equipped with pegs inside the jet for the subsequent shrinkage measurement by means of comparators. The maturation phases were measured with the comparators but also monitored by the DIC, which allowed to obtain detailed information on the tensile response of the mortar paste and the location of micro-crack during the shrinkage time.

The comparison between the data analyzed by the DIC technique and the values measured manually by means of the comparators confirmed the validity and precision of the DIC to perform laboratory measurements even of very small and microscopic values such as deformations due to shrinkage. The test results also made it possible to integrate information about a technical atlas on different mortar mixes for different types of maintenance on the existing building stock [3, 6].

Keywords: Shrinkage; DIC; repair mortar; durability; laboratory test.

Fig. 1. Chapel n. 13 of the Sacri Monti of Varallo (Italy)

2. References

[1] P. Bocca, A. Grazzini, D. Masera, A. Alberto and S. Valente (2011). Mechanical interaction between historical brick and repair mortar: experimental and numerical tests, *J. of Physics: Conf. Series,* **305**, 1-10, doi: 10.1088/1742-6596/305/1/012126.

[2] P. Bocca and A. Grazzini (2013). Mechanical properties and freeze-thaw durability of strengthening mortars, *J. of Mat. in Civil Eng.,* **25**, 274-280, doi: 10.1061/(ASCE)MT.19435533.0000597.

[3] S. Fasana, A. Grazzini and M. Zerbinatti (2018). Mortars and plasters mixes for ancient buildings and their mechanical characteristics. First results of a research project (in progress), in *Proc. of the 34th Convegno Internazionale Scienza e Beni Culturali - Intervenire sulle superfici dell'architettura tra bilanci e prospettive (in italian)*, Bressanone, Italy.

[4] A. Grazzini, G. Lacidogna, S. Valente and F. Accornero (2018). Delamination of plasters applied to historical masonry walls: Analysis by acoustic emission technique and numerical model, *IOP Conf. Series: Mat. Sc. Eng.,* **372**, 1-7, doi: 10.1088/1757-899X/372/1/012022.

[5] P. Tarizzo, A. Formia, J.M. Tulliani, M. Zerbinatti and A. Schiavi (2013). A new non invasive method to evaluate the detachments of plasters. First results, *Int. J. Cons. Sc.*, **4**, 587-592.

[6] A. Grazzini, M. Zerbinatti and S. Fasana (2019). Mechanical characterization of mortars used in the restoration of historical buildings: an operative atlas for maintenance and conservation, *IOP Conf. Series: Mat. Sc. Eng.,* **629**, 1-7, doi: 10.1088/1757-899X/629/1/012024.

[7] G. Minafò, L. La Mendola, J. D'Anna, G. Amato and J.F. Chen (2019). On the use of digital image correlation (DIC) for evaluating the tensile behaviour of BFRCM strips, in *6th International Conference on Mechanics of Masonry Structures Strengthened with Composite Materials, MuRiCo6 2019*, Bologna Italy, *Key Eng. Mat.,* **817**, 377-384.

DETECTION OF CORROSION ON STEEL STRUCTURES USING AUTOMATED IMAGE PROCESSING

M. Khayatazad[1,2], L. De Pue[1] and W. De Waele[1]
[1] SOETE LABORATORY, Department of Electromechanical, Systems and Metal Engineering, Faculty of Engineering and Architecture, Ghent University, Gent, Belgium
[2] SIM vzw, Technologiepark 48, 9052 Zwijnaarde, Belgium (project number 179P04718W).

1. Abstract

The traditional method used for corrosion damage assessment is visual inspection which is timeconsuming for vast areas, impossible for inaccessible areas and subjective for non-experts. A promising way to overcome the aforementioned drawbacks is to develop an artificial intelligencebased algorithm that can recognize corrosion damage in a series of photographic images. This paper reports on the implementation and use of an algorithm that quantifies and combines two visual aspects – roughness and color – in order to locate the corroded area in a given image. For the roughness analysis, the uniformity metric calculated from the gray-level co-occurrence matrix is considered. For the color analysis, the histogram of corrosion-representative colors extracted from a data-set in HSV color space is used. The algorithm has been applied to a large dataset of photographs of corroded and non-corroded components and structures. Our findings show that the developed algorithm can effectively and efficiently locate corroded areas.

2. Introduction

Corrosion is a frequently occurring damage mechanism for steel structures exposed to harsh environments. For engineering components this mechanism takes the lead in terms of frequency of failure with 42% according to [1]. Early detection of structural degradation prior to failure does not only have its financial benefits but can also prevent catastrophic collapses of structures and avoid harmful situations for both humans and the environment. The occurrence of corrosion comes with two main visual characteristics. In the first place it creates a rough surface texture, and secondly the colors of the by-products are situated within a characteristic color spectrum. Therefore the use of texture analysis and color analysis, or a combination of both, is often used to develop algorithms for corrosion detection. These two features can be applied on a stand-alone basis or implemented in a pattern recognition technique. In this paper, the algorithm proposed by Bonnin-Pascual and Ortiz [2] is implemented and optimized.

3. Roughness step

A non-corroded surface has a quite uniform color distribution, but a corroded surface has a nonuniform distribution of corrosion colors. One way to measure the color distribution of an image is to measure its so-called *uniformity* [3]. For this, one first needs to convert the color image to a gray scale with a predefined number of gray levels. Following, for every pixel a general neighborhood is defined and the number of co-occurrences of two specific gray levels is counted and extracted as a matrix, the so-called gray level co-occurrence matrix (GLCM) [3]. Using the GLCM, one can calculate the *uniformity* of the image. If the calculated *uniformity* is less than a threshold, the investigated region is considered as a potentially corroded patch.

4. Color step

By-products of steel corrosion in atmospheric conditions are characterized by shades of red, yellow and red-brown. By quantifying image colors and comparing them with quantified corrosion colors, one can make a classifier for corrosion detection. In this paper the HSV color space is used for quantification. Among hue (H), saturation (S) and value (V), V can just be used to prevent the wellknown instabilities in the computation of hue and saturation when the color is close to white or black. In that case, the pixel is classified as non-corroded [2]. Regarding H and S, one can apply two methods. The first method is to apply rough limitations on the H and S. The second one, called histogram method and applied in this work, is a normalized histogram of H and S values of corrosion colors on which a two-dimensional filter is applied. Since a normalized histogram is used, applying a threshold means to filter out the low-probability combinations of H and S that represent a corrosion color.

5. Results

The benefit of combining both steps in the corrosion analysis are illustrated in the first and second examples in Fig. 1. The first row of images concerns a detail of a steel bridge with corroded region at the top and a region with the original green paint. The roughness analysis defines almost the entire image as 'rough'. Because not every rough surface implies corrosion, the color classification filters out the corroded area.. In the second example, both in the roughness step and in the color step, too many areas are labelled as corroded. The roughness analysis includes rougher parts of the white surface and a part of the orange bar, while the color analysis includes the rust stains and parts of the orange bar. By combining the two classifiers, additional areas are filtered out and at the end the corroded area is quite accurately determined.

(a) original images   (b) roughness analysis   (c) color analysis   (d) Combination
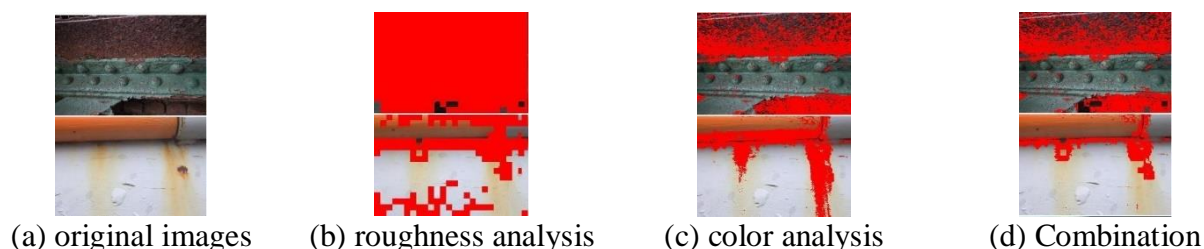
Fig. 1. Results of the corrosion detection algorithm in which red indicates the corroded areas.

6. Conclusion

The results confirm that the implemented algorithm is a promising tool for the detection of corrosion by image analysis. It does not yield a 100% performance in corrosion recognition due to the rather simple classification method and the trade-off between the roughness and color steps that has to be made. Images with non-uniform illumination show most limitations when parts of the image are under or over-exposed or part of the image is covered with a shadow. The authors are working on this issue to further improve the algorithm.

7. References

[1] Z. Petrovic, "Catastrophes caused by corrosion," Vojnoteh. Glas., vol. 64, no. 4, pp. 1048–1064, 2016.
[2] F. Bonnin-Pascual and A. Ortiz, "Corrosion Detection for Automated Visual Inspection Visual Inspection," in Developments in Corrosion Protection, INTECH, 2014, pp. 619–632.
[3] A. Baraldi and F. Parmiggiani, "An investigation of the textural characteristics associated with Gray Level Co-occurrence Matrix statistical parameters," Geosci. Remote Sensing, IEEE Trans., vol. 33, pp. 293–304, 1995.

ACOUSTIC MONITORING OF CEMENTITIOUS COMPOSITE PLATES FOR LOAD-BEARING APPLICATIONS

N. Ospitia[1], E. Tsangouri[1], A. Hardy[2], A. Van Driessche[1], A. Si Larbi[2] and D.G. Aggelis[1]
[1] Department of Mechanics of Materials and Constructions, Vrije Universiteit Brussel, Brussels, Belgium
[2] École Nationale d'Ingénieurs de Saint-Étienne – ENISE, St. Etienne, France

1. Introduction

Acoustic emission (AE) is used in laboratory and in-situ conditions to evaluate the structural condition of materials and structures. Its advantages concern the non-destructive, non-hazardous and relatively easy application, while the recent developments in sensors' technology and signal analysis, render it an excellent candidate for monitoring of the structural condition. Specifically, in cementitious composite members for construction purposes including reinforcement and repair, AE has proven its ability to characterize the fracture mode as well as the developed strain field based on the AE waveform parameters. Cracking events are registered with higher frequency content while debonding between layers or between the plate and the substrate usually obtain longer duration characteristics [1,2]. At the same time, it allows evaluation and 3D damage localization something not possible by visual inspection. Still, the absolute capacity of the technique is not yet reached insitu mainly because of phenomena that mask the initial information from the source. These include the wave propagation path, reflections, frequency dispersion due to plate geometry that causes elongation of the signal, scattering as well as attenuation [3]. All these factors change the received acoustic waveform and complicate the assessment in large scale. This paper wishes to address the influence of the plate geometry and specifically the curvature and the width of the plates, in order to allow the correct interpretation of the results.

2. Experimental details

Several textile reinforced cement (TRC) plates and beams were manufactured. The matrix is inorganic phosphate cement (IPC) and the reinforcing mat consists of randomly oriented chopped E-glass fibers. The final volume fraction averages at 20%. The laminates were tested in three-point bending according to the photograph of Fig. 1. Several AE sensors resonant at 150 kHz were used to capture the transient elastic waves emitted during the fracture process of the specimens.
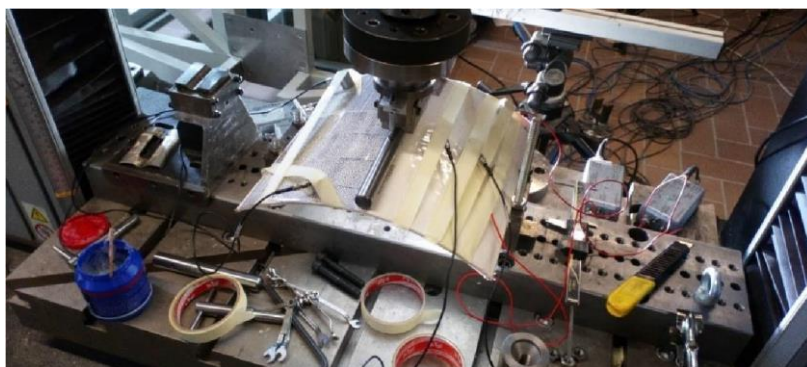
Fig. 1. Photograph of the experimental setup

3. Results

Results indicate that the same fracture mechanisms are registered with quite different AE characteristics depending on the shape of the plate. Specifically, frequency and amplitude are higher for beam specimens, while duration characteristics are longer for plates. Fig. 2 shows AE parameters of the matrix cracking source for beams and plates. It is obvious that there is a significant shift in the results which necessitates extra consideration when upscaling the conclusions from small laboratory coupons to large and realistic plate geometries.
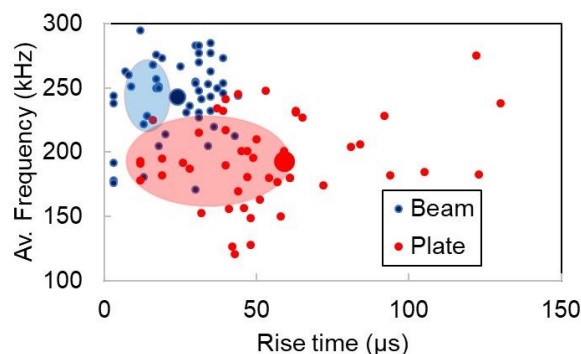
Fig. 2. AE parameters of waveforms
recorded during matrix cracking for beam and plate TRC specimens

4. Conclusions

The effect of geometry (curvature and width) of TRC plates in the AE behavior of the material is discussed. This combined study of AE and wave propagation is necessary for the correct interpretation of the acoustic data, while confirmation of the damage mode by optical methods (digital image correlation) applied on the surface is also conducted.

5. References

[1] Aggelis, D.G., De Sutter, S., Verbruggen, S., Tsangouri, E., Tysmans, T., Acoustic emission characterization of damage sources of lightweight hybrid concrete beams, (2019) Engineering Fracture Mechanics, 210, pp. 181-188.

[2] Ohtsu M. (2010) Recommendation of RILEM TC 212-ACD: acoustic emission and related NDE techniques for crack detection and damage evaluation in concrete, Test method for damage qualification of reinforced concrete beams by acoustic emission, Materials and Structures, 43(9), 1183-1186.

[3] Scholey JJ, Wilcox PD, Wisnom MR, Friswell MI. (2010). Quantitative experimental measurements of matrix cracking and delamination using acoustic emission. Compos A 41:612–23

ACOUSTIC EMISSION INVESTIGATION IN THE FRACTURE BEHAVIOR OF FIBER-REINFORCED MORTAR SPECIMENS

A.C. Mpalaskas[1], I.F. Giannoulakis[1], D.G. Aggelis[2] and T.E. Matikas[1]
[1] Department of Materials Science and Engineering, University of Ioannina, Greece
[2] Department of Mechanics of Materials and Constructions, Free University of Brussels, Belgium

1. Abstract

The present paper deals with the acoustic emission (AE) monitoring of fracture behavior on (steel fiber-reinforced mortar, SFRM) beams. The aim is to characterize the influence of fiberreinforcement in mortar specimens utilizing acoustic emission technique and ultrasonic testing (UT) as a supplementary NDE method.

Reliable nondestructive evaluation (NDE) of the material condition is essential for accurate structural health monitoring (SHM). The wave propagation commonly referred to as ultrasonic testing (UT) offers this nondestructive nature along with certain benefits. One of the most tangible benefit is that wave velocity is directly connected to the elastic constants [1]. In this specific study, the different fiber-reinforced mortar specimens were ultrasonically interrogated and the correlation between the ultrasound pulse velocity and the final strength was investigated employing statistical analysis. Apart from the well-known association of pulse velocity to strength for building materials, which also holds for the materials used in this study, AE provides a unique insight into the fracture behavior of the specimens. Parameters like the frequency of the waveforms and their amplitude among others show a transition with the load. According to their maximum strength, the samples exhibit distinct AE characteristics even at low load, allowing to estimate their final strength class after having sustained just a small percentage of their ultimate load [2]. The data of AE monitoring have been processed using modern statistical methods to investigate the correlation with the strength of the specimens. For achieving a statistical analysis with accurate and robust results, the number of samples has been increased up to 25 per batch.

As far as the experimental procedure is concerned, the mortar specimens have been reinforced with three different types of steel fibers (straight, waved and hooked) by means of shape and geometry and were tested in three-point bending according to EN 13892-2:2002 [3] and compression according to ASTM C109[4] for determination of their mechanical properties. Consequently, four different mortar mixtures were produced consisting of 25 specimens each. One was plain mortar (PM) and the other included 0.5% (vol.) of straight, waved and hooked steel fibers (steel fiber reinforced mortar, SFRM). The same mix proportions were used in all four batches with the only difference in the addition of 39.3 kg/m^3 steel fibers for each type used. The specimens were 40x40x160 mm in size. In order to secure that the crack would initiate at the center of the specimen, a notch was created by inserting a small wooden stick in the midspan of the side to be placed at the bottom during bending (tensile side). As to AE monitoring, two AE piezoelectric sensors, namely the R15 (Physical Acoustics Corp., PAC) with resonance nominally at 150 kHz were attached to the side of the specimen. Honey was used for acoustic coupling, while the sensors were secured by the use of tape during the experiment. The horizontal distance between the sensors was 40 mm and they were positioned symmetrical besides the centre of the side of the specimen as seen in Fig.1. The signals were recorded by a two-channel monitoring board PCI-2, PAC with a sampling rate of 5 MHz. The threshold was set to 40 dB to avoid ambient noise and the acquired signals were preamplified by 40 dB[5].

Fig. 1. Positioning of the R15 sensors during three-point bending

It is concluded, that (UT) together with (AE) monitoring during a proof loading can provide useful insight information of the materials, characterize the reinforcement used in SFRM specimens and also provide an efficient prediction of the level of ultimate strength make them a valuable asset for NDE in the expanded sector of building materials

Keywords: Acoustic emission, mortar, frequency, steel fiber-reinforced, ultrasound

2. References

[1] A. C. Mpalaskas, O. V. Thanasia, T. E. Matikas, and D. G. Aggelis, "Mechanical and fracture behavior of cement-based materials characterized by combined elastic wave approaches," Constr. Build. Mater., vol. 50, pp. 649–656, 2014, doi: 10.1016/j.conbuildmat.2013.10.022.

[2] E. Tsangouri, D. G. Aggelis, T. E. Matikas, and A. C. Mpalaskas, "Acoustic emission activity for characterizing fracture of marble under bending," Appl. Sci., vol. 6, no. 1, pp. 1– 12, 2016, doi: 10.3390/app6010006.

[3] EN 13892-2:2002, "Methods of test for screed materials. Part 2: Determination of flexural and compressive strength," 2002.

[4] I. Kett, "Compressive Strength of Hydraulic Cement Mortars (C 109)," Eng. Concr., pp. 29– 31, 2009, doi: 10.1201/9781420091175-c5.

[5] D. G. Aggelis, A. C. Mpalaskas, D. Ntalakas, and T. E. Matikas, "Effect of wave distortion on acoustic emission characterization of cementitious materials," Constr. Build. Mater., vol. 35, pp. 183–190, 2012, doi: 10.1016/j.conbuildmat.2012.03.013.

ACOUSTIC MONITORING FOR CURING AND CHARACTERIZATION OF ADVANCED CEMENTITIOUS MATERIALS

G. Lefever[1], D. Snoeck[1,2], N. De Belie[2], D. Van Hemelrijck[1] and D.G. Aggelis[1]
[1] Department Mechanics of Materials and Constructions, Vrije Universiteit Brussel (VUB)
[2] Magnel-Vandepitte Laboratory for Structural Engineering and Building Materials,
*Department of Structural Engineering and Building Materials, Faculty of Engineering
and Architecture, Ghent University*

1. Abstract

In this study, acoustic emission (AE) is used to monitor the hydration of mortar specimens with and without superabsorbent polymers (SAPs). AE is a non-destructive measuring technique that monitors transient elastic waves, generated by the release of energy inside the material under test. The acoustic activity recorded in a chosen time frame, allows to determine diverse processes occurring such as chemical and autogenous shrinkage cracking [1] or hydration [2]. Projections to the final properties can also be done based on the AE rate during the exothermal phase [3].

Moreover, from the received waves various parameters can be extracted, related to the energy, or the waveform shape among others. Differences in these wave parameters can be used to further elaborate the knowledge on the occurring phenomena. For example, several studies on the use of AE during fracture of cementitious mixes showed that different fracture modes could be characterized by analyzing the rise time, amplitude and frequency of the received wave signals [4]. Also, in a study on self-healing concrete, where an encapsulated healing agent was placed inside the specimen, the concrete fracture could be distinguished from the breaking of glass tubes inside the cementitious matrix, characterized by an increased energy level [5].

The main setup used in this experimental campaign is depicted in Figure 1, where a metallic mold can be seen, equipped with three piezoelectric sensors. Figure 1a shows a top view with two AE sensors, kept in place by magnetic holders, at the sides of a covered mortar specimen. In figure 1b the side view of the set-up is presented, revealing also an AE sensor, resonant at 150 kHz on the bottom of the specimen.

(a) top view

(b) side view

Fig. 1. Set-up for hydration monitoring

In addition, pencil lead break (PLB) tests were carried out on different mortar compositions. PLB is often used for excitation of broadband wave signals [6].

As the generated wave travels through the material, the analysis of the wave parameters such as velocity and amplitude can provide us extra information on the material's inner structure.

Figure 2 shows the used set-up for PLB testing. In this case, two broadband sensors were used, having a peak frequency at 450 kHz. The PLB is performed multiple times, alternating the position of the pencil lead. In this way, the effect of different additives, such as superabsorbent polymers and nanosilica, on the AE parameters was revealed. The measurements were repeated during the autogenous healing cycles of cementitious materials with and without SAPs in order to check the possible healing effect and its accordance to mechanical measurements conducted on the same specimens.

Fig. 2. Set-up of the pencil lead break test

2. Acknowledgements

3. References

[1]	P. Lura, J. Couch, O.M. Jensen and J. Weiss (2009). Early-age acoustic emission measurements in hydrating cement paste: Evidence for cavitation during solidification due to self-desiccation, *Cement and Concrete Research*, **39**(10), 861-867

[2]	Iliopoulos, S.N. et al. (2016). Towards the Establishment of a Continuous Nondestructive Monitoring Technique for Fresh Concrete, *Journal of Nondestructive Evaluation*, **35**(3), no. 37.

[3]	V.V. Bardakov and A.I. Sagaidak (2016). Forecasting of concrete strength during the hardening process by means of Acoustic Emission method, *PROGRESS in ACOUSTIC EMISSION XVIII*, p.105-110, Editors T.Shiotani, S.Wakayama, M.Enoki, S.Yuyama.

[4]	K. Ohno and M. Ohtsu (2010). Crack classification in concrete based on acoustic emission, *Construction and Building Materials*, **24**(12), 2339-2346

[5]	E. Tsangouri, D.G. Aggelis, K. Van Tittelboom, N. De Belie and D. Van Hemelrijck (2013). Detecting the activation of a self-healing mechanism in concrete by acoustic emission and digital image correlation, *Health Monitoring of Civil Infrastructure and Materials*, 10 pages

[6]	V.A.D. de Almeida, F.G. Baptista and P.R. de Aguiar (2014). Piezoelectric transducers assessed by the pencil lead break for impedance-based structural health monitoring, *IEEE Sensors Journal*, **15**(2), 693-702

11. Thermomechanical Behaviour of Metallic Alloys

IN SITU OBSERVATION OF FATIGUE CRACK CLOSURE IN WELDED JOINTS THROUGH THERMOGRAPHIC STRESS ANALYSIS

L. Bercelli[1], B. Levieil[1], C. Doudard[1] and F. Bridier[2]
[1] ENSTA Bretagne, UMR CNRS 6027, IRDL, Brest, France
[2] Naval Group, Technocampus Océan, Bouguenais, France

1. Introduction

Welded joints are the place of both a strong residual stress field and stress concentrations when subjected to a mechanical loading. They are prone to fatigue cracks initiation and propagation which depend on both the macroscopic loading ratio R and the residual stress field. Indeed, for strong loading ratios ($R \ll 0$ and $R \gg 1$), i.e. in compression, a crack closure phenomenon appears, meaning that only a portion of the fatigue loading cycle actually takes part in the propagation of fatigue cracks. The aim of the present study is to propose, on the one hand, an experimental method for crack propagation tracking through infrared measurement, and on the other hand, a fatigue model for welded joints, identified using the infrared data, that considers the stress ratio effect.

2. Material and experimental set-up

The considered welded joint configuration is a ferritic steel T-joint with double-sided fillet weld. Samples are mounted in a four-point bending test fixture in a hydraulic tension-compression machine of a 100 kN capacity. The samples are monitored through infrared thermography using an infrared mirror tilted at 45°, sending back the image of both weld beads to an infrared camera. In order to explore the effect of both the loading ratio and the residual stress field on the crack closure phenomenon, different test configurations are considered, with as-welded and pre-loaded samples, at loading ratios R=0.1 and R=10.

3. Thermographic Stress Analysis

As detailed in reference [1], the presence of surface cracks can be detected on the temperature's first harmonic θ_{fr} field, which can be linked to the thermoelastic coupling, computed from infrared films. Under adiabatic conditions, i.e. assuming negligible conduction, this temperature is proportional to the amplitude of the stress tensor's first invariant I_{1_a}. The presence of an open fatigue crack in mode I is then visible in the temperature's first harmonic θ_{fr} field given the presence of a zero stress at the free edges of the crack. This is the case at a loading ratio of R=0.1 (Figure 1).
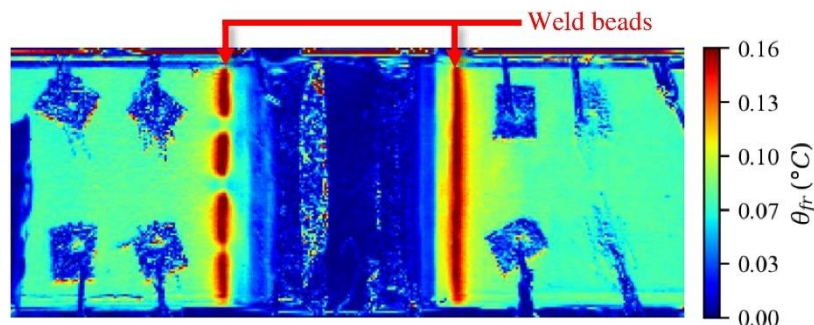
Fig. 1. Image of a $\boldsymbol{\theta_{fr}}$ field on a welded joint at $\boldsymbol{R}$=**0.1**;
three cracks are visible on the left weld bead

In the case of a compressive cyclic stress at the weld bead (R=10), the crack is not necessarily open during the whole loading cycle. As a result, the temperature signal near the crack is no longer a linear response to the mechanical loading (clipped sine). The computation of the temperature's first harmonic θ_{fr} field is no longer relevant to detect closing cracks. Instead, the skewness indicator γ_1 is computed for each pixel, revealing where the thermal response the temperature signal takes the form of a clipped sine. An example is shown in Figure 2 where no cracks are detected in the θ_{fr} field while, on the γ_1 field, four cracks on the right weld bead and two on the left weld bead are visible.

(a)   (b)
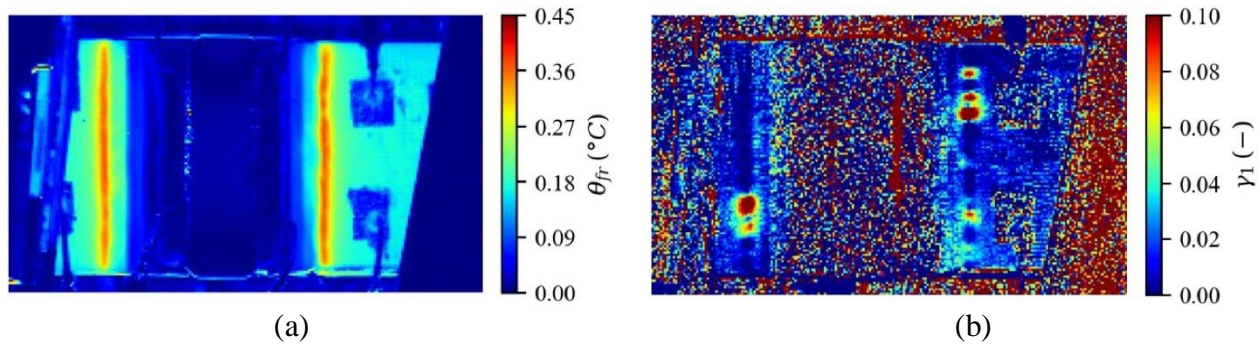
Fig. 2. Comparison of the temperature's first harmonic $\boldsymbol{\theta_{fr}}$ field (a) and the skewness γ_1 field (b) on a welded joint at R=10

4. Model and results

By post-processing infrared films, the propagation of cracks on a weld bead can be tracked. In particular crack propagation kinetics parameters are identified at different load ratios. From these results, a fatigue prediction model based on a crack propagation approach is identified. The definition of an effective stress range $\Delta\sigma_{eff}$ is proposed, i.e. the stress range that takes part in the opening of a fatigue crack

(1) $$\Delta\sigma_{eff} = \left(\frac{1-bR_{eff}}{1-R_{eff}}\right)\Delta\sigma_{nom},$$

where R_{eff} is the effective stress ratio considering residual stresses close to the weld (determined by X-ray analysis), b a material parameter determined from infrared experimental results at different effective stress ratios R_{eff} and $\Delta\sigma_{nom}$ the applied nominal stress range.

The complete identification of this model was performed using the experimental infrared data. Its predictions are in very good agreement with results from an independent experimental database of fatigue lives (determined using an ACPD crack detection method) at various stress ratios.

5. Acknowledgements

6. References

[1] L. Carteron, C. Doudard, S. Calloch, B. Levieil, J. Beaudet, F. Bridier (2020). *Naval welded joints local stress assessment and fatigue cracks monitoring with quantitative thermoelastic stress analysis*, Theoritical and Applied Fracture mechanics, **110**

IDENTIFICATION OF THE DAMAGE SCENARIOS UNDER CYCLIC LOADING OF A COATED 300M STEEL BY INFRARED THERMOGRAPHY MEASUREMENTS

P. Lepitre[1,2], S. Calloch[1], C. Doudard[1], M. Dhondt[1] and M. Surand[2]
[1] *École Nationale Supérieure des Techniques Avancées, ENSTA Bretagne, UMR CNRS 6027, IRDL*
[2] *Safran Landing Systems, Vélizy-Villacoublay*

1. Introduction

Determining a full S/N curve is a time consuming and expensive task. Since numerous parameters influence fatigue properties, generating fatigue curves for every configuration is impractical. The self-heating method under cyclic loading can be used to quickly determine fatigue properties by coupling them with intrinsic dissipation. Where an empirical approach can provide estimation of the fatigue limit [1], the method may provide more information such fatigue life. Understanding and modelling of dissipation mechanisms are then required to link them to fatigue ones [3].

300M is an ultra-high tensile strength steel with good fatigue properties ($\sigma_D \approx 830$ MPa, R = -1) [2]. It is used in aerospace for landing gears to achieve resistance and lifespan requirements. To prevent wear and corrosion, a WC-CoCr coating is applied by High Velocity Oxygen Fuel (HVOF) [4]. The elastic and thermal properties mismatch and the projection effects adversely affect bare material fatigue performance [5]. To reduce this impact, 300M is shot-peened prior to coating. With high temporal and special resolution temperature fields, infrared measurements can provide qualitative and quantitative information on dissipation mechanisms and materials behavior.

2. IR measurements

Additional characterizations were conducted to improve knowledge on the fatigue behavior of the coating. The coating is deemed to be relatively brittle and cracks initiate at strength levels below 300M tensile strength. To investigate this aspect, one bare and one HVOF coated test coupons were tested with cyclic axial loads (R=-1). With a loading frequency of 10 Hz, blocks of 200 cyclic loadings, of increasing stress amplitude, were applied from 0 to $0.59\sigma^*$ for the bare configuration and from 0 MPa until σ^* for the HVOF configuration. For every block, the last 100 cycles were recorded at a frequency of 40 Hz with an InfraTec ImageIR® 10300 camera.

As the HVOF configuration is heterogeneous (300M substrate coated with WC-CoCr) and the Fourier number is significant higher than one ($F_o = 4\lambda t / \rho c_p d^2 \approx 200$), test is not adiabatic. Thus, the temperature amplitude does not correspond to the coating thermo-elastic coupling but an average of the coating and steel one. The term "first harmonic" will be subsequently used instead. The first harmonics were determined with the mean amplitude of the gauge length (calculated with the lock-in method). Both slopes (bare: 0.91 mK.MPa^{-1}; HVOF: 0.73 mK.MPa^{-1}) are slightly lower than the set 300M (1.04 mK.MPa^{-1}) and WC-CoCr (0.79 mK.MPa^{-1}) coupling term value (estimated with literature properties) (fig. 1). Those results validate the magnitude order of the thermal expansion coefficient ($\alpha \approx 6 \times 10^{-6}$ K^{-1}) for WC-CoCr (since the density ρ and the specific heat cp are known).

To detect cracking, the first harmonic amplitude map and the skewness map were calculated. Where no crack appears, the two maps are homogenous (fig. 2.a & 2.b). For $0.94\sigma^*$ (fig. 2.c. & 2.d) a first crack occurs and for σ^*, 4 cracks are observed (fig. 2.e & 2.f). Cracks appear brighter in amplitude maps and darker in skewness maps. After 2 000 cycles at σ^*, the coating seems to be completely cracked (fig. 2.g & 2.h).
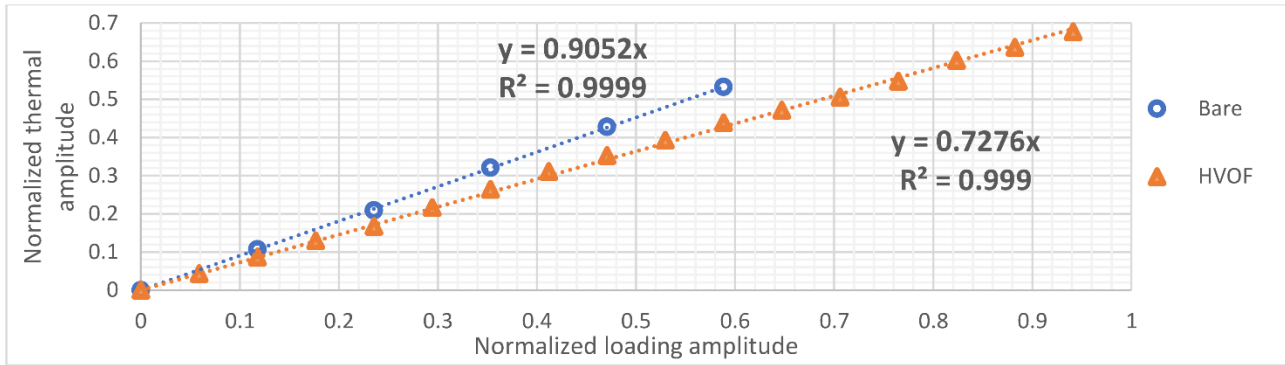
Fig. 1. Mean thermal amplitude according to the loading amplitude
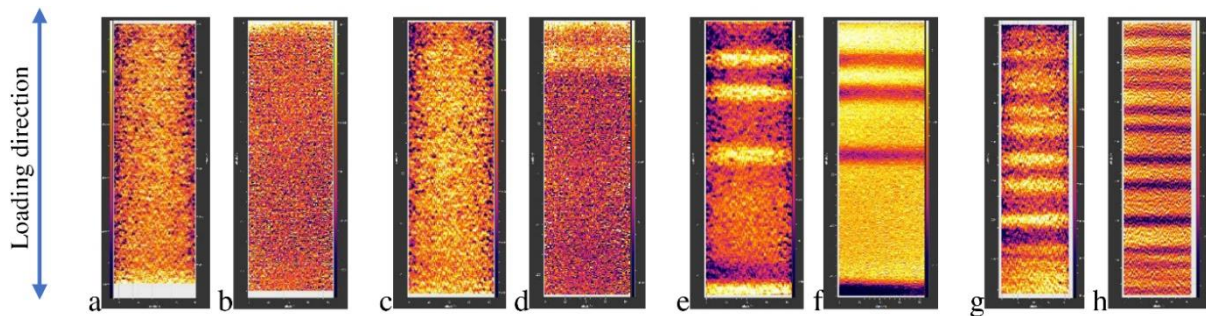
Fig. 2. First harmonic amplitude and skewness maps for 0.88σ* (2.a. and 2.b.), 0.94σ* (2.c. and 2.d.), σ* (2.e. and 2.f.) and after 2 000 cycles (2.g and 2.h)

The coating shows a brittle behavior with no plasticity before crack indication. The first harmonic amplitude increases near the cracks, indicating that they affect the coating and substrate stress state. Complete coating cracking appears after $\approx$ 2 000 cycles and shows a steady inter-cracks step of $\approx$ 1 mm. IR measurements provide access to valuable data, such as crack initiation and kinetics.

As the HVOF configuration test is highly non-adiabatic, the thermal signal cannot be directly interpreted. Further quantitative analyses have to be conducted using thermo-mechanical finite element simulations to interpret dissipation mechanisms and materials behavior.

3. Acknowledgements

4. References

[1] C.E. Stromeyer (1914). The determination of fatigue limits under alternating stress conditions, *Proc. R. Soc. Lond. A*, **90**, 411–425.

[2] H. Xue, P. Liu, P. Chen, J. Wang (2012). Fatigue life assessment of a high strength steel 300M in the gigacycle regime, *Theoretical and Applied Mechanics Letters*, **2**, 031006.

[3] R. Munier, C. Doudard, S. Calloch, B. Weber (2014). Determination of high cycle fatigue properties of a wide range of steel sheet grades from self-heating measurements, *International Journal of Fatigue*, **63**, 46–61.

[4] P.L. Ko, M.F. Robertson (2002). Wear characteristics of electrolytic hard chrome and thermal sprayed WC–10 Co–4 Cr coatings sliding against Al–Ni–bronze in air at 21 °C and at −40 °C, *Wear*, **252**, 880–893.

[5] A. Vackel, S. Sampath (2017). Fatigue behavior of thermal sprayed WC-CoCr- steel systems: Role of process and deposition parameters, *Surface and Coatings Technology*, **315**, 408–416.

POSTERS

EVALUATION OF DEPLOYMENT SYSTEM
FOR NEW GENERATION PERSONNEL RESCUE PARACHUTE
WITH THE USE OF DYNAMIC SCALE PARACHUTE MODELS

K.S. Szafran[1] and I. Kramarski[2]
[1] Łukasiewicz Research Network – Institute of Aviation, Warsaw, Poland
[2] HORNET, Nowy Dwor Mazowiecki, Poland

1. Abstract

A new generation of nylon parachute fabrics is characterised by increased specific strength and significantly lower weight. In order to use new fabrics, conceptual work was undertaken on a new generation of aviator rescue parachute, characterised by reduced unit weight, and also to meet the requirements of ETSO C23d aviation regulations relating to personnel rescue parachutes and reserve parachutes.

A comparative analysis of personnel rescue parachutes was performed, in which a different method of opening the canopy of the parachute was used: with the unfurling of suspension lines first followed by filling the canopy (parachutes SP-6 by Polish company Aviotex and GQ 350 by British company GQ) and simultaneous unfurling of suspension lines and filling the canopy (parachutes SK94 by Polish company AIR-POL and EB-80 by British company Irvin-GQ). The first method offers less overloading during canopy opening, but with greater loss of height. The second method gives higher overloads, but the parachute is opened with less height loss.

A personnel rescue parachute is used in the event of an emergency egress, which often occurs at the last moment before a crash into the ground or water. Therefore, the amount of height loss during parachute opening is a critical performance indicator, especially for rescue over built-up areas or industrial installations where the height of standing buildings or industrial facilities reduces the available height for proper opening of a rescue parachute.

A geometric model of the filling canopy was developed, in which a pear-shaped canopy consists of a spherical part at the top and a conical part below. The model also takes into account the existence of canopy folds during the filling process, which compared to the geometric models used so far, increases the area of air intake of the canopy and the volume of air flowing into the canopy, and thus more realistically reproduces the parachute canopy dynamics during opening process. For each of the opening methods, a version of the dynamic model with appropriately selected equations of system motion during the parachute opening process was developed. The model takes into account the stiffness properties of the canopy structure considering limited possibilities of scaling the lines properties, fabric and reinforcing tapes due to the availability of a limited range of raw materials on the market. Scalable models of the new generation of lightweight parachute fabric were developed to test the manufacturing properties of the new generation of parachute fabric. The fabric's susceptibility to manual and machine cutting was investigated, and the fabric's seams were tested using standard parachute threads. The ability of the canopies to be packed was checked and the correct opening of the canopies on the ground tests was conducted. All the tests were completed with a positive result.

Personnel rescue parachute is designed for pilots and crew members of aircraft and helicopters. The regulations require correct opening of the parachute at speeds up to 278 km/h (150 KTS) and at the loss of altitude during its opening not more than 90 m at the opening speed of 111 km/h (60 KTS). When jumping from a helicopter in a hover, a loss of altitude of up to 150 metres is allowed. Based on these requirements and in order to ensure that rescue parachutes can be used from a fixed-wing

and rotary-wing aircrafts, a flight test programme has been developed using appropriate unmanned aerial vehicles (UAVs).

To simulate the use of parachute from a board of a fixed-wing aircrafts, Neo and Giez UAVs from MSP company were used, and to simulate the use of parachute from a board of a rotary-wing aircrafts, multi-copter Zawisak UAV from MSP was also used. The available unmanned aerial vehicles allowed to examine parachutes with suspended weighs from 5 to 15 kg and in the range of speeds from zero to 100 km/h. Each of the UAV used in flight tests was equipped with a set of acceleration sensors and autopilot using GPS space navigation signals, which allowed to record of speed and acceleration data from two independent measurement subsystems. During the flight tests, parachutes were introduced to the work by means of a pyrotechnic ejector, which simulated the opening of the parachute with a good approximation. A comparative test of parachute models manufactured from standard F-111 ripstop nylon parachute fabric and lightweight Q fabric was also made, which showed a noticeable difference in the descending velocity of canopies produced from different fabrics. Detailed analysis confirmed the obtained results, indicating better performance of the canopy made of lightweight fabric, and in particular its higher coefficient of aerodynamic drag, which allows it to descend at a slower rate, i.e. with less kinetic energy to disperse during landing, or allows it to use smaller canopies with the same descending speed, i.e. with less weight and volume of parachute system.

It was found that further investigations with the use of dynamic scalable models of parachute canopies were necessary in order to obtain more results and thus to obtain quantitative data, and not only qualitative behaviour of parachute canopies made of lightweight Q fabric. Such tests are planned to be performed in laboratory conditions with the use of an innovative method of launching parachutes from a mortar with the use of a pyrotechnic cartridge. Such a test stand is already under construction.

Keywords: parachute systems, personnel rescue parachute, lightweight ripstop nylon fabric, aviation safety, dynamic scalable models.

2. Basic References

[1] T.W. Knacke (1991). *Parachute Recovery Systems Design Guide*, Naval Weapon Center, China Lake, USA.
[2] J. Pleasants,(1974). *Parachute Mortar Design,* Journal of Aircraft, Vol. 11, No. 4, April 1974.
[3] E. Huckins (1974), *Techniques for Selection and Analysis of Parachute Deployment Systems,* NASA Technical Note D-5619.
[4] H. Johari, K. J. Desabrais (2003). *Stiffness Scaling for Solid-Cloth Parachutes*, Journal of Aircraft, Vol. 40, No. 4, July-August 2003.
[5] *Pyrotechnics and and Retro Rocket System*, Gemini Guide, geminiguide.com
[6] *Instrukcja użytkowania nr 092-06 spadochronu ratowniczego SK-94*, Wydanie IIIC,, Legionowo 2013, AIR-POL.
[7] *Instrukcja użytkowania spadochronu ratowniczego plecowego SP-6*, Legionowo, Aviotex.
[8] *Packing and Servicing Instruction for the Irvin-GQ Ltd Emergency Parachute Assembly type EB-80*, MRI IRV 844, Issue 2, Sept 2002.
[9] *Instruction Manual No. 720, Parachute Assembly GQ Security Type 350 Mk 2*, MRI GQ 1277, Issue 2, December 2000.

FATIGUE OF THE HIGH STRENGTH STEEL AND ITS WELD

T. Szymczak[1], P. Prochenka[2], K. Makowska[1] and Z.L. Kowalewski[3]
[1] Motor Transport Institute, Warsaw, Poland
[2] Military University of Technology, Warsaw, Poland
[3] Institute of Fundamental Technological Research, Warsaw, Poland

1. General

Despite of the fact that modern materials possess attractive mechanical parameters they are still requiring additional testing especially under cyclic loading in order to get better characterisation of their fatigue phenomenon. This is extremely important from exploitation point of view. Fatigue examinations are conducted by means of specimens of various shapes and dimensions. Their selection depends on technical details of a test, volume of the materials tested and dimensions of the objects in question. Usually, two control signals are applied: stress or strain. A type of control signal depends on the parameters of future exploitation or diagnostic methodology. For example, if strain are taken to assess a state of the structure, then test should be stress controlled.

An importance of the fatigue process for exploitation is still treated as the crucial point [1]. Particularly the fractography and microscopic analysis provides evidence in this matter. Thanks to data from such tests typical features of fatigue zones can be captured, and as a consequence, essential reasons of damage evolution can be indicated. It has to be emphasised that our current knowledge on fatigue features is still limited, particularly for new materials or materials introducing in new structures. Therefore, the aim of this paper focuses on examination of the S700MC steel behaviour and its weld under cyclic loading at various fatigue stages up to fracture.

2. Specimens, material, testing

All tests were conducted using 8874 Instron servohydraulic testing machine at room temperature. The geometry of specimens (Fig. 1) was designed according to the requirements of the ASTM standards: E468-90 "Standard Practice for Presentation of Constant Amplitude Fatigue Test Results for Metallic Materials". The axial strain was measured using the 2620-603 Instron extensometer on the gauge length of 10 mm, Fig. 2. Stress signals in the form of the sinusoidal function having the amplitude values from 900 to 300 MPa and frequency of 10 Hz at R = 0 were used.
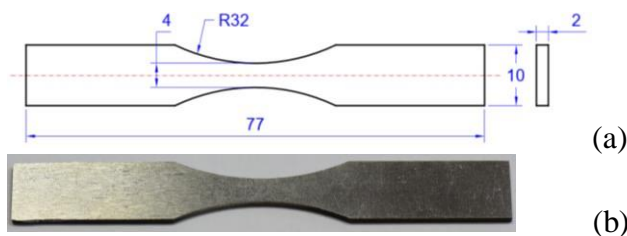
Fig. 1. The specimen dimensions (a) and shape after manufacturing (b)
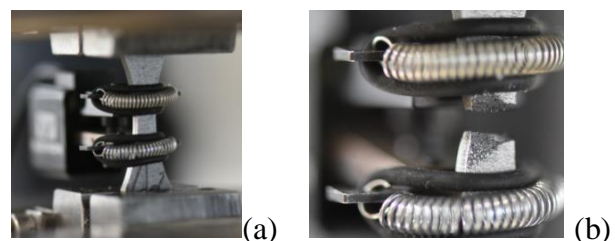
Fig. 2. The specimen with extensometer (a) and after test (b), respectively

Thin sheets of the S700MC steel were chosen for the tests. The specimens made of parent material and laser welded were selected from the perpendicular direction with respect to rolling. Mechanical parameters of the S700MC were: $E = 2.2$ GPa, $\sigma_h = 453$ MPa, $\sigma_{0.2} = 735$ MPa, $\sigma_m = 778$ MPa. In the case of the weld the proportional limit, yield point and ultimate tensile strength

had higher values, i.e.: $\sigma_h = 583$ MPa, $\sigma_{0.2} = 805$ MPa, $\sigma_m = 865$ MPa, respectively. The parent material and weld subjected to cyclic loading were analysed on the basis of variations of the axial strain versus cycle number up to fracture. The relationship between the axial stress and strain was also taken into an account. Finally, the limited fatigue life and fatigue limit of the parent and welded material were determined.

3. Results

The parent material and weld exhibited the ratcheting effect, Figs. 3a, 4a. Before the fracture variations of the mean strain at constant stress amplitude were identified, Fig. 3b. In the case of the cycles close to fracture (Figs. 3c, 4b) the parent material reached larger strain values than the weld, expressing brittle-plastic fracture Figs. 3c, 4b. An influence of the weld on fatigue durability was expressed by fatigue limit variations, particularly for lower stress amplitudes, Fig. 5.
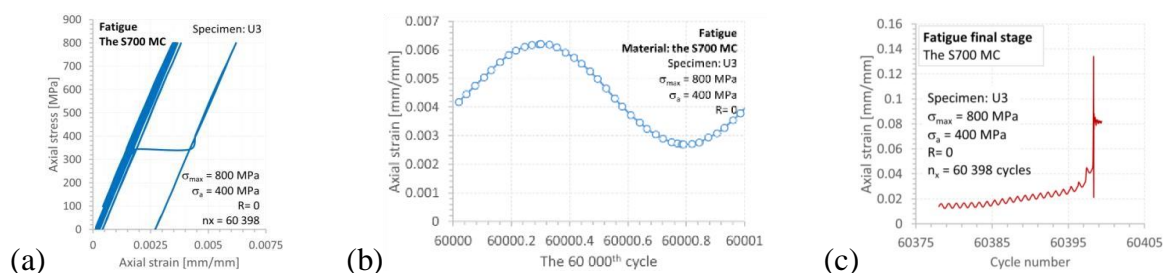
Fig. 3. Stress versus strain (a); strain at the cycles before (b) and during fracture (c)
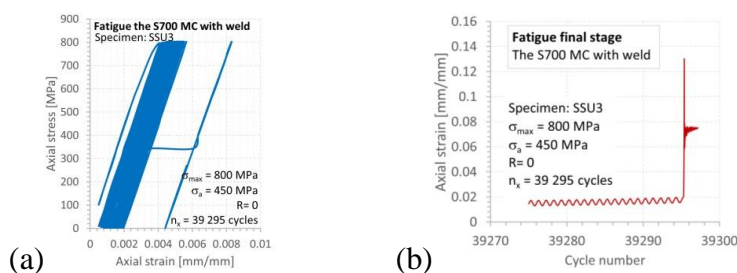
Fig. 4. Stress versus strain (a); $\sigma = f(N)$ (b)   Fig. 5. The Wöhler diagram of the S700MC and its laser weld
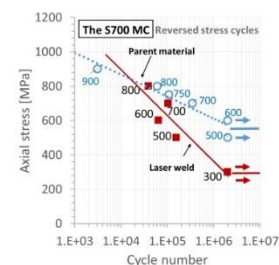
4. Summary

The S700MC steel is very sensitive on the welding processes. In comparison to the result obtained for the parent material the fatigue limit of the welded material was reduced even by a factor of 2 for the lowest stress amplitudes taken into account.

5. Acknowledgment

6. References

[1] *Fatigue and Fracture of Engineering Materials*, Willey, Editors: Y. Hong, R.W. Neu, M. Endo, 42, 9, 2019, 1845-2203.
[2] T. Szymczak, A. Brodecki, K. Makowska, Z.L. Kowalewski (2019). *Tow truck frame made of high strength steel under cyclic loading*, Materials Today Proceedings, 12, 2, 207-212.

IMPACT ENERGY ABSORBTION
OF ADDITIVELY MANUFACTURED LIGHTWEIGHT STRUCTURES

S. Szałkowski and G. Socha

Łukasiewicz Research Network – Institute of Aviation, Warsaw, Poland

1. Introduction

Lightweight energy-absorbing cellular materials are of concern to a variety of industries, including military, aerospace, automotive and shipbuilding. Additively manufactured lattices are one of the types of lightweight structure with promising capabilities comparable to honeycombs or foams [1] and [2]. The additive manufacturing (3D printing) becomes more and more popular nowadays. It allows producing a different structural elements with complicated shapes and which are not possible to manufacture with conventional methods like casting or machining.

In the article, selective laser melting (SLM) lattice structures based on simple architecture - a body-centred cubic structure with vertical struts (BCC-Z) under quasi-static and dynamic compressive loads have been analyzed. Both 3D continuum and beam finite element models have been developed to predict the compressive response of lattice structures. Simulations were performed using LS-Dyna software package.

Modelling and computer simulation of the impact requires use of appropriate yield condition, flow rule and failure criterion. Two failure criteria have been used in the case of reported investigations: simple constant equivalent strain criterion and mixed strain-stress Hancock - Mackenzie ductile failure model. This model takes account for the influence of the stress state on the failure strain. New method for calibration of Hancock-Mackenzie model has been proposed [5]. The results of FE simulation, including failure modes were compared with experimental data. Good agreement of the experiment and simulation results has been achieved.

2. Material characterization and failure criterion

In most FE analyses simple fracture criterion is used where fracture is assumed to occur in a material element when the equivalent plastic strain reaches a critical value [3]:

$$(1) \qquad \bar{\varepsilon} = \varepsilon_f^-$$

Material data for 3D printed, 316L stainless steel for the calibration of this criterion can be derived from tensile tests results.

For the 3D printed alloy used by authors in presented research failure criterion was assumed in the following form [4]:

$$(2) \qquad \bar{\varepsilon}_f = \alpha e^{-\frac{3}{2}\eta}$$

where ε_f is the failure strain, η is the triaxiality factor (ratio of first and second invariant of the stress tensor). Coefficient α was determined using procedure described in [5].

3. Model, test conditions and results

Lattice structure in the shape of cube with side length of 100 mm consisted of BCC-Z unit cells has been modeled using both beam and solid elements. Both, quasi-static compression by rigid surface and impact of 1.7 kg projectile at 45 m/s velocity have been simulated. Contact and friction between struts have been taken into account which allowed to predict densification region of the

stress-strain curve. In Fig. 1 example of impact simulation results is presented in comparison to test results. As it can be seen from this figure general agreement between simulation and test results was obtained.
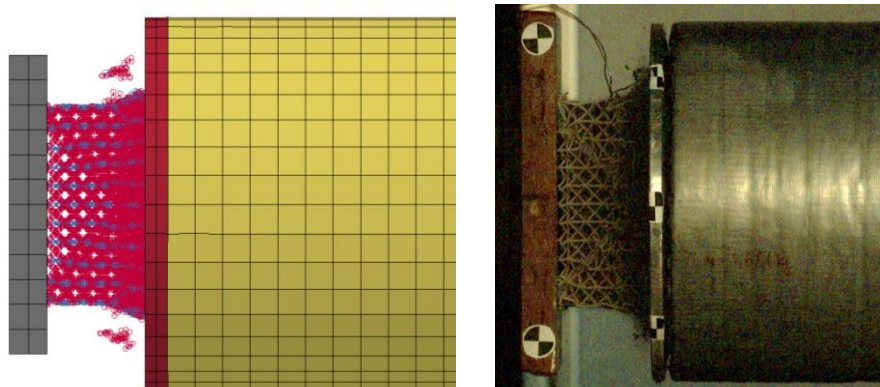
Fig. 1. Impact simulation compared to test results

4. Conclusions

Computer simulation of failure and energy absorption of 3D printed structures requires use of proper plasticity and failure models. Such models shall take into account phenomena characteristic for 3D printed materials: anisotropy of yield limit and influence of stress state on the failure strain. In this paper mixed, strain-stress failure criterion sensitive for the stress state was used with good result. General agreement between simulation and test results was obtained. For the accurate prediction of absorbed energy also anisotropy of the yield limit shall be taken into account.

5. References

[1] M. G. Rashed, Mahmud Ashraf, R. A. W. Mines, Paul J. Hazell, *Metallic Microlattice Materials: A Current State of The Art on Manufacturing,* Mechanical Properties and Applications, Materials Design, 2016.

[2] M. Smith, Z.Guan, W.J.Cantwell, *Finite element modelling of the compressive response of lattice structures manufactured using the selective laser melting*, International Journal of Mechanical Sciences, 67 (2013) 28–41.

[3] Wierzbicki T. et al., *Calibration and evaluation of seven fracture models*, International Journal of Mechanical Sciences, Vol.47, pp. 719-743, 2005

[4] Hancock J.W., Mackenzie A.C., *On the mechanisms of ductile failure in high-strength steels subjected to multi-axial stress-states,* J. Mech. Phys. Solids, Vol.24, pp.147-169, 1976

[5] Socha G., *A method and accessory for determination of failure strain for ductile materials subject to arbitrary stress state in the wide range of temperatures*, Polish Patent Office, patent pending 77P43754 PL00

EXPERIMENTAL VERIFICATION
OF A NEW CONSTITUTIVE MODEL OF COMPOSITE MATERIALS

A. Wiśniewska[1], A. Liber-Kneć[1] and H. Egner[1]
[1] Faculty of Mechanical Engineering, Cracow University of Technology, Cracow, Poland

1. Introduction

The design of composite materials involves methods for predicting their effective properties. The most known analytical models are the Voigt and Reuss approximations [1]-[2], the Hashin- Shtrikman bounds [3] and the Mori-Tanaka theory [4]. In the presented research a new methodology of effective properties determination is considered, based on the mechanical equivalence hypothesis. The analytical results are validated with the available experimental data.

2. Basic ideas

An isotropic composite is considered as an elastic-plastic two-phase material consisting of the matrix and randomly distributed inclusions. The proposed method relies on the concept of the Representative Volume Element (RVE). The true state of a material within the RVE is mapped to a material point of the effective quasi-homogeneous continuum. The hypothesis of total energy equivalence is here proposed in the following way [5]:

At any time, to an RVE in its real configuration, described by the set of state variable pairs, we associate an unchanged equivalent fictive configuration, the state of which is described by the effective state variables – in such a manner that the total internal energy defined over the two (real and fictive) configurations is the same.

3. Effective properties

According to the hypothesis of total energy equivalence the isotropic moduli $K(\xi)$, $\mu(\xi)$, can be expressed in a general form:

$$(1) \quad \begin{cases} K(\xi) = \xi \alpha^I K^I + (1-\xi)\alpha^M K^M \\ \mu(\xi) = \xi \beta^I \mu^I + (1-\xi)\beta^M \mu^M \end{cases}$$

where α^I, α^M, β^I, β^M, are concentration factors, and ξ is the volume fraction of inclusions.

Equations for concentration factors can be expressed in the following way:

$$(2) \quad \alpha^I = \frac{\xi\sqrt{K^I} + (1-\xi)\sqrt{K^M}}{\sqrt{K^I}} , \; \alpha^M = \frac{\xi\sqrt{K^I} + (1-\xi)\sqrt{K^M}}{\sqrt{K^M}} , \; \beta^I = \frac{\xi\sqrt{\mu^I} + (1-\xi)\sqrt{\mu^M}}{\sqrt{\mu^I}} , \; \beta^M = \frac{\xi\sqrt{\mu^I} + (1-\xi)\sqrt{\mu^M}}{\sqrt{\mu^M}}$$

4. Results

The effective properties obtained with the use of model where compared with experimental results for the case of polyacetal matrix (POM) containing a carbon short fibers. The length of fibers was in the range of 120-200 μm. The volume fraction of inclusion was from 5 to 30 percent. The uniaxial tensile test was performed using MTS Insight 50 testing machine with TestWorks4 software according to PN-EN ISO 527-1:2012 standard. The mechanical extensometer was attached to specimens to measure the displacement. The Poisson ratio was investigated using electroresistant tensometric method. The average values of the Young's modulus and Poisson's ratio were determined based on the conducted tests, which were then compared with analytical results (Fig. 1).

a)   b)
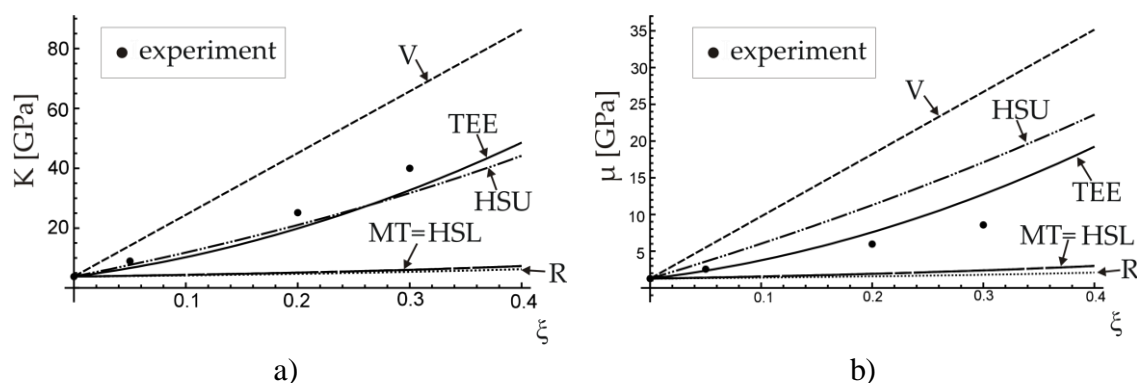
Fig. 1. Isotropic moduli a) $K(\xi)$, b) $\mu(\xi)$ distribution obtained from proposed method (TEE)
and other approaches: V – Voigt, R – Reuss, MT – Mori-Tanaka, HSU– Hashin- Shtrikman
upper bound, HSL – Hashin- Shtrikman lower bound for carbon short-fiber reinforced polyacetal

The analytical results are also validated with the experimental data available in the literature [6].
Fig. 2 shows the distribution of Young's modulus for graphene-copper composites.
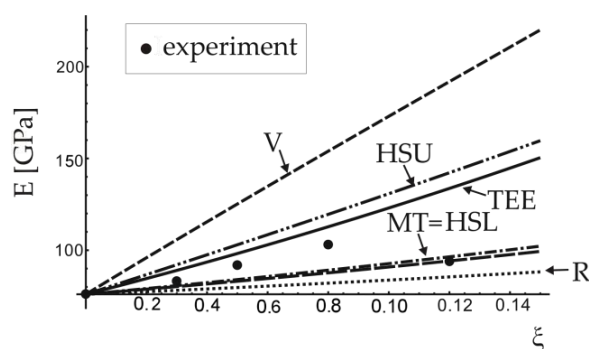
Fig. 2. Young`s modulus distribution obtained from proposed method (TEE) and other approaches:
V – Voigt, R – Reuss, MT – Mori-Tanaka, HSU– Hashin- Shtrikman upper bound,
HSL – Hashin- Shtrikman lower bound for graphene-copper composites

5. Acknowledgemets

6. References

[1] W. Voigt (1889). Über die Beziehungen zwischen den beiden Elastizitäskonstanten isotroper Körper. *Wied. Ann.*, **38**, 573–587.

[2] A. Reuss (1929) Berechnung der Fliessgrenze von Mischkristallen auf Grund der Plastizitätsbedingung für Einkristalle. *Z. Angew. Math. Mech.*, **9**, 49–58.

[3] Z. Hashin and S. Shtrikman (1962). A variational approach to the theory of the elastic behaviour of polycrystals. *J. Mech. Phys. Solid.*, **10**, 343–352.

[4] T. Mori and K. Tanaka (1973). Average stress in matrix and average elastic energy of materials with misfitting inclusions. *Acta. Metall.*, **21**, 571–574.

[5] A. Wiśniewska, S. Hernik, A. Liber-Kneć and H. Egner (2019). Effective properties of composite material based on total strain energy equivalence. *Compos. Part B: Eng.*, **166**, 213220.

[6] K. Chu, C. Jia (2014). Enhanced strength in bulk graphene–copper composites, *Phy.s Status. Solidi. A*, **211**(1), 184-190.

ELASTICITY MEASUREMENT OF SKIN BY PHASE STABILITY IMPROVED OPTICAL COHERENCE ELASTOGRAPHY

Y. Hu[1], C. Sun[1] and J. Chen[1]
[1] Department of mechanics, Tianjin university, Tianjin, China

1. Introduction

The mechanical properties of the skin are important tissue parameters for understanding the pathophysiology of the skin and for medical diagnosis and treatment, such as scleroderma and skin cancer. Most skin lesions result in changes in elasticity and thickness[1]. Currently, most qualitative diagnoses of skin diseases are based on palpation by dermatologists. In palpation, the histopathologic region can be identified by a different strain response to the applied pressure compared to the surrounding healthy tissue. This diagnosis is highly subjective among dermatologists. Phase-sensitive optical coherence elastography has been widely studied as a rapid, inexpensive and non-invasive method for the analysis and quantification of skin mechanical properties[2, 3]. It has nanoscale displacement resolution and sub-nanoscale sensitivity. The stability of laser is the key to realize the function. How to realize accurate measurement under unstable condition is the main research content of this paper.

2. Method

A schematic of the home-made mechanical-OCE (M-OCE) system is shown in Figure 1. The structure has a typical SS-OCT structure and a mechanical excitation module, but the sweep laser source is very unstable. A more economical and commonly used method was used to correct the phase noise caused by laser instability, i.e., a stationary mirror was placed on the sample arm to correct the phase[4]. Generally, the correction mirror is positioned so that the image appears near the maximum imaging depth. In this unstable system, it is not the best solution. Not only will the edge of the sample image be blurred, but also the phase wrapping will appear. The modified and unwrapped phase $\Delta\phi_{i j}$, and displacement u_z can be calculated by the following equation:

$$(1) \qquad \Delta\hat{\phi}_{i,j} = \Delta\phi_{i,j} - \left(\frac{i}{m}\right)\Delta\phi_{m,j} + \frac{i}{m}\left(2k\pi\right)$$

$$(2) \qquad u_z\left(i,j\right) = \frac{\Delta\hat{\phi}_{i,j}}{4\pi n}\lambda$$

where i and m are the depth index of the measured position and correction mirror, respectively.
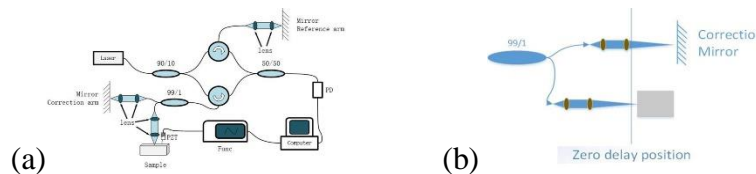
Fig. 1. (a) Structure diagram of M-OCE. (b) Structural diagram of correction arm

The velocity of the surface wave is directly related to the elastic property of the material[5]. In the current system, the direct use of peak tracking method will cause a very large error due to the phase noise. A method for calculating the wave velocity c by combining the spectrum analysis and phase

analysis is presented. In the far field, the displacement field of the surface wave can be expressed as a simple harmon ic function, and the scanning speed v of OCT can be expressed as follows:

(3) $\quad u_z(x,t)=A\cos(\omega x(1/v-1/c))$

We can realize that this is a function of observed position x, and find its main period by Fourier transform to solve the surface wave velocity c.

3. Results and discussion
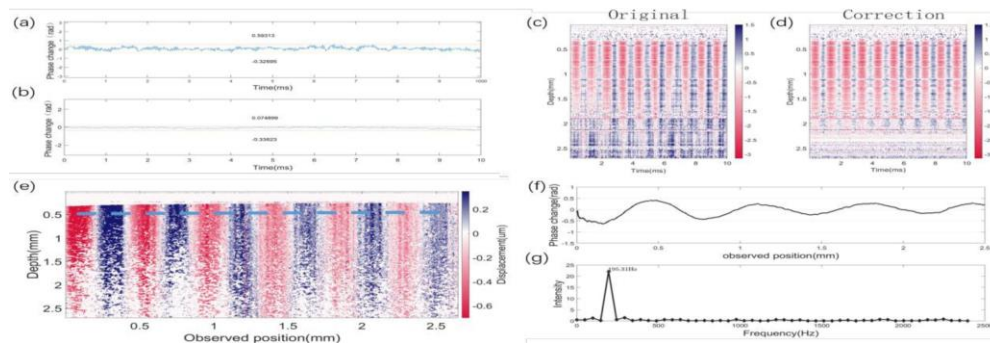
Fig. 2 (a), (b) Phase correction effect in static state; (c), (d) Phase correction renderings of motion samples; (e) Displacement field obtained during OCT scanning; (f) is a detailed drawing of the position of the blue dotted line in (e); (g) is the Fourier transform of (f)

It can be concluded from figure 2 (b), (d) that this correction scheme has a certain effect. So placing the correction arm near the zero path is optimal for three reasons: it provides a recognizable phase correction signal, effectively utilizing the imaging space, and does not affect the imaging of the sample. It can be seen from figure 2 (e) that the displacement is interfered by random phase noise, and the propagation time cannot be accurately obtained. In the frequency domain graph (g), it has a single frequency component. When the sampling rate of the system is high, the acquisition of the wave velocity is completely decoupled from the phase noise, that is, the accurate wave velocity is obtained in the system with low stability. It is proved by tensile test that the method has high accuracy.

4. Acknowledgement

5. References

[1] C. Li, G. Guan, S. Li, Z. Huang, and R. K. Wang, "Evaluating elastic properties of heterogeneous soft tissue by surface acoustic waves detected by phase-sensitive optical coherence tomography," *Journal of Biomedical Optics,* vol. 17, no. 5, p. 057002, 2012.

[2] C. Li, G. Guan, R. Reif, Z. Huang, and R. K. Wang, "Determining elastic properties of skin by measuring surface waves from an impulse mechanical stimulus using phase-sensitive optical coherence tomography," *J R Soc Interface,* vol. 9, no. 70, pp. 831-41, May 7 2012.

[3] S. Song, Z. Huang, and R. K. Wang, "Tracking mechanical wave propagation within tissue using phase-sensitive optical coherence tomography: motion artifact and its compensation," *J Biomed Opt,* vol. 18, no. 12, p. 121505, Dec 2013.

[4] B. Vakoc, S. Yun, J. de Boer, G. Tearney, and B. Bouma, "Phase-resolved optical frequency domain imaging," *Opt Express,* vol. 13, no. 14, pp. 5483-93, Jul 11 2005.

[5] C. Glorieux, W. Gao, S. E. Kruger, K. V. D. Rostyne, W. Lauriks, and J. J. J. o. A. P. Thoen, "Surface acoustic wave depth profiling of elastically inhomogeneous materials," vol. 88, no. 7, pp. 4394-4400, 2000.

EXPERIMENTALLY MOTIVATED FATIGUE DAMAGE MODEL FOR P91 STEEL

W. Egner[1], P. Sulich[1], S. Mroziński[2] and H. Egner[1]
[1] Institute of Applied Mechanics, Faculty of Mechanics,
Cracow University of Technology, Cracow, Poland
[2] Faculty of Mechanical Engineering, UTP University of Science and Technology,
Bydgoszcz, Poland

1. Introduction

In the presented research the analysis of fatigue damage behavior of P91 steel is considered. First the experimental stress and strain controlled tests are performed. Then, based on the observed material behavior a dissipation-based constitutive model of fatigue damage is developed within the framework of thermodynamics of irreversible processes with internal state variables. Next the material parameters are identified, and the model is validated on the basis of the available experimental data.

2. Influence of test conditions

The selected test conditions should depend on the intended use of the obtained material data. Nevertheless, low-cycle fatigue tests are carried out mainly at constant strain amplitude (due to the lack of material flow observed during tests at constant stress amplitude). This may result in erroneous fatigue life predictions if testing conditions do not correspond to the operation mode of the considered mechanical facilities [1]. This problem seems to be particularly important for the P91 grade steel, since it exhibits continuous cyclic softening without the period of cyclic properties stabilization, which makes it difficult to design experimental tests for various types of control so that their results are comparable.

To investigate the influence of test conditions, the results of both stress and strain controlled tests were compared in terms of the Ramberg-Osgood type fatigue relation coefficients. The results revealed the noticeable difference between both cases, while the increasing test temperature enhanced the mismatch (cf [2], see Fig. 1a). What is interesting, there is no effect of test conditions on the dissipated energy (see Fig. 1b). This observation may impose the approach for fatigue damage modelling. Although the differences visible in Fig. 1 are not large, but accumulated in thousands of cycles can lead to significant errors in lifetime predictions. For this reason the dissipation-based fatigue damage modelling [3] is proposed instead of the classical ductile damage approach [4].

3. Results

Both damage models mentioned above were implemented numerically, and model parameters were identified for strain and stress controlled tests independently. For both damage models a very good agreement was obtained between numerical simulations and experimental tests (see Fig. 2). In general, the advantage of the entropy-based approach is that the simulated curves are smooth, and there is less model parameters to be identified. However, the real advantage of the dissipation-based approach is revealed when the parameter values are analyzed. For the dissipation based approach the set of optimal values is almost the same for both controlling schemes, while for the ductile damage description a significant differences take place (up to 39%). These results validate the benefits of using the dissipation-based approaches in the analysis of the low-cycle fatigue process, in particular for the materials that do not exhibit stabilization.
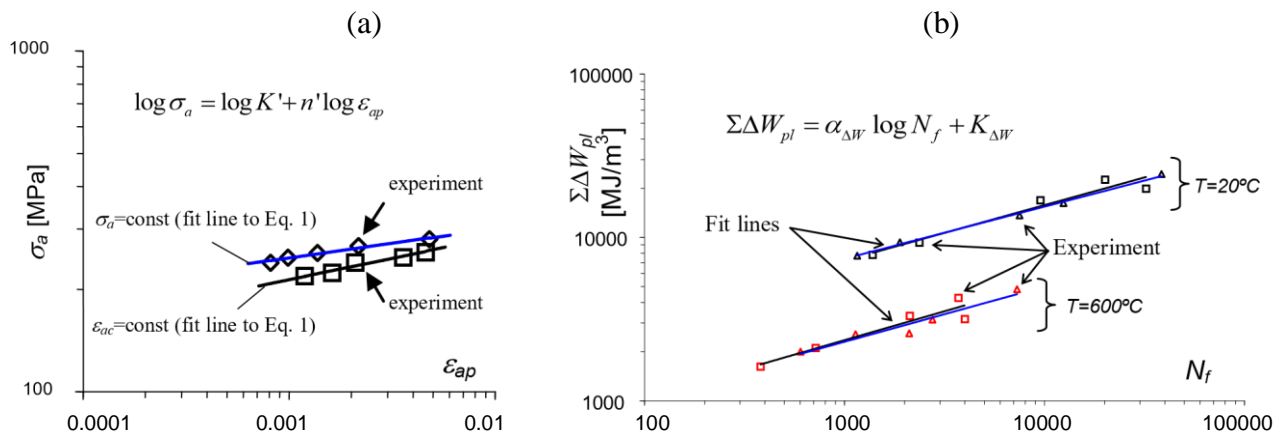
Fig. 1. Comparison of stress- and strain-controlled experimental results:
(a) Ramberg-Osgood approximation; (b) Dissipated energy
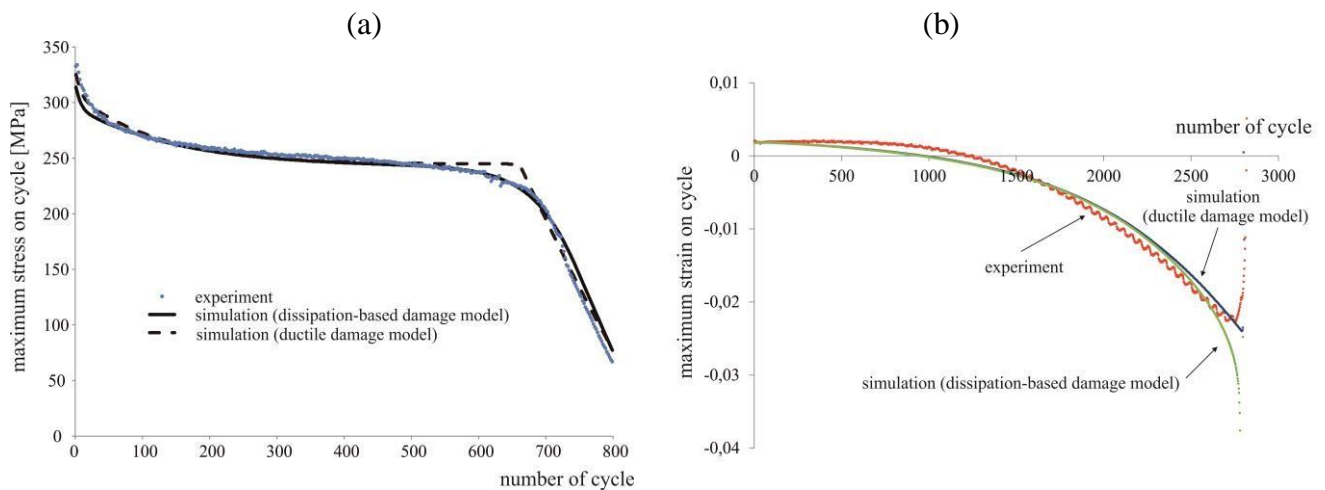
Fig. 2. Comparison of experimental and numerical results for:
(a) strain-controlled test (T=600°C, ε_{ac}=0.5%); (b) stress-controlled test (T=600°C, σ_a=257 MPa)

4. Acknowledgements

5. References

[1] D. Wu, P. Zhao, Q. Wang, F. Xuan (2015). Cyclic behavior of 9–12% Cr steel under different control modes in low cycle regime: A comparative study, *Int. J. Fatigue*, **70**, 114-122.
[2] S. Mroziński, H. Egner, M. Piotrowski (2019). Effects of fatigue testing on low-cycle properties of P91 steel, *Int. J. Fatigue,* **120**, 65-72.
[3] C. Basaran and S. Nie (2004). An Irreversible Thermodynamics Theory for Damage Mechanics of Solids, *Int. J. Damage Mech.*, **13**, 205-223.
[4] J. Lemaitre (1992). A course on damage mechanics, Springer, Berlin 2nd Edition (1996).

COMPARISON OF MEASUREMENTS AND PREDICTIONS FOR A THERMALLY-INDUCED DEFORMATION OF A STAINLESS-STEEL TUBE

S.N. Eseigbe[1], M. Bankhead[2], R.J. Taylor[2] and E.A. Patterson[1]
[1] School of Engineering, University of Liverpool, Liverpool, United Kingdom
[2] School of Mechanical, Aerospace, and Civil Engineering, The University of Manchester, Manchester, United Kingdom [2]National Nuclear Laboratory, Birchwood, United Kingdom

1. Abstract

A temperature-displacement analysis of a cladding was performed using digital image correlation (DIC) technique to acquire full-field displacement data. The data-rich displacement fields were decomposed using orthogonal image decomposition into information-preserved data set of reduced dimensionality that facilitates a quantitative comparison between the experiment and the model. The model was validated by experimental results, and the results show a good correlation.

Keywords: digital image correlation, multi-physics, image decomposition, finite element, fuel cladding, validation

2. Introduction

Many engineering systems involve some level of complexity and multiple physics domains such as hypersonic vehicles and nuclear energy systems. The cladding in fission nuclear reactors is an example of a nuclear energy component that deforms due to multiple physics phenomena, e.g. heat transfer, fluid flow, irradiation, and structural loading. The cladding can be described as thinwall tube housing the annular ceramic fuel pellets. Due to a relatively high temperature (650^OC) and overpressure of the CO_2 coolant in the core, the cladding creeps until initial contact with the pellet occurs resulting in pellet-cladding interactions (PCI) [1]. During a power ramp, PCI induces large stresses in the cladding, which can lead to failure. Therefore, the analysis of stresses and strains due to combined temperature and mechanical load is vital for assessing its structural integrity. Computational models are often used to evaluate the structural integrity of complex systems. It is, therefore, important to demonstrate the reliability of such models through a validation exercise [2].

The work reported here is for the temperature-induced displacement component of a planned thermo-mechanical experiment and validation assessment, and is part of a progression towards achieving a multi-physics validation exercise for the validation of a similar computational model.

3. Methodology

An idealised fuel cladding made of 316l stainless steel tube (modulus of elasticity = 193 MPa) was employed as the specimen. The diameter, length, and thickness of the tube are 25.4 mm, 310 mm, and 1.65 mm respectively. The tube was subjected to a thermal load from ambient temperature to 200ºC, using an infrared heating element, and was simply-supported in a horizontal position by specially designed end caps to allow thermal expansion. Surface displacement fields were acquired using a commercially-available DIC system. A reference image of the undeformed specimen was captured at room temperature and at increments of 25°C up to a temperature of 200°C.

Similarly, the numerical analysis was performed using a commercially-available finite element (FE) software package (ABAQUS). The tube was modelled in three-dimensions and comprised of

approximately 6500, hexahedral elements for a temperature-displacement analysis. The reference temperature was set at 23°C and ramped to a final temperature of 200°C in increments of 25°C.

4. Results and Discussion

The displacement fields obtained from the experiment and the model were treated as images and were decomposed using orthogonal image decomposition by fitting Chebyshev polynomials to the data fields, to obtain shape descriptors that facilitate a quantitative comparison. The predicted and measured shape descriptors are plotted, as indicated in Figure 1.
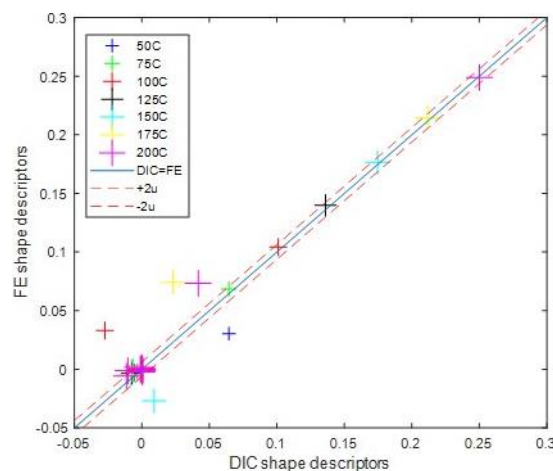
Fig. 1. Comparison of shape descriptors representing the measured
and predicted axial displacement fields at different thermal loads.
The dashed lines represent the extended minimum measurement uncertainty

The allowable scatter in the plot was defined as the minimum measurement uncertainty, which was obtained following a procedure detailed in the CEN guideline [3]. The shape descriptors representing the predicted and measured axial displacement fields exhibited a high degree of linearity. The model can be said to be a good representation of the experiment because most of the shape descriptors fall within the uncertainty bounds.

5. Conclusions

A temperature-displacement analysis of a planned thermo-mechanical experiment was successfully performed as a progression towards achieving a multi-physics validation exercise. Comparison of the axial displacement between the measured and prediction show good agreement as most of the shape descriptors fall within the uncertainty bounds.

6. References

[1] P. Van Uffelen, J. Hales, W. Li, G. Rossiter, and R. Williamson, "A review of fuel performance modelling," *J. Nucl. Mater.*, vol. 516, pp. 373–412, Apr. 2019.
[2] E. A. Patterson, M. . Feligiotti, and E. . Hack, "On the integration of validation, quality assurance and non-destructive evaluation," *J. Strain Anal. Eng. Des.*, vol. 48, no. 1, pp. 48– 58, 2013.
[3] CEN, "Validation of Solid Mechanics Models. CEN Workshop Agreement," vol. CWA 16799, 2014.

DEVELOPMENT OF ONE-SHOT SHADOW MOIRÉ SYSTEM FOR SURFACE PROFILE MEASUREMENT

T.Y.-F. Chen, C.-C. Lee and F.-Y. Cheng
Department of Mechanical Engineering, Nation Cheng Kung University, Tainan, Taiwan

1. Introduction

Shadow moiré method is an effective optical technique for surface profile measurement of diffusely reflecting objects. For accurate measurement, phase-shifting technique is usually adopted. However, the specimen or system may be moved during the time of image capture, and not suitable for dynamic measurement. In order to overcome this drawback for dynamic measurement, a shadow moiré system consisted of two light source of different color, and a color CCD camera is developed. The phase shift is introduced by using two light sources illuminate the grating from different position, and the two moiré fringe patterns captured by the color camera simultaneously are processed by an automated fringe analysis scheme using spiral phase transform (SPT), optical flow and digital filtering techniques. The proposed one-shot system was applied to simulated surface profile and real specimen. The principles and test results are presented. The intensity distribution of the two color images and the influence of incident angle of light source on the range of measurement were investigated.

2. Principles

The schematic of experimental set-up for shadow moiré with two light sources is shown in Fig. 1. The intensity of moiré fringe pattern, I, can be described by

(1) $\qquad I(x,y)=a(x,y)+b(x,y)\cos[\Theta(x,y)]$

where (x,y) is the position, a(x,y) is the background intensity, b(x,y) is the amplitude, and θ(x,y) is the phase of moiré fringe. After removing the DC term, SPT operator can be applied to obtained cosine signals and their quadrature signals given as [1]

(2) $\qquad b(x,y)\sin[\Theta(x,y)]=-i\exp(-i\beta)SPT\{\bar{I}(x,y)\}$

The parameter, β, in Eq. 2 can be obtained by calculating the fringe orientation angle using optical flow approach [2]. The wrapped phase can be determined from

(3) $\qquad \Theta(x,y)=\arctan\{[-i\exp(-i\beta)SPT\{\bar{I}(x,y)\}]/\bar{I}(x,y)\}$

After unwrapping, the height of surface can be calculated. The flow chart of the fringe phase analysis is given in Fig. 2.
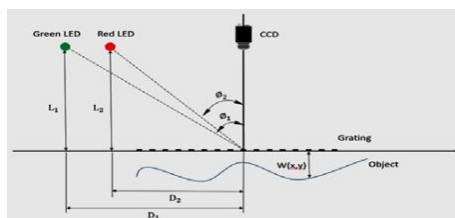
Fig. 1. Schematic of one-shot shadow moiré system
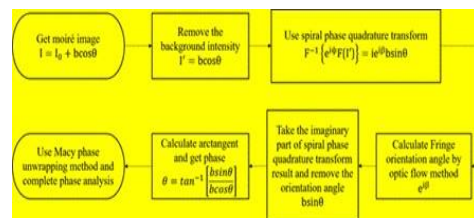
Fig. 2. Fringe phase analysis flow chart

3. Experimental Results and Conclusion

Since the grey level range is different between the two images, a first-order linear image stretching was applied to the images. The influence of incident angle of light source on the range of measurement is plotted in Fig. 3. Figure 4 shows the result of a convex circular disk. Comparison to the result obtained by using four-step phase shifting method, a RMS error of 8 μm can be achieved for a height of 370 μm.
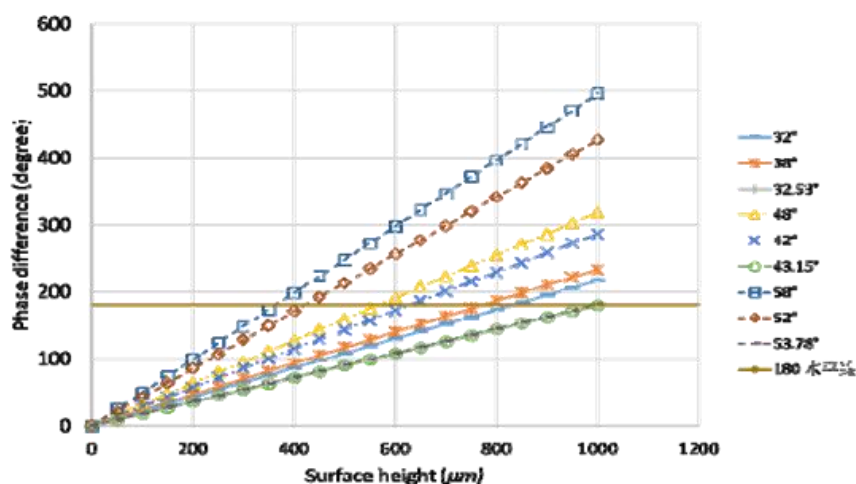
Fig. 3. The influence of incident angle of light source on the surface hight measurement

| (a) | (b) | (c) | (d) |
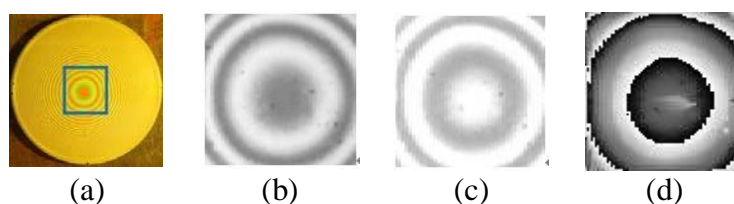
Fig. 4. (a) convex plate specimen, (b) green fringe pattern,
(c) red fringe pattern, and (d) wrapped phase

4. Acknowledgement

5. References

[1] Du, H., H. Zhao, and B. Li., Proc. of SPIE, 8681, (2013) 86812A-6.
[2] Vargas, J., Quiroga, J. Antonio., Sorzano, C. O. S., Estrada, J. C. Carazo, J. M., Optics Letters, (2011) 36(17): 3485-3487.

STRUCTURAL AND MICROMECHANICAL PROPERTIES OF LASER MARKING STAINLESS STEEL (AISI 304)

P. Dywel[1,2] and L. Skowronski[1]

[1] *Institute of Mathematics and Physics, UTP University of Science and Technology, Kaliskiego 7, 85-796 Bydgoszcz, Poland*
[2] *Faculty of Mechanical Engineering, UTP University of Science and Technology, Kaliskiego 7, 85-796 Bydgoszcz, Poland*

1. Introduction

Nowadays, laser surface treatment techniques such as laser marking and graving are widely used to improve various of functional properties of many different kinds of materials. It is achieved by means of short pulsed laser beams interaction with the material surface and resulting with rapid phase and microstructure modification, mainly due to fast heating, melting and solidification. The laser marking process can also affect directly on optical properties of irradiated material, therefore there have been a number of longitude studies describing the influence of laser marking strategies on the optical properties such as obtained colour and its sensitivity [1].

Among others, various grade stainless steel such as AISI 304 and AISI 316 are frequently influenced by the laser treatment aimed at improving robust level of protection against corrosion as well as improving its hardness and wear. It derives directly from the ubiquity of stainless steel application and outstanding mechanical properties.

2. Experimental

The purpose of the present investigation is to roughly examine microstructure and micromechanical properties of commonly used stainless steel i.e. AISI 304 through Nd:Yag (1064 nm) after pulsed laser surface modification. The samples were laser-proceeded varying processparameters: scanning speed in the range 20 – 80 mm/s and pulse repetition rate from 20 to 1000 kHz. The paper covers in detail how process parameters affects on different morphologies formation, the surface topography and micromechanical properties such as microhardness and local elastics modulus. Moreover, the study offers some important insights into relation between laser process parameters and the sample colour obtained.

In this study the continuous stiffness measurement (CSM) technique was applied for microhardness and nanohardness identification [2]. This instrumental indentation measuring hardness and elastic modulus technique is adopted especially for characterization of mechanical behaviour of materials at small scale. Microhardness (HIT) and local young modulus (EIT) was calculated using Oliver-Pharr approach based on indentation load and contact stiffness ratio [3]. The surface topography including the roughness parameters determination was examined by means of confocal laser microscopy. The XRD analysis was performed for crystal structure identification. Additionally, for more detailed chemical phase identification of laser-irradiated specimens Raman spectroscopic characterization has been carried out in the range 50-1600 cm^{-1}.

3. Results

The surface topography of laser proceeded stainless steel treated under various process parameters are presented in Figure 1. The clear single overlapping traces can be reported for most of presented images. The roughness parameters calculated for irradiated samples are in range from 0.14 µm to

7.26 µm for R_a and R_q, respectively. The XRD spectra for laser-treated steel revealed the presence of austenitic phases (FCC) for each considered sample. Alongside the austenitic specimens one can observe the α'–Fe peaks. Phase identification spectra also gives the evidence of Fe_2O_3/Cr_2O_3 presence. With instrumented nanoindentation testing, the highest level of microhardness HIT = 2501 MPa was observed for sample treated with scanning speed v = 80 mm/s and pulse frequency f =10 kHz. It can be seen that surface microhardness of laser proceeded regions is significantly improved compared to the untreated one HIT_{304} = 2263 MPa. In general the increase in surface microhardness compared to untreated steel was observed for samples modified with highest considered scanning speed i.e. v = 80 mm/s and the lowest pulse repetition rate f =10 kHz. Moreover, for the same process parameters the value of local elastic modulus EIT was fixed at 164 GPa, similar to untreated one.
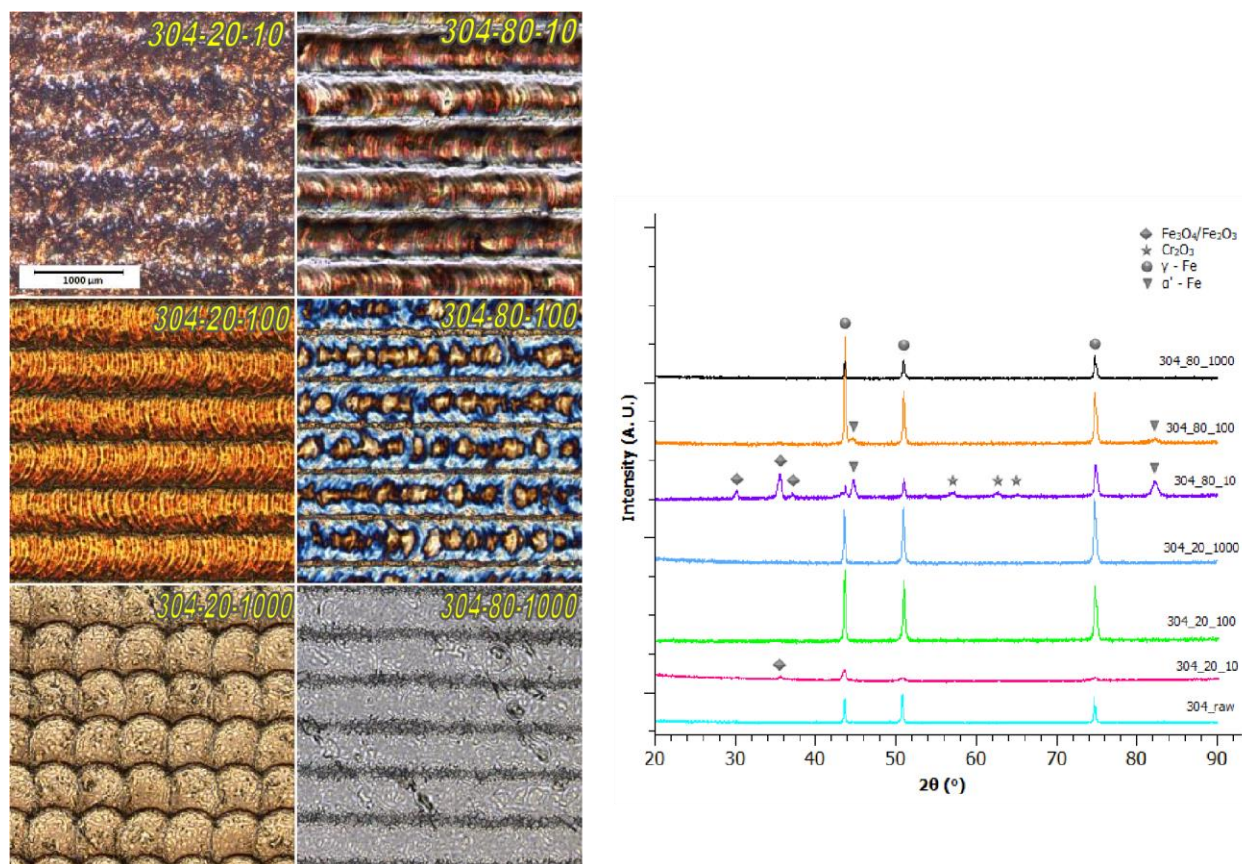
Fig. 1. Left: The 304 SS COM images of surfaces treated with different process parameters
(sample id. - scanning speed (mm/s) - pulse repetition rate (kHz)),
Right: XRD patterns of 304 SS

4. References

[1] A. J. Antonczak et al. (2013). Laser-induced colour marking- Sensitivity scaling for a stainless steel, *Appl. Surf. Sci.*, **264**, 229-236.

[2] X. Li, B. Bhushan. (2002). A review of nanointendation continuous stiffness measurement technique and its applications, *Mater. Charact.*, **48**, 11-36.

[3] W. C. Oliver, G. M. Pharr. (2004). Measurment of hardness and elastic modulus by instrumented intendation: Advances in understanding and refinements to methodology, *J. Mater. Res.*, **19**, 3-20.

IDENTIFICATION OF THE YIELD SURFACE OF THE Al/Cu BIMETALLIC SHEET

R. Uścinowicz
Bialystok University of Technology, Bialystok, Poland

1. Introduction

Modern materials like metal composites consisting of aluminium and copper layers are important in the sector of power energy, electricity and consumer electronics. The advantages of these composites are good thermal and electrical conductivity, reduced total weight, elimination the galvanic corrosion.

It is necessary to adopt an appropriate yield criterion for the proper design of mechanical structures using materials with variable of physical properties in cross section and in complex stress state. The application of correct criterion needs experiments checking material properties in the range of small elasto-plastic deformations. This is particularly difficult with respect to the bimetal in the form of sheet metal.

2. Material & experimental procedure

The experimental tests were carried out on a Al/Cu bimetallic sheet with fraction content of components: Al(48.4%), Cu(51.6%). Permanent connection of layers was obtained by cold rolling. The Szczepinski's [1] method used in this study allows determining the contour of yield surface of the material in the sheet form by using simple tensile tests. Testing procedure of experimental study consisted of cutting large size flat specimens in the rolling direction. They were stretched on the testing machine, what permitted to obtain permanent deformation $\varepsilon = 0.75\%$. The flat mini specimens for tests were cut from large specimens in seven directions at an angle $\alpha = 0°$, 15°,..., 60°, 75°, 90° to the maximum pre-strain direction. Mini specimens were extended with a monotonic strain rate.

3. Analysis of experimental data

Assuming that an initial model of material is the isotropic and homogeneous body, yield criterion in plane stress state can be represented as the rotary ellipsoid in three rectangular coordinate system σ_x-σ_y-τ_{xy}, where B_x-B_y and A_x-A_y were axes of ellipsoid. The exemplary mathematical model of ellipsoid can be presented by Huber-von Mises-Hencky (H-M-H) (Fig. 1a) and equation can be written in the form:

$$(1) \qquad \sigma_p^2 = \sigma_x^2 - \sigma_x \sigma_y + \sigma_y^2 + 3\tau_{xy}^2$$

where σ_x-σ_y-τ_{xy} - components of stress tensor, σ_p - yield stress.
When the cross-cut of an ellipsoid by perpendicular plane $\sigma_p = \sigma_x + \sigma_y$ will be made then the contour in the form of the ellipse A-D-G will remain on the ellipsoid. Substituting the above equation of the plane to equation (1) we obtain the formula which is a mathematical representation of the ellipse:

$$(2) \qquad \sigma_x \sigma_y = \tau_{xy}^2$$

Points A, B,…,F, G lying on ellipse A-D-G correspond to values of the proof stress obtained from monotonic tensile test of mini specimens in directions 0°, 15°,..., 90° relative to the direction of primary plastic pre-strain. Stress values σ_x, σ_y, τ_{xy} were determined from the following formulas:

$$(3) \qquad \sigma_x = 0.5 R_{p_{\varepsilon_i}}\left(1+\cos 2\alpha\right), \; \sigma_y = 0.5 R_{p_{\varepsilon_i}}\left(1-\cos 2\alpha\right), \; \tau_{xy} = 0.5 R_{p_{\varepsilon_i}} \sin 2\alpha$$

where $R_{p_{\varepsilon_i}}$ - a set of proof stress for the permanent deformation $\varepsilon_i=\varepsilon_H, 0.05\%...,0.3\%$; ε_H - proportionality limit.
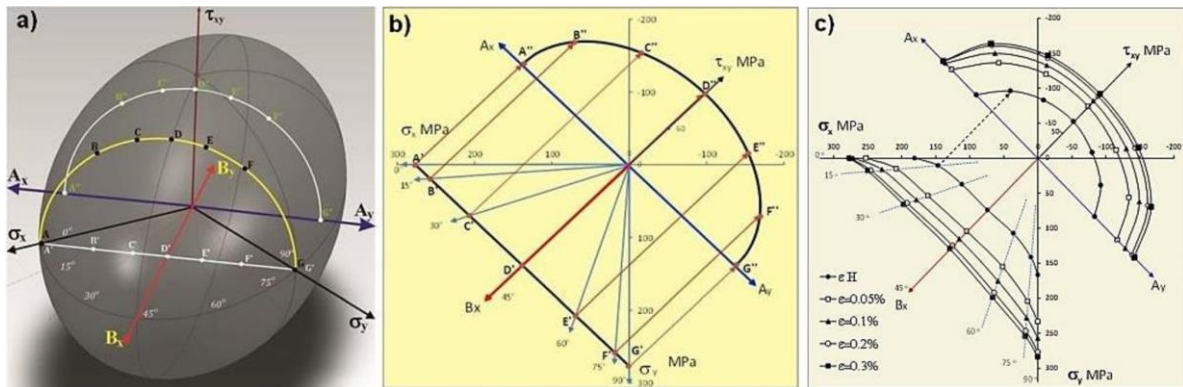
Fig. 1. Scheme of determination of yield surface: a) ellipsoid of H-M-H's yield criterion, b) lines representing sectors of H-M-H's yield surface, c) lines of yield surfaces for Al-Cu bimetal

Fig. 1b illustrated the course of two types of characteristic lines which position were analysed. The first type of lines is presented in the lower left corner of the Fig. 1b and the second one in the shape similar to a half ellipse in the upper right corner These lines correspond to the yield surface and refer to permanent deformation. The first type of lines is the orthogonal projection of the interpolated lines on the plane σ_x-σ_y and the second type of lines is the revolved section of the rectangular projection of the curve consisting of seven points A, B,…,F, G on the plane formed by axis τ_{xy} and small axis A_x-A_y.

4. Yield surface of tested Al/Cu bimetal

The method presented above gave a possibility to plot and identify evolution of lines representing the yield surfaces of tested Al/Cu bimetal sheet (Fig.1c). It was observed that plotted surfaces are asymmetrical in relation to axis τ_{xy}. The largest asymmetry of the shape was observed for the yield surface corresponding to the proportional limit strain and the difference of values was 7 MPa for extreme directions 0° and 90°. These differences were reduced with increasing permanent strains ε_i and at the level of $\varepsilon=0.3\%$ the difference was 3.1 MPa. The stress increment was the smallest with increasing the strains ε_i from 0.2% to 0.3%, which was the result of the bimetal hardening process. The analysis of evolving shapes of the yield surface suggested that the hardening process had an isotropic nature.

The yield surfaces of Al/Cu bimetal demonstrated isotropic hardening. Yield surfaces corresponding to the proof strength for $\varepsilon=0.2\%$, obtained from tests for Al/Cu bimetal were different from the surface calculated on the basis the Huber-von Mises-Hencky criterion.

5. References

[1] W. Szczepiński. (1984). Metody doświadczalne mechaniki ciała stałego. T10. PWN. Warszawa.

6. Acknowledgements

HIGH STRAIN RATE DUCTILITY OF THE SELECTED METALS FOR SHAPED CHARGE LINERS

J. Janiszewski[1], J. Sienkiewicz[1], W. Burian[2], A. Kowalski[2], A. Żak[3] and P. Prochenka[1]
[1] Military University of Technology, Warsaw, Poland
[2] Łukasiewicz Research Network – Institute of Non-Ferrous Metals, Gliwice, Poland
[3] Łukasiewicz Research Network –Institute for Ferrous Metallurgy, Gliwice, Poland

1. Introduction

The penetration capability of a shaped charged jet depends mainly on density of a shaped charge liner (SCL) material ρ_j and the maximum length of the jet L. The theoretical possible penetration depth P can be estimated by applying the following equation:

$$(1) \qquad P = L\sqrt{\frac{\rho_j}{\rho_t}}$$

where by ρ_t denotes the target material density [1].

The maximum length of the jet is determined by two factors: jet velocity gradient, i.e. the velocity difference between jet tip v_{jmax} and cut-off velocity v_{jmin}, and jet fragmentation time t_f. In turn, both v_{jmax} and t_f are limited by other parameters. The maximum jet tip velocity v_{jmax} is limited by the bulksound velocity of the SCL material, whereas jet fragmentation time t_f depends directly on the ductility of the SCL material. In the literature of the field [1, 2, 3], it is emphasized the liner material ductility is critical for achieving high penetration capability of the jet. Therefore, the main problem of liner manufacturing technology, besides the achievement of required liner geometry, is to obtain the desired mechanical properties of the final SCL material such as high ductility under high strain loading.

There are several experimental techniques for high strain rate ductility testing of engineering materials. The tensile split Hopkinson pressure bar technique is often applied to this purpose, however, it seems an expanding ring experiment is an excellent tool for examining the ductility behaviour of metals.

2. Experimental procedure

The experimental investigation presented in the work was performed with the use of the electromagnetic expanding ring technique. A detailed description of the device applied in the present studies for an electromagnetic launch of the ring specimen is presented in [4, 5]. The experimental observations on selected SCL metals with various physical-mechanical properties, i.e. the OFE copper manufactured by continuous extrusion forming (ConForm method), aluminum alloy AW 2017A, Armco iron are reported. The cross-sectional area of the ring specimens for all tested materials was the same and equal to 1mm x 1 mm, however, the mean diameter of rings differed slightly and was as follows: for OFE copper and Al 2017A – 32.2 mm, and for Armco iron – 33.2 mm. Ductility of studied materials was expressed by uniform strain ε_u and strain at fracture ε_f. The parameter of ε_u was estimated by measuring changes in cross-sectional areas in the uniform strain portions of the recovered ring fragments, whereas ε_f was calculated on the basis of direct measurement of lengths of the recovered fragments captured into the soft medium (wax ring) [5]. By using the Phantom v1612 digital high-speed camera and specialized TEMA Automotive software rings expansion velocities were determined with satisfactory accuracy.

3. Results and discussion

All high strain rate experiments were carried out under similar loading conditions, i.e. maximum expansion velocities involved a range from 141 m/s to 165 m/s, which corresponds to an average strain rate of the order of 7×10^3 s^1. The highest maximum expansion velocities were reached for the rings made of OFE copper, whereas, the rings manufactured from Armco iron were expanded at the lowest velocities. Ductility behavior at applied dynamic loading for all tested metals is illustrated in Tab. 1.

Ring materials	Strain at fracture ε_f (high strain rate) [-]	Uniform strain ε_u (high strain rate) [-]	Uniform strain ε_u (quasi-static) [-]
OFE copper	0.49	0.41	0.31
Al 2017A	0.17	0.19	0.21
Armco iron	0.25	0.24	0.24

Table 1. Ductility parameters for tested SCL materials determined under quasi-static and high strain rate testing conditions

The parameters collected in Tab. 1 allow to conclude that the ductility of copper specimens is the highest and increases under electromagnetic ring expansion experiments in relation to the static one. In turn, the ductility of aluminum alloy Al 2017A is the lowest from all tested SCL metals and surprisingly drops slightly under applied dynamic loading conditions. Interesting that the dynamic ductility of Armco iron is almost at the same level of ductility obtained from a quasi-static tensile test.

4. Conclusion

In accordance with the data presented in the literature [1–3], the obtained results show that the OFE copper with the highest ductility under electromagnetic expanding ring experiment should meet requirements for SCL materials. Thus, it can be assumed that the application of the tested OFE copper as the liner material should ensure the high penetration capability of a shaped charge jet. Moreover, the obtained results for Armco iron reveal its good ductility properties under dynamic loading and thus a possibility of applying the tested Armco iron in the manufacturing of shaped charge liners.

5. References

[1] W.P.Walters, J.A. Zukas (1991). *Fundamentals of shaped charg*es, John Wiley and Sons, New York – Chichester – Brisbane – Toronto – Singapore.
[2] A. Lichtenberger (1995). *Ductile behavior of some materials in the shaped charge jet*, [in:] Metallurgical and Materials Applications of Shock-Wave and High-Strain-Rate Phenomena, L.E. Murr, K.P. Staudhammer, M.A. Meyers [Eds.], Elsevier Science B.V.
[3] A. Lichtenberger (1989). *Some criteria for choice of shaped charge copper liners*, 11th International Symposium on Ballistics, Brussels, Belgium.
[4] J. Janiszewski, W. Pichola (20090. *Development of electromagnetic ring expansion apparatus for high-strain-rate test*. Solid State Phenom., 645–650.
[5] J. Janiszewski J (2012). *Ductility of selected metals under electromagnetic ring test loading conditions*, International Journal of Solids and Structures, 49, 1001–1008.

MECHANICAL AND INTERFACIAL PROPERTIES TESTING OF PHYSICAL VAPOR DEPOSITED METALLIC FILMS AFTER RAPID THERMAL ANNEALING

T.H. Yang and K.-S. Chen

Department of Mechanical Engineering, National Cheng-Kung University, Tainan, Taiwan, 70101

1. Introduction

Metallic films deposited by physical vapor deposition (PVD) are widely used in semiconductor devices during post-processing for interconnection [1]. Their microstructures and defects are prone to the deposition and the subsequent thermal processing. Consequently, the associated electrical and mechanical properties such as residual stress and interfacial toughness would possibly be changed and the device reliability is also affected [2]. In this paper, the influences of thermal processing condition to the above-mentioned mechanical properties are investigated with different rapid thermal annealing (RTA) conditions for evaluating the properties variations and failure mechanisms to provide information of mechanism-based assessment of semiconductor device reliability.

2. Experimental Plan

The experimental plan, schematically shown in Figure 1. Aluminum films deposited evaporation (ULVAC EBX-6D) with deposition rates from 4-8 (Å/s) and the achieved final thickness between 500 and 700 nm. Meanwhile, copper films are realized by using sputtering (Ion Tech Microvac 450CB) with rates of 0.4 to 0.8(Å/s) and thickness of 300-500 nm. After deposition, the films are then treated with additional RTA using different temperatures and durations based on the experimental plan. Subsequently, various structure and mechanical characterizations are then followed by using scanning electron microscopy for topology, nano-indentation/scratch for fracture and adhesion toughness, curvature measurement for residual strength, and X-ray diffraction (XRD) for evaluating microstructure evaluation.
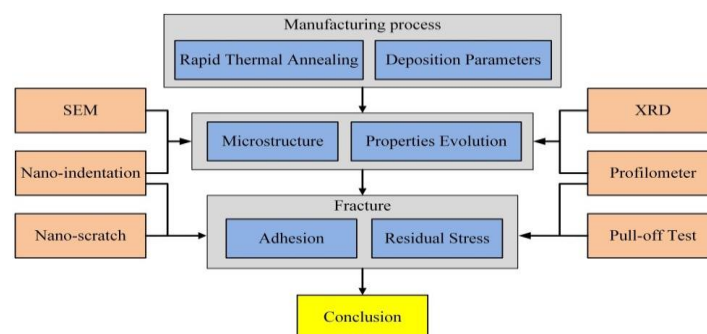
Fig. 1. Overall plan characterization flow

3. Experimental Results

The residual stresses of Al films after RTA are shown in Figure 2. When RTA temperature increases, residual stresses of metallic films also increased. It may be attributed to the effect of grain growth and coalescence, as well as defect elimination in microstructure. After RTA with temperatures over 400°C, the residual stresses decrease possibly due to stress relaxation of films and substrates.

Meanwhile, as shown in Figure 3, the modulus and hardness of aluminum films obtained by nono-indentation [3] reveals that a higher RTA temperature effectively reduces both of them. Finally, the interfacial strength of those films are then evaluated by both indentation and scratch. Figure 4 shows typical scratch results of aluminum films after different RTA. It can be seen that the films exhibit plastic deformations at the condition without RTA or RTA temperature below 300ºC. As RTA temperatures exceed 300ºC, the toughness gradually deceases and more cracks are founded. Same testing procedures are performed on copper films and the results are similar. The results will be useful for evaluating the influence of thermal processing on the reliability of interconnection structures.
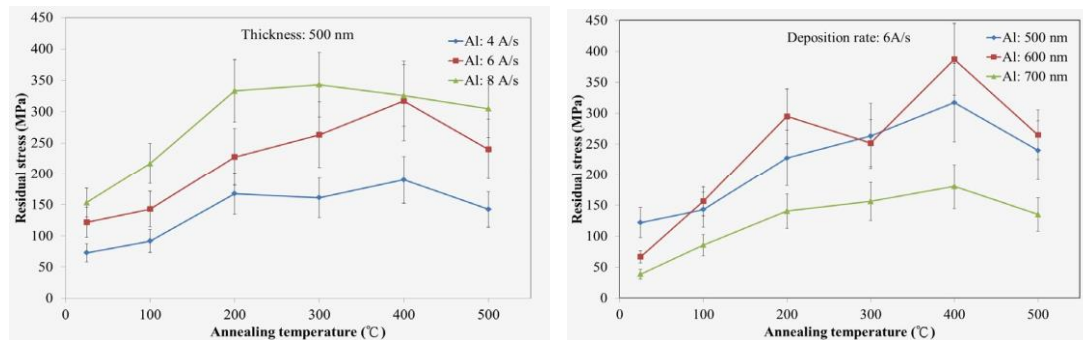
Fig. 2. Residual stress of Al films after RTA with different deposition (a) rate and (b) thickness
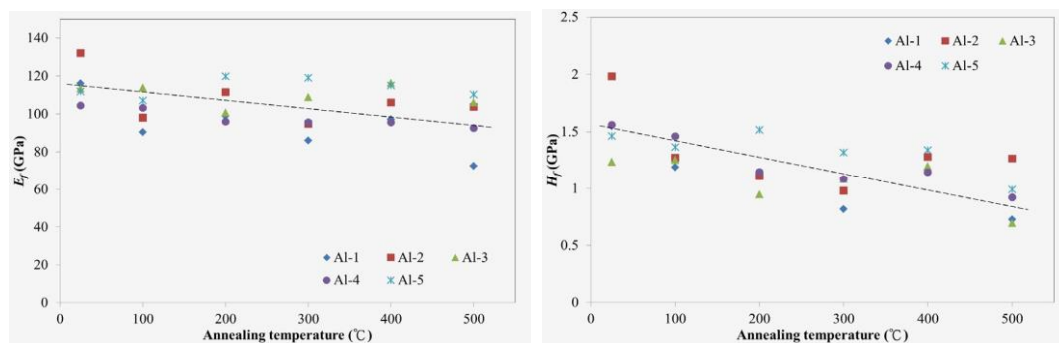
Fig. 3. Effect of RTA temperature on the modulus and hardness of aluminum films
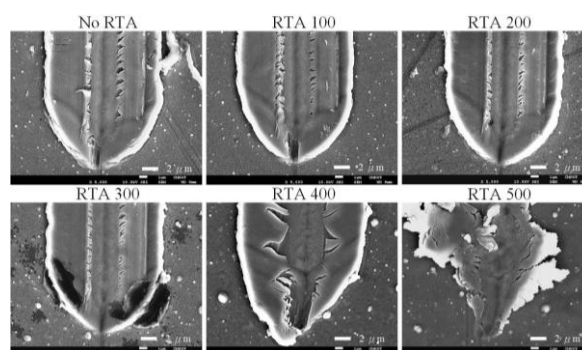
Fig. 4. Nanoscratch results of aluminum films with different RTA temperatures

4. References

[1] M. Ohring (1992), *The Materials Science of Thin Films,* Academic Press.

[2] S. Hyun, W. L. Brown, and R. P. Vinci (2003), "Thickness and temperature dependence of stress relaxation in nanoscale aluminum films", *Applied physics letters*, **83**, 4411-4413. [3] A. C. Fischer-Cripps (2000), *Nanoindentation Testing*, Springer New York.

NDE OPTICAL BASED METHODS FOR LINERS ASSESSMENT FOR HYDROGEN STORAGE

K. Wachtarczyk[1], P. Gąsior[1], J. Kaleta[1] and N. Yadav[2]
[1] Department of Mechanics, Materials and Biomedical Engineering,
Wrocław University Of Science And Technology, Wrocław, Poland
[2] Processing of Composites Group, Department Polymer Engineering and Science,
Montanuniversität Leoben, Leoben, Austria

1. Introduction

Due to increasing requirements for the energy sources efficiency, storage methods are being widely studied. Combination of fuel cells with high pressure vessels is an alternative method for electricity production to li-ion batteries for vehicles, machines and stationary equipment. One solution to store hydrogen is a high pressure type IV composite vessel. It consists of the polymer a liner with a boss and a composite winded on its surface. The liner is a barrier for the gas stored inside, while composite strengthens the structure. Many papers focused on the optimization of the composite because of its price [1]. On the other hand, even though the liner is the cheapest part of the vessel, its defects often lead to failure of the whole vessel. There is only a limited number of papers focused on liner defects.

In our works, we show usage of the different NDE optical methods for inspection and monitoring of the liner. Strain field under internal pressure was investigated with fiber Bragg grating (FBG) sensors and digital image correlation (DIC) method. Additionally, visual analysis was used to find defects inside the material.

2. Experiment description and results

The HDPE 60 liter liner was used for the tests. First, visual analysis of the defects inside the material were performed. Red bar LED light was placed at the 45 degree angle to the surface on the outside of the liner and image with CCD camera was acquired. This setup increased the contrast of the material's defects. The visual inspection allowed to find defects inside the material, e.g. concentration of the air bubbles around the boss was observed.

In the next step 11 FBG sensors and FBG-based rosette were attached to the surface and speckle pattern for DIC measurements was sprayed on the liner (fig. 1). Paint was removed where sensors were attached to avoid disturbances. The liner was pumped with a compressed air up to 1 bar and 3-D DIC system was used to investigate the strain field on the surface.
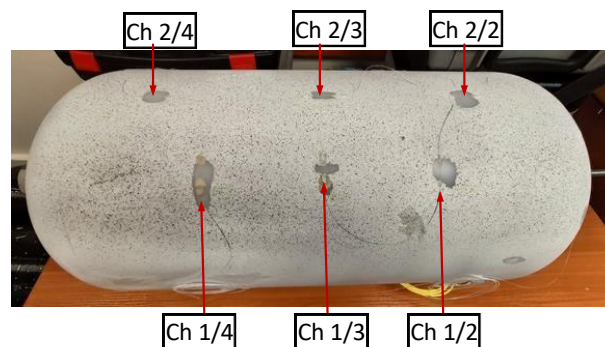
Fig. 1. View of the liner a) with surface installed FBG sensors and DIC speckle pattern

DIC and FBG results were compared. Difference in measured values didn't exceed 5%. Strain field analysis showed that the cylindrical part of liner is mostly deformed in the circumferential direction, while dome is in the longitudinal. Highest value of strain (10000 με) was observed in the radial direction on the middle of the liner.

Two fiber sensors were placed symmetrically to the middle of the liner (Ch1/2 and Ch1/4), on the cylindrical part in the circumferential direction. Difference in the strains from the FBG sensors placed symmetrically were observed (difference up to 25%). It can be a reason of the material thickness difference between those areas.

Small compression in the circumferential direction on the dome was observed for both FBG and DIC method. It means that collapse of the liner on the dome part was observed. This behavior can be an initiation point for the defect of the liner.

3. Summary

Three different optical based NDE methods were presented. They can be useful for liner assessment at different stages of the life-time of the pressure vessel. Image analysis can be used after manufacturing of the liner for the quality verification of the final product before winding of a composite. DIC method can be used on the development stage for both the liner and whole vessel [2], because it allows to see anomalies in the strain field, caused by e.g. different thickness of the material., but requires speckle pattern. Optical FBG sensors, embedded inside composite material, can be used for the structural health monitoring (SHM) of the vessel during its manufacturing and exploitation.

4. References

[1] Barthelemy, H., Weber, M., & Barbier, F. (2017). Hydrogen storage: Recent improvements and industrial perspectives. *International Journal of Hydrogen Energy*, *42*(11), 7254–7262. https://doi.org/10.1016/j.ijhydene.2016.03.178

[2] Gąsior, P., Malesa, M., Kaleta, J., Kujawińska, M., Malowany, K., & Rybczyński, R. (2018). Application of complementary optical methods for strain investigation in composite high pressure vessel. *Composite Structures*. https://doi.org/10.1016/j.compstruct.2018.07.060

USING OF ELECTRICAL RESISTANCE TOMOGRAPHY FOR LOCALIZATION OF DAMAGE OF THIN CARBON LAYER

M. Stepnowski and P. Pyrzanowski
Warsaw University of Technology, Institute of Aeronautics and Applied Mechanics, Warsaw, Poland

1. Introduction

Minor damage to machinery and equipment often occurs during operation. Due to their surface nature, they are difficult to detect by typical methods such as measuring the changes in shape or strain. In such cases, a method of measuring the change in resistance of the thin conductive layer applied to the surface may be helpful. A very thin layer of graphene or graphite can be used, applied on the surface being tested, with a thickness of several or over a dozen □m. Damage to the surface of the element causes the discontinuity of this layer and subsequently lead to a change in the current density distribution in its individual fragments. These changes can be estimated by measuring the change in resistance between the respective electrical contacts installed in the layer [1]. This paper proposes a method to improve the accuracy of the defects location by means of multiple measurements of resistance changes along various cross-sections as well as the use of the twodimensional function of the reduction of the area edgeinfluence.

2. Specimen, methodology

A small, square-shaped 50x50 mm sample of graphite with a thickness of about 10µm was used. 18 silver electrodes about 0.4 mm wide were applied along each of the 4 edges. The spacing between the electrodes was 2.54 mm. The sample used was the same as at work [2]. To make accurate resistance measurements, especially for carbon composites, a 4-wire measurement method should be used [3]. However, due to the relatively high layer resistance (several dozen to several hundred ohms) and very high quality (low resistance) of electrode-layer connections it was possible to use a much simpler 2-wire method.

A special analog multiplexer connected the ohmmeter with each pair of 2 contacts, which in total gives $(4*18)!/(4*18-2)!/2=2556$ independent measurements. Then the entire analyzed area was divided into a grid of 500x500 small areas, hereinafter referred to as pixels. When the distance of the center of the pixel from the line connecting the electrode contact points with the layer was less than the assumed value, the given measurement was taken into account for the given pixel. Then the value of the change in resistance was averaged taking into account the number of valid measurements for each pixel.

Then the result was corrected by its multiplication by the function eliminating the edge effect determined by the equation:

$$F = \left(\left(\left(1 - \frac{1}{w \cdot x + s}\right) + \left(1 - \frac{1}{w \cdot (50 \cdot s - x) + s}\right)\right) - 0{,}95\right) \cdot \left(\left(\left(1 - \frac{1}{w \cdot y + s}\right) + \left(1 - \frac{1}{w \cdot (50 \cdot s - y) + s}\right)\right) - 0{,}95\right)$$

where: x, y – horizontal and vertical coordination respectively;
w – edge influence correction factor equal to 0.4;
s – grid resolution equal to 10 pixels per mm.
The shape of the correction function is shown in Fig. 1.
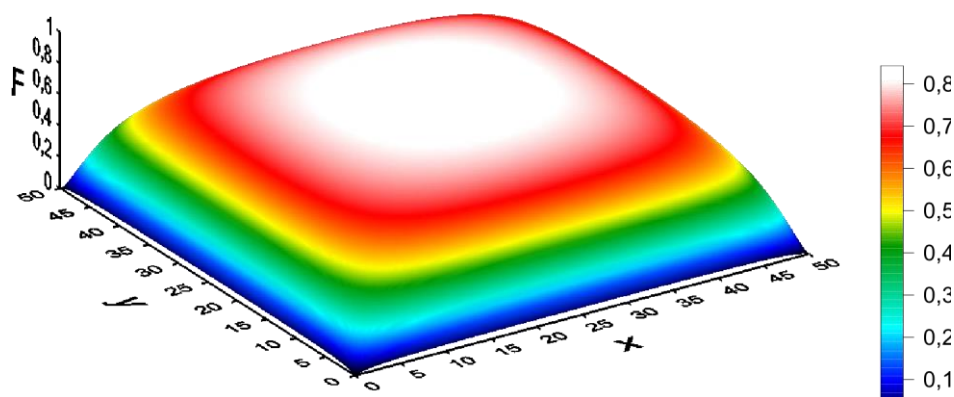
Fig. 1. The shape of the correction function

3. Results

The described method was used to determine the location of the defect in the graphite layer, shown in Fig. 2a.The damage is visible as a thin line marked in red circle on the drawing. Figure 2b shows the experimentally determined damage location. As it could be noticed the location was determined very accurately. Some concerns regarding its shape may occur, but in practice the issue is much less important.
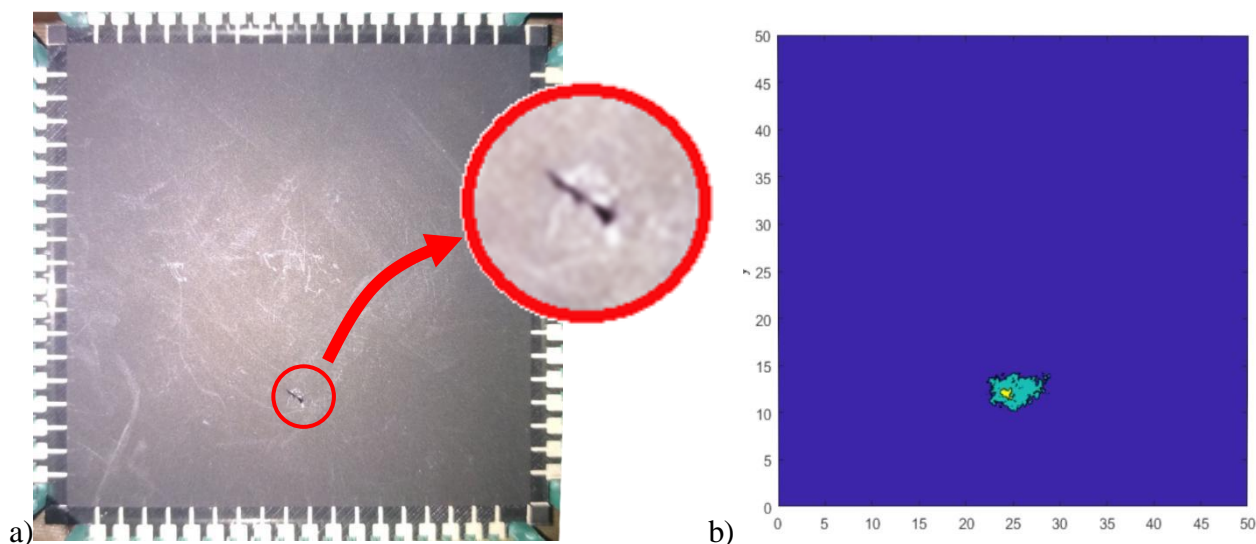
Fig. 2. Damage shape: a) real; b) experimentally determined

4. References

[1] X. Zhou, P. Bhat, H. Ouyang, J. Yu, Localization of cracks in cementitious materials under uniaxial tension with electrical resistance tomography, *Construction and Building Materials*, **138** (2017) 45-55.

[2] M. Stepnowski, D. Janczak, M. Jakubowska, P. Pyrzanowski, Detection of surface damage using resistance tomography in thin graphite layer, *Materials Today: Proceedings*,**12** (2019) 484–490

[3] J. Gadomski, P. Pyrzanowski, Experimental investigation of fatigue destruction of CFRP using the electrical resistance change method, *Measurement*, **87** (2016) 236-245.

THE STRESS ANALYSIS IN POLYETHYLENE TIBIA COMPONENT OF UNICOMPARTMENTAL KNEE IMPLANTS USING FINITE ELEMENT METHOD

M. Żak[1] and J. Mika[2]
[1] Department of Mechanics, Materials and Biomedical Engineering,
Wroclaw University of Science and Technology, Wroclaw, Poland
[2] Interdepartmental Scientific Circle of Biomechanics,
Wroclaw University of Science and Technology

1. Introduction

Modular components of an unicompartmental knee arthroplasty (UKA) allow customizing of the implant to the patient and are less invasive alternative to total knee arthroplasty (TKA). However, aseptic mechanical loosening and polyethylene (PE) wear remain are among the most common causes for failure after UKA. The introduction of new implants and designs has slightly reduced the number of failures. Many studies have underlined that PE wear as the predominant mechanism failure and is a complication inherent in the design of fixed implants [1,2].

Our study aimed to analyze the effects of shape and height of the polyethylene replacement of cartilage used in an unicompartmental knee arthroplasty. Especially since the design of polyethylene affect the distribution contact stress and may lead to severe wear and damage in an artificial joint.

2. Material and method

Femoral component, tibial insert, and tibial component dimensions was constructed based on of the JOURNEY UNI knee systems. Two different tibial insert models, used in fixed-bearing UKA, were developed: a flat (F) and spherical (S) design (Fig.1). In addition, it was assumed that the height of the polyethylene insert can be: 5mm, 8mm and 11mm. In these studies, finite element analysis software ANSYS Workbench 19 was used for numerical estimation of mechanical properties of unicompartmental knee models.
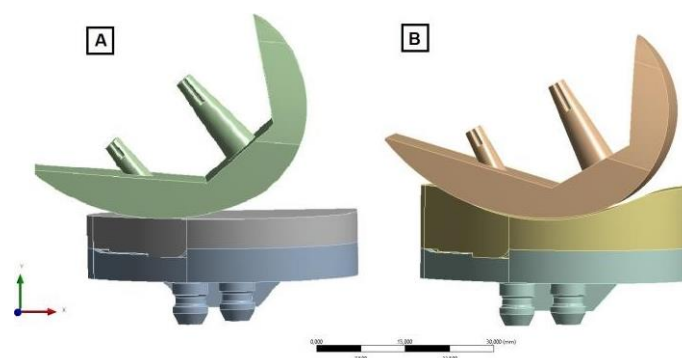
Fig. 1. Unicompartmental knee models with different tibial insert: a) flat (F); b) spherical (S)

A contact condition was specified at the femoral component and tibial insert interface with a friction coefficient of 0.002. Whereas, the polyethylene insert is rigidly bonded to the tibial component. The model simulated the process of rotation the tibial component through the tibial insert (by selecting the vertical and horizontal force components). The amount of load increased gradually

to its maximum level of 1200N. Numerical models made it possible to assess stress distribution in the whole endoprosthesis as well as in its individual elements.

3. Results and conclusions

The maximum stress values in endoprosthesis models decreased with the increase of polyethylene insert height (Tab.1). Comparing the PE inserts of the same height with different shapes, higher stress values were obtained for spherical inserts (not including models with 5mm PE inserts). For the height of 8 mm PE inserts (F8 and S8) the highest stress values were found on femoral component with similar values (140 MPa model F8 and 150 MPa model S8). The highest stress in the models with 11 mm high PE inserts was observed in the tibia. Only in the case of model F5 the maximum stress values, in endoprosthesis elements made of titanium alloy, exceed the permissible stress values.

σ_{MAX} [MPa]					
F5	F8	F11	S5	S8	S11
775	140	112	183	150	148

Tab. 1. The maximum von Mises stresses in unicompartmental knee implants.

The interpretation of the obtained values of stress distributions in PE insert made it possible to assess the prepared models in terms of fulfilling their function in a safe and permanent way (Fig.2). One of the models F5 was not able to carry the applied load. In the case of the other models, it cannot be clearly determined whether they will not be damaged. However, attention should be paid to models F5 and S8, as their PE inserts have generated a stress in excess of the UHMWPE permissible stress, which, during the cyclic operation of the load, can cause faster wear of the insert.
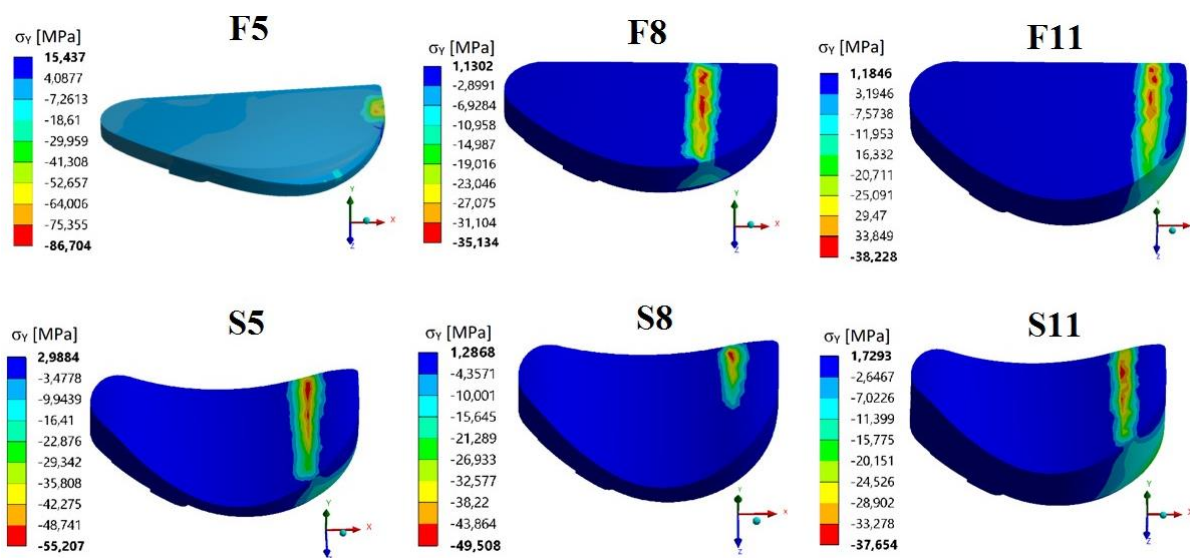
Fig. 2. Distribution of maximum axial stress values (σ_Y) in polyethylene inserts

4. References

[1] Y.G. Koh, K.M. Park, H.Y. Lee, and K.T. Kang (2019). Influence of tibiofemoral congruency design on the wear of patient-specific unicompartmental knee arthroplasty using finite element analysis. Bone & joint research, 8(3), 156–164.

[2] M. Vasso, A. Antoniadis, N. Helmy (2018). Update on unicompartmental knee arthroplasty: Current indications and failure modes. EFORT Open Rev., 3(8), 442–448.

FIRST ATTEMPTS TO DESCRIBE THE FATIGUE STATE OF THE MATERIAL USING X-RAY DIFFRACTION METHODS

E. Gadalińska, M. Malicki and B. Madejski

Łukasiewicz Research Network – Institute of Aviation, Warsaw, Poland

1. Introduction

The fatigue phenomena are of the crucial importance for the exploitation life of airplanes, cars, in power engineering (turbine blades, boilers, pipelines), cutting tools and many others. From the perspective of the fatigue life the determination of the moment of fatigue crack initiation is the most important [6]. It is possible when the state of the material is known. As for now the fatigue phenomena were investigated with different methods having their roots in different sciences and in different research methods. Many authors investigated the fatigue induced material damage and evolution of structure with different methods i.e.: scanning electron microscopy [8], electron transmission microscopy [2], optical microscopy and two-beam interferometry [4] or / and with modelling [1]. The possibilities of diffraction methods were developed through the last decades and this powerful tool of research can be utilized as an experimental method for determination of the fatigue state of the material [7], [3].

The aim of this work is to find out the relationship between the residual stress and dislocation density evolution applying the X-ray diffraction methods. The dislocations multiply and reorganize during monotonic and cyclic deformation, so their evolution can be a valuable information for investigation of fatigue phenomenon [3].

The diffraction methods are non-destructive methods for quantitative analysis of grain level deformation [5]. In this study X-ray diffraction is employed to acquire the information about the evolution of elastic lattice strains and changes in dislocation density after fatigue cycling of austenitic steel.

2. Methodology and some results

In this work the X-ray diffraction has been employed to assess the damage level under HCF and LCF conditions and under the tensile test. The subject undertaken in this work was the observation of changes of the diffraction peaks shape and position for specimens on different levels of the fatigue tests. As the material of the first attempt the common austenitic steel 316L was chosen. The stress/strain curve is presented in Fig. 1a and the specimen shape and geometry is shown in Fig.1b.

Diffraction experiments were performed in two configurations to achieve the goals set by the research program. The first one was the well known rocking curve measurement geometry combined with the analysis of the diffraction peaks broadening. The second was the standardized $\sin^2\psi$ method of determination of the first order stresses. Additionally the texture measurements with diffraction were performed as well. This type of measurements were made in one point in the specimen in the initial state and in 5 points along the specimen axis. Additional experimental methods utilized here were tomography, optical and scanning electron microscopy which allowed to determine the material microstructure and its changes as well as the possible microcracks during the fatigue tests. The hardness measurements were combined with the results of diffraction experiments as well. Moreover the tensile testing allowed to identify the mechanical properties of examined material, i.e. Young modulus, yielding point and ultimate tensile strength.
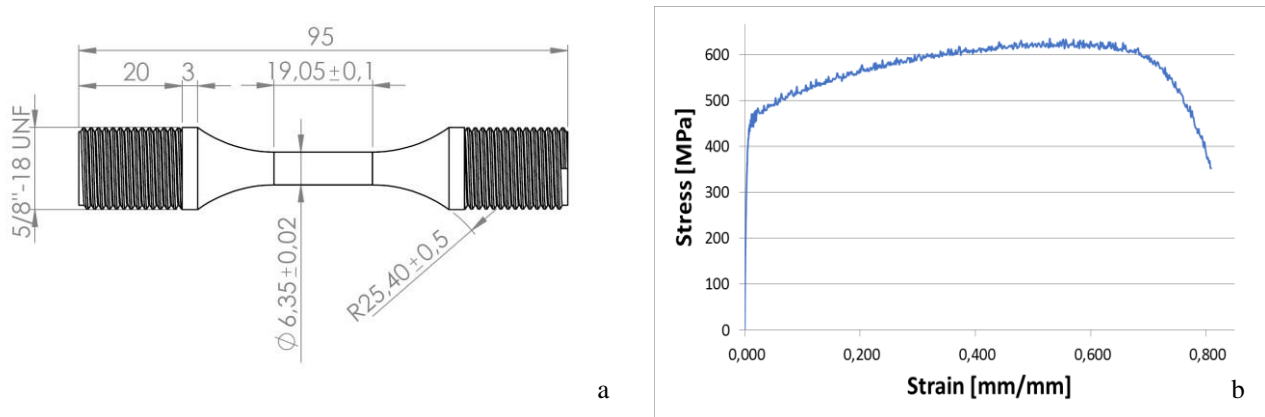
Fig. 1. a) The drawing of the specimen used,
b) the stress/strain curve for the material used in the research

3. References

[1] J.P. Dingli, A. Abdul-Latif, K. Saanouni (2000). *Predictions of the complex cyclic behavior of polycrystals using a self-consistent modeling*, International Journal of Plasticity, 16411–437.

[2] P.B. Hirsch, M.J. Whelan (1960). *A kinematical theory of diffraction contrast of electron transmission microscope images of dislocations and other defects*, Phil. Trans. R. Soc. Lond. A. **252**, 499–529.

[3] E.-W. Huang, R.I. Barabash, B. Clausen (2010). Y.-L. Liu, J.-J. Kai, G.E. Ice, K.P. Woods, P.K. Liaw, F*atigue-induced reversible/irreversible structural-transformations in a Ni-based superalloy*, International Journal of Plasticity **26**, 1124–1137.

[4] W.H. Kim, C. Laird (1978). *Crack nucleation and stage I propagation in high strain fatigue—I. Microscopic and interferometric observations*, Acta Metallurgica **26**, 777–787.

[5] A.M. Korsunsky, K.E. James, M.R. Daymond (2004). *Intergranular stresses in polycrystalline fatigue: diffraction measurement and self-consistent modelling*, Engineering Fracture Mechanics **71**, 805–812.

[6] Z.L. Kowalewski (2011). *Zmęczenie materiałów - podstawy, kierunki badań, ocena stanu uszkodzenia*, presented on Siedemnaste Seminarium Nieniszczące Badana Materiałów, Zakopane.

[7] M. Tahara, H.Y. Kim, H. Hosoda, S. Miyazaki (2009). *Cyclic deformation behavior of a Ti–26 at.% Nb alloy*, Acta Materialia **57**, 2461–2469.

[8] P. Zhang, Q.Q. Duan, S.X. Li, Z.F. Zhang (2008). *Cyclic deformation and fatigue cracking behaviour of polycrystalline Cu, Cu–10 wt% Zn and Cu–32 wt% Zn*, Philosophical Magazine **88**, 2487–2503.

USING WELD-ON STRAIN GAUGES FOR ELEVATED TEMPERATURES

J. Chvojan, J. Václavík, O. Weinberg and J. Német

Výzkumný a zkušební ústav Plzeň s.r.o., Tylova 1581/46, 301 00 Plzeň, Czech Republic

1. Introduction

There are two main possibilities how to attach the strain gauges on to the specimen surface for the measurement at higher temperatures: using adhesive or spot welding. However when the structure is permanently hot, only welding strain gauges can be used. The producers offer very good weld-on strain gauges usable till 600°C or higher temperatures, but the price is relatively high. Even for elevated temperatures up to 250°C the mentioned gauges have to be used. Recently HBM introduced new type of weld-on strain gauges LS31HT (M-series strain gauge glued with EP310N on metal carrier), which cover this temperature range. The aim of this article is the comparison of these strain gauges and self-made weld-on strain gauges during operational stress measurement on the ash hoper body on the power station.

2. Object of the investigations

The object of presented investigations was to determine the stresses, occurring on the ash hopper body, used in the conventional power stations for flue-dust separation. The goal was to ensure that during non-standard states of filled-up ash hopper body the stresses not exceed the allowable limit. Except of quasi-static pressure the dynamic stresses were expected by reason of the ash rippling with the compressed air. Using FEA model the critical nodes were identified on very bad accessible positions on the body corner (Fig 1a), red). Nevertheless it was found, that the nominal stress on the carrying horizontal cross U-beams good represents the pressure in the hopper. Thus the measured places were chosen in the middle of this beams and the value of stress peaks was then recalculated.

3. Instrumentations

The strain gauge LS31HT was installed on the uncovered part of the insulation above the beam using standard spot welder and the same compensation one on the free steel plate; Wheatstone bridge was completed in the measuring amplifier.

However this task was very good opportunity to compare the conventional strain gauges with self-made ones. The second self-made strain gauge was manufactured from metal carrier 0.2 mm thick with HBM LY11-6/350 strain gauge glued with HBM Z70 cyanoacrylate adhesive. The behavior of these strain gauges was in advance successfully tested in laboratory up to 100°C. Two strain-gauges were used on upper and bottom U-beams, with two the same compensating strain gauges attached to the U-beam coupled to the full bridge. The installation was performed again with the spot welder. Installed strain gauges are presented in the Fig. 1b). The temperature of measured place was about 90°C.

The cables from strain gauges were led to the small terminal box clamped to the hopper insulation and from this place the standard shield cables of 20 m length were led to the measuring system, installed at the larger distance from the heat source.

The measuring unit enables on-line measurement of stresses at sampling frequency 400 Hz for about 2 months. The LTE connection enables the unit control and data management.

The taw data were stored in daily records on the system hard disc. The figures of stress time histories and files with extreme values were sent to the operator server.

a) FEA model – left max. stress, right measured   b) Installed strain gauges – left LS31HT
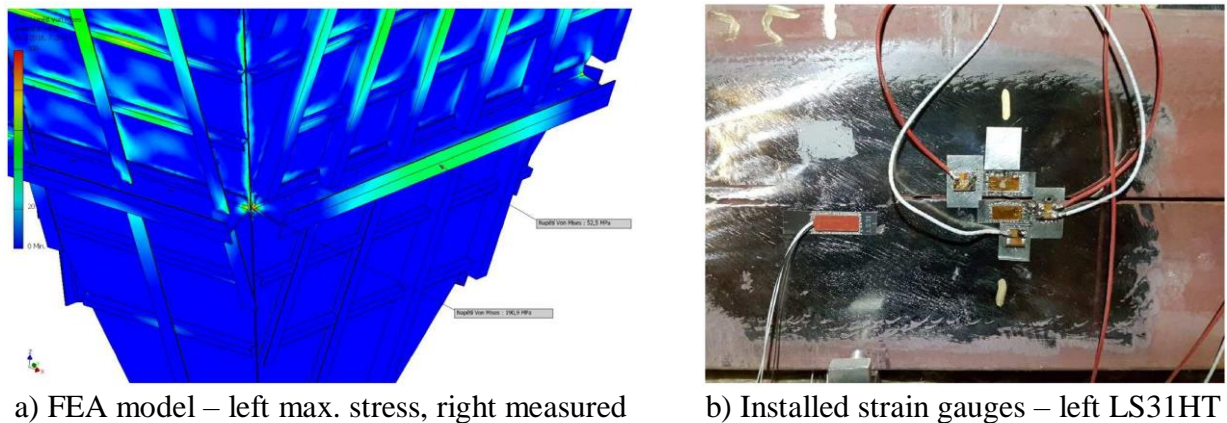
Fig. 1. Measured place on the ash hopper

4. Results and conclusions

The long term measurement detected so date not known behavior of the hopper body during nonstandard loading events.

It has been found at the same time, that the measured strains using self-made weld-on strain gauges corresponded with those, measured with professional HBM LS31HT ones (see Fig. 2). No offset was observed during 2 month test.
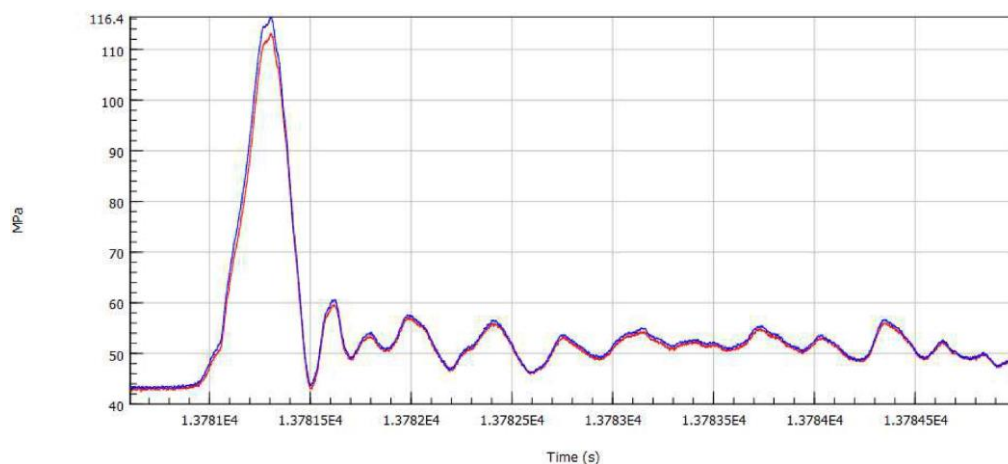
Fig. 2. Comparison of stress time histories on both measuring strain-gauge channels
(red LS31HT, blue 6LY11/350)

5. Acknowledgement

6. References

[1] HBM LS31HT, Instruction for use, DVS A04340_02_Y00_00_HBM.
[2] J.Vaclavik. (2019) *Ash hooper strain gauge test.* Testing report VYZ-1854Z-0050-01N, VZÚ Plzeň (in Czech).

DIGITAL IMAGE CORRELATION EMPLOYING THERMAL MARKING

F. Andrés-Castro[1], L.A. Felipe-Sesé[1], Á.J. Molina-Viedma[1], E. López-Alba[2] and F.A. Díaz[2]

[1] *Departamento de Ingeniería Mecánica y Minera, Campus Científico Tecnológico de Linares, Universidad de Jaén, 23700, Linares, Spain*
[2] *Departamento de Ingeniería Mecánica y Minera, Campus Las Lagunillas, Universidad de Jaén, 23071, Jaén, Spain*

1. Introduction

Digital Image Correlation (DIC) is a widely employed technique which allows obtaining full field displacement and shape measurement even at high speed rates [1], leading to grate improvements in studies such as impact or vibration. However, it requires the spraying of a speckle pattern on the surface. This could be a big inconvenient in some applications such as biomechanical studies. In this work a new DIC methodology has been developed by the employment of thermal cameras and non-invasive thermal patterns which disappear completely after a certain time. Physical printing will be no longer necessary, presenting great potential in various fields.

2. Methodology

DIC using thermal cameras and patterns, is based on the use of the temperature distribution presented by the surface under study as speckle pattern for obtaining displacements and strains. Figure 1 a) presents the traditional sprayed pattern on a specimen for the use of DIC with visible spectrum camera and in Figure 1 b) it is presented the non-invasive thermal pattern on a face.

Despite previous approaches where speckle pattern was projected [2], in this case thermal speckle is marked on the analyzed object, and it deforms and displace with it, allowing not only the digitalization but also the strain measurement. The duration of the thermal pattern will depend on the thermal diffusivity of the study material [3].

a) b)
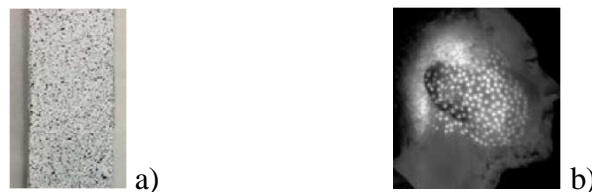
Fig. 1. a) Physical pattern on a specimen, b) Thermal pattern made on the profile of a face

It was developed different devices to perform the thermal marking which presented a randomly distributed metal blunt peaks. Those devices were warmed up previously to contact with the specimen and start the test. Two different sets of tests were performed. In the first set, 2D DIC was employed to measure a controlled solid rigid movement test in order to validate the methodology. The support material was polycarbonate and different coatings were analyzed. In a second set of test, 3D-DIC was employed on different human body parts, among others, on face, hand and arm. The 3D calibration was performed employing a special calibration target visible for thermal camera.

3. Results

In Figure 2 it is presented the evolucion of the measured displacement on a solid rigid displacement test on a policarbonate specimen from initial state, to 5mm diplacement and then back to initial point

in 10 seconds. As observed, a certain kind of peelable paint could obtain good results but no coating is also offering close to real values of displacements.
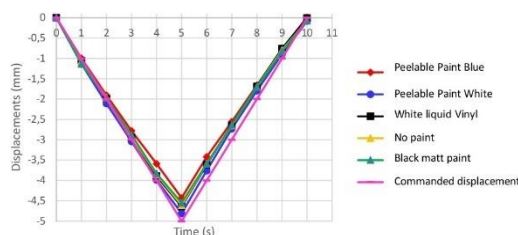
Fig. 2. Graphic showing measured displacement on solid rigid 2D displacement test using different surface coatings

In the case of 3D measurements, an analysis of a human hand was performed, by applying a speckle pattern of 5mm diameter at 45ºC. Results show in Fig 2.
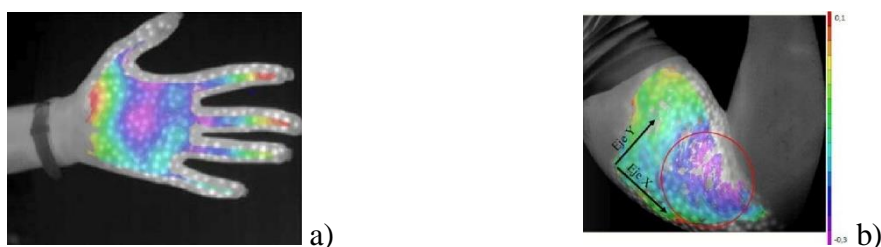
Fig. 3. a) Scanning in the direction of the z axis (mm), seen in 2D b) 3D scanning, created by VIC 3D

Next, the strains generated in the contraction and relaxation of a biceps is shown. Strains in x-axis direction are presented in Figure 3. It can be clearly seen how in the area of the arm where the fold between the forearm and the biceps occurs, a compression (negative) strain is generated, however, in the biceps area, strain is positive.

4. Conclusions

The results show a great advance, opening a path to future works that allow this technique to be developed successively. As for the 3D study, the validity of this technique has been demonstrated without the need for surface preparation (NON INVASIVE technique), obtaining good results from both 3D recreated forms and deformations and displacements.

However, it should be taken into account that the value of this temperature will vary during the performance of the test or analysis mainly for two reasons, the first one will be due to a heat transfer by conduction that will tend to reduce the temperature gradient until the temperature is equalized at the different points of the body, The second factor is due to the thermoelastic effect.

5. References

[1] M.A. Sutton, J.J. Orteu, H.W. Schreier, Image Correlation for Shape, Motion and Deformation Measurements- Basic Concepts, Theory and Applications, Image Rochester NY. (2009) 341. doi:10.1007/978-0-387-78747-3.

[2] H. Nguyen, Z. Wang, P. Jones, B. Zhao, 3D shape, deformation, and vibration measurements using infrared Kinect sensors and digital image correlation, Appl. Opt. 56 (2017) 9030. doi:10.1364/ao.56.009030.

[3] M.E.H. (University of S. Ortiz, Novel Developments of Moiré Techniques for Industrial Applications, 11 (2004).

IMPACT OF CHEVRON ORIFICE GEOMETRY ON THE NOISE REDUCTION AND FLOW PROPERTIES OF SYNTHETIC JET

E. Smyk

Faculty of Mechanical Engineering, UTP University of Science and Technology,
al. Prof. S. Kaliskiego 7, 85-796 Bydgoszcz, Poland

Keywords*: ZNMF; efficiency; noise; vortex; turbulence*

1. Introduction

The synthetic jet (SJ) is generated by periodic expulsion and injection of fluid (mostly air or water) through an orifice or nozzle to a closed cavity. Because the time-averaged mass flow rate in the orifice is equal zero, SJ are called zero-net mass- flux jet (ZNMF). However, some volume of fluid being expelled through the orifice moves away under self-induced velocity. This phenomenon repeats periodically due to the using movable or deformable element, as for example piezoelectrics diaphragm (piezoelectrics SJA), piston (mechanical SJA) or loudspeaker (acoustic SJA).

The vortex nature of SJ makes that they are used in many fields of science and technology, as electronic cooling [1], flow control [2], mixing [3], and other. The cooling application of SJ is very promising. However, in the case of large area electronic devices the used of acoustic SJA is necessary and this type of SJA generates nuisance noise, which should be reduces to a minimum.

There are many methods to reduce the sound pressure level (SPL) of synthetic jet actuator (SJA). Arik [4] closed the SJA in cube with a muffler and Smyk et. all [5] placed a heat sink inside the actuator chamber. However, this simplest method of SJA noise reduction is the used of chevron nozzle [6] or chevron orifice [7].

The acoustic and flow properties of SJA will be investigated in this paper for 8 different orifices. The impact of a number of chevrons in the orifice, and chevron cutouts rounding on chosen parameters was tested.

2. Materials

The SJA with eight different orifices was investigated. The measurements method and utilized actuator was similar as in [7]. The chevrons were isosceles triangles with the same base and height length. In case ,,a" the orifices was classic chevron orifice and in case ,,b" the bottom of cutouts was rounded with radius equal R = 1/6 h. In the Fig. 1 differences between the case ,,a" and ,,b" of orifices and the dimensions were presented.

For all cases the SJ characteristic frequency has been designated, ad such parameters as the supply real power, the energetic efficiency, the characteristic velocity were measured. The hot-wire anemometer was used for the flow velocity measurements.

In the end, the SPL for each case were measured and on the basis of previous and current measurements, the most favorable geometric case has been selected.

	d [mm]	l [mm]	Number of Chevrons	h [mm]	R [mm]
Case 1a	20	40	4	16.8	-
Case 1b	20	40	4	16.8	2.8
Case 2a	20	40	7	10.4	-
Case 2b	20	40	7	10.4	1.73
Case 3a	20	40	10	7.4	-
Case 3b	20	40	10	7.4	1.23
Case 4a	20	40	14	5.3	-
Case 3b	20	40	14	5.3	0.88

Table 1. Specification of the synthetic jet actuator orifce
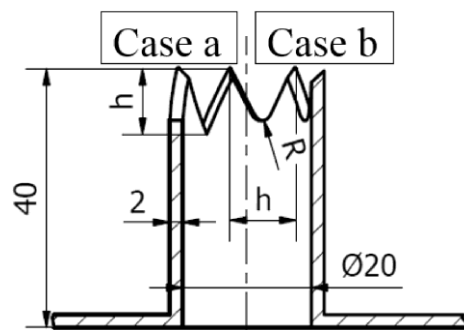
Fig. 1. Schema of orifice

3. Acknowledgements

4. References

[1] G. Krishan, K.C. Aw and R.N. Sharma (2019). Synthetic jet impingement heat transfer enhancement – A review, *Appl. Therm. Eng.,* **149**, 1305–1323.

[2] E. Smyk (2017). Numerical simulation of axisymmetric valve operation for different outer cone angle, *EPJ Web Conf.*, **143**, 02112.

[3] P. Wang and C. Bing Shen (2019). Characteristics of mixing enhancement achieved using a pulsed plasma synthetic jet in a supersonic flow, *J. Zhejiang Univ. Sci. A.*, **20**, 701–713.

[4] M. Arik (2007) An investigation into feasibility of impingement heat transfer and acoustic abatement of meso scale synthetic jets, *Appl. Therm. Eng.*, **27**, 1483–1494.

[5] E. Smyk, P. Gil, R. Gałek and Ł. Przeszłowski (2020). Acoustic and Flow Aspects of Novel Synthetic Jet Actuator, *Actuators.*, **9**, 100.

[6] H. Xia, P.G. Tucker and S. Eastwood (2009). Large-eddy simulations of chevron jet flows with noise predictions, *Int. J. Heat Fluid Flow.*, **30**, 1067–1079.

[7] E. Smyk and M. Markowicz (2021). Acoustic and flow aspects of synthetic jet actuators with chevron orifices, *Appl. Sci.,* **11**, 652.

MEASUREMENT OF STRESSES IN POLYCRYSTALLINE MATERIALS USING ENERGY-DISPERSIVE X-RAY DIFFRACTION

A. Oponowicz[1], M. Marciszko-Wiąckowska[2], A. Baczmański[1],
M. Klaus[3], Ch. Genzel[3], S. Wroński[1], M. Wróbel[4]
AGH-University of Science and Technology, [1]WFiS, [2]ACMiN, [4]WIMiIP,
al. Mickiewicza 30, 30-059 Kraków, Poland
[3] Abteilung für Mikrostruktur- und Eigenspannungsanalyse, Helmholtz-Zentrum Berlin
für Materialien und Energie, Albert-Einstein-Str. 15, Berlin 12489, Germany

1. Introduction

The microstructure and residual stresses are important characteristics of materials affecting their mechanical properties. The stress state and material properties are usually heterogeneous in the near-surface volume of the machined samples. There are a number of experimental methods that allow for an accurate description of the stress distribution and can be effectively applied to many polycrystalline materials exhibiting both cubic and hexagonal crystal structures. One of the non-destructive techniques for stress measurements is the reflection-mode X-ray diffraction method - the so-called XSA (X-ray stress analysis). In this work a combination of standard X-ray diffraction with synchrotron measurements was proposed and tested on materials such as titanium, tungsten and austenitic steel subjected to grinding or polishing surface treatment.

2. Experimental methodology

The idea of the new MMXD method is based on the ED (energy-dispersive) diffraction measurement combined with the *sin2ψ* analysis for multiple *hkl* reflections [1]. In this case, data are collected for one constant *2θ* angle but with a white synchrotron beam [2].
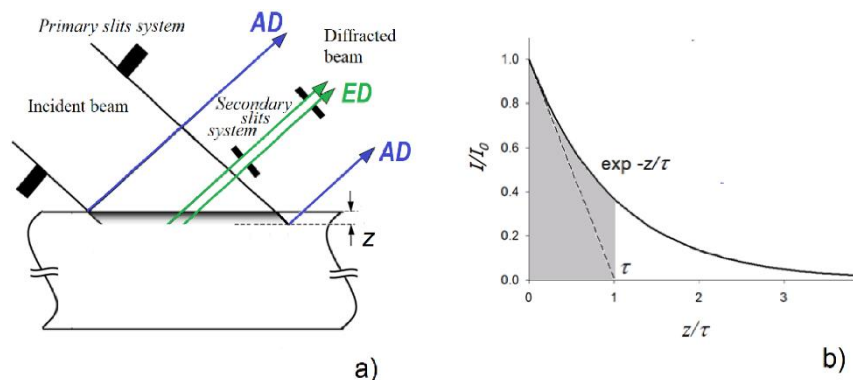
Fig. 1. The information depth limited by absorption of the radiation: a) the beam optics used in AD - angular dispersion and ED – energy-dispersive techniques; b) variation of the beam intensity with depth (z) below the surface and definition of penetration/information depth τ

During experiments, the information gauge is determined by exponential attenuation of the beam intensity, which can be characterized by penetration depth τ, defined in Fig. 1. In the case of the MMXD method, data are grouped for strictly chosen information depths. In this way, it is possible to perform the residual stress analysis layer by layer in the sample and perform a study for a much deeper profile compared to classical X-ray methods with characteristic radiation on laboratory diffractometer [1].

3. Results and conclusion

Proposed in this work MMXD analysis (multireflexion and multiwavelength X-ray diffraction) allowed to determine depth-dependent stress profile vs. penetration depth with a step of 2 μm, up to the maximum depth of about 10-14 μm. For the mechanically treated surfaces of tungsten, titanium alloy and austenitic samples, a very good convergence of stresses measured by synchrotron radiation (MMXD) and stresses determined by Cu Kα radiation on a laboratory diffractometer (MGIXD multi-reflection grazing diffraction [3]) was obtained (Figs. 1 and 2).
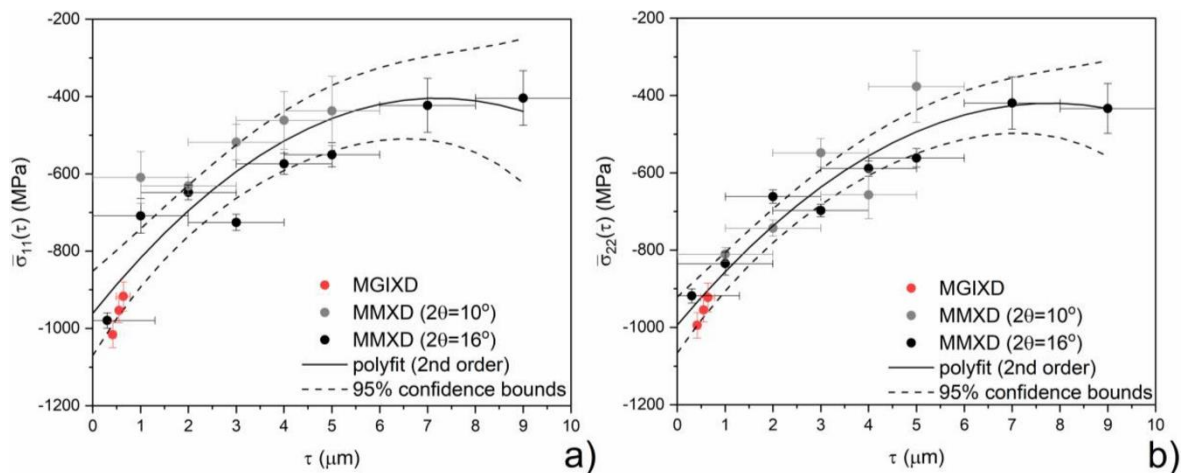
Fig. 2. Residual stress depth-dependent profiles in the function of penetration depth (τ) *for* polished tungsten. Results were gathered from classical diffractometer (MGIXD) and synchrotron experiment (MMXD for two *2θ* angles)

It can be concluded that the MGIXD and MMXD methods become a powerful and unique tools for stress measurement in subsurface volume, which cannot be investigated with other techniques. These methods can be used to study residual stresses resulting from surface finishing processes, such as mechanical polishing.

4. Acknowledgments

5. References

[1] M. Marciszko, A. Baczmański, M. Klaus, C. Genzel, A. Oponowicz, S. Wroński, M. Wróbel, C. Braham, H. Sidhom and R. Wawszczak (2018). Gradient of residual stress and lattice parameter in mechanically polished tungsten measured using classical X-rays and synchrotron radiation, *J. Appl. Cryst.,* **51**, 732-745.

[2] Ch. Genzel, I.A. Denks, J. Gibmeier, M. Klaus, and G. Wagener (2007). The materials science synchrotron beamline EDDI for energy-dispersive diffraction analysis, *Nucl. Instrum. Methods Phys. Res. Sect. Accel. Spectrometers Detect. Assoc. Equip.*, **578**, 23–33.

[3] M. Marciszko, A. Baczmański, C. Braham, M. Wróbel, S. Wroński, G. Cios (2017). Stress measurements by multi-reflection grazing-incidence X-ray diffraction method (MGIXD) using different radiation wavelengths and different incident angles, *Acta Mater.*, **123**, 157–166.

IMPACT COMPRESSION TESTING OF PURE ICE USING SPLIT HOPKINSON BAR METHOD AND HIGH-SPEED CAMERA

Y. Nakao[1], H. Yamada[1] and N. Ogasawara[2]
[1] Graduate School of Science and Engineering, National Defense Academy, Japan
[2] Department of Mechanical Engineering, National Defense Academy, Japan

1. Introduction

The Split Hopkinson Bar (SHB) method proposed by Kolsky [1] is one of the impact test methods to measure the deformation of materials under high strain rates. The SHB compression testing apparatus consists of three long bars: the striker, the input bar, and the output bar. The specimen is sandwiched between the input and the output bars. The dynamic stress-strain relationship of this specimen is obtained by the propagation of elastic stress waves generated by the striker colliding with the input bar. Since this test method can be applied to various specimens in principle, its application has been developed not only for metallic materials but also for non-metallic materials in recent years.

In this study, we focus on the application of the SHB method to ice that exhibits brittle fracture behavior at high strain rates [2-3]. Ice is one of the well-known materials, and is used in a wide range of applications. On the other hand, the ice causes several problems such as damage to cars and buildings subjected to hail, collision of sea ice and ships, and falling of ice blocks from aircraft. In this regard, the mechanical properties of ice must be elucidated, especially at impact strain rates. We constructed a test apparatus that combines the SHB compressive testing machine with a cooling chamber, and evaluated the compressive strength of ice at strain rates from 10^0 to 10^3 s^{-1}. At the same time, a high-speed camera was used to observe the state of cracks inside the ice during impact deformation.

2. Material and method

Commercially available pure ice was used as the test material. The specimens were 20 mm in length and width, and four different heights (5, 10, 20, and 25 mm) were prepared. Figure 1 shows a schematic diagram of the SHB compression testing apparatus with a cooling chamber. The diameter of the input and output bars was 16 mm respectively. The aluminum alloy flanges with a diameter of 34 mm and a thickness of 4.5 mm were attached to the tip of these bars. The specimen was sandwiched between these flanges. The cooling chamber was connected to a cooling system using liquid nitrogen. The testing temperature for ice specimen was -10±0.3°C.

The states of deformation and fracture of the ice were recorded using a high-speed camera (ULTRA Cam HS-106E; nac Image Technology Inc.) with frame rates of 500000 fps installed in front of the observation window of the chamber. A strobe was used as the light source and illuminated from the rear of the specimen.
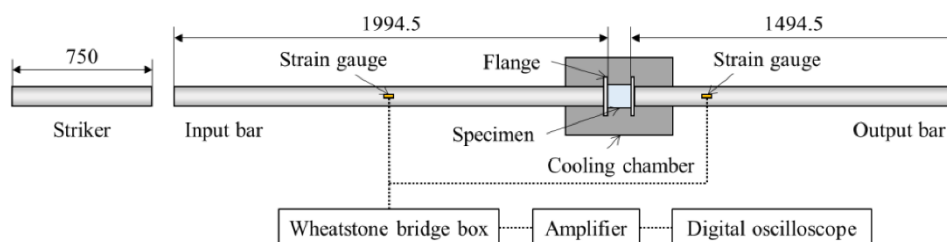
Fig. 1. Schematic of SHB compression testing apparatus

3. Results and discussion

Figure 2 shows an example of the stress-strain relationship at strain rates of 12.7 and 608 s^{-1}. The maximum stress increased with increasing strain rate. The high-speed camera images showed that many cracks had already appeared in the specimen near the maximum stress, regardless of the strain rate. However, after the stress reached its maximum value, the flow stress slowly decreased. This was probably due to the high deformation rate. From the observation results of the high-speed camera, the ice remaining between the flanges continued to be compressed. This is considered to be an inertia effect after the fracture.
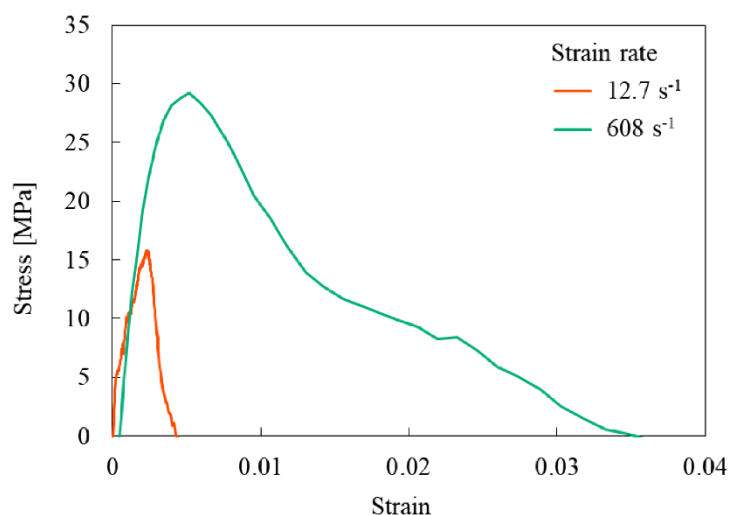
Fig. 2. Relationship between stress and strain at strain rates of 12.7 and 608 s^{-1}

4. Conclusions

In this study, we conducted the SHB compression tests with flanged bars on pure ice at -10°C. The maximum stress of the ice showed a positive strain rate dependence at strain rates of 10^0 to 10^3 s^{-1}. Furthermore, it was confirmed that cracks propagated inside the ice, which led to the fracture from the high-speed camera images.

5. References

[1] H. Kolsky (1949). An investigation of the mechanical properties of materials at very high rates of loading, *Proc. Phys. Soc. B*, **62**, 676–700.
[2] L.W. Gold (1977). Engineering properties of fresh-water ice, *J. Glaciol.* **19**, 197–212.
[3] E.M. Schulson (2001). Brittle failure of ice, *Eng. Fract. Mech.*, **68**, 1839–1887.

PLANAR SHEAR SPECIMENS FOR HIGH STRAIN-RATE TESTING OF ENGINEERING MATERIALS USING THE CONVENTIONAL SHPB TECHNIQUE: EXPERIMENTAL AND NUMERICAL INVESTIGATIONS

K. Cieplak, M. Grązka, Ł. Konwerski and J. Janiszewski
Military University of Technology, Warsaw, Poland

1. Introduction

Shear stress states dominate in many technical applications. Some examples of these are sheet metal forming, high-speed machining and ballistic impact. These processes are often associated with very high strain rates, which can even reach the level of 10^7 s^{-1} [1]. In order to understand better material behavior at such complex and extreme loading condition, or to select properly material for given application, or to conduct correct numerical simulations, it is necessary to determine the shear stress-strain response in a wide range of strain rates. Over the past decades, several techniques have been developed to study the dynamic shear behavior of engineering materials, however the split-Hopkinson pressure bar (SHPB) is the most widely used experiment [2]. The specific nature of SHPB tests, however, imposes limitations that result from the selection of the appropriate specimen geometry and the method of fixing the specimen. Many different design solutions of the SHPB system and various specimen geometries have been proposed for dynamic simple shear testing. A detailed review on the SHPB experiments include the torsion specimens, hat shape specimens, double shear specimens or shear-compression specimens was presented in [1-3]. However, despite the large variety of shear sample geometries, new solutions are still proposed to improve the accuracy of material data describing dynamic shear behavior. In the present work, it is considered three specimen geometries, which slightly differs from the shape of the shear specimens presented in the literature, and which are adapted to making them from sheet metal. The goal is to figure out for which specimen shape, the shear stress is most uniformly distributed over the gauge section and force equilibrium state within specimen is achieved.

2. Experimental procedure

The experimental and numerical investigations presented in the work was performed with the use of three planar (flat) specimens with single or double shear zones, the dimensions of which are well-defined by the following parameters: width w, height h and thickness t (Fig. 1).
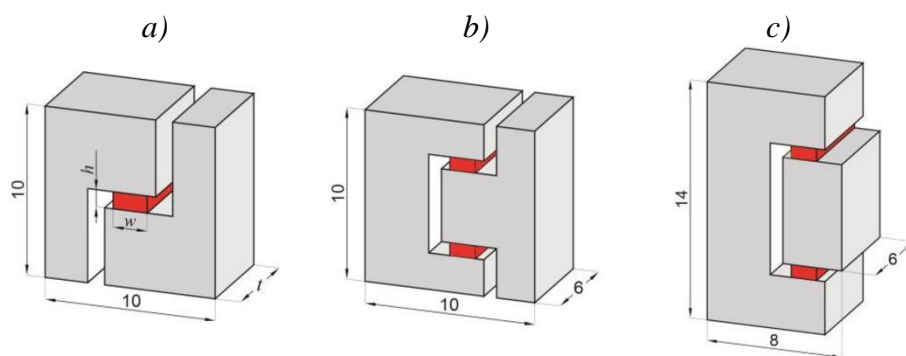
Fig. 1. Considered geometries of flat samples for simple shear tests: a) SSS specimen; b) DSS specimen; c) D2S specimen

The thickness of shear zone corresponds to the thickness of the sheet from which the specimens were cut away. The nominal dimensions of the shear zones of the specimens used in the tests are $1.5 \times 0.7 \times 6$ mm, respectively. All specimens were made of the Ti-6Al-4V alloy with the use of the wire electro discharge machining (WEDM) technology. The shear strength tests of the proposed specimens were performed under quasi-static and dynamic loading conditions. Quasi-static tests were carried out using the MTS C45 Criterion testing machine with strain rates of $0.001 \, \text{s}^{-1}$. In turn, high strain-rate shear tests were carried out with the use of the split Hopkinson pressure bar setup, the design solution of which is based on a typical design of the compression SHPB test equipped in maraging steel bars with dimension of 12 mm and length of 1200 mm. The high-speed Phantom v1612 camera was also used to record the process of dynamic shear deformation of the specimens.

3. Results and discussion

Based on the obtained shear stress-strain curves for Ti-6Al-4V alloy, the averaged level of plastic stress is almost the same for all tested specimen geometries, i.e., 630 MPa at the strain rate level of $10\,000 \, \text{s}^{-1}$. The obtained shear stress value corresponds well with the data presented in the literature [2, 4]. However, the results of numerical investigations reveal that the most uniformly distributed values of stress triaxiality η and Lode angle parameter θ in the shear zone are obtained for specimens with the geometry designated as D2S (Fig. 2a). Moreover, the force equilibrium in the D2S specimen is achieved after relatively short time (Fig. 2b).
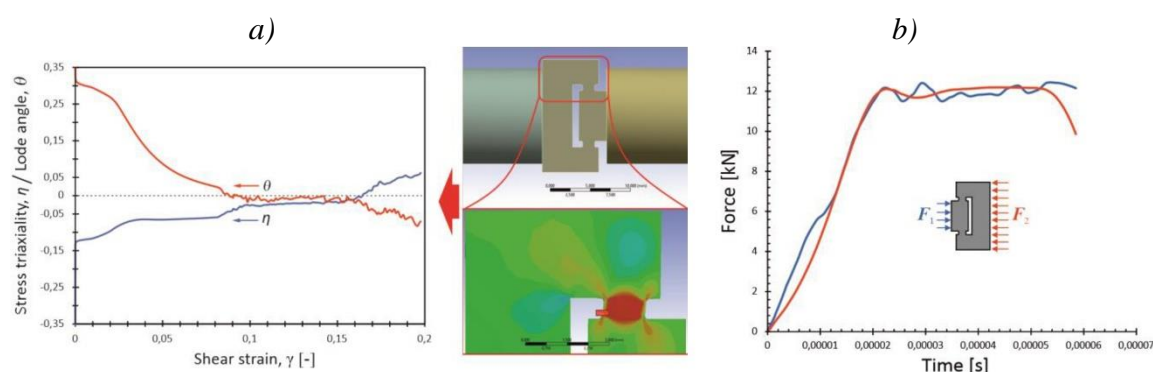
Fig. 2. a) Value distribution of stress triaxiality η and Lode angle parameter θ at the middle point of shear zone of D2S specimen; b) force equilibrium of the D2S specimen.

4. Conclusion

The tested specimen geometries are designed to be simple and are easy to manufacture by conventional WDEM technology. Lack of any clamping specimen system does not induce waves disturbance and allows to obtain good accuracy of the calculated load and deformation. However, of all the specimens tested, the D2S specimen guarantees the best quality of obtained experimental data, i.e., smooth profile of reflected and transmitted waves and a good force equilibrium state.

5. References

[1] N. Yan, Z. Li, Y. Xu, M.A. Meyers (2021). *Shear localization in metallic materials at high strain rates*, Progress in Materials Science, **119**, 100755.
[2] P. Verleysen (2018). *Shear Testing Using the Kolsky-Hopkinson Bar Machine,* in book: *Kolsky-Hopkinson Bar Machine: Selected Topics,* Springer, 75-120.
[3] L.W. Meyer, T. Halle (2011). *Shear strength and shear failure, overview of testing and behavior of ductile metals*. Mech. Time-Depend Mater, **15**, 327–340.
[4] Y. Guo, Y. Li (2012), *A Novel Approach to Testing the Dynamic Shear Response of Ti-6Al-4V*. Acta Mech. Solida Sin. 25, 299–311.

ASSESSMENT OF THE NON-NEWTONIAN LIQUID FILLED CELL POTENTIAL TO MITIGATE THE IMPACT FORCE

A.N. Rotariu[1], L.C. Matache[1], F. Bucur[1], F. Dîrloman[1,2], P. Turtoi[2], C. Enescu[2,3] and E. Trană[1]
[1] Military Technical Academy, Bucharest, Romania
[2] Politechnica University of Bucharest, Bucharest, Romania
[3] SC STIMPEXSA, Bucharest, Romania

1. Introduction

Anti-trauma pads based on the textile layers imbibed by non-Newtonian were recently studied through laboratory and ballistic tests [l, 2]. The attention paid to these combinations of materials is justified by the behavioral changes that occur in the flow of fluids in the conditions of high pressures caused by ballistic impact or shock waves. By using such pads cells, the maximum forces exerted on and the mechanical momentums transferred to the protected tissues are expected to decrease significantly. The present study reports experimental results obtained in impact tests in which cells made of thin polymer film with a core of 3D fabric filled with glycerin were used. For some tests the impact surface was spherical with a radius of 72.5 mm. The characteristic size of the spherical surface was established starting from the average width of the human male skull [4].

2. Experimental setup

A 60 mm caliber compressed air gun was used to accelerate the projectile. The triggermg of the projectile movement was controlled by means of a solenoid valve. By loading the air tank at different initial pressures the impact velocity of the projectile was also varied. The 0.76 kg aluminum projectile was fitted with a removable, flat/concave spherical head.

The samples were attached with an adhesive tape to a rigid body with a flat/convex spherical surface, in front of the barrel of the air gun. The rigid body mount was supported during the test on a 200C20 PCB force transducer. The movement of the transducer during the test was blocked by a massive target. A detail of the experimental configuration is shown in Figure l.

A PHOTRON high speed camera was used to determine the impact velocity at a shooting rate of 50 400 frames per second.

Fig. 1. Image with the projectile before impact on the cell attached to the curved surface

Two types of 3D fabrics with the same thickness were used for the core of the cells. In addition to the imbibed cell tests a series of dry cell tests and of free impact tests, without any damping cells, were performed.

3. Results

Based on the images obtained by the camera, both the impact velocity and the return velocity of the projectile were determined. The aim was to get three impact velocities: I - 6 m/s, II - 9 m/s, III - 12 m/s, which is why the measured impact velocities are grouped around these three values.

The data obtained with the force transducer were used to determine the maximum values recorded for each test. The figures below show by test categories the values of the maximum forces recorded depending on the impact velocity.
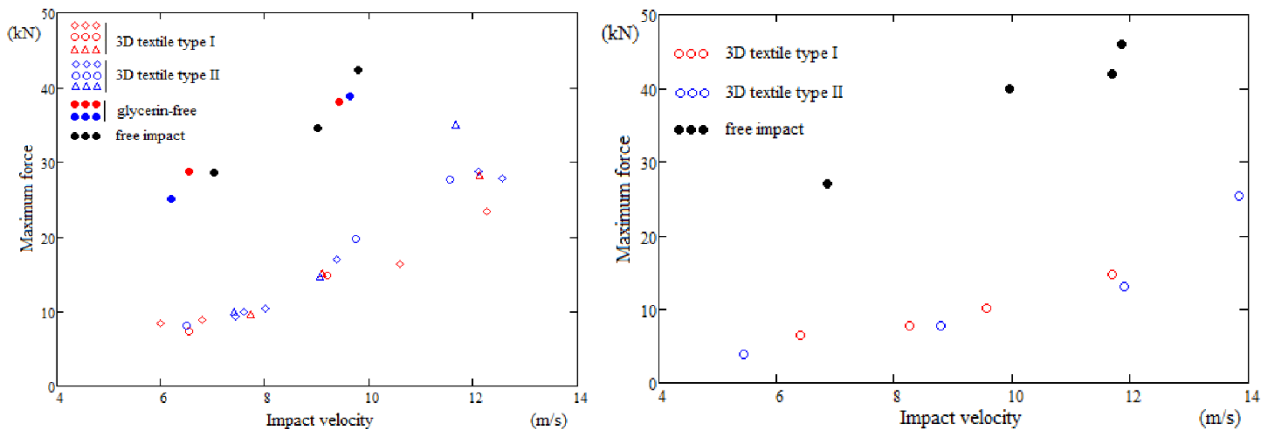
Fig. 2. Maximum values of forces depending on the impact velocity for the impact on the flat surface (left) and on the spherical surface (right)

4. Conclusions

Tests performed on dry, glycerin-free cells showed that 3D fabric only marginally contributes to shock attenuation through its deformation. Regarding the damping measured by comparison with the maximum values of the force at free impact, the presence of the imbibed cells at impact on the flat surface ensures a reduction of the maximum force by 70-50%, depending on the impact speed. There is also a reduction in efficiency of damping cells as the impact velocity increases. In the case of impact on the curved surface, the reduction of the maximum force is higher and less dependent on the velocity, the max. forces being in the range of 25-35% of the values obtained at free impact.

5. References

[1] D. Pacek, P. Zochowski and A. Wisniewski (2016). *Anti-trauma pads based on non-Newtonian materials for flexible bulletproof inserts*, 29th International Symposium on Ballistics, Edinburgh, Scotland, UK, May 9-13.

[2] P. Turtoi, M. Pascovici, T. Cicone, A. Rotariu, C. Puică, M. Istrate (2018). *Experimental proof of squeeze damping capacity of imbibed soft porous layers subjected to impact, IOP Conference Series: Materials Science and Engineering*, **444**(2), 022010.

[3] H. Li, J. Ruan, Z. Xie, H. wang, W. Lill (2007). Investigation of the critical geometric characteristics of living human skulls utilising medical image analysis techniques, *Int. J. Veh. Saf.*, **2**, 345-367.

6. Acknowledgments

ASSESMENT OF A NEW THERMOMARIC-EFP TANDEM CHARGE CONCEPT

L.C. Matache, A.N. Rotariu, E. Trană, M. Ungureanu, F. Dîrloman and F.I. Pană
Military Technical Academy "Ferdinand I", Bucharest, Romania

1. Introduction

Tandem charge it is a concept of two or many explosives charges that detonate in a controlled manner in order to enhanced the destructive effect. Usually tandem ammunition are designated to fight against reactive armour, but can fight also against non-explosive reactive armour as well.

Starting from this type of dual charge, we propose in this paper an assessment of a new tandem charge concept formed of two stages: explosively formed projectile and thermobaric.

Generaly, the thermobaric explosives (TBX) and enhanced blast explosives (EBX) are defined and categorized as liquid and solid mixtures, and advanced compositions including layer charges. In this concept thermobaric explosive (TBX) consists of a central charge (called the core), which is a high explosive, and an external secondary charge (fuel-rich formulation) [1]. Shock wave produced by thermobaric charge detonation has a longer positive phase and a bigger magnitude of impulse than a classical condensed explosive, even the maximum peek pressure is lower, as you can see in Figure 1.
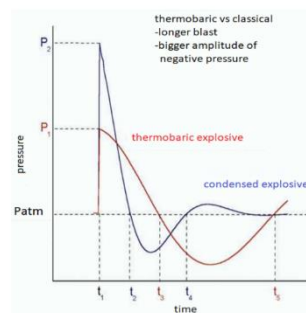
Fig. 1. Comparation between thermobaric and condensed explosives [2]

2. EFP/TB tandem charge concept

In order to assess the concept proposed we designed and manufactured a test configuration of EFP/TB charge concept, as you can see in Figure 2.

Fig. 2. EFP/TB Tandem charge test configuration

For the thermobaric charge we synthesized a high blast explosive composition, with low sensitivity, based on RDX explosive, Al, Mg and polyurethane.

3. Experimental setup

In order to evaluate the EFP/TB effect, tandem charge configuration was subjected to dynamic test conditions by firing it in to a 10 mm steel plate, disposed at 50 m distance from the weapon. Impact between tandem charge and target was recorded using Photron SA-Z high speed camera at 60.0000 fps.

4. Results and conclusions

Successive aspects of the phenomenon are presented in Figure 3. In can be observed the EFP first stage functioning in the left and in the right the detonation of thermobaric charge.

Fig. 3. Impact between tandem charge and target steel plate

The effect on target steel plate and on the concrete test building can be observed in Figure 4.

Figure 4. The effect on 10 mm target steel plate and on the concrete test building.

In conclusion, to assess a new of EFP/TB tandem charge concept an experimental configuration was subjected to a dynamic test by firing on a 10 mm steel plate disposed on the concrete test building. After experimental firing the two stages of the tandem charges were noticed using high speed camera and the EFP effect by observing and measuring the steel plate.

5. References

[1] M.-I. Ungureanu, L.-C. Matache, T. Rotariu, Cristian Barbu, F.-M. Dîrloman (2021), High blast explosive composition for annular thermobaric ammunitions, *UPB Scientific Bulletin, Series B: Chemistry and Materials Science* **83,** 3, 263-272.
[2] O.- G. Iorga, M. Munteanu, T.-V. Țigănescu, G. Epure (2018), Experimental and theoretical aspects regarding design and testing of thermobaric munitions for recoilless armament systems, *International Conference KNOWLEDGE-BASED ORGANIZATION,* **XXIV**, 3, 107-117.

6. Acknowledgments

SUITABILITY OF DIGITAL IMAGE CORRELATION FOR FATIGUE DAMAGE DEVELOPMENT MONITORING IN X10CrMoVNb9-1 POWER ENGINEERING STEEL

A. Brodecki, M. Kopec and Z.L. Kowalewski
Institute of Fundamental Technological Research, Warsaw, Poland

1. Introduction

Material behaviour under various loading types could be successfully determined by using different measurement techniques. The most conventional method includes extensometer recordings during both, static and fatigue tests for subsequent strain component measurements. Such methodology enables continuous recording of strain changes in a particular direction defined at the beginning of mechanical test. Moreover, the extensometers can only monitor a displacement on the limited strain gauge, and more importantly, give only an average values of it. This is a serious limitation of the technique, particularly in the case of fatigue investigations. Although fatigue phenomenon has been investigated by many research centres for more than two ages, there are still a lot of difficulties in the prediction of crack initiation under cyclic loading, especially under multiaxial stress conditions. It is well known that the process of fatigue damage development and structural degradation is of local nature, and as a consequence, an application of the above-mentioned conventional extensometers for strain measurements cannot reflect strain distribution along the gauge length of the specimen tested and the indication of the crack initiation location within the gauge length is practically impossible using the conventional extensometers. Such a problem may be effectively solved by the application of DIC full-field optical method. DIC is a stereoscopic technique in which two CCD cameras, light sources and computational software are used. A mathematical theory of DIC was presented by Chu et al. [1]. In this method, a specimen needs to be covered with a special pattern (black dots on a bright background) [1, 2]. Such pattern defines the x and z coordinates which are further used to run the test under strain control. The origins of rectangular- or square-shaped pattern are directly applied to calculate the displacement/strain. The results obtained are presented in the form of full-field strain distribution maps [2]. The DIC method is mainly used for static measurements in which tensile and compressive behaviour [3], fracture toughness [4] and the geometrical imperfection effects on mechanical response [2] are investigated in detail.

2. Results and discussion

To assess an applicability of the DIC methodology, fatigue tests were performed up to the specimen fracture under stress amplitude equal to 500 MPa. As it is shown in Fig. 1a, DIC technique enabled an identification of the strain accumulation area, being a potential location of possible damage initiation, after just a single cycle (Fig. 1a). A subsequent fatigue process up to 100 000 cycles enabled to clearly indicate an area of the potential crack initiation (Fig. 1b). Further loading cycles evidenced its development (Fig. 1c, d) up to the specimen fracture. The effectiveness of DIC method was confirmed by additional tests carried out for the stress amplitude equal to 600 MPa, 630 MPa and 640 MPa. For each experiment, the area of potential crack initiation was precisely determined after selected initial number of fatigue cycles. As the final results of each of these tests shown, the specimens fractured exactly in the initially specified regions. It should be mentioned, however, that in order to clearly present a strain distribution the highest values of stress amplitude were required which enabled the strain scale unification.
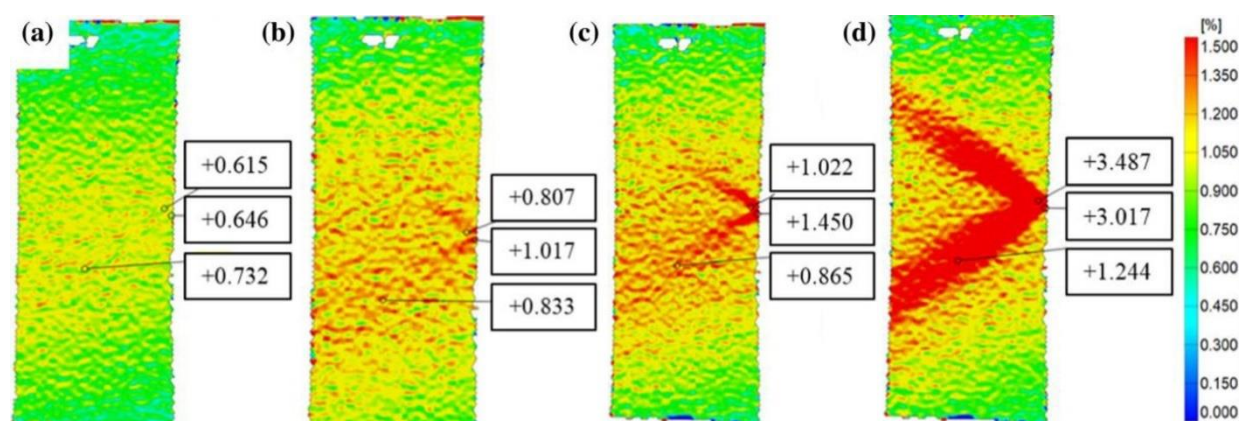
Fig. 1. DIC strain maps determined for the stress amplitude equal to 500 MPa with the unified scale after: 1 cycle (a); 100 000 cycles (b); 250 000 cycles (c); 301 251 cycles (d) [5]

3. Conclusions

In this research, steel specimens subjected to fatigue loadings in the range of stress amplitude from ± 400 to ± 640 MPa were monitored by DIC optical technique. A quality of the technique was assessed in terms of its effectiveness during fatigue damage development monitoring of P91 power engineering steel. It was found, that DIC enables an effective monitoring of the fatigue behaviour and accurate indication of an area of the potential failure at early stage of fatigue damage development.

Key Words: Fatigue development · Damage · P91 steel · Digital image correlation (DIC)

4. References

[1] T.C. Chu, W.F. Ranson, M.A. Sutton, W.H. Peters (1985). *Application of digital-image-correlation techniques to experimental mechanics*. Exp Mech. **25**, 232–244.

[2] J.D. Lord (2009). *Digital image correlation (DIC)*, 2nd ed. J. Eaton-Evans, J.M. Dulie-Barton, R.L. Burguete, Modern stress and strain analysis. A state of the art guideto measurement techniques. British Society for Strain Measurement, 14–15.

[3] J. Forster, A. Theobald, S. Engel, R. Pasmann (2012). *Using optical measuring system for identification of material parameters for finite element analysis*. In: 11. LS-DYNA, DYNAmore GmbH, Ulm, 1–9.

[4] E. Durif, J. Réthoré, A. Combescure, M. Fregonese, P. Chaudet (2012). *Controlling stress intensity factors during a fatigue crack propagation using digital image correlation and a load shedding procedure*. Exp. Mech. **52**, 1021–1031.

[5] M. Kopec, A. Brodecki, D. Kukla, Z.L. Kowalewski (2021), *Suitability of DIC and ESPI optical methods for monitoring fatigue damage development in X10CrMoVNb9-1 power engineering steel*, Archives Of Civil And Mechanical Engineering, **21**, 167.

PROBABILISTIC STUDY ON CRACKING EVOLUTION AND FRACTURE ENERGY CHANGE OF STEEL FIBER-REINFORCED CONCRETE

I. Pokorska[1,2], M. Poński[3], W. Kubissa[4], T. Libura[1], A. Brodecki[1] and Z.L. Kowalewski[1]
[1] *Institute of Fundamental Technological Research, Polish Academy of Sciences, Warsaw, Poland*
[2] *Częstochowa University of Technology, Faculty of Civil Engineering, Częstochowa, Poland*
[3] *Desigma Engineering (civil engineering company), Częstochowa, Poland*
[4] *Warsaw University of Technology, Faculty of Civil Engineering, Mechanics and Petrochemistry, Warsaw, Poland*

1. Introduction

The fracture mechanics defines concrete as a quasi-brittle material. Concrete cracking process is a common problem, because a period to the first micro-cracks may occur even before it is loaded. This is due to the loss of moisture from the concrete. The production method, admixtures, porosity, hardening conditions, maximum aggregate size, etc., as well as its inherent disadvantages are the main reasons that the process of cracks formation in concrete and their subsequent growth up to failure is complex. The use of fracture mechanics helps to better understand this process. The results of fracture energy (G_f) in the three-point bending test of steel-fiber reinforced high-strength concrete (SFRHSC) beams with notches and tensile strength (f_{ct}, f_l) were presented by Bywalski et al. [1]. They recorded two relationships, i.e. force-displacement (F- δ) and crack tip opening displacement (CTOD). On the basis of data captured, the parameters f_{ct}, f_l and G_f were estimated as a function of the fiber reinforcement coefficient.

On the other hand, the probabilistic fracture mechanics (PFM) is becoming more and more popular for realistic assessment of the fracture response and reliability of structures. However, the application of stochastic nonlinear computational mechanics to real world applications faces a major impediment as detailed information is lacking on the stochastic properties of the material parameters related to the problem. The process of the stochastic fracture-mechanical parameters determination is presented in [2] for C25/30 concrete together with stochastic models. The experimental procedure consisted of specimens compression, three-point bending tests of notched beams and splitting the wedges on the notched specimens. The inverse analyzes based on an artificial neural network were performed in order to identify material parameters. A quantitative influence of the freshly mixed concrete consistency on its mechanical cracking was determined. Moreover, the temporal development of fracture-mechanical parameters and their variability were investigated. Neha et al. [3] were used Two Parameter Weibull Distribution for the statistical analysis of the fracture energy of plain concrete and concrete reinforced by natural fibers. Weibull reliability curves show fracture energy at each reliability level. This enables the fracture energy to be selected for a given concrete mix in order to ensure reliability and a safety limit. This method can be applied in analyzing the scattered experimental results.

2. Materials and Methods

Concrete mixture of 380 kg/m³ cement by 0.44 w/c ratio was prepared. Fraction of river sand of 0 ‑ 2 mm and natural gravel fraction of 2 ‑ 8 mm were used. Aggregates were kept at laboratory air-dry condition. The sand point was established to be SP=37% and used 12% sand and 88% gravel what allowed for the aggregate grading curves fit between the boundary curves. Superplasticizer Atlas Duruflow PE-220 and VMA admixture Atlas Duruflow VM-500 were used according to

PN-EN 934-2. A regular tap water was applied as the mixing water. Steel fibers of 0.8 mm diameter and 40 mm length were used.

The specimens for the basic test were produced in horizontally placed molds with dimensions of 500x500x50 mm. Based on the experience presented in the works [4, 5], it was decided to form the specimens horizontally, which enables better compaction and homogeneity of the mixture than in the case of vertical forms. The specimens were formed and compacted in two layers. In order to minimize segregation of the mixture and the separation of milk on the upper surface, the F2 consistency was chosen. It enabled the correct concentration of simple-shaped specimens, and VMA application. The specimens of 500x200x50 mm were cut out of the boards 20 days after forming, approximately, using a laboratory saw, and a notch of 10 mm high and 4 mm wide was manufactured in the middle of the longest wall.

Specimens for the compressive strength and bending tensile strength determination (beams with dimensions 500x100x100 mm) were also produced. After taking them out of the molds, they were stored together with the boards/beams in the air-dry laboratory conditions t = 20°C ± 2°C, RH = 50% ± 10%. Tests were carried out after 134 days of their production. The compressive strength tests were conducted on 100 mm cubic specimens after either 28 or 134 days of hardening. The tests were carried out in accordance with PN-EN 12390-3 by using a ToniTechnik instrument of 3000 kN compression force capacity. The flexural strength tests were conducted on the beams with dimensions of 500x100x100 mm after 134 days of hardening. The tests were carried out in accordance with PN-EN 12390-5 by using a Matest instrument of 300 kN compression force capacity. The rate of loading was maintained at 0.5 MPa/s for compressive strength tests and at 0.05 MPa/s for tensile splitting strength tests.

3. Conclusions

The paper presents the results of analysis concerning an evolution of the fracture process developing in the fibro-concrete specimens subjected to several types of mechanical tests. The results elaborated in the form of probability distributions and force - CMOD curves enabled to check suitability of the stochastic constitutive models with special emphasis of taking into account the random nature of the parameters describing the material tested and the analysis of cross-correlation of these parameters.

4. References

[1] C. Bywalski, M. Kaźmierowski, M. Kamiński, M. Drzazga, (2020), Material Analysis of Steel Fibre Reinforced High-Strength Concrete in Terms of Flexural Behaviour. Experimental and Numerical Investigation, *Materials*, 13, (7), 163.

[2] T. Zimmermann, A. Strauss, D. Lehký, D. Novák, Z. Keršne, (2014), Stochastic fracture-mechanical characteristics of concrete based on experiments and inverse analysis, *Construction and Building Materials*, Volume 73, 30 December, 535-543.

[3] P. Neha Asrani, G. Murali, J. Arthika, K. Karthikeyan, M.K. Haridharan, (2019), Probabilistic Fracture Energy Assessment of Natural Fibre Reinforced Concrete by Two Parameter Weibull Distribution International, *Journal of Engineering & Technology*, 7 (3.12), 407-410.

[4] C.G. Hoover, Z. Bažant, J. Vorel, R. Wendner, M. Hubler, (2013), Comprehensive concrete fracture tests: Description and results. *Engineering Fracture Mechanics,* 114, 92, 103, doi:10.1016/j.engfracmech.2013.08.007.

[5] C.G. Hoover, Z. Bažant, (2013), Comprehensive concrete fracture tests: Size effects of Types 1 & 2, crack length effect and postpeak. *Engineering Fracture Mechanics* 110, 281-289, doi:10.1016/j.engfracmech.2013.08.008.

MEASURING DISPLACEMENTS AND STRAINS DURING FATIGUE TESTING OF 31 METER WIND TURBINE BLADE USING DIGITAL IMAGE CORRELATION WITH DISPERSED FIELDS

A. Styk[1], O. Sobiecki[1], S. Semenow[2], M. Jankowski[3] and M. Kujawińska[1]
[1] *Institute of Micromechanics and Photonics, Warsaw University of Technology, Warsaw, Poland*
[2] *Technical University of Denmark, Kongens Lyngby, Denmark*
[3] *Institute of Metrology and Biomedical Engineering, Warsaw University of Technology, Warsaw, Poland*

Renewable energy sources have become increasingly popular over the last decades as green energy trends grow in importance. The development strategy for offshore wind energy adopted by the European Union foresees increased capacity from the currently installed 12 GW to 300 GW in 2050. The plan places enormous demands on new wind turbine designs. The largest 14 MW turbine has a blade length of 108 meters. New solutions require developing modern measurement methods to cope with technical problems resulting from the increasing blades' size. Limitation of the total blade weight forces the design of lightweight structures with lower rigidity. The operation of blades with higher aeroelasticity fundamentally changes the entire rotor and the supporting structure dynamics. As a result, we observe many negative dynamic phenomena such as VIV - Vortex Induced Vibrations accelerating fatigue processes and, as a result, intensifying blade wear. Reliable identification of large blades' structural dynamics requires applying innovative experimental and measurement techniques to improve reliability and reduce operating and repair costs.

The work presents the preliminary results of 31m wind turbine blade (WTB) fatigue testing with different flap-wise loads and cycle counts. The investigated WTB had a specially introduced defect, a partial shear web debonding. One of the main aims of the investigations was to observe the debonding growth over the increasing number of fatigue cycles and loads from the outer side of the blade. For this purpose, the 3D Digital Image Correlation (3D DIC) was used. 3D DIC is an optical noncoherent technique that measures shape and displacements in the full 3D vector (u,v,w) and in-plane strains (εxx, εyy and εxy) mechanical structure subjected to an external force [1]. In the research, we used multi field of view approach, which required setting a few 3D DIC systems (6 systems altogether – four under the blade and two above the blade) and further calibrating them to the common coordinate system [2]. The proposed calibration required a specially designed calibration procedure using custom made calibration targets and a laser tracker. Figure 1 presents the stitching procedure concept and calibration target.
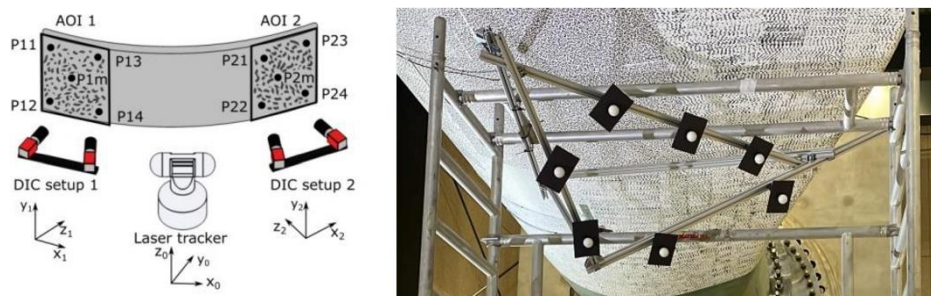
Fig. 1. Stitching concept (left) and used ball calibration target (right)

One hundred sixty-two data sets containing 100 stereo pair images were captured during the experiment. The data was captured asynchronously to the blade excitation frequency to assure the

scanning over the single period of motion with higher accuracy than provided by the camera FPS, as the used camera's frame rate was insufficient. That approach allowed us to evaluate the WTB single cycle motion after reshuffling the evaluated data on displacement and strains in every FOV.

The preliminary results of shape calculation for two FOVs and their merging into one larger FOV are presented in Figure 2. The further part of the work assumes the development of the techniques enabling coercion of non-overlapping FOVs.
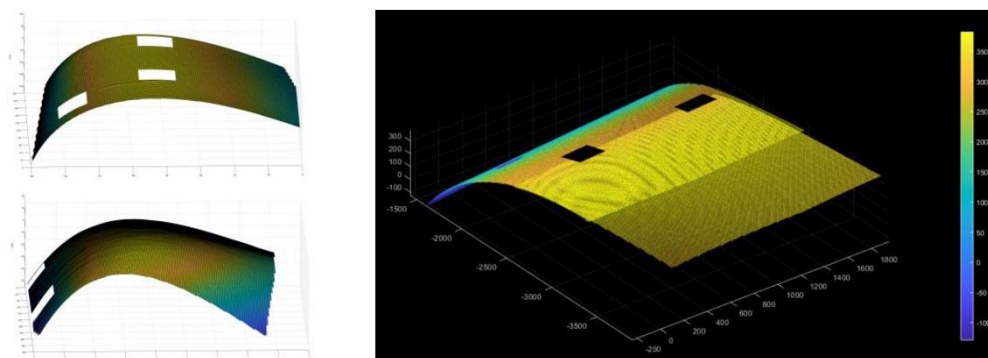
Fig. 2. Calculated shapes of two overlapping FOVs of an object (left) and the result of stitching operation (right)

The preliminary results of W displacement (along the Z-axis of the stereo system) captured in one of these two FOVs are presented in Figure 3.
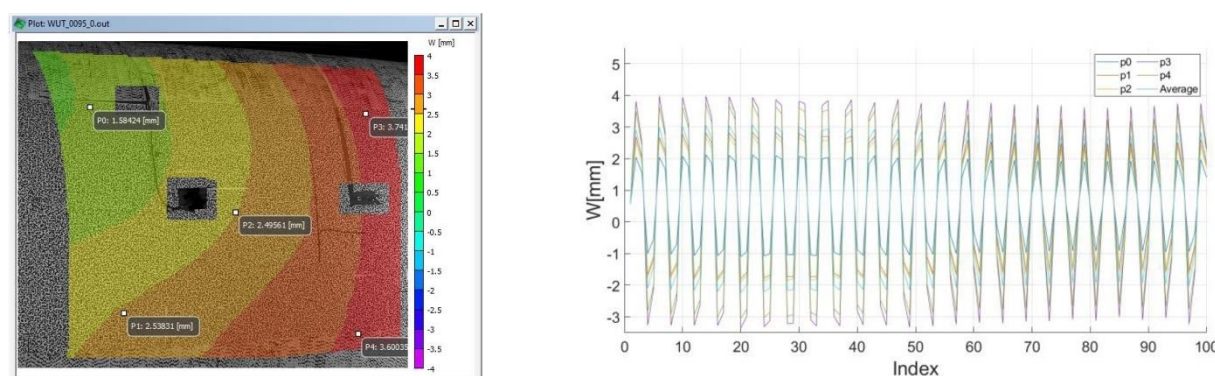
Fig. 3. The selected map of W displacement in one stereo DIC system (left) and the time plot of changes of W displacement in the selected points over 100 captured frames (right)

The proposed method obtained allows to refine the digital blade models, i.e., improve the opto-numerical feedback used in the hybrid structure design. It also potentially detects damages, such as cracks in the reinforcing baffle between the two blade surfaces (pressure and suction sides). It provides a starting point for continuing works toward early detection of damage within the blade, increasing its structural reliability. This type of testing predicts operating faults and minimises the risk of severe turbine damage and unplanned power outages.

References

[1] Sutton MA., Orteu JJ., Schreier HW., "Image Correlation for Shape, Motion and Deformation Measurements," Springer Science+Business Media, LLC 2009;
[2] Malowany, K., Malesa, M., Kowaluk, T., Kujawinska, M., "Multi-camera Digital Image Correlation method with distributed fields of view." Optics and Lasers in Engineering 98, 198-204 (2017).

AUTHORS INDEX

NOVEL NON-DESTRUCTIVE TESTING

STRESS ASSESSMENT IN STEELS

NNT designs and manufactures equipment for non-destructive, rapid diagnosis of the stress state in steels. We offer the **MagStress** family of equipment using the Barkhausen effect. We also provide services in the field of stress state measurements both with our equipment and other solutions.

MagStress5c - compact, hand-held device for determining uniaxial stress state

- unidirectional sensors
- possibility of autonomous operation
- basic tool for industrial and laboratory use

MagSress5d - powerful system for fast, complete 2D stress state analysis

- multi-directional sensors
- automatic calibration system option
- dedicated to advanced testing applications
- base for complex industrial systems

EXPERTISES, LABORATORY TESTS

We offer a non-standard and flexible approach to experimental laboratory testing not only in the field of stress measurement, but also in other areas, such as vibration testing, strength testing and others. Tests are carried out both in our laboratory and with our partners.

R&D PROJECTS WITH EU FINANCING

We assist in obtaining EU funding for R&D works (including preparation of application forms), we implement such projects and participate in them as subcontractors.

Visit our booth in the exhibition space!

MagStress5c

MagStress5d
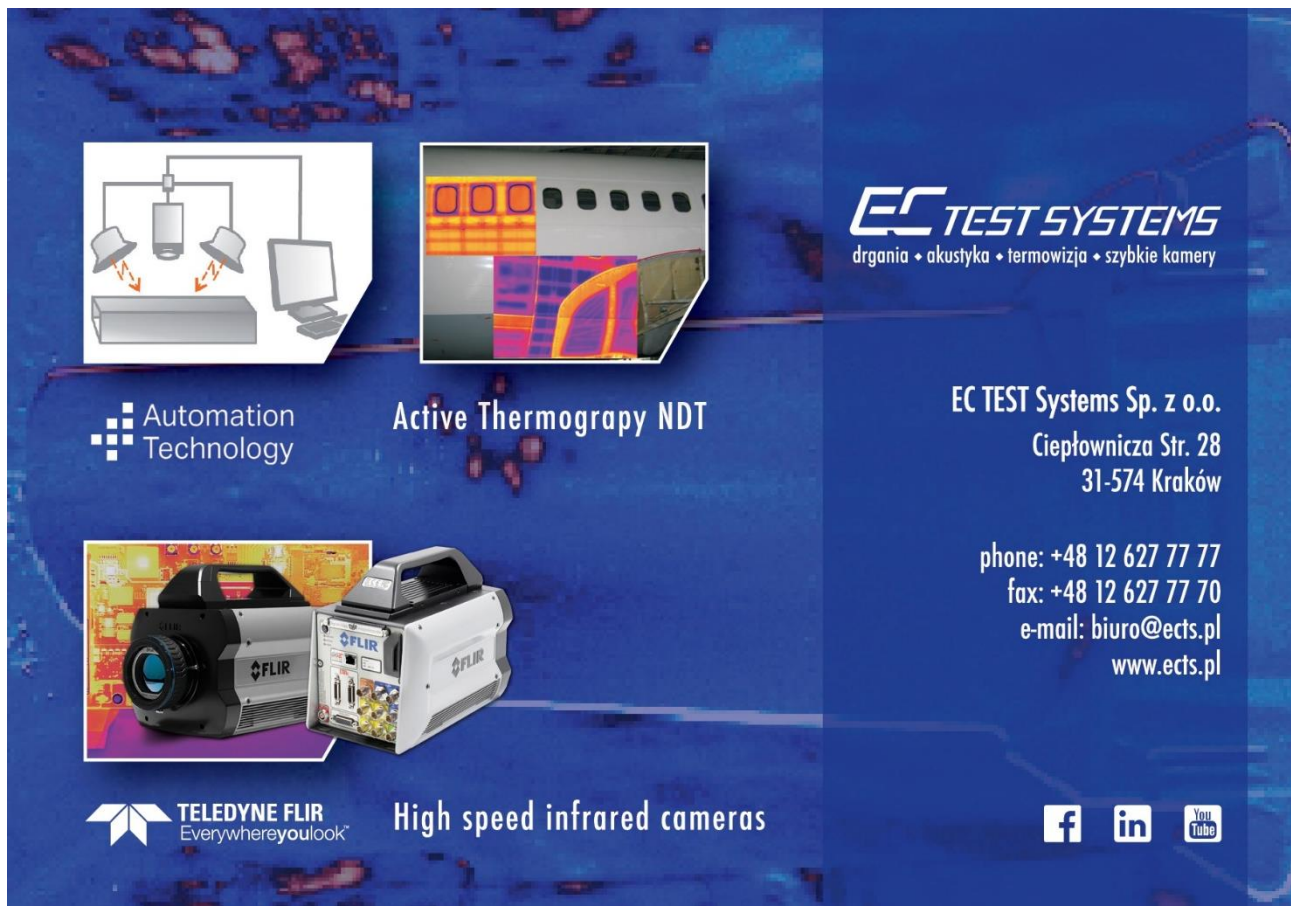
If you have any questions, please do not hesitate to contact us.
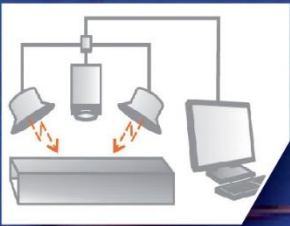
Adam Augustyniak
+48 502 060 080
adam.augustyniak@nntlab.com

NNTLAB.COM

Institute of Fundamental Technological Research (IPPT PAN), established in 1953, is the largest institute of the Polish Academy of Sciences in the field of engineering. The main mission of the Institute is to conduct high quality research in the areas which are the focus of the world's science and technology. The most important fields of the Institute's expertise include theoretical and applied mechanics, theory of coupled mechanical and physical fields, theoretical and experimental mechanics of materials and structures, and biomechanics.

Extensive research is conducted in the areas of nanoscience and nanotechnology, multicomponent and multifunctional materials, micro-, nano- and biomaterials, computational mechanics, computational materials science, computational intelligence, computational biology, bioinformatics, bioengineering, ultrasonic medical diagnostics and smart technologies. Advanced works of the Institute scientific staff are also closely connected with several branches of fundamental science and technology, such as: physics and thermodynamics of continua; fluid mechanics; laser beam interaction with metal surfaces, nano-photonics, applied mathematics and informatics.

IPPT PAN has maintained the highest scientific category A+, assigned during the last scientific evaluation, performed by the Ministry of Science and Higher Education.

Getting the highest category in the quality of research is the effect of the extensive experience, great scientific potential of our scientific staff and the Institute's high scientific activity in Poland and abroad, including spearheading consortia, projects, organizing scientific conferences, memberships of prestigious scientific committees and societies, and also running doctoral schools, exchanging scientists, creating patents and developing the modern scientific infrastructure. IPPT PAN scientific research is carried out in 8 independent research sectors:

- Department of Biosystems and Soft Matter
- Department of Experimental Mechanics
- Department of Intelligent Technologies
- Department of Information and Computational Science
- Department of Mechanics of Materials
- Department of Ultrasound
- Department of Theory of Continuous Media and Nanostructures
- Laboratory of Polymers and Biomaterials